61st International Conference for Students of Physics and Natural Sciences

Open Readings 2018

March 20-23, 2018

Vilnius, LITHUANIA

Programme and Abstracts

CONFERENCE CHAIRS

Edvinas Skliutas, *Faculty of Physics, Vilnius University & SPIE Chapter of Vilnius University*

ORGANIZING COMMITTEE

Sonata Adomavičiūtė, *Faculty of Physics, Vilnius University*
Bernadeta Balčiukynaitė, *Faculty of Physics, Vilnius University*
Vytautas Bubilaitis, *Faculty of Physics, Vilnius University*
Živilė Čerškutė, *Faculty of Physics, Vilnius University*
Gintarė Kuksėnaitė *Faculty of Physics, Vilnius University*
Mantas Kulnickas, *Faculty of Physics, Vilnius University*
Dovilė Lengvinaitė, *Department of General Physics and Spectroscopy, Faculty of Physics, Vilnius University*
Mažena Mackoit, *Center for Physical Sciences and Technology & EPS YM Vilnius*
Giedrius Pakalka, *Faculty of Physics, Vilnius University*
Edvinas Skliutas, *Faculty of Physics, Vilnius University & SPIE Chapter of Vilnius University*
Gabrielė Stanionytė, *Faculty of Physics, Vilnius University*
Jurgita Strakšytė, *Faculty of Physics, Vilnius University*
Matas Tartėnas, *Faculty of Physics, Vilnius University*
Laura Tauraitė, *Faculty of Physics, Vilnius University*
Raimis Urbonas, *Faculty of Physics, Vilnius University*

PROGRAMME COMMITTEE:

Kastytis Zubovas, *Fundamental Research Department, Center for Physical Sciences and Technology*
Andrius Gelžinis, *Department of Theoretical Physics, Faculty of Physics, Vilnius University*
Mangirdas Malinauskas, *Laser Research Center, Vilnius University*
Tomas Serevičius, *Institute of Photonics and Nanotechnology, Faculty of Physics, Vilnius University*
Ramūnas Aleksiejūnas, *Institute of Photonics and Nanotechnology, Faculty of Physics, Vilnius University*
Renata Butkutė, *Department of Optoelectronics*, *Center for Physical Sciences and Technology*
Audrius Gegeckas, *Institute of Biotechnology, Life Sciences Center, Vilnius University*
Rasa Pauliukaitė, *Department of NanoEngineering, Center for Physical Sciences and Technology*
Jevgenij Chmeliov, *Department of Theoretical Physics, Faculty of Physics, Vilnius University*
Justinas Čeponkus, *Department of General Physics and Spectroscopy, Faculty of Physics, Vilnius University*
Vilmantas Gėgžna, *Institute of Photonics and Nanotechnology, Vilnius University*

Conference programme

20 March, TUESDAY

09:00	**CONFERENCE OPENING**		
09:05	**Audrius Alkauskas,** Center for Physical Sciences and Technology, *Lithuania* **DEFECT IS A DEVICE**		
	ORAL SESSION O1		
10:00	Laima Busaite, Marcis Auzinsh, Andris Berzins, Ruvin Ferber, Florian Gahbauer, Reinis Lazda **LEVEL ANTI-CROSSING SIGNAL DEPENDENCE ON NITROGEN-VACANCY CENTRE'S ORIENTATION IN MAGNETIC FIELD**	O1-1	17
10:15	Monika Richter, Maciej Kozarzewski, Anna Gorczyca-Goraj, Maciej Maska **NEURAL NETWORKS AS A TOOL FOR IDENTIFICATION OF PHASES OF MATTER**	O1-2	18
10:30	Beata Zjawin, Piotr Ablewski, Kyle Beloy, Slawomir Bilicki, Marcin Bober, Roger Brown, Roman Ciurylo, Robert Fasano, Hidekazu Hachisu, Tetsuya Ido, Jerome Lodewyck, Andrew Ludlow, William McGrew, Piotr Morzynski, Daniele Nicolodi, Marco Schioppo, Mamoru Sekido, Rodolphe Le Targat, Piotr Wcisło, Peter Wolf, Xiaogang Zhang, Michał Zawada **SEARCHING FOR DARK-MATTER SIGNATURES WITHIN THE INTERCONTINENTAL OPTICAL ATOMIC CLOCK NETWORK**	O1-3	19
10:45	Miriam Kosik, Karolina Finc, Kamil Bonna, Włodzisław Duch, Simone Kühn **DIFFERENCES BETWEEN MODALITIES – FUNCTIONAL NETWORK REORGANIZATION DUE TO VISUOSPATIAL AND AUDITORY WORKING MEMORY TASK OF INCREASING DIFFICULTY**	O1-4	20
11:00	COFFEE BREAK		
	ORAL SESSION O2		
11:15	Matas Tartėnas, Kastytis Zubovas **MODELLING OF BLACK HOLE ACCRETION INDUCED BY DYNAMICAL PERTURBATIONS**	O2-1	21
11:30	Stanislav Komarov, Alexander Gorbatsievich, Alexander Tarasenko **REDSHIFT OF LIGHT FROM THE SOURCE IN BINARY SYSTEM THAT MOVES IN THE GRAVITATIONAL FIELD OF KERR BLACK HOLE**	O2-2	22
11:45	Aidas Sadauskas, Kastytis Zubovas **DETERMINING THE AGE OF FERMI BUBLES USING HYDRODYNAMIC SIMULATIONS**	O2-3	23
12:00	Simonas Draukšas, Thomas Gajdosik **AUTOMATIZING THE GRIMUS-NEUFELD MODEL**	O2-4	24
12:15	Monika Stangret **TRANSITING HOT JUPITERS**	O2-5	25
12:30	Anton Kuncinas, Per Osland **EXTENDED STANDARD MODEL HIGGS SECTOR: ANALYSIS OF THE S3-SYMMETRIC THREE-HIGGS-DOUBLET MODEL**	02-6	26
12:45	BREAK		
13:15-15:00	**POSTER SESSION P1**		
15:00	**Andrius Baltuška,** Vienna University of Technology, *Austria* **STRONG-FIELD PHYSICS WITHIN ONE OPTICAL CYCLE**		
16:00	COFFEE BREAK		
	ORAL SESSION O3		
16:15	Paulius Mackonis, Augustinas Petrulėnas, Aleksej M. Rodin **SCALABLE PUMPING SOURCE FOR TW-CLASS OPCPA BASED ON YB:YAG RODS WITH 1 PS 20 MJ OUTPUT PULSES AT 100 HZ**	O3-1	27
16:30	Vitalis Vosylius, Sergej Orlov **ANALYSIS OF PULSED VECTOR MATHIEU BEAMS WITH FEMTOSECOND DURATION**	O3-2	28
16:45	Karolis Adomavičius, Maksym Ivanov, Danas Buožius, Žilvinas Svirskas **SPATIAL EFFECTS INDUCED BY LASER–PREFORMED PLASMA ON THZ SIGNAL GENERATION IN AIR BY BICHROMATIC LASER PULSES**	O3-3	29
17:00	Rokas Stonys, Juozas Dudutis **FORMATION OF ASYMMETRICAL BESSEL-LIKE LASER BEAMS FOR GLASS PROCESSING**	O3-4	30
17:15	Gedvinas Nemickas, Titas Tičkūnas, Vytautas Purlys **FABRICATION OF MICROSTRUCTURES IN SAPPHIRE BY FS-LASER INDUCED SELECTIVE ETCHING**	O3-5	31
17:30	Rūta Pakalnytė, Simonas Varapnickas **DETERMINATION OF OPTIMAL SPATIAL RESOLUTION CONDITIONS TO PRODUCE PHASE MICRO-OPTICAL COMPONENTS USING THE SUSPENDED BAR STRUCTURE METHOD VIA 3D LASER LITHOGRAPHY**	O3-6	32
17:45	BREAK		
18:00	**WELCOME EVE**		

21 March, WEDNESDAY

09:00	**Roel Baets,** Ghent University, *Belgium* **SILICON PHOTONICS: FROM TRANSCEIVERS TO LIFE SCIENCES APPLICATIONS**		
	ORAL SESSION O4		
10:00	Rokas Jasiunas **FABRICATION AND INVESTIGATION OF LAMINATED SOLUTION-BASED NON-FULLERENE ORGANIC SOLAR CELLS**	O4-1	33
10:15	Andrius Žemaitis, Mantas Gaidys, Mindaugas Gedvilas **EFFICIENT ULTRASHORT PULSED LASER ABLATION FOR 3D ENGRAVING**	O4-2	34
10:30	Mindaugas Gicevicius, Arunas Ramanavicius **ELECTROCHEMICAL DEPOSITION OF CONDUCTING POLYMER POLYANILINE ONTO TEXTILE ELECTRODE**	O4-3	35
10:45	Egle Ezerskyte, Arturas Katelnikovas **UPCONVERSION LUMINESCENCE OF LU6(W,MO)O12:YB3+/ER3+ PHOSPHORS WITH RHOMBOHEDRAL AND CUBIC CRYSTAL STRUCTURE**	O4-4	36
11:00	COFFEE BREAK		
	ORAL SESSION O5		
11:15	Dominik Kreil, Michaela Haslhofer, Helga M. Böhm **COLLECTIVE MODES IN SNOM REFLECTIVITY OF DOPED GRAPHENE ON A SUBSTRATE**	O5-1	37
11:30	Mikhail Lobanok, Andrei Novikau, Stanislau Prakopyeu, Peter Gaiduk **EFFECT OF HYDROGEN PRE-TREATMENT ON SIC-ON-SI EPITAXIAL GROWTH**	O5-2	38
11:45	Sandra Stanionytė, Vaidas Pačebutas, Bronislovas Čechavičius, Andrius Bičiūnas, Virginijus Bukauskas, Andrejus Geižutis, Arūnas Krotkus **INFLUENCE OF THERMAL ANNEALING ON THICK GAINASBI LAYERS**	O5-3	39
12:00	Martynas Skapas, Renatra Butkutė, Sandra Stanionytė, Evelina Pozingytė **HRTEM STUDY OF SIZE-CONTROLLED BI QUANTUM DOTS IN ANNEALED GAASBI/ALAS MQW STRUCTURE**	O5-4	40
12:15	Leigh Weston, Darshana Wickramaratne, Mažena Mackoit, Audrius Alkauskas, Chris G. Van de Walle **NATIVE POINT DEFECTS IN HEXAGONAL BORON NITRIDE**	O5-5	41
12:45	BREAK		
13:15-15:00	**POSTER SESSION P2**		
15:00	**Peter Uhd Jepsen,** Technical University of Denmark **THE (ULTRA)FAST-MOVING WORLD OF TERAHERTZ TECHNOLOGY**		
16:00	COFFEE BREAK		
	ORAL SESSION O6		
16:15	Andrius Vaitkunas, Michael Feiginov **TOWARDS SUB-THZ RESONANT-TUNNELLING-DIODE OSCILLATORS WITH HIGH EMISSION EFFICIENCY**	O6-1	42
16:30	D. Čibiraitė, M. Bauer, A. Rämer, S. Chevtchenko, A. Lisauskas, V. Krozer, W. Heinrich, and H. G. Roskos **ALGAN/GAN HEMT-BASED THZ DETECTORS FOR A HIGH-RESOLUTION THZ CAMERA**	O6-2	43
16:45	Ieva Beleckaitė, Lukas Burakauskas, Ramūnas Adomavičius **INVESTIGATION OF A P-TYPE INAS USING A NOVEL MODIFIED DOUBLE-PUMP-PULSE TERAHERTZ EMISSION METHOD**	O6-3	44
17:00	Domantas Berenis, Dovydas Banevičius, Edvinas Radiunas, Karolis Kazlauskas, Saulius Juršėnas **PHENANTHROIMIDAZOLE HOSTS FOR RED OLEDS EXHIBITING THERMALLY ACTIVATED DELAYED FLUORESCENCE**	O6-4	45
17:15	Tomas Steponavičius, Augustas Vaitkevičius, Gintautas Tamulaitis, Mikhail Korjik, Etiennette Auffray. **INFLUENCE OF TETRAVALENT CERIUM ON THE LUMINESCENCE PROPERTIES OF GARNET-TYPE SCINTILLATORS**	O6-5	46

22 March, THURSDAY

09:00	**Julija Krupič,** University College London, *UK* **INTERNAL GPS: HOW DO WE PERCEIVE SPACE**		
	ORAL SESSION O7		
10:00	Tadas Penkauskas, Marija Jankunec, Gintaras Valincius **TETHERED BILAYER LIPID MEMBRANES FOR PICOMOLAR DETECTION OF PORE-FORMING TOXINS**	O7-1	47
10:15	Marijonas Tutkus, Giedrė Karzaitė, Šarūnė Ivanovaitė, Danielis Rutkauskas, Danielis Rutkauskas **FLUORESCENCE MICROSCOPY STUDIES OF DNA AND DNA RESTRICTION ENZYMES INTERACTIONS AT THE SINGLE MOLECULE LEVEL**	O7-2	48
10:30	Mantas Žiaunys, Tomas Šneideris, Vytautas Smirnovas **UNDERSTANDING DIFFERENT PATHWAYS OF INSULIN AGGREGATION**	O7-3	49
10:45	Migle Kazlauskiene, Auguste Rimaite, Giedre Tamulaitiene, Gintautas Tamulaitis, Virginijus Siksnys **CSM6 - THE LATENT RIBONUCLEASE IN CYCLIC OLIGOADENYLATE SIGNALLING PATHWAY**	O7-4	50
11:00	COFFEE BREAK		
	ORAL SESSION O8		
11:15	Agata Gołębiewska, Jakub S. Otrębski, Przemysław P. Michalski, Tomasz K. Pietrzak **NANOCRYSTALLIZATION OF LITHIUM-BORATE GLASSES**	O8-1	51
11:30	Anastasiya Rysiavets, Andrey Panarin, Sergei Terekhov **DETECTION OF SILVER NANOPARTICLES BASED ON PORPHYRINE-INDUCED AGGREGATION**	O8-2	52
11:45	Uladzislau Humennik, Alexander S. Fedotov, Vadim Bayev **INFLUENCE OF COBALT NANOPARTICLES AT PARAMETERS OF WEAK LOCALIZATION IN BILAYER GRAPHENE**	O8-3	53
12:00	Vytautas Žalandauskas, Audrius Alkauskas **MODELLING OF POINT DEFECTS IN HEXAGONAL BORON NITRIDE USING FORCE FIELDS**	O8-4	54
12:15	Anna Matsukovich, Oleg Nalivaiko, Kirill Chizh, Sergey Gaponenko **AU/SI-GE AND AU/GE NANOSTRUCTURES FOR SURFACE-ENHANCED RAMAN SCATTERING**	O8-5	55
12:30	Viktorija Padolskytė, Darius Gailevičius, Simas Šakirzanovas, Subhashri Chatterjee, Linas Jonušauskas, Roaldas Gadonas, Kestutis Staliunas, Vygantas Mizeikis, Saulius Juodkazis, Mangirdas Malinauskas **STUDY OF THE ORGANIC-INORGANIC PHOTORESIST SZ2080 AND ITS PROPERTIES AFTER DIRECT LASER STRUCTURING AND HEAT-TREATMENT**	O8-6	56
12:45	BREAK		
13:15-15:00	**POSTER SESSION P3**		
15:00	**Richard B. Hoover**, NASA, *USA* **MICROFOSSILS AND BIOMOLECULES IN METEORITES**		
16:00	COFFEE BREAK		
	ORAL SESSION O9		
16:15	Toleikienė Monika, Žvirdauskienė Renata, Skaidrė Supronienė, Akelaitis Paulius, Žydrė Kadžiulienė **EFFECT OF ORGANIC PLANT-BASED FARMING TO SOIL MICROBIAL FUNCTIONAL DIVERSITY**	O9-1	57
16:30	Andrii Netreba, Yriy Kyiashko, Andrii Komarov **THE SENSITIVITY OF MR-IMAGING WEIGHTED BY THE SPINE DENSITY AND TEMPORAL RELAXATION CHARACTERISTICS IN ACCORDANCE TO THE GRADIENTS PARAMETERS**	O9-2	58
16:45	Rita Banciul, Kristina Daniūnaitė, Ieva Sadzevičienė, Sonata Jarmalaitė **APC GENE PROMOTER METHYLATION IN BREAST CANCER**	O9-3	59
17:00	Kristina Žukauskaitė, Kristina Daniūnaitė, Arnas Bakavičius, Sonata Jarmalaitė **ASSOCIATION BETWEEN PROMOTER METHYLATION OF TUMOR SUPPRESSOR GENES AND PROSTATE CANCER**	O9-4	60
17:15	Armina Morkeliūnė, Neringa Rasiukevičiūtė, Alma Valiuškaitė **ANTRACNOSE - RAPIDLY SPREADING STRAWBERRY DISEASE**	O9-5	61
17:30	Giedrė Skiauterytė, Aida Vitkevičienė, Rūta Navakauskienė **ASSESSMENT OF CELL DIFFERENTIATION AND GENE EXPRESSION IN APL PATIENT CELLS AND NB4 CELLS TREATED WITH 3-DEAZANEPLANOCIN A, BELINOSTAT AND RETINOIC ACID**	O9-6	62
17:45	BREAK		
18:00	**DISCUSSION**		

23 March, FRIDAY

09:00	**Andrea Alù,** University of Texas, *USA* **FROM CLOAKING TO ONE-WAY MIRRORS: THE FASCINATING PHYSICS OF METAMATERIALS**		
	ORAL SESSION O10		
10:00	Sonata Adomaviciute, Martynas Velicka, Valdas Sablinskas. **DETECTION OF ASPIRIN TRACES IN BLOOD BY SURFACE ENHANCED RAMAN SCATTERING**	O10-1	63
10:15	Jekaterina Borzova, Vitaly Kocherbitov, Justas Barauskas, Gediminas Niaura **MARKER BANDS OF LYSOZYME FOR HYDRATION STUDIES BY RAMAN SPECTROSCOPY. LIMITS OF NATIVE STRUCTURE REGAINING**	O10-2	64
10:30	Antanas Bukartas, Robert Finck, Jonas Wallin, Christopher Rääf **BAYESIAN BASED METHOD FOR MAPPING IONIZING RADIATION SOURCES – A FEASIBILITY TEST**	O10-3	65
10:45	Agnė Zdaniauskienė, Tatjana Charkova, Ieva Matulaitienė, Olegas Eicher-Lorka, Algirdas Matijoška, Martynas Skapas, Algirdas Selskis, Gediminas Niaura **SHELL-ISOLATED NANOPARTICLE-ENHANCED RAMAN SPECTROSCOPY STUDY OF THE POSITIVE CHARGE BEARING MONOLAYER**	O10-4	66
11:00	COFFEE BREAK		
	ORAL SESSION O11		
11:15	Monika Skruodiene, Ramunas Skaudzius **TB3+ TO CR3+ ENERGY TRANSFER IN CO-DOPED Y3AL5O12 (YAG) HOST**	O11-1	67
11:30	Artsiom Antanovich, Anatol Prudnikau, Kirill Grzhegorzhevskii, Andrey Chuvilin, Mikhail Artemyev **SYNTHESIS AND PROPERTIES OF CORE-SHELL SEMICONDUCTOR AIIBVI HETERONANOPLATELETS WITH TUNABLE SHELL COMPOSITION AND MORPHOLOGY**	O11-2	68
11:45	Eglė Bukartė, Anja Haufe, Claudia Büchel, Donatas Zigmantas **TWO DIMENSIONAL SPECTROSCOPY OF CHLOROPHYLL-C** **WHERE DID ALL THE BEATINGS GO?**	O11-3	69
12:00	Sabina Brazevic, Gotard Burdzinski **ELECTRONIC AND VIBRATIONAL TRANSITIONS ANALYSIS IN 3H-NAPHTHOPYRANS - INSIGHTS FROM EXPERIMENT AND THEORY**	O11-4	70
12:15	Darya Meniailava, ?liaksandr Nikitsin, Anna Matsukovich, Maksim Shundalau **PREDICTION OF UV/VIS SPECTRA OF ORGANIC MOLECULES WITH CHARGE TRANSFER: MULTI-REFERENCE PERTURBATION THEORY VS. TIME-DEPENDENT DFT**	O11-5	71
12:30	Nikola Goleš **SIMULATING INTERACTIONS BETWEEN FLAMES AND ELECTRIC FIELDS BY APPLYING MODELS USED IN PLASMA PHYSICS**	O11-6	72
12:45	BREAK		
13:15-15:00	**POSTER SESSION P4**		
15:00	**Rasuolė Lukošė,** Center for Physical Sciences and Technology, *Lithuania* **MATERIALS FOR PULSED MAGNETIC FIELD SENSORS**		
19:00	**CONFERENCE PARTY and AWARD CEREMONY**		

List of poster presentations

20 March, TUESDAY

13:15-15:00 **POSTER SESSION P1**

WITHDRAWED Dzianis Marmysh MONTE-CARLO METHOD FOR CALCULATING DAMAGEABILITY	P1-01	73
Arkadiusz Bochniak REVERSE ENGINEERING FOR THE LORENTZIAN NONCOMMUTATIVE STANDARD MODEL OF PARTICLE PHYSICS	P1-02	74
Maciej Kościelski, Jan Chwedeńczuk QUANTUM METROLOGY AND THE LOCAL REALISM	P1-03	75
Piotr Gładysz, Karolina Słowik INTERACTION OF AN ASYMETRIC TWO-LEVEL QUANTUM SYSTEM WITH LIGHT	P1-04	76
Augustinas Povilas Fedaravičius, Kęstutis Pyragas OPTIMAL WAVEFORM FOR THE ENTRAINMENT OF A SPIKING NEURON WITH THE MINIMUM MEAN ABSOLUTE VALUE OF THE STIMULATING CURRENT	P1-05	77
Svajūnas Korsakas, Darius Abramavičius APPLICATION OF THE REDFIELD RELAXATION EQUATION FOR A TIME EVOLUTION OF A SIMPLE EXCITONIC SYSTEM	P1-06	78
Gabrielė Stankūnaitė THEORETICAL STUDY OF XE I HYPERFINE STRUCTURE	P1-07	79
Kasparas Kizlaitis, Mantas Šimėnas, Evaldas Tornau PLANAR SELF-ASSEMBLY OF TMA MOLECULES: ASYMMETRY OF MOLECULE IN A HEXAGONAL CAGE	P1-08	80
Ulada Vysotskaya, Irina Shapochkina BROWNIAN MOTORS CONTROLLED BY HARMONIC FLUCTUATIONS OF POTENTIAL ENERGY	P1-09	81
Fyodor Morozko, Andrey Novitsky OPERATOR APPROACH TO THE ELECTRODYNAMICS IN TIME-DEPENDENT LINEAR MEDIA	P1-10	82
Yuliya A. Kamysh, Irina V. Shapochkina STOCHASTIC PROCESSES WITH DETERMINISTIC DICHOTOMOUS CHANGES OF TRANSITION RATES AS A MATHEMATICAL MODEL OF A BROWNIAN FOTOMOTOR	P1-11	83
Augustinas Stepšys, Saulius Mickevičius, Darius Germanas, Ramutis Kazys Kalinauskas DIFFERENT TYPES OF CLUSTERIZATION OF SIX BODY SYSTEMS USING JACOBI COORDINATES	P1-12	84
Henrikas Vaickus, Jonas Reklaitis SIMULATION OF ELECTRON ENERGY SPECTRUM IN LASER PULSE GENERATED PLASMA	P1-13	85
Ivan Shershan, Tatiana Shishkina POLARIZATION EFFECTS FOR SINGLE GAUGE BOSON PRODUCTION IN LEPTON-PHOTON COLLISIONS	P1-14	86
Vytautas Dūdėnas, Thomas Gajdosik GAUGE PARAMETER DEPENDENCE OF THE NEUTRINO MASS RENORMALIZATION	P1-15	87
Carlos Viscasillas, Ehsan Moravveji, Andrés Moya Bedón ASTEROSEISMICS DIAGNOSTICS OF QUASI-ADIABATICITY OF THE CORE OVERSHOOTING REGIONS IN B-STARS	P1-16	88
Marijus Ambrozas, Andrius Juodagalvis DRELL-YAN PROCESS BACKGROUND ESTIMATION USING DATA-DRIVEN METHODS	P1-17	89
WITHDRAWED Uladzislava Yevarouskaya EVENT SELECTION AND BACKGROUND ESTIMATION FOR FORWARD-BACKWARD ASYMMETRY MEASUREMENT AT THE CMS DETECTOR AT THE LHC	P1-18	90
WITHDRAWED Michał Naskręt FEW WORDS ABOUT HYDRO SIMULATIONS IN HEAVY ION COLLISIONS	P1-19	91
Anna Abramowicz, Ryszard Chybiorz DYNAMIC CHANGES IN BURNING COAL-WASTE DUMPS IN THE UPPER SILESIAN COAL BASIN (POLAND)	P1-20	92
Paul Drozd KOHONEN'S NEURAL NETWORKS FOR CUSTOMER SEGMENTATION	P1-21	93
Laurynas Klimavičius THE IMPACT OF SPRING AIR TEMPERATURE ON VEGETATION CONDITIONS IN THE EASTERN PART OF THE BALTIC SEA REGION	P1-22	94
Antanas Vaitkus, Andrius Merkys, Yassine El Mendili, Saulius Gražulis THE USE OF INTERCONNECTED OPEN DATA FOR MATERIAL IDENTIFICATION	P1-23	95

Pavel Labatsevich POLARIZATION BISTABILITY IN VERTICAL CAVITY SURFACE-EMITTING LASERS	P1-49	121
Lukas Ramalis, Lina Grinevičiūtė, Rytis Buzelis and Tomas Tolenis INVESTIGATION OF POROUS ANISOTROPIC THIN FILMS FOR ZERO ANGLE POLARIZERS	P1-50	122
Domas Jokubauskis, Linas Minkevičius, Mindaugas Karaliūnas, Sergejus Orlovas, Gintaras Valušis BESSEL ZONE PLATE DESIGN FOR TERAHERTZ IMAGING	P1-51	123
Yaraslau Okrut, Yana Tsitavets ULTRASHORT LOW-ENERGY LASER HEATING WITH DONUT-SHAPED PULSES	P1-52	124
Adomas Gasperaitis, Viktorija Tamulienė INFLUENCE OF DISPERSION TERMS ON SINGLY RESONANT SYNCHRONOUSLY PUMPED OPTICAL PARAMETRIC OSCILLATOR: THEORETICAL INVESTIGATION	P1-53	125
Robertas Grigutis, Andrius Melninkaitis HOW TO PREDICT THE FUTURE OF OPTICS?	P1-54	126
Ernestas Nacius, Sergejus Orlovas, Alfonsas Juršėnas EXPERIMENTAL REALIZATION OF FOCAL LINE WITH CONTROLLED LONGITUDINAL INTENSITY PROFILE	P1-55	127
Justas Baltrukonis, Sergej Orlov, Pavel Gotovski EXPERIMENTAL IMPLEMENTATION OF THE FOCAL LINE ENGINEERING WITH WEBER BEAMS USING SPATIAL LIGHT MODULATOR	P1-56	128
WITHDRAWED Danas Buožius, Žilvinas Svirskas, Karolis Adomavičius, Maksym Ivanov RESEARCH ON LASER–PREFORMED PLASMA INDUCED EFFECTS ON THZ RADIATION GENERATION IN AIR BY BICHROMATIC LASER PULSES	P1-59	129
Greta Krivickaitė, Aidas Matijošius, Valerijus Smilgevičius, Maksym Ivanov PHASE AND POLARIZATION SINGULARITIES OF VECTOR VORTEX BEAM	P1-60	130
Artūras Grabusovas, Vitalis Vosylius, Sergej Orlov “OPTICAL KNIVES” – EXPERIMENTAL MATHIEU BEAM ENGINEERING USING SPATIAL LIGHT MODULATOR	P1-61	131
Kamilė Kasačiūnaitė, Antanas Urbas, Sergėjus Orlovas, Mindaugas Mikutis, Orestas Ulčinas. USING LASER INDUCED VOLUME MODIFICATIONS FOR CONROLLING CHEMICAL ETCHING OF THE GLASSES.	P1-62	132
Maksym Ivanov, Aidas Matijošius, Valerijus Smilgevičius OPTICAL PARAMETRIC AMPLIFICATION OF ELLIPTICALLY POLARIZED BEAMS AND SPATIAL DISTRIBUTION OF DEPLETED PUMP BEAM	P1-63	133
Mantas Gaidys, Andrius Žemaitis, Paulius Gečys, Mindaugas Gedvilas STUDY OF EFFICIENT COPPER LASER ABLATION	P1-64	134
Algirdas Jasinskas, Lina Grinevičiūtė, Tomas Tolenis INVESTIGATION OF SIO2 MIRRORS OPTICAL AND STRUCTURAL PROPERTIES AT HIGH DEPOSITION RATE	P1-65	135
Ivan Vatlin, Ulrich Pacher PASSIVELY Q-SWITCHED SUB-NANOSECOND IR LASERS IN CERAMIC MULTILAYERS DEPTH PROFILING BY LIBS METHOD	P1-66	136
Miglė Kuliešaitė, Julius Vengelis, Vygandas Jarutis MEASUREMENT OF PHOTONIC CRYSTAL FIBER DISPERSION BY MEANS OF SUPERCONTINUUM GENERATION AND CROSS-CORELLATION FREQUENCY- RESOLVED OPTICAL GATING	P1-67	137
Julius Skruibis, Kotryna Remeikaitė, Ona Balachninaitė A COMPARISON OF SINGLE AND MULTIPLE PULSE FEMTOSECOND LASER-INDUCED BREAKDOWN SPECTROSCOPY ANALYSIS	P1-68	138

21 March, WEDNESDAY

13:15-15:00 **POSTER SESSION P2**

Julija Grigorjevaite, Arturas Katelnikovas SYNTHESIS AND OPTICAL PROPERTIES OF K2BI(PO4)(MOO4):PR3+ PHOSPHORS FOR SECURITY PIGMENT APPLICATIONS	P2-01	139
Indrė Mackevičiūtė, Arturas Katelnikovas SYNTHESIS AND CHARACTERIZATION OF NOVEL LUMINESCENT SECURITY PIGMENTS BASED ON GDBSB2O8 HOST	P2-02	140
Lukas Osipovič, Mantas Šimėnas, Marius Burkanas, Jonas Venius, Jūras Banys EPR PROBING OF IRRADIATED DIMETHYLAMMONIUM ZINC FORMATE [(CH3)2NH2][ZN(HCOO)3] HYBRID FRAMEWORK	P2-03	141
Marius Navickas, Mantas Šimėnas, Eva Gjuzi, Frank Hoffman, Michael Fröba, Jūras Banys EPR OF METAL-ORGANIC FRAMEWORKS CONTAINING RADICAL LINKERS AND COPPER PADDLE WHEEL UNITS	P2-04	142

Olena Litsis, Nataliia S. Kariaka, Tatiana Yu. Sliva, Yu.V. Kolomzarov, I.E. Minakova, Vladimir M. Amirkhanov
EUROPIUM COORDINATION COMPOUNDS BASED NANODIMENSION THIN FILMS FOR LIGHT-EMITTING DEVICES

22 March, THURSDAY

13:15-15:00 **POSTER SESSION P3**

Robertas Sičiovas, Nicola Tiso, Audrius Maruška CYCLODEXTRIN GLUCANOTRANSFERASE PRODUCTION BY ALKALIPHILIC BACTERIA ISOLATED FROM POTATO SOIL	P3-01	193
Egle Paskeviciute, Bernadeta Zudyte, Zivile Luksiene CHLOROPHYLLIN-BASED PHOTOSENSITIZATION FOR MICROBIAL CONTROL OF FOODS	P3-02	194
Egle Surkaite, Justina Vaicekauskaite, Jolita Ostrauskaite BIODEGRADATION OF CROSS-LINKED EPOXIDIZED LINSEED OIL-BASED POLYMERS AND THEIR COMPOSITES	P3-03	195
Veronika Lutsenko, Daria Grigorieva, Irina Gorudko, Alexey Sokolov DETECTION OF HYPOCHLOROUS ACID-PRODUCING ACTIVITY OF NEUTROPHILS IN RESPONSE TO PLANT LECTINS USING CELESTINE BLUE B	P3-04	196
Alena Kavalenka, Elizaveta Kavalenka, Alexandra Zayko REGULATION OF NEUTROPHIL ACTIVITY BY REACTIVE OXYGEN, NITROGEN AND CLORINE SPECIES	P3-05	197
Elizaveta Kavalenka, Artemiy Yushkevich, Alena Kavalenka ALTERATION OF FUNCTIONAL ACTIVITY OF HUMAN BLOOD NEUTROPHILS AFTER EXPOSURE TO CONSTANT ELECTRIC FIELD WITH STRENGTH UP TO 1 V/SM	P3-06	198
WITHDRAWED Maria Trawkina, Alexander Ivanchyk, Aliaksey Yantsevich ALTERATIONS IN RAT BRAIN MITOCHONDRIA PHOSPHOPROTEOME INDUCED BY PSYCHOEMOTIONAL STRESS	P3-07	199
Greta Musteikytė, Vytautas Smirnovas METHYLENE BLUE ACTS AS AMYLOID REMODELLING AGENT ON SUPEROXIDE DISMUTASE I AGGREGATION	P3-08	200
Dovilė Daunoraitė, Marius Gedgaudas, Aurelija Mickevičiūtė, Daumantas Matulis, Egidijus Kazlauskas CLONING, EXPRESSION AND PURIFICATION OF TOXOPLASMA GONDII HSP90 N DOMAIN	P3-09	201
Romuald Stanilko, Tomas Šneideris, Vytautas Smirnovas IMPACT OF ENVIRONMENTAL FACTORS ON INSULIN AGGREGATION KINETICS	P3-10	202
Tomas Šneideris, Vytautas Smirnovas EFFECT OF TEMPERATURE AND DENATURANT CONCENTRATION ON ELONGATION OF DISTINCT MOUSE PRION PROTEIN FIBRIL STRAINS	P3-11	203
Maria Terekhova, Anatoly Kokhan, Daria Grigorieva, Irina Gorudko, Semak Igor, Alexey Sokolov THE ASSOCIATION BETWEEN HALOGENATIVE STRESS-INDUCED LACTOFERRIN AND CALCIUM SIGNALING IN NEUTROPHILS	P3-12	204
Indre Aleknaviciene, Gintaras Valincius ANALYSIS OF ANCHOR MOLECULES FOR TETHERED BILAYER LIPID MEMBRANE FORMATION ON NOVEL SERS ACTIVE BIOSENSOR	P3-13	205
Vaida Paketurytė, Edita Čapkauskaitė, Asta Zubrienė, Daumantas Matulis BINDING AND INHIBITION OF CATALYTICALLY ACTIVE HUMAN CARBONIC ANHYDRASES BY THIAZOLE-SUBSTITUTED BENZENESULFONAMIDES	P3-14	206
Aistė Imbrasaitė, Dovilė Stravinskienė, Aurelija Žvirblienė. EPITOPE MAPPING OF MONOCLONAL ANTIBODIES AGAINST HUMAN CARBONIC ANHYDRASE XII	P3-15	207
Justinas Babinskas, Visvaldas Kairys, Inga Matijošytė AB INITIO METHOD APPLICATION FOR ANALYSIS OF ELECTRON AND PROTON TRANSFER AT LACCASE T1 CU SITE	P3-16	208
Viktorija Zaranko, Marija Jankunec THE EFFECT OF HYDRATION ON NANOMECHANICAL RESPONSE OF PORCINE SKIN	P3-17	209
Yuliya Kunitskaya, Tatiana Kochetkova, Elizaveta Kavalenka, Elena Golubewa, Pavel Bulai DIRECTION OF CELL GROWTH UNDER LONG-TERM ELECTRICAL STIMULATION	P3-18	210
Irmantas Mogila, Brighton Samatanga, Ralf Seidel, Gintautas Tamulaitis, Virginijus Siksnys TEMPORAL REGULATION OF TYPE III CRISPR-CAS EFFECTOR COMPLEX ACTIVITY	P3-19	211
Mantas Dūdėnas, Žydrūnas Stanius, Vilma Kaškonienė, Tomas Drevinskas, Audrius Sigitas Maruška, Ona Ragažinskienė, Kęstutis Obelevičius QUENCHER PROCEDURE FOR ANALYSIS OF BIOLOGICALLY ACTIVE COMPOUNDS OF HOP (HUMULUS LUPULUS L.) LEAVES AND CONES	P3-20	212
Elžbieta Kulicka, Tomas Šneideris, Vytautas Smirnovas POLYMORPHISM OF MOUSE PRION PROTEIN	P3-21	213
Domantas Armonavičius, Audrius Maruška, Vilma Kaškonienė, Rūta Mickienė IDENTIFICATION AND EVALUATION OF ANTIBACTERIAL AGENTS PRODUCED BY MICROORGANISMS IN LOCAL RAW MATERIALS	P3-22	214

Mindaugas Juodenas, Adrien Chauvin, Domantas Peckus, Tomas Tamulevicius, Abdel-Aziz El Mel, Pierre-Yves Tessier, Sigitas Tamulevicius POLARIZATION DEPENDANT ULTRAFAST PLASMON RELAXATION DYNAMICS IN GOLD NANOWIRES	P3-47	239
WITHDRAWED	P3-48	240
Nadia Khinevich, Sergey Zavatski, Hanna Bandarenka, Asta Tamuleviciene, Sigitas Tamulevicius, Iuliia Mukha SERS AND FLUORESCENCE-BASED ULTRASENSITIVE DETECTION OF ORGANIC DYE USING COMBINATION OF GOLD COLLOID AND SILVERED POROUS SILICON		
Rokas Vargalis, Dovile Baziulyte-Paulaviciene, Simas Sakirzanovas SYNTHESIS OF NAGDF4:YB3+,ER3+@NAGDF4 UPCONVERTING NANOPARTICLES AND CHARACTERIZATION OF OPTICAL PROPERTIES	P3-49	241
Piotr Pasza Storożenko IMPACT OF PRESYTHESIS ON ELECTRICAL AND STRUCTURAL PROPERTIES OF SAMPLES WITH COMPOSITION LIFE0.85V0.10PO4 NANOCRYSTALISED FROM GLASSY PHASE.	P3-50	242
Andrii Netreba, Yriy Kyiashko, Andrii Komarov RECONSTRUCTION OF THE MR-IMAGES BY PARTIALLY INTERPOLATED SIGNAL DATA	P3-51	243
Algirdas Grybauskas, Saulius Gražulis MODELLING THE SIDE-CHAINS OF AMINO ACIDS USING ROBOTICS-INSPIRED METHODS	P3-52	244
Nerijus Karlonas DEVELOPMENT AND VALIDATION OF MIXED-MODE SOLID PHASE EXTRACTION METHOD FOR THE DETERMINATION OF MEDICINE DRUGS IN BIOLOGICAL MATRICES	P3-53	245
Tomas Kairys, Artautas Mackevičius ANALYSIS OF VALUE OF C REACTIVE PROTEIN IN COMPARISON TO BISAP SCORE IN PREDICTING THE SEVERITY OF NEWLY PRESENT ACUTE PANCREATITIS	P3-54	246
Dovilė Čepukoit, Aurelija Putramentaitė, Daiva Burokienė MICROBIAL DIVERSITY OF INVASIVE FABACEAE PLANTS	P3-55	247
Migle Kalvaityte, Egidijus Simoliunas, Milda Alksne, Virginija Bukelskiene THE IMPACT OF 3D PRINTED PLA SCAFFOLDS MICROSTRUCTURIZATION ON RAT'S DPSC OSTEOGENIC DIFFERENTIATION	P3-56	248
Iveta Mikalajūnaitė ACCUMULATION OF CHEMOTHERAPEUTIC AGENTS IN 3D SPHEROID CELL CULTURES	P3-57	249
Sandra Saunoriūtė, Ona Ragažinskienė, Audrius Sigitas Maruška, Erika Šeinauskienė GERANIUM ROBERTIANUM L. INTRODUCTION, BIOLOGICALLY ACTIVE COMPOUNDS IN OVERGROUND	P3-58	250
Dalia Smalakyte, Thomas Fricke, Michal Pastor, Agnieszka Kolano, Gintautas Tamulaitis, Virginijus Siksnys, Matthias Bochtler TARGETED RNA KNOCKDOWN BY TYPE III-A CRISPR-CAS EFFECTOR COMPLEX IN ZEBRAFISH	P3-59	251
Rūta Maleckaitė, Kristina Daniūnaitė, Sonata Jarmalaitė DNA METHYLATION ANALYSIS OF METALLOTHIONEIN CODING GENES IN RENAL AND PROSTATE TUMORS	P3-60	252
Ieva Sadzevičienė, Kristina Daniūnaitė, Rasa Sabaliauskaitė, Valerijus Ostapenko, Sonata Jarmalaitė TP53 MUTATION ANALYSIS IN THE ETIOLOGY OF BREAST CANCER	P3-61	253
Deimante Simanaviciute, Ramune Rutkaite, Rima Klimaviciute, Valdas Jakstas, Liudas Ivanauskas INVESTIGATION OF INTERACTIONS BETWEEN CHITOSAN AND CAFFEOYLQUINIC ACID DERIVATIVES OF ARTICHOKE EXTRACT	P3-62	254
Vetra Markeviciute, Medeine-Silene Markeviciute, Pranas Serpytis DEMOGRAPHIC CHARACTERISTICS OF PATIENTS WITH PULMONARY EMBOLISM IN LITHUANIA	P3-63	255
Dovile Majauskyte, Egle Kontrimaviciute, Giedrius Volbekas BRACHIAL PLEXUS TRACK IN THE INTERSCALENE GAP: ANATOMICAL VARIATIONS AND THEIR CLINICAL SIGNIFICANCE	P3-64	256
Giedrė Grigalevičiūtė, Daiva Baltriukienė, Evaldas Balčiūnas, Linas Jonušauskas, Mangirdas Malinauskas FABRICATION OF FLEXIBLE MICROPOROUS 3D SCAFFOLDS VIA STEREOLITHOGRAPHY AND OPTIMIZATION OF THEIR BIOCOMPATIBILITY	P3-65	257
WITHDRAWED	P3-66	258
Arsenii Orlov, Tatiana Baikova, Sergey Gonchukov, Alexander Sundukov, Tatiana Svistunova DETECTION OF MENINGITIS BACTERIA IN THE SPINAL FLUID VIA RAMAN SPECTROSCOPY		
Julija Mažeikaitė, Viktorija Andrejevaitė ANXIETY DISORDERS AND LIPID METABOLISM MARKERS CORRELATION AMONG SMOKING MEN	P3-67	259

23 March, FRIDAY

13:15-15:00 **POSTER SESSION P4**

Raminta Mazėtytė, Urtė Bubnienė, Arūnas Ramanavičius, Renata Karpič SPECTROSCOPIC PROPERTIES AND ACTIVITY OF GLUCOSE OXIDASE	P4-01	260

23 March, FRIDAY

13:15-15:00 **POSTER SESSION P4**

LEVEL ANTI-CROSSING SIGNAL DEPENDENCE ON NITROGEN-VACANCY CENTRE'S ORIENTATION IN MAGNETIC FIELD

Laima Busaite, Marcis Auzinsh, Andris Berzins, Ruvin Ferber, Florian Gahbauer, Reinis Lazda

Laser Centre, University of Latvia, 19 Rainis Boulevard, Riga, Latvia, LV-1586
laima.busaite@lu.lv

Nitrogen-vacancy (NV) centers are powerful instruments in many areas of research, including quantum information, magnetometry and nanoscale sensing. They have been used to detect individual electron spins and spin ensembles, measure the magnetic field distributions in biological signals, measure temperature and electric fields [1].

NV centres are defects in diamond crystal consisting of paired nitrogen (N) and vacancy (V). The NV centre has a triplet ground state with a zero-field splitting between the $m_s = 0$ and $m_s = \pm 1$ ground state sublevels of 2.87 GHz. Due to nonradiative decay path from the excited state via singlet state that preferentially populates the $m_s = 0$ ground-state sublevel, the NV centre can be polarized optically, and the fluorescence from exciting $m_s = 0$ sublevel is more intense than the fluorescence from exciting the $m_s = \pm 1$ sublevels. In presence of microwave field population of $m_s = 0$ can be transferred to $m = \pm 1$ levels, decreasing the total detected fluorescence. However, if the magnetic field is applied along NV centre axis (which defines quantization axis in the system), the $m_s = \pm 1$ energies are shifted by $g_e \mu_B B_z$ or 2.8 MHz/G. At around 1025 G a crossing of sublevels $m_s = 0$ and $m_s = -1$ appear and due to nuclear spin interaction of ^{14}N

$$H = DS_z^2 + \gamma_e B \cdot S + S \cdot \overline{A} I + Q I_z^2 - \gamma_n B \cdot I, \tag{1}$$

the hyperfine states of $m_s = 0$ and $m_s = -1$ are mixed and anticrossing is formed (Fig.1 inset).

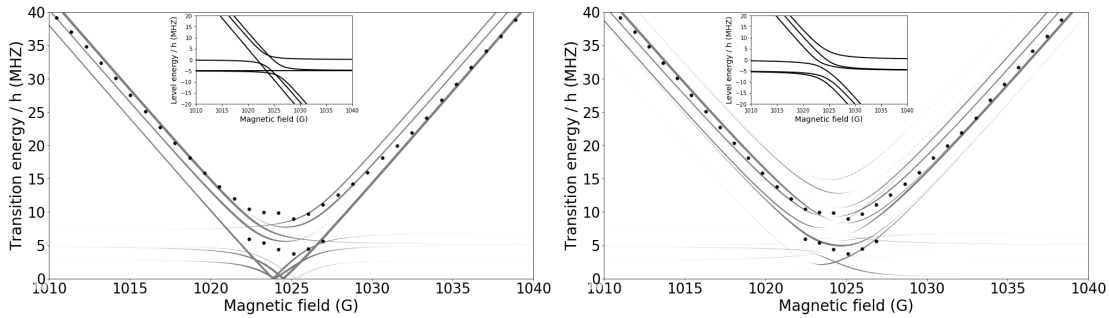

Fig. 1 Transition frequencies $m_s = 0 \rightarrow m_s = -1$ transition near anticrossing point. Transverse magnetic field $B_x = 0$ G (left) and $B_x = 1.85$ G (right).

At the point of the anticrossing the wave functions of the ground state $m_s = 0$ and $m_s = -1$ hyperfine sublevels are mixed, modifying the probabilities for magnetic-dipole transition of microwave field.

Adding additional magnetic field in transverse direction changes the ODMR signal significantly, due to mixing of all levels. For $m_s = 0 \rightarrow m_s = -1$ transitions (MW range 0 - 30 MHz) even small perturbation of NV center orientation (0.1°) changes transition frequencies considerably (Fig. 1 right).

This research was kindly supported by the M-ERA.NET project MyND no. Z/15/1366.

[1] L. Rondin et al., *Magnetometry with nitrogen-vacancy defects in diamond, Reports on Progress in Physics*, **77**, 056503 (2014), arXiv:1311.5214

[2] G. D. Fuchs et al., *A quantum memory intrinsic to single nitrogenvacancy centres in diamond* Nature Physics **7**, 789793 (2011)

Neural Networks As A Tool For Identification Of Phases Of Matter

Monika Richter, Maciej Kozarzewski, Anna Gorczyca–Goraj, Maciej M. Maśka

University of Silesia, Institute of Physics, Katowice, Poland
monika.richter@smcebi.edu.pl

In the last years machine learning has attracted, also among physicists, great attention. It turned out that the algorithms, while having vast applications in the decision–making (for example in games such as chess or AlphaGo), pattern recognition, medical diagnosis and finance, can be applicable also in the area of condensed matter physics.

The study of many–body systems is a challenging task, as the size of the Hilbert space and consequently the amount of data to analyze, grow exponentially with the size of the system. Therefore, such systems seem to be a perfect 'material' for machine learning algorithms, which are especially well suited to deal with big and complex sets of data. Such an approach has already been successfully used, e.g., for the Ising model. By analyzing Monte Carlo-generated samples, deep neural networks were able to identify with quite good precision the transition temperature [1].

However, a problem arises when one has to deal with non–conventional phase transitions, such as the Berezinsky–Kosterlitz–Thouless (BKT) transition occurring without an ordered phase or symmetry breaking. As a result, the difference between the high– and low–temperature phases is much more subtle than in the case of Ising–type models. Therefore, unambiguous identification of the critical temperature is much more difficult. The BKT transition transforms the system from bound vortex–antivortex pairs at low temperatures to unpaired vortices and anti–vortices above the critical temperature. Thus, it is topological in nature. It was demonstrated in Ref. [2] that it is difficult to determine the BKT phase transition in the classical XY model with the help of neural networks.

In our study, we demonstrate how one can overcome some of these difficulties. We test our approach on the classical XY model but also on its quantum version as well as on the phase–fermion model [3], where the BKT transition also occurs.

[1] J. Carasquilla, R. G. Melko, Machine learning phases of matter, Nature Physics **13**, 431 (2017).
[2] M. J. S. Beach, A. Golubeva, and R. G. Melko, Machine learning vortices at the Kosterlitz–Thouless transition, Phys. Rev. B **97**, 045207 (2017).
[3] M. M. Maśka and N. Trivedi, Temperature–driven BCS–BEC crossover in a coupled boson-fermion system, arXiv:1706.04197 (2017).

SEARCHING FOR DARK-MATTER SIGNATURES WITHIN THE INTERCONTINENTAL ATOMIC CLOCK NETWORK

Beata Zjawin[1], Piotr Ablewski[1], Kyle Beloy[2], Sławomir Bilicki[1,3], Marcin Bober[1], Roger Brown[2], Roman Ciuryło[1], Robert Fasano[2], Hidekazu Hachisu[4], Tetsuya Ido[4], Jérôme Lodewyck[2], Andrew Ludlow[2], William McGrew[2], Piotr Morzyński[1,4], Daniele Nicolodi[2], Marco Schioppo[2], Mamoru Sekido[4], Rodolphe Le Targat[3], Piotr Wcisło[1], Peter Wolf[3], Xiaogang Zhang[2] and Michał Zawada[1]

[1]Institute of Physics, Faculty of Physics, Astronomy and Informatics, Nicolaus Copernicus University, Grudziadzka 5, 87-100 Torun, Poland
[2]National Institute of Standards and Technology, 325 Broadway, Boulder, CO 80305, USA
[3]SYRTE, Observatoire de Paris, PSL Research University, CNRS, Sorbonne Universités, UPMC Univ. Paris 06, LNE, 61 avenue de l'Observatoire, 75014 Paris, France
[4]National Institute of Information and Communications Technology
4-2-1 Nukuikitamachi, Koganei, 184-8795 Tokyo, Japan
279076@fizyka.umk.pl

We present the data collected by the intercontinental atomic clock network. We show results of analysis of clocks readouts aimed on searches for dark-matter signatures.

Astrophysical observations indicate that the Universe contains five times more dark matter than standard matter, however its nature still remains an unsolved mystery. Dark matter candidates like topological defects and oscillating massive scalar fields can be searched for by a single optical atomic clock [1, 2]. Being the most precise scientific instrument, optical atomic clock makes great candidate for searches for physics beyond the standard model. Its two main components, ultra-stable optical cavity and cold atoms, have different susceptibilities to possible variations of the fine-structure constant, what makes an optical atomic clock sensitive to dark matter. This approach can be applied to many clocks, both distant and closely spaced, without the use of phase-noise compensated optical fibre links. It means that a global network can be established from currently operating optical atomic clocks since they are already collecting data needed for dark matter searches.

We describe the optical atomic clocks readouts analysis and provide a direct recipe for combining already existing optical atomic clocks to search for dark-matter signatures. Furthermore, we report new limits on both topological defects and oscillating massive scalar fields couplings to standard matter obtained from our transcontinental network. Our results exceed previously reported limits, showing that synchronization of the already existing optical atomic clocks is crucial for the future dark matter studies.

Fig. 1. Already existing optical atomic clocks that could potentially contribute to the network in the future.

[1] A. Arvanitaki, J. Huang, and K. Van Tilburg, "Searching for dilaton dark matter with atomic clocks", Phys. Rev. D, vol. 91, p. 015015, 2015.
[2] P. Wcisło, P. Morzyński, M. Bober, A. Cygan, D. Lisak, R. Ciuryło, and M. Zawada, "Experimental constraint on dark matter detection with optical atomic clocks", Nat. Astro., vol. 1, p. 0009, 2016.

DIFFERENCES BETWEEN MODALITIES – FUNCTIONAL NETWORK REORGANIZATION DUE TO VISUOSPATIAL AND AUDITORY WORKING MEMORY TASK OF INCREASING DIFFICULTY

Miriam Kosik[1,2], Karolina Finc[1], Kamil Bonna[1,2], Włodzisław Duch[1], Simone Kühn[3,4]

[1] Centre for Modern Interdisciplinary Technologies, Nicolaus Copernicus University, Toruń, Poland
[2] Institute of Physics, Faculty of Physics, Astronomy and Informatics, Nicolaus Copernicus University, Poland
[3] Center for Lifespan Psychology, Max Planck Institute for Human Development, Berlin, Germany
[4] University Medical Center Hamburg - Eppendorf, Hamburg, Germany
mkosik@doktorant.umk.pl

Several studies have shown that functional network reorganizes from more segregated to more integrated pattern when demands of a cognitive task increase. This pattern of network reorganization was found especially for working memory (*n*-back) task [1-3]. However, differences in network reorganization during a working memory task engaging different modalities and information processing were so far not investigated. Here, we compare how increasing cognitive demands of visuospatial and auditory n-back are reflected in the whole-brain functional network topology.

Forty-seven healthy subjects (aged 18-26) were examined using the functional magnetic resonance imaging (fMRI) technique during resting-state and while performing visuospatial and auditory working memory n-back tasks at increasing levels of difficulty (from 1-back to 2-back). FMRI data were pre-processed using a standard pipeline and denoised with aCompCor method [4]. We calculated correlation matrices for each participant, task type, and task condition (1-back, 2-back and resting-state) for 264 ROIs functional brain parcellation [5]. For connectivity analysis the Brain Connectivity Toolbox for MATLAB was used [6]. The comparison of strength of individual edges was examined with use of Network-Based Statistic method which is implemented in the NBS Toolbox [7].

We showed that the brain reorganizes itself while switching from the lower- to the higher-demand task. Both for auditory and for visuospatial tasks, the highest modularity occurred in the resting-state, and the modularity in 2-back was lower than in 1-back condition. However, the modularity during the 1-back auditory task was lower than in the visuospatial 1-back task. NBS analysis showed that for both auditory and visuospatial conditions the majority of weakened network edges consist of edges within the default mode network (DMN) and the largest group of edges in the strengthened network link DMN with other brain systems (Fig. 1).

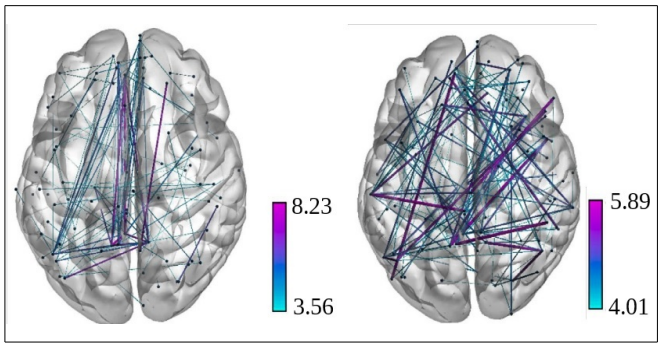

Fig. 1. Weakened (left, 1-back > 2-back) and strengthened (right, 2-back > 1-back) networks in terms of predefined brain systems while performing visuospatial tasks.

These results confirm the previous findings that the brain adapts to increasing cognitive demands and extend these conclusions for different modalities. Such outcomes can shed new light on the understanding of the differences between various working memory modalities.

This project is supported by the National Science Centre, Poland (2015/17/N/HS6/03549; 2017/24/T/HS6/00105).

[1] Braun, U., Schäfer, A., Walter, H., Erk, S., Romanczuk-Seiferth, N., Haddad, L., … Bassett, D. S (2015), *Dynamic reconfiguration of frontal brain networks during executive cognition in humans,* Proceedings of the National Academy of Sciences, 112(37), 11678–83.
[2] Finc, K., Bonna, K., Lewandowska, M., Wolak, T., Nikadon, J., Dreszer, J., Duch, W., Kühn, S. *Transition of the functional brain network related to increasing cognitive demands*. (2017), Human Brain Mapping 38 (7), 3659–74.
[3] Bassett, D. S., Wymbs, N. F., Porter, M. A., Mucha, P. J., Carlson, J. M., & Grafton, S. T. (2011), *Dynamic reconfiguration of human brain networks during learning*. Proceedings of the National Academy of Sciences, 108(18), 7641-46.
[4] Behzadi, Y., Restom, K., Liau, J., Liu, T. T. (2007), *A component based noise correction method (CompCor) for BOLD and perfusion based fMRI*. NeuroImage, 37(1), 90-101.
[5] Power J. D., Cohen A. L., Nelson S. M., Wig G. S., Barnes K. A., Church J. A., Vogel A. C., Laumann T. O., Miezin F. M., Schlaggar B. L., Petersen S. E. (2011), *Functional network organization of the human brain*. Neuron 72, 665–678
[6] Rubinov M, Sporns O (2010), *Complex network measures of brain connectivity: Uses and interpretations*., NeuroImage 52:1059-69.
[7] Zalesky A, Fornito A, Bullmore ET (2010), *Network-based statistic: Identifying differences in brain networks*. NeuroImage. 53(4):1197-1207.

MODELLING OF BLACK HOLE ACCRETION INDUCED BY DYNAMICAL PERTURBATIONS

Matas Tartėnas[1], Kastytis Zubovas[1,2]

[1]Faculty of Physics, Vilnius University, Lithuania
[2]Department of Fundamental Research, Center for Physical Sciences and Technology, Vilnius, Lithuania
matas.tartenas@gmail.com

Currently, the black hole at the center of the Milky Way is inactive, but there are reasons to believe it was not always so and there were at least two activity periods in the recent past [1]. The first of these, happening a few million years ago, could be responsible for the formation of the Fermi bubbles [2]. It is suggested that such an event could be initiated by a perturbation of the molecular gas ring that surrounds the black hole by an infalling molecular cloud.

We aim to reproduce this process with a hydrodinamical model. The model consists of three main components: central black hole ($M_{bh} \sim 4 \times 10^6 \mathrm{M}_\odot$), a ring of molecular gas ($R_{in} = 1.5$ pc, $R_{out} = 4$ pc) and a molecular cloud ($R_{cloud} = 1$ pc). The initial masses of both the ring and the cloud are chosen similar to the lower estimates of the mass of the circumnuclear ring ($M_\mathrm{r} \simeq M_\mathrm{cl} \sim 10^4 \mathrm{M}_\odot$). By varying the initial inclination angle (γ) of the orbit of the molecular cloud we change the outcome of the encounter, including the rate of black hole accretion and the morphology of resulting structures.

We find that the black hole accretion rate is dependent on the initial angle and reaches up to $\sim 0.8 \dot{M}_{Edd}$. Also the morphology of the system is affected by the change in γ - systems with initial angle $<= 60^\circ$ do not produce a central disk and more highly inclined initial orbits lead to a more compact and less massive resulting ring. Energy liberated during the nuclear activity period is equal to about 3% of the energy required for Fermi bubble formation with initial ring mass $\sim 10^4 \mathrm{M}_\odot$. The highest possible ring mass ($\sim 10^6 \mathrm{M}_\odot$), combined with an equivalent cloud mass, would produce the required energy.

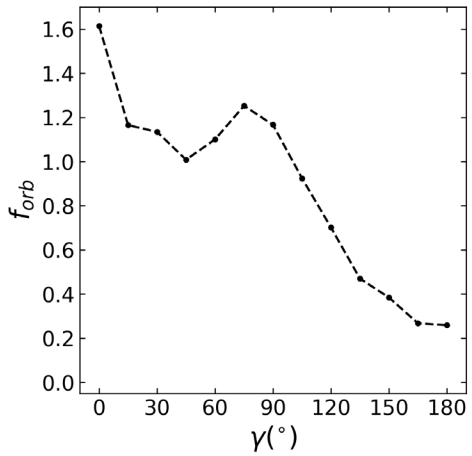

Fig. 1. The ratio of resultant and starting average circularization orbits after ~ 0.5 Myr

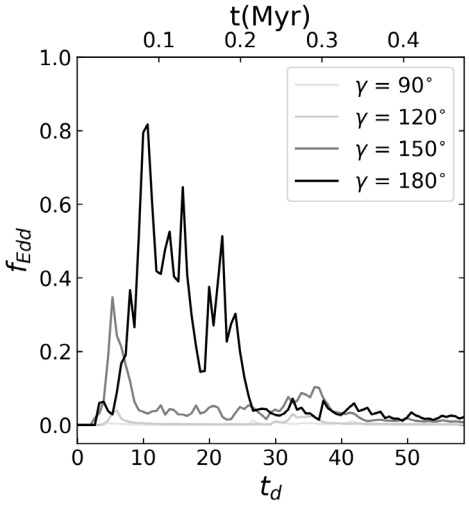

Fig. 2. The rate of accretion of the black hole in units of $\dot{M}_{Edd}$. Dynamical time t_d is at 1.5 pc.

[1] Ponti G., Morris M. R., Terrier R., Goldwurm A., 2013, in Rays Cosmic Rays in Star-forming Enviroments, edited by D. F. Torres, O. Reimer, vol. 34 of Astrophysics and Space Science Proceedings, 331.
[2] Zubovas K., Nayakshin S., 2012, MNRAS, 424, 666.

REDSHIFT OF LIGHT FROM THE SOURCE IN BINARY SYSTEM THAT MOVES IN THE GRAVITATIONAL FIELD OF KERR BLACK HOLE

Stanislav Komarov*, Alexander Gorbatsievich, Alexander Tarasenko

Department of Theoretical Physics and Astrophysics, Belarusian State University, Nezavisimosti av., 4, 220030 Minsk, Belarus

*staskomarov@tut.by

The results of observation and analysis of the stars in the Galactic Center region show that the supermassive black hole (Sagittarius A*) exists in this region (see e. g., [1]). The studying of the redshift of light of these stars gives us possibilities for testing theories of gravity (see e. g., [2, 3]). The binary systems can exist among these stars (see e. g., [4]). And this provide possibilities for calculation of addition parameters of motion and hence, for more exact tests.

In the general case the gravitational field of astrophysical black hole can be considered as a Kerr metric. In this work we present the method for the calculation of redshift as a function of time for the source in binary star system that moves in external gravitational field of Kerr black hole. For the calculation of the redshift it is necessary to solve the edge problem for the isotropic geodesics in external gravitational field (see Fig. 1). For this purpose we use the decomposition of redshift into two parts. The first one gives the redshift from the source that moves along geodesic, and the second part is the redshift from the relative motion of the two stars (see [5]). We use the analytical expressions for the geodesics in Kerr metric and this gives us possibilities to use our results in the case of strong gravitational field, when binary system moves very close to the supermassive black hole horizon.

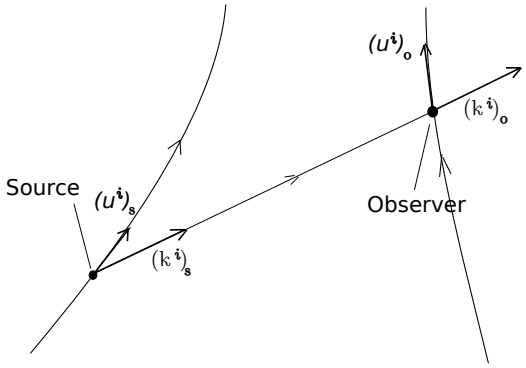

Fig. 1. The observer can detect only rays of light that propagate along the isotropic geodesic intersecting both: source worldline and observer worldline.

The assumption about the existence of large number of binary pulsars in the vicinity of Sagittarius A* is presented in many scientific publications (see e. g. [6]). Due to the simple relation between the redshift and the time delay of the pulse of pulsar (see e. g. [6]) one can use our results also for studying of the Galactic Center pulsar timing data.

[1] R. Genzel, S. Gillesen, The Galactic Center massive black hole and nuclear star claster, Rev. Mod. Phys, **82**, P. 3144-3195 (2010).

[2] Y. Zhang, Y. Lu, Q. Yu, On testing the Kerr metric of the massive black hole in the Galactic Center via stellar orbital motion: full general relativistic treatment, ApJ, **809**, P. 127 (2015).

[3] A. Tarasenko, Reconstruction of a compact object motion in the vicinity of a black hole by its electromagnetic radiation, Phys. Rev. D, **81**, P. 123005 (2010).

[4] S. Devid Chu. Investigating the binarity of S0-2: implications for its origins and robustness as a probe of the laws of gravity around a supermassive black hole. arXiv: 1709.04890v1 [astro-ph.SR] 14 Sep 2017

[5] S. Komarov, A. Gorbatsievich, A. Tarasenko. Time delay of radiation from pulsar in a binary system that moves in field of Schwarzschild black hole, Lithuanian Journal of Physics, **2**, Pp. 88-93 (2017).

[6] F. Zhang, Y. Lu, and Q. Yu. On the existence of pulsars in the vicinity of the massive black hole in the Galactic Center. The Astrophysical Journal, **784**, Pp. 1-8, (2014)

DETERMINING THE AGE OF FERMI BUBLES USING HYDRODYNAMIC SIMULATIONS

Aidas Sadauskas[1], Kastytis Zubovas[1,2]

[1]Faculty of Physics, Vilnius University, Lithuania
[2]Department of Fundamental Research, Centre for Physical Sciences and Technology, Lithuania
a.sadauskass@gmail.com

Active Galactic nuclei (AGN) are arguably one of the most important ingredients in galaxy formation and evolution theories. Some observational facts indicate that the Milky Way's central supermassive black hole Sgr A* might have been active in the recent past. Giant gamma-ray structures known as the Fermi bubbles, discovered in 2010, could be one of the Sgr A* activity footprints. However, the origin of these bubbles still remains debatable even eight years after their discovery. Therefore understanding the origin and evolution of these structures may help us better understand how AGN feedback influences host galaxies.

In this work we study the morphology and kinematics of the Fermi bubbles. Using a hydrodynamic model, we aim to determine the age and lifetime of these structures, assuming that their origin is wind feedback from an accretion episode of Sgr A*.

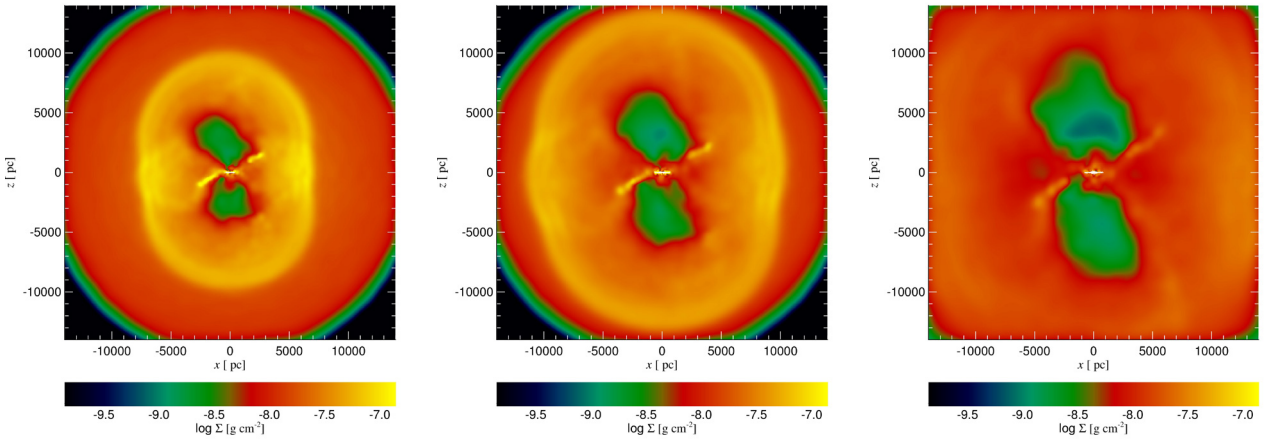

Fig. 1. Evolution of Fermi bubble morphology: left - 6 Myr, center - 10 Myr, right - 20 Myr.

We conclude, based on kinematics and morphology of the simulated bubbles, that the age of the observed structures should be between 6 and 10 Myr. Also the lifetime of Fermi bubble structures should not exceed 20 Myr. Our research contributes to the understanding of the history of Galactic evolution and the formation of Fermi bubbles and their analogues in other galaxies.

Automatizing the Grimus-Neufeld model

Simonas Draukšas[1], Thomas Gajdosik[1,2]

[1] Faculty of Physics, Vilnius University, Lithuania
[2] Institute of Theoretical Physcis and Astronomy, Vilnius University, Lithuania
s.drauksas@gmail.com

In the Standard Model neutrinos are massless and experimentally that is not the case. Incorporating their masses theoreticlly has a couple of difficulties. First of all, right-handed neutrinos are not observed and therefore the usual Higgs mechanism is unable to give masses to the neutrinos. Secondlly, masses of the neutrinos are very small, hence why they were thought to be massles to begin with. The Grimus-Neufeld model [1] gives a possible mechanism to incorporate these small neutrino masses. This model has two Higgs doublets written in the Higgs basis and a single heavy Majorana neutrino, that couples as a right-handed particle. These two parts use the seesaw mechanism and 1-loop corrections to generate masses for the massless Standard Model neutrinos.

Our first goal was to implement the model, i.e. prepare it for calculations, in the following software packages: `SARAH` [2], `SPHENO` [3] and `FlexibleSUSY` [4]. `SARAH` provides analytical expressions while `SPHENO` and `FlexibleSUSY` use those expressions to do numerical calculations. We have implemented the model in two spectrum generators to be sure that the model is decribed correctly in model files of the software packages. In the present we are interested in doing calculations, for example, we want to do a sweep of parameters as well as look at the masses of neutrinos.

In the presentation we will discuss the model and present the work that has been done so far.

The authors thank the Lithuanian Academy of Sciences for the support (the project DaFi2017).

---

[1] W. Grimus and H. Neufeld. "Radiative neutrino masses in an SU(2) × U(1) model". In: Nuclear Physics B 325.1 (1989), pp. 18 –32. DOI: https://doi.org/10.1016/0550-3213(89)90370-2.

[2] F. Staub. "Sarah". In: ArXiv e-prints (June 2008). arXiv: 0806.0538 [hep-ph].

[3] W. Porod. "SPheno, a program for calculating supersymmetric spectra, SUSY particle decays and SUSY particle production at e^+e^- colliders". In: Computer Physics Communications 153 (June 2003), pp. 275–315. DOI: 10.1016/S0010-4655(03)00222-4. eprint: hep-ph/0301101.

[4] Peter Athron et al. "FlexibleSUSYA spectrum generator generator for supersymmetric models". In: Comput. Phys. Commun. 190 (2015), pp. 139–172. DOI: 10.1016/j.cpc.2014.12.020. arXiv: 1406.2319 [hep-ph].

Transiting Hot Jupiters

Monika Stangret

Centre for Astronomy, Faculty of Physics, Astronomy and Informatics, Nicolaus Copernicus University, Grudziadzka 5, 87-100 Torun, Poland
stangret.galaxy@gmail.com

Exoplanets are the planets which orbit the stars other than Sun. So far, we detected 3741 such planets with various methods (exoplanet.eu catalogue). Hot Jupiters are the first exoplanets discovered by transit and radial velocities methods because of their large radii, high masses and short periods up to several days. Studying Hot Jupiters using transit method (photometric and spectroscopic) we can determine the orbit parameters, the size of the planet, temperature and the chemistry of the atmosphere.

In my presentation I will to show the transits of the hot jupiters: GJ 436b, WASP-3b, KELT-1b, KELT-3b. Those exoplanets were observed throughout full transits during the nights in 2017 and 2018 using a CCD camera mounted at the 60 cm Cassegrain reflector at the Centre for Astronomy in Piwnice near Torun, Poland.

Because of the close orbits of the Hot Jupiters there is possibility that the star leads the tidal distortion of the planet. Having the high precision light curves and determine the orbit paramiters, size and period of the hot jupiters we can check if the star affects the planet.

All data reduction was carried out using the AstroImageJ (AIJ, Collins et al. 2016).

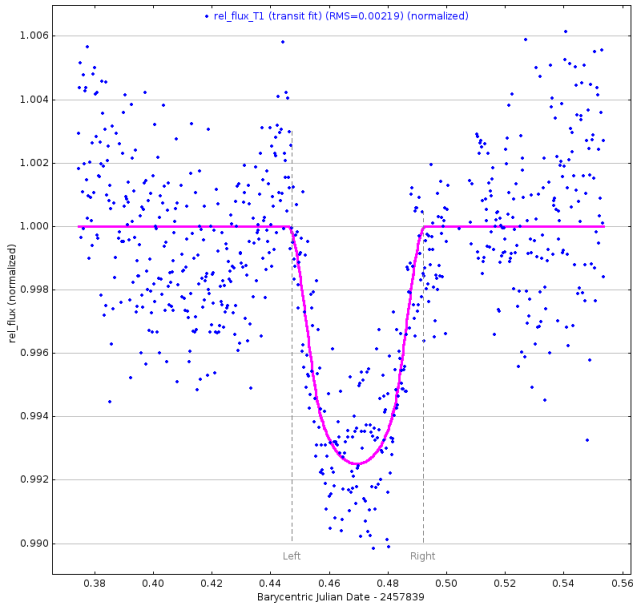

Fig. 1. Photometric light curve for GJ 436b and fitting transit model (pink line).

[1] Collins, K.A., Kielkopf, J.F., Stassun, K.G., 2016, arXiv:1601.02622.

EXTENDED STANDARD MODEL HIGGS SECTOR: ANALYSIS OF THE S_3-SYMMETRIC THREE-HIGGS-DOUBLET MODEL

Anton Kuncinas, Per Osland

Department of Physics and Technology, University of Bergen, Norway
Anton.Kuncinas@protonmail.com

Nearly six years have passed since the discovery of the Standard Model (SM) like Higgs boson in 2012. The combined measured mass of the Higgs boson is $m_h = 125.09 \pm 0.21(\text{stat.}) \pm 0.11(\text{syst.})$ GeV [1] based on data from the ATLAS and CMS experiments. There is still no experimental verification that it is the only Higgs boson although a lot of experimental data accumulated during the past few decades suggest that the SM is a good model. Acknowledging the fact that the SM is the theory, which describes an approximate observable world it is worth taking a note that there is physics beyond the SM. Some of the physical phenomena, which do not fit the frame of the SM are: neutrino masses, dark matter etc. An extension of the Higgs sector would solve some of the issues. Thus we propose and are motivated that such extension could potentially solve several problems.

The extension of the SM Higgs sector we are interested in is the so-called three-Higgs-dublet model (3HDM). In the case of the SM, only one Higgs $SU(2)_L$ doublet is present, while in the 3HDM two additional doublets are added:

$$\phi_i = \begin{pmatrix} \varphi_i^+ \\ \frac{1}{\sqrt{2}}(\rho_i + \eta_i + i\chi_i) \end{pmatrix},\ \{\varphi_i^+,\ \rho_i\} \in \mathbb{C},\ \{\eta_i,\ \chi_i\} \in \mathbb{R}\ , i = \overline{1,3}. \tag{1}$$

Such extension leads to six additional scalar fields with respect to the SM: two neutral CP-even Higgs bosons H_i^0, two neutral CP-odd Higgs bosons A_i^0 and a pair of charged Higgs bosons $H_i^\pm$, where $i = \{1,2\}$. In general all scalar fields mix to form physical Higgs states. Based on mixing this can lead to some interesting properties.

We are interested in the specific case of the 3HDM, that is the S_3-symmetric 3HDM. S_3 is a non-Abelian group and is the permutation group of three objects, in this case permutation of the three Higgs doublets: $\{\phi_1,\ \phi_2,\ \phi_3\}$. S_3 consists of two ^{1}D irreducible representations, $\mathbf{1}_\text{S}$ and $\mathbf{1}_\text{A}$, and a ^{2}D doublet irreducible representation, $\mathbf{2}$. We chose the following ^{3}D representation:

$$\begin{aligned} \mathbf{2}\text{:} \qquad & \begin{pmatrix} h_1 \\ h_2 \end{pmatrix} = \begin{pmatrix} \frac{1}{\sqrt{2}}(\phi_1 - \phi_2) \\ \frac{1}{\sqrt{6}}(\phi_1 + \phi_2 - 2\phi_3) \end{pmatrix}, \\ \mathbf{1}\text{:} \qquad & h_S = \frac{1}{\sqrt{3}}(\phi_1 + \phi_2 + \phi_3), \end{aligned} \tag{2}$$

The most general renormalizable scalar potential invariant under $SU(3)_C \otimes SU(2)_L \otimes U(1)_Y \otimes S_3$ symmetry can be written as ref.[2]:

$$\begin{aligned} V_2 =& \mu_1^2\left(h_1^\dagger h_1 + h_2^\dagger h_2\right) + \mu_0^2 h_S^\dagger h_S, \\ V_4 =& \lambda_1\left(h_1^\dagger h_1 + h_2^\dagger h_2\right)^2 + \lambda_2\left(h_1^\dagger h_2 - h_2^\dagger h_1\right)^2 + \lambda_3\left[\left(h_1^\dagger h_1 - h_2^\dagger h_2\right)^2 + \left(h_1^\dagger h_2 + h_2^\dagger h_1\right)^2\right] \\ &+ \left[\lambda_4\left(\left(h_S^\dagger h_1\right)\left(h_1^\dagger h_2 + h_2^\dagger h_1\right) + \left(h_S^\dagger h_2\right)\left(h_1^\dagger h_1 - h_2^\dagger h_2\right)\right) + \text{h.c.}\right] \\ &+ \lambda_5\left[\left(h_S^\dagger h_S\right)\left(h_1^\dagger h_1 + h_2^\dagger h_2\right)\right] + \lambda_6\left[\left(h_1^\dagger h_S\right)\left(h_S^\dagger h_1\right) + \left(h_2^\dagger h_S\right)\left(h_S^\dagger h_2\right)\right] \\ &+ \lambda_7\left[\left(h_1^\dagger h_S\right)^2 + \left(h_2^\dagger h_S\right)^2\right] + \lambda_8\left(h_S^\dagger h_S\right)^2. \end{aligned} \tag{3}$$

In our research we analyze a specific case of vacuum configuration, which is presented as C-III-c in ref.[3]:

$$\{\hat{\omega}_1 e^{i\sigma_1},\ \hat{\omega}_2 e^{i\sigma_2},\ 0\}, \tag{4}$$

along with suppressing some fields mixing, $\lambda_4 = 0$. Although vacuum consists of complex values it does not lead to spontaneous CP violation. We take a look at how the S_3 3HDM C-III-c model changes by softly breaking the S_3 symmetry. This leads to an inert doublet scenario, which is written as h_S. We believe that due to such behaviour h_S might be a possible dark matter candidate. We present preliminary results by taking a look at experimental and theoretical constraints ref.[4].

[1] G. Aad *et al.* [ATLAS and CMS Collaborations], Phys. Rev. Lett. **114** (2015) 191803 doi:10.1103/PhysRevLett.114.191803.

[2] S. Pakvasa and H. Sugawara, Phys. Lett. **73B** (1978) 61. doi:10.1016/0370-2693(78)90172-7
E. Derman, Phys. Rev. D **19** (1979) 317. doi:10.1103/PhysRevD.19.317
J. Kubo, H. Okada and F. Sakamaki, Phys. Rev. D **70** (2004) 036007 doi:10.1103/PhysRevD.70.036007.

[3] D. Emmanuel-Costa, O. M. Ogreid, P. Osland and M. N. Rebelo, JHEP **1602** (2016) 154 Erratum: [JHEP **1608** (2016) 169] doi:10.1007/JHEP08(2016)169, 10.1007/JHEP02(2016)154

[4] W. Grimus, L. Lavoura, O. M. Ogreid and P. Osland, Nucl. Phys. B **801** (2008) 81 doi:10.1016/j.nuclphysb.2008.04.019.
D. Das and U. K. Dey, Phys. Rev. D **89** (2014) no.9, 095025 Erratum: [Phys. Rev. D **91** (2015) no.3, 039905] doi:10.1103/PhysRevD.91.039905, 10.1103/PhysRevD.89.095025.

SCALABLE PUMPING SOURCE FOR TW-CLASS OPCPA BASED ON Yb:YAG RODS WITH 1 ps 20 mJ OUTPUT PULSES AT 100 Hz

Paulius Mackonis[1], Augustinas Petrulėnas[1], Aleksej M. Rodin[1,2]

[1] Solid State Laser Laboratory,
Department of Laser Technologies, Center for Physical Sciences and Technology, Lithuania

[2] Ekspla Ltd, Lithuania

pauliusandco@gmail.com

Significant efforts have been made all over the world to create TW-class laser systems [1] that take up a lot of space, while development and maintenance costs limit their distribution. Therefore, such systems are usually shared by many scientists with limited access time. For the wide distribution of high peak power lasers among the scientific community, it is vitally important to pay special attention to reducing the size and cost. We report on the current state of development of a cost-effective and compact pumping source for TW-class Optical Parametric Chirped Pulse Amplifier (OPCPA) containing a fiber seed laser, a pulse picker, a two-cascaded double-pass Chirped Pulse Amplifier (CPA) based on Yb:YAG rods and a pulse compressor. With a scalable output of 20 - 60 mJ and a pulsewidth of ~ 1 ps at a repetition rate of 100 Hz, the experimental setup includes commercially available components and is easily reproduced.

A two-stage double-pass CPA operates at a repetition rate of 100 Hz [2,3]. Seed pulses were selected using a Pockels cell with an extinction ratio of over 30 dB from a fiber laser operating at 10 kHz. The first CPA cascade is based on 2 × 2 × 20 mm^3, 2 % at. Yb:YAG rod pumped by ~ 7 ms pulses, emitted from the high brightness laser diode. The induced thermal lens was compensated by adjusting the distance between the spherical mirror and the laser rod. Faraday rotators, located after the first pass of Yb:YAG CPA stages, suppress the depolarization. Pulses with an output energy of up to 2 mJ, a pulsewidth of ~ 150 ps and a spectral width of ~ 1.8 nm were directed to a second CPA cascade designed to achieve an output energy of several tens of mJ. To reduce the incident energy density, the input beam was expanded to ~ 1.5 mm. Larger aperture: 5 × 5 × 20 mm^3 rod with 2 % at. Yb-doping was pumped by a combined output of seven laser diodes providing pulses of ~ 2 ms with a total average power of ~ 90 W at a repetition rate of 100 Hz. Spatial beam cleaning with an insignificant energy loss of < 6 % eliminates the impact of spherical aberration (Fig.1, left).

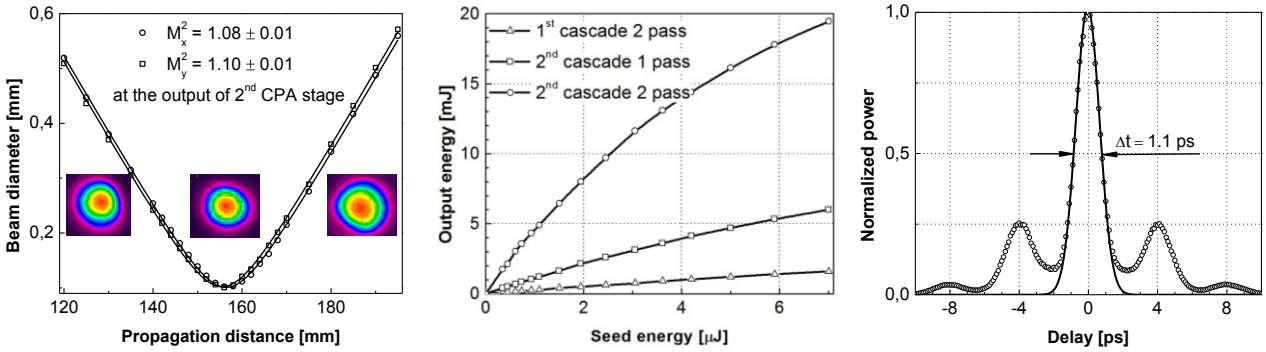

Fig. 1. M^2 measurement of amplified beam at ~ 20 mJ (left), amplified output energy versus seed energy (middle) and autocorrelation trace of compressed pulses at ~ 18 mJ with Gaussian fit (right).

Amplified pulses with a total gain of ~ 2800, an output energy of ~ 20 mJ (Fig. 1, middle) and an excellent beam quality of M^2 ~ 1.1 (Fig. 1, left), pulsewidth of ~ 90 ps and spectral width of ~1.6 nm were directed to a compact folded compressor based on a diffraction grating of 1842 grooves/mm and a diffraction efficiency of more than 97 %. Although the gain narrowing to a spectral width ~ 1.6 nm FWHM after amplification, we obtained pulses of ~ 1.1 ps (Fig. 1, right), 1.1 times of transform limited for measured bandwidth. The overall efficiency of a 4-pass compressor exceeds 90 %. Combining of 19 pcs of pumping diodes with the commercially available fiber beam combiner enable an increase in the output energy to ~ 60 mJ. The optimization of the temperature gradient applied to the fiber stretcher in the seed source is ongoing to improve the temporal contrast of the compressed pulses. Output pulses converted to the second harmonics at 515 nm wavelength in an LBO crystal are used for pumping of 1 TW-class OPCPA.

This work has been funded by Research Council of Lithuania under contract LAT-10/2016.

[1] National Academies of Sciences, Engineering, and Medicine, Opportunities in Intense Ultrafast Lasers: Reaching for the Brightest Light, Washington, DC: The National Academies Press (2018). https://doi.org/10.17226/24939.

[2] A.M. Rodin, E. Zopelis, Optimized configuration for two cascaded double-pass Yb:YAG chirped pulse amplifier, Conference on Lasers and Electro-Optics Digest, Paper CA-P.7 TUE, Munich, Germany (2017).

[3] A. M. Rodin and E. Zopelis, Comparison of Yb:YAG single crystal fiber with larger aperture CPA pumped at 940 nm and 969 nm, Conference on Lasers and Electro-Optics Pacific Rim (CLEO-PR), Singapore, 1-5 (2017). doi: 10.1109/CLEOPR.2017.8118912.

ANALYSIS OF PULSED VECTOR MATHIEU BEAMS WITH FEMTOSECOND DURATION

Vitalis Vosylius[1,2], Sergej Orlov[1]

[1] Center for Physical Sciences and Technology, Sauletekio av. 3, Vilnius, Lithuania
[2] Faculty of Physics, Vilnius University
vitalis.vosylius@ff.stud.vu.lt

Mathieu beams are solutions of Helmholtz wave equation in elliptical coordinate system and are part of non-diffracting beam family. Due to unique asymmetric transverse intensity profile of zeroth order even Mathieu beam it can be perceived as "Optical Knife" and has many applications including material processing, medicine etc. Superposition of Bessel beams with different frequencies and amplitudes results in non-diffracting pulses where, diffraction spreading and dispersive broadening is compensated by a given angular dispersion. These non-diffracting and non-dispersing wave packets are also known as X-waves or Focus Wave Modes. Scalar non-diffracting pulses containing Bessel, parabolic and Mathieu beams analyzed previously [2], but a deeper analysis of pulsed vector Mathieu beams is still needed.

In this work we introduce Mathieu beams and use them to create pulses with different polarizations in a fashion similar to Focus Wave Modes. Vector solutions to Mathieu beams are obtained from scalar ones using classical technique described in [1]. Pulses with different topological charges (m) and eccentricity parameters (which control the width of "Optical Knife") are presented in detail. Transverse distribution of intensity of a pulse with m = 0 ("Optical Knives" case) can be seen in Fig.1.

Moreover, angular spectrum of femtosecond Mathieu beams and its properties will be discussed.

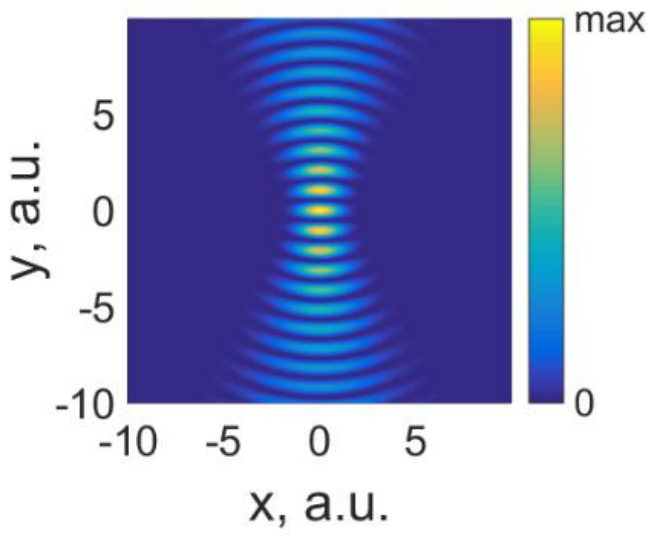

Fig. 1. Transverse intensity distribution of a pulsed Mathieu beam with *m = 0*

Furthermore, ways of creating these beams and possible challenges will be presented as well as applicability and importance of these pulsed beams.

[1] J. Stratton, Electromagnetic Theory, An IEEE Press classic reissue (Wiley, 2007).

[2] Josue Davila-Rodriguez and Julio C. Gutiérrez-Vega, Helical Mathieu and parabolic localized pulses, Vol. 24, No. 11/November 2007/ J. Opt. Soc. Am. A

[3] P. Saari, and K. Reivelt, "Evidence of X-shaped propagation-invariant localized light waves," Phys. Rev. Lett. 79, 4135 (1997)

[4] M. Ornigotti, C. Conti and A. Szameit, "Universal form of the carrier frequency of scalar and vector paraxial X waves with orbital angular momentum and arbitrary frequency spectrum," Phys Rev. A 92, 043801 (2015).

SPATIAL EFFECTS INDUCED BY LASER–PREFORMED PLASMA ON THZ SIGNAL GENERATION IN AIR BY BICHROMATIC LASER PULSES

Karolis Adomavičius, Maksym Ivanov, Danas Buožius, Žilvinas Svirskas

Vilnius University Laser Research Center, Saulėtekio Ave. 10, LT-10223 Vilnius, Lithuania
Karolis.Adomavicius@ff.stud.vu.lt

Terahertz (THz) radiation represents the region in the electromagnetic spectrum between far-infrared and microwave radiation and has frequency between 0.1 THz and 10 THz (wavelength varies from 3 mm to 0.03 mm). Terahertz radiation has been investigated by scientists and engineers for over a decade; however compact and efficient THz sources and detectors are still to be developed. Therefore the research efforts in this field are rising, because THz radiation has many interesting and unique properties: for example it is non-ionizing and safe for the living organisms. Moreover, it can easily pass through wood, paper, clothing, various plastics and ceramics. Furthermore, rotational and vibrational transitions of various molecules have energies in THz frequency range. This leads to a wide range of applications, such as spectroscopy, biological and medical imaging, detection of hazardous materials, security screening, etc.

As a pump source the Ti:Sapphire laser system (central wavelength about 790 nm) operating at 1 kHz and delivering 9 mJ pulses of 35 fs (FWHM) duration was used. THz radiation and prepulse were generated in ambient air with energies of 5.2 and 1.65 mJ respectively. In the experiment THz radiation was generated by mixing laser and its second harmonic pulses (bichromatic pump [1]) and prepulse was generated using fundamental harmonic only. The prepulse was propagated and focused in the orthogonal direction with respect to the main beam to generate a plasma filament that intercepted the main beam path.

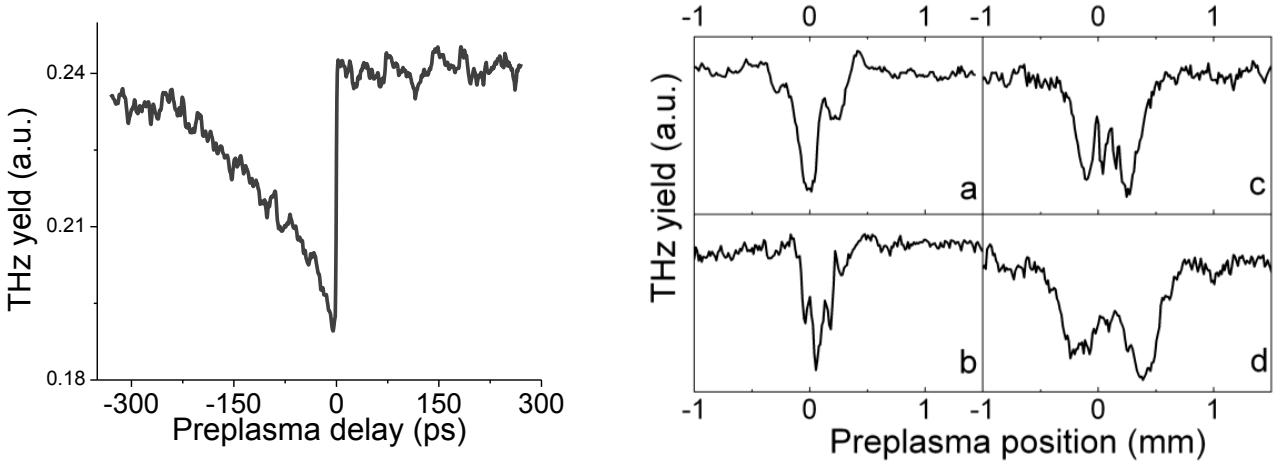

Fig. 1 THz radiation yield dependence on prepasma delay (left) and on preplasma position (right).

During the experiments the dependencies of various THz radiation properties depending on position, delay and power of prepasma been investigated (Fig. 1). The THz signal significantly decreases when the precreated plasma is present in the path of the pump beam. The impact of the preplasma on the yield of THz generation was strongly dependent on the timing between the pump pulse and prepulse: the amplitude of THz signal didn‘t change when the prepulse was sent after the main pulse, and rapidly decreased, when the delay between these pulses reversed the sign. After the initial dropdown the THz signal slowly recovered with a time constant of a few hundred picoseconds (Fig. 1 (left)). In addition, the dependence of THz attenuation on the mutual position of two plasma filaments have been observed: depending on the position of interception point along the main beam (along the z coordinate axis) the THz yield as a function of preplasma position along the y coordinate mainly had either one or two minimum (Fig. 1 (right)). Obtained results of preplasma interaction with THz generating filament could be explained by at least two different mechanisms: pump beam diffraction and THz radiation screening induced by preplasma filament [2].

[1]V. Pyragaitė, V. Smilgevičius, K. Steponkevičius, B. Makauskas, and V. Vaičaitis, “Phase shifts in terahertz wave generation by tightly focused bichromatic laser pulses,” JOSA B **31**(7) 1430–1435 (2014).
[2] J. Zhao, Zhang, T. Wu, C. Zhang, Y. Zhao, “Terahertz wave absorption via preformed air plasma,” Opt. Commun. **380**, 87-90 (2016).

Formation of asymmetrical Bessel-like laser beams for glass processing

Rokas Stonys*, Juozas Dudutis

Center for Pfysical Sciences and Technology, Savanoriu Ave. 231, LT-02300 Vilnius, Lithuania
*rokas.stonys@ff.stud.vu.lt

Conventional processing methods of glass cannot fulfil evergrowing industrial requirements for processing speed and quality. For that reason these days glass processing is usually done by employing various laser-based techniques. One of the most material and energy efficient glass cutting techniques is to locally weaken the material along the cutting path by generating cracks or material modifications and then separate the sheets by applying thermal or mechanical load. This method results in a smooth cut with an infinitely thin kerf width and in most cases there is no need of additional processing [1].

Bessel-Gaussian beams are very appealing for glass processing because of their authentic properties such as the long non-diffracting propagation length and rapid reconstruction behind an obstacle. However generating glass modifications with a symetrical Bessel-Gaussian beam is not ideal as glass modifications are random and negatively influence speed and quality of the cut, thus arises a need to make the modifications directional and easily controlled.

It was shown that the asymmetrical Bessel-Gaussian beams can be formed by filtering its spectrum of spacial frequencies after compensating the aberrations emerged because of the axicon's elliptical base [2]. We have proved that such beams in turn generate directional cracks in the bulk of the glass.

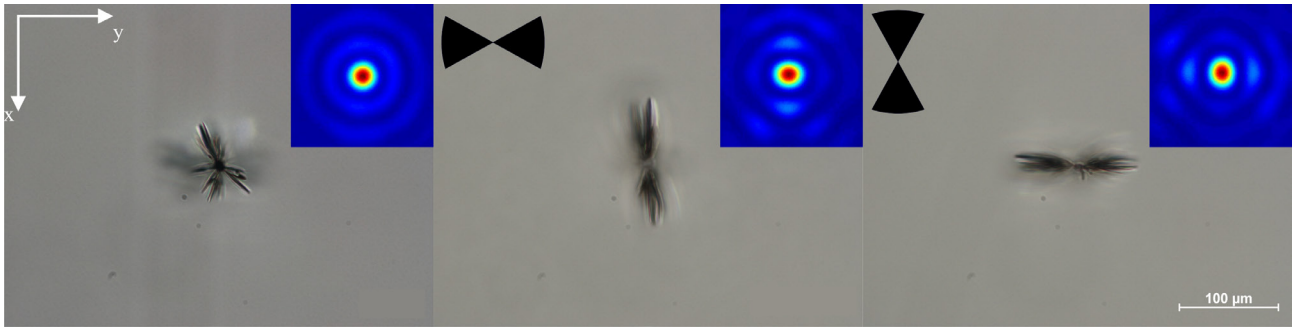

Fig. 1. Images of directional cracks made by an asymmetrical Bessel-like beam as seen from the direction of beam's propogation

Furthermore, generated cracks are easily controlled by changing the filter's position in respect to the cutting direction. Also, when compared with cracks made by a non-filtrated beam without the correction of aberrations, the cracks made by a filtrated beam with compensated aberrations were more than twice as large in respect of cracked area. These results are indeed promising as the cracks generated using such asymmetrical beams could greatly increase both speed and quality of the cutting process.

[1] S. Nisar, L. Li, M. A. Sheikh. Laser glass cutting techniques - A review. Journal of Laser Applications, **25**(4), 42010 (2013).
[2] R. Meyer, M. Jacquot, R. Giust, J. Safioui, L. Rapp, L. Furfaro, F. Courvoisier. Single-shot ultrafast laser processing of high-aspect-ratio nanochannels using elliptical Bessel beams. Optics Letters, **42**(21), 4307 (2017).

FABRICATION OF MICROSTRUCTURES IN SAPPHIRE BY FS-LASER INDUCED SELECTIVE ETCHING

Gedvinas Nemickas[1,2], Titas Tičkūnas[1,2], Vytautas Purlys[1,2]

[1] Laser Research Center, Vilnius University, Saulėtekio ave. 10, Vilnius, Lithuania
[2] UAB „Femtika“, Saulėtekio ave. 15, Vilnius, Lithuania
gedvinas@femtika.lt

Recently lasers have been widely applied in various materials processing. As one of laser techniques, light can be used for cutting or drilling metals, polymers, glasses. Femtosecond lasers can be characterized as a tool owning unique properties to process transparent materials in their volume. Due to their high-peak intensities, tightly focused femtosecond laser beams can modify locally the volume of material. Subsequently, these laser affected zones could be etched much faster that unexposed material zones. This technology is known selective laser etching and it enables to fabricate three-dimensional structures of the volume of transparent material.

There have been shown many publications of researches of selective laser etching for various transparent materials, especially fused silica, but there are just a few for sapphire [1]. However, sapphire could be desirable material for the processing where long and narrow channels, steep edges are required, because of its greater selectivity (sapphire – 10 000:1, fused silica – 100:1) [2].

The main goal of this research was to find out optimal parameters of femtosecond laser processing in order to form 3D structures of sapphire.

As a result, we investigated the etching speed dependence on processing parameters, such as laser writing speed, laser repetition rate and the average power of the laser. Moreover, we found that combination of selective laser etching and thermal shock allows fabrication of arbitrary geometry 2D objects, such as squares or cylinders. Furthermore, the etched sapphire sides had less than 200 nm roughness.

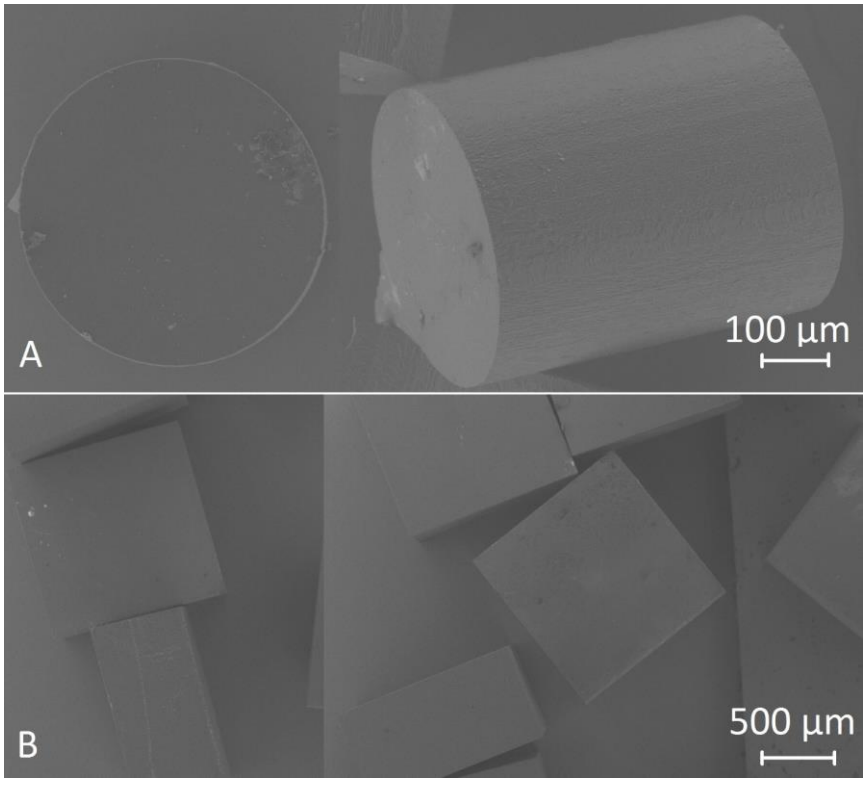

Fig. 1. Microstructures made in the volume of sapphire using selective laser etching and thermal gradient: a) cylinders; b) squares.

[1] M. Hörstmann-Jungemann, J. Gottmann, and M. Keggenhoff, 3D-microstructuring of sapphire using fs-laser irradiation and selective etching, J. Micromech. Microeng, **5**(2), 145-149 (2010).

[2] Y. Bellouard, A. Said, M. Dugan, and P. Bado, Fabrication of high-aspect ratio, micro-fluidic channels and tunnels using femtosecond laser pulses and chemical etching, Opt. Express, 12(10), 2120-2129 (2004).

DETERMINATION OF OPTIMAL SPATIAL RESOLUTION CONDITIONS TO PRODUCE PHASE MICRO-OPTICAL COMPONENTS USING THE SUSPENDED BAR STRUCTURE METHOD VIA 3D LASER LITHOGRAPHY

Rūta Pakalnytė, Simonas Vanagnickas

Laser Research Center, Physics Faculty, Vilnius University, Vilnius, Lithuania
ruta.pakalnyte@ff.stud.vu.lt

Three-dimensional laser lithography (3DLL) is applied in the field of photonics. Under certain conditions, 3DLL can be used for photonic crystals [1]; therefore, this could also be applied in the production of phase micro-optical components [2]. Phase micro-optical components are different from other micro-optical elements, because they are wave phase modulation devices, also called meta-surfaces. For the production of meta-surfaces such as q-plates, high spatial resolution is essential because components are formed from filaments of lateral linewidths smaller than the wavelength of light. 3DLL is still the only technology capable of creating high-resolution (less than 100 nm has been achieved [3]) full-3D structures.

In order to achieve high spatial resolution in 3DLL, it is necessary to select appropriate focusing conditions and to understand the material's response to the laser beam as each material reacts to the light differently. For this reason, suspended bar structures of three materials (SZ2080, SZ2080 + IRG (1%), SZ2080 + DMAEMA) were formed to determine the optimal conditions for high-resolution polymerization and the influence of additives (photoinitiators and quenchers) on the dimensions of the bars. The sample were scanned at different speeds (10, 50, 100, 200, 1000 μm/s) to determine which speeds are the most suitable for high spatial resolution fabrication. To perform the 3DLL experiments in this research, a femtosecond laser *Pharos* (*Light Conversion*) was used. A YbKGW crystal has been used as the laser active element, generating a pulse duration of less than 300 fs, pulse repetition rate of 200 kHz, and the wavelength λ = 515 nm. For tight focus, a 63x magnifying lens (Zeiss) with the numerical aperture NA = 1.4 and transmission T = 41 % was used.

After the research, it was found that the best resolution is achieved by using the additives of the quencher (d_q = 0.16 μm/s < d_p = 0.18 μm/s < d_{pi} = 0.22 μm/s) because their diffusion inhibits the movement of free radicals to areas not affected by laser light [4]. Fabrication of the prepolymer with photoinitiator additives resulted in wider strands because radicals diffuse beyond the beam waist position. The thinnest bars were fabricated at the scanning speed of 200 μm/s, results are shown in Fig. 1. In accordance with the best conditions suggested by the research, a phase micro-optical element, a q-plate with line widths of 0.24 μm, was produced (Fig. 2).

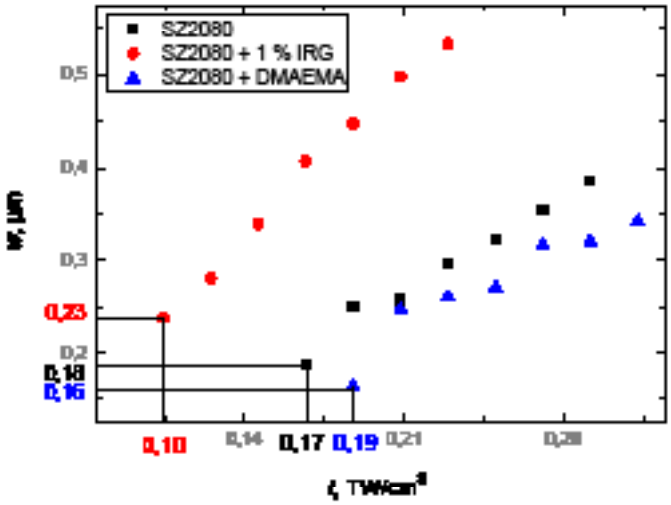

Fig. 1. Suspended bar structure strand width dependence on the exposure intensity, at the scanning speed of 200 μm/s in pure SZ2080, SZ2080 + 1 % IRG, SZ2080 + DMAEMA materials. The dotted line marks values of polymerization threshold.

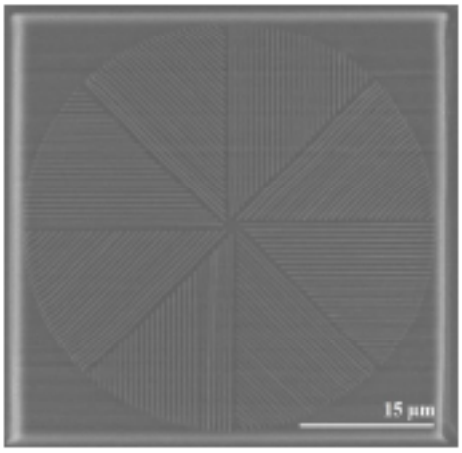

Fig. 2. A picture of a q-plate, fabricated in accordance with research results, produced using a scanning electron microscope.

[1] D. Gailevičius et al., Photonic Crystal Microchip Laser, Sci. Rep. 6, 34173 (2016).
[2] X. Wang, A. A. Kuchmizhak, P. Bosshard, S. Juodkazis, Dielectric geometric phase optical elements fabricated by femtosecond direct laser writing in photoresists, Appl. Phys. Lett. 118, 181101 (2017).
[3] J. Fischer, M. Wegener, Three-dimensional optical laser lithography beyond the diffraction limit, Laser Photonics Rev., 7, 22–44 (2013).
[4] I. Sakellari, E. Kabouraki, D. Gray, V. Purlys, C. Fotakis, A. Pikulin, N. Bityurin, M. Vamvakaki, M. Farsari, Diffusion-Assisted High-Resolution Direct Femtosecond Laser Writing, ACS Nano, 6 (3), 2302–2311 (2012).

FABRICATION AND INVESTIGATION OF LAMINATED SOLUTION-BASED NON-FULLERENE ORGANIC SOLAR CELLS

Rokas Jasiūnas

Department of Physics, Chemistry and Biology, Linköping University, Sweden
rokas.jasiunas@ftmc.lt

As demand for cheap and environmental friendly energy is expected to increase more and more in following decades both industry and academia are on a quest to produce technology as a supply for this demand. Organic Photovoltaic (OPV) is one of most promising candidate for such demand owing to its possibility of extremely low-cost solution-based production. Here we present highly attractive fabrication process of laminated all-polymer solar cells on flexible and transparent plastic substrate having both electrodes and active layer deposited from solutions. As well results of brief charge carrier migration investigation in fabricated bilayer solar cells.

We were able to laminate devices with active layer as thin as 40 nm and made several sets of devices with thickness varying up to 400 nm. Even though cells were made in bilayer structure best Power Conversion Efficiency (PCE) reached over 1% and is comparable with conventional and more efficient bulk heterojunction structure with evaporated aluminum cathode for the same active layer materials. Exposure to oxygen was minimized after printing electrodes in ambient conditions, but was not completely avoided, which contributed to poor reproducibility of devices. Nevertheless, all different device sets showed familiar tendencies in performance.

We were able to probe Charge Transfer (CT) states at bilayers interface by investigating electroluminescence spectrum. We observed CT states red-shift with increasing active layer thickness, which we attribute to thermalization of injected charge carrier migrating from electrode to donor-acceptor interface.

EFFICIENT ULTRASHORT PULSED LASER ABLATION FOR 3D ENGRAVING

Andrius Žemaitis*, Mantas Gaidys, Mindaugas Gedvilas

Center for Physical Sciences and Technology, Savanoriu Ave. 231, LT-02300 Vilnius, Lithuania
andrius.zemaitis@ftmc.lt

Ultrashort pulsed lasers are the first choice considering high quality, precise material processing. Picosecond (ps) laser pulses compared to nanosecond (ns) provide less heat affected zone and melt-free surface. Since most of the metals have picosecond range (copper ~10 ps [1]) electron-phonon thermalisation time, there is no need to use femtosecond (fs) laser pulses, which are more expensive than ps laser sources. So, ps lasers combine both precision and cost-efficiency.

The high throughput of laser ablation is a key factor for industry companies, especially for large area surface structuring [2]. This work was dedicated to the optimisation of ps laser ablation process taking into account many processing parameters: laser fluence, beam scanning speed, hatch distance (distance between lines which fill drawing) and pulse repetition rate.

It was shown that optimum fluence point where ablation rate is highest could be found by two methods. We have proved that material removal rate also depends on the lateral distance between pulses on the sample surface and has optimum value as well (Fig. 1).

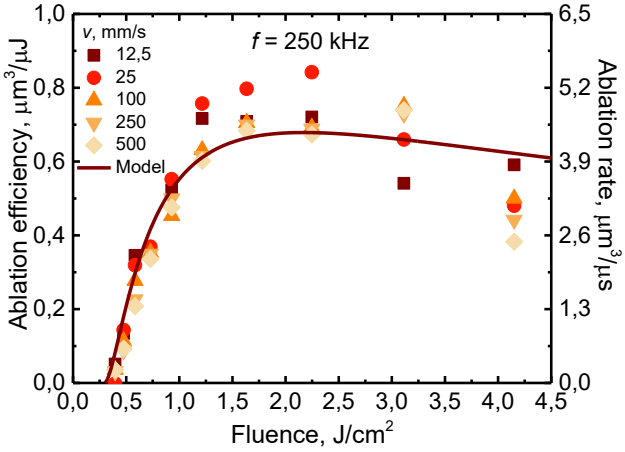

Fig. 1. Laser ablation rate and efficiency have optimum fluence and beam scanning speed points.

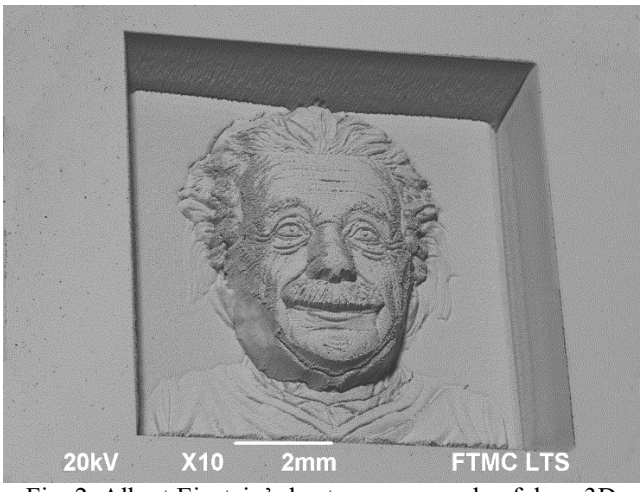

Fig. 2. Albert Einstein's bust as an example of deep 3D laser engraving.

Furthermore, the processed surface had the highest quality at optimum processing parameters. That means that optimisation of ablation rate automatically optimises quality as well. This is very important for laser micromachining as a developing technology since both ablation rate and quality are the most crucial parameters. From experimental results of cavities ablation in copper, we have estimated laser processing parameters, which later were used for deep 3D engraving of Albert Einstein's bust (Fig. 2).

[1] J. Winter, S. Rapp, M. Schmidt, and H. P. Huber, Ultrafast laser processing of copper: A comparative study of experimental and simulated transient optical properties, *Appl. Surf. Sci.* **417**, 2–15 (2017).

[2] B. Jaeggi, S. Remund, R. Streubel, B. Goekce, S. Barcikowski, and B. Neuenschwander, Laser Micromachining of Metals with Ultra-Short Pulses : Factors Limiting the Scale-Up Process, *J. Laser Micro/Nanoeng.* **12**, 267–273 (2017).

ELECTROCHEMICAL DEPOSITION OF CONDUCTING POLYMER POLYANILINE ONTO TEXTILE ELECTRODE

Mindaugas Gicevicius[1,2*], Arunas Ramanavicius[1,3]

[1] Department of Physical Chemistry, Faculty of Chemistry and Geosciences,
Vilnius University, Naugarduko str. 24, Vilnius, Lithuania
[2] NanoTechnas – Center of Nanotechnology and Materials Science, Faculty of Chemistry and Geosciences,
Vilnius University, Naugarduko str. 24, Vilnius, Lithuania
[3] Department of Material Science and Electrical Engineering,
Center for Physical Sciences and Technology, Saulėtekio av. 3, Vilnius, Lithuania
mindaugas.gicevicius@gmail.com

Development of new functional materials and composites may accelerate the advancement of modern technology. The combination of textile fabrics and conducting polymers would open the path for advancement of wearable and flexible electronics, including various sensors [1], adaptive camouflage [2] and wearable displays [3]. The presented research was aimed to examine the combination of conducting polymer polyaniline and textile via electrochemical polymerization and investigate the prospects of such composites for applied use.

Polyester (PES) fabric PES/INOX (stainless steel/metal fibre) 20 tex blended yarn (80 : 20 %) known as S-shield PES [4], was produced by Schoeller GmbH & CoKG and supplied by Institute of Textile, Centre for Physical Sciences and Technology, Kaunas, Lithuania. Scanning electron microscopy image of S-Shield PES textile is given in figure 1. Alongside regular polyester yarns it contains electrically conducting stainless steel fibres which can be utilised as flexible electrodes within PES fabric matrix. This opens the prospects of both pre- and post-weaving textile surface modification via electrochemical methods and later employment of these methods to achieve greater functionality of textiles beyond traditional applications.

Deposition of conducting polymer polyaniline was performed electrochemically using cyclic voltammetry technique. The polymer was deposited from 0.5 M sulfuric acid solution containing 50 mM of the monomer. Experiments were carried out using conventional three-electrode cell where S-Shield PES served as the working electrode, Pt wire as counter electrode and Ag wire as reference electrode. Electrochemical deposition was performed by potential cycling between -0.3 V and 1.0 V for 10 cycles at 100 mV/s.

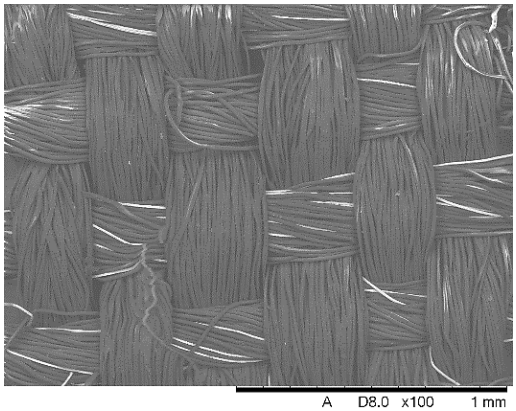

Fig. 1 Scanning electron microscopy micrograph of S-Shield PES textile

A green, well-adhered solid was observed to have formed on the surface of PES S-Shield textile electrode indicating a successful deposition of conducting polymer polyaniline. The modified textile was characterized by electrochemical and optical methods. It revealed that the polyaniline-modified textile exhibited reversible electrochemical and spectroelectrochemical character. This leads to a conclusion that textile and conducting polymer composites hold a great promise for future applications.

Acknowledgment This research was partially supported by a grant (No. 09.3.3-LMT-K-712-03-0063) from the Research Council of Lithuania.

[1] P. Calvert, D. Duggal, P. Patra, A. Agrawal, and A. Sawhney, "Conducting polymer and conducting composite strain sensors on textiles," *Mol. Cryst. Liq. Cryst.*, vol. 484, 2008.
[2] W. Kang, M. F. Lin, J. Chen, and P. S. Lee, "Highly Transparent Conducting Nanopaper for Solid State Foldable Electrochromic Devices," *Small*, pp. 1–8, 2016.
[3] M. A. Invernale, Y. Ding, and G. A. Sotzing, "All-Organic electrochromic spandex," *ACS Appl. Mater. Interfaces*, vol. 2, no. 1, pp. 296–300, 2010.
[4] S. Varnaite, "The use of conductive yarns in woven fabric for protection against electrostatic field," *Medziagotyra*, vol. 16, no. 2, pp. 133–137, 2010.

UPCONVERSION LUMINESCENCE OF $Lu_6(W,Mo)O_{12}:Yb^{3+}/Er^{3+}$ PHOSPHORS WITH RHOMBOHEDRAL AND CUBIC CRYSTAL STRUCTURE

Egle Ezerskyte, Arturas Katelnikovas

Faculty of Chemistry and Geosciences, Vilnius University, Naugarduko 24, LT-03225 Vilnius, Lithuania
eglezerskyte@gmail.com

There are many factors contributing to the colour of upconversion emission such as chemical composition of matrix, crystalline structure of upconverting materials, etc. The purpose of this research is to determine whether the colour of upconversion emission can be controlled by modifying the band gap of the host matrix. Therefore, the matrix of $Lu_6(W,Mo)O_{12}$ was chosen for this research since by changing the ratio of tungsten and molybdenum band gap can be easily manipulated.

With regard to establish band gap variations in these upconverting phosphors, samples of $Lu_6(W,Mo)O_{12}$ with rhombohedral structure were synthesized via high temperature solid-state reaction. The stoichiometric amounts of precursors (Lu_2O_3, WO_3, MoO_3) were blended in the agate mortar employing acetone as the grinding media. The obtained powders were transferred to the corundum crucibles and annealed at 1600 °C for 5 h in air. The process of calcination was repeated twice. Compounds with cubic crystal structure were prepared by aqueous sol-gel method with final sintering of the gel at 1000 °C for 2 h in air. The same methods were applied to produce $Lu_6(W,Mo)O_{12}:Yb^{3+}/Er^{3+}$ samples (precursors: Lu_2O_3, WO_3, MoO_3, Yb_2O_3 and Er_2O_3) with intent to analyse the influence of band gap and crystal structure on the upconversion luminescent properties in these compounds [1] [2].

The investigation of structural, morphological and optical properties of the synthesized compounds was carried by powder X-ray diffraction (XRD), scanning electron microscope (SEM) analysis and UV-Visible spectroscopy.

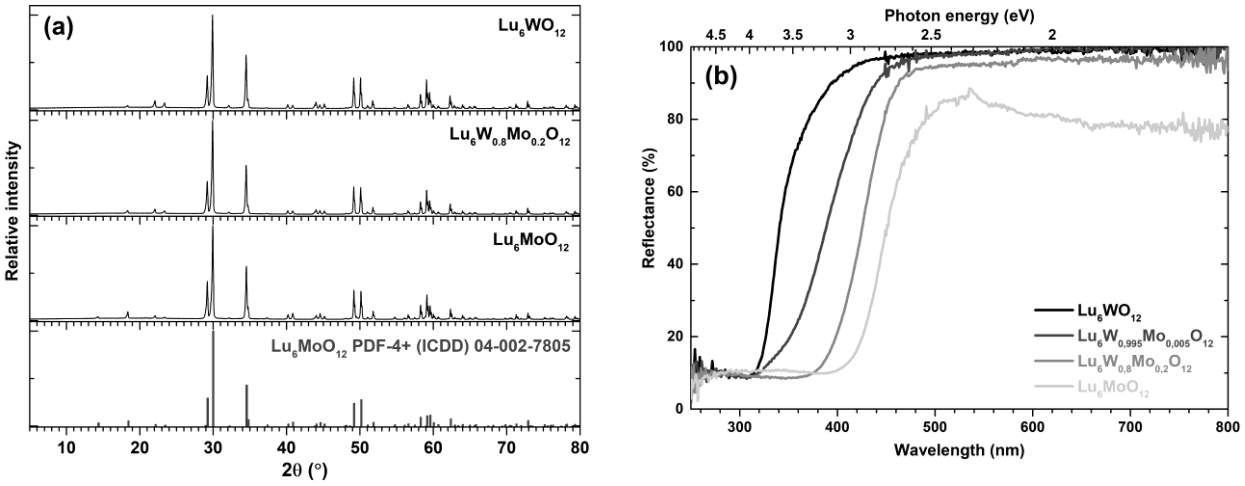

Fig. 1. XRD patterns (a) and reflection spectra (b) of rhombohedral $Lu_6(W,Mo)O_{12}$ samples with different W/Mo ratios.

XRD patterns of $Lu_6(W,Mo)O_{12}$ samples with rhombohedral crystal structure are shown in Fig. 1a. Single phase compounds are obtained at any W/Mo ratio. The reflection spectra of $Lu_6(W,Mo)O_{12}$ samples with rhombohedral crystal structure are given in Fig. 1b. The absorption of the host shit to the longer wavelengths when Mo concentration in the structure increases. Moreover, the band gap values of the synthesized $Lu_6(W,Mo)O_{12}$ samples were calculated from reflection spectra applying Kubelka-Munk function. Depending on tungsten and molybdenum ratio in prepared $Lu_6(W,Mo)O_{12}$ samples band gap varies from 2.66 eV (467 nm) to 3.57 eV (348 nm).

Upconversion emission (λ_{ex} = 980 nm) spectra of $Lu_6(W,Mo)O_{12}:Yb^{3+}/Er^{3+}$ samples were also measured and analysed. The strongest emission was observed in the red spectral range. Moreover, the CIE colour space coordinates and luminous efficacies were calculated and will be discussed.

[1] N. Diot, P. Benard-Rocherulle, R. Marchand, X-ray powder diffraction data and Rietveld refinement for Ln_6WO_{12} (Ln=Y, Ho), Powder Diffraction 15 (4), 220-226 (2000).

[2] A. V. Shlyakhtina, S. N. Savvin, N. V. Lyskov et al., Polymorphism in the family of $Ln_{6-x}MoO_{12-\delta}$ (Ln = La, Gd – Lu; x = 0, 0.5) oxygen ion- and proton-conducting materials, J. Mater. Chem. A 2017 (5), 7618-7630 (2017).

Collective modes in SNOM reflectivity of doped graphene on a substrate

Dominik Kreil, Michaela Haslhofer, Helga M. Böhm

Institut für Theoretische Physik, Johannes Kepler University, Linz Austria
dominik.kreil@jku.at

Since the first fabrication of graphene by Geim and Noveselov [1], honored with a Nobel Price in 2010, the run for this intrinsic two-dimensional (2D) material is far from coming to a rest. Electrons near the K point of the conduction– and valence band behave like massless Dirac fermions, ensuring extraordinary conductivity and promising cost-effective applications via graphene plasmonics [2]. With conventional 2D systems, e.g. semiconductor heterostructures, graphene shares a square-root plasmon dispersion for small wave vectors, so that studying this collective mode in thin systems with light is a challenge. Fei et al. [3] overcame this difficulty by measuring the reflectivity of a graphene sheet on SiO_2 using optical scanning near field microscopy (SNOM), and succeeded in exciting and detecting plasmons in the graphene. For damped collective modes the definition of their dispersion is quite ambiguous and depends on the experimental setup. They are all based on the complex dielectric function $\varepsilon(q,\omega) = \varepsilon_{\mathrm{I}}(q,\omega) + i\,\varepsilon_{\mathrm{II}}(q,\omega)$ (with energy- and momentum-transfer $\hbar\omega$ and $\hbar q$, respectively), and, though closely related, are equivalent only in damping-free regions [4]. Here, we compare the plasmon dispersion in graphene obtained from the following conventions:

(a) the loss function, $-\mathrm{Im}\,\varepsilon^{-1}(q,\omega)$, proportional to the scattering cross section, being maximal at $\omega_{\mathrm{pl}}^{(\mathrm{a})}(q)$

(b) the complex $\varepsilon(q,\omega)$ vanishing for complex ω_0 with $\omega_{\mathrm{pl}}^{(\mathrm{b})}(q) \equiv \Re e\,\omega_0(q)$, determining reflection coefficients

(c) the frequent approximation of the latter as the zero of $\Re e\,\varepsilon(q,\omega)$ at $\omega_{\mathrm{pl}}^{(\mathrm{c})}(q)$ (with $\omega_{\mathrm{pl}}^{(\mathrm{c})}$ always lower than $\omega_{\mathrm{pl}}^{(\mathrm{a,b})}$)

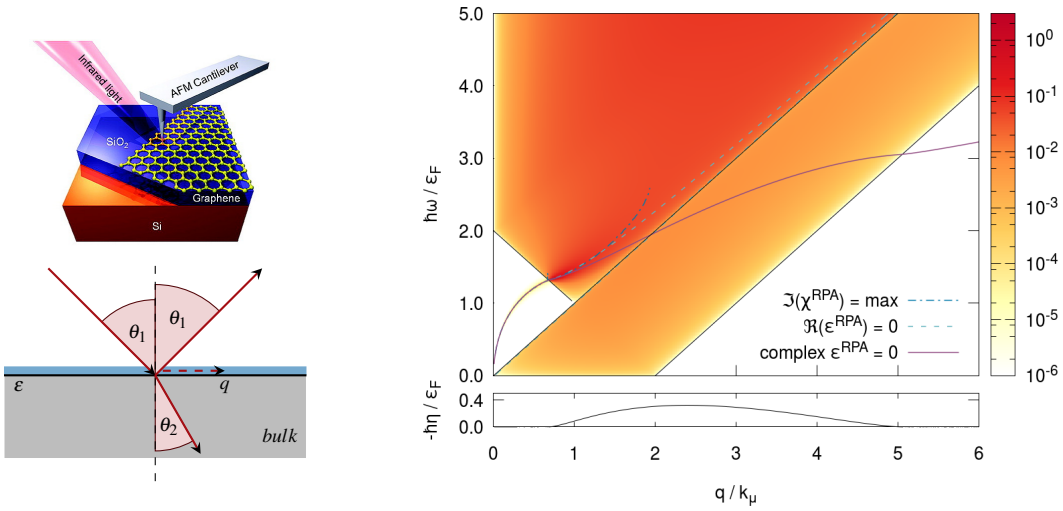

Fig. 1. (**left:**) SNOM setup [3] (top) with the graphene sheet on a SiO_2 bulk substrate. An AFM tip illuminated with infrared light induces longitudinal excitations in the sheet. Compared to a typical scattering experiment (bottom), the perpendicular wave vector in SNOM is very small. (**right:**) Calculated RPA loss function of graphene on SiO_2. The lines give the collective modes for the three different definitions. On the bottom, the damping of the plasmon is shown. Here, k_{F} denotes the the largest ground-state wave vector and ε_{F} the corresponding energy.

After a brief introduction to the theory of sheet reflectivity, we present calculations of the dielectric function as well as the sheet reflectivity of graphene on a bulk sybstrate. Here, we use linear response theory and the random phase approximation (RPA) [3, 5]. The loss function obtained this way, togehter with the prospective collective modes $\omega_{\mathrm{pl}}^{(\mathrm{a,b,c})}(q)$ are shown in Fig.1 (right). We discuss the discrepancies resulting from the different definitions of the plasmon and compare them to the available experimental results. To better include correlation effects for large q, advanced techniques have to be used [6]. In future work, we plan to include spin-orbit coupling into the theory. This will also cover more complex materials like MoS_2, a promising candidate for valleytronics.

[1] Kostya S Novoselov, Andre K Geim, SV Morozov, D Jiang, Y_ Zhang, SV Dubonos, IV Grigorieva, and AA Firsov. Electric field effect in atomically thin carbon films. Science, 306(5696):666–669, 2004.

[2] A. N. Grigorenko, M. Polini, and K. S. Novoselov. Graphene plasmonics. Nature Photonics, 6(11):749–758, 2012.

[3] Zhe Fei, Gregory O Andreev, Wenzhong Bao, Lingfeng M Zhang, Alexander S. McLeod, Chen Wang, Margaret K Stewart, Zeng Zhao, Gerardo Dominguez, Mark Thiemens, et al. Infrared nanoscopy of Dirac plasmons at the graphene–SiO2 interface. Nano Letters, 11(11):4701–4705, 2011.

[4] Raphael Hobbiger, Jürgen T. Drachta, Dominik Kreil, and Helga M. Böhm. Phenomenological plasmon broadening and relation to the dispersion. Solid State Communications, 252:54 – 58, 2017.

[5] Gabriele Giuliani and Giovanni Vignale. Quantum theory of the electron liquid. Cambridge University Press, 2005.

[6] Dominik Kreil, Raphael Hobbiger, Jürgen T Drachta, and Helga M Böhm. Excitations in a spin-polarized two-dimensional electron gas. Physical Review B, 92:205426, 2015.

EFFECT OF HYDROGEN PRE-TREATMENT ON SiC-ON-Si EPITAXIAL GROWTH

Mikhail Lobanok, Andrei Novikau, Stanislau Prakopyeu, Peter Gaiduk

Department of Physical electronics and nanotechnology, Belarusian State University, Minsk
mishalobanok@gmail.com

Silicon Carbide (SiC) and its polytypes are of huge interest for power and opto-electronic devices. SiC has a unique combination of physical and chemical properties: a wide bandgap, attractive thermal and chemical properties, elevated electron drift velocity and high break-down voltage. On the other hand, SiC substrates are too expensive for commercial mass-production, therefore the development of the methods for defect-free epitaxial growth of SiC layers on the Si substrates is of great necessity. The task of SiC-on-Si growth is very complex because Si and SiC have different thermal expansion coefficients and there is a significant lattice misfit [1-2]. Another reason for defects in hetero-epitaxial SiC is the presence of SiO_2 islands on the surface of Si-substrate [3]. These islands might be removed by interaction with hydrogen atoms during thermal treatment in vacuum [3]. In addition, high-temperature treatment in hydrogen-containing vacuum is expected to saturate surface layer with hydrogen atoms resulting in modification of lattice parameters and reduction of structural defects. Therefore, in this work we used hydrogen treatment of Si substrate to make it relevant for the growth of thin epitaxial SiC layers.

The (100) Si wafers are used in this study. Just before high-temperature processing in a vacuum chamber, the samples are chemically cleaned and their surface is refreshed in 5% $HF+H_2O$ solution. Thermal treatment of the samples and the growth of SiC layer is proceeded in a tungsten-foil-based heating cell. The cell is constructed in a vacuum chamber and is equiped with a thermocouple and two gas inputs. The process is carried out in four stages. At the first stage the chamber was evacuated to $1 \cdot 10^{-3}$ Pa. After that the hydrogen is injected up to a vacuum of $8 \cdot 10^{-3}$ Pa and the samples are heated to 700 ºC for 10 min. At the third stage the temperature is increased and the carbon containing gas is injected to the heating cell. The growth of SiC layers takes place at the fourth stage and the process is carried out at 1100°C for 10 min in a vacuum better than $1 \cdot 10^{-3}$ Pa.

The structure of Si/SiC layers is finally studied by scanning electron microscopy (SEM), transmission electron microscopy (TEM), and transmission electron diffraction (TED). The LEO 1455VP and TEM Hitachi H-800 devices are used for SEM and TEM investigations respectively. The samples are prepared for TEM study by using routine chemical etching from the back side.

Fig. 1 shows representative SEM image and TED patterns of SiC layers grown on different Si substrates at 1100° C for 10 min. Comparison of diffraction spots indicates an improvement in the structural quality of SiC layers grown on a substrate treated in a hydrogen-enriched atmosphere. SEM investigations shows (Fig 1a) that the SiC layer is about 40 nm thick and the surface is rough due to nanometer-size pores in the Si substrate. The mechanisms of the growth is discussed taking into account chemical reactions on the surface and Kirkendall assisted pore formation in the Si substrate.

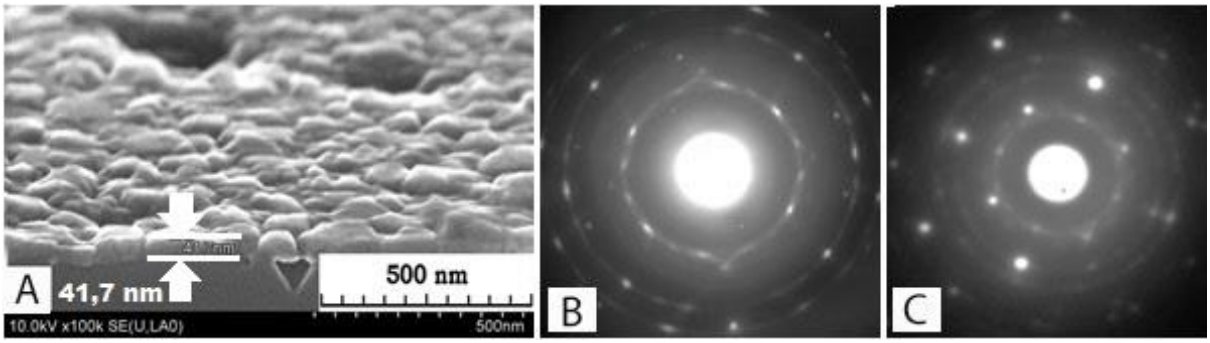

Fig 1. SEM image (a) and TED patterns (b,c) of epitaxial SiC layers, grown on the top of Si (100) substrate with (a,c) and without (b) preliminar H-plasma treatment.

[1] S.A. Kukushkin, A.V. Osipov FTT (2008) V. 50, P. 1188-1195.
[2] G. Ferro, "3C-SiC Heteroepitaxial Growth on Silicon: The Quest for Holy Grail"// Critical Reviews in Solid State and Materials Sciences, 40:56–76, 2015
[3] K.V.Ravi. Imperfections and Impurities in Semiconductor Silicon. Wiley, NY., 1981, 379 p.

Influence of thermal annealing on thick GaInAsBi layers

Sandra Stanionytė, Vaidas Pačebutas, Bronislovas Čechavičius, Andrius Bičiūnas, Virginijus Bukauskas, Andrejus Geižutis, Arūnas Krotkus

Center for Physical Sciences and Technology, Saulėtekio ave. 3, LT-10257, Vilnius, Lithuania
sandra.stanionyte@ftmc.lt

AIII-BV group compounds are attractive due to their wide applications in optoelectronics. GaInAs compound lattice-matched to InP for a quite long time was suitable for optoelectronics devices operating in telecommunications "windows" and in near-infrared region up to ~1.7 μm wavelengths. Dilution of GaInAs by Bi could lead to engineering of good alternative compound for longer wavelengths applications. It was demonstrated that even low content of Bi can considerably reduce the bandgap (Eg) of semiconductor. Moreover, the conditions for epitaxial growth of lattice-matched GaInAsBi to InP substrate can be realized by optimization of In and Ga ratio as well Bi content. Theoretically the working range of such GaInAsBi/InP systems can reach 6 μm [1].

In this work, thick GaInAsBi epitaxial layers were grown by molecular beam epitaxy (MBE) on semi-insulating (100)-oriented InP:Fe substrates with GaInAs buffer layer. The buffer layer thickness varied from 100 nm to 650 nm. Two compositions of buffers were used: lattice-matched to InP:Fe substrate and lattice-matched to bismide layer. 300 nm thick bismide layers were grown at 280°C-300°C substrate temperature with growth rate of 300 nm/h. Two different flux ratios of In/Ga were kept for GaInAsBi layers growth on different buffer layers. The Bi/Ga flux ratio in both cases varied in order to introduce the larger content of bismuth and fulfil the conditions of lattice-matching of buffer and bismide in-plane. The effect of the annealing on structure and optical characteristics of quaternary GaInAsBi alloy were investigated. Layers were annealed at rapid thermal annealing oven for 180 s at temperatures ranging from 450°C to 750°C.

For evaluation of structural quality the ω-2θ rocking curves of (004) reflex and reciprocal space mappings (RSM) of (115) reflex were measured and analysed. The modelling of measured rocking curves allowed estimating the incorporation of Bi up to 3.6% in quaternary compound lattice. The reciprocal space mapping measurements demonstrated that both buffer and the bismide layers are fully strained (Fig. 1).

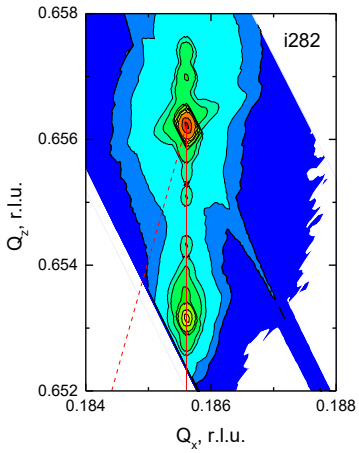

Fig. 1. Reciprocal space map of (115) reflex measured for the GaInAsBi with 3,6% Bi layer

Both annealed and as-grown GaInAsBi layers were characterized by optical absorption, photomodulated reflectance, photoluminescence (PL) measurements. The carrier lifetimes were determined from the optical pump – THz probe measurements. Complex study of GaInAsBi properties showed an improvement of optical characteristics. It was found that rapid thermal annealing at temperatures in the range of 650-700°C improves photoluminescence intensity, extends carrier lifetime and enhances electron mobility. Strong PL signals at longer than 2.2 μm light wavelengths and relatively long lifetimes evidence that this quaternary compound could be prospective for IR optoelectronic applications.

[1] J. P. Petropoulos, Y. Zhong, J. M. O. Zide. Optical and electrical characterization of InGaBiAs for use as a mid-infrared optoelectronic material. Applied Physics Letters 99 031110 (2011).

HRTEM STUDY OF SIZE-CONTROLLED BI QUANTUM DOTS IN ANNEALED GAASBI/ALAS MQW STRUCTURE

Martynas Skapas[12], Renata Butkutė[1], Sandra Stanionytė[1], Evelina Pozingytė[1]
[1] Center for Physical Science and Technology, Lithuania
[2] Faculty of Physics, Vilnius University, Lithuania
Martynas.skapas@ftmc.lt

High Resolution Transmission Electron Microscopy (HRTEM) is the premier tool for understanding of the internal microstructure of materials at nanometer level. This method allows to distinguish real-space nano-scale peculiarities in material, and simultaneously from Fast Fourier Transform (FFT) diffraction patterns obtain the information about crystalline lattice of the investigated specific regions in the nanostructures, such us, nanoparticles, quantum dots, and etc.

In this work, MBE grown and thermally treated GaAsBi/AlAs quantum wells were studied by structural (High-Resolution X-ray Diffraction, HRTEM) and optical (PL) characterizations. The analysis of profile of GaAsBi/AlAs QWs containing Bi-nanoparticles measured by HRTEM and Scanning Transmission Electron Microscopy in High-Angle Annular Dark-Field (STEM HAADF) mode were performed to evaluate the influence of annealing on orientation of nanoparticles and strain distribution in whole quantum structure. Energy Dispersive X-ray Spectroscopy (EDS) mapping and STEM HAADF revealed re-distribution of Bi atoms in GaAsBi quantum wells during high temperature annealing and formation of semiconducting Bi nanoparticles in the wells of GaAsBi with lower Bi content. The significant changes in crystalline lattice of GaAsBi quantum wells were shown by HRXRD ω-2θ scans. Also, the PL measurements demonstrated the additional low-energy peak appeared in the spectra after thermal treating, and attributed to semiconducting Bi-nanoparticles.

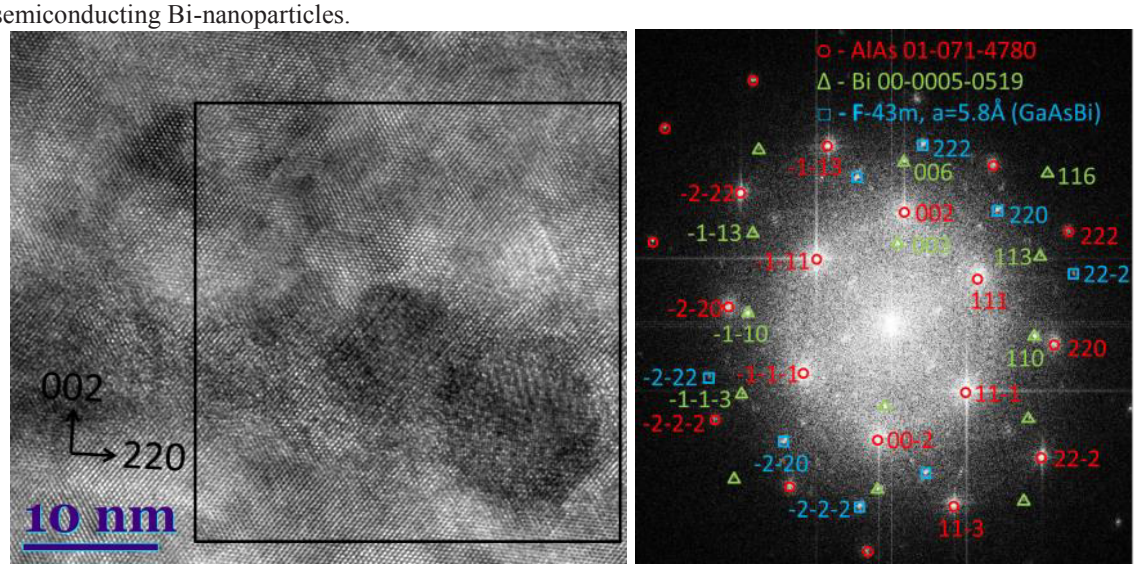

Fig. 1. HRTEM micrograph of AlAs/GaAsBi QW (left) and FFT transform of selected area with determined chemical phases (right)

[1] R. Butkutė, G. Niaura, E. Pozingytė, B. Čechavičius, A. Selskis, M. Skapas, V. Karpus, A. Krotkus, "Bismuth Quantum Dots in Annealed GaAsBi/AlAs Quantum Wells". Nanoscale research letters, 12 (2017) 436. doi: 10.1186/s11671-017-2205-7

COMPARATIVE ANALYSIS OF RECOMBINATION CHARACTERISTICS AND PHOTOIONIZATION SPECTRA IN REACTOR NEUTRONS IRRADIATED GaN

Laimonas Deveikis, Tomas Čeponis, Eugenijus Gaubas, Dovilė Meškauskaitė, Jevgenij Pavlov, Vytautas Rumbauskas

Institute of Photonics and Nanotechnology, Vilnius University, Saulėtekio av. 3, LT-10221, Vilnius, Lithuania
laimonas.deveikis@ff.stud.vu.lt

GaN is a promising wide band-gap material for fabrication of the solar-blind photo-sensors and radiation tolerant particle detectors applied in high energy physics, radiation monitoring and other fields [1]. Wide band-gap determines low leakage current and proper radiation hardness of devices made of these materials. High luminescence efficiency is also an attractive characteristic of GaN. Crystals of large thickness (300-600 μm) and high resistivity ($\geq 10^6$ Ωcm) can also be used for manufacturing of the capacitor type particle sensors with high sensitivity. Acceptor type impurities are often introduced during growth of GaN to reach high resistivity of the material. However, technological defects and impurities introduced during crystal growth process affect functional characteristics of devices made of GaN material. Radiation interacting with material can also produce damage which determines the degradation of functional parameters of devices. Therefore, it is important to characterise the initial and irradiated material by identifying the existing defects and their concentrations for manufacturing of devices of high quality. The spectroscopic methods are highly effective tools for the investigation of these defects.

In this work the pristine and reactor neutrons irradiated GaN samples of 400 μm thickness doped with Mg and Mn impurities have been investigated by contact-less techniques. Recombination characteristics have been investigated by microwave probed photoconductivity transient (MW-PC) technique. Defects and impurities have been identified by employing pulsed photoionization spectroscopy (PPIS) technique. A comparative analysis of photoionization spectra and variations of recombination characteristics in pristine and irradiated by reactor neutrons at different fluences (10^{12} - 5×10^{16} cm^{-2}) GaN samples has been performed.

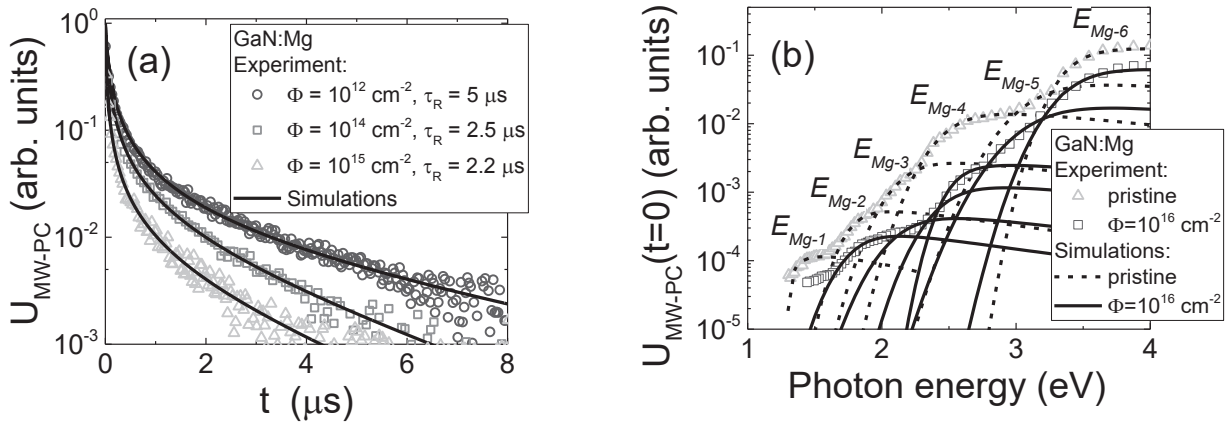

Fig. 1. (a) – Experimental (symbols) and simulated (solid curves) MW-PC transients in reactor neutrons at different fluences irradiated GaN:Mg samples. (b) – Experimental (symbols) PPIS spectra of pristine and reactor neutrons at fluence of Φ=10^{16} cm^{-2} irradiated GaN:Mg samples compared with simulated (solid and dashed curves) using Kopylov and Pikhtin model [2] energy levels.

Analysis of the MW-PC transients allowed us to determine the impact of neutron irradiation for the excess carrier lifetime in GaN. It was found that carrier lifetime drops by the factor of 60 in GaN:Mg and 3 in GaN:Mn samples irradiated by reactor neutrons at fluence of Φ=5×10^{16} cm^{-2} in comparison with the pristine GaN material. The analysis of PPIS spectra allowed us to identify the existing defects and impurities in pristine and reactor neutrons irradiated GaN samples. The comparative analysis of the MW-PC transients and PPIS spectra as well as the procedure for identification of defects and impurities in pristine and reactor neutrons irradiated GaN material doped with Mg and Mn impurities will be presented.

[1] S. J. Pearton, *GaN and related materials II*, (Gordon and Breach Science Publishers, Amsterdam, 2000).
[2] A. A. Kopylov and A. N. Pikhtin, Profiles of absorption and luminescence spectra of deep centers in semiconductors (oxygen in gallium-phosphide), Sov. Phys. Solid State **16**, 1200 (1975).

TOWARDS SUB-THZ RESONANT-TUNNELLING-DIODE OSCILLATORS WITH HIGH EMISSION EFFICIENCY

Andrius Vaitkūnas, Michael Feiginov

TU Wien, EMCE Institute, THz-electronics group, Austria
andrius.vaitkunas@tuwien.ac.at

Terahertz (THz) frequency range lies between infrared and microwave frequencies, therefore both electronic and optical devices are being investigated as THz sources [1]. As scientific equipment, THz sources and systems are well developed and available in many research laboratories nowadays. However, the THz sources are still extremely complex, bulky and expensive for practical applications. Resonant-tunneling-diode (RTD) oscillators have reemerged in the recent years as a promising enabling technology of room-temperature THz and sub-THz sources for real-world applications [2,3]. RTD oscillators are operating close to 2 THz nowadays, they can emit up to ~0.5 mW of the output power at sub-THz frequencies and they could be as small as a fraction of mm^2. Nevertheless, the output power and efficiency of RTD oscillators still need to be improved to meet the application requirements.

An RTD oscillator consists of a resonant antenna (usually, a slot one) integrated with an RTD. RTD provides gain in a wide frequency range and a resonant antenna is required to define the frequency of an oscillator, see schematic in Fig.1a. Since THz RTDs have relatively high capacitance (~10 $fF/\mu m^2$), they have a strong impact on the resonant properties of the antenna. The oscillation frequency is determined by the interplay of the parameters of the RTD and of the antenna. E.g., due to high capacitance of the RTD, the slot antenna dimensions are usually much smaller than the radiation wavelength, therefore such antennas have a low radiation efficiency. Design of an efficient RTD oscillator is not a trivial task. One needs to find a proper balance between the properties of the antenna (e.g., by adjusting its dimensions) and RTD (its area, gain and other parameters). For example, the antenna radiation efficiency should be sufficiently high to make an efficient oscillator, but it should not be too high, otherwise the RTD gain will not be sufficient to compensate for the oscillator losses.

In this work, we optimize the parameters of slot antenna and RTD dimensions to maximize the oscillator output power. We have been considering slot antennas with the geometry typical for on-chip RTD oscillators, Fig.1a. Such oscillators are mounted on Si-lenses for collimation of the emitted radiation. We were varying the width and the length of the slot and adjusting the RTD area to match the target oscillation frequency, which was 300 GHz in this optimization run. The antenna characteristics have been calculated with the 3D electromagnetic simulator (CST STUDIO SUITE® 2018). Then they were combined with the RTD parameters, calculated with high-frequency RTD models developed by us in the past [4, 5]. In the work, we were using RTDs with the parameters similar to those used in the previous experimental works [3]. The optimization results indicate, that such RTD oscillators could provide an output power at the level of ~0.5 mW (see Fig.1b), which is a quite high value, considering a relatively small RTD area of ~1 μm^2 and very low RTD current density of ~2.5 $mA/\mu m^2$. The simulations also indicate that the DC to sub-THz conversion efficiency (η) could be at the level of ten or even tens percents, which is a surprisingly high level compared to η at the level of few percents reported in the literature till now. The optimization results should be verified experimentally at a later stage.

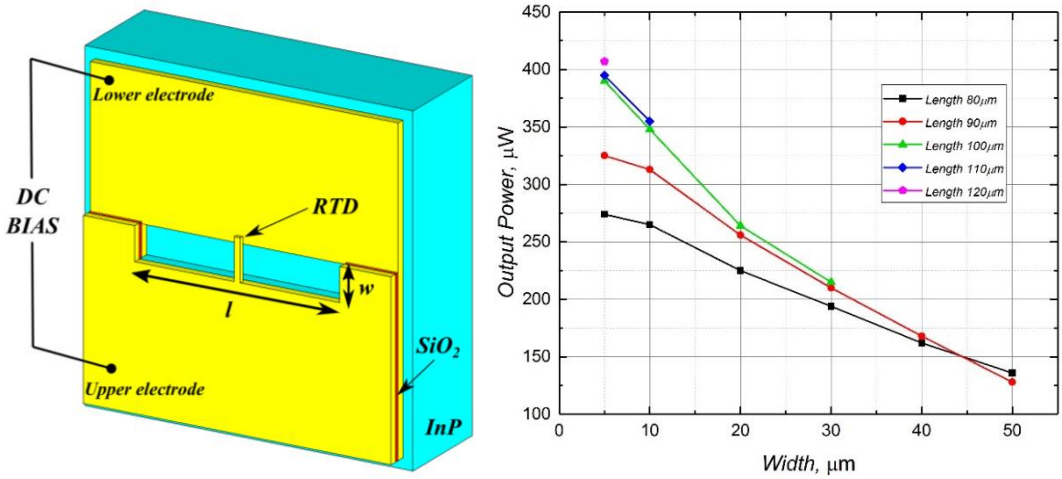

Fig. 1. (a) Schematic view of RTD oscillator slot antenna. (b) Device output power dependence on the width of slot antenna. Oscillation frequency - 300GHz.

[1] M. Tonouchi, Nat. Photonics 1, 97–105 (2007).
[2] S. Suzuki, M. Asada, A. Teranishi, H. Sugiyama, and H. Yokoyama, Appl. Phys. Lett. 97, 242102 (2010).
[3] M. Feiginov, C. Sydlo, O. Cojocari, and P. Meissner, Appl. Phys. Lett. 99, 233506 (2011).
[4] M. N. Feiginov, Appl. Phys. Lett. 76, 2904 (2000).
[5] M. N. Feiginov, Appl. Phys. Lett. 78, 3301 (2001).

AlGaN/GaN HEMT-based THz Detectors for a High-Resolution THz Camera

Dovilė Čibiraitė[1], Maris Bauer[2], Adam Rämer[3], Serguei Chevtchenko[3], Alvydas Lisauskas[1,4], Viktor Krozer[1,3], Wolfgang Heinrich[3], and Hartmut G. Roskos[1]

[1]Physikalisches Institut, Goethe-Universität Frankfurt, 60438 Frankfurt am Main, Germany
[2]Fraunhofer ITWM, Kaiserslautern, Germany
[3]Ferdinand-Braun-Institut, Leibniz-Institut für Höchstfrequenztechnik, 12489 Berlin, Germany
[4]Department of Radiophysics, Vilnius University, 01513 Vilnius, Lithuania
cibiraite@physik.uni-frankfurt.de

THz detection based on resistive mixing and enhanced by plasmonic effects at high frequencies is an important feature in the THz photonics field [1, 2]. Until now, the highest sensitivity has been reached with silicon CMOS devices with narrow-band antennas, which exhibit an optical noise-equivalent power (NEP) of ≥10 pW/√Hz [3]. To improve robustness against electrostatic shock, which is a crucial aspect in many applications, as well for a multiple-pixel array, we use III-V group materials, namely GaN/AlGaN HEMTs, for an effective THz detection [4]. After an extensive optimization effort on the single device fabrication technology and the device design, published in [5, 6], here we present the device characterization and sensitivity enhancement at low temperatures.

GaN/AlGaN TeraFETs were developed to work with various types of integrated broadband antennas and substrate-side radiation coupling. The best performance is achieved with FETs with integrated bow-tie antenna. These devices have a gate width of 3 µm, a channel length of 900 nm, and a small gated-channel length of only 100 nm, which is possible by advances of the fabrication technology.

The room-temperature optical NEP of these TeraFETs was measured at frequencies from 0.1 THz to 1.2 THz with a Toptica TeraScan 1550 system and a RPG radiation source. The data for the two different sources are compared with each other in figure 1. At room temperature, we determine a state-of-the-art optical NEP for quasi-optical detectors of 25.4 pW/√Hz at 490 GHz. The maximum current responsivity $\mathscr{R}_I$ reaches 104 mA/W. These values are usually achieved only with narrow-band antennas in other material systems. Concerning these key quantities, GaN/AlGaN TeraFETs are now competitive with Si CMOS room-temperature THz detectors.

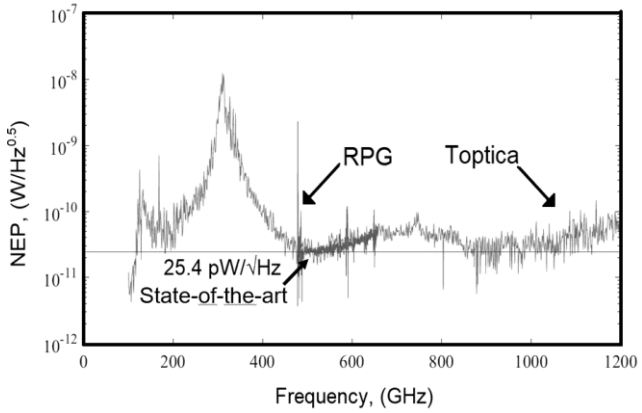

Fig. 1. Room-temperature optical NEP of broadband GaN/AlGaN bow-tie TeraFET with the gated-channel length of 100 nm measured with Toptica TeraScan 1550 system (light gray line) and RPG source (black line). Arrow shows the state-of-the-art optical NEP at 490 GHz frequency.

Further characterization of GaN/AlGaN TeraFETs proved the noise limitation to be given only by thermal noise as it is the case also for other material systems. Upon cryogenic cooling of a device, we observed an improvement of the best NEP by a factor of 13.8 and of the maximum current responsivity by a factor of 3.8 at 630 GHz at liquid nitrogen temperature. Measurements at cryogenic temperatures enable us also to adapt the Dyakonov-Shur responsivity formula for real devices and to use this advanced device model as the main tool for the extraction of internal device parameters needed for further device improvement. From such devices, we have already built a 12 x 12 pixel integrated array for a camera implementation.

[1]. W. Knap et al., Nonresonant detection of terahertz radiation in field effect transistors, J. Appl. Phys. **91**, 9346-9353, (2002).
[2] S. Boppel et al., CMOS integrated antenna-coupled field-effect transistors for the detection of radiation from 0.2 to 4.3 THz, IEEE Trans. Microw. Theory Tech. **60**, 3834–3843, (2012).
[3] M. V. Ryzhii et al., Fundamental And Applied Problems Of Terahertz Devices And Technologies, RJUSE TeraTech, 23, (Oct. 31 – Nov. 4 2016).
[4] M. Bauer et al., High-sensitivity wideband THz detectors based on GaN HEMTs with integrated bow-tie antennas, Proc. 10th Europ. Microw. Integr. Circ. Conf. (EuMiC 2015), Paris, 1–4, (Sep. 7-8, 2015).
[5] M. Bauer et al., Highly-sensitive AlGaN/GaN HEMT terahertz detectors with integrated broadband bow-tie antennas, submitted to IEEE Trans. Terahertz Sci. Technol.
[6] M. Bauer et. al., Optimization of the design of terahertz detectors based on Si CMOS and AlGaN/GaN field-effect transistors, Internat. J. High Speed Electr. and Syst. **25**, 1640013, (2016).

INVESTIGATION OF A P-TYPE InAs USING A NOVEL MODIFIED DOUBLE-PUMP-PULSE TERAHERTZ EMISSION METHOD

Ieva Beleckaitė[1], Lukas Burakauskas[1,2], Ramūnas Adomavičius[1]

[1]Center for Physical Sciences and Technology, Saulėtekio av. 3, Vilnius, Lithuania
[2]Department of Physics, University of Oxford, Parks Rd, Oxford OX1 3PU
ieva.beleckaite@ftmc.lt

In recent years terahertz (THz) time-domain (TDS) spectroscopy systems have become more accomplished and found its application in various fields. One of the main component of such systems is a THz pulse emitter which could be made of various semiconductors, their compounds and nanostructures. In order to create more effective THz emitter it is important to understand the physical mechanisms responsible for THz generation. For this purpose a lot of modified THz TDS methods were created. One of the modification is double-pump-pulse THz emission (DPP) method that was first mentioned in 2002 by Tanouchi *el al* [1]. The main idea of this method is to use two excitation pulses instead of usually used one. In this work we have analysed standard DPP method, relieved its drawbacks and suggested a novel modification of DPP (MDPP) measurements. We use MDPP method for the investigation of THz emission efficiency dynamics in p-type InAs that is best-known THz surface emitter.

In MDPP measurements the First pulse creates photocarriers with the frequency of mechanical chopper and affects the THz generation process initiated by the Second pulse. In the other words it is possible to measure an indirectly modulated THz pulse which reflects the difference in THz emission initiated by the Second pulse due to the influence of the First pulse. In Fig. 1 the amplitude of indirectly modulated THz pulse dependence on a time delay between the First and the Second pulses is shown. It is obvious that THz generation properties strongly depend on the polarization of the Second pulse (Fig. 1a). The polarization of the First pulse does not affect THz generation process so heavily, nevertheless small difference under s and p polarized excitation could be seen (Fig. 1b). We have found out that the First pulse builds electric fields near the surface, while the Second pulse creates THz radiating electric dipoles upon the influence of these electric fields. In addition, we have noticed that the polarization of the optical excitation pulses could be used to change the orientation of the mentioned electric fields and dipoles. Thus it is possible to observe the influence of variously oriented electric fields upon the formation of electric dipoles and their ability to emit THz pulses. Moreover, the MDPP method becomes a tool to investigate the dynamics of the electric fields created after photoexcitation.

Our suggested method is shown to be a precise and sensitive way to study electric fields in semiconductors and electric properties of photocarriers after photoexcitation. Received results would lead to a better understanding of THz generation process that could help to create more efficient THz emitters. Furthermore, the time resolution of MDPP method is a few hundreds of femtoseconds therefore it is a promising tool to investigate rapid processes, such as the ballistic electron transport dynamics.

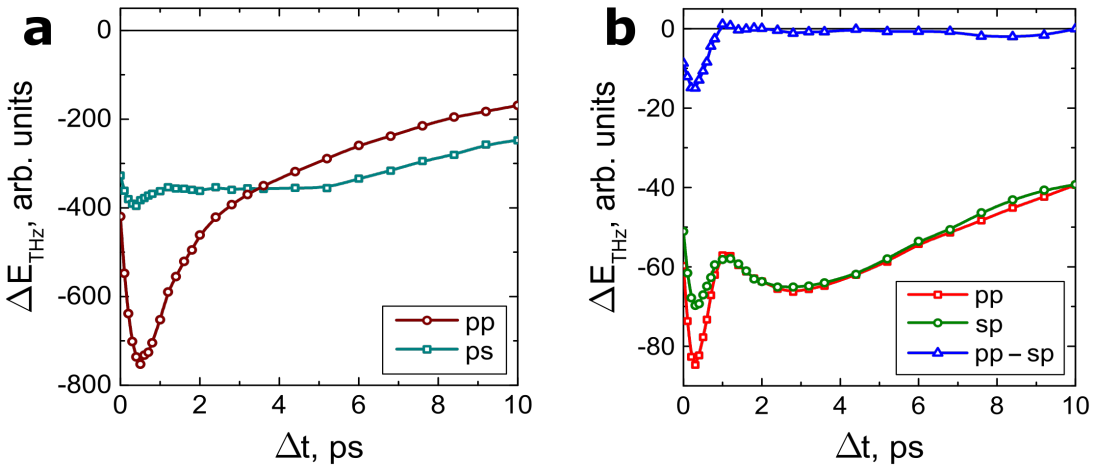

Fig. 1. Indirectly modulated THz pulse amplitude dependence on a time delay between two excitation pulses. (a) The First pulse is always p-polarized while the Second pulse is p-polarized (pp) or s-polarized (ps). (b) The Second pulse is always p-polarized while the First pulse is p-polarized (pp) or s-polarized (sp). Blue curve represents the difference in THz generation under p and s polarization of the First pulse. Results in (a) and (b) were obtained at a different azimuthal angle.

[1] M. Tonouchi, N. Kawasaki, T. Yoshimura, H. Wald, and P. Seidel, Pump and Probe Terahertz Generation Study of Ultrafast Carrier Dynamics in Low-Temperature Grown-GaAs, Japanese Journal of Applied Physics **41**(Part 2, No 6B), L706 (2002)

PHENANTHROIMIDAZOLE HOSTS FOR RED OLEDS EXHIBITING THERMALLY ACTIVATED DELAYED FLUORESCENCE

Domantas Berenis, Dovydas Banevičius, Edvinas Radiunas, Karolis Kazlauskas, Saulius Juršėnas

Institute of Photonics and Nanotechnology, Vilnius University, Lithuania
domantas.berenis@ff.stud.vu.lt

Organic light-emitting devices (OLEDs) already dominate the smartphone and tablet display market due to low power consumption, relatively cheap mass production technology and potential flexibility [1]. In most cases phosphorescent OLEDs capable of converting 100% of created excitons into photons are used. Unfortunately, emitters in these devices contain heavy metal (typically iridium or platinum) atoms, which make them rather expensive. Recently, next generation OLEDs based on thermally activated delayed fluorescence (TADF) were realized. This phenomenon also enables achieving 100% of internal quantum efficiency by reverse inter-system crossing (RISC) from exciton triplet state to radiative singlet state in the materials with small singlet-triplet energy separation (of a few k_BT) [2]. Although substantial progress has been made in research of blue-orange TADF OLEDs only a few attempts were made to realize efficient red TADF OLEDs. Main difficulties arise from the enhanced non-radiative decay in low bandgap emitters. Moreover, to avoid emitter concentration quenching in OLEDs, emissive (guest) molecules are doped in a host material at low concentration. TPBi is a widely used host [3,4], however, due to the wide energy gap between the highest occupied and lowest unoccupied molecular orbitals and relatively small hole mobility, it may not be the optimal host option. In this work we investigate new host materials (alternatives to TPBi) based on phenantroimidazole, possessing narrower energy gap and exhibiting bipolar charge transport.

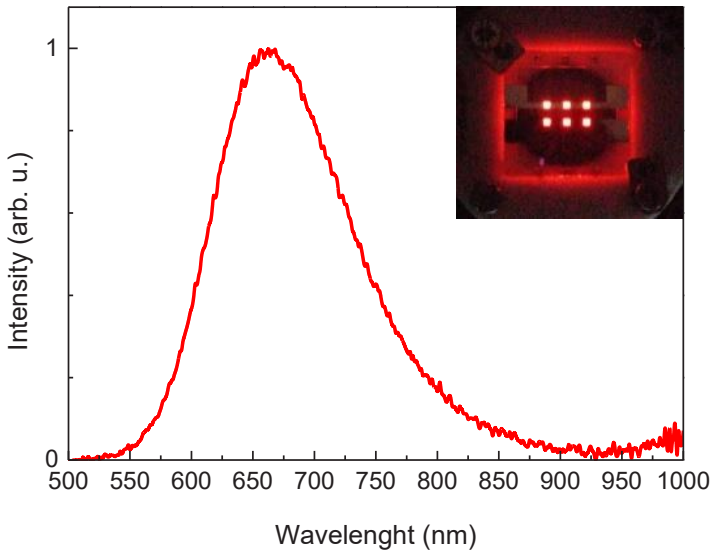

Fig. 1. Electroluminescence spectra of fabricated TADF OLED. Inset shows picture of the device.

The search of the suitable host material for deep red TADF emitter – TPA-DCPP (TPA = triphenylamine; DCPP = 2,3-dicyanopyrazino phenanthrene), referred as a guest, was conducted by estimating Förster resonance energy transfer rate from various phenantroimidazole hosts to the guest. To this end, we evaluated fluorescence spectrum, internal quantum efficiency (IQE) and excited state lifetime of the hosts and absorption spectrum of the guest. Additionally, concentration quenching experiments were carried out for the guest-host films with different guest concentrations (0.1 - 10%) to find the optimal one. Triplet energies of the hosts were deduced from their phosphorescence spectra to assure sufficient triplet exciton confinement in the emitter, i.e. negligible back-energy-transfer to a host. Finally, the selected optimal hosts were tested in red TADF OLEDs fabricated by thermal evaporation in a high vacuum. Main OLED characteristics, i.e. external quantum efficiency (EQE), current efficiency, efficiency roll-off, I-V characteristics, and electroluminescence spectra were measured. OLED structure optimization was done considering electron and hole current balance. Optimized OLED was compared with a device using conventional TPBI host.

[1] R. Mertens, The OLED Handbook (2016 edition), Lulu.com, 2012.
[2] Ch. Adachi, Third-generation organic electroluminescence materials, Japanese Journal of Applied Physics 53, 060101 (2014)
[3] P. Anzenbacher, S.Y. Takizawa, V.A. Montes, Phenylbenzimidazole-Based New Bipolar Host Materials for Efficient Phosphorescent Organic Light-Emitting Diodes, Chem. Mater. 21 (2009) 2452–2458. doi:10.1021/cm9004954.
[4] S. Wang, X. Yan, Z. Cheng, H. Zhang, Y. Liu, Y. Wang, Highly Efficient Near-Infrared Delayed Fluorescence Organic Light Emitting Diodes Using a Phenanthrene-Based Charge-Transfer Compound, Angew. Chemie - Int. Ed. 54 (2015) 13068–13072. doi:10.1002/anie.201506687.

Influence of tetravalent cerium on the luminescence properties of garnet-type scintillators

Tomas Steponavičius[1], Augustas Vaitkevičius[1], Gintautas Tamulaitis[1], Mikhail Korjik[2], Etiennette Auffray[3]

[1]Institute of Photonics and Nanotechnology, Vilnius University, Saulėtekis Avenue 9-3, Vilnius 10222, Lithuania.
[2]Research Institute for Nuclear Problems, Belarusian State University, Minsk, Belarus.
[3]CERN, Geneva, Switzerland.
tomas.steponavicius@ff.stud.vu.lt

In the late 1990s, swift developments in the fields of particle physics and medical tomography have been made. As a result, need for high quality ultra-fast scintillator materials has increased. One of the most perspective type of materials for use in the field of ultrafast detectors are garnets doped with cerium. The parameters of garnet structure materials cause it to be an attractive option for use in ionizing radiation detector systems. By changing the doping or co-doping element and the amount of it in garnet - it is possible to vary its luminescence properties. However, the processes behind the change of these properties are not well known. One of the most recent and promising discoveries is gadolinium aluminum gallium garnet $Gd_3Al_3Ga_2O_{12}$ (GAGG).

The work was aimed at investigating photoluminescence properties of GAGG:Ce. This material is known to have some of the most immense values light yield (LY), yet its decay time of PL signal is relatively large. By co-doping GAGG:Ce with Mg^{2+} it is possible to reduce decay time. However, after introducing magnesium, LY also decreases. The change of the photoluminescence properties can be assigned to the stabilization of cerium ion in a tetravalent state and because of that, it was attempted to examine the influence of magnesium co-doping on the PL parameters.

Two samples of garnets were analyzed: GAGG:Ce and GAGG:Ce,Mg. These crystals were grown in the same conditions and the only difference between them was Mg-codoping of one of the crystals.. The measurements were executed utilizing photoluminescence spectrometry equipment in semi-stationary state using adjustable values of excitation energy: 4.88 eV (254 nm) and 3.61 eV (343 nm). The samples were also investigated with confocal microscope *WITec Alpha Alpha 300* with the resolution of 250 nm.

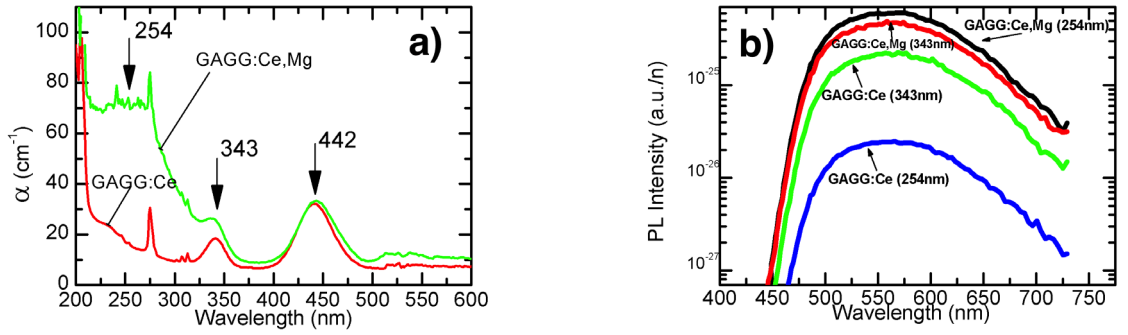

(a) (b)

Fig. 1. Absorption (a) and photoluminescence spectra (b) of GAGG:Ce and GAGG:Ce,Mg. The PL spectra are normalized by phoexcited carrier density and were measured at different excitation energies, indicated in (b) and by arrows in (a).

During the investigation, the absorption spectra (figure 1(a)) of GAGG:Ce and GAGG:Ce,Mg were measured and spatially integrated spectra were obtained. Spatial distributions of the luminescence parameters were mapped. In this work it is reported that the shape of photoluminescence spectra (figure 1(b)) of GAGG:Ce stays the same during both: excitation of electrons from 4f to 5d level and by excitation of charge transfer band. It does also not depend on co-doping. This implies that the mechanism behind the luminescence process can always be assigned to electron tranisitions of cerium ion. The co-doping of GAGG:Ce by magnesium results in deterioration of photoluminescence intensity by approximately 20 times when charge transfer (CT) band is excited and only three times when electron transitions $4f \rightarrow 5d$ of Ce^{3+} are excited. This shows that when exciting the CT band a noticeable part of photons are absorbed by non-radiative recombination centers. It is also evident that co-doping by Mg^{2+} does not influence the homogeneity of distribution of photoluminescence parameters.

TETHERED BILAYER LIPID MEMBRANES FOR PICOMOLAR DETECTION OF PORE-FORMING TOXINS

Tadas Penkauskas[1], Marija Jankunec[1], Gintaras Valincius[1]

[1] Department of Bioelectrochemistry and Biospectroscopy, Vilnius University Life Sciences Center, Lithuania
tadas.penkauskas@bchi.vu.lt

Formation of plasma membrane is considered as a crucial event during evolution and life, as known today, would not be possible without them. Actual plasma membranes contain a complex, heterogeneous distribution of lipids and membrane proteins which interact to create important biological functions. To investigate this complex membrane environment significant progress has been made to model native membranes. The most common systems include lipid monolayers, lipid vesicles, and supported lipid bilayers (SLBs) [1]. Particular group of solid supported bilayers, tethered bilayers (tBLMs), are considered as perspective experimental platforms for membrane biosensors [2]. In particular, the modulation of the ionic conductance of tBLMs may be utilized to develop biosensors of the membrane damaging agents such as pore-forming toxins [3].

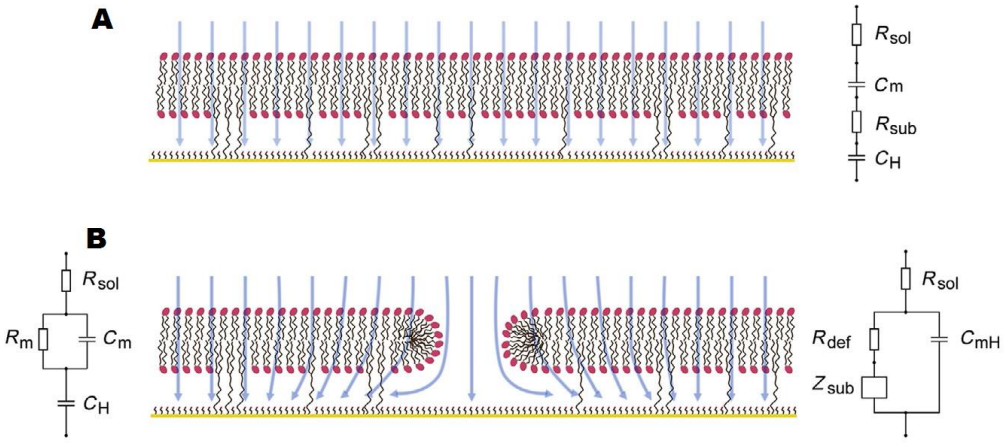

Figure 1. Electric equivalents of different bilayer membrane systems: (A) defect-free tethered bilayer, and (B) defect-containing tethered bilayer [4].

We have used the tBLM platform for the detection and visualization of cholesterol-dependent cytolysins (CDCs), using electrochemical impedance spectroscopy (EIS) and atomic force microscopy (AFM) techniques. tBLM modification in aqueous environment has been performed, using Methyl-β-cyclodextrin (MβCD) and cholesterol complex, to achieve picomolar CDC sensitivity.

[1] I. Koper, Insulating tethered bilayer lipid membranes to study membrane proteins, Mol. BioSyst. 3 (10), 651–657 (2007).
[2] D. J. McGillivray et al., Molecular-scale structural and functional characterization of sparsely tethered bilayer lipid membranes, Biointerphases 2 (1), 21–33 (2007).
[3] G. Preta, M. Jankunec, F. Heinrich, et al., Tethered bilayer membranes as a complementary tool for functional and structural studies: The pyolysin case, Biochim. Biophys. Acta 1858 (9), 2070–80 (2016).
[4] G. Valincius, M. Mickevicius, Chapter Two – Tethered Phospholipid Bilayer Membranes: An Interpretation of the Electrochemical Impedance Response, Advances in Planar Lipid Bilayers and Liposomes 21, 27–61 (2015).

FLUORESCENCE MICROSCOPY STUDIES OF DNA AND DNA RESTRICTION ENZYMES INTERACTIONS AT THE SINGLE MOLECULE LEVEL

Marijonas Tutkus[1], Giedrė Karzaitė[1], Šarūnė Ivanovaitė[1], Danielis Rutkauskas[1], Mindaugas Zaremba[2]

[1] Vilnius University, Institute of Biotechnology, Saulėtekio Avenue 7, LT-10257 Vilnius
[2] Center for Physical Sciences and Technology, Savanorių pr. 231, LT-02300 Vilnius
giedre.karzaite@gmail.com

Restriction endonucleases (REases) recognize specific nucleotide sequences in a double stranded DNA and cleave both strands of the duplex. In vivo REases protect their host bacteria from viral attacks by cleaving foreign DNA. In vitro, they are widely used as a molecular tool for various DNA manipulations [1]. Restrictase BfiI belongs to the phospholipase D (PLD) superfamily and does not require metal ions for DNA cleavage. It recognizes an asymmetric DNA sequence, 5'-ACTGGG-3', and cuts top and bottom strands at fixed positions downstream of this sequence [2].

Here we are studying several versions of BfiI REase: WT BfiI, BfiI-SS, BfiI-K107A, BfiI-K107A-SS. The wild-type BfiI is a native protein. In BfiI-SS protein SS bridge is linking the dimer interface [3]. In BfiI-K107A protein mutation was introduced in the active center at residue 107 - Lysine was changed to Alanine. BfiI-K107A-SS protein contains both mentioned mutations.

In this research we have studied interaction between DNA and BfiI restriction enzymes using single – molecule Forster Resonance Energy Transfer (smFRET) total internal reflection (TIR) microscopy. Biotinylated DNA molecules bearing two targets for BfiI and FRET pair dyes close to these targets were immobilized on a silanized and PEGylated (metoxy-PEG and biotin PEG mixture) glass surface via neutravidin. The protein induces formation of DNA loop: one BfiI site binds one target and second another, and therefore brings the FRET pair in close proximity (Fig. 1).

Our acquired smFRET signals have shown multiple FRET level lasting for several seconds. We observed that FRET efficiency and duration was affected by BfiI mutation, Cross-linking and Mg^{2+} ions/ ion strength.

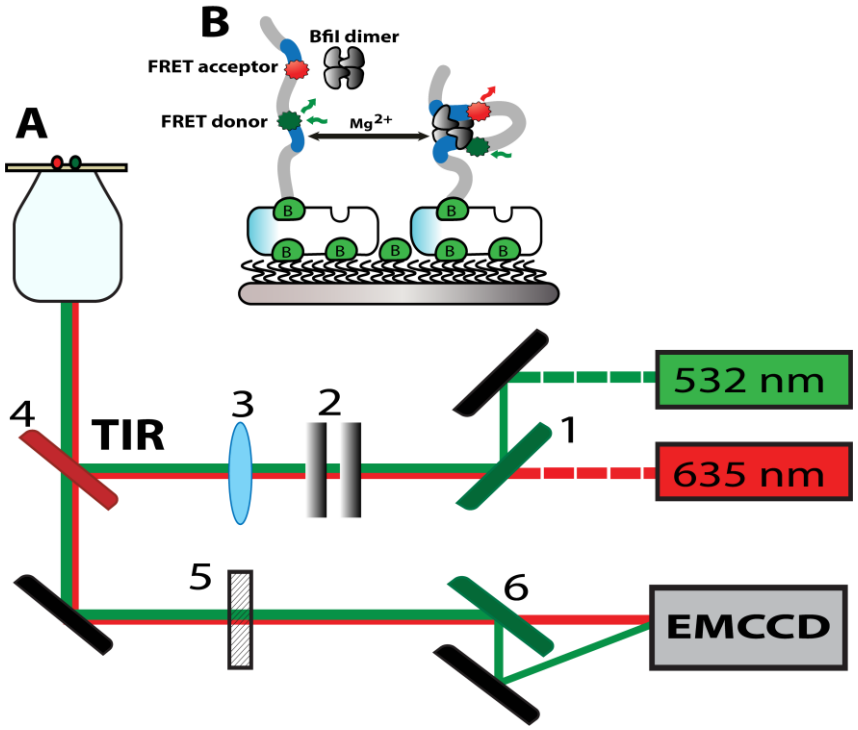

Figure 1. Experimental setup: (A) microscope setup scheme for total internal reflection fluorescence (TIRF) microscopy, (B) surface immobilization strategy.

[1] D. Rutkauskas, M. Petkelyte, P. Naujalis, G. Sasnauskas, G. Tamulaitis, M. Zaremba, V.Siksnys. Restriction enzyme Ecl18kI-induced DNA looping dynamics by single-molecule FRET. J. Phys. Chem. B (2014).
[2] G. Sasnauskas, S. E. Halford, V. Siksnys. How the BfiI restriction enzyme uses one active site to cut two DNA strands. Proc. Natl. Acad. Sci. U. S. A. (2003).
[3] M. Zaremba, V. Siksnys. An Engineered SS Bridge Blocks the Conformational Change Required for the Nuclease Activity of BfiI. Biochemistry (2015).

UNDERSTANDING DIFFERENT PATHWAYS OF INSULIN AGGREGATION

Mantas Žiaunys, Tomas Šneideris, Vytautas Smirnovas

Department of Biothermodynamics and Drug Design, Vilnius University Institute of Biotechnology, Vilnius, Lithuania
mantas.ziaunys@gmail.com

Amyloids are self-assembled, highly ordered, closely packed peptide or protein aggregates and their formation is associated with neurodegenerative diseases, such as Alzheimer's, Parkinson's and prion diseases [1]. Amyloidogenic protein aggregation mechanism dependence on environmental factors, such as ionic strength and pH are still poorly understood [2].

Insulin amyloid-like fibrils were prepared by incubation of fresh insulin solution in 100 mM phosphate buffer pH 2.4 (with and without 0.1 M NaCl) at 60 °C for 24 hours in quiescent conditions. 5.0 mg/ml insulin solutions were used in dynamic light scattering analysis and formed fibrils were examined with atomic force microscopy and infrared spectroscopy. Aggregation kinetics of insulin solutions (0.5 – 5.0 mg/ml) were recorded at constant 60 °C temperature by measuring Thioflavin -T fluorescence intensity. Kinetic data was analysed using “classic” and “saturated elongation” models [3] as well as our proposed “classic” + tetramer and “classic” + “capping” model (Fig. 1.).

In this work we observed unusual insulin aggregation kinetics at pH 2.4 under two ionic strength conditions that could not be explained by any currently predominant models. Our proposed additional tetramer formation and aggregation center "capping" steps greatly improved the "classic" aggregation model's ability to fit the abnormal kinetic data. The addition of salt also shifted the monomer-tetramer equilibrium towards higher oligomeric form creation.

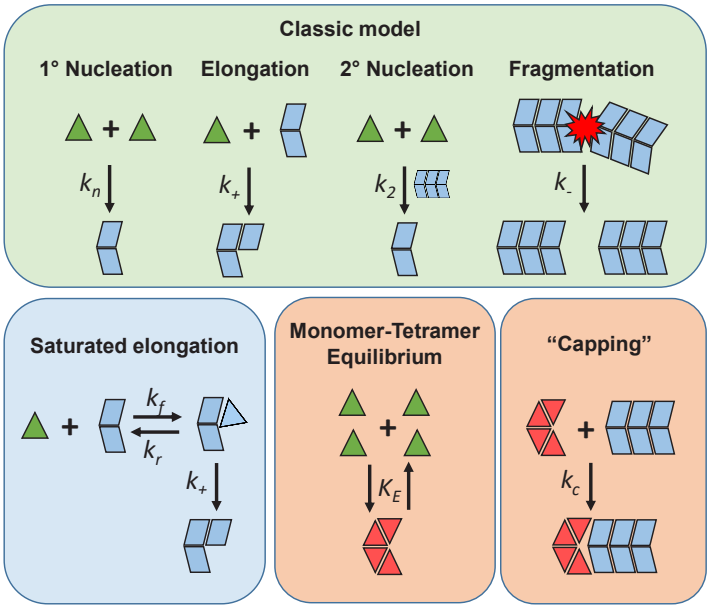

Fig. 1. The classic model of amyloid self-assembly and a possible saturated elongation step, as well as our proposed additional reaction steps.

[1] F. Chiti, C. M. Dobson, “Protein Misfolding, Functional Amyloid, and Human Disease,” *Annu. Rev. Biochem.* **75,** 333–366, (2006).
[2] G. Meisl, et al., “Molecular mechanisms of protein aggregation from global fitting of kinetic models,” *Nat. Protoc.* **11,** 252–272, (2016).
[3] G. Meisl, et al., “Scaling behaviour and rate-determining steps in filamentous self-assembly,” *Chem. Sci.* 7087–7097, (2017).

CSM6 – THE LATENT RIBONUCLEASE IN CYCLIC OLIGOADENYLATE SIGNALLING PATHWAY

Miglė Kazlauskienė[1], Augustė Rimaitė[1], Giedrė Tamulaitienė[1], Gintautas Tamulaitis[1], Virginijus Šikšnys[1]

[1] Institute of Biotechnology, Life Sciences Center, Vilnius University, Lithuania
migle.kazlauskiene@gmail.com

CRISPR-Cas systems protect prokaryotes against viruses and other foreign nucleic acids. This protection is adaptive and sequence specific due to crRNA molecules that recognize the targets and guide the effector complex to them. It is known that type I, II and V effector complexes (Cascade, Cas9-RNA and Cpf1-RNA, respectively) cleave foreign DNA while type III and VI complexes (Csm/Cmr and Cas13) degrade foreign RNA [1]. Additionally, binding of target RNA by the type III complexes activates their Cas10 subunit to degrade DNA [2] and synthesize cyclic oligoadenylates from ATP. The cyclic oligoadenylates serve as unique messengers that activate a stand-alone ribonuclease Csm6 [3, 4]. In this study we aimed to understand the regulation of Csm6 from *Streptococcus thermophilus*. For this, we optimised the protein expression and purification protocols and performed screening of crystallisation conditions. We employed RNA cleavage assays to determine suitable ligands and evaluate the quality of purified proteins. Understanding of the Csm6 structural changes could lead to improvement of the controllable ribonuclease and design of novel regulable proteins.

[1] Koonin, E. V., Makarova, K. S., Zhang, F. Diversity, classification and evolution of CRISPR-Cas systems. *Curr. Opin. Microbiol.* **37,** 67–78 (2017).

[2] Kazlauskiene, M., Tamulaitis, G., Kostiuk, G., Venclovas, Č., Siksnys, V. Spatiotemporal Control of Type III-A CRISPR-Cas Immunity: Coupling DNA Degradation with the Target RNA Recognition. *Mol. Cell* **62,** 295–306 (2016).

[3] Kazlauskiene, M., Kostiuk, G., Venclovas, Č., Tamulaitis, G., Siksnys, V. A cyclic oligonucleotide signaling pathway in type III CRISPR-Cas systems. *Science* **357,** 605-609 (2017).

[4] Niewoehner, O., Garcia-Doval, C., Rostøl, J. T., Berk, C., Schwede, F., Bigler, L., Hall, J., Marraffini, L. A., Jinek, M. Type III CRISPR–Cas systems produce cyclic oligoadenylate second messengers. *Nature* **548**, 543–548 (2017).

NANOCRYSTALLIZATION OF LITHIUM-BORATE GLASSES

Agata Gołębiewska, Jakub S. Otrębski, Przemysław P. Michalski, Tomasz K. Pietrzak

Faculty of Physics, Warsaw University of Technology, Poland
agata.golebie@gmail.com

Nowadays, energy storage field is becoming more significant. Therefore, when it comes to portable devices, the development of the battery field has an extremely crucial role in it. It has also a huge impact on electric cars industry – especially now, when European Union insists on reducing the level of pollution [1] and many countries introduced subsidies for eco-cars. Moreover, renewable energy sources should be supported by efficient energy storage system. Taking all of these into consideration, the need for electrochemical cells is growing. Essential part of every Li-ion cell is cathode material, so the investigation on new cathode components is becoming more important in energy storage field.

Some time ago, interesting compounds with the composition $LiMBO_3$ (M = Fe, Mn) have emerged as potential cathode materials for Li-ion batteries [2]. Unfortunately, the polycrystalline samples of those materials have exhibited too low conductivity and insufficient practical gravimetric capacity. Herein, we present our recent results of studies on compounds obtained by thermal nanocrystallization of glasses, synthesis of glassy sample and selected physical properties of nanocrystallized analogs. Previously, we have successfully applied this method in case of several glassy systems, e.g. V_2O_5-P_2O_5 and Li_2O-FeO-V_2O_5-P_2O_5. The heat-treated materials exhibited an advantageous microstructure and significantly enhanced electric conductivity (up to 10 orders of magnitude!) [3].

Borates are really good glass-forming materials and are widely used for commercial purposes, such as amorphous optical materials, electrolytes in Li-ion batteries, solid state lasers and have been recently reported to be applied as cathode materials. Lately, $LiFeBO_3$ and $LiMnBO_3$ glassy materials were successfully synthesized and nanocrystallized. Compound with manganese exhibited better glass-forming properties and high increase of electric conductivity after nanocrystallization, but even though, the final conductivity was pretty low. Addition of iron gave better conductivity, but caused lower glass-forming properties. In order to improve conductivity, addition of vanadium was also introduced [4] and $LiMn_{1-3/2x}V_xBO_3$ compound was successfully obtained. Another attitude was to use both, manganium and iron – $LiFe_xMn_{1-x}BO_3$, where x = 0.25, 0.5 and 0.75.

All of the above samples were synthesized using melt-quenching method and characterized with thermal (DTA), structural (XRD, SEM) and electrical (IS) methods. Therefore, this work aims to give better overview on the properties of nanocrystallized lithium-borate glasses.

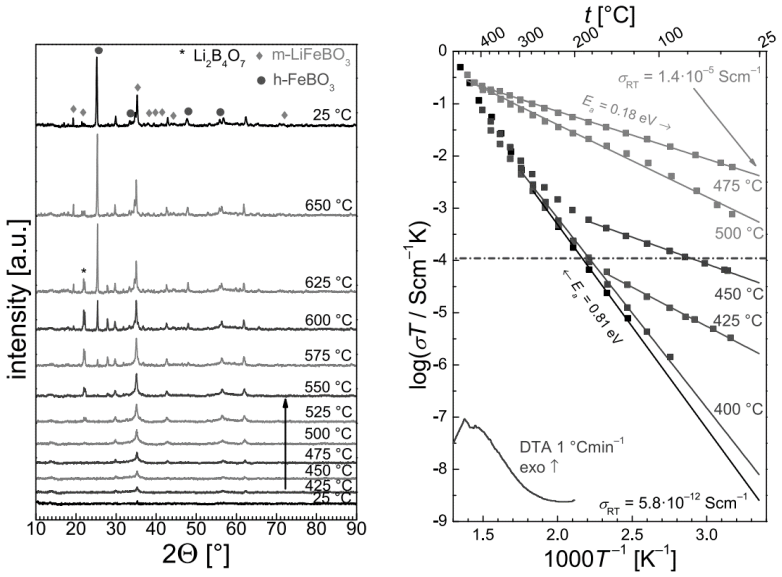

Fig. 1. Results for the $LiFeBO_3$ sample [5]. XRD patterns in the elevated temperatures with the phases marked on the chart (left) and temperature dependence of electric conductivity presented in Arrhenius coordinates (right). The lowest points represent the data obtained during heating, the rest – during cooling after heating to various temperatures given. DTA curve and the conductivity value for crystalline $LiFeBO_3$ (dotted line) are shown for comparison.

[1] Communication from the European Commission: EUROPE 2020 A strategy for smart, sustainable and inclusive growth, passed in Brussels, 3rd March, 2010.
[2] V. Legagneur, Y. An, A. Mosbah, R. Portal, A. Le Gal La Salle, A. Verbaere, D. Guyomard, Y. Piffard. Solid State Ionics **139** (2001) 37–46.
[3] T.K. Pietrzak, M. Wasiucionek, P.P. Michalski, A. Kaleta, J.E. Garbarczyk. Materials Science and Engineering B **213** (2016) 140–147.
[4] J. Hong, C. S. Wang, X. Chen, S. Upreti, M. S. Whittingham. Electrochemical and Solid-State Letters, **12** (2) (2009) A33–A38.
[5] P. P. Michalski, T. K. Pietrzak, J. L. Nowiński, M. Wasiucionek, J. E. Garbarczyk. Solid State Ionics **302** (2017) 40–44.

DETECTION OF SILVER NANOPARTICLES BASED ON PORPHYRINE-INDUCED AGGREGATION

Anastasiya Rysiavets[1], Andrey Panarin[2], Sergei Terekhov[2]

[1]Department of Physics, Belarusian State University, Belarus
[2]B.I. Stepanov Institute of Physics NASB, Belarus
anrisevets@gmail.com

Silver nanoparticles (AgNPs) with their unique optical properties due to excitation of localized plasmons have recently been objects of intensive research. Such NPs have the broad spectrum of analytical usage in biosensorics and genomics, cellular structures visualization, precision drug delivery, treatment of tumor diseases, etc. An expansion of AgNPs application will lead to the growth of their production volume, increase in the probability of entering the environment and, as a result, accumulation in the human body. There is concern about the potential human and ecosystem hazards associated with their exposure to silver nanoparticles [1]. In this situation, it is important to develop a simple, reliable and sensitive method of detection small quantities of AgNPs in solutions.

In order to analyse plasmonic particles, particularly silver NPs, we propose to use the resonance light scattering spectroscopy. To enhance sensitivity of the method, preliminary analyte-induced aggregation was applied. Such approach is driven by the fact that the cross-section of scattering process significantly increases with the increase of particle size. As an agglomerate forming molecules we used water-soluble cationic and anionic porphyrins, which act as electrostatic bridges between the metallic NPs.

To develop a scattering-based technique for determining of silver NPs spectral manifestation of the surface plasmon resonance of nanoparticles upon their interaction with porphyrins has to be characterized. Thus this study focuses on interaction of cationic Cu(II)-tetrakis(4-N-methylpyridyl) porphyrin (CuTMPyP4) and Cu(II)-tetrakis(2-N-methylpyridyl) porphyrin (CuTMPyP2), as well as anionic Cu(II)-5,10,15,20-tetrakis(4-sulphonatophenyl) porphyrin (CuTPPS4) with colloidal solution of Ag NPs.

Silver NPs were synthesized by reduction of $AgNO_3$ with glucose (50 mM) in water solution of 10 mM $NaHCO_3$ (as a pH-regulator) and 1 mM sodium citrate (as a stabilizer). The resulting silver particles were purified from the synthesis medium components by centrifugation (20000 rpm, 30 min). The size of Ag NPs assessed by transmission electron microscopy and extinction spectra was about 30 nm.

It was observed, that in the presence of cationic porphyrins (CuTMpyP4 and CuTMpyP2) the surface plasmon resonance maximum in the absorption and light scattering spectra of Ag NPs has been significantly increased and shifted to the longer wavelengths. It has been suggested that such behaviour is due to aggregation of nanoparticles. This was supported by transmission electron microscopy images which showed formation of agglomerates of Ag NPs. On the other hand, addition of anionic porphyrin (CuTPPS4) to Ag NPs solution did not lead to any meaningful spectral changes. The described observations can be explained by Coulomb attraction between cationic porphyrin molecules and negatively charged AgNPs, and repulsion between the nanoparticles and anionic CuTPPS4 molecules. These results give a foundation for the development of optical method of detection noble metal NPs in aqueous solutions.

In order to progress with practical application of the method, it is important to evaluate the limit of detection of NPs. For this reason extinction and scattering spectra for different amount of NPs in mixture with cationic porphyrin CuTMPyP4 were registered. To calculate the concentration of NPs in solutions we also measured extinction spectra of NPs in absence of porphyrin. Accordingly to the position and intensity of the bands in these spectra and taking into the account the data which are presented in work [2], concentrations of NPs were determined. Based on the calculated results we can conclude that $0{,}5 \cdot 10^{-12}$ M is the limit of detection of Ag NPs by scattering spectra. To use the measured data for determination of NPs in solutions we have built the calibrated dependency of scattering intensity on concentration of NPs.

Thereby, the resonance light scattering spectroscopy allows a quantitative analysis of containment of silver NPs in solution.

[1] Buzea, C.; Pacheco, I. I.; Robbie, K. Nanomaterials and nanoparticles: Sources and toxicity. Biointerphases. 2007, 2, MR17– MR71.

[2] D. Paramelle, A rapid method to estimate the concentration of citrate capped silver nanoparticles from UV-visible light spectra / D. Paramelle, A. Sadovoy // Royal society of chemistry – 2014- p. 4855-4861.

INFLUENCE OF COBALT NANOPARTICLES AT PARAMETERS OF WEAK LOCALIZATION IN BILAYER GRAPHENE

Uladzislau Humennik[1], Alexander S. Fedotov[1], Vadim Bayev[2]

[1]Faculty of Physics, Belarusian State University, The Republic of Belarus
[2]Institute for Nuclear Problems, Belarusian State University, The Republic of Belarus
fiz.gumennik@bsu.by

The study of electronic properties of modified graphene is of a great demand in modern applied science within the trend of its application in future nanoelectronics [1]. In this work we study the influence of electrochemical deposition of cobalt nanoparticles on the electrical transport properties and parameters of weak localization of bilayer twisted graphene.

Sheets of twisted graphene 10×10 mm were fabricated by chemical vapor deposition (CVD) on 25 μm thick cooper foil (Alfa Aesar 99.8 % purity) from the *n*-decane precursor with nitrogen as a carrier gas [2]. Electrochemical deposition of cobalt Co nanoparticles with an average diameter of 220 nm onto the surface of graphene on the Cu substrate was carried out in electrolyte contained 0.96 g/l of cobalt(II) sulphate heptahydrate $CoSO_4 \cdot 7H_2O$ and 0.064 g/l of sodium chloride $NaCl$ at a constant current, at room temperature.

In order to study electrical properties, the sheets of twisted graphene were transferred onto the SiO_2 substrate. Magnetoresistance $R(B)$ of graphene samples (G/Si) and graphene with Co nanoparticles on substrate of SiO_2 $(Co-G/Si)$ was studied in the range temperature range T=4−300 K under magnetic field B up to 8 T. At temperatures T up 10 K samples do demonstrate typical field dependences of magnetoresistance typical for the weak localization phenomena. The approximation of experimental $R(B)$ dependencies by expressions (1) and (2) allowed to estimate the characteristic times and lengths of coherence for charge carriers in graphene before and after the cobalt nanoparticles deposition.

$$\Delta\rho(B) = -\frac{e^2\rho^2}{\pi h}\left(F\left(\frac{B}{B_\phi}\right) - F\left(\frac{B}{B_\phi + 2B_i}\right) + \left(\frac{B}{B_\phi + B_*}\right)\right). \quad (1)$$

$$F(x) = \ln x + \psi\left(\frac{1}{2} + \frac{1}{x}\right), B_{\phi,i,*} = \frac{\hbar}{4De}\tau^{-1}_{\phi,i,*}. \quad (2)$$

Here $\psi(x)$ is the digamma function; τ_ϕ is the decoherence time; τ_i is the intervalley scattering time; $\tau_*^{-1} = \tau_w^{-1} + \tau_i^{-1}$, where τ_w is the time between scattering events [3, 4].

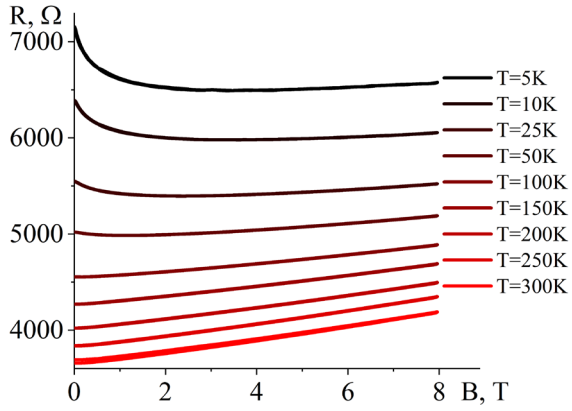

Fig. 1. Magneto field dependence of (G/Si)

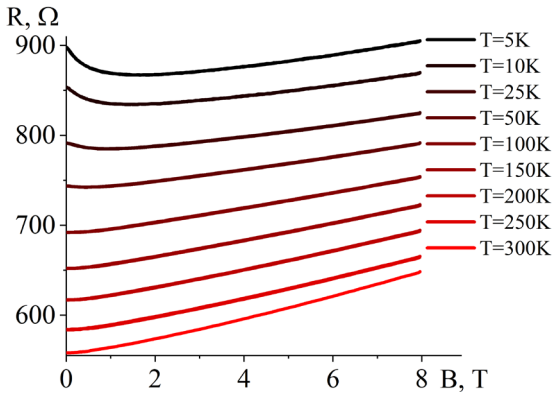

Fig. 2. Magneto field dependence of $(Co-G/Si)$

As is seen from Figures 1 and 2 the deposition of cobalt nanoparticles leads to the decrease of electrical resistance by an order of magnitude. It should be noted that the weak electron localization in studied system is caused by amorphous structure of grain boundaries between the crystallites of graphene [5]. Most likely, the increase of electrical conductivity and a decrease of negative magnetoresistance in samples $(Co-G/Si)$ are caused by an interaction of cobalt nanoparticles with graphene underlayer and the shunting of the grain boundaries.

In summary, it was shown that in magnetic field B up to 0.2 T magnetoresistance of samples (G/Si) and $(Co-G/Si)$ can be described by the theory of quantum corrections. The values of decoherence times and lengths for studied temperature range: $\tau_\phi \approx (0.6-2)\cdot 10^{-12}$ s and $L_\phi \approx (1-2)\cdot 10^2$ nm, and intervalley scattering times and lengths for the correction are: $\tau_i \approx (0.1-1)\cdot 10^{-13}$ s and $L_i \approx (0.2-5)\cdot 10^1$ nm.

[1] A. Luican et al., Single-Layer Behavior and Its Breakdown in Twisted Graphene, Physical Review Letters **106**, 126802 (2011).
[2] I.V. Komissarov et al., Nitrogen-doped twisted graphene grown on copper by atmospheric pressure CVD from aa decane precursor, Beilstein Journal of Nanotechnology **8**, 145-158 (2017)
[3] E. McCann et al., Weak-Localization Magnetoresistance and Valley Symmetry in Graphene, Physical Review Letters **97**, 146805 (2006).
[4] K. Kechedzhi et al., Influence of Trigonal Warping on Interference Effect in Bilayer Graphene, Physical Review Letters **98**, 176806 (2007).
[5] Qingkai Yu et al., Control and characterization of individual grains and grain boundaries in graphene grown by chemical vapour deposition, Nature Materials **10**, 443-449 (2011).

MODELLING OF POINT DEFECTS IN HEXAGONAL BORON NITRIDE USING FORCE FIELDS

Vytautas Žalandauskas[1,2], Audrius Alkauskas[1]

[1] Department of Fundamental Research, Center of Physical Sciences and Technology, Lithuania
[2]Faculty of Physics, Vilnius University, Lithuania
vytautas.zalandauskas@ff.stud.vu.lt

Layered van der Waals crystals are attracting increasing attention due to their excellent chemical and physical properties, leading to potential applications in next-generation photo-electronic devices.

The discovery of quantum emision in commercially available hexagonal boron nitride (h-BN) in early 2016 opens up applications in quantum computing, quantum communication and nanoscale sensing [1,2]. However, it is still unclear what is the exact mechanism of the measured quantum emission from defects in h-BN. Accurate modelling methods are required to garner extensive knowledge of these defects. Studies show that observed photoluminescence may come from point deffects located on linear defects like grain boundaries and dislocations. Using quantum chemistry calculations is too computationally expensive to model such large scale systems. Therefore, the goal of the present work is to use force field (FF) methods to model these systems.

In this study we used the classical Tersoff potential, developed for covalent systems, to model well known point defects in h-BN as a test for the accuracy of the potential. Eight different parameter sets for B-N systems, developed by different groups from 1996, were identified and used in this work. The results were compared with accurate density functional theory (DFT) calculations from other studies to find a parameter set most suited to model defects in h-BN.

Pristine h-BN monolayers of 2048 atoms were created with optimised geometry using periodic boundary conditions. Defect formation energies and geometries (bond lengths) of Stone-Wales (SW) and double antisite (AS) point defects (Fig. 1) were calculated for available Tersoff potential parameter sets.

We find that defect formation energies are up to several eV larger than DFT calculation values. One specific parameter set gives rather accurate defect formation energy values however bond lengths are up to 0.15 Å longer than in *ab-initio* calculations. Accurate bond length values are required to correctly model large scale linear defects like grain boundaries or dislocations. We show that most widely used parameter set by Kınacı et al. for h-BN and graphene heterostructures is suited to model pristine monolayers but not to describe point defects [3]. These results show underlying problems in using currently available parameter sets to model defects in hexagonal boron nitride. New parametrisation for structures with defects is required, especially for nitrogen-nitrogen interactions.

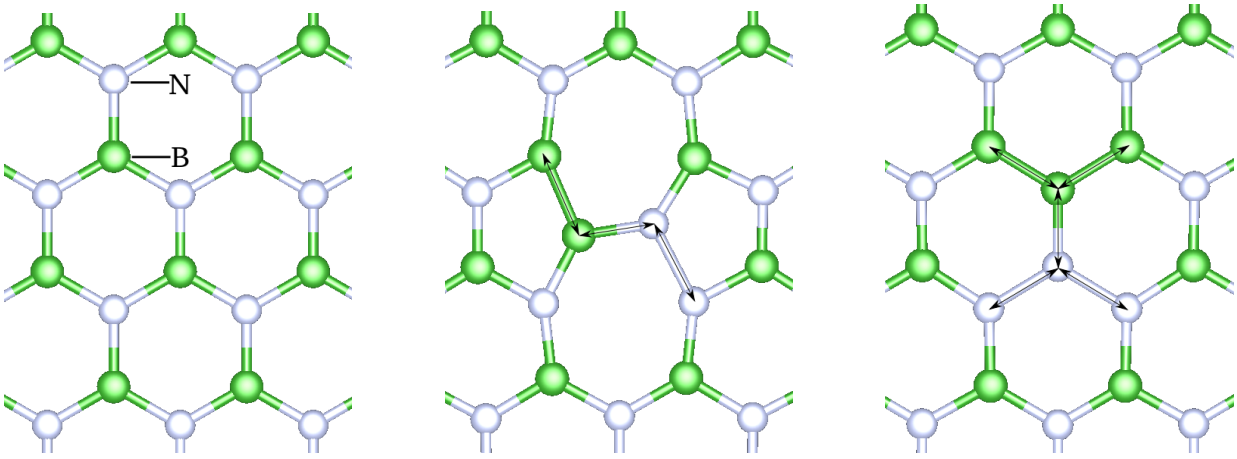

(a) Pristine (b) Stone-Wales (c) Double antisite

1 Fig.. Visualisation of pristine h-BN and SW, AS defect geometries.

[1] T. T. Tran, K. Bray, M. J. Ford et al. Boron nitride substrates for high-quality graphene electronics. *Nature Nanotechnology* **11**, 37-41 (2016).
[2] Z. Shotan, H. Jayakumar, and C. R. Considine *et al.* Photoinduced Modification of Single-Photon Emitters in Hexagonal Boron Nitride. *ACS Photonics*, **3**(12), 2490-2496 (2016).
[3] A. Kınacı, J. B. Haskins, C. Sevik, and T. Çağın. Thermal conductivity of BN-C nanostructures. *Phys. Rev. B*, **86**(11), 115410 (2012).

Au/Si-Ge and Au/Ge nanostructures for surface-enhanced Raman scattering

Anna Matsukovich[1], Oleg Nalivaiko[2], Kirill Chizh[3], Sergey Gaponenko[1]

[1] B.I. Stepanov Institute of Physics, National Academy of Sciences of Belarus, Belarus
[2] JSC "INTEGRAL" - Holding Management Company, Belarus
[3] A. M. Prokhorov Institute of General Physics, Russian Academy of Sciences, Russia
a_matsukovich@tut.by

Surface-enhanced Raman scattering (SERS) is a powerful spectroscopic analytical tool of determining structural information for molecules adsorbed on noble metal nanostructures. In addition, noble metal/semiconductor hetero-junctions, which have wide applications in nanoelectronics, optoelectronics, plasmonics, medical diagnostics, catalysis, drug delivery, and chemical sensing, also have shown effective enhancements in Raman scattering and were demonstrated to be appropriate as versatile SERS substrates [1, 2, 3].

This work shows SERS-activity of the novel semiconductor-metal hybrid nanostructures that consists of Si-Ge and Ge coated with Au film.

Three types of Au/Si-Ge and Au/Ge nanostructured substrates were used to obtain SERS spectra of mitoxantrone ($M=10^{-5}$ M). Au/Si-Ge surfaces are characterized by cone-shaped roughnesses (height is 50-150 nm, diameter is 0.5-1 μm). Au/Ge surfaces are characterized by roughnesses of 40-60 nm in height and 1 μm in diameter. Also Au/Ge III surface has some structures with height about 250 nm. The thickness of Au layer is 15 nm. The experiment was conducted with laser excitation at wavelengths λ = 632.8 and 785 nm. Exposure time was 5 s.

SERS spectra of mitoxantrone have an intensive peak at 1300 cm^{-1} (Fig.1). The intensity of this peak at excitation wavelength 632,8 nm is about 2000 a.u. for Au/Ge I, 700 a.u. for Au/Ge II and 1200 a.u. for Au/Ge III substrates. The intensity of this peak is about 2000 a.u. for Au/Si-Ge I and Au/Si-Ge II, and 3000 a.u. for Au/Si-Ge III substrates.

Using the excitation wavelength at 785 nm gives additional enhancement of SERS signal up to 1,7 times for Au/Ge I and III substrates and up to 4 times for Au/Ge II. The effect of excitation wavelength is more pronounced for Au/Si-Ge substrates. We can see additional enhancement of SERS up to 2,5 times for Au/SiGe I, up to 5,5 times for Au/SiGe II and up to 1,5 times for Au/SiGe III substrates.

Raman signals of analyte on the Si-Ge and Ge substrates without Au layer were not detected under same excitation conditions. Thus we conclude the using of Au/Si-Ge and Au/Ge substrates allows to obtain the surface-enhanced Raman scattering of mitoxantrone on 2-3 orders of magnitude.

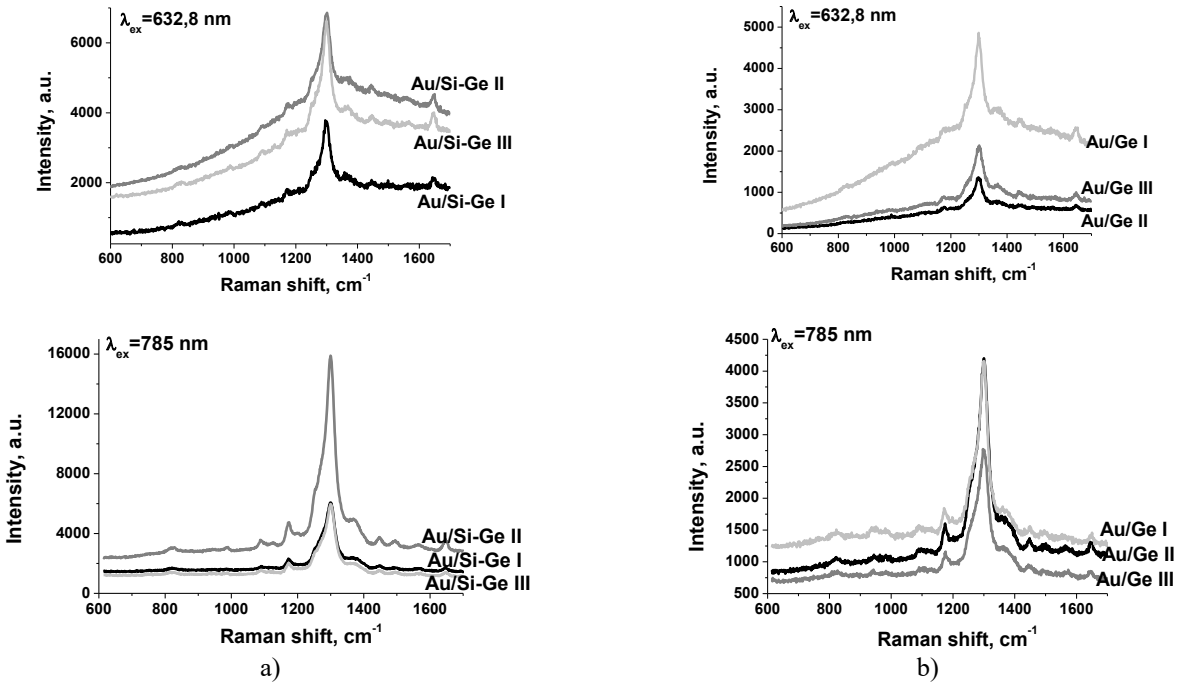

a) b)

Fig. 1. SERS spectra of mitoxantrone on a) Au/Si-Ge and b) Au/Ge substrates.

[1] E. V. Klyachkovskaya et al., Enhancement of Raman Scattering by Ultramarine Using Silver Films on Surface of Germanium Quantum Dots on Silicon. Optics and Spectroscopy. **110 (1)**. 48–54 (2011).
[2] . V. Klyachkovskaya et al., Enhanced Raman Scattering of Ultramarine on Au-coated Ge/Si-nanostructures. Plasmonics **6**. 413–418. (2011)
[3] T. Wang, Zh. Zhang et l., The Effect of Dielectric Constants on Noble Metal/Semiconductor SERS Enhancement: FDTD Simulation and Experiment Validation of Ag/Ge and Ag/Si Substrates. Scientific reports **4:4052**, P.1-8 (2014).

STUDY OF THE ORGANIC-INORGANIC PHOTORESIST SZ2080 AND ITS PROPERTIES AFTER DIRECT LASER STRUCTURING AND HEAT-TREATMENT

Viktorija Padolskytė[1,2], Darius Gailevičius[1,2], Simas Šakirzanovas[3], Subhashri Chatterjee[4], Linas Jonušauskas[1,2], Roaldas Gadonas[1,2], Kestutis Staliunas[5,6], Vygantas Mizeikis[4], Saulius Juodkazis[7,8], Mangirdas Malinauskas[1]

[1]Laser Research Center, Vilnius University, Lithuania
[2]Femtika Ltd., Lithuania
[3]Faculty of Chemistry and Geosciences, Vilnius University, Lithuania
[4]Research Institute of Electronics, Shizuoka University, Japan
[5]Departament de Física, Universitat Politcnica de Catalunya, Spain
[6]Instituci Catalana de Recerca i Estudis Avancats, Spain
[7]Swinburne University of Technology, Australia
[8]Melbourne Centre for Nanofabrication, ANFF, Australia
viktorija.padolskyte@ff.stud.vu.lt

Direct laser writing (DLW) lithography, known as two-photon polymerization (2PP) is a technique for micro- and nano-structuring that allows fabrication of complex 3D objects. We present a systematic study on post process heat treatment's influence on direct laser structured non-photosensitized [1] organic-inorganic photoresist SZ2080 material. The effects of pyrolysis on polymer micro- and nano-structures have been firstly studied in relatively low heating temperatures [2]. It is observed that post-process heat treatment method improves the resolution and reduces dimensions of structures fabricated with 2PP in organic-inorganic materials [3, 4].

We used various geometry structures fabricated from ultra-low shrinkage Si and Zr containing polymer SZ2080 using the DLW method and applied a hard bake procedure that reduces it into a more inorganic spatially shrunk 3D structure. We performed heating in air, Ar and O_2 gas environments while the temperature ranged from 200 to 1500 °C at varied time intervals. We examined the resulting properties of different structures, mainly focusing on geometry retention, e.g. bulk structures, scaffolds of macroscopic dimensions, woodpile photonic crystals (photonic-bandgap). In addition, we tested the material resiliency to plasma etching, FIB milling and wet etching by acid.

The results of the research shows that the geometry of the structures can be permanently and homogeneously scaled down to 60 % of their original size and the structures also showed an increased resiliency to FIB milling (Fig. 1). We confirmed that heat treatment has reduced the organic part of the material leaving the glass-ceramic component of the hybrid. In conclusion, the heat treated DLW structured photoresist SZ2080 is a good candidate as an engineering material for hot and reactive environments.

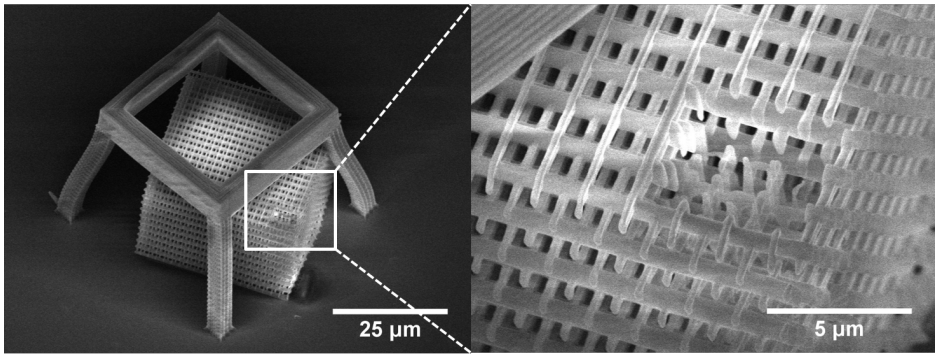

Fig. 1. SEM micrograph of a woodpile photonic crystal, which shrunk and retained its geometry during heat-treating at 300 °C for 3 h, and FIB milling. Inner geometry is revealed on the right. Resiliency to milling is observed.

[1] L. Jonušauskas, D. Gailevičius, L. Mikoliūnaitė, D. Sakalauskas, S. Šakirzanovas, S.Juodkazis, M. Malinauskas, Optically Clear and Resilient Free-Form μ-Optics 3D-Printed via Ultrafast Laser Lithography, Materials **10**, 12 (2017).
[2] K. Takada, K. Kaneko, Y. D. Li, S. Kawata, Q. D. Chen, and H. B. Sun, Temperature effects on pinpoint photopolymerization and polymerized micronanostructures, Appl. Phys. Lett. **92**, 041902 (2008).
[3] J. Li, B. Jia, and M. Gu, Engineering stop gaps of inorganic-organic polymeric 3D woodpile photonic crystals with post-thermal treatment, Optics Express **16**(24), 20073 (2008).
[4] G. Seniutinas, A. Weber, C. Padeste, I. Sakellari, M. Farsari, C. David, Beyond 100 nm resolution in 3D laser lithography - post proccessing solutions, Microelectron. Eng. in press (2018).

INFLUENCE OF ORGANIC PLANT-BASED FARMING ON SOIL MICROBIAL FUNCTIONAL DIVERSITY

Toleikienė Monika, Žvirdauskienė Renata, Skaidrė Supronienė, Akelaitis Paulius, Kadžiulienė Žydrė, Arlauskienė Aušra

Institute of Agriculture, LAMMC, Lithuania
toleikiene.monika@lammc.lt

The soil is a natural resource that provides crucial life for ecosystem services. An alternative to traditional mineral fertilization for improving soil quality is the application of organic green manures [1]. The application of plant-based organic manure has been shown to be an adequate strategy for increasing the level of organic matter in soils, with benefits for the development of soil microorganisms and plants.

However, microbial composition and biological activity remains uncertain in differently fertilized soils. Soil microbial status can be differently affected by amount and type of organic matter inputs [2]. Microbial community composition is sensitive to plant residues type because different forms of green manure stimulate structurally different microbial communities. In some cases, the organic amendment soil attend to have linear relationship between the microbial functional diversity and soil carbon availability, altering significant increases in average well-color development AWCD, richness and Shannon-Weaver index [3]. Therefore, these are the reasons of additional green manure preparation by composting and ensiling legume mass to reduce C:N ratio and keep fertilizing effect in all crop rotation.

Methods: Field experiments were conducted in 2015 - 2017 cropping system. Trial was carried at the Lithuanian Centre for Agriculture and Forestry, in Akademija (55°24′ N), Lithuania. Crop rotation: 2015 - winter wheat, 2016 - spring wheat, 2017 - spring barley. For monitoring the activity of soil microorganisms, 6 fertilization treatments were chosen: C - control with no fertilizers, RC - red clovers intercropped in the fall, FerRC - fermented red clover ground mass (N50), FerP+W - fermented peas and summer wheat mass (N25), ComRC+S - red clover and straw compost (N 50), GCM - granulated cattle manure (N50).

Since it has been found, that organic substrates (organic carbon) are the main factor controlling the growth of microorganisms in soil, a method based on the ability of microorganisms to catabolize different sources of carbon in the medium has been used, called CLPP - Community Level Physiological Profiling. For this Biolog EcoPlates (BIOLOG Inc, Hayward, CA, USA) containing 31 different C sources, respectively, plus a water control have been used. To assess the changes in microorganisms' communities in the soil, the trend of microorganisms' growth after 48 hours was determined by the AWCD, richness (R), Shannon diversity index (H), Simpson index (D) and McIntosh index (U).

Results: Rates of AWCD were significantly affected by sampling time and ranged from avg. 0.23 (at 17 May 2016) to avg. 0.65 (at 18 July 2017). AWCD was higher in all fertilized plots comparing with untreated control, but the differences were statistically insignificant. In first vegetation season, fermented red clovers, fresh mass of red clovers and green cattle manure had higher levels of AWCD. Fermented pea with wheat mass and composted red clovers did not show effect in first year, but had higher AWCD level on second year. Best not interrupted effect on AWCD in both year was observed applying granulated cattle manure. Few tendencies were noticed in our research: in first stage (than substrates consumption starts to differ significantly) microbial activity most of all increases on complex carbon sources' and amines' substrates. Amines dominate in RC and FerRC with narrow C:N, complex carbon sources - in GCM and ComRC+S with more broad C:N ratio. In later stage, significantly differ carbohydrates (in GCM and ComRC+S). Lastly, the peak of microbial activity is reached on amino acid substrates (in RC and GCM). The best microbial well coloring development was observed in D-galacturonic acid, L-asparagine and D-mannitol wells. After 14 months highest AWCD values were reached.

Conclusions: All organic manure increased microbial functional diversity in organic farming system. Fermented red clovers, fresh mass of red clovers had higher effect in first vegetation season. Fermented pea with wheat mass and composted red clovers - on second year. Best not interrupted effect in both year observed applying granulated cattle manure. Rates of microbial functional diversity varied significantly due to seasonal changes.

[1] K. Melcher, L.-M. Ng, E. Zhou et al., A gate-latch-lock mechanism for hormone signaling by abscisic acid receptors, Nature **462**, 602-608 (1990).
[2] M. A. Green, *High Efficiency Silicon Solar Cells* (Trans. Tech. Publications, Switzerland, 1987).
[3] J. Belovickis, Acoustooptic interaction of leaky surface acoustic waves in YX-LiTaO3 crystals, 54th scientific conference for young students of physics and natural sciences Open Readings 2011, ISSN 2029-4420, Vilnius University, 103-104 (2011).

THE SENSITIVITY OF MR-IMAGING WEIGHTED BY THE SPINE DENSITY AND TEMPORAL RELAXATION CHARACTERISTICS IN ACCORDANCE TO THE GRADIENTS PARAMETERS

Andrii Netreba, Yriy Kyiashko, Andrii Komarov

Department of Radiophysics, Electronics and Computer Systems, Taras Shevchenko National University of Kyiv, Ukraine
avn@univ.kiev.ua

The method for modeling of the operation of a magnetic resonance tomograph is proposed in the work under the condition that the experimental points deviate from the regular grid positions in the gradient K-space. The dependence of the stability of the reconstruction of tomograms weighted on the spin density and relaxation times was investigated. These studies are relevant today in connection to the development of the new diagnostic technologies and new types of mobile medical equipment [1].

The signal of the free induction decay (FID) in general form can be represented by the expression

$$S(t_1,t_2)=\sum_{x,y}\rho(x,y)\times(1-e^{-\frac{TR}{T_1(x,y)}})\times(e^{-\frac{TE}{T_2(x,y)}})\times(e^{[i\gamma(xG_xt_1+yG_yt_2]}), \quad (1)$$

where $\rho(x,y)$ - spine density, $T_1(x,y)$ - spin-lattice relaxation time, $T_2(x,y)$ - spine-spine relaxation time, TE - time of spin echo, TR - repetition time. Coordinates in a gradient K-space can be written as $k_{x,y}=\gamma G_{x,y}t_{1,2}$, where γ - gyromagnetic ratio for hydrogen, $G_{x,y}$ - value magnetic fields gradient, $t_{1,2}$ - pulse sequence parameters that change on each repetition cycle and are responsible for phasing and frequency coding of signals. The work assumes the modeling of the instability of the work of gradient systems by describing the Gas-like law of the probability distribution with respect to the positions of the experimental points in K space [2]:

$$F(\tilde{k})=\frac{1}{\sqrt{2\pi}\sigma_k}\exp\left(-\frac{(\tilde{k}-m_k)^2}{2\sigma_k^2}\right), \text{ where}$$

random variable in K-space is equal $\tilde{k}=|\Delta\vec{k}|$, $\Delta\vec{k}=\{\Delta k_x,\Delta k_y\}$ σ_k - the mean square deviation, m_k - mathematical expectations.

Fig. 1. Reconstruction of MR-images under condition of unsteadiness of positions of signal measurement points in gradient K space (original as test object, image reconstruction with σ_k=10 and σ_k=5).

For different values of the instability of the FID signal recording and the complete restoration of the tomograms were simulated (Fig.1). The arrays of signals and result images were calculated by using of our own design software with using of the expression (1). Several dozens of such model reconstruction experiments were carried out. Complete dependencies of the quality of diagnostics on instability parameters are obtained. The presented results allow to estimate critical values of instability for practical application. For example, the value of σ_k=5 is quite acceptable for working with the results of reconstruction.

[1] Ralf Ladebeck, Diana Martin, Sebastian Schmidt, "Mobile combined MRI/PET apparatus", US20090043189 – A1, (2009).
[2] Netreba A.V., Komarov A.O., Influence of the Transverse Gradient Magnetic Fields Instability to Reconstruction in MR Imaging, 2017 IEEE International Young Scientists Forum on Applied Physics and Engineering YSF, (2017).

APC GENE PROMOTER METHYLATION IN BREAST CANCER

Rita Banciul[1,2], Kristina Daniūnaite[2,3], Ieva Sadzeviciene[2], Sonata Jarmalaite[2,3]

[1] Vilnius Gediminas Technical University, Faculty of Fundamental Sciences, Lithuania
[2]Human Genome Research Group, Institute of Biosciences, Life Sciences Center, Vilnius University, Lithuania
[3]National Cancer Institute, Lithuania
rita.banciul@stud.vgtu.lt

Breast cancer is the most common oncological disease among women in Lithuania and many western countries. It is also responsible for the main part of deaths from malignant diseases [1]. Since early diagnosis increases the chance of survival, it is of high importance to search for biomarkers, which would enable clinicians to detect breast cancer at its early stages. Initiation and progression of cancer depends not only on genetic alterations but also on epigenetic changes such as DNA methylation. DNA methylation biomarker is defined as a molecular target that undergoes DNA methylation changes in carcinogenesis. Aberrant DNA methylation in the promoter regions of genes is well-defined in tumors and is commonly associated with silencing of tumor suppressor genes. Such epigenetic biomarkers might be utilized for early diagnosis of cancer, predicting and/or monitoring the therapeutic response [2].

The aim of this study was to analyze the promoter methylation of *APC* gene, which is a tumor suppressor gene and plays a critical role in several cellular processes, and therefore has a potential to be a biomarker for breast cancer diagnosis.

In the present study, 74 breast carcinomas and 29 control samples (breast tissue samples from women with benign breast diseases) were analyzed for *APC* promoter methylation. First, bisulfite conversion was used to convert unmethylated cytosine to uracil. Methylation specific PCR (MSP), which uses different primers for methylated and unmethylated DNA, was used in order to qualitatively determine the methylation status. MSP products were visualized by agarose gel electrophoresis.

Methylation frequency of *APC* was 54.6% and 0% in breast tumors and control samples, respectively ($p < 0.0001$), showing its potential diagnostic value for breast cancer diagnostics (fig. 1). *APC* methylation was also analyzed according to clinical-pathological patients' parameters. Statistically significant methylation frequency difference was found between luminal A (61%) and triple negative (18%) breast cancer molecular subtypes, which are the two most distinct subtypes of breast cancer. No associations were found between *APC* methylation status and patient's age, tumor stage, tumor size, or disease recurrence/progression.

In conclusion, our study revealed that *APC* gene promoter methylation could be utilized for diagnostics of breast cancer. However, further validation in independent cohort is needed.

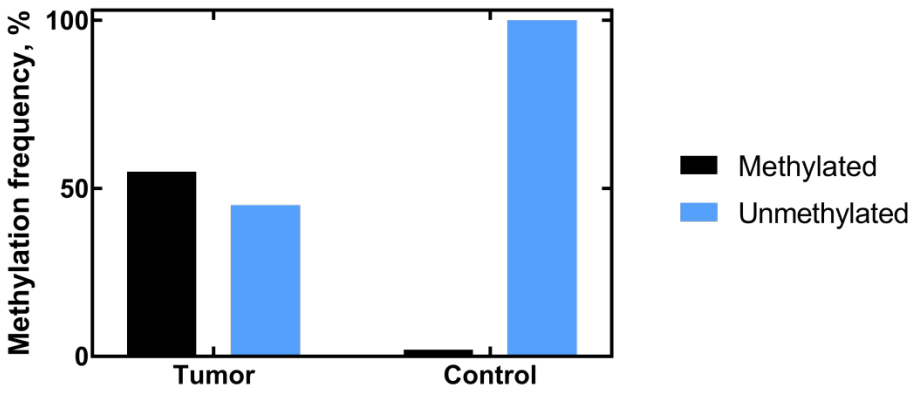

Fig. 1. The methylation frequency of *APC* gene promoter in breast tumors and control samples.

[1] Lithuanian Cancer Registry (National Cancer Institute, Vilnius, 2012).
[2] S. Fukushige, A. Horri, DNA methylation in cancer: a gene silencing mechanism and the clinical potential of its biomarkers, Tohoku J Exp Med. **229**, 173-85 (2013).

ASSOCIATION BETWEEN PROMOTER METHYLATION OF TUMOR SUPPRESSOR GENES AND PROSTATE CANCER

Kristina Žukauskaitė[1], Kristina Daniūnaitė[1,2], Arnas Bakavičius[2], Sonata Jarmalaitė[1,2]

[1] Human Genome Research Group, Life Sciences Center, Vilnius University, Vilnius, Lithuania
[2] National Cancer Institute, Vilnius, Lithuania
kristina.zukauskaite@gf.stud.vu.lt

Prostate cancer (PCa) is the second most prevalent malignancy in men and the sixth leading cause of death in males with cancer worldwide [1]. It is known that PCa can be effectively treated if detected at early stages. The most common method for early PCa diagnosis is prostate-specific antigen (PSA) screening. However, this method has only 20% specificity, which often leads to unnecessary biopsies and overtreatment [2]. For this reason, the development of new molecular biomarkers for PCa is vitally necessary. Epigenetic silencing of tumor suppressor genes is a common feature of many cancers. Aberrant methylation of CpG islands in promoter region is considered as the earliest somatic genome change in cancer [3]. Thus, promoter methylation of tumor suppressor genes could be used as a potential biomarker for the early diagnosis of PCa.

The aim of this study was to evaluate the promoter methylation status of three tumor suppressor genes, namely, *RARB, RASSF1*, and *GSTP1*, in clinical PCa samples as potential biomarkers.

In the present study, 112 prostate adenocarcinoma samples and 16 noncancerous prostate tissue (NPT) samples from 113 PCa patients were analyzed for promoter methylation. The tissue samples were collected during 2008-2014 at Vilnius University Hospital "Santaros Klinikos". Tumor suppressor genes were analyzed by means of methylation-specific polymerase chain reaction (MSP). Also, DNA from voided urine samples of 44 PCa patients were tested using quantitative MSP (QMSP). Prior to analysis, purified genomic DNA was bisulfite-treated in order to convert unmethylated cytosines to uracils, while the methylated cytosines remained unchanged.

The results of our study revealed significant methylation differences of tumor suppressor genes *RARB*, *RASSF1*, and *GSTP1* comparing PCa and NPT samples (all $p < 0.0001$; Fig. 1). The sensitivity for PCa was up to 99%, while specificity reached 87%. Moreover, we analyzed differences of DNA methylation in patients' groups, divided according to their age, prostate mass and Gleason grade groups. Methylated *GSTP1* promoter status was associated with larger prostate mass ($p = 0.0112$), and similar tendencies were observed between methylation of the three genes and higher Gleason grade group (defined according to the recommendations of International Society of Urological Pathology; ISUP). Furthermore, promoter methylation of *RARB*, *RASSF1*, and *GSTP1* was also detectable in urine, where mean methylation levels comprised 0.02%, 0.04%, and 0.01%, respectively.

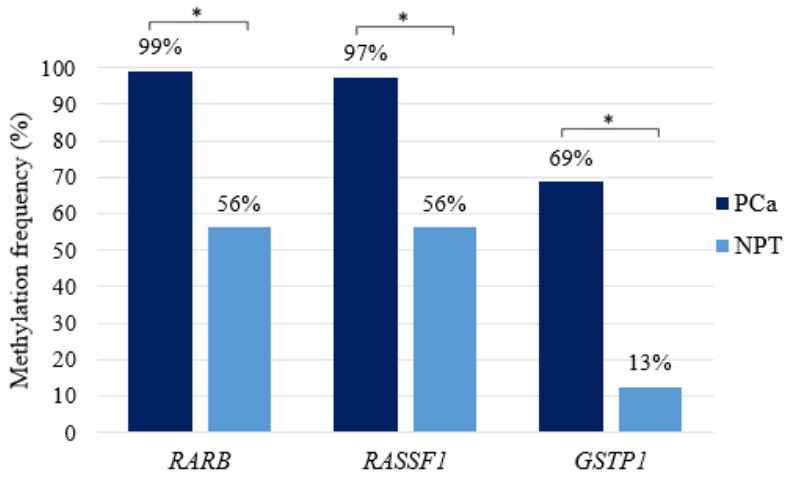

Fig. 1. Methylation frequencies of tumor suppressor genes *RARB*, *RASSF1*, and *GSTP1* in prostate cancer (PCa) and noncancerous prostate tissue samples (NPT); * – $p < 0.0001$

In conclusion, our analysis revealed frequent PCa-specific promoter methylation of *RARB, RASSF1*, and *GSTP1*, which might serve as novel epigenetic biomarkers for PCa diagnostics. Adding *RARB, RASSF1*, and *GSTP1* promoter methylation status to currently used clinical tests has the potential to improve early prostate cancer detection. Further investigation is needed to validate the prognostic and predictive value of the proposed biomarkers.

[1] Jamel A, Center MM, DeSantis C, Ward EM. Global patterns of cancer incidence and mortality rates and trends. Cancer Epidemiol Biomarkers Prev. 19: 1893-1907 (2010).
[2] van Leeuwen PJ, Connolly D, Gavin A, Roobol MJ, Black A et al. Prostate cancer mortality in screen and clinically detected prostate cancer: estimating the screening benefit. Eur J Cancer 46: 377-383 (2010).
[3] Esteller, M. Epigenetics in cancer. N Engl J Med. 358: 1148-1159 (2008).

ANTRACNOSE – RAPIDLY SPREADING STRAWBERRY DISEASE

Armina Morkeliūnė[1], Neringa Rasiukevičiūtė[1], Alma Valiuškaitė[1]

[1] Institute of Horticulture, Lithuanian Research Centre for Agriculture and Forestry, Kauno Str. 30, LT-54333 Babtai, Kaunas dist.
a.morkeliune@lsdi.lt

Rising requirement of fresh strawberry production demanded new varieties import from warmer climate zones to Lithuania. New growing technologies developed and applied to prolong fresh fruits season from early spring to late autumn.

Anthracnose is a limiting factor for strawberry fruits and plants caused by *Colletotrichum* spp. pathogens. It infects several parts of a strawberry plant (berries, flowers, leaves, roots), fruit infections are visible only on ripe berry, yield losses can reach up to 80% [1]. The pathogen is widespread in warm climate zone countries. The optimal temperature for its development is from +26.7 to 32 ° C. Under rainy and warm season conditions for the disease spread is very quickly and may destroy the entire plant. The pathogen can adapt to cooler climatic conditions due to warm-days period influenced by climate change [2, 3]. *Colletotrichum* spp. is very difficult to control then the environmental conditions are favourable for disease development. Anthracnose can be partially controlled by applying protective fungicides from flowering through to harvest, however, chemical control is often not sufficient. The strawberry susceptibility to anthracnose is considered as a polygonal and quantitative inheritance [1, 2]. Anthracnose becomes one of the major pathogen necessitates exploring novel control strategies, especially for day – neutral strawberries [1]. The day-neutral and traditional strawberries require different plant protection technologies and a new approach to harmful organism's control. The growing resistance to chemical pesticides need new solutions in controlling diseases before and after harvest [1, 3].

Essential oils are one of the non-toxic plant protection product controlling plant pathogens. Phenolic compounds of plants play an important role in protection against fungal pathogens. The findings of plant extract antimicrobial ant antifungal activities; low toxicity and biodegradability make it potential for use in plant protection against pathogens instead of chemicals [4].

The aim of this study was to evaluate antifungal effect of *T. vulgaris* essential oil against strawberry anthracnose causing pathogen *Colletotrichum* spp. The research was carried out at the LAMMC Institute of Horticulture. The essential oil of *T. vulgaris* were extracted from local material. The inhibition of mycelial growth was evaluated at concentrations 200 µl/l, 400 µl/l, 600 µl/l, 800 µl/l and 1000 µl/l. Small purified isolate fragment of about 10-mm diameter was placed in the centre of a sterile Petri dish of PDA with different essential oil concentrations. Plates were incubated 25 ° C in darkness and evaluated after 2, 4, 6 days. The antifungal activity of *T. vulgaris* essential oil was compared with chemical fungicide (difenoconazole 125 g/l + cyflufenamid 15 g/l). The results showed that *T. vulgaris* essential oils inhibited completely of *Colletotrichum* spp. growth at concentrations > 200 µl/l. The results of *T. vulgaris* essential oil study show that it could be an effective biocontrol agent to control strawberry *Colletotrichum* spp.

[1] R. Baroncelli, A. Zapparata, S. Sarrocco, S. A. Sukno, C. R. Lane, M. R. Thon, G. Vannacci, E. Holub, Molecular Diversity of Anthracnose Pathogen Populations Associated with UK Strawberry Production Suggests Multiple Introductions of Three Different *Colletotrichum* Species, PLoS One 10(6), e0129140 (2015).

[2] E. Feliziani, G. Romanazzi, Postharvest decay of strawberry fruit: Etiology, epidemiology, and disease management, Journal of Berry Research 6, 47–63 (2016).

[3] W. J. Janisiewicz, F. Takeda, D. M. Glenn, M. J. Camp, Dark period following UV-C treatment enhances killing of *Botrytis cinerea* conidia and controls gray mold of strawberries, Phytopathology 4 (106), 386-394 (2016).

[4] L. Šernaitė, Plant extracts: antimicrobial and antifungal activity and appliance in plant protection (Review), Sodininkystė ir daržininkystė 36(3-4), 58–68 (2017).

ASSESSMENT OF CELL DIFFERENTIATION AND GENE EXPRESSION IN APL PATIENT CELLS AND NB4 CELLS TREATED WITH 3-DEAZANEPLANOCIN A, BELINOSTAT AND RETINOIC ACID

Giedrė Skiauterytė, Aida Vitkevičienė, Rūta Navakauskienė

Department of Molecular Cell Biology, Institute of Biochemistry, Life Sciences Center, Vilnius University, Lithuania
giedre.skiauteryte@gf.stud.vu.lt

Acute promyelocytic leukemia (APL) is a hematological malignancy driven by a chimeric oncoprotein containing the C terminus of the retinoic acid receptor-α (RARα) fused to a N-terminal partner, most commonly promyelocytic leukemia protein (PML) [1]. The main genetic feature (90% APL cases) of this disease is chromosomal translocation t(15;17) (q22;q12). Normally RARα regulates gene expression through a co-repressor complex containing histone deacetylase (HDAC) activities that induces chromatin condensation and transcriptional repression. When mutated PML-RARα protein forms, it does not respond to its natural ligand retinoic acid (RA) allowing uncontrolled cells proliferation at the promyelocyte stage. Pharmacological doses of RA are used to treat patients in so-called differentiation therapy [2]. However, RA has limited activity as single therapeutic agent and not all patients respond to RA treatment, or after initial success relapse can arise. RA therapy could be improved with combinations of epigenetic agents, such as histone deacetylases, methyltransferases.

In the present study, we aimed to investigate the effects of combination of retinoic acid, histone deacetylases inhibitor belinostat (Bel) and histone methyltransferase EZH2 inhibitor 3-deazaneplanocin A (DZNep) on NB4 cell line and APL patient bone marrow cells with PML-RARα translocation. Cell proliferation and viability were evaluated by the trypan blue exclusion test. Cell differentiation was determined by microscopic nitroblue tetrazolium assay and gene expression changes were evaluated by using RT-qPCR.

NB4 cell treatment with combination of RA, Bel and DZNep decreased cell viability from 97% to 75% after 72 hours, but had no significant impact on NB4 cell proliferation rates. Meanwhile, APL patient cell viability did not change, proliferation decreased. The combination of RA, Bel and DZNep significantly increased differentiation in NB4 and APL patient cells. Gene expression experiment following treatment with RA, Bel and DZNep revealed effects on multiple genes: *ATM* (G1/S cell cycle arrest regulator) and *C/EPBα* (has positive effects on granulocytic maturation) expression increased in both NB4 and patient cells. *TER* (maintains telomere ends) expression decreased in both cases. Oncogenes *MYC, WT1* expression decreased in NB4 and patient cells (Fig. 1).

Consequently, we suggest that the combination of RA with Bel and DZNep could be used as an option for development of new treatment strategies for APL.

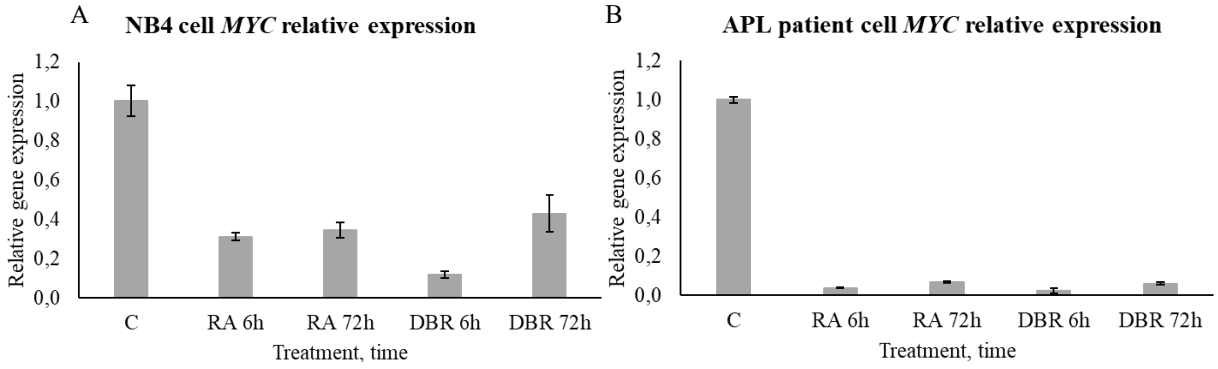

Fig. 1. NB4 (A) and APL patient (B) cell relative *MYC* gene expression after treatment with RA (1 μM) and DBR (0,5 μM DZNep + 0,2 μM Bel + 1 μM RA) compared to untreated cells (C - Control).

[1] Santos G. A., Kats L., Pandolfi P. P., Synergy against PML-RARa: targeting transcription, proteolysis, differentiation, and self-renewal in acute promyelocytic leukemia, J. Exp. Med. **210**(13), 2793–2802 (2013).

[2] Borutinskaitė V., Navakauskienė R., The Histone Deacetylase Inhibitor BML-210 Influences Gene and Protein Expression in Human Promyelocytic Leukemia NB4 Cells via Epigenetic Reprogramming, Int. J. Mol. Sci. **16**(8), 18252–18269 (2015).

DETECTION OF ASPIRIN TRACES IN BLOOD BY SURFACE ENHANCED RAMAN SCATTERING

Sonata Adomaviciute, Martynas Velicka, Valdas Sablinskas

Vilnius University, Institute of Chemical Physics, Vilnius, Lithuania
sonata.adomaviciute@ff.stud.vu.lt

Over-the-counter anti-inflammatory drugs, such as aspirin, are sold extensively throughout the world [1]. Overdose and rapid use of this medication may lead to serious drug-induced liver injury and even to death [2]. The concentration of active metabolite of aspirin – salicylic acid – in patients' blood is commonly tested using chromatography. In order to achieve better accuracy of the drug detection in blood, more sensitive method should be used. Therefore, surface enhanced Raman scattering (SERS) might be employed since it is capable to detect molecules in solutions on ppm level. Nevertheless, for achieving the highest enhancement of Raman scattering, nanoparticles (NPs) must be chosen correctly.

The aim of this study is to determine optimal experimental conditions and to find the most suitable metal nanoparticles for the detection of aspirin in blood. For this purpose, silver and gold nanoparticles were synthesized by employing different wet-chemical approaches. Nanoparticles were tested by examining the enhancement of Raman scattering of salicylic acid. The viability of detection of salicylic acid in blood at low concentrations was verified with SERS measurements of aspirin dissolved in animal blood serum.

Overall, four different types of AgNPs and two types of AuNPs were synthesized including citrate and polymer capped NP's with different polydispersity and shapes (Fig. 1). Citrate capped Silver nanoparticles were synthesized according to Lee – Meisel method [3]. Other synthesis included sodium borohydride ($NaBH_4$) as a reducing agent and polyvinylpyrrolidone (PVP) or citrate and PVP – as a stabilising agents reasoning very different shapes and sizes of NPs synthesized by seed mediated growth mechanism (Fig. 1). For synthesis of polymer capped nanoparticles, PVP was used in a polyol process to acquire nanoparticles covered by the polymer film [4]. For synthesis of gold nanoparticles 2-morpholinoethanesulfonic acid (MES) was used as a reducing agent and PVP as a stabilizing agent. For non-spherical Au nanoparticles PVP was used as both the reducing and the stabilizing agent [5]. The assessment of polydispersity, shape and size of particles were made by collecting UV-Vis absorbtion spectra of the synthesied colloids.

Further preparation of different NPs involved washing colloids with distilled water or concentrating them with a centrifuge. Samples for Raman measurements were prepared by drying 25 µl of colloidal solution on aluminium substrate and putting a drop of 1 mM salycilic acid solution on top of it.Results showed that silver nanoparticles have a greater enhancement of Raman signal (Fig. 2), though signal-to-noise ratio may decrease if citrate capped AgNPs are too much concentrated. This leads to distortion of salycilic acid spectrum. A recourse for this could be the use of polymeric nanoparticles instead of citrate capped ones. So far the measurements of salycilic acid in serum revealed that 0.1 mM salycilic acid might be distinguished in blood by spectroscopic analysis.

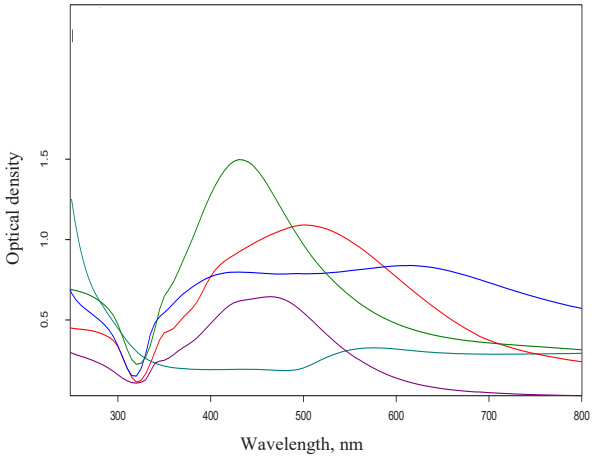

Fig. 1. Absorption spectra of plasmonic nanoparticles, synthesized by different wet-chemical methods.

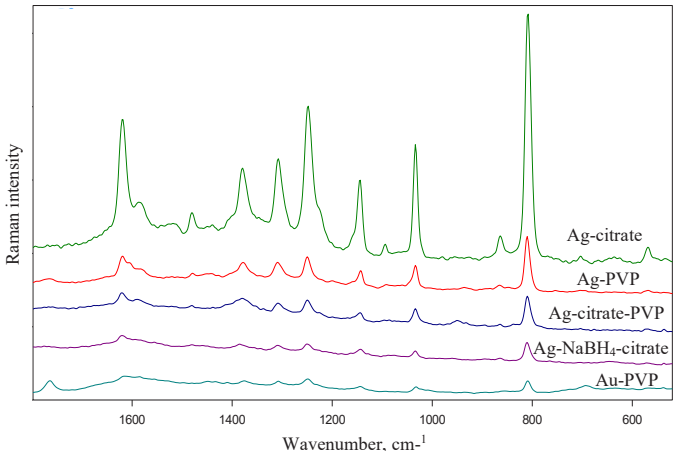

Fig. 2. SERS spectra of 1 mM salicylic acid on different plasmonic nanoparticles.

[1] J.B. Mowry, D.A. Spyker, D.E. Brooks, N. McMillan, J.L. Schauben, Annual Report of the American Association of Poison Control Centers' National Poison Data System (NPDS): 32nd Annual Report, Clin Toxicol (Phila) 3, 962-1147 (2015).
[2] M. Locquet, G. Honvo, V. Rabenda, T. Van Hees, J. Petermans, J. Y. Reginster, O. Bruyere, Adverse Health Events Related to Self-Medication Practices Among Elderly: A Systematic Review, Drugs Aging 34, 359-365 (2017).
[3] P. C. Lee, D. Meisel, Adsorption and Surface-Enhanced Raman of Dyes on Silver and Gold Sols, J. Phys. Chem. 86, 3391-3395 (1982).
[4] Ch. Wu, B. P. Mosher, K. Lyons, T. Zeng, Reducing Ability and Mechanism for Polyvinylpyrrolidone (PVP) in Silver Nanoparticles Synthesis, Journal of Nanoscience and Nanotechnology 10, 2342–2347 (2010).
[5] M. Zhou, Synthesis of Icosahedral Gold Nanocrystals: A Thermal Process Strategy, J. Phys. Chem. B 110, 4510–4513 (2006).

MARKER BANDS OF LYSOZYME FOR HYDRATION STUDIES BY RAMAN SPECTROSCOPY. LIMITS OF NATIVE STRUCTURE REGAINING.

Jekaterina Borzova[1], Vitaly Kocherbitov[2], Justas Barauskas[2], Gediminas Niaura[1]

[1] Vilnius University Life Science Center, Vilnius, Lithuania
[2] Biomedical Science, Faculty of Health and Society, Malmö University, Sweden
Latynis@gmail.com

Hydration plays a fundamental role in maintaining the three-dimensional structure and function of proteins. In this study, Raman spectroscopy was used to probe the hydration induced structural changes at various sites of lysozyme (lyz) under isothermal conditions in the range of water contents from 0 to 44 wt %. Raman hydration curves were constructed from detailed analysis of marker bands. Transition inflection points (w_m) and onsets determined from the hydration curves have shown that structural changes start at 7−10 and end at about 35 wt % water. The onset of structural changes coincides with the onset of the broad glass transition earlier observed in this system. The increase of α-helix content starts at very low concentrations of water with w_m = 12 wt %. Monitoring the development of importance for enzymatic action hydrophobic clusters has revealed w_m = 15 wt % and completion of the process at 25 wt %. The parameters of 621 cm^{-1} (Phe) and 1448 cm^{-1} (CH_2 bending) modes were found to be sensitive to hydration, suggesting changes in organization of water molecules near the protein surface [1].

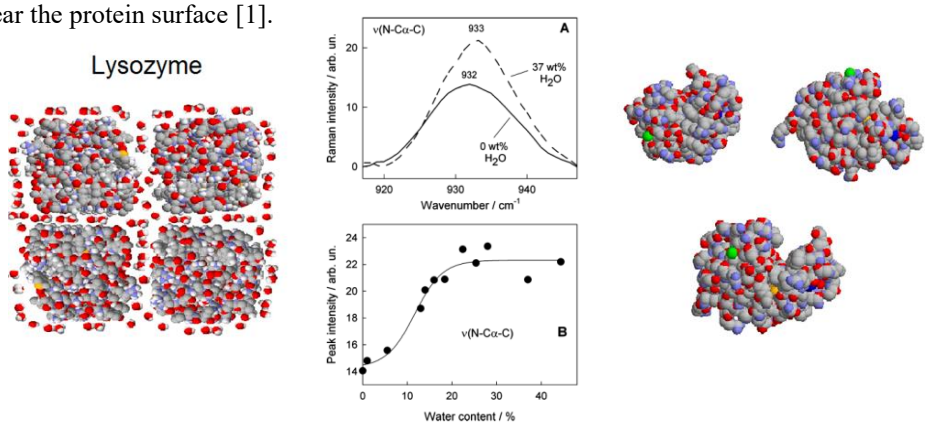

Fig. 1. (A) Raman spectra of lyz in the α-helix marker mode ν(N−Cα−C) spectral region at two hydration states (0 and 37 wt % water). (B) Hydration induced dependence of the band intensity. The solid line transition inflection point value w_m of 11.7 ± 1.6 wt %.

According to simulations by Donev et al. [2] the volume fraction of packed prolate spheroids with aspect ratio 5:3 is about 0.715. In other words, the minimum theoretical water content needed for existence of native structure in lyz is 28.5 vol % or 22 wt % assuming a density of lyz of 1.4 g/cm^3 [3]. In reality, the minimum water content should be higher because we expect at least one layer of water molecules to be present at the interface between lyz molecules. This leads to the following ratio:

$$\frac{V_W}{V_L + V_{BW}} = \frac{0.285}{0.715} \quad (1)$$

where V_W, V_L, and V_{BW} are volumes of free water, lyz, and bound water, respectively.
Calculations of the area and the volume of a prolate spheroid based on approximate dimensions of lyz molecules of 5 × 3 nm give 4150 $Å^2$ and 23560 $Å^3$, respectively. Assuming that a half of a water molecule belongs to every lyz molecule at the "touching" interface, the volume of the bound water is 6225 $Å^3$, which gives the volume of free water of 11 870 $Å^3$. Finally, the water to lyz ratio is calculated as:

$$h = \frac{V_W + V_{BW}}{d_L V_L} \quad (2)$$

Using a density of native lyz d_L of about 1.4 g/cm^3 [2] one arrives at an h value of 0.55 or 35 wt % water. Thus, from simple geometrical considerations, at about 35 wt % water, one can expect formation of the native structure of lyz. At water contents above 35 wt %, dehydration does not change the lyz structure and only removal of water occurs. Below 35 wt %, water dehydration has an effect on the structure of lyz because further removal of water cannot happen without geometrical distortion of lyz molecules.

[1] V.Kocherbitov, J.Latynis at al., Hydration of Lysozyme Studied by Raman Spectroscopy J.Phys.Chem.B. **117,** 4981−4992 (2013)
[2] A. Donev at al., Improving the Density of Jammed Disordered Packings Using Ellipsoids. Science **303**, 990−993 (2004)
[3] H. Fischer at al., Average Protein Density is a Molecular-Weight-Dependent Function. Protein Sci. **13**, 2825−2828 (2014)

BAYESIAN BASED METHOD FOR MAPPING IONIZING RADIATION SOURCES – A FEASIBILITY TEST

Antanas Bukartas[1],Robert Finck[1], Jonas Wallin[2], Christopher Rääf[1]

[1]Department of Medical Physics, Lund University, Sweden
[2]Department of Statistics, Lund University, Sweden
antanas.bukartas@med.lu.se

When an ionizing radiation source falls out of the regulatory control, it has to be localized and retrieved as quickly as possible to avoid unnecessary radiation exposure to the environment. Usually, mobile gamma spectrometry systems are used for these tasks [1]. In real-world situations, signal from the source might be drowned by the statistical, spatial or even temporal fluctuations of the background radiation [2]. Significant effort is being made to decrease the influence of the radiation background to the measurements – e.g. fitting the spectrum with natural decay series eliminating most of the non-anthropological background, subtracting the rolling average background level from the acquired spectra or even displaying only the deviation from rolling average for easier identification of changing radiation intensity [3, 4, 5]. Existing methods use frequentistic inference approaches to detect a significant increase in a background radiation – a consequence of a ionizing radiation source nearby.

In this work we present a first feasibility study on testing of the Bayesian inference methods in mobile gamma spectrometric applications – development of a data analysis method that automatically estimates position and activity of the source. For this first feasibility study, the created method is limited to solve for only one source in an off-line setting. The method was tested with data acquired experimentally with various mobile gamma spectrometry vehicles equipped with HPGe and NaI detectors and theoretically by calculating the gamma particle fluence at the detector. A number of sources (Cs-137, I-131, Co-60 and Ba-130) were set up at various distances from the road – from 30 to 90 meters. Posterior distributions for position and activity of the source were estimated using the method, and compared to the known actual values. The difference between estimated and actual activity and position of the source for this first feasibility test is $20-50\%$. Such a big difference can be explained with the Poisson nature of number of counts in the detector, observed systematic inaccuracies of GPS systems, uncertainties in efficiency calibration of the detector in the vehicle, etc. Despite the mentioned uncertainties, current results are promising. This method is going to be developed and tested further. An example of posterior distributions for position and activity from experimental measurements of a 298 MBq Cs-137 source situated at 30 meters from the road are displayed in Fig. 1.

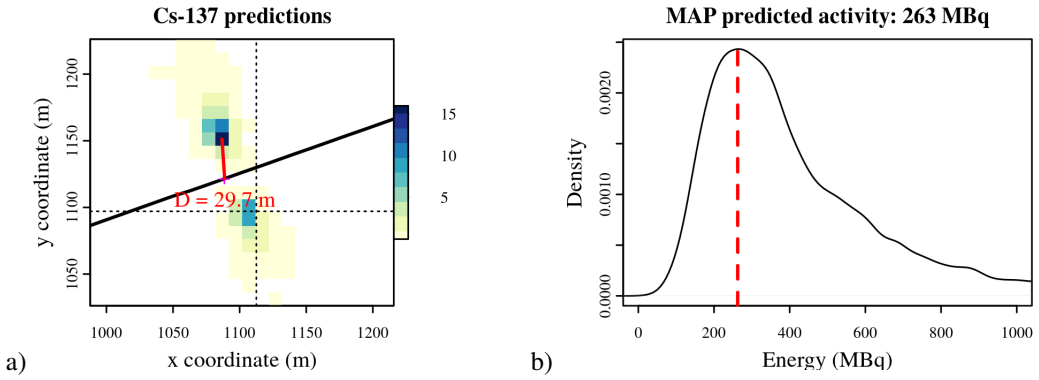

Fig. 1. a) Posterior probability distribution for source position. Solid black line represents the path of the vehicle with the detector. Actual position of the source is marked by the crossing of dashed vertical and horizontal lines. Size of the grid is 5 m. Color of the grid box is relative to the posterior distribution of spatial source position. The ends of the red line marks positions of the grid box with largest relative probability and maximum number of counts in detector. The D in red text marks the distance of this line. b) Posterior distribution of activity of the source. Red dashed line marks the maximum aposteriori (MAP) value (263 MBq) of the acquired posterior distribution.

[1] H. K. Aage, U. Korsbech, Search for lost or orphan radioactive sources based on NaI gamma spectrometry, Applied Radiation and Isotopes **58**, 103-113 (2003).
[2] P. Kock, C. Rääf, C. Samuelsson, On background radiation gradients - the use of airborne surveys when searching for orphan sources using mobile gamma-ray spectrometry, Journal of Environmental Radioactivity **128**, 84-90 (2014).
[3] E. Mauring, M. A. Smethurst, Reducing noise in radiometric multi-channel data using noise-adjusted singular value decomposition (NASVD) and maximum noise fraction (MNF).
[4] A. J. Cresswell, D. C. W. Sanderson, The use of dierence spectra with a ltered rolling average background in mobile gamma spectrometry measurements, Nuclear Instruments and Methods in Physics Research, Section A: Accelerators, Spectrometers, Detectors and Associated Equipment **607 (3)**, 685-694 (2009).
[5] P. Kock, R. R. Finck, J. M. C. Nilsson, K. Östlund, C. Samuelsson, A deviation display method for visualising data in mobile gamma-ray spectrometry, Applied Radiation and Isotopes **68 (9),** 1832-1838 (2010).

SHELL-ISOLATED NANOPARTICLE-ENHANCED RAMAN SPECTROSCOPY STUDY OF THE POSITIVE CHARGE BEARING MONOLAYER

Agnė Zdaniauskienė[1,2], Tatjana Charkova[1], Ieva Matulaitienė[1], Olegas Eicher-Lorka[1], Algirdas Matijoška[1], Martynas Skapas[1], Algirdas Selskis[1], Gediminas Niaura[1,2]

[1]Department of Organic Chemistry, Center for Physical Sciences and Technology, Lithuania
[2] Faculty of Physics, Vilnius University, Lithuania
agne.zdaniauskiene@gmail.com

Self-assembled monolayers (SAMs) from organethiol molecules adsorbed on noble metals are widely used to create interfaces with desirable properties. SAMs with positive charge bearing terminal group have attracted growing attention in the last few decades for few reasons. Such SAMs have electrostatic ability to attract inorganic anions and peptides from the solution phase. In addition, monolayers bearing positively charged terminal group have been used for sensing the anions and for the fabrication of bioelectronics devices [1, 2].

Surface-enhanced Raman spectroscopy (SERS) is one of the most sensitive vibrational spectroscopic method for probing the bonding, structure, and orientation of adsorbed molecules at certain nanostructured metals (mostly Au, Ag, and Cu). On the other hand, the limited number of SERS-active substrates and requirement to use roughened surfaces restricts the applicability of this method for analysis of technologically important surfaces. Consequently, Tian et al. approached a novel SERS technique named "shell-isolated nanoparticle-enhanced Raman spectroscopy" (SHINERS). The method is based on enhancement of Raman signal by strong electromagnetic field provided by gold core nanoparticles surrounded by a few nanometre thick inert silica shell (Au@SiO_2) [3].

The present work focused on *in situ* SHINERS study of positive charge bearing SAM formed from N-(6-mercapto)hexylpyridinium (MHP) at smooth Au electrode in aqueous $NaClO_4$ solutions. SHINERS was used to probe the electrochemical potential effect on bonding with surface, ion-pairing, and molecular structure of MHP.

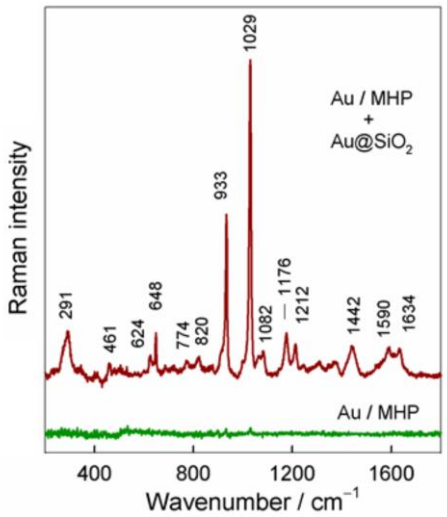

Fig. 1. Raman spectrum of MHP adsorbed on smooth Au electrode (Au/MHP) and SHINERS spectrum from smooth Au electrode with adsorbed MHP (Au/MHP + Au@SiO_2). Spectra were recorded in aqueous solution containing 0.01 M $NaClO_4$. Excitation wavelength is 785 nm.

During this study, it was found that metal-adsorbate vibrational mode ν(Au−S) was detected in the SHINERS spectra at 282−305 cm^{-1} (Fig. 1). Near linear potential-induced blue shift of this mode was revealed as electrode potential was tuned to more positive values. Spectroscopic analysis showed formation of ion-pairs between the positively charged pyridinium group of MHP and ClO_4^- anions in the solution phase.

SHINERS is emerging recently as a novel technique that uses shell-isolated nanoparticles to improve the applicability of SERS. SHINERS overcomes the long-term limitation of SERS because it allows SERS measurements on various target systems that were inaccessible previously because of the material and surface morphology issues. Moreover, SHINERS can be used in many complicated environments such as in aqueous solutions and biological systems.

[1] P. Lamberg et al., Electrical activity of cellobiose dehydrogenase adsorbed on thiols: influence of charge and hydrophobicity. Bioelectrochemistry **115**, 26−32 (2017).
[2] V. Krikstolaityte et al., Mediatorless carbohydrate/oxygen biofuel cells with improved cellobiose dehydrogenase based bioanaode. Fuel Cells **14**, 792−800 (2014).
[3] J. F. Li et al., Shell-isolated nanoparticle-enhanced Raman spectroscopy. Nature **464**, 392−395 (2010).

Tb^{3+} to Cr^{3+} ENERGY TRANSFER IN CO-DOPED $Y_3Al_5O_{12}$ (YAG) HOST

Monika Skruodiene[1*], Ramunas Skaudzius[1]

[1] Institute of Chemistry, Faculty of Chemistry and Geosciences, Vilnius University,
Naugarduko 24, LT-03225 Vilnius, Lithuania
monika.skruodiene@gmail.com

Luminescent materials, also known as phosphors, are widely used in nowadays. Optical technologies, emissive displays, fiber-optic telecommunication systems, lasers, etc. are the area of major applications. In last two decades, many new phosphors that are more efficient than the previous ones were invented. Inorganic phosphors are composed of an inert host lattice and optically active ion (activator), for example 3d or/and 4f metal ions, such as Cr^{3+}, Ce^{3+}, Eu^{3+}, Tb^{3+}, etc.[1-4]

For a successful growth of plant the photo-physiological processes need to be satisfied and this requires light in far-red (700 – 760 nm), red (620 – 680 nm), and blue (400 – 500 nm) spectral ranges [5]. Chromium doped garnets are perfect candidates for this purpose. It is well known that yttrium aluminum garnet (YAG) doped Cr^{3+} possess a broad absorption bands at ca. 450 and 650 nm. These bands correspond to $^4A_2 \rightarrow {}^4T_1$ and $^4A_2 \rightarrow {}^4T_2$ transitions, respectively. Emission originates in red and far-red spectral region with $^2E \rightarrow {}^4A_2$ transition at around 610 – 800 nm [6, 7].

External quantum efficiency (EQE) is very important factor for phosphors in their practical evaluation [8]. G. A. Torchia *et al.* has reported that $LiNbO_3$:ZnO:Cr^{3+} congruent crystal exhibit 10%±2% absolute quantum yield [9], while the luminescent quantum yield for the Cr^{3+} doped Cs_2NaAlF_6 was found to be 68±3% [10]. S. S. Pedro *et al.* has demonstrated that the quantum yield for $Be_3Al_2(SiO_3)_6$:Cr^{3+} and Cs_2NaAlF_6:Cr^{3+} crystals varied from 54% up to 78% depending on host lattice and dopant concentration . The quantum efficiency (QE) of YAG depends on its phase purity. Besides garnet phase, there are two intermediate phases: $Y_4Al_2O_9$ – yttrium aluminum monoclinic (YAM) and $YAlO_3$ – yttrium aluminum perovskite (YAP). If any of these phases coexist, the quantum efficiency decreases [11].

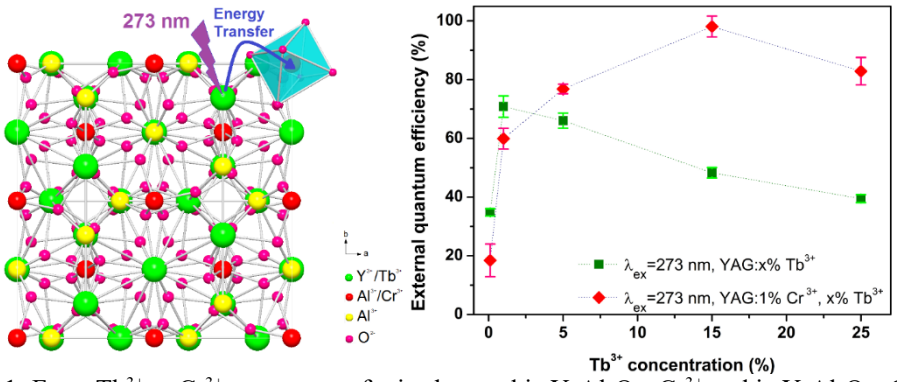

Fig. 1. From Tb^{3+} to Cr^{3+} energy transfer is observed in $Y_3Al_5O_{12}$:Cr^{3+} and in $Y_3Al_5O_{12}$:Cr^{3+},Tb^{3+}

Strong absorption and high quantum efficiency are the key features for any phosphor. Chromium and terbium co-doped yttrium aluminum garnets (YAG) are perfect candidates for luminescence. All samples of doped and co-doped YAG were prepared by the sol-gel route which is advantageous and useful to obtain single phase garnets. Samples were annealed at 1500 °C in order to avoid crystal lattice defects and to obtain better luminescence properties. It was found out, that optimal Tb^{3+} doping concentration in YAG:x%Tb^{3+} was x = 1% with external quantum efficiency (EQE) of nearly 71%. Optimal Tb^{3+} co-doping concentration in YAG:1%Cr^{3+},x%Tb^{3+} was x = 15% with EQE of more than 98% (excited at 273 nm). All series of samples of YAG:Tb^{3+} and YAG:Cr^{3+},Tb^{3+} were characterized by X-ray diffraction analysis, steady state and kinetic luminescence measurements.

[1] C. R. Ronda, T. Justel, et al. Rare earth phosphors: fundamentals and applications. Journal of Alloys and Compounds **275**, 669-676, (1998).
[2] L. Pavasaryte, A. Katelnikovas, et. al. Eu^{3+}-Doped $Y_{3x}Nd_xAl_3O_{12}$ garnet: synthesis and structural investigation. *Royal Society of Chemistry* **19**, 3729-3737, (2017)
[3] P. F. S. Pereira, M. G. Matos, et. al. Red, green and blue (RGB) emission doped $Y_3Al_5O_{12}$ (YAG) phosphors prepared by non-hydrolytic sol-gel route. Journal of Luminescence **130 (3),** 488-493, (2010).
[4] A. A. Setlur, W. J. Heward, et. al. Crystal chemistry and luminescence of Ce^{3+}-doped (LuCaMg$_2$)-Ca-2(Si, Ge)(3)O-12 and its use in LED based lighting. Chemistry of Materials **18 (14),** 3314-3322, (2006).
[5] A. Zabiliute, S. Butkute, et. al. A., Sol-gel synthesized far-red chromium-doped garnet phosphors for phosphor-conversion light-emitting diodes that meet the photomorphogenetic needs of plants. Applied Optics **53 (5),** 907-914, (2014).
[6] E. Raudonyte, H. Bettentrup, et. al. On the Ce^{3+} -> Cr^{3+} energy transfer in $Lu_3Al_5O_{12}$ garnets. Optical Materials **37**, 204-210, **(2014)**.
[7] Y. Li, et al.,Tailoring of the trap distribution and crystal field in Cr^{3+}-doped non-gallate phosphors with near-infrared long-persistence phosphorescence. Npg Asia Materials **7**, **(2015)**.
[8] J. Grigorjevaite, A. Katelnikovas, Luminescence and Luminescence Quenching of $K_2Bi(PO_4)(MoO_4)$:Eu^{3+} Phosphors with Efficiencies Close to Unity. ACS Applied Materials & Interfaces **8 (46),** 31772-31782, (2016).
[9] G. A. Torchia, J. A. Muñoz, et. al. The luminescent quantum efficiency of Cr^{3+} ions in co-doped crystals of $LiNbO_3$:ZnO determined by simultaneous multiple-wavelength photoacoustic and luminescence experiments. Journal of Luminescence **92 (4),** 317-322 (2001).
[10] G. A. Torchia, et al. The luminescent quantum efficiency of Cr^{3+} ions in Cs_2NaAlF_6 single crystals. Optical Materials **20 (4),** 301-304, (2002).
[11] J. Bouman, et al., On the deep-red luminescence of Cr^{3+} in $Y_3Al_{5-x}Ga_xO_{12}$: Cr^{3+} garnets. Ghent University, 2016.

SYNTHESIS AND PROPERTIES OF CORE-SHELL SEMICONDUCTOR $A^{II}B^{VI}$ HETERONANOPLATELETS WITH TUNABLE SHELL COMPOSITION AND MORPHOLOGY

Artsiom Antanovich[1]*, Anatol Prudnikau[1], Kirill Grzhegorzhevskii[2], Andrey Chuvilin[3,4], Mikhail Artemyev[1]

[1] Research Institute for Physical Chemical Problems of the Belarusian State University, Minsk, Belarus
[2] Ural Federal University named after the B.N. Yeltsin, Institute of Natural Science and Mathematics, Ekaterinburg, Russia
[3] CIC nanoGUNE, Tolosa Hiribidea, 76, E-20018 Donostia – San Sebastian, Spain
[4] Ikerbasque, Basque Foundation for Science, 48013 Bilbao, Spain
artsiom.antanovich@gmail.com

Nanoplatelets or colloidal quantum wells with strong one-dimensional confinement are the most recently discovered class of semiconductor nanocrystals composed of cadmium chalcogenides. They were shown to exhibit optoelectronic properties that are superior to those of respective quantum dots or nanorods, such as extremely narrow absorption and photoluminescence bands, large linear and two-photon absorption coefficients, high electooptical response, low lasing thresholds etc.

However implementation of semiconductor nanocrystals for practical applications generally requires overcoating them with a shell composed of other semiconductor materials with wider bandgap. Such overcoating passivates dangling bonds on the particle surface thus increasing radiative recombination rates, protects nanocrystal cores from the environment and enhances their photo- and chemical stability. Shell deposition on cadmium chalcogenide nanoplatelets is quite challenging, since traditional approaches for overcoating fail in their case and alternative approaches are more sophisticated and less reliable.

It this work we report novel convenient and scalable procedure for overcoating CdSe nanoplatelets with $Zn_xCd_{1-x}S$ (x = 0 - 1) shells using single-source precursors – Zn or Cd diethyldithiocarbamates and study the morphology, structure and optical properties of obtained core-shell heteronanoplatelets (Figure 1).

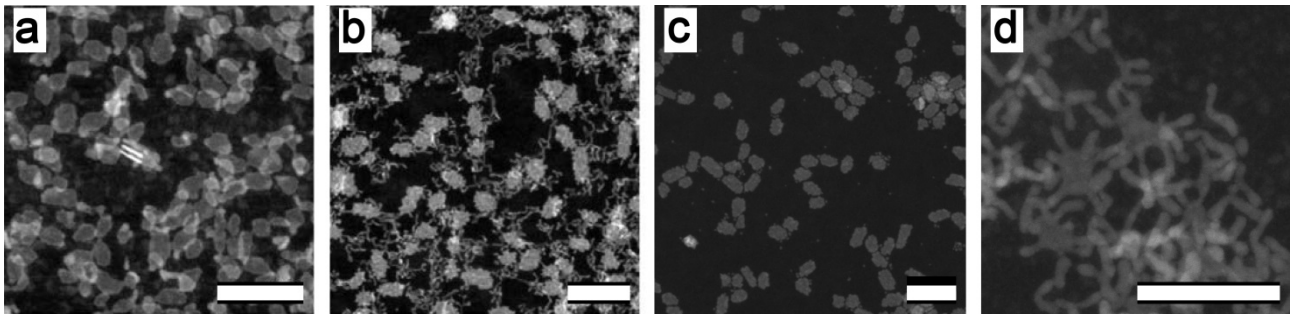

Fig. 1. STEM images of CdSe nanoplatelets prior to (a) and after the overcoating with ZnS (b), ZnCdS (c) and CdS (d) shells. All scale bars are 50 nm.

Using transmission electron microscopy, X-ray diffraction, Raman and optical spectroscopy we investigate the effect of shell composition and related strain at the core-shell interface on the shell morphology and optical properties of final heteronanoplatelets. We demonstrate that among studied materials due to the combination of structural and electronic factors ZnCdS shells provide the best passivation of nanoplatelet core thus yielding CdSe/ZnCdS two-dimensional core-shell heterostructure with the photoluminescence quantum yield of ~ 60 %.

Additionally we introduce a method for the preparation of novel nanocrystals with mixed dimensionality – 2D-1D CdSe/CdS heteronanoplatelets formed due to the inherent zinc blende-wurtzite polytypism of cadmium chalcogenides that can be manipulated by the type of ligands present in the reaction mixture. Such CdSe/CdS heteronanostructures exhibit enhanced light absorption in ultraviolet and blue regions that can be modulated by the length of 1D-branches. Such structures can be considered as promising materials for luminescent solar converters and concentrators or photocatalysts with directional electron transport.

Authors acknowledge financial support from BRFFI grant № X16SRBG-001 and “Chemreagents” program.

TWO DIMENSIONAL SPECTROSCOPY OF CHLOROPHYLL-*c*
Where did all the beatings go?

Eglė Bukartė[1], Anja Haufe[2], Claudia Büchel[2], Donatas Zigmantas [1,*]

[1] Division of Chemical Physics, Lund University, Sweden
[2] Institute of Molecular Biosciences, Goethe University Frankfurt, Germany.

egle.bukarte@chemphys.lu.se

The principal pigments related to absorption of light and transfer of excitation energy towards reaction centers are chlorophylls (Chls). In addition, Chls play a role in charge separation and electron transfer [1]. These molecules are known to have two electronic Qy and Qx transitions, with almost perpendicular polarization with respect to each other, as well as prominent vibrational progressions. The interplay among these electronic excited states and their vibrational degrees of freedom – vibronic coupling – is known to mix the characters from both states. In practice this means that a vibrational side band of the Qy state can absorb (or emit) in both Qy and Qx polarization directions [2].

In photosynthetic molecular systems (Reaction centers, Fenna-Matthews-Olson complexes), vibronic coupling is suggested to play a role in charge transfer [3, 4] and influence the lifetime of coherences within the system [5, 6].

Vibronic coupling can be probed using specialized measurements, such as two-dimensional electronic spectroscopy (2DES), where short coherent laser pulses can excite ladders of states in phase. The coupling is detectable throughout a quantum coherence – a superposition between two levels – and is observed as oscillatory beatings between those levels.

Although known to be of a great importance, no beatings between two electronic levels were observed in Chls using 2DES spectroscopy. One of the most probable explanations being that transition dipole moment of Qx level is just too weak to be probed. In this work we present a 2DES polarization study of Chlorophyll *c* molecule, where Qy and Qx transitions are almost of the same intensity (See Fig. 1), in order to find out: *where did all the beatings go*?

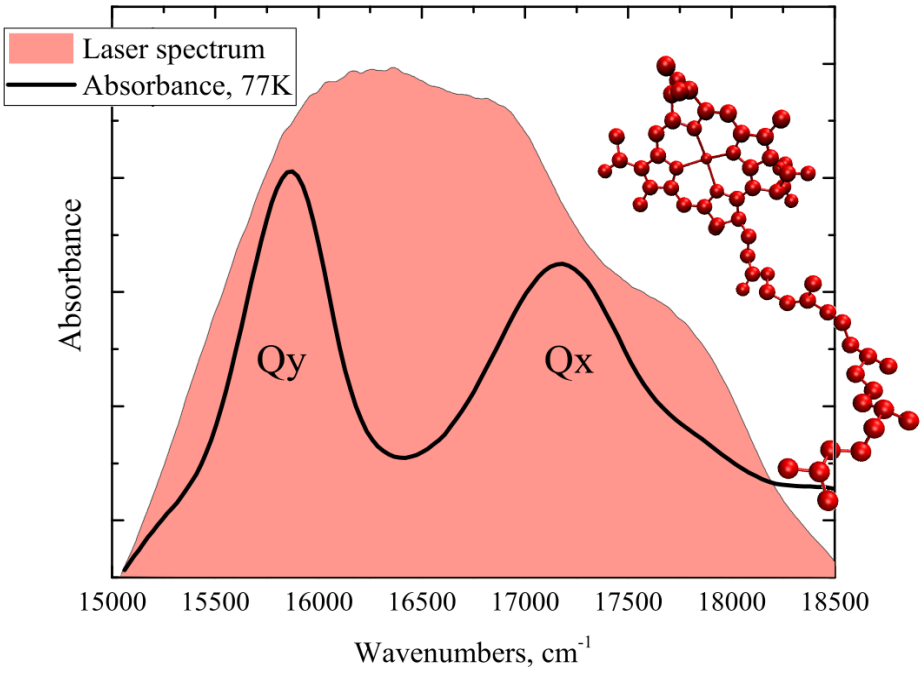

Fig. 1. Low temperature (77 K) absorption spectrum (thick black line) of chlorophyll *c* and a laser spectrum (shaded). The structure of chlorophyll *c* is presented on the right side of the spectrum.

[1] R. E. Blankenship, *Molecular mechanisms of photosynthesis* (Blackwell Science Ltd, Oxford, UK., 2002).
[2] J.R. Reimers, Z.L. Cai, R. Kobayashi, M. Rätsep M, A. Freiberg, E. Krausz, Assignment of the Q-Bands of the Chlorophylls: Coherence Loss via Qx − Qy Mixing, Scientific reports, Nature Publishing Group **3**, 2761 (2013)
[3] F. D. Fuller, et al., Vibronic coherence in oxygenic photosynthesis, Nature chemistry **6**, 706-711 (2014).
[4] E. Romero, et al., Quantum coherence in photosynthesis for efficient solar-energy conversion, Nature physics **10**, 676-682 (2014).
[5] N. Christensson, H. F. Kauffmann, T. Pullerits, T. Mančal, Origin of Long-Lived Coherences in Light-Harvesting Complexes, The Journal of Physical Chemistry B **116**, 7449-7454 (2012).
[6] V. Butkus, L. Valkunas, D. Abramavicius, Vibronic phenomena and exciton–vibrational interference in two-dimensional spectra of molecular aggregates, The Journal of chemical physics **140**, 034306 (2014).

ELECTRONIC AND VIBRATIONAL TRANSITIONS ANALYSIS IN 3*H*-NAPHTHOPYRANS – INSIGHTS FROM EXPERIMENT AND THEORY

Sabina Brazevic, Gotard Burdzinski

Quantum Electronics Laboratory, Faculty of Physics, Adam Mickiewicz University in Poznań, Poland
sabina.brazevic@amu.edu.pl

3*H*-naphthopyrans are valuable photochromic compounds that have been applied in commercially available photochromic lenses. On the molecular level UV-light irradiation initiates a ring-opening reaction as a consequence of C-O bond cleavage. Two colored isomers: transoid-*cis* (TC) and transoid-*trans* (TT) are typically generated. Although the coloration is quite fast, the decoloration process is usually slower which leads to the persistence of a long-lived color for several minutes/hours and this is a serious issue for their application. The photoreaction can be free from residual species simply by replacing a bulky substituent to the 2-position of the naphthopyrans [1]. The application of both, time-resolved electronic and vibrational spectroscopies allows us to detect various intermediates involved in photoreaction of 3*H*-naphthopyrans [2]. However, transient absorption data analysis and interpretation is not straightforward. Quantum-chemical calculations can facilitate data interpretation by giving predictions for electronic and vibrational transitions related to the species involved in the photoreaction. Herein, parent derivative of 3*H*-naphthopyran (3,3-diphenyl-3*H*-naphtho[2,1-*b*]pyran) and its derivatives with various aryl substituents (phenyl, naphthalenyl and pyrenyl, Fig. 1) at the 2-position were studied. Transient species involved in the photoreaction over time-scale from subpicosecond to hundreds of microseconds were characterized by time-resolved UV-vis and mid-IR optical spectroscopies. Additionally, quantum-chemical calculations were performed with the B3LYP functional, 6-311++G(3df,3pd) basis set (the largest Pople-style basis set) and the polarizable continuum model (PCM) for acetonitrile implemented in Gaussian 09.

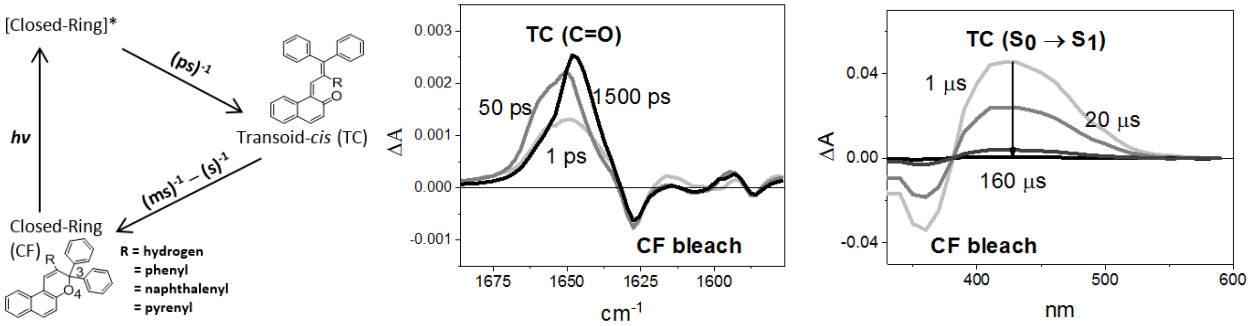

Fig. 1. Photochromic reaction mechanism for 3*H*-naphthopyrans. Exemplary transient mid-IR and UV-vis absorption data obtained in acetonitrile-d_3 after photoexcitation of 2-Ph-NP (λ_{exc} = 320 nm).

Table 1. Theoretical and experimental data for CF and TC forms.

Absorption \ R		H		Ph		Np		Py	
		CF	TC	CF	TC	CF	TC	CF	TC
$S_0 \rightarrow S_1$ transition [eV]	experiment (*ps, **ns)	3.44	2.93*	3.42	2.88* 2.88**	3.36	2.83* 2.82**	3.35	2.78* 2.82**
	theory	3.52	2.56	3.23	2.52	3.30	2.38	2.97	2.16
C = O [cm^{-1}]	experiment	-	1638	-	1648	-	1647	-	1647
	theory	-	1642	-	1638	-	1637	-	1639

The calculated spectral position (cm^{-1}) of vibrational C=O stretching mode of TC isomers of all studied 3*H*-naphthopyran derivatives is in a good agreement with experimental data showing positive transient band at about 1645 cm^{-1}. On the basis of TD-DFT calculations it was possible to obtain excitation energies and oscillator strengths of $S_0 \rightarrow S_1$ electronic transitions for CF and TC in agreement with experiment too (Table 1).

In summary, theoretical calculations allow us to assign spectroscopic data to species involved in the photoreaction and mechanistic details of the photochromic reaction can be explored.

[1] K. Arai, Y. Kobayashi, J. Abe, Rational Molecular Designs for Drastic Acceleration of the Color-Fading Speed of Photochromic Naphthopyrans, Chem. Commun. **51**, 3057-3060 (2015)
[2] S. Brazevic, M. Sliwa, Y. Kobayashi, J. Abe, G. Burdzinski, Disclosing Whole Reaction Pathways of Photochromic 3*H*-Naphthopyrans with Fast Color Fading, J. Phys. Chem. Lett. **8**, 909-914 (2017)

PREDICTION OF UV/VIS SPECTRA OF ORGANIC MOLECULES WITH CHARGE TRANSFER: MULTI-REFERENCE PERTURBATION THEORY VS. TIME-DEPENDENT DFT

Darya Meniailava[1], Aliaksandr Nikitsin[1], Anna Matsukovich[2], Maksim Shundalau[1]

[1] Faculty of Physics, Belarusian State University, Belarus
[2] B.I. Stepanov Institute of Physics, National Academy of Science of Belarus, Belarus
meniailava@bsu.by

Analysis and prediction of the absorption spectra of organic and inorganic molecules in the visible and ultraviolet regions are important theoretical and practical tasks. Nowadays, the most widely applied method for calculating the electronic structure and modeling the electronic spectra of polyatomic molecules is Time-Dependent Density Functional Theory (TDDFT). It is a well-known fact that the frequently used functionals in the TDDFT calculations of excited state energies gives a large deviation in comparison with the experimental values (up to 0.4 eV). It is also noticeable that TDDFT calculations are unsuccessful in the case of intramolecular charge transfer (ICT) excitations. However, there is an alternative to the TDDFT method which is called multi-reference approximation (for example, multi-reference perturbation theory, or MRPT).

The objectives of this study are to evaluate the success of using the above-mentioned approximations for the comprehensive analysis of UV/Vis absorption spectra of widespread organic compounds, most of which are characterized by ICT, as well as, on the basis of the results obtained, to analyze and interpret the UV/Vis spectra of a number of adamantane-containing compounds, perspective for medicinal chemistry and for drugs design. The following compounds are investigated in terms of the first objective: aniline, *trans*-azobenzene, benzaldehyde, glycine, phenol, phenyl isocyanate, pyridine, pyrimidine. We have altered these ones due to available experimental data, it is also known about the ICT for mentioned molecules and they are widely used in biological and chemical industry.

We carry out calculations of spectral and energetic characteristics of the excited singlet electronic states for the above mentioned compounds at the TDDFT approximation using the hybrid CAM-B3LYP functional and perform the *ab initio* calculations at the multi-reference perturbation theory CASSCF/XMCQDPT2 approximation. All calculations are carried out using the cc-pVDZ basis set. The influence of solvents was taken into account by the approximation of the Solvation Model Density (SMD) for TDDFT calculations.

The results of the calculations are shown in Fig. 1. It follows that in most cases TDDFT calculations overestimate energy (underestimate wavelength) of the $S_1 \leftarrow S_0$ и $S_2 \leftarrow S_0$ transitions and the second approximation results a good agreement with the experimental spectra. It is worth mentioning that namely *ab initio* multi-reference (configuration interaction, perturbation theory) should be recommended for simulations and predictions of the UV/Vis spectra.

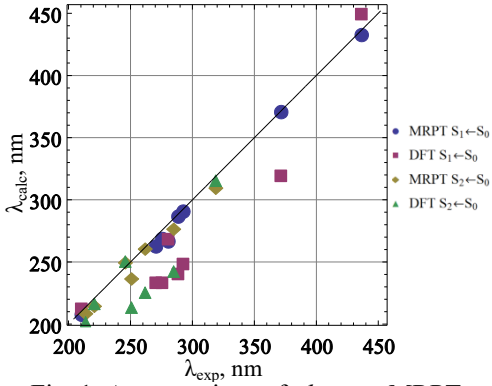

Fig. 1. A comparison of *ab initio* MRPT with DFT calculations for the $S_1 \leftarrow S_0$ and $S_2 \leftarrow S_0$ electronic transitions of 8 molecules under consideration.

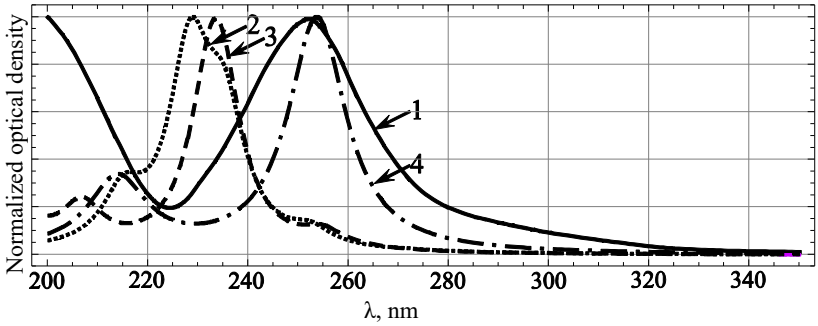

Fig. 2. Experimental (1) and calculated (2, 3, 4) at the TDDFT/CAM-B3LYP/cc-pVDZ (2), TDDFT/CAM-B3LYP/cc-pVDZ + SMD (ethanol) (3) and CASSCF(2,4)/XMCQDPT2 (4) levels of theory UV/Vis spectra of the compound IV.

We use the same approximations to interpret the UV/Vis spectra of solution of 5 adamantane-containing compounds in ethanol: *N'*-(adamantan-2-ylidene)benzohydrazide (I), (3-(adamantan-1-yl)-1-[(4-benzylpiperazin-1-yl)methyl]-4-phenyl-1*H*-1,2,4-triazole-5(4*H*)-thione (II), 3-(adamantan-1-yl)-4-phenyl-1-[(4-phenylpiperazin-1-yl)-methyl]-1*H*-1,2,4-triazole-5(4*H*)-thione (III), 3-(adamantan-1-yl)-4-ethyl-1-[(4-phenyl-piperazine-1-yl)methyl]-1*H*-1,2,4-triazole-5(4*H*)-thione (IV), ethyl-4-{[3-(adamantan-1-yl)-4-phenyl-5-sulfanylidene-4,5-dihydro-1*H*-1,2,4-triazol-1-yl]methyl}piperazine-1-carboxylate (V). The results of calculations for one of these compounds (IV) are shown in Fig. 2. Here one can see that TDDFT approximation predicts zeroth intensity for the $S_1 \leftarrow S_0$ transition with overestimated wavelength and this band has been short-wavelength shifted when one takes into account the solution model. We assume that the errors in the TDDFT calculations are due to the possibility of the ICT. At the same time the results of the multi-reference perturbation theory calculations are in good agreement with the experimental data.

SIMULATING INTERACTIONS BETWEEN FLAMES AND ELECTRIC FIELDS BY APPLYING MODELS USED IN PLASMA PHYSICS

Nikola Goleš

Department of Physics, Faculty of Sciences, University of Novi Sad, Serbia
df.nikola.goles@student.pmf.uns.ac.rs

Recent research in the field of flame manipulation and fire suppression has yielded admirable results. In the reference [1] a method is described for manipulating laboratory-grade flames by applying time-varying oscillating electric fields. Described methods could potentially be used in the future as a means of suppressing fires from a distance in places inaccessible to firefighters. In order to construct effective apparatus utilizing this effect, we must first explore in depth the nature of flame-field interactions.

In this project, a computer simulation of a laminar hydrogen flame is constructed, capable of demonstrating and quantifying its interactions with external electro-magnetic fields. This simulation could be used to extrapolate existing empirical data on flames of other sizes and fuels, thus allowing for a better understanding of the behavior of flames in externally applied fields.

Since flame is the unstable transitional stage of a combustion reaction and it consists of electrons, ions and neutral particles moving at high speeds and recombining frequently [2], we propose that it is possible to make a numerical model of flames as plasmas of low temperatures and densities. A suitable method for such simulations is called the *Particle-in-Cell (PIC)* method (described in [3]), due to its faithful representation of the interaction between plasma particles and external fields. This method reduces the complexity of the simulation by using the Lorentz equation instead of the Coulomb relation for calculating the force exerted on a particle, while utilizing the Debye shielding effect to group individual particles into superparticles, thus further reducing computational cost. Electric field values (external and self-induced by the particles) are calculated only in discrete points in space defined by the nodes of a square lattice positioned over the simulated plasma interface, and are derived using the finite-difference method. As part of the presentation, the *PIC* model and its application to this specific problem will be explained, focusing on its benefits over other possible simulation methods.

We have constructed a 2D electrostatic *PIC* simulation of a premixed hydrogen flame using the *MatLab* toolkit, which has the capabilities to demonstrate the behavior of flames in homogenous time-invariant external electric fields, as illustrated in Fig. 1. Here, negatively charged species of a flame are shown to be deflecting towards the positive electrode in a homogenous electric field. This confirms that models used in plasma physics (such as *PIC*) could potentially be used as reliable simulation methods in combustion physics.

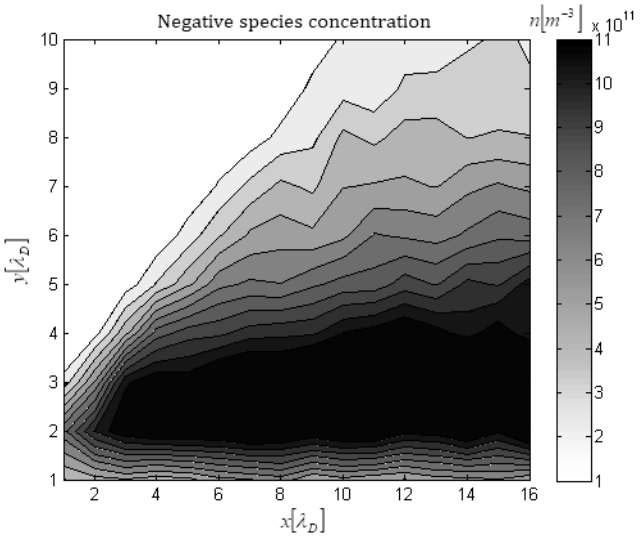

Fig. 1. Negative species concentration for a flame in external applied homogenous electric field of strength 75 kVm^{-1}; simulated interface is located on the lower left corner of the flame, just above the tip of the burner's barrel.

In order to further develop the model, we are adding the ability to simulate time- and space-varying electric fields. To simulate the magnetic components of EM waves we will be using the Boris integrator method [3] for evaluating the velocity vector rotation in a magnetic field arising from the Lorentz force. Finally, since real flames contain many neutral species which are unaffected by EM fields, we will include an adequate "drag factor" as a proposed method to account for the flow-restricting nature of collisions between neutral and charged particles in a flame.

[1] A. M. Drews, L. Cademartiri et al., AC fields drive steady flows in flames, Phys. Rev. E **86**/3:036314 (2012).
[2] C. K. Law, *Combustion physics* (Cambridge University Press, Cambridge, United Kingdom, 2006).
[3] C. K. Birdsall, A. B. Langdon, *Plasma physics via computer simulation* (McGraw-Hill, New York, USA, 1985).

MONTE-CARLO METHOD FOR CALCULATING DAMAGEABILITY

Dzianis Marmysh[1]

[1] Department of Mechanics and Mathematics, Belarusian State University, Belarus
marmyshdenis@mail.ru

The research of the damageability of power systems makes it possible to explain some patterns of behavior of individual nodes and units of mechanisms. The general concepts of dangerous volumes and damageability of power system was considered in [1, 2].

If we have a certain value of stress σ at the point A of continuum Ω, it is possible to determine the local relative damage φ at the point A by the formula

$$\varphi = \frac{\sigma}{\sigma^{(\lim)}},$$

where $\sigma^{(\lim)}$ – limit stress.

If $\varphi \geq 1$, it is said continuum Ω damaged at the point A. As is know, in real systems acting stress σ more than limit stress $\sigma^{(\lim)}$ not only at one point but in some closed region of the continuum. Damageability of the continuum can be described by two parameters: dangerous volume (V) and integral damageability (Ψ), which are defined as follows

$$V = \int\limits_{\substack{\Omega \\ \varphi \geq 1}} dV, \quad \Psi = \int\limits_{\substack{\Omega \\ \varphi \geq 1}} \varphi dV.$$

In this way, the problem of determining the damageability of a system is reduced to the problem of determining the volume V of the figure by a given inequality $\varphi \geq 1$ or $\sigma \geq \sigma^{(\lim)}$. We note that this problem is a special case of calculation the volume of a figure in an n-dimensional Euclidean space.

The solution of inequality $\sigma \geq \sigma^{(\lim)}$ analyticaly is impossible, therefore different numerical approaches are used. In this paper is used Monte-Carlo method for calculation of value of dangerous volume and integral damageability in half-plane when the normally distributed pressure acts on its boundary. The results are obtained with accuracy $\varepsilon = 10^{-2}$ mm^2. The normally distributed pressure are used for simulation: a) elliptic pressure $p(x) = p_0\sqrt{1 - x^2/a^2}$; b) indentation by a rigid flat punch $p(x) = p_0 \Big/ \sqrt{1 - x^2/a^2}$.

The algorithm for calculating of of dangerous volume and integral damageability consists of the following steps:

1) dividing the segment of load distribution into n sub-segments and approximation on each of them by a uniform pressure;
2) determination of the stress state at the point of the half-plane from the action of the load for each sub-segment;
3) sum of actions for each of the n sub-segments [3];
4) generation of random points $A_i(x_i, y_i)$ $(i = 1, 2, ..., N)$ for the area $D = \{(x, y) : x_1 \leq x \leq x_2; y_1 \leq y \leq y_2\}$, which contains dangerous volume V;
5) calculation of the number of points K, where $\sigma \geq \sigma^{(\lim)}$ ($K < N$).

After performing steps 1-5 we can calculate the measures of dangerous volumes and damageability by the formula

$$V = K \cdot dV, \quad \Psi = dV \sum_{i=1}^{K} \frac{\sigma_i}{\sigma^{(\lim)}}, \quad dV = \frac{(x_2 - x_1) \cdot (y_2 - y_1)}{N}.$$

Figure 1 show the graphs measures of dangerous volumes V and damageability Ψ depending by the number of sub-segments n for elliptic pressure and indentation by a rigid flat punch for $a = 3$ mm and $\sigma^{(\lim)} / p_0 = 0.88$.

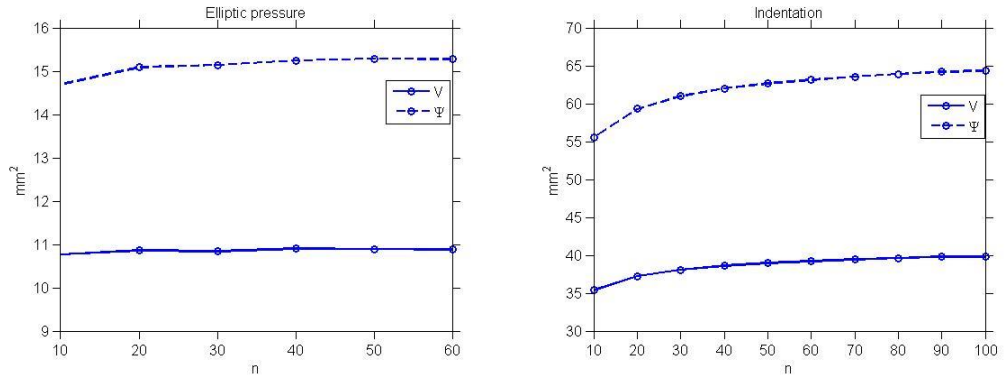

Fig. 1. Measures of dangerous volumes V and damageability Ψ

[1] L. A. Sosnovskiy. Tribo-Fatigue. *Wear-fatigue damage and its prediction* (Springer, 2004).
[2] S.S. Sherbakov, M.A. Zhuravkov. Interaction of Several Bodies as Applied to Solving Tribo-Fatigue Problems, Acta Mechanica **224**, 1-13 (2013).
[3] Д.Е. Мармыш. Численно-аналитический метод граничных элементов в плоской контактной задаче теории упругости, Вести нац. акад. наук Беларуси **3**, 42-46 (2013).

REVERSE ENGINEERING FOR THE LORENTZIAN NONCOMMUTATIVE STANDARD MODEL OF PARTICLE PHYSICS

Arkadiusz Bochniak[1]

[1]Institute of Physics, Jagiellonian University, Poland
arkadiusz.bochniak@student.uj.edu.pl

The approach to the Standard Model based on Connes' ideas of Noncommutative Geometry [3] is a very useful and predictive tool that allows for deep mathematical analysis of the structure of models used in Particle Physics [1]. It reveals the origin of the spontaneous symmetry breaking in the Standard Model and allows for the geometrization of this model. In that approach bosonic parameters can be calculated from the fermionic one using spectral action formalism and renormalization group techniques. The first versions of that model had few problems related to the difference in the mass of the Higgs boson[1], Higgs vacuum instability, fermion doubling, neutrino contents and see-saw mechanism. Moreover, that constructions was based on the Euclidean version of the theory and there were added some additional mathematical assumptions which use is debatable and taking into account possible changes in that structure allows for analysing possible extensions of the Standard Model, like Grand Symmetry[8] or Pati-Salam models[2]. Nowadays, there are a lot of reformulations of this approach using some modifications in the mathematical structure like twisted spectral triples [6] and Morita equivalence for the Clifford modules and the relation with the Hodge-de Rham structures [4],[5]. Furthermore, the Lorentzian versions was also analysed [10],[9],[11],[12],[7], but there are many inequivalent formulations and some of them require additional assumptions to be well-defined and it is not obvious that they are satisfied in real Particle Physics models.

In my master thesis I am trying to implement the reverse engineering methods to analyse what kind of geometric structures can be find in the Standard Model on the pseudo-Riemannian level, without assuming to much a priori. There are a lot of intriguing questions about possible extensions of the Standard Model, the role of S^0-symmetry, the possibility of leptoquarks and the role of the Lorenzian structure. In my talk I will briefly present the main ideas, show preliminary results and formulate working hypothesises.

[1] A. H. Chamseddine, A. Connes, M. Marcolli, Gravity and the standard model with neutrino mixing , Adv. Theor. Math. Phys. **11**, 991-1089 (2007).
[2] A. Chamseddine, A. Connes, W. van Suijlekom, Beyond the spectral standard model: Emergence of Pati-Salam unification, J. High Energy Phys. **11**, 132 (2013).
[3] A. Connes, Noncommutative geometry and reality, J. Math. Phys. **36**, 6194 (1995).
[4] F. D'Andrea, L. Dąbrowski, A. Sitarz, The Standard Model in noncommutative geometry: fundamental fermions as internal forms, arXiv:1703.05279v1 [math-ph].
[5] L. Dąbrowski, On noncommutative geometry of the Standard Model: fermion multiplet as internal forms, arXiv:1711.06492v1 [math-ph].
[6] A. Devastato, Noncommutative geometry, Grand Symmetry and twisted spectral triple, J. Phys.: Conf. Ser. **634** 012008 (2015).
[7] A. Devastato, S. Farnsworth, F. Lizzi, P. Martinetti, Lorentz signature and twisted spectral triples, arXiv:1710.04965 [hep-th].
[8] A. Devastato, F. Lizzi, P. Martinetti, Grand symmetry, spectral action, and the Higgs mass, J. High Energy Phys. **01** 042 (2014).
[9] K. van den Dungen, Krein spectral triples and the fermionic action, Math. Phys. Anal. Geom. **19** (2016).
[10] M. Eckstein, N. Franco, Noncommutative geometry, Lorentzian structures and causality, arXiv:1409.1480 [math-ph].
[11] N. Franco, Temporal Lorentzian Spectral Triples, Rev. Math. Phys., Vol. **26**, No. 8, 1430007 (2014).
[12] M. Paschke, A. Sitarz, Equivariant Lorentzian Spectral Triples, arXiv: math-ph/0611029.

QUANTUM METROLOGY AND THE LOCAL REALISM

Maciej Kościelski[1], Jan Chwedeńczuk[2]

[1]Department of Physics, University of Warsaw, Poland
[2]Institute of Theoretical Physics, Department of Physics, University of Warsaw, Poland
koscielski.maciej at gmail.com

Quantum metrology is a rapidly developing branch of applied quantum mechanics. It requires entangled states of light or matter to beat the classical limits for the measurement precision [1, 2]. For instance, the LIGO gravitational-wave interferometers [3] are soon expected to operate on squeezed vacuum states of light to provide ultra-sensitive detection of the astronomical signal [4]. Also entangled many-body matter waves are a promising tool for precise measurements of fundamental forces, such as gravitation at micrometer distances [5, 6].

On the other hand, the quantumness of a system can manifest through its non-locality, which lies at the heart of the Einstein-Podolsky-Rosen paradox and is witnessed by a broad family of Bell inequalities [7, 8, 9, 10, 11].

In my talk I will focus on the relation between the metrologically useful entanglement and the non-locality. I will show a relation between the correlations responsible for the sub shot-noise sensitivity and the possibility to violate the postulates of local realism.

[1] Vittorio Giovannetti, Seth Lloyd, and Lorenzo Maccone. Quantum-enhanced measurements: beating the standard quantum limit. Science, 306(5700):1330–1336, 2004.
[2] Luca Pezzé and Augusto Smerzi. Entanglement, nonlinear dynamics, and the heisenberg limit. Phys. Rev. Lett., 102(10):100401, 2009.
[3] Benjamin P Abbott et al. Observation of gravitational waves from a binary black hole merger. Physical Review Letters, 116(6):061102, 2016.
[4] LIGO Scientific Collaboration. A gravitational wave observatory operating beyond the quantum shot-noise limit: Squeezed light in application. Nat. Phys., 7:962, 2011.
[5] G. Ferrari, N. Poli, F. Sorrentino, and G. M. Tino. Long-lived bloch oscillations with bosonic sr atoms and application to gravity measurement at the micrometer scale. Phys. Rev. Lett., 97:060402, 2006.
[6] N. Poli, F.-Y. Wang, M. G. Tarallo, A. Alberti, M. Prevedelli, and G. M. Tino. Precision measurement of gravity with cold atoms in an optical lattice and comparison with a classical gravimeter. Phys. Rev. Lett., 106:038501, 2011.
[7] A. Einstein, B. Podolsky, and N. Rosen. Can quantum-mechanical description of physical reality be considered complete? Phys. Rev., 47:777–780, 1935.
[8] J. S. Bell. On the einstein podolsky rosen paradox. Physics, 1:195, 1964.
[9] Nicolas Brunner, Daniel Cavalcanti, Stefano Pironio, Valerio Scarani, and Stephanie Wehner. Bell nonlocality. Rev. Mod. Phys., 86:419–478, Apr 2014.
[10] Ryszard Horodecki, Paweł Horodecki, Michał Horodecki, and Karol Horodecki. Quantum entanglement. Rev. Mod. Phys., 81:865–942, Jun 2009.
[11] N. David Mermin. Hidden variables and the two theorems of john bell. Rev. Mod. Phys., 65:803–815, Jul 1993.

INTERACTION OF AN ASYMETRIC TWO-LEVEL QUANTUM SYSTEM WITH LIGHT

Piotr Gładysz, Dr Karolina Słowik

Institute of Physics, Faculty of Physics, Astronomy and Informatics, Nicolaus Copernicus University, Grudziadzka 5, 87-100 Torun, Poland
pg@atomista.pl

This presentation is about quantum systems with broken inversion symmetry (for example Fig. 1) subject to a strong electric field, which can be used as a tunable radiation source.

A two-level quantum system characterized with inversion symmetry and coupled to a classical electromagnetic field undergoes so-called Rabi oscillations where the population flips between the ground and excited levels.

I will discuss how the dynamics is modified if a system of broken inversion symmetry is exploited instead [1]. Then, the eigenstates are characterized with an extra electric dipole moment originating from the polarisation of charges, which plays a significant role. Apart from Rabi oscillations between the energy levels, additional effective oscillations of eigenenergies of these levels can be identified.

Spontaneous emission has been also taken into consideration by using master equation to describe interaction with vacuum fluctuations. I will demonstrate how all of the additional parts lead to radiation emission not only at the transition frequency of the system but also with the modified Rabi frequency [2].

The latter could reach even the terahertz domain if the quantum system is driven by strong electromagnetic fields, e.g. at close vicinity of plasmonic nanostructures [3].

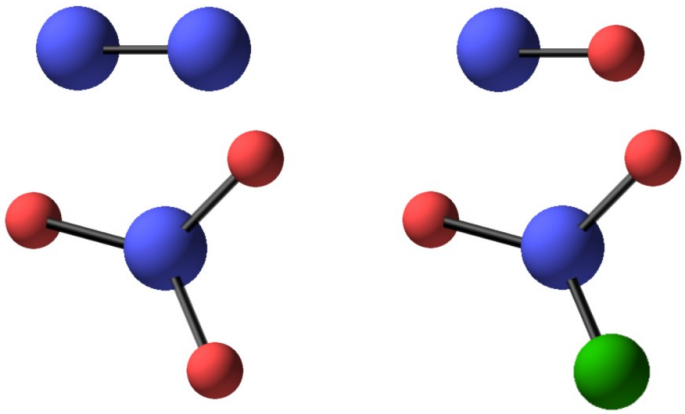

Fig. 1. An example of systems with inversion symmetry (left) and without it (right).

[1] O. V. Kibis, G.Ya. Slepyan, S.A. Maksimienko, A. Hoffman, Matter Coupling to Strong Electromagnetic Fields in Two-Level Quantum Systems with Broken Inversion Symmetry, Physical Review Letters, 2009.
[2] P. Gładysz, Asymetryczny układ dwupoziomowy w oddziaływaniu ze światłem, bachelor's thesis, Toruń (2017).
[3] L. Novotny, N. van Hulst, Antennas for light, Nature Photonics, 5, 83–90 (2011).

OPTIMAL WAVEFORM FOR THE ENTRAINMENT OF A SPIKING NEURON WITH THE MINIMUM MEAN ABSOLUTE VALUE OF THE STIMULATING CURRENT

Augustinas Povilas Fedaravičius, Kęstutis Pyragas

Center for Physical Sciences and Technology, LT-10257 Vilnius, Lithuania
apfedaravicius@gmail.com

We consider the problem of optimal entrainment of a spiking neuron to a periodic external stimulation using the mean absolute value of the stimulating current as a performance measure to be minimized. We denote this functional $\mathcal{J}^*$. The choice of such a performance measure is motivated by the desire to minimize the damage to neural tissue under stimulation. We refer to this problem as a minimum-current control problem. We take into account the clinically relevant charge-balance condition ($\int_0^T I(\omega t)\,\mathrm{d}t = 0$) and the amplitude limitation of the stimulating current ($I_- < I < I_+$). Using phase reduction theory [1] and Pontryagin's maximum principle [2], we derived an algorithm for constructing the optimal waveform that provides the entrainment of a spiking neuron to the stimulating current with the conditions mentioned above.

The optimal waveform is of the bang-off-bang type:

$$I^*(\vartheta) = I_\pm H[z(\vartheta) - z_2] + I_\mp H[z_1 - z(\vartheta)]. \tag{1}$$

Here $I^*(\vartheta)$ is the optimal current, $H(\cdot)$ is the Heaviside step function, $z(\vartheta)$ is the phase response curve (PRC) and ϑ is the phase. The optimal current depends on the sign of the frequency mismatch $\Delta\omega$ between the natural frequency of the neuron and the external stimulation. The upper and the lower subscripts correspond, respectively, to $\Delta\omega > 0$ and $\Delta\omega < 0$. z_1 and z_2 ($z_1 < z_2$) are parameters determined from the equations

$$I_\pm M_+(z_2) + I_\mp M_-(z_1) = \Delta\omega, \tag{2}$$

$$I_\pm N_+(z_2) + I_\mp N_-(z_1) = 0, \tag{3}$$

where $M_\pm(\xi)$ and $N_\pm(\xi)$ are auxiliary functions. Then the value of the functional computed on the optimal trajectory (1) is

$$\mathcal{J}^* \equiv \mathcal{J}[I^*] = |I_\pm| N_+(z_2) + |I_\mp| N_-(z_1). \tag{4}$$

Along with the minimization of tissue damage, the minimum-current control algorithm has another practical advantage. For small $\Delta\omega$, the minimum-current waveform does not require the knowledge of the whole PRC. On the contrary, it is determined only by the distance between the absolute extrema of the PRC and the PRC amplitude. It can thus be written as:

$$I^*(\vartheta) = I_\pm \Pi\left(\frac{\vartheta - \vartheta_{max}}{\Delta\vartheta_+}\right) + I_\mp \Pi\left(\frac{\vartheta - \vartheta_{min}}{\Delta\vartheta_-}\right), \tag{5}$$

where $\Pi(x)$ is the rectangular function that satisfies $\Pi(x) = 1$ for $|x| < 1/2$ and $\Pi(x) = 0$ for $|x| > 1/2$, ϑ_{max} and ϑ_{min} are the extrema of the PRC and $\Delta\vartheta_+$ and $\Delta\vartheta_-$ are the respective widths of the positive and negative pulse.

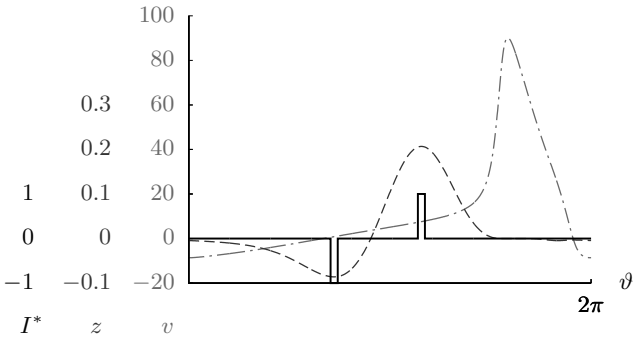

Fig. 1. The membrane potential (dash-dot) of the spiking Hodgkin-Huxley neuron for a direct current $I_d = 20$ μA/cm^2, the PRC (dashed) and the optimal waveform [Eq. (5)] (solid) for $I_+ = -I_- = 1$ μA/cm^2 and $\Delta\omega = 0.01$ rad/ms.

In a real experiment, the parameters of the optimal bang-off-bang waveform can hopefully be estimated empirically, without recourse to the neuron model and phase reduction theory.

[1] Nakao, Hiroya. "Phase reduction approach to synchronisation of nonlinear oscillators." *Contemporary Physics* 57.2 (2016): 188-214.

[2] Pontryagin, Lev Semenovich, et al. "The mathematical theory of optimal processes." (1962).

APPLICATION OF THE REDFIELD RELAXATION EQUATION FOR A TIME EVOLUTION OF A SIMPLE EXCITONIC SYSTEM

Svajūnas Korsakas[1], Darius Abramavičius[1]

[1]Institute of Chemical Physics, Vilnius University, Sauletekio ave. 9, Build. 3, LT-10222 Vilnius, Lithuania
svajunas.korsakas@ff.stud.vu.lt

Quantum mechanics describes quantum static and dynamic effects in molecular systems. One of most popular used examples nowadays is light energy collection, exciton energy transfer between molecules, and charge separation effects [1, 2, 3]. But quantum mechanics application in condensed phase systems is very complicated problem. In recent decades there were new methods developed to calculate dynamic evoliution of quantum systems in thermal environment. But it is still hard to calculate numerically the excitation dynamics. Redfield relaxation equation is one of most used to describe nonequalibrium dynamics at arbitrary temperature.

In this work we take a look on to Redfield relaxation equation, we calculate density matrix elements time evoliution in excitonic system and density matrix elements dependance on temperature. At low temperature (5-100K) dependence on the temperature is weak, but at higher temperature (100-300K) differences between density matrix time evolutions are much higher. It is due to the thermal energy approaching the energy gap value between excitonic states $k_bT \rightarrow E_1 - E_0$. Coherences (Fig. 1) oscillate in broader intervals in high temperature and decay faster. Comparing amplitudes of coherences and populations it can be concluded that the coherences have a very small impact on excited state density matrix dynamics. Nonlinear dependence of relaxation coefficient values at low temperatures $k_bT < \gamma$ are do to transition from quantum environment, $\gamma > k_bT$, into classical $\gamma < k_bT$, where γ - spectral density maximum.

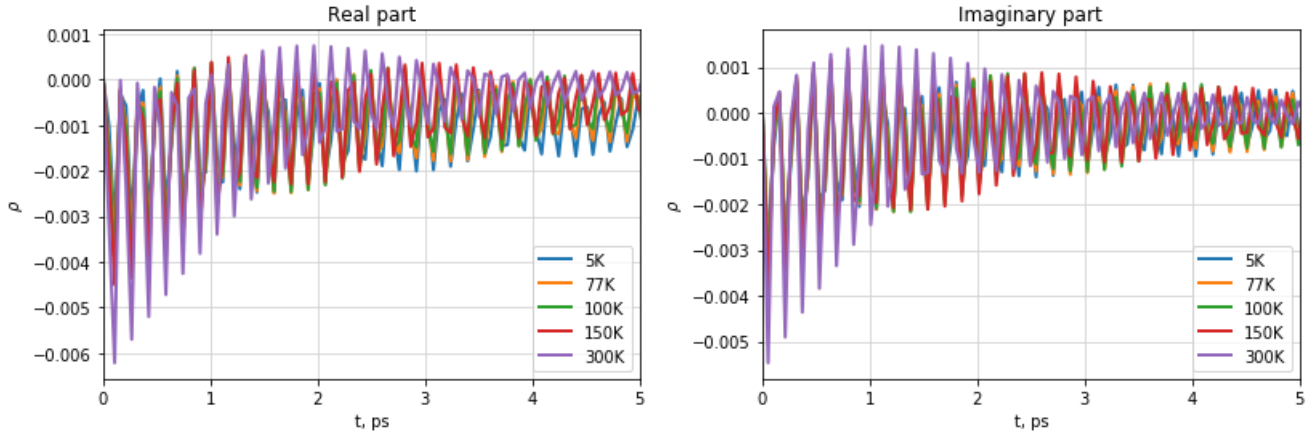

Figure 1. Coherences of mixed state $|1\rangle\langle 0|$.

[1] G. Panitchayangkoon, D. Voronine, D. Abramavičius, J. R. Caram, N. H. C. Lewis, S. Mukamel, G. S. Engel, *Direct Evidence of Quantum Transport in Photosynthetic Light-harvesting Complexes,* Proceedings of the National Academy of Sciences of USA **108**, 20908 (2011).

[2] V. Balevičius, A. Gelžinis, D. Abramavičius, T. Mančal, L. Valkūnas, *Excitation Dynamics and Relaxation in Molecular Heterodimer*, The Journal of Chemical Physics **404**, 94 (2012).

[3] M. Mohseni, P. Rebentrost, S. Lloyd, A. Aspuru-Guzik, *Environmental-assisted Quantum Walks in Photosynthetic Energy Transfer,* The Journal of Chemical Physics **127**, 174106 (2008).

THEORETICAL STUDY OF XE I HYPERFINE STRUCTURE

Gabrielė Stankūnaitė

Institute of Theoretical Physics and Astronomy,Vilnius University, Lithuania
gabriele.stankunaite@ff.stud.vu.lt

Accurate measurements of hyperfine structure (HFS) in atoms can provide important information about the coupling of the nucleus with its electronic environment. Therefore, the purpose of this study was to calculate the HFS constants (A) by applying the multiconfiguration Dirac–Hartree–Fock method. The General-purpose relativistic atomic structure package Grasp2K [1], which was used to execute the calculations, is based on this method.

With the help of the MDHF method 51 states were computed from $5p^6, 5p^5\{6s, 6p, 5d, 4f, 5g\}$ configuration list. Configuration state functions were generated by using the active space method. The active space is formed by selecting an orbital set, which is considered to be active. Then every possible configuration formed from this set of orbitals with corresponding space and spin symmetry forms the active space.

To compute the HFS constants, 5 different active space generation strategies were applied during the study. It was discovered that the most accurate strategy was the one where single and double substitutions were allowed from $5s, 5p, nl$, in this case nl: $6s, 6p, 5d, 4f, 5g$, shells into the active space [2]. The active space was increased by adding 3 additional sets of virtual orbitals (layers). These layers had the orbital symmetry $l = s - g$ and total angular momentum $J = 0 - 6$. In order to examine, whether it is possible to achieve even more accurate results, relativistic configuration interaction calculation including Breit interaction and quantum electrodynamics effects was performed.

The interaction between electrons and nucleus in the atom is described by the total momentum $F = I + J$, which couples the nuclear I and electronic J total angular momenta. Therefore, the HFS of Xe I atom can be examined and the accuracy of generated radial wave and atomic state functions can be evaluated in layers, which are close to the nucleus. The HFS of atomic energy levels is the result of interaction between electrons and electromagnetic multipole moments of the nucleus. The Hamiltonian of this can be expressed as [3]:

$$\hat{H}_{hfs} = \sum_{k\geq 1} \hat{\boldsymbol{T}}^{(k)} \cdot \hat{\boldsymbol{M}}^{(k)}, \tag{1}$$

where $\hat{\boldsymbol{T}}^{(k)}$ and $\hat{\boldsymbol{M}}^{(k)}$ are spherical tensor operators of rank k in the electronic and nuclear spaces, respectively. The nuclear tensor operator is related to the usual nuclear magnetic dipole moment μ_I by relation:

$$\mu_I = \left\langle \Psi(\nu I M_I) \middle| \hat{\boldsymbol{M}}_0^{(1)} \middle| \Psi(\nu I M_I) \right\rangle, \quad M_I = I. \tag{2}$$

The calculated A constants were evaluated by comparing them with experimental results computed by other authors. Constants of levels $6s'\,^2[1/2]_1$ and $6s\,^2[3/2]_1$ are listed in a table below and compared with the results of other authors [4, 5].

Table 1. Comparison of computed A constants (in MHz) with experimental results of other authors.

	[4]	[5]	a6	b6	c4	d5	f3
$6s'\,^2[1/2]_1$	-5788(5)	-5808(2)	-5373	-5372	-5469	-5654	-6119
$6s\,^2[3/2]_1$	-965(1)	-959.1	-951	-951	-940	-990	-901

The first two columns present the experimental values of A constants calculated by other authors. The 1st column represents the best and the 2nd column represents the worst match of experimental values with theoretical results computed when applying the 4th strategy. The other 5 columns represent A constants computed by applying different strategies to generate the active space. The strategy $S\{5s\}\{5p, nl\}$, where single substitutions were allowed from $5s, 5p, nl$ shells into the active space, is marked as a6. The second strategy $Sh\{5s\}\{5p, nl\}$, when the active space was increased by adding the h orbital symmetry, is marked as b6. The strategies, where $4d$ and $\{4p, 4d\}$ shells were move to the active set of orbitals from the core, are marked as c4 and d5 accordingly. The most accurate $SD\{5s\}\{5p, nl\}$ strategy is marked as f3. The hyperfine structure for the rest of the states of Xe will be presented during the conference.

[1] P. Jönsson, J. Bieroń, C. Froese Fischer, G. Gaigalas, I. P. Grant, New version GRASP2K relativistic atomic structure package, Comp. Phys. Com. **9** (184), 2179-2203 (2013).
[2] G. Stankūnaitė, Teoriniai Xe I energijos spektro tyrimai,Vilnius University, 1-30, (2018).
[3] P. Jönsson, F.A. Parpia, C. Froese Fischer, HFS29: a program for relativistic atomic hyperfine structure calculations, Comp. Phys. Com. **96**, 301-310 (1996).
[4] E. Pawelec, S. Mazouffre, N. Sadegh, Spectrochimica acta part B **66**, 470-475 (2011).
[5] G. Damico, G. Pesce, A. Sasso, Isotope-shift and hyperfine-constant measurements of near-infrared xenon transitions in glow discharges and on a metastable Xe($^3P_2$) beam, Phys. Rev. A **60**, 4409-4416 (1999).

PLANAR SELF-ASSEMBLY OF TMA MOLECULES: ASYMMETRY OF MOLECULE IN A HEXAGONAL CAGE

Kasparas J. Kizlaitis[1*], Mantas Šimėnas[1], Evaldas E. Tornau[2]

[1] Faculty of Physics, Vilnius University, Lithuania
[2] Semiconductor Physics Institute, Center for Physical Sciences and Technology, Lithuania
kasparas.kizlaitis@ff.stud.vu.lt

The ordered monolayers of the trimesic acid (TMA) molecules are one of the simplest examples of a two-dimensional self-assembly. These triangular molecules usually form honeycomb-like patterns on noble metal and graphite surfaces. It was also observed that the centers of the hexagons constituting such honeycombs can be occupied by the TMA or other molecules. This makes such orderings highly attractive examples for studying guest-host interactions. However, the experimental scanning tunneling microscopic techniques lack resolution to fully resolve the position and orientation of these guest molecules [1]. Thus, theoretical ab-initio and statistical (Monte Carlo) calculations serve as an alternative tool for detailed understanding of such orderings.

In this work, we propose a relatively simple statistical model to describe the ordering of TMA molecules into honeycomb phase with filled hexagons. The model consists of two types of the short-range TMA-TMA interactions that are caused by the H-bonds between the molecules. The main interaction is responsible for formation of the honeycomb phase (see Fig. 1a). The weaker interactions occur between the central molecule in the hexagon and the rest of the honeycomb. The relative values of these interactions are calculated with by the density functional theory (DFT), while the whole model is simulated using the Monte Carlo method.

During the simulations, we calculated energy and heat capacity of the TMA system for various temperatures and molecular concentrations. The obtained snapshots of simulation (Fig. 1) display the low-temperature ordered structures including the honeycomb, the honeycomb with filled hexagons and dense phases.

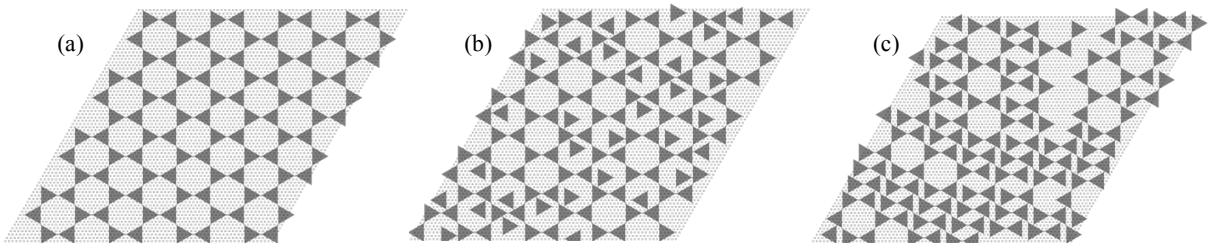

Fig. 1. Snapshots of simulations for TMA concentration of: (a) c_{HON}, (b) $4/3 \cdot c_{HON}$, (c) $3/2 \cdot c_{HON}$, where c_{HON} is the stoichiometric concentration of the honeycomb phase.

[1] D. C. Y. Nguyen et al., Deposition-Temperature- and Solvent-Dependent 2D Supramolecular Assemblies of Trimesic Acid at the Liquid−Graphite Interface Revealed by Scanning Tunneling Microscopy, J. Phys. Chem. C **120**, 11027–11036 (2016).

BROWNIAN MOTORS CONTROLLED BY HARMONIC FLUCTUATIONS OF POTENTIAL ENERGY

Ulada Vysotskaya, Irina Shapochkina

Department of Physics, Belarusian State University, Belarus
vladavysockaya@mail.ru

Mechanisms of energy conversion of nonequilibrium fluctuations of different nature into directed mechanical motion are an object of both methodological and applied interest. The reasons of the interest lie in the desire to understand principles that govern molecular (protein) motors operation and causes of their high efficiency, as well as in designing of artificial devices which can demonstrate controlled movement at the nanoscale [1-3].

One of the main models which describe mechanisms of appearance of nanoparticles directed motion is a so-called Brownian motor (ratchet). For motor operation, both breaking the spatial inversion symmetry and existence of nonequilibrium fluctuations are required. Harmonic fluctuations are the simplest and widely used ones for governing various motor systems.

In our work, we consider a stochastic Brownian motor which motion is induced by small harmonic (in coordinate) fluctuations of the particle potential energy. The basis of the model is the Smoluchowski equation describing the overdamped motion of a Brownian particle in a periodic potential $U(x,t) = u(x) + \sigma(t)w(x)$, where $u(x)$ and $\sigma(t)w(x)$ is, respectively, a stationary and a fluctuating (control) component of the potential energy; $u(x+L) = u(x)$, $w(x) = \cos(2\pi x/L)$, L is a period. Our analytical and numerical analysis is based on the following general expression for the motor average velocity [4]

$$\langle v\rangle = LJ, \quad J = \beta^2 D^2 \int_0^L dx q(x) w'(x) \int_0^L dx' S(x,x') \frac{\partial}{\partial x'} w'(x') \rho^{(0)}(x') \qquad (1).$$

Here β is the inverse thermal energy, D is the diffusion coefficient, $q(x) = e^{\beta u(x)} / \int_0^L dx e^{\beta u(x)}$, $\rho^{(0)}(x) = e^{-\beta u(x)} / \int_0^L dx e^{-\beta u(x)}$. The function $S(x,x')$ is the Laplace representation of the Green's function for the diffusion in the potential $u(x)$. A detailed study of the properties of $S(x,x')$ function is given in our works [4-6]. The function $u(x)$ is chosen as a piecewise linear (sawtooth) one. The high-temperature approximation made it possible to analyse regimes of motor operation analytically, while, out of this approximation, the motor characteristics have been calculated numerically, by quadrature formula for integrals. We have analyzed the behavior of the average motor velocity as a function of the phase shift λ_0 of the control signal relative to the stationary component of the potential energy. It is shown that while within the high-temperature approximation the average velocity is multiplicative with respect to the model parameters [4], the consideration beyond this approximation violates the multiplicativity (so that the roles of temporal and spatial control parameters cannot be analyzed separately). At the same time, for certain fixed values of the asymmetry parameter κ of the stationary component $u(x)$, an increase in its amplitude βu_0 leads to an increase in the size of the region of positive values of the motor velocity and to a decrease in the size of the region of negative values. This allows one to assume the existence of regimes in which the choice of the parameter βu_0 will suppress the negative values at all. The influence of the asymmetry parameter κ on both the magnitude and direction of the average motor velocity is demonstrated: It is shown that the competition between the parameters κ and λ_0 plays a decisive role. The behavior of the motor stopping points with temperature changes has been studied. We have also demonstrated the possibility of the choice of optimal parameters for motor operating (which are determined by the maxima of the dependencies).

The results can be of interest for practical applications in the field of nanoengineering, biophysics, surface chemistry, which use the effect of rectifying nonequilibrium fluctuations into the directed motion of nanoparticles. The use of a spatially harmonic signal as a source of perturbation of a stationary spatially periodic asymmetric potential profile shows great promise: Signals of this type are easily realized and widely used in various applications.

[1] P. Reimann, Brownian motors: noisy transport far from equilibrium, Phys. Rep. **361,** 57 – 265 (1990).
[2] J. Howard, *Mechanics of Motor Proteins and the Cytoskeleton* (Sinauer, Sunderland, MA, 2001).
[3] P. Hänggi and F. Marchesoni, Artificial Brownian motors: Controlling transport on the nanoscale, Rev. Mod. Phys. **81**, 387 - 442 (2009).
[4] U. A. Vysotskaya, I. V. Shapochkina, V. M. Rosemaum et al, Stochastic Brownian motors with small potential energy fluctuations, Chemistry, Physics and Technology of Surface **8**, 299-309 (2017).
[5] U. A. Vysotskaya, I. V. Shapochkina, V. M. Rosemaum et al, Diffusion of Brownian particles in a spatially periodic potential with a finite life-time, Journal of the Belarusian State University. Physics **3**, 33-40 (2017).
[6] U. A. Vysotskaya, I. V. Shapochkina, Diffusion of a Brownian particle in a periodic potential with a finite life-time, 60th Scientific Conference for Students of Physics and Natural Sciences Open Readings 2017, ISSN 2029-4425, Vilnius University, 119 (2017).

OPERATOR APPROACH TO THE ELECTRODYNAMICS IN TIME-DEPENDENT LINEAR MEDIA

Fyodor Morozko[1], Andrey Novitsky[1,2]

[1]Department of Theoretical Physics and Astrophysics, Belarusian State University, Belarus
[2]DTU Fotonik, Technical University of Denmark, Denmark
fyodormorozko95@gmail.com

Recent research has shown that time-dependent media can lead to a number of novel effects. Among others there are optical time-reversal [1], excitation of standing waves with infinite group velocity in temporally periodic medium [2], "time Faraday effect" [3] and "time birefringence" [4] in magnetoelectric-coupled media, parametric resonance of defect modes in photonic crystals [5].

It would be convenient to have an apparatus applicable to the variety of time dependent material parameters. Here we demonstrate that operator method known in electrodynamics of stratified media [6] well suits for this purpose. The technique in ref. [6] uses linear operators to describe spatial evolution of an electromagnetic mode. Namely the mode field at some point z is connected to starting point z_0 by means of evolution operator (propagator)

$$W(z) = F(z, z_0) W(z_0). \tag{1}$$

Operator approach can be employed for the accurate field calculations, as well as for approximate ones including homogenization and perturbation theory [7, 8].

In this work we propose a similar approach applied to the electrodynamics of time-dependent media. The analogy between stratified medium and uniform nonstationary medium is in the fact that material parameters in both cases depend on a single coordinate. In the case of stratified medium the coordinate is normal to layer interfaces and in the case of nonstationary medium the coordinate is time.

In the framework of developed method we consider the case of time-stratified medium (i. e. the medium which has stationary material parameters within a time interval) and obtain tensorial time-refraction and time-reflection coefficients. We also propose a perturbation theory analogous to that described in [8] for the case of weak time dependencies.

[1] S. Vezzoli, et al., Optical time reversal from time-dependent epsilon-near-zero media, Phys. Rev. Lett. **120** (2018)
[2] J. S. Martinez-Romero, P. Halevi, Standing waves with infinite group velocity in a temporally periodic medium, Phys. Rev. A **96** (2017)
[3] R.-Y. Zhang et al., Time circular birefringence in time-dependent magnetoelectric media, Scientific Reports **5** (2015)
[4] S. R. Lin et al., Electromagnetic wave propagation in time-dependent media with antisymmetric magnetoelectric coupling, Phys. Lett. A **380** (2016)
[5] V. Konotop, V. Kuzmiak, Parametric resonance of a defect mode in a 2D photonic crystal, Phys. Rev. B **64** (2001)
[6] G. Borzdov, Frequency domain wave-splitting techniques for plane stratified bianisotropic media, J. Math. Phys **38** (1997)
[7] V. Popov, A. Lavrinenko, A. Novitsky, Operator approach to effective medium theory to overcome a breakdown of Maxwell Garnett approximation, Phys. Rev. B **94** (2016).
[8] A. Furs, T. Alexeeva, Reflection and transmission of weakly inhomogeneous anisotropic and bianisotropic layers calculated by perturbation method, J. Phys. A: Math. Theor. **41** (2008) .

STOCHASTIC PROCESSES WITH DETERMINISTIC DICHOTOMOUS CHANGES OF TRANSITION RATES AS A MATHEMATICAL MODEL OF A BROWNIAN FOTOMOTOR

Yuliya A. Kamysh, Irina V. Shapochkina.

Department of Physics, Belarusian State University, Belarus
juliak1995@mail.ru

An interest in the phenomenon of transformation of chaotic Brownian motion into directional transport of nanoparticles arose long ago. During the last decades, systems which can demonstrate this phenomenon, called Brownian motors, have been actively studied, simulated and realized in real devices [1-4]. Such systems are based on the general principle: for the directional motion of a particle, its potential energy, as a periodic function of coordinates, must be spatially asymmetric and time-dependent; and a driving force, which it entails, must be unbiased [1]. In Brownian photomotors [5], the change, with time, in particle potential energy is induced by cyclic laser pulses that are resonate with certain levels of its electronic subsystem. As a result, a dependence of the particle charge distribution on time, $P(\mathbf{r}',t)$, appears. Then the potential energy of the particle interaction with a polar substrate $U(\mathbf{r},t)$, which is a source of the electrostatic potential $\varphi(\mathbf{r})$, also acquires time dependence, $U(\mathbf{r},t)=\iiint_V d\mathbf{r}'P(\mathbf{r}',t)\varphi(\mathbf{r}+\mathbf{r}')$.

Usually, the time dependence $U(\mathbf{r},t)$ is modeled as a step function, so $U(\mathbf{r},t)$ describes a dichotomous process with the potential relief $U_+(\mathbf{r})$ and $U_-(\mathbf{r})$ when the laser is turned on and off, respectively. Typically, the system response is not instantaneous, and one must take this fact into account.

The aim of the work was to study, analytically and numerically, characteristics of Brownian motors governed by stochastic processes with dichotomous changes in transition rates. We study the kinetics of a three-level system with arbitrary rate constants of transitions between the levels. The mathematical model is a system of differential equations for the population of the particle electronic levels $n_j(t)$ [5]:

$$\begin{aligned} dn_1^{\pm}(t)/dt &= -k_{12}I\delta_{\pm}n_1^{\pm}(t)+\left[k_{21}I\delta_{\pm}+\tau_{21}^{-1}\right]n_2^{\pm}(t)+\tau_{31}^{-1}n_3^{\pm}(t),\\ dn_2^{\pm}(t)/dt &= k_{12}I\delta_{\pm}n_1^{\pm}(t)-\left[k_{21}I\delta_{\pm}+\tau_{21}^{-1}+\tau_{23}^{-1}\right]n_2^{\pm}(t),\\ dn_3^{\pm}(t)/dt &= \tau_{23}^{-1}n_2^{\pm}(t)-\tau_{31}^{-1}n_3^{\pm}(t). \end{aligned} \qquad (1)$$

Knowledge of $n_j(t)$ allows one calculating the particle charge distribution $P(\mathbf{r},t)$. The parameter δ is responsible for the "on" and "off" states of the laser with the intensity of the pulse I; the forward (backward) transitions between the ground electronic state 1 and the excited one 2, when the laser is turned on (off), are characterized by the transition constants $k_{12}I$ ($k_{21}I$); the inverse lifetimes $\tau_{21}^{-1},\tau_{23}^{-1},\tau_{31}^{-1}$ of the states characterize spontaneous transitions.

The model (1) is a particular case of the Pauli equation arising in the description of a stochastic Markov process of transitions between N (here $N=3$) states for the conditional probability $\rho_{nn'}(t)$ to find the system at the time t in the state n, provided that at the previous, initial, time $t=0$ it was in the state n':

$$\frac{d}{dt}\rho_{nn'}(t)=\sum_{n''}\Gamma_{nn''}(t)\rho_{n''n'}(t)=0,\ \rho_{nn'}(0)=\delta_{nn'}. \qquad (2)$$

Here, the matrix Γ is time dependent, that is, it is different for the time intervals τ_+ with the laser turned on ($\Gamma_{nn''}^{(+)}$) and τ_- with the laser turned off ($\Gamma_{nn''}^{(-)}$), and thus is described as a deterministic dichotomous process:

$$\Gamma_{nn''}(t)=\begin{cases}\Gamma_{nn''}^{(+)}, & (r\tau<t<r\tau+\tau_+)\\ \Gamma_{nn''}^{(-)}, & (r\tau+\tau_+<t<(r+1)\tau)\end{cases},r=0,1,\ldots;\quad \tau=\tau_++\tau_-. \qquad (3)$$

This model is analyzed analytically (under the certain assumptions about the values of the system characteristic times) and numerically (in the general case). The behavior of $n_j(t)$ quantities with time is illustrated graphically. The ways in which the level populations are redistributed with time under the cyclic laser pumping have been demonstrated, as well as the changes in photomotor potential energy as a result of it. The conditions under which the maximum photomotor velocity is reached have been analyzed. The results are discussed in the context of a Brownian photomotor based on a semiconductor nanocluster [5].

[1] P. Reimann, Brownian motors: noisy transport far from equilibrium, Phys. Rep. **361,** 57 – 265 (1990).
[2] P. Hanggi, F.Marchesoni, Artificial Brownian motors: Controlling transport on the nanoscale. Rev. Mod. Phys. **81**, 387 – 441 (2009).
[3] V. Serreli, C.F.Lee, E.R.Kay et.al., A molecular information ratchet. Nature (London). **445**, 523 – 527 (2007).
[4] J. Siegel, Inventing the nanomolecular wheel. Science. **310**, 63 – 64 (2005).
[5] V.M. Rozenbaum, M.L. Dekhtyar, Sh.H. Lin et.al, Photoinduced diffusion molecular transport. J.Chem.Phys. **145**, 0641101-12 (2016).

DIFFERENT TYPES OF CLUSTERIZATION OF SIX BODY SYSTEMS USING JACOBI COORDINATES

Augustinas Stepšys[1], Saulius Mickevičius[2], Darius Germanas[3], Ramutis Kazys Kalinauskas[3]

[1]Department of Theoretical Physics,Faculty of Physics of Vilnius University, Saulėtekio Avenue 9,build. 3, 10222, Vilnius , Lithuania

[2]Vytautas Magnus University, K. Donelaičio str. 58, LT-44248, Kaunas, Lithuania

[3]Center for Physical Sciences and Technology, Savanoriu str. 231, LT-02300 Vilnius, Lithuania

augustinas.stepsys@ff.vu.lt

The antisymmetrization of a given system and the center of mass (CM) elimination must be ensured for the wave function of nuclear system. CM problem is easily solved by direct construction of the CM free wavefunction in terms of the relative (Jakobi) coordinates of an identical fermions. If the Jakobi coordinates are used, then the antisymetrization procedure can be done in isospin formalism and the use of Slater determinants is not needed. By using this type of approach the spurious state elimination is avoided and significant reduction of matrix dimensions is achieved.

Wavefunction antisymmetrization for a six body system can be based on eigenvalue calculation of two particle transposition operator P of a symmetry group S_6. In this method, six particle system can partitioned into different types of sub-clusters. For example, six particle system can be partitioned into three particle subclusters and subclusters made from four and two particles. (Fig.1). The basis states of subclusters must be antisymmetrized before the antisymmetrization of whole system [1]. Then the six body system can be characterized by good quantum numbers: Oscillator quanta E, total angular momentum J, parity π, isospin T and additional integer quantum number Δ for unambiguous enumeration of the basis states.

In presentation, the procedure of antisymmetric basis state construction for six particle nuclear system in different types of clusterization will be given, as well as calculation results..

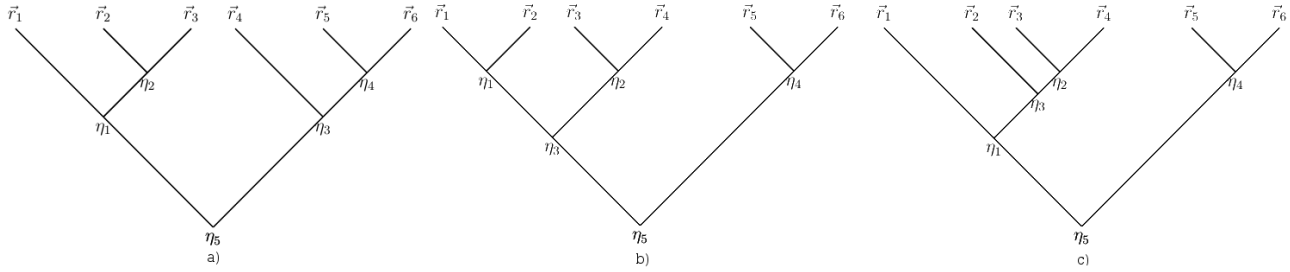

Fig. 1. Six body system in Jacobi coordinates with intrinsic clusterization. A) refers to system partitioned 6=3+3; b) refers to partitioning 6=(2+2)+2; c) refers to partitioning 6=(1+3)+2

[1] S. Mickevičius, D. Germanas, R. K. Kalinauskas, Cent. Eur. J. Phys. **11** (2013), 568.

SIMULATION OF ELECTRON ENERGY SPECTRUM IN LASER PULSE GENERATED PLASMA

Henrikas Vaickus[1], Jonas Reklaitis[2]

[1]Vilnius university Faculty of Physics, Saulėtekio av. 9, Bld. III, LT- 10222 Vilnius, Lithuania.
[2]Center for Physical Sciences and Technology, Savanorių ave. 231, LT-02300 Vilnius, Lithuania
Henrikas.vaickus@ff.stud.vu.lt

Considering the promising alternative of X-rays generation by plasma accelerated ultrafast electrons [1], in this work we investigate electrons acceleration in a laser pulse generated plasma. As the main tool of research in this area, we consider electron energy spectrum, as a result we will pay attention for electron energy distribution dependencies on laser parameters in more detail.

To begin with, there were foreseen to model a physical system of electrons acceleration. In addition, some theoretical assumptions were made. Firstly, here we describe a single electron, which is initially at rest. Then electron starts to oscillate in high intensity fields of an electromagnetic wave with a random initial phase (from 0 to π). As we will see, random phase in the beginning of oscillations provides results, which describe multiple electron systems. It is important to mention, that we do not consider the interaction between electrons and ions, nor take into account the frequency distribution of laser pulse.

Second task was the implementation of the physical system in the "Matlab" environment. During the modeling part, the system was set to original parameters, used for a calibration of the model: the laser intensity was 3×10^{18} W/cm^2, the wavelength of 800 nm and pulse duration of 120 fs. Later, these parameters were varied in order to find out dependencies of the spectrum.

Final part involved the generation of electrons spectrums by using the created model and analysis of the energy distributions. A set of spectrums were got, which had similar properties as experimental results during electrons acceleration in plasma [2][3]. Considering this fact, we made a conclusion that our generated spectrums could be considered as a suitable approximation for experimental data. The analysis of main results showed the electron spectrum evolution in the first period, the linear dependency on a laser intensity (Fig. 1) and the square dependency on a wavelength (Fig. 2).

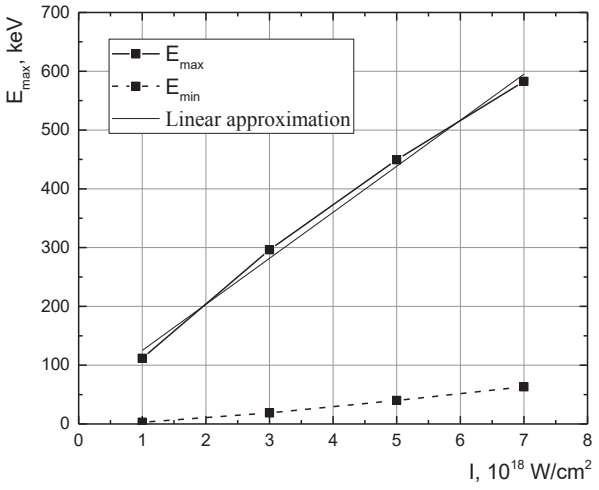

Fig. 1. Electron spectrum dependency on laser intensity.

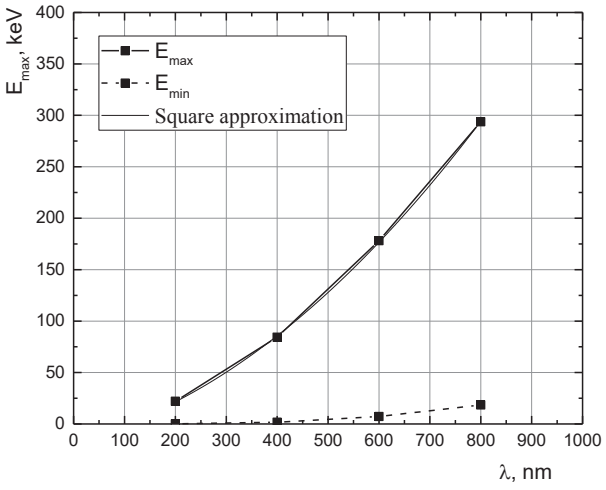

Fig. 2. Electron spectrum dependency on laser wavelength.

[1] A. Baguckis, A. Plukis, J. Reklaitis, V. Remeikis, L. Giniūnas, M. Vengris. Generation of plasma X-ray sources via high repetition rate femtosecond laser pulses. *Applied Physics B,* 123:290, 2017.
[2] L. M. Chen, J. Zhang, Q. L. Dong, H. Teng, T. J. Liang, L. Z. Zhao, Z. Y. Wei. Hot electron generation via vacuum heating process in femtosecond laser – solid interactions. *Physics of Plasmas*, vol. 8, No. 6, 2001.
[3] B. Chichkov, Y. Kato. Electron distribution function in an intense femtosecond laser field, Physical Review A, vol. 46, no. 8, 1992.

POLARIZATION EFFECTS FOR SINGLE GAUGE BOSON PRODUCTION IN LEPTON-PHOTON COLLISIONS

Ivan Shershan[1], Tatiana Shishkina[1]

[1] Department of Theoretical Physics and Astrophysics, Belarusian State University, Republic of Belarus
undershroud@gmail.com

Modern high-energy physics is aimed at both the confirmation of already established theories (such as the Standard Model (SM) and quantum chromodynamics (QCD)), and the search for different kinds of deviations from the formed theories. However, it would be presumptuous to assume that the existing electroweak theory is the only one possible. Therefore, the search for deviations from the Standard Model is an important task of modern fundamental science.

One of the most progressive areas of such research is studying the lepton flavor violating processes (involving neutrino oscillations). However, neutrino detection is a very difficult task for high-energy experimental physics. In this case, the lepton–photon interactions study has great potential. This is due to the linear colliders high accuracy and the nonzero lepton number in the final state [1]. Moreover, these processes can be implemented in the future at the International Linear Collider (ILC) [2].

In this paper single gauge bosons production polarization effects in photon-lepton collisions were investigated [3]. Precise covariant analytical expressions and graphs for total cross sections and asymmetries in the cases of photon interaction with electrons and muons were obtained. Electron interaction asymmetries $A^{e\gamma}$ and asymmetries difference $\Delta A^{l\gamma}$ for leptons of different generation defined as

$$A^{l\gamma}_{PP';KK'}(X)=\frac{\sigma^{l\gamma}_{PP'}(X)-\sigma^{l\gamma}_{KK'}(X)}{\sigma^{l\gamma}_{PP'}(X)+\sigma^{l\gamma}_{KK'}(X)}\times 100\%;\quad \Delta A^{l\gamma}_{PP';KK'}(X)=A^{e\gamma}_{PP';KK'}(X)-A^{\mu\gamma}_{PP';KK'}(X), \tag{1}$$

where $\sigma^{l\gamma}_{PP'}(X)$ is the total cross section of X boson production process in $l\gamma$–interaction; $P(P')$ is initial(final) lepton polarization. Corresponding graphics for different processes are presented in Fig. 1.

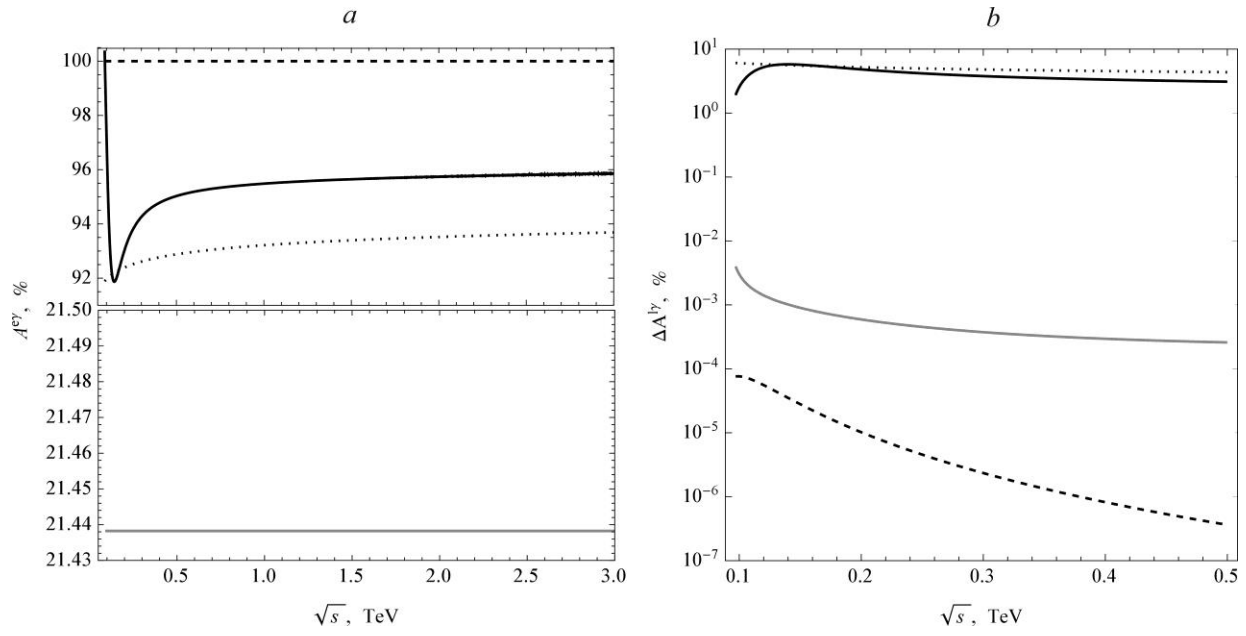

Fig. 1. Asymmetries $A^{e\gamma}_{PP';KK'}(X)$ (a) and asymmetries difference $A^{l\gamma}_{PP';KK'}(X)$ (b) in following cases (X,PP',KK'): (γ,LL,LR) – dotted line, (Z,LL,LR) – solid line, (W,LL,LR) – dashed line, (Z,LR,RL) – gray line.

Deviations from the obtained values (with the exception of radiation corrections) may indicate observed deviations from the Standard Model.

[1] I.F. Ginzburg et al., Colliding γe and γγ beams based on single-pass e^+e^- accelerators II. Polarization effects, monochromatization improvement. Nuclear Instruments and Methods in Physics Research **219.1,** 5-24 (1984).
[2] H. Baer et al., The International linear collider technical design report-Volume 2: Physics. *arXiv preprint* ***arXiv:1306.6352*** (2013).
[3] A. Denner, S. Dittmaier, Gauge-boson production in electron-photon collisions. *arXiv preprint* ***hep-ph/9308360*** (1993).

GAUGE PARAMETER DEPENDENCE OF THE NEUTRINO MASS RENORMALIZATION

Vytautas Dūdėnas, Thomas Gajdosik

Institute of Theoretical Physics and Astronomy, Faculty of Physics, Vilnius University, Lithuania
vytautasdudenas@inbox.lt

The main building blocks of any model in a quantum field theory are postulated gauge symmetries and the phenomenological parameters such as masses and couplings. The observables, however, are not directly the masses or the couplings, but decay rates and cross sections constructed from amplitudes. The amplitudes then have to be independent of the gauge choice, since they are directly related to the observables of the model. The amplitudes depend on the parameters of the theory, hence from the information of the measured decay rates and cross sections we can indirectly "measure" those phenomenological parameters. From the theoretical point of view these parameters need not be gauge parameter independent: the dependence just has to cancel when calculating the amplitude. Despite that, it is desirable to have gauge independent masses and couplings, as they would more directly correspond to our physical intuition of what a mass and a coupling should be. This, however, is not always an easy task, if one goes to a higher accuracy than the tree level approximation.

To calculate amplitudes with higher accuracy than at tree level, one needs to renormalize the theory. This means that the renormalized parameters of the theory are now determined from the renormalization conditions at a given order of accuracy. So now we are the ones that determines what our parameters mean and if we are not careful enough, we might accidentally introduce unwanted gauge dependent terms into the parameters.

We study the mass renormalization of the neutrinos in a two Higgs doublet model extended by one sterile neutrino allowing radiative mass generation, the model introduced by [1]. We adapt the complex mass scheme for neutrinos [2] as it is formally shown to give gauge invariant definitions for masses at all loop levels [3]. When calculating explicitly, the mass renormalization constants for neutrinos turn out to depend on the gauge fixing parameter, which means that the bare mass parameter becomes gauge dependent. The solution to this problem is to add the tadpole functions to the definition of the counterterm as briefly discussed in [4]. This method is inspired by the pinch technique [5], in which the gauge dependent terms of the Green's functions of the theory are separated systematically. These tadpole functions actually come from the renormalization of the Higgs vacuum expectation value, hence adding the tadpole functions to the mass counterterms also effects the so-called tadpole conditions. This also affects the Legendre transform of the generating functional of the theory. Nevertheless, this technique is useful in defining the gauge independent part of the counterterm leaving the gauge dependent part for bookkeeping reasons.

We present the algebraic structure of the relationship between the neutrino mass and the Higgs sector renormalization paying attention to the gauge dependences at one loop order. We discuss different basis choices for the fields and for the renormalization constants. We outline the steps done to arrive at the analytic checks using the Mathematica packages FeynArts[6], FormCalc[7] and Sarah[8].

Acknowledgements: The authors thank the Lithuanian Academy of Sciences for the support (the project DaFi2017).

[1] W. Grimus and H. Neufeld, Nucl. Phys. B **325** (1989) 18. doi:10.1016/0550-3213(89)90370-2
[2] V. Dūdėnas, T. Gajdosik, Acta. Phys. Polonica B **56** (2017). doi:10.5506/APhysPolB.48.22434
[3] P. Gambino, P.A. Grassi, Phys. Rev. **D62**(2000) doi: 10.1103/PhysRevD.62.076002
[4] S. Liebler, W. Porod, Nucl. Phys. **B849** (2011) 213-249 doi:10.1016/j.nuclphysb.2011.10.033
[5] J.M. Cornwall, J. Papavassiliou, D. Binosi, "The Pinch Technique and its Applications to Non-Abelian Gauge Theories", Cambridge University Press (2010)
[6] T. Hahn, Comput. Phys. Commun. **140** (2001) 418 doi:10.1016/S0010-4655(01)00290-9 [hep-ph/0012260]
[7] T. Hahn and M. Perez-Victoria, Comput. Phys. Commun. **118** (1999) 153 doi:10.1016/S0010-4655(98)00173-8 [hep-ph/9807565]
[8] F. Staub, arXiv:0806.0538 [hep-ph]

ASTEROSEISMICS DIAGNOSTICS OF QUASI-ADIABATICITY OF THE CORE OVERSHOOTING REGIONS IN B-STARS.

Carlos Viscasillas[1], Ehsan Moravveji[2], Andy Moya[3]

[1]Institute of Theoretical Physics and Astronomy, Saulėtekio av., Vilnius 10222, Lithuania
[2]Instituut voor Sterrenkunde, KU Leuven, Leuven 3001, Belgium
[3]School of Physics and Astronomy, University of Birmingham, Birmingham B15 2TT, UK
cviscasillas@uc.cl

In this poster we present a theoretical and computational study for obtaining the oscillation dipole modes of pulsating main sequence B type stars (SPB and β Cep), constraining the behaviour of the temperature profile in the overshooting region. This is a critical but poorly-understood phenomenon which affect different parameters outside classical convection zones. Convective core overshooting is important because it extends the main-sequence lifetime of a star, thus modifying their evolution. We discuss some uncertainties in that region, concerning the quasi-adiabaticity in B stars. We focus on the g-mode behavior in that zones surrounding the convective core. For that we use the numerical codes MESA [1] and GYRE [2] for stellar evolution and oscillation respectively. We found obvious differences between the radiative and the adiabatic model, based on asteroseismological techniques.

The inclusion of quasi-adiabaticity in the overshooting region produces significant differences in the temperature gradients, properties of oscillation modes, period spacing and Brünt-Väisälä frequency. In the case of SPB, these differences are more significant for long periods and less evolved models. Recent studies can model perfectly the period spacing of KIC7760680 [3] for short-period modes, but observations and models show an anti-correlation towards the high order g-modes. One possible explanation is that was ignored the quasi-adiabaticity. The ongoing project includes revisiting KIC7760680 considering quasi-adiabaticity in overshooting region to confirm the hypothesis.

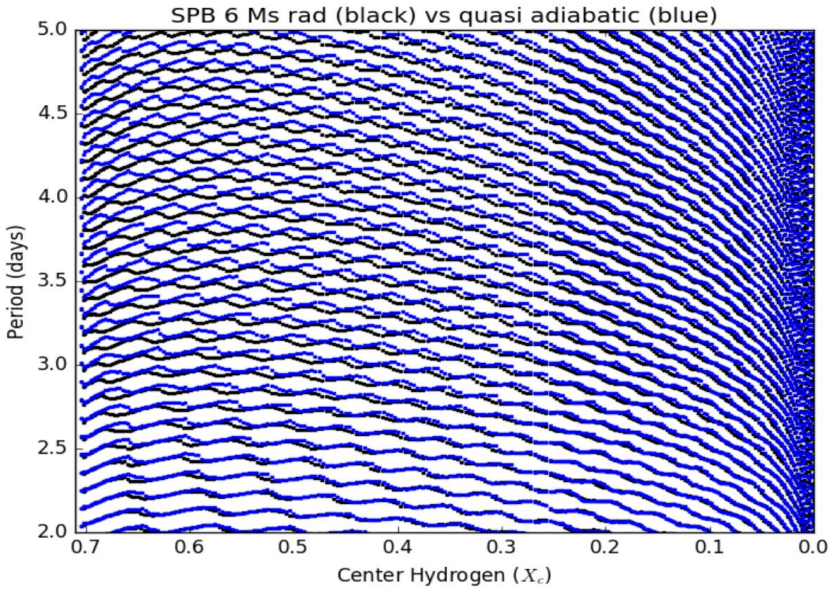

Fig.1. Composition of periods for both models (radiative and quasi-adiabatic in the overshooting region) for 6 solar masses SPB model from ZAMS to TAMS for the higher periods (low frequencies).

[1] B. Paxton, et al., ApJS, 192, 1 (2011)
[2] R. Townsend, S. Teitler, B. Paxton, Proceedings IAU Symposium, 301. (2013)
[3] E. Moravveji, et al., ApJ, 823, 2 (2016)

DRELL-YAN PROCESS BACKGROUND ESTIMATION USING DATA-DRIVEN METHODS

Marijus Ambrozas, Andrius Juodagalvis

Institute of Theoretical Physics and Astronomy, Faculty of Physics, Vilnius University, Lithuania
marijus.ambrozas@ff.stud.vu.lt

Interactions between proton component parts, named "partons" (quarks and gluons), might occur in high-energy proton-proton collisions. The inner structure of the proton is described using parton distribution functions (PDFs). The probabilities of parton-parton interactions depend on the the types of partons and the amount of energy they have. Therefore, calculations of probabilities of rare events are quite dependent on the precision of the PDFs.

Drell-Yan process is a quark-antiquark annihilation resulting in a lepton-antilepton pair. Theoretical predictions for the differential cross section of the Drell-Yan process are available at next-to-next-to-leading order (NNLO) in perturbative quantum chromodynamics (QCD). The experimental analysis of this process allows to constrain parton distribution functions. Precise measurements of the standard model processes including the differential Drell-Yan cross section allow to test perturbative QCD and the theoretical predictions of higher-order corrections [1].

The measurements of the differential Drell-Yan cross section are carried out by different experiments at the Large Hadron Collider (LHC) at CERN. They are done at various proton-proton collision energies [1-4]. Some uncertainties of the measurement are related to the response of the detector. A significant contribution to the measurement uncertainty of the Drell-Yan process originates from simulation of distinct background processes. In order to reduce these uncertainties, the number of background events is estimated using data-driven methods. A background-dominated control region is defined, and the number of background events from this region is transformed into the number of background events in the signal region. Background processes which can independently produce different or same type of leptons are estimated using the $e\mu$ method. Other processes, in which jets (streams of particles) might be produced, are estimated using the fake rate method. These two methods and their accuracy will be discussed during the presentation in the context of the measurement at CMS.

Study of the differential Drell-Yan cross section at the CMS experiment is supported by the Lithuanian Academy of Sciences.

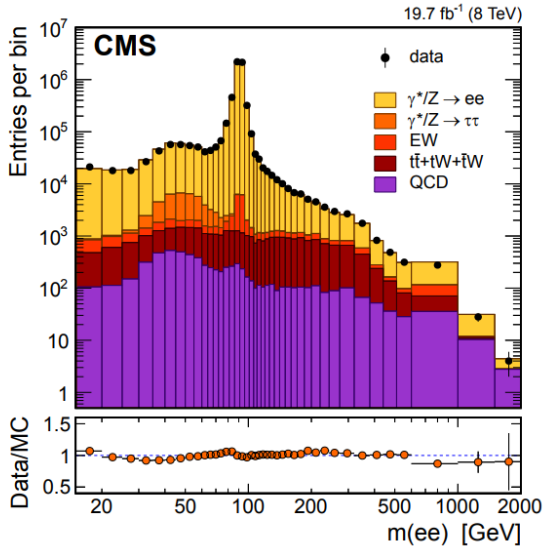

Fig. 1. Dielectron invariant mass spectrum at the proton-proton collision energy of 8 TeV. The black dots represent the number of events measured with the CMS detector. The colors represent contribution of different processes. Yellow color marks the signal – the Drell-Yan process events. EW denotes diboson and W+Jets processes. The black vertical lines represent statistical uncertainties. [2].

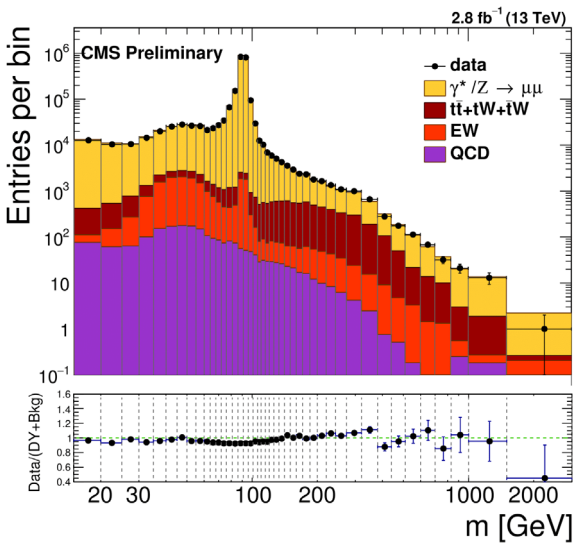

Fig. 2. Dimuon invariant mass spectrum measured with the CMS detector at the collision energy of 13 TeV [1]. The markings are the same as in Fig.1, only the DY $\to \tau\tau$ process is included into the EW contribution.

[1] CMS Collaboration, Measurement of the differential Drell-Yan cross section in proton-proton collisions at 13 TeV, CMS PAS SMP-16-009 (2016).
[2] CMS Collaboration, Measurements of differential and double-differential Drell-Yan cross sections in proton-proton collisions at 8 TeV, Eur. Phys. J. C **75**, 147 (2015).
[3] ATLAS Collaboration, Measurement of the low-mass Drell-Yan differential cross section at $\sqrt{s} = 7$ TeV using the ATLAS detector, JHEP **06**, 112 (2014).
[4] CMS Collaboration, Measurement of the differential and double-differential Drell-Yan cross sections in proton-proton collisions at $\sqrt{s} = 7$ TeV, JHEP **12**, 030 (2013).

Event selection and background estimation for Forward-Backward Asymmetry measurement at the CMS detector at the LHC

Uladzislava Yevarouskaya[1], The CMS Collaboration[2]

[1]Research Institute for Nuclear Problems of Belarusian State University, Belarus
[2]CERN, Switzerland

The Large Hadron Collider (LHC) was built to confirm, expand and rather disprove the existing concepts of the modern theory of the universe – The Standard Model (SM). The achieved center-of-mass energy of 13TeV in proton-proton collisions at the LHC makes it possible to obtain a sufficiently large amount of statistical data for studying the Forward-Backward Asymmetry (AFB) of the muon channel of well-understood Drell-Yan process. The studies of AFB allow to measure the weak mixing angle $\sin^2\theta_W$, to constrain the parton distribution function (PDF) and make it possible to point out the existence of processes beyond the SM, such as an existence of new neutral gauge bosons, super-symmetric particles, extra dimensions and structure of quarks and leptons. The procedure of Drell-Yan process extracting from muons signatures in the muon chamber of CMS detector and further AFB calculations, involves an estimating and subtracting of background processes with the similar muon final states, as well as the application of corrections related to detector misalignments, the multiplicity of simultaneous pp collisions (pile-up), the registration efficiency difference between data and simulations. The forward-backward asymmetry was measured as a function of dimuon invariant mass on Data Samples collected in 2016 with the CMS detector at the LHC of total integrated luminosity 36.23 fb^{-1}. The obtained results in a good agreement with the theoretical predictions presented with the Monte Carlo simulations. Unexpected deviations from the Standard Model are not observed.

FEW WORDS ABOUT HYDRO SIMULATIONS IN HEAVY ION COLLISIONS

Michał Naskręt[1,2]

[1]Department of Physics and Astronomy, University of Wroclaw, Poland
[2]CERN, Geneva, Switzerland
michal.naskret@uwr.edu.pl

The quark model of hadron classification proposed by Murray Gell-Mann [1] and George Zweig [2] in 1964 motivated the opinion that a new state of matter, namely strongly interacting matter composed of subhadronic constituents, may exist. Soon thereafter, quantum chromodynamics (QCD) was formulated as the theory of strong interactions, with quarks and gluons as elementary constituents.

At low temperatures and baryonic chemical potentials (e.g. in the nuclei) quarks are always confined in hadrons. Increasing temperature and density of hadrons lets us unleash the elementary constituents of matter. The state that is formed is called the quark-gluon plasma (QGP) [3, 4, 5]. Assuming that conditions connected to thermal equilibrium are fulfilled, the time evolution of QGP can be described by the laws of fluid dynamics. This approach proved to be useful in description of relativistic heavy ion collisions [6].

In my talk I will aim to guide through the basic concepts of relativistic hydrodynamics. The description will contain algorithms used to extract observables from the fluid description. Finally, I will compare the latter to the results obtained in heavy ion experiments at CERN.

[1] M. Gell-Mann,Physics Letters 8, 214-125 (1964),
[2] G. Zweig,CERN Report No.8182/TH.401 (1964),
[3] Collins Perry, Phys. Rev. Lett. 34, 151 (1975),
[4] J.Rafelski, Phys. Rep. 88, 331–347 (1982),
[5] Müller, Rep. Prog. Phys. 58, 611–636 (1995),
[6] P. Huovinen and P.V. Ruuskanen, Ann.Rev.Nucl.Part.Sci.56:163-206,(2006),

DYNAMIC CHANGES IN BURNING COAL-WASTE DUMPS IN THE UPPER SILESIAN COAL BASIN (POLAND)

Anna Abramowicz, Ryszard Chybiorz

Faculty of Earth Sciences, University of Silesia in Katowice, Poland
abramowiczanna@gmail.com

The strong development of the hard coal mining industry has led to the dramatic increase in the number of coal-waste dumps next to the Polish mines. They required reclamation and proper management, but the lack of regulations and due care for the environment led to the disregard of the coal-waste dumps problem. Over the years, the dumps have been subjected to many external infuences – have been dismantled, liquidated or left without a specific plan of development, and in the meantime the new ones have emerged. However, the fires caused by self-heating of coal-waste dumps are the greatest ecological threat. They affect the condition of the atmosphere, soils, water and most of all - the health of local residents. The better knowledge of this phenomenon may help to control it [1].

Using five open-access databases and satellite data, currently burning coal-waste dumps in the Upper Silesian Coal Basin (Poland) have been identified and classified. The classification was made based on the stages of fires. The spatial distribution analysis of coal-waste dumps has been carried out. Selected objects have been used to accomplish numerous analysis regarding their detailed construction (shape, area, capacity, used material). First of all, the course of changes in the construction of the dumps was restored based on historical materials and data. It allowed to select the most important factors affecting the construction of selected objects and trends in their changes. The fire of dumps became the main object of interest. Its participation in the analyzed changes is undeniable, but the separation of other factors was quite problematic.

[1] G. B. Stracher, A. Prakash, E. V. Sokol, Coal and Peat Fires: A Global Perspective: Volume 3: Case Studies – Coal Fires, ISBN 0444595112, Elsevier (2014).

Kohonen's neural networks for Customer Segmentation

Paul Drozd[1]

[1]Department of Intelligent Systems, Belarussian State University, Belarus
rct.drozdPS@bsu.by

This study describes an approach for solving market segmentation problem using Kohonen's self-organizing maps [1] and hierarchical cluster analysis. Z-score and principal component analysis were used for data pre-processing [2]. This approach eliminates the need for redesigning the neural network architecture in exploratory data analysis when the number of expected clusters changes [3]. We have developed a toolkit (in R programming language) that allows non-technical specialists, such as marketers, to analyze customers and find patterns in the data of their companies. The toolkit can be integrated with various CRM systems, such as Salesforce.

The method was tested on the Ta-Feng dataset, which was laid out in free access by ACM RecSys. It contains information about purchases of various goods made by more than 32 thousand unique customers. Each of the 817741 records describes one transaction made by the buyer with the help of nine characteristics (transaction date, transaction amount, etc.). The sample result of applying our approach to this dataset is given below (Fig. 1).

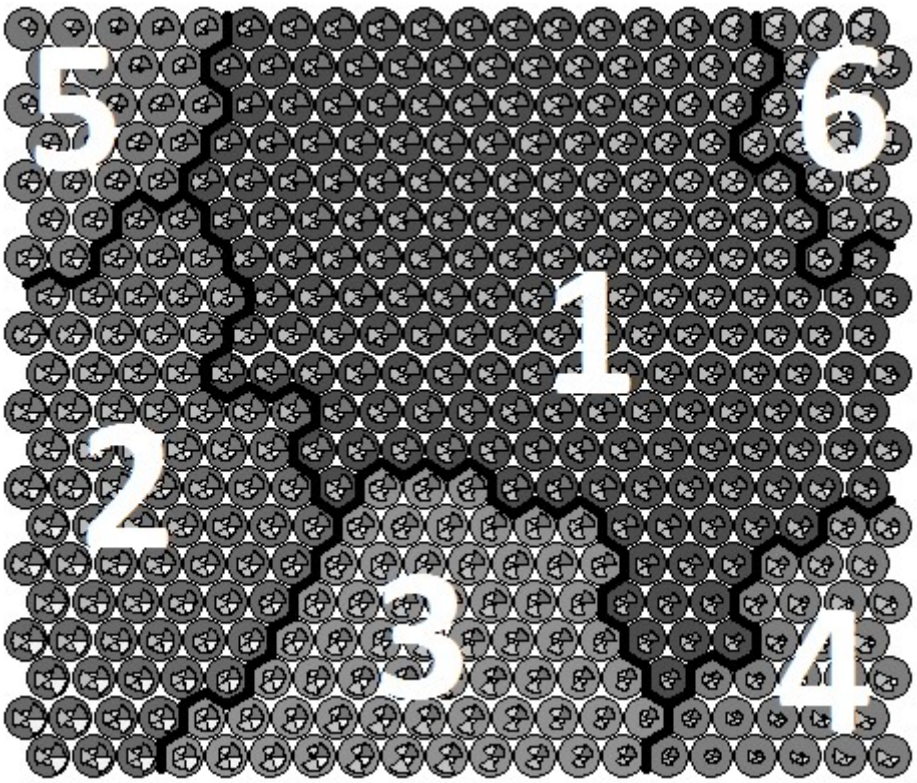

Fig. 1. Customer Segmentation results

For example, there are mostly VIP-customers in cluster 6. They make very expensive purchases, but the company doesn't have significant profit from them. On the other hand, the company can focus its marketing policy on cluster 5, which contains aged people - they bring a lot of income on the weekends. Thus, the company can optimize its business processes.

[1] Kohonen, T. Self-Organizing Maps (Third Extended Edition) / T. Kohonen // New York – 2001.-502 p.
[2] Kaufman, L. Finding Groups in Data: An Introduction to Cluster Analysis / L. Kaufman, P. J. Rousseeuw // John Wiley and Sons, Inc – 2005.-342 p.
[3] Yazkov, N. N. Data mining: methodical instructions to laboratory works / N. N. Yazkov, I. P. Shingarev // Minsk:BSU. – 2012.-51 .

THE IMPACT OF SPRING AIR TEMPERATURE ON VEGETATION CONDITIONS IN THE EASTERN PART OF THE BALTIC SEA REGION

Laurynas Klimavičius

Institute of GeoSciences, Vilnius University, Vilnius, Lithuania
laurynas.klimavicius@gf.stud.vu.lt

Many meteorological factors have an impact on vegetation: precipitation, soil moisture, air temperature and etc. However, spring air temperature is especially important as it does not only set the time of the beginning of the vegetation period but also predetermine the further development of vegetation. The impact of spring air temperature on vegetation conditions in the eastern part of Baltic Sea region is a little studied – only a few researches were made in Lithuania and Poland [1,2].

Normalized Difference Vegetation Index (NDVI) and Vegetation Condition Index (VCI) were used in this research as parameters which describe vegetation conditions in the investigated area. In this research the NDVI and VCI values during period from 1982 till 2016 were analyzed. NDVI data were obtained from Advanced Very High Resolution Radiometer (AVHRR) sensor which is installed in NOAA-7,9,11,14,16,18,19 satellites [2] while VCI was calculated as NDVI's deviation from the mean. 322 cells (0.25×0.25°) located in Estonia, Latvia, Lithuania and northern Poland were analysed. Five types with different land use were distinguished according CORINE land cover data. NDVI values of each year's 10th-30th weeks and air temperature values of January-June were investigated.

The main objectives of this study are to assess the differences of development of vegetation in five types of land use (pastures, wetlands, broad-leaved forests, coniferous forests and arable land) in spring and to evaluate the impact of spring air temperature on vegetation.

The study showed that the maximum average value of NDVI in all types of land use were observed at the beginning of summer. This value was highest in broad-leaved forests while lowest - in coniferous forests. The maximum average value of NDVI was reached earlier in coniferous forests and wetlands than in the other types of land use. The observed increase of NDVI values during investigation period (1982-2016) can be related with early spring temperature rise in the eastern part of Baltic Sea region. However, statistically significant positive changes in NDVI values were identified in all types of land use only in April and May. The influence of spring air temperature on vegetation conditions is found to be greatest in arable land and pastures, while the least important in coniferous forests. Moreover, analysis showed that only in the middle of the summer (in July) the impact of spring air temperature on vegetation conditions is no longer significant.

[1] Dabrowska-Zielinska K., Kogan F., Ciolkosz A., Grusxsczynska M., Kowalik W. 2002. Modelling of crop growth conditions and crop yield in Poland using AVHRR-based indices. *International Journal of Remote Sensing.* 23: 1109-1123. doi: 10.1080/01431160110070744.
[2] Rimkus E., Stonevičius E., Kilpys J., Mačiulytė V., Valiukas D. 2017. Drought identification in the Eastern Baltic region using NDVI. *Earth System Dynamics.* 8: 627-637. doi: 10.5194/esd-8-627-2017.

THE USE OF INTERCONNECTED OPEN DATA FOR MATERIAL IDENTIFICATION

Antanas Vaitkus[1], Andrius Merkys[1,2], Yassine El Mendili[3], Saulius Gražulis[1,2]

[1]Vilnius University Institute of Biotechnology, Saulėtekio 7, LT-10257 Vilnius, Lithuania
[2]Vilnius University Faculty of Mathematics and Informatics, Naugarduko 24, LT-03225 Vilnius, Lithuania
[3]Normandie Université, CRISMAT-ENSICAEN, UMR CNRS 6508, Université de Caen Normandie, 14050 Caen, France
antanas.vaitkus90@gmail.com

One of the main driving forces behind modern day scientific research is openness. As a result, open-access data repositories play an increasingly important role in the scientific community. The Crystallography Open Database (COD, `http://www.crystallography.net/cod`) [1] is one such resource – over the last 15 years it has become the largest curated and validated open-access collection of inorganic and non-polymeric organic crystal structures encompassing over 390 000 entries. More than 155 000 of these entries have been enhanced by manually adding the SMILES descriptors and as a result enabling the substructure search within the given subset. Recently, a number of computer programs capable of automatically determining stoichiometrically [2] and chemically sound molecules from the crystallographic data have also been developed; this, in turn, enabled the automated generation of structural formulae descriptors and eased the establishment of cross-links between the COD and other open-access resources such as PubMed, DrugBank and Wikipedia. New strides have also been made in relating spectral data to their corresponding crystal structures. The COD was chosen as the back-end database in the wide scale on-site sample analysis of the "Sonic Drilling coupled with Automated Mineralogy and chemistry On-Line-On-Mine-Real-Time" (SOLSA, `http://www.solsa-mining.eu`) project that focuses on developing highly efficient, cost-effective and sustainable exploration technologies. Since part of the sample analysis involves material identification via the means of Raman spectroscopy, reference spectra aggregation from various sources was initialised choosing CIF [3, 4] as the homogeneous data carrier format for both XRD and spectral data; this, in turn, stipulated the development of spectroscopy oriented DDLm dictionary [5] and the creation of the Raman Open Database (ROD, `http://solsa.crystallography.net/rod`). These new developments will allow the SOLSA project to present various aspects of mineral characterization such as Raman spectra, XRD structures and fluorescence data in the COD database in a uniform, computer-readable way.

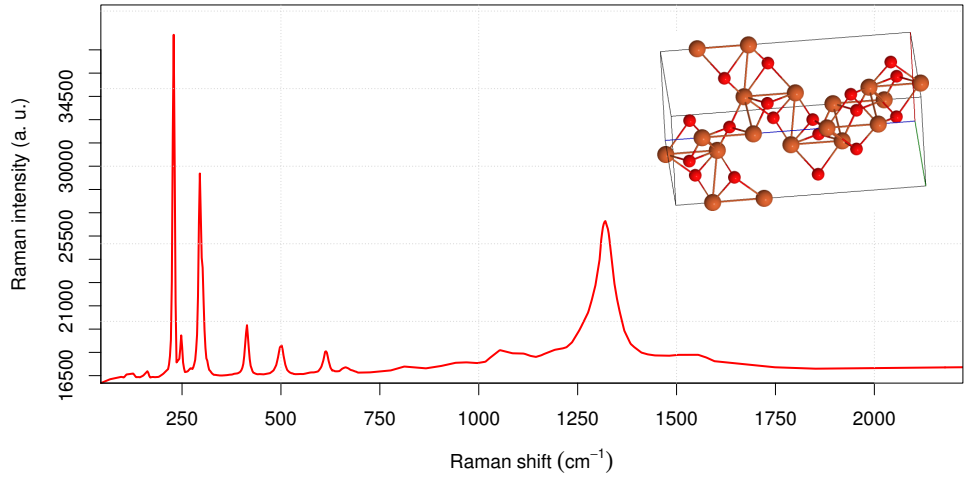

Fig. 1. The Raman spectra and the related crystal structure of hematite. ROD ID 1000001, COD ID 1546383.

[1] Gražulis, S.; Daškevič, A.; Merkys, A.; Chateigner, D.; Lutterotti, L.; Quirós, M.; Serebryanaya, N. R.; Moeck, P.; Downs, R. T. & Le Bail, A. Crystallography Open Database (COD): an open-access collection of crystal structures and platform for world-wide collaboration. Nucleic Acids Research, 2012, 40, D420-D427, doi: 10.1093/nar/gkr900.

[2] Gražulis, S.; Merkys, A.; Vaitkus, A. & Okulič-Kazarinas, M. Computing stoichiometric molecular composition from crystal structures. Journal of Applied Crystallography, 2015, 48, 85-91, doi: 10.1107/S1600576714025904.

[3] Hall, S. R.; Allen, F. H.; Brown, I. D. The crystallographic information file (CIF): a new standard archive file for crystallography. Acta Crystallographica Section A, 1991, 47, 655-685, doi: 10.1107/S010876739101067X.

[4] Bernstein, Herbert J.; Bollinger, John C.; Brown, I. David; Gražulis, Saulius; Hester, James R.; McMahon, Brian; Spadaccini, Nick; Westbrook, John D.; Westrip, Simon P. pecification of the Crystallographic Information File format, version 2.0. Journal of Applied Crystallography, 2016, 49, 277-284, doi: 10.1107/s1600576715021871.

[5] Spadaccini, Nick; Hall, Sydney R. DDLm: A New Dictionary Definition Language. Journal of Chemical Information and Modeling, 2012, 52, 1907-1916, doi: 10.1021/ci300075z.

HELIUM MIGRATION IN GROUNDWATER OF LITHUANIA

Vytautas Samalavičius

Department of Hydrogeology and Engineering Geology, Vilnius University, Lithuania
vytautas.samalavicius@chgf.vu.lt

Helium (^{4}He) is an element with a nucleus containing two neutrons and two protons. It is being emanated during nuclear decay of radioactive elements as an alpha particle. Geological massifs containing minerals and rocks which have uranium and thorium are the source of helium on Earth [1, 3]. In Lithuania ^{4}He can be detected in groundwater of the Baltic Artesian Basin (BAB). Crystalline basement is mainly made of magmatic and metamorphic rocks which contains radioactive elements emanating alpha particles. Alpha particles are being ionized shortly and become helium. Due to ^{4}He nature it tends to escape geological environment through faults and porous media. Part of helium dissolve in groundwater (^{4}He solubility in water is worst of all gases) [1, 2, 3]. Permeability of aquifers and aquitards are the key factor determining helium concentration in groundwater. The better the groundwater is confined the more likely helium would accumulate. In BAB groundwater helium concentration correlate with aquifer depth. The deeper and more confined aquifer groundwater is more saturated with the helium gas than shallow layers. Helium anomalies can be detected in the fault zones, where deep groundwater (usually brakish or brine) forms an intrusion to the shallow aquifers. In these cases shallow and deep groundwater mixing occurs leading to alteration chemical, isotopical and gas composition of groundwater [2, 3, 4].

During the fieldworks fifteen samples of groundwater were collected for this study. Eight samples were extracted from shallow wells of Quaternary aquifer system (up to 125 m depth) and seven samples from deep boreholes (300 – 1011 m depth). Sampling sites were selected to represent most of the BAB aquifers in Lithuania. Samples were prepared for chemical, isotopical and helium analysis which was executed in the laboratory. Physical-chemical parameters (pH, Eh, T) were measured during sampling process. Helium is a very volatile element, therefor sampling procedure is complicated. Each sample is collected in to the glass bottle which has to be quickly filled with water and clogged with a rubber cork to avoid helium escape.

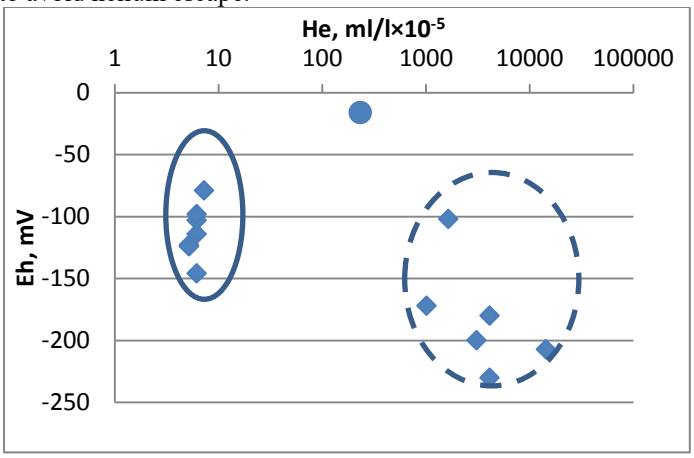

Fig. 1. Different hydrogeochemical environments based oxidation reduction potencial (Eh, mV) and helium concentration data (ml/l×10^{-5})

The shallow aquifer groundwater helium concentration is equal to atmospheric. Helium is not being accumulated and most of it coming from below is released into the atmosphere except small portion of ^{4}He, which shows equilibrium. Deep aquifer groundwater helium concentration values are between 232 and 14430 ml/l×10^{-5}. Comparing helium data with the chemical composition of the groundwater reveals that metamorphisation degree ((rNa^++rCl^-)/$rHCO_3^-$) and chloride is proportional to helium concentration. Deep aquifers groundwater composition is different from the shallow because of the recharge intensity, interaction with a surrounding minerals, mean residence time, etc. Oxidation-reduction potencial (Eh, mV) and helium concentration graph (Figure 1) shows two distinct groundwater environments. Shallow aquifers groundwater with small amounts of helium have Eh values -150 – -60 mV (smooth circle line). Deep groundwater with the accumulated helium have Eh -230 – -100 mV (dash circle line). An exception is in Telšiai site (well Tichė) were groundwater type is calcium – sulphate type (circle point). This groundwater type deviates from usual BAB groundwater also altering hydrogeochemical environment (Eh).

[1]Appelo C. A. J., Postma D., *Geochemistry, groundwater and pollution*. A. A. Balkema/ Rotterdam/ Brookfield. 536 p. (1993).
[2]Juodkazis V., *Fundamentals of regional hydrogeology*. Vilnius. Vilniaus universiteto leidykla. 171 p. (2003). [In Lithuanian]
[3]Mokrik R., Mažeika J., *Hydrogeochemistry*.Vilnius. VUL. 248 p. (2006). [In Lithuanian]
[4]Zuzevičius A., Mažeika J., Baltrūnas V., *A model of Brakish groundwater formation in the Nemunas River valley, Lithuania*. Geologija Nr. 60. 63-75 p. (2007).

EMOTION RECOGNITION BY IMAGE AND HUMAN SPEECH PROCESSING

Elizaveta Plyshevskaya, Elena Kozlova

Faculty of Radiophysics and Computer Technologies, Belarusian State University, Minsk, Belarus
l.tarakanowa@gmail.com

Emotion recognition problem is hard to solve and formulate. People express emotions in many ways: by face mimics, gestures, speech intonations and content. Also physical state of a person is different when experiencing different emotions. So it is important to analyze different components when recognizing emotions.

The idea of the present study is to improve an emotion recognition algorithm using Intel RealSense technology [1] that recognizes emotion by analyzing image of the person's face by adding speech emotion recognition module to the system. Analyzing both speech and face components allows to get a more accurate result, especially in such cases, as, for example, when a person is lying or has a face injury.

Emotion recognition algorithm using Intel RealSense consists of six steps and uses the emotion classification described in Paul Ekman[2] studies and the mimic codes of emotional states. The picture is grabbed from the camera, than a face and facial landmark points are detected. As it is done the program counts the key values such as mouth and eyes being open in percents. Then the classification starts and the result is presented.

Emotion recognition by speech is performed by a convolutional neural network for small-footprint keyword spotting, because it is comparatively simple, fast and quick to train. At first spoken words are defined by grouping the audio samples into segments and calculating the strength of frequencies across a set of bands. Then the model gets a spectrogram for an audio sample. Spectrogram can be treated as a single-channel image, as it appears to be a two-dimensional array, created by vectors that are actually one-dimensional arrays of frequency strengths for each audio segment of an audio sample.

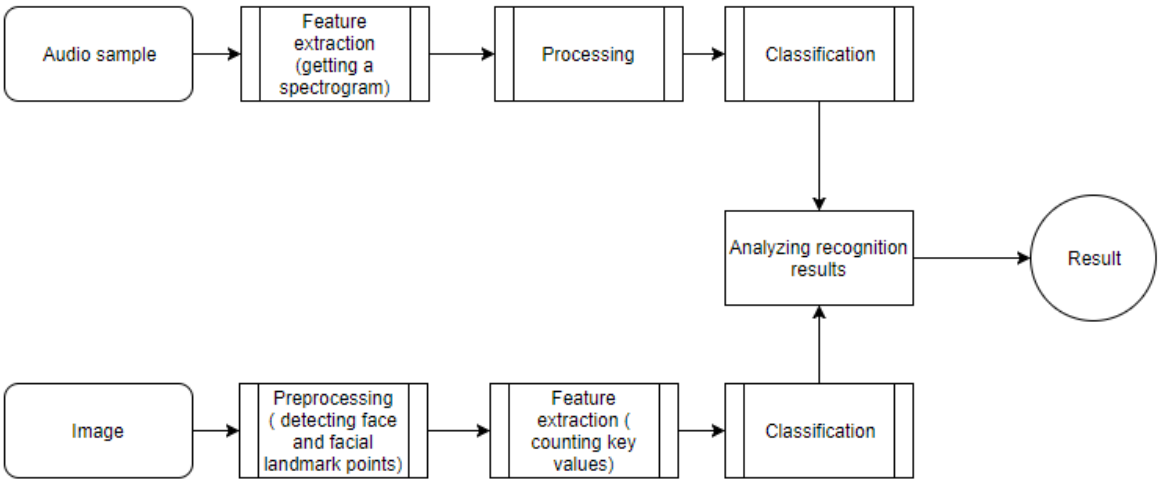

Fig. 1. Emotion recognition system with two modules.

Average accuracy for emotion recognition by image is about 80% when the system recognizes seven emotions with video frame rate about 30 fps, when average accuracy for emotion recognition by speech is about 82% for 10000 epochs of learning using dataset with 21000 audio samples.

Combining and analyzing the recognition results of the two modules can help to increase the average accuracy and get more reliable results about the emotional state of a person.

[1] E. Tarakanova, E. Kozlova, *Emotion recognition algorithm based on Intel RealSense technology* (Trans. Open Readings Programme and Abstracts, 2017).

[2] P. Ekman, W. Friesen, *Unmasking the Face: A Guide to Recognizing Emotions from Facial Clues* (Trans. Piter Publishing house, Russia, 2010).

PNEUMATIC ASSEMBLY LINE

Viktor Kovalevskyi, Vytautas Bučinskas, Andrius Dzedzickis, Vytenis Sinkevičius, Linas Sinkevičius

Department of Mechatronics, Robotics and Digital Fabrication, Vilnius Gediminas Technical University, Lithuania
viktor.kovalevskyi@vgtu.lt

Nowadays the automatic conveyor systems and robots increasingly substitute human labor overtaking various manufacturing processes such as palletizing, packing and transporting goods within manufacturing department [1] [2]. The reason is that automatic conveyors and robots have many advantages over human labor, for example: i) much higher performance speed; ii) better quality and higher positioning accuracy; iii) possibility to work without any break; iv) lower operating costs; v) possibility to avoid errors produced by people because of their emotional state and fatigue.

We have created a mini version of a pneumatic assembly line Fig. 1. and connected it to the existing robot. We are planning that the new equipment will be controlled via robot control unit. In such a way we will be able to simulate different work processes conducted by both the robot and the conveyor. Also, we will be able to find the best solution for each task associated with goods transportation.

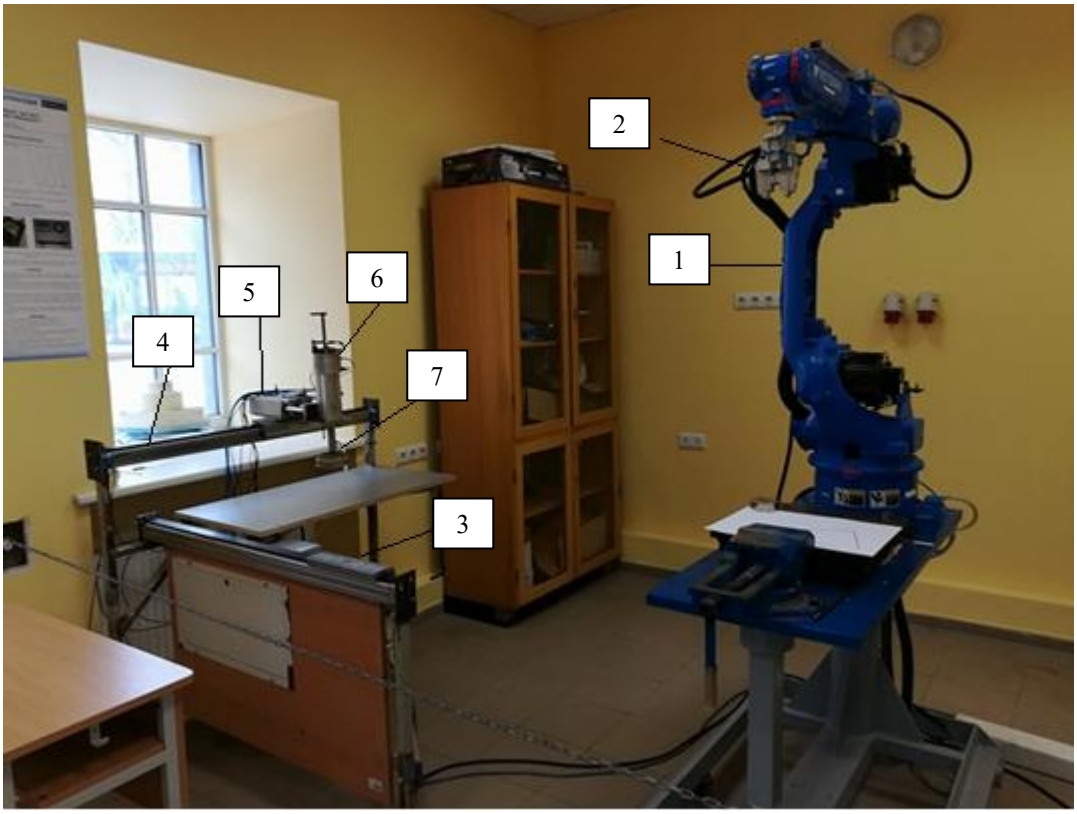

Fig. 1. Pneumatic assembly line: 1) robot MOTOMAN SSF2000; 2) capturing tool of robot; 3) first cylinder – motion in x axis; 4) second cylinder - motion in y axis; 5) third cylinder; 6) fourth and fifth cylinders; 7) vacuum capturing tool.

Despite the fact that our model is already constructed, there is possibility to attach several more sensors, for example: on the table can be installed capacitive sensor, ultrasonic or other sensor to detect if there any object or not. So, if there are some ideas how to modernize this project, they will be taken into to make our model more efficient and interesting in teaching process.

[1] Markin RS, Tackett EL, Hoskinson SJ, inventors; Board Of Regents-Univ. Of Nebraska, assignee. Automated laboratory conveyor system. United States patent US 5,351,801. 1994 Oct 4.
[2] Southworth PR, Baxter GR, inventors; Nacom Industries, Incorporated, assignee. Conveyor system. United States patent US 4,682,927. 1987 Jul 28.

MAGNETIC SUSCEPTIBILITY A PROXY FOR HEAVY METAL POLLUTION DETECTION ON THE SOUTHEASTERN BALTIC SEA COAST

Dovilė Karlonienė[1], Veronika Vilčinska[1], Donatas Pupienis[1,2]

[1] Department of Hydrology and Climatology, Vilnius University, Lithuania
[2] Institute of Geology and Geography, Nature Research Centre, Lithuania
dovile.karloniene@chgf.vu.lt

Heavy metals (HM) are among the most common environmental pollutants, and their occurrence in sediments derives from natural or anthropogenic sources. The geochemistry and magnetic susceptibility (MS) methods applied to beach sediments remains an underdeveloped field of research. Authors [1] pointed out that MS method can be very useful when targeting and selecting sampling sites for geochemical analyses. A good relationship between MS and HM were determined in a new studies related to HM pollution on the coast [2, 3, 4, 5]. As an example, authors [2] determined high positive correlation between higher in-situ MS values measured on the beach and higher Cu, Cr, Zn and Ni concentrations, the other authors [5] indicated that the MS values of the beach sand have a positive relationship with the higher concentrations of Fe, Mn, Cr, Ni, As and Pb.

The aim of our study was to investigate the possibilities of the indication of places possible polluted with the HMs using MS measurements along the southeastern Baltic Sea coast. The research was performed on the entire Curonian spit and mainland sea coast of Lithuania (136 km) in 2014. The beach along the southeastern Baltic Sea coast is backed by a vegetated foredune or moraine cliffs. The beach consists predominantly of quartzoze (enriched with heavy minerals) sand. A MS field survey was undertaken along the coast in the middle of the beach at equal distance every 1 km. In total, 135 surface sand samples were measured. To characterize the relative concentrations of heavy minerals (HMCs), a Bartington MS3 field scanning sensor was used for rapid and effective measurements of low-field volume MS. It is indicated that the in-situ MS values of $\kappa<50$ μSI defines the quartz-rich sands with low HMCs, and values higher than 50 μSI indicates the existence of higher surface HMCs, in other words the higher the MS value the higher possibility of determination the pollution with HM.

The MS values along the investigated sea coast ranges from 11.2 to 4977.9 μSI (Fig. 1). The mean MS value of entire coast is 170.9 μSI (σ = 451.0 μSI). The mean MS value on mainland coast reaches 274.5 μSI (σ = 158.0 μSI), and whereas on the Curonian spit it is 130.8 μSI (σ = 517.4 μSI).

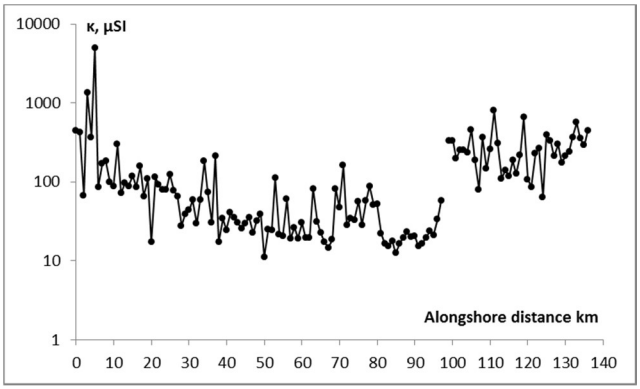

Fig. 1. Magnetic susceptibility (κ) distribution along the southeastern Baltic Sea coast. The alongshore distance (0 km) is shown from Zelenogradsk.

The greatest mid-beach MS values ($\kappa>1000$ μSI) occurs in the southern part of the Curonian spit. The greatest MS values on the mainland coast are less than measured on Curonian spit mid-beach. The greatest mid-beach MS values ($500< \kappa <1000$ μSI) on the mainland occurs near the Palanga, Šventoji seaside resorts and cliffs (Olando kepurė, Šaipiai).

These MS measurements illustrates that the main places with higher heavy mineral concentrations, which can be enriched with heavy metals, alongshore the southeastern Baltic Sea coast are located near the cliffs, on the beaches with high erosional processes and influenced by the intense human activities (beach nourishment, port jetties, groynes and etc.). For further investigation and data validation the geochemical analysis will be performed.

[1] Lourenço, A.M., Sequeira, E., Sant'Ovaia, H., Gomes C.R. 2014. Magnetic, geochemical and pedological characterisation of soil profiles from different environments and geological backgrounds near Coimbra, Portugal. Geoderma. 213, 408–418.
[2] Bandaru, V.L., Gawali, P.B. Hanamgond, P.T. Kannan, D. 2016. Heavy metal monitoring of beach sands through environmental magnetism technique: a case study from Vengurla and Aravali beaches of Sindhudurg district, Maharashtra, India. Environ Earth Sci, 75:678
[3] Yalcin, M.G. 2009.Heavy mineral distribution as related to environmental conditions for modern beach sediments from the Susanoglu (Atakent, Mersin, Turkey). Environ. Geol. 58, 119–129.
[4] Ra, K., Kim E.S., Kim, K.T., Kim, J.K., Lee, J.M., Choi, J.Y. 2013. Assessment of heavy metal contamination and its ecological risk in the surface sediments along the coast of Korea. Journal of Coastal Research. 65(1), 105-110.
[5] Wang, Y., Huang, Q., Lemckert, C., Ma, Y. 2017. Laboratory and field magnetic evaluation of the heavy metal contamination on Shilaoren Beach, China. Marine Pollution Bulletin, 117, 291–301.

INFLUENCE OF GAS-DYNAMIC PARAMETERS OF AN AIR PLASMA JET ON THE MICROORGANISMS INACTIVATION PROCESS

Alena Vabishchevich[1,2], Aliaksandra Kazak[2], Leanid Simonchik[2], OlgaEmeliyanova[3]

[1] Faculty of Physics, Belarusian State University, Minsk,Belarus
[2] Institute of Physics of the National academy of sciences of Belarus, Minsk,Belarus
[3] Republican unitary enterprise Scientific Practical Centre of Hygiene, Minsk, Belarus
elena199713.elena@mail.ru

Among a variety of plasma sources special attention is focused on the development and application of plasma jets [1]due to the possibility to treat objects of complex shapes and sizes outside a closed discharge volume.

The cold plasma jet is formed by direct current glow discharge in air at atmospheric pressure [2]. Interelectrode gap is fixed at 0.7 mm. Discharge is maintained by DC power supply with an output voltage up to 3 kV and ballast up to 80 kOhm. Air flow can be varied in the range of 1-10 l/min. Plasma generated in the discharge is blown out with the gas through anode hole into surrounding air. As a result, a glow of plasma jet of 2-3 mm in diameter and several centimeters in length is observed (Fig. 1, a and b). In almost all articles about plasma medicine the accent is made on the bactericidal action of RONSs (e.g., NO, O_3, OH, H_2O_2, etc.) generated by the plasma jets [3]. Determination of the concentration of long-living chemically active species in the plasma jet is performed by IR absorption spectroscopy [4]. In the absorption spectra of air jet, NO, NO_2, $HNO_2$and N_2O bands are observed. Molar fractions of these active species at the zone of the jet impact on the bacteria are 40 ppm, 20 ppm, 10 ppm and 2 ppm, correspondingly. The temperature field was measured with a thermocouple and compared with the schlieren images. Three separate temperature regions with well-defined boundaries were observed along the diameter of the jet. The first one is a central narrow hot area that corresponds to the area of the visible luminous jet. It has gas temperature of 30 to 120ºC depending on the gas low rate and distance from the anode. It is surrounded by a warm "coat" of diameter of about 1 cm with a temperature of 25 to 50ºC (the boundary of this zone is shown in Fig. 1, c). The last region is an ambient air area surrounding the plasma jet and having the room temperature.

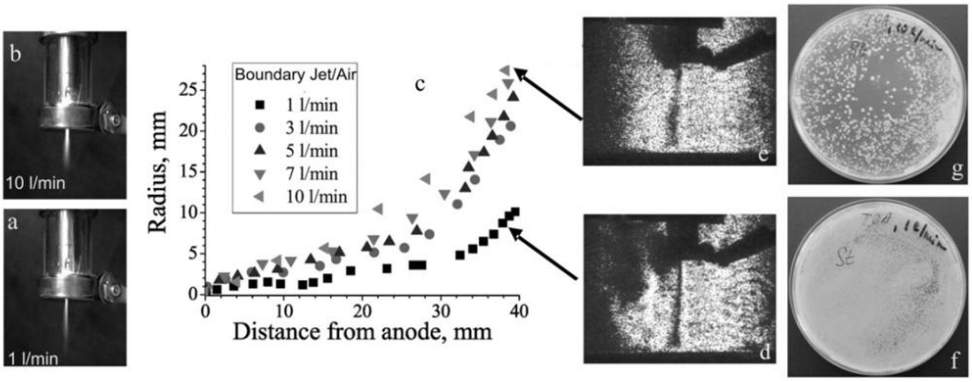

Fig. 1. (a, b) Air plasma jet photos and (c) their boundary radii at different air flows; (d and e) shadow images of jets flowing onto a Petri dish at flows of 1 and 10 l / min and (f, g) photos of corresponding Petri dishes (right), treated for 5 minutes.

The plasma jet effectiveness was evaluated on test-strains of *Staphylococcus aureus* with an initial concentration of microorganisms of 10^6CFU/ml. The temperature in the Petri dish was controlled by a FLIR E4 thermal imager and did not exceed 30 °C. Inactivation ability is demonstrated by inhibition zones (Fig. 1, f and g). At a flow 1 l/min, the inhibition zone is difficult to detect. With increasing gas flow, the zone becomes more pronounced, "clean" regions are formed, and the radius of the zone grows. As it follows from the shadow images, this can be due to the increase in the radius of the plasma jet itself (Fig. 1c).The best effect is observed at 10 l/min, inactivation in this case takes place in the whole Petri dish. Also, as the flow increases, a decrease in the gas temperature of plasma jet in the region of the sample from 50 ºC to 35 ºC.

The work is partially supported by the grant of BRFFR F17RM-050.

1. K. H. Schoenbach and K. Becker, 20 years of microplasma research: a status report. Eur. Phys. J. D, 2016, **70**: p. 29.
2. V.I. Arkhipenko et al. Bactericidal components in an air plasma jet at dc and ripple current regimes, Proceedings of the National academy of sciences of Belarus, Physic and mathematics series, 2015, **3**: p. 104-110.
3. X. Lu et al. Reactive species in non-equilibrium atmospheric-pressure plasmas: Generation, transport, and biological effects. Physics Reports, 2016, **630**: p. 1–84.
4. A.A. Kirillov et al. Bactericidal components in an atmospheric pressure air plasma jet at different current regimes. 22thInternational symposium of plasma chemistry, 5–10 July 2015, Antwerpen, Belgium, P-II-11-7, 2015, [Electronic resource] http://www.ispc-conference.org/ispcproc/ispc22/P-II-11-7: p. 5.

LITHUANIAN BALTIC SEA COAST VARIABILITY AND STABILITY

Viktoras Karaliūnas, Darius Jarmalavičius

Laboratory of Geoenvironmental Research, Nature Research Centre, Lithuania
viktoras.karaliunas@gamtostyrimai.lt

The beach is one of the most sensitive elements of sandy coast, changing constantly during short period of time. Hydrodynamic and aeolian processes act as the main driving forces changing the cross-shore sediment exchange between nearshore, beach and foredune. However, despite the extremely dynamic environment, morphological elements of coast (beach, foredune) remain stable.

The aim of this paper is to determine changes in the beach morphometry during accretion and erosion dominated periods.

In order to evaluate the change of beach profile in sectors with dominated accretion (Smiltynė) and erosion (I Melnragė) processes, the changes in beach morphometry that occurred during 2002-2017 period were analyzed. The leveling of the beach cross-sections has been performed in May of every year in calm weather conditions since 2002. The following morphometric indicators were chosen for analysis of morphological changes of the beaches: beach width (horizontal distance from the coastline to the foredune toe), beach slope (θ – the ratio of the beach height near the foredune toe and beach width), beach volume and position of shoreline. These parameters were selected as being the best to represent the features of beach profile.

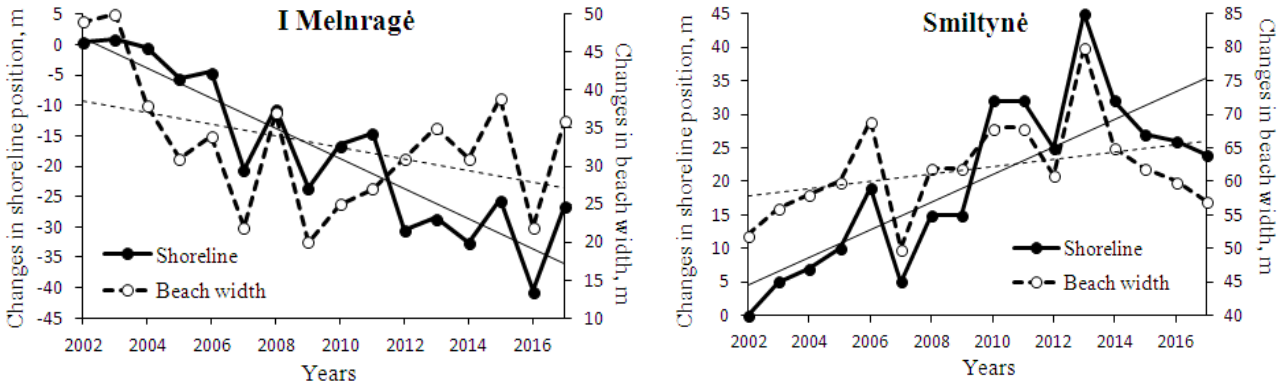

Fig. 1. Changes in shoreline position and beach width in I Melnragė and Smiltynė between 2002 and 2017.

Analysis of change in beach morphology has shown (Fig. 1) that, despite an intensive fluctuation of shoreline position, the beach width and volume remained almost unchanged. In case of I Melnragė where shoreline position during 2002-2017 period moved landward more than 30 m, beach width shrunk only 15 m (from 50 to 35 m). Whereas in case of Smiltynė where shoreline position moved about 30 m seaward, beach widened only 5 m (from 50 to 55 m).

Their temporal stability can be explained the formation of incipient dune near established foredune toe in the coastal sectors with prevailing accretion period. In the coastal sectors with prevailing erosion, the narrowing of beaches allows the waves to erode the foredune. Eroded material from foredune nourished the beach, resulting in the recovery of beach profile. In such way, the beach profile retains quasi– stability in the coast dominated by accretion processes as well as in the coast with prevailing erosion processes. Thus, the beach profile tries to return into equilibrium with the forming factors.

THE INFLUENCE OF 3G AND GSM RADIO WAVES ON THE GERMINATION, GROWTH AND DEVELOPMENT OF COMMON WHEAT PLANTS AND CHERRY TOMATOES

Natalia Gubceac[1,2], Gabriel-Octavian Lazar[1]

[1]Department of Environmental Engineering, "Vasile Alecsandri" University of Bacau, Romania;
[2]Department of Human physiology and biophysics, "Nicolae Testemitanu" State University of Medicine and Pharmacy, Republic of Moldova.
natalia.gubceac@usmf.md

The impetuous development of modern communication technologies as well as the increase of the life rhythm generated the enhancement of communication needs and connections to data services at high speeds. These led to a corresponding increase of the energy consumed and respectively released into the ether. It should be borne in mind that usually the speeding up of wireless communication is done by moving to higher frequencies, which leads to the increase of energy emitted in the corresponding frequency domain in order to cover required area. The purpose of this study is to study the influence of some radiation in the GSM and 3G frequencies on the germination and growth of wheat grains and tomato seeds. These frequencies were selected following previous observations as the most intense in the urban area. As trial samples, wheat cultures (*Triticum aestivum L., Dropia spp.*) and cherry tomatoes (*Lycopersicum esculentum*) were selected, the radiation being produced and controlled by two radio frequency amplifiers for the 3G (UL1920-1990, DL2110-2180) and GSM (UL880-915, DL925-960). For wheat there was a variation of the germination rate in the range of 62% to 79.3%, depending on the applied radiation. For tomatoes, the germination rate vary from 56% to 62.6%. As control samples, the plantlets were grown in a Faraday cage and under normal laboratory conditions. The germination rate at the 14th day, the length of the stem and root of the plantlets, as well as the number of plantlets for which the first leaves appeared, all were studied.

APPLICATION OF LASER BREAKDOWN FOR RECORDING INFORMATION INSIDE OPTICALLY TRANSPARENT MATERIALS

Julia Lyudchik[1], Olga Lyudchik[2]

[1] Faculty of Radiophysics and Computer Technologies, Belarusian State University, Belarus
[2] Faculty of Computer Science, TU Dresden, Germany
lyudchikj@gmail.com

The search for alternative methods of recording and storing information is relevant in the age of rapid development of information technology. Existing methods allow to record huge data streams in a miniature form, but in these cases there is a risk of information loss under various external factors like high temperatures, influence of electric and magnetic fields, as well as radiation.

The first publications devoted to the development of methods for recording information inside transparent materials appeared in the last 5-7 years [1]. These methods are devoid of the above disadvantages and at the same time have a sufficiently high recording density. However, specialized high-precision optical equipment is required to read the information.

The purpose of this paper is to develop a method of recording information inside transparent materials using the phenomenon of laser breakdown and precision laser processing [2], for reading which the simplest optical equipment can be used.

After a detailed study of the phenomenon of laser breakdown, we found that the microdefect has an asymmetric structure of complex shape close to an ellipsoid with a system of microcracks. To form microdefects inside the glass the ELS-02M device is used. The changing of the energy of the pump lamp makes it possible to create regions of microbreakdown of different size. This fact formed the basis of the method of recording information.

To form information states in the glass, microdefects of two sizes are created. The absence of a microdefect is defined as the third information state. Areas without a microdefect are assigned an information state of "0", and microdefects arranged in ascending order of sizes are assigned states of "1" and "2", respectively.

Considering the small size of microdefects, the reading algorithm is based on the layerwise registration of the defect arrays observed through an optical microscope with the necessary resolution.

An application was designed to read the recorded information. It allows you to convert photos of microdefect regions to the corresponding matrix of states. The program consists of two main blocks. At the first stage, the program processes primary images of microdefects and converts them into binarized images. The second block, based on machine learning algorithms, converts microdefect images into digital code. The workflow of the application is shown in Fig. 1.

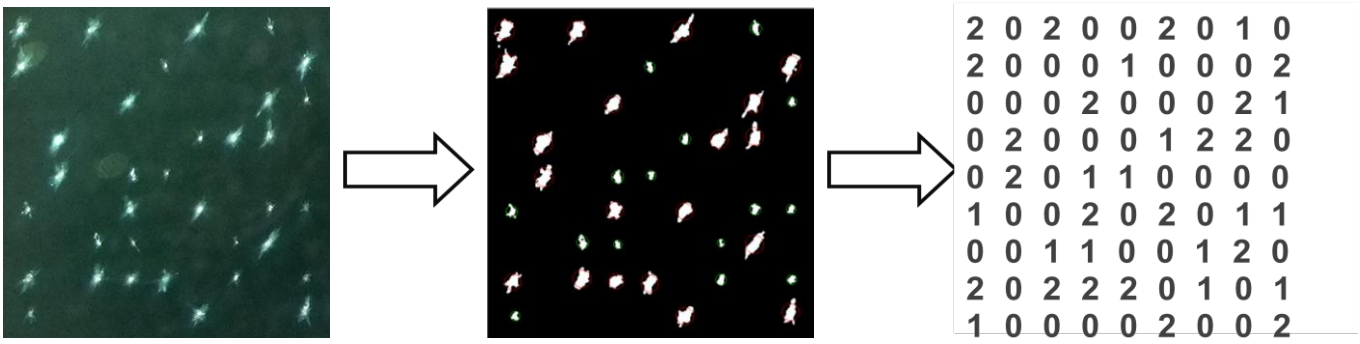

Fig. 1. Application workflow

The proposed method has a sufficiently high recording density, since one region of microbreakdown corresponds to 3 information states, and for our experimental conditions, about 80,000 defects can be formed in a cubic centimeter of the glass. The developed system of information reading was successfully tested on experimental data sets. Unlike the analogues, for data recognition we need only a simple optical microscope and a digital camera.

[1] J. Zhang, M. Gecevičius, M. Beresna. Seemingly unlimited lifetime data storage in nano-structured glass // Phys. Rev. Lett. 112, 2014.
[2] N.B. Delone. Interaction of laser radiation with matter. - Moscow: Nauka, 1989.

ASSESSMENT OF BEACH NOURISHMENT IMPACT IN PALANGA COASTAL ZONE, LITHUANIA

Veronika Vilčinska[1], Dovilė Karlonienė[1], Donatas Pupienis[1,2]

[1] Department of Hydrology and Climatology, Vilnius University, Lithuania
[2] Institute of Geology and Geography, Nature Research Centre, Lithuania
veronika.vilcinska@chgf.vu.lt

The coastal zone is a dynamical system which is constantly changing. This system is quite sensitive to changes of extreme hydrodynamical processes but even more sensitive to human activity. The coastal zone of Palanga was distinguished by wide beach with light-yellow fine grained quartz sand bordered by foredunes. An increase in erosion processes from the end of the 20th century determined a retreat of shoreline and coastal zone sediment loss. These problems led to a decision to nourish the beach. The beach nourishment is a modern, effective and ecological method to protect the coastal zone from erosion. The Palanga beach was nourished with 574 648 m³ of sand during 2006-2012 [1].

The aim of this study was to analyse the changes in sediment budget in Palanga recreational zone during 1975-2015. To achieve the aim, cross-shore levelling in 9 profile were carry out along a 2.5 km long stretch from Rąžės stream to Birutės hill. Output results such as shoreline displacement, beach width, annual and total subaerial beach volume were calculated on the bases of levelling of cross-shore profile data [2].

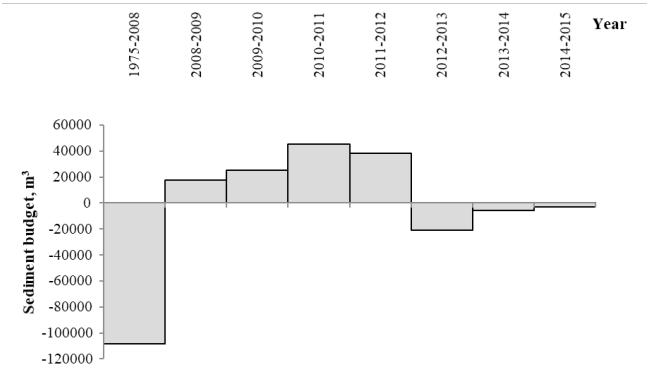

Fig. 1. The changes in sediment budget in Palanga recreational zone

The results revealed that the beach in Palanga recreational coastal zone narrowed from 80 to 20 m with sediment loss amounted on 108 593 m^3during 1975 – 2008 (Fig. 1). During the subsequent period of 2008-2012 the average width of the beach expanded by 80 m as a result of the beach nourishment.

a b

Fig. 2. Palanga recreational zone after beach nourishment northern (a) and southern section (b)

Beach nourishment completed in 2012 and groyne reconstruction at Palanga pier have slowed down an erosion processes in a southern section (Birutės hill –Palanga pier stretch). However, in a northern section (Palanga pier – Ražės stream stretch) erosion processes have become more intensive (Fig. 2).

[1] Pupienis, D., Jarmalavičius, D., Žilinskas, G., Fedorovič, J., 2014. Beach nourishment experiment in Palanga, Lithuania. Journal of Coastal Research, SI. 70, 490-495.

[2] Jarmalavičius D., Satkūnas J., Žilinskas G., Pupienis D. 2012. Dynamics of beaches of Lithuanian coast (the Baltic Sea) for the period 1993-2008 based on morfometric indicators. Environmental Earth Sciences, 65 (6), 1727–1736.

RESEARCH OF THE DISTRIBUTION OF ATMOSPHERIC REFRACTIVE INDEX

Esterė Vedrickaitė[1], Stasys Tamošiūnas[2], Milda Tamošiūnaitė[2*]

[1] Faculty of Physics, Vilnius University, Lithuania
[2] Center for Physical Sciences and Technology (FTMC), Lithuania
estere.vedrickaite@ff.stud.vu.lt

Every telecommunications system involves the transmission of an information-bearing electromagnetic signal through the atmosphere, where part of its energy is lost because of absorption and scattering. This is the reason why a radio wave propagated through the atmosphere attenuates and changes its trajectory because of refractive index, causing lower connection quality. Previous researches show that changes in temperature and relative humidity have the biggest influence in refractive index.

Since it became possible to collect and analyze meteorological data from different sources in particular locations in short time ranges, this research was started in September 2017. In this work relation between hourly and monthly changes in temperature and related humidity and their impact on refractive index was analyzed in Vilnius from September to December in 2017, based on methods suggested by International Telecommunication Union (ITU-R)[1]. The results were compared with records from 2012[2].

The results of analyzed years were quite similar based on air humidity changes. The best time to delineate correlation between refractive index and daytime is between 9AM and 10PM. To observe the changes in this time range quadratic polynomial was derived. Correlation between refractive index and daytime relates to correlation between water vapor partial amount (density) and daytime. The impact of temperature is important only for water vapor changes in the air. Although partial amount of saturation vapor increases with rising temperature, in daytime, when air is drying up, its relative humidity is decreasing as well as absolute humidity and refractive index. Therefore, evaluation of water vapor impact on refractive index is more important.

[1]RECOMMENDATION ITU-R P.453-13 „The radio refractive index: its formula and refractivity data“ . 2017m.
[2]E. Brilius. Lietuvos atmosferos lūžio koeficiento tyrimas ir žemėlapio sudarymas. Magistrantūros studijų baigiamasis darbas. 2013 m.

SPATIALLY CONSISTENT LOS/NLOS MODEL FOR TIME-VARYING MIMO CHANNELS

Rimvydas Aleksiejunas[1], Albert Cesiul[1], Kestutis Svirskas[1]

[1] Institute of Applied Electrodynamics and Telecommunications, Vilnius University, Lithuania
albert.cesiul@ff.vu.lt

A cluster scattering MIMO channel model is proposed combining advantages of map-based models such as spatial consistency as well as stochastic properties of more general statistical models. The model is constructed by generating clusters based on LOS/NLOS visibility regions and generating stochastic MIMO channel coefficients according to temporal, spatial and spectral correlations between large and small scale fading parameters.

For constructing MIMO channel models two main approaches have been used: map-based deterministic models usually implemented using ray-tracing [1] and geometric stochastic models based on statistical properties of multipath fading correlation properties [2]. Recently a hybrid map-based and geometric stochastic models have received wide attention especially related to METIS channel model proposal [3, 4].

Line-of-sight or non-line-of-sight (LOS/NLOS) visibility conditions are required for radio wave propagation modeling to properly select empirical path loss model. For Monte Carlo statistical simulations a random generator of visibility states should be design according to a given spatial probability density. The radio channel model is constructed following 3GPP 3D channel model framework [5] for a stationary base station transmitter and mobile receiver in an urban scenario taking into account spatially consistent LOS/NLOS visibility state model.

In this way a discrete channel model is formed with time sampling interval corresponding to the Doppler frequency within each WSSUS path segment. This enables saving simulation time when processing slower paths without reducing the accuracy of the model.

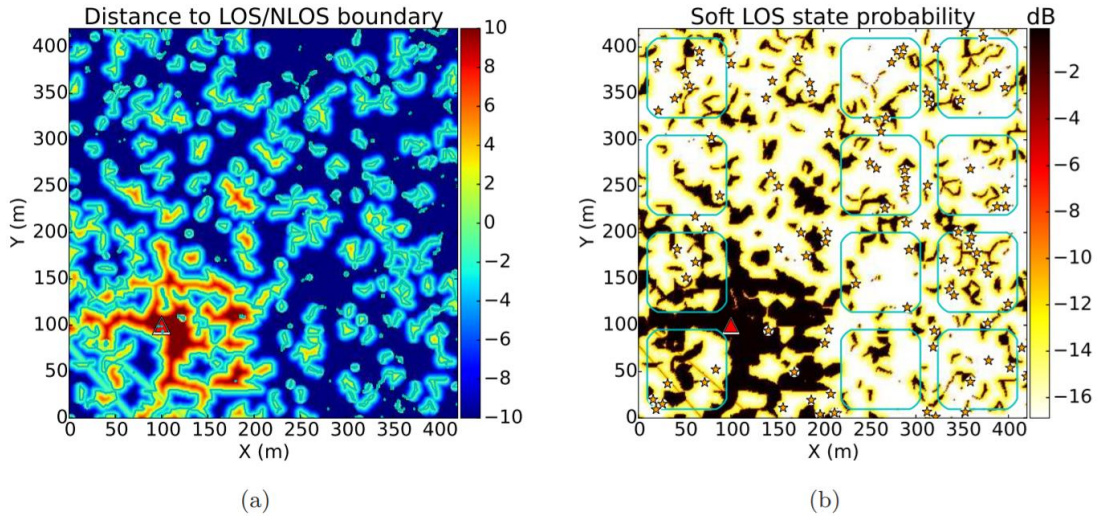

Fig. 1. ure 3: Distance to LOS/NLOS boundaries in meters (a) for a specific snapshot of LOS probability distributions and corresponding soft LOS probability in logarithmic units (b) estimated using the distances to LOS/NLOS boundaries. Figure (b) also displays scattering cluster centers represented by star symbols.

The presented MIMO channel model is based on a discrete statistical cluster scattering description but also takes advantage of spatial consistency via LOS/NLOS visibility zone assignment and large scale fading parameter generation. It can combine properties of stochastic and map-based channel models.

Being a discrete model it is suitable for efficient computer simulations. After splitting into WSSUS stationarity regions, the model can be applied in parallel to multi-processor systems by dividing whole path into array of route parts which can be processed independently.

[1] Z. Yun and M. Iskander, "Ray Tracing for Radio Propagation Modeling: Principles and Applications," IEEE Access, vol. 3, pp. 1089–1100, 2015.
[2] A. Molisch, H. Asplund, R. Heddergott, M. Steinbauer, and T. Zwick, "The COST259 Directional Channel Model-Part I: Overview and Methodology," IEEE Transactions on Wireless Communications, vol. 5, no. 12, pp. 3421–3433, Dec. 2006.
[3] L. Raschkowski, P. Kysti, K. Kusume, T. Jms, V. Nurmela, A. Karttunen, A. Roivainen, T. Imai, J. Jrvelinen, J. Medbo, J. Vihril, J. Meinil, K. Haneda, V. Hovinen, J. Ylitalo, N. Omaki, A. Hekkala, R. Weiler, and M. Peter, "METIS Channel Models (D1.4)," Deliverable ICT-317669-METIS/D1.4, Feb. 2015.
[4] P. Kysti, J. Lehtomki, J. Medbo, and M. Latva-aho, "Map-Based Channel Model for Evaluation of 5G Wireless Communication Systems," IEEE Transactions on Antennas and Propagation, vol. 65, no. 12, pp. 6491–6504, Dec. 2017.
[5] 3GPP TR 36.873, "Study on 3D channel model for LTE," Tech. Rep. Version 12.6.0, Sep. 2017. [Online]. Available: http://www.3gpp.org/dynareport/36873.htm

NARROWBAND POWER-LINE COMMUNICATION TECHNOLOGY ANALYSIS

Vladislovas Čižas, Pranciškus Vitta

[1] Institute of Photonics and Nanotechnology, Vilnius University, Lithuania
vladislovas.cizas@gmail.com

In today‘s world we can observe an incredible boom of electronic technology. A great amount of new devices are being integrated into more and more different fields of human activity. Concerning this, it is no wonder that there is a huge demand for high-quality data transfer channel between different devices and control center.

During last decade PLC (power-line communication) technology is becoming more and more popular as cheap and low noise-dependent technology. In PLC, the communication is implemented by transferring data using AC power cables by modulating signal with much higher frequencies than AC mains. One of the greatest advantages of such a communication is the fact that it can be easily implemented in already existing electrical infrastructure, because it doesn’t require any additional wiring. Furthermore, improved modulation and data coding techniques allowed to create long-distance (>100km) PLC communication devices. These aspects make PLC especially popular for different Smart City features. Unfortunately invented in 90-ies, PLC wasn‘ popular for a long time due to high noise level in power grids. This made PLC to develop in different directions and nowadays we have a huge amount of different incompatible and competing PLC modules with different communication approaches.

During this study we were analysing different PLC parameters (different modulations, transfer protocols, regulations) trying to find the optimal combination, suitable for small package transfer by low-voltage power lines. Moreover, several already existing PLC chips were compared. Furthermore, we were trying to lay a foundation for combining different technology PLC chips to expand already existing Smart City possibilities in Vilnius and other cities.

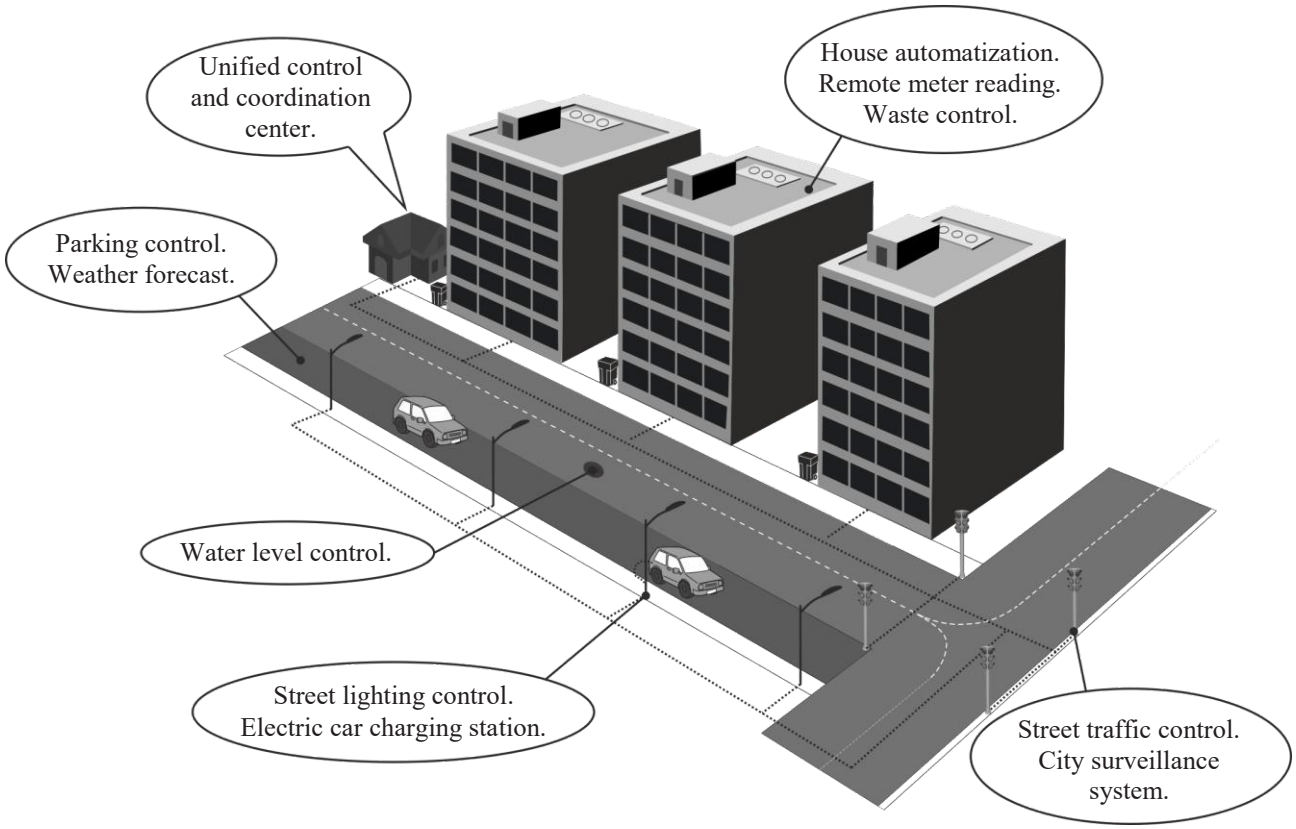

Fig. 1. Vast of PLC application for Smart City features.

[1] H.C. Ferreira et al., Power Line Communications: Theory and Applications for Narrowband and Broadband Communications over Power Lines, Wiley & Sons, 528 (2010).

TREATMENT OF YEAST CELLS BY ELECTRIC FIELD

Antanas Zinovicius[1,2], Vilius Aukscionis[4], Inga Morkvenaite-Vilkonciene[1,3], Jurate Jolanta Petroniene[4], Aura Kisieliute[4], Neringa Petrasauskiene[2], Aliona Kirdeikiene[3], Rimantas Ramanauskas[3], Arunas Ramanavicius[3,4]

1 Vilnius Gediminas Technical University, Faculty of Mechanics, J. Basanavičiaus g. 28, 03224 Vilnius, Lithuania
2 Kaunas University of Technology, Faculty of Chemical technology, Radvilėnų pl. 19, 50299 Kaunas, Lithuania
3 Center for Physical Sciences and Technology, Saulėtekio 3, 10257 Vilnius, Lithuania
4 Faculty of Chemistry and Geosciences, Naugarduko g. 24 03225 Vilnius, Lithuania
inga.morkvenaite-vilkonciene@vgtu.lt

Saccharomyces cerevisiae (S. cerevisiae) – is a simple eukaryote cell, which serves as a model system for eukaryotes, as it is homologous to animal and plant cells, periodically used for studying fundamental cellular processes [1]. Yeast cells can be used as a bioreceptor in biosensors [1, 2]. Scanning electrochemical microscopy (SECM) provides the means to monitor cells in the specialized medium using non-invasive methods. SECM can be used to investigate changes in biosensors' surface and to determine their reaction to different changes in the surrounding conditions, such as mediators and the effect of a temporary electric field.

Atomic force microscopy (AFM) provided valuable information about the cell's surface changes e.g. shape, size or any deformability induced in the cell's membrane, the cytoskeleton and the cytosol. From force-distance curves, measured by AFM, it is possible to get additional information about the physical properties of biological samples, such as Young's modulus and adhesion forces [3]. The influence of mediators and additionally applied electric field on cell viability can be determined from morphological data.

The plasma membrane protects the cell from an outside environment and ensures its homeostasis. Yeast cells affected by an electric field could form hydrophilic or non-hydrophilic pores in the membrane, it may increase transportation of compounds which are usually not supposed to be transported to the inside of the cell.

A study was conducted using a double mediator based system, lipophilic, which takes part in redox reactions inside the cell with NAD, NADP and many others, a hydrophilic mediator which is the final electron acceptor [1]. From the mediators used in the study the most effective for SECM cell imaging was found to be 9,10-phenanthraquinone (PQ), which acts as a second redox mediator in the charge transfer chain of yeast cells, when ferricyanide is used as a first redox mediator [2]. The UME current, measured with PQ as a second redox mediator, was more than 3 times higher than with other evaluated hydrophilic redox mediators. Therefore, the toxicity of PQ is also 3 times higher than other redox mediators. Yeast cells, affected by PQ, were measured by AFM in contact mode. The results show, that after exposure with 0.05 mM PQ, cell morphology was not greatly affected, but an increase in cells' surface roughness was observed. After a second exposure with the same conditions, the cell's surface appears smoother, which is a sign of decreased cell viability.

Therefore, SECM and AFM are suitable for researching the effects of toxicity. Furthermore, going to continue investigation of the electric field application and its effects on yeast cell.

This research was funded by the European Social Fund under the No 09.3.3-LMT-K-712 "Development of Competences of Scientists, other Researchers and Students through Practical Research Activities" measure.

[1] I. Morkvenaite-Vilkonciene, A. Ramanaviciene, and A. Ramanavicius. Sens. Actuat. B, 228 (2016) 200-206.
[2] A. Ramanavicius, I. Morkvenaite-Vilkonciene, A. Kisieliute, J. Petroniene, A. Ramanaviciene. Coll. Surf. B., 149 (2017) 1-6.
[3] I. Morkvenaite-Vilkonciene, A. Ramanavicius, and A. Ramanaviciene. Medicina, 49 (2013). 155-164.

INFLUENCE OF X-RAY BEAM CENTRATION ON DOSES IN ORGANS AND TISSUES FOR THORAX RADIOGRAPHY

Krystsina Makarevich[1,2], Viktor Minenko[2], Semen Kutsen[2]

[1] Department of Nuclear Physics, Belarussian State University, Belarus
[2] Institute for Nuclear Problems , Belarussian State University, Belarus
kristinanevdokh@tut.by

It is important to determine radiation doses of patients in order to optimize the image quality contemporaneously with negative consequences of the radiological procedure. But there are a number of factors that cause uncertainties in the process of estimating doses to patients [1]. This paper is devoted to estimating the uncertainties that X-ray beam centration brings to the values of the absorbed doses in critical organs and tissues.

The thorax radiography in posterior-anterior projection was chosen as one of the most frequent X-ray examinations. In order to estimate the energy absorbed in organs and tissues the Monte-Carlo modelling of X-ray transport within the human body was performed. The reference voxel phantoms of an adult male and female were used as the models of human body [2]. All calculating were made for the following parameters: anode voltage 70 kV, 3 mm filtration of aluminum, voltage ripple 5%, the focus-film distance was 100 cm, the field size on the film was 30×40 cm^2.

The reference centration (RC) was defined as the centration to the geometrical center of lungs. For the male phantom it corresponded to 40 cm and for the female phantom – 36.8 cm down from the top of the head. The cases of ±5%RC, ±10%RC, ±15%RC and ±20%RC to this centration were considered. The results of calculations were normalized by kerma-area product estimated for such examinations. Some of them are shown on the Fig. 1.

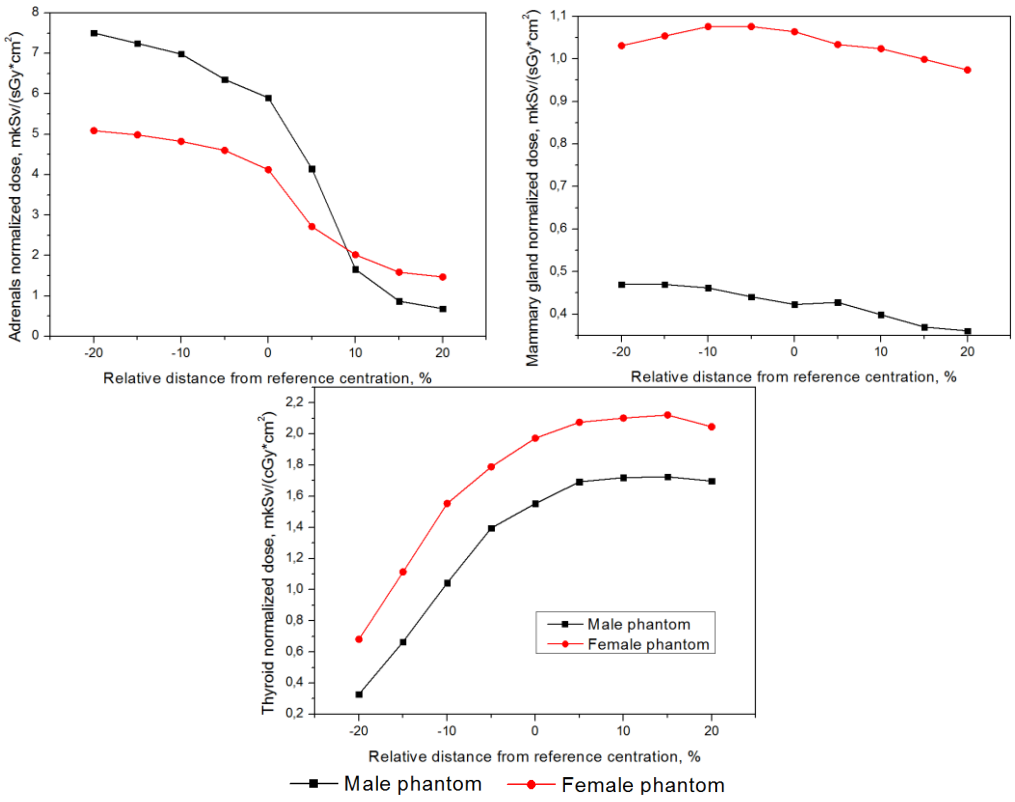

Fig. 1. Normalized doses calculated for adrenals, mammary gland and thyroid of male and female phantoms.

According to our research the position of X-ray beam causes large uncertainties (up to ten times) for organs that originally were out of the direct field of radiation or were partially in the field. For extended organs and tissues such as lungs, muscle or skin this changes are not so great (<20%) but nevertheless they should be taken into account for patient's dose assessment. Also it should be considered that doses to female organs practically in all cases are larger than doses to the same organs of male phantom. It can be explained by differences in their bodies' constitutions. Thus, all these findings will be taken into account by our team that develops the program for patients' doses assessment.

[1] P. Toroi, A. Kaleranta, P. Vock et. al., Interpretation of measured dose data in X-ray imaging, IRPA 2012, Glasgow, UK.
[2] International Commission on Radiological Protection. Adult Reference Computational Phantoms. ICRP Publication 110. Ann ICRP, Peragamon Press, 2009.

ROCK MAGNETIC SUSCEPTIBILITY APPLICATION FOR PALEOENVIRONMENTAL RECONSTRUCTION OF THE LOWER PALAEOZOIC SHALEY SUCCESSION, LITHUANIA

Anna Cichon-Pupienis

Department of Geology and Mineralogy, Vilnius University, Lithuania
anna.cichon-pupienis@gf.vu.lt

Magnetic susceptibility (MS) is a parameter which reflects changes in mineralogical composition of sedimentary rock. The changes in MS signal are controlled by variations in ferromagnetic minerals such as magnetite, paramagnetic fraction encompassing less magnetic phases mainly clay minerals, iron carbonates, pyrite, and diamagnetic portion (quartz, calcite). Paramagnetic minerals are generally of lower importance in regard to MS, but the overall signal coming from those minerals may prevail in the measured MS values [1].

Core rock shale samples from Upper Ordovician, Lower Silurian Llandovery and Wenlock section from a well located in western Lithuania were analysed. These greenish-grey and black, organic and graptolite-rich, locally calcareous shales and claystones were deposited in marine deep shelf environment in the eastern part of the Baltic sedimentary basin placed on the western margin of the East European Craton. Rock magnetic susceptibility, geochemical (X-Ray Fluorescence - XRF) and mineralogical (X-Ray Diffraction - XRD) investigations were carried out on whole rock samples with the aim to recognize depositional paleoenvironment of shaley horizons.

Bulk mineralogy investigation (XRD) performed on the selected samples showed very similar mineralogical composition in all of the samples; the dominant phases were quartz, clay minerals, feldspars, carbonates and iron sulphide. Clay minerals+mica constitute the largest group (34-59 %) among silicates which content ranges from 68 to 91 %. Feldspars contribution was minor up to 5 %. The carbonate portion was amounted from 4 to almost 30 % in Wenlock section. Pyrite occurs in all of the samples, but with varying content from < 1 to over 13%.

The MS values in the studied section range widely (κ 39 - 559 μSI), but the most stable MS values and of lowest amplitudes of fluctuation were observed in the Llandovery Telychian section. In this interval MS curve imitates well the gamma-ray log suggesting that MS signal primarily comes from phyllosilicate minerals such as illite and chlorite, which are the most abundant clay minerals according to XRD analysis. General long-term slightly decreasing trend of MS upward this section that coincides with progressively increasing trend of grain size and higher rates of carbonate fraction is interpreted as shallowing-upward trend. Here, MS values reflect growing dilution of terrigenous material by carbonate portion. A sharp shift toward very high MS values (change reaches κ 355 μSI) near the Llandovery-Wenlock boundary seems to be controlled by fluxes of detrital material during enhanced falling sea-level. Higher values of calculated excess (authigenic/diagenetic) Fe-fraction [2] and determined Degree of Pyritization [3, 4] corresponding in some intervals with elevated MS values suggests that MS signal is supported by presence of minerals such as ferrous dolomite or ankerite and pyrite, which were also identified in different quantities by XRD.

The results imply that origin of magnetic minerals controlling variations in MS signal is linked to detrital input and authigenic/diagenetic mineral phases. MS measurements complemented by geochemical proxies may serve as a record of change in ancient sea-level fluctuation and provide valuable information on mineralogical phase which in turn gives clues on sediment depositional paleoenvironment.

---

[1] Ellwood, B., Crick, R., Hassani, A., Benoist, S.L., Young, R.H. 2000. Magnetosusceptibility event and cyclostratigraphy method applied to marine rock: Detrital input versus carbonate productivity. Geology, 28, 1135-1138.

[2] Riquier, L., Averbuch, O., Devleeschouwer, X., Tribovillard, N. 2010. Diagenetic versus detrital origin of the magnetic susceptibility variations in some carbonate Frasnian–Famennian boundary sections from Northern Africa anWestern Europe: implications for paleoenvironmental reconstructions. International Journal of Earth Sciences, 99(1), S57-S73.

[3] Dean, W., Arthur, M. 1989. Iron-sulfur-carbon relationships in organic-carbon-rich sequences: Cretaceous Western Interion Seaway. American Journal of Science, 289, 708-743.

[4] Arthur, M.A., Sageman, B.B. 1994. Marine Black Shales: Depositional Mechanisms and Environments of Ancient Deposits. Annual Review of Earth and Planetary Sciences, 22, 499-551

THEORETICAL AND EXPERIMENTAL RESEARCH OF SPLIT-CAVITY OSCILLATOR

Ilia Moroz[1,2], Anatoli Rouba[2]

[1] Department of Nuclear Physics, Belarussian State University, Belarus
[2] Institute for Nuclear Problems , Belarussian State University, Belarus
miwa-holod@yandex.ru

High-power microwaves (HPM) have a wide range of applications in plasma heating, particle acceleration, high-power radar, and many other industrial and military fields. There are lots different types of HPM sources: klystron amplifiers, backward wave oscillators (BWO), travelling wave tubes (TWT), transit-time oscillator (TTO), virtual cathode oscillator (vircator), etc. Despite the great success in their development, their use is often limited by large size or low efficiency. For this reason Barry M. Marder with his group developed new device, called split-cavity oscillator (SCO) [1, 2], which was improved by others scientists [3, 4]. SCO does not require external magnetic guide field, therefore has a smaller size then BWO or TWT, and has a larger efficiency then TTO or vircator. SCO consists of a cylindrical resonator with a conducting screen walls splitted by a conducting screen (Fig.1) which an electron beam can pass. This configuration has additional fundamental electromagnetic modes (see Fig. 1) in comparison with a hollow resonator.

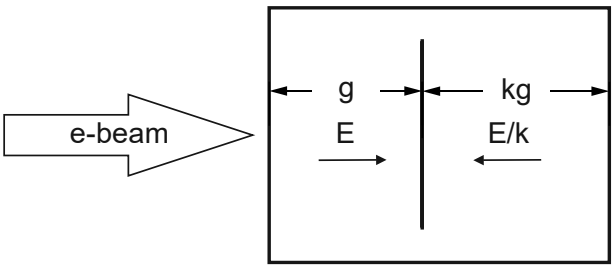

Fig. 1. Schematic representation of SCO, where g is longitudinal size of cavity, E is electric field, k is parameter.

The research is devoted to theoretical and experimental research of HPM source based on the SCO. Interaction between electron beam and fundamental mode was considered. Expressions of a beam-energy change were obtained 1) for an asymmetric resonator taking into account the space charge of beam and 2) for relativistic beam. The small-signal analysis showed that the optimal configuration is symmetric, the space charge almost does not effect on the resonator size, increasing of electron velocity decreases energy transfer efficiency to electromagnetic field.

Experimental research confirmed theoretical predictions. HPM generation was obtained on the calculated frequency (Fig.2). Method of tuning frequency was developed and HPM radiation was detected in range of 2.5-3 GHz.

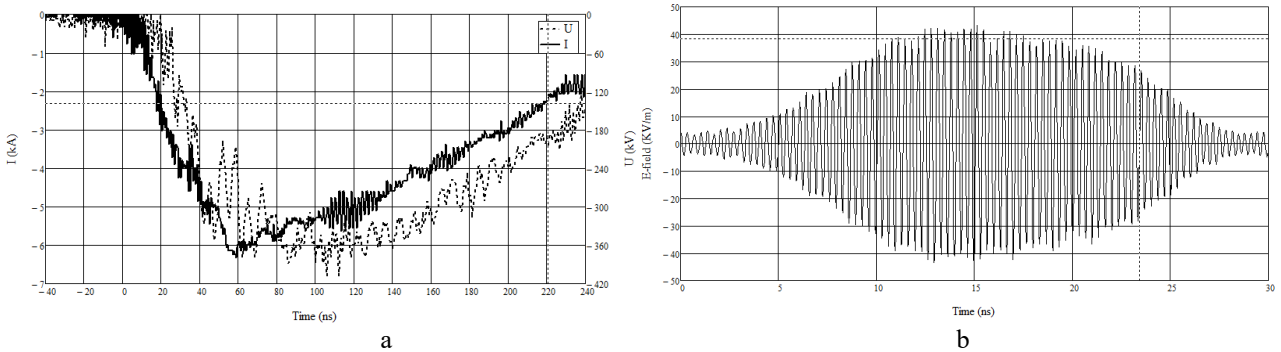

a b

Fig. 2. Experimental results: (a) beam current (I) and accelerating voltage (U); (b) electric field at 6 m distance.

[1] Barry M. Marder, M. Collins Clark, Larry D. Bacon, James M. Hoffman, Raymond W. Lemke, P. Dale Coleman, The split-cavity oscillator: a high-power E-beam modulator and microwave source, IEEE TRANSACTIONS ON PLASMA SCIENCE. – 1992. – V20, №3 – C.312–331.
[2] Raymond W. Lemke, M. Collins Clark, Barry M. Marder ,Theoretical and experimental investigation of a method for increasing the output power of a microwave tube based on the split-cavity oscillator, Journal of Applied Physics. – 1994. – V75, №10 – C.5423–5432.
[3] G.V. Sotnikov, Yu.V. Tkach, S.L. Scherbina, Eigen frequencies and field structure of axially symmetric split-cavities, Electromagnetic Phenomena. – 2008. – V8, №1(19) – c.46-61.
[4] ZHANG Yun-Jian, MA Qiao-Sheng, LUO Xiong , Study of a compact external magnetic field radial split-cavity oscillator, Chinese Physics C. – 2011. – V35, №4 – c.381-386.

COMPLEX THERAPY FOR HYPERTROPHIC SCARS TREATMENT

Akvilė Andziukevičiūtė-Jankūnienė[1], Daiva Mikučionienė[1], Virginija Jankauskaitė[1]

[1]Department of Production Engineering, Kaunas University of Technology
akvilea@gmail.com

Wound healing is a very complex process, which can be divided into hemostasis and inflammation, tissue growth, called proliferation and tissue remodeling [1]. Usually wound contractions result scarring, which can result different consequences, ranging from body disfigurement to organ dysfunction [2]. There are a lot of complex scar treatment methods, but these therapies often result in inadequate results like relapses or side effects. Therefore, non-invasive treatment methods, such as compression therapy, silicone gel films, and the herbal extracts (Table 1) are becoming very popular.

Table 1. Some topical non-invasive hypertrophic scar and keloids therapies [3]

Therapy	Preparation method	Use	Pros	Cons	Efficacy
Compression therapy	Custom-made elastic compression garment of different shape	Worn all day until scar is mature; new garment made very 6–8 weeks	Low cost	Limited use on face and high-motion areas; low patient compliance; subjective pressure measurements; side effects of local skin maceration	+
Silicone sheeting	Soft, extensible tacky or nontacky gel or soft rubber sheets	12–24 h/d for 2–4 months	Easy to use, more effective than silicone gel alone	Cumbersome application, especially in areas of movement; side effects of superficial maceration	+ +
Herb extracts	Transparent gels and creams	3–4 times/d for 8 weeks on new scars (after wound closure) and 2–6 months on old scars	Good for exposed areas, widespread availability	Few documented effects on scars	+/–

The goal of this investigation is to create textile compression means with silicone and medical plants extract composite layer for complex scar treatment.

3D knitted structures must ensure compression higher than capillary pressure (about 24 mmHg) to decrease blood flow and hypoxia [4]. Compression fabric of high tensility in all directions, permeability, and durability, could be used. These properties was ensured by compression means knitted from elastomeric yarns – polyurethane core double wrapped with polyamide 6.6 yarn that generated pressure of 25 mmHg.

Meanwhile, silicone relieves scar redness, paint, improves elasticity [5]. Prosthetics, highly biocompatible, cross-linked polydimethylsiloxane (PDMS) with 2 methyl groups, from Wacker Chemie AG, was used for scar treatment. This silicone has low hardness (Shore 00 – 25) and strength, is hydrophobic, viscoelastic (elongation at break – 550%), and repels water and dust. PDMS layer of 2 mm thickness can be easy formed and adhered to knitted compression textile surface with biocompatible silicone adhesive (adhesion strength – 390 N/m with cohesive failure mode).

Medicinal plants show several different effects on hypertrophic scars: proliferation inhibition of fibroblasts, promotion of apoptosis, suppression of mitosis, decrease of scar tissue fibrosis [6]. The antihypertrophic scar activity of medical plants results from a variety of components (i.e., bioflavonoids) contained in these plants. Red onion (*Allium cepa*) extract shows antiproliferation of hypertrophic scars fibroblast activity due to the presence of quercetin, cepalin, kaempferol, and other flavanoids. Addition of *Allium cepa* extract freeze-dry particles reduces the PDMS composite surface wettability in 1-3 %. Onion extract blocked PDMS cross-linking, therefore, additionally silica nanoparticles were added. Low amount (1%) of onion extract/silica nanocomposite increases mechanical properties at tension up to 26 %, though 4 % of additive decrease tensile strength and elongation.

ACKNOWLEDGEMENT. This research is funded by the European Social Fund under the No 09.3.3-LMT-K-712 “Development of Competences of Scientists, other Researchers and Students through Practical Research Activities” measure.

[1] H. P. Lorenz, M. T. Longaker. Wounds: biology, pathology, and management. Surgery: Basic Science and Clinical Evidence, 2nd ed. 191-208 (New York, 2008).

[2] M.T. Longaker, D. J. Whitby, M. W. Ferguson, et al. Adult skin wounds in the fetal environment heal with scar formation. Annal of Surgery **219**, 65–72 (1994).

[3] J. M. Zurada, D. Kriegel, I. C. Davis. Topical treatments for hypertrophic scars. Journal of American Academy Dermatology **55(6)**, 1024-1031 (2006).

[4] A. Katsambas, T. Lotti, C. Dessinioti, A. M. D'Erme, (Eds.). European Handbook of Dermatological Treatments, 3rd ed. (Springer-Verlag Berlin Heidelberg, 2015).

[5] T. A. Mustoe. Evolution of silicone therapy and mechanism of action in scar management, Aesthetic Plastic Surgery **32**, 82-92 (2008).

[6] Qi Ye, Su-Juan Wang, Jian-Yu Chen, Khalid Rahman, Hai-Liang Xin, Hong Zhang. Medicinal Plants for the Treatment of Hypertrophic Scars, Evidence-Based Complementary and Alternative Medicine (2015), Article ID 101340, 15 p.

SATELLITE SOIL MOISTURE RELATIONSHIP WITH METEOROLOGICAL PARAMETERS

Viktorija Mačiulytė[1]

[1] Institute of Geosciences, Vilnius University, Vilnius, Lithuania
viktorija.maciulyte@meteo.lt

Soil moisture is an important factor in the hydrological cycle controlled by precipitation, air temperature, evapotranspiration and infiltration into deeper layers [2]. Water content in soil is one of the main determinants of the vegetation conditions, because it determines the growth and productivity of the plant [1]. Soil moisture measurements are necessary in modelling and drought estimation. *In situ* point measurements have better accuracy, but poor spatial representation. Also, it is quite expensive. Remote sensing methods, like satellite information, could help to improve spatial resolution of soil moisture [3].

The goal of this research is to estimate relationship between satellite soil moisture and meteorological parameters in eastern Baltic Sea region (53–60°N and 20–30°E) covering the period from 1979 to 2016 warm season (April - October). Remote sensing soil moisture data were used from ESA Soil Moisture CCI Project soil moisture product created from merged active and passive products (water amount m^3/m^3) with 25 km spatial and daily temporal resolution. For meteorological conditions it was used minimum, maximum and daily mean air temperature and daily precipitation amount from E-OBS with 25 km spatial resolution.

It was found that highest air temperature and most precipitation is in July compared with other months in analyzed area. Meanwhile, soil moisture in July is the lowest (the average area of the whole area was 0.17 m^3/m^3). The highest moisture content in the soil is in April and October (0.21–0.22 m^3/m^3).

In different years, meteorological parameters can vary greatly in the same month. The most variegated values is in July (standard deviation for temperature reach 1.7 °C and for precipitation 41 mm.) Meanwhile, soil moisture varies the most in October (0.02 m^3/m^3).

Soil moisture is most strongly determined by the combination of air temperature and precipitation. The strongest correlation was found between daily precipitation and one day later soil moisture (1 day inertia) (correlation coefficient reach r=0.5)

However, the total amount of precipitation over long periods is also important for soil moisture. Analyzing sums of precipitation in last 2, 3, 5, 10 and 15 days found that the soil moisture is mostly determined by the amount of precipitation in the last 2–10 days (mostly 5 days).

Research showed that different parts of analyzed area have few relationship patters (Fig. 1). Precipitation and soil moisture relationship is stronger in northern and southern part (r=0.4–0.5), but in central part is more important air temperature (r=-0.4–-0.5), especially in the Middle Lithuania and Žemaičiai heights.

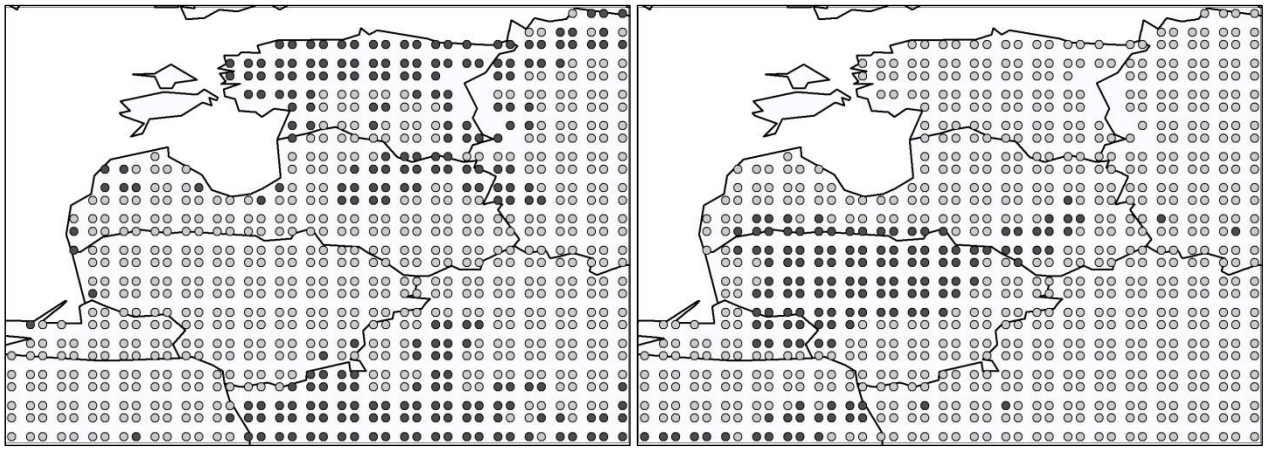

Fig. 1. Correlation between soil moisture and precipitation amount of 3 days (left) and air temperature (right). Darker points show correlation coefficients more than 0.4 (left) and less than -0.4 (right).

These results show that remote sensing soil moisture data has relationship with meteorological parameters. Relationship has lagging time until 10 days, so using meteorological forecast it is possible to predict soil moisture too.

[1] D. Valiukas, Analysis of droughts and dry periods in Lithuania, Doctoral dissertation, Vilnius University (2015).
[2] J. Jian, P. Pan, Y. Chen, W. Yang, Soil Moisture Retrieval Quantitatively with Remotely Sensed Data and Its Crucial Factors Analysis, *J. Water Resource and Protection* 1, 439-447 (2009), doi:10.4236/jwarp.2009.16053.
[3] L. A. Méndez-Barroso, E. R. Vivoni, C. K. Watts, J. C. Rodrķguez, Seasonal and interannual relations between precipitation, surface soil moisture and vegetation dynamics in the North American monsoon region, *Journal of Hydrology* 377, 59–70 (2009), doi:10.1016/j.jhydrol.2009.08.009.

RESEARCH OF HUMAN ERGONOMIC PRESSURE ADJUSTMENT TO THE SITTING SUFACE

Ieva Miagkovaite[1], Vytautas Bucinskas[1], Inga Morkvenaite-Vilkonciene[1,2]
1 Vilnius Gediminas Technical University, Faculty of Mechanics, J. Basanavičiaus g. 28, 03224 Vilnius, Lithuania
2 Center for Physical Sciences and Technology, Saulėtekio 3, 10257 Vilnius, Lithuania
E-mail: ieva.miagkovaite@stud.vgtu.lt

Researches of pressure measurements are mostly made for the laying body pressure on a bed like surfaces. The analysis for sitting position is realized for car or agricultural vehicle seats to find most comfortable materials and designs. Although, analysis of human fatigue in a seated working place based on pressure measurements is not widely investigated. Most papers of sitting pressure measurements [1] made to prevent development of pressure ulcers for disable people, who cannot move and do not have feeling in a lower body, while seated in wheelchairs [2].

The motivation for this topic comes from fatigue behavior of human tests and ergonomics of seated working places. As studies have shown, many adults spend 70% of their waking hours sitting and little or no time exercising in a result experiencing pain in the back, neck, and shoulders. Sitting in uncomfortable chair requires greater muscular force and control to maintain stability and equilibrium, which leads to fatigue and discomfort [3]. Project tests would analyze people behavior while sitting on different surfaces (different size of chair cushions and design of chair) based on the measured pressure and find parts where the highest pressure is concentrated.

In this project, main objective is to design the sensing mat (Fig. 1) and test it. The pressure-measuring mat should be adjustable in purpose to move it through different sitting surfaces. In this project pressure sensing is done with Interlink Electronics force sensing resistors (FSR-part no. 402), which increase the resistance with increasing force applied on the sensing area. Sensor connected with resistor of known value creates voltage divider, where drop of input voltage corresponds to weight applied on the sensor. The program of measurement reading and visualization is created in Matlab package Simulink. Where, data from 16 sensors is obtained in 10 Hz sampling time and converted from voltage change to grams by prescribed function. Values of sensors are visualized as color matrix corresponding to sensor placement. Moreover, data measured over time is stored in Matlab workspace, where it can be reused for further examinations.

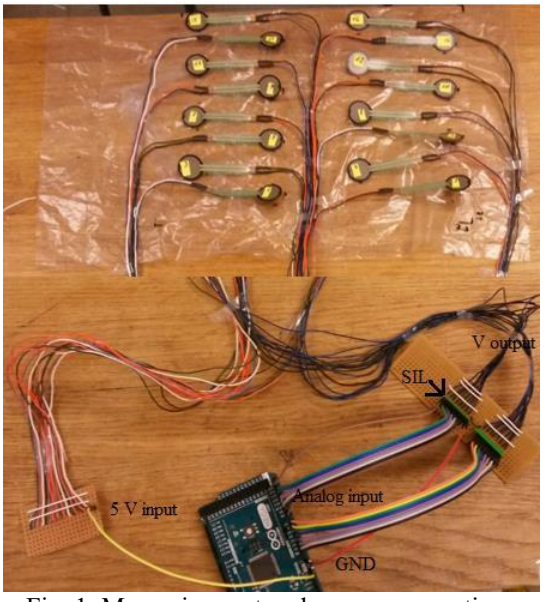

Fig. 1. Measuring mat and sensor connections

Measurements show that, pressure measuring mat can be affective with matrix 4x4. Having more sensors that can cover all sitting surface can represent data of leg position more detailed. Furthermore, small spacing between sensors can result in very low readings of particular places where is low pressure. Spacing of the sensors also depends on tested body anatomy for important data reflection.

Measured value can change from 20 g to 60 g depending on the sitting surface (hard or soft), because of this variation precise tests have to be performed on different surfaces. For this reason, mat can be used for comparison of pressure of different parts, but not precise measurements of the weight.

Humans of different body physique should be tested to find optimal spacing of the sensors. Fatigue study should be run, to show how pressure changes over long period of time not changing sitting position.

[1] Jawad, A.; Andersson, H.; Sidén, J. 2017. Sitting posture recognition using screen printed large area pressure sensors, IEEE Sensors.
[2] Jun, Y.; Cho. E.; Park, S. H. 2016. Body pressure distribution measurement for comfort evaluation of a coccyx seating mat, 3rd International Mega-Conference on Green and Smart Technology.
[3] Anderson, S., *et al*. 2013. Correlating air cushion pressure to maximum interface pressure on the buttocks, Resna annual conference.

OPTICAL PROPERTIES OF THE URBAN AEROSOL PARTICLES IN VILNIUS

Julija Pauraitė, Kristina Plauškaitė, Genrik Mordas and Vidmantas Ulevicius*

[1] Center for Physical Sciences and Technology, Vilnius, Lithuania
julija.pauraite@ftmc.lt

Atmospheric aerosols can significantly influence local and global climate and their loadings have substantially increased since preindustrial times. The impact of particles depends on their chemical composition and physical properties (e.g. optics). The light scattering and the light absorption are two main interaction processes in the atmosphere between aerosol particles and solar radiation. Large uncertainties in estimating the aerosol radiative forcing [1] urge a better understanding of optical processes in the atmosphere.

We investigated aerosol optical properties in spring-summertime in Vilnius (urban background site). During experiments in May-June 2017, we deployed an Aerosol Chemical Speciation Monitor (ACSM), a 7-wavelength Aethalometer and an integrating Nephelometer (TSI). Ancillary measurements included the meteorological parameters (relative humidity, temperature, wind speed and solar radiation). We used Positive matrix factorization (PMF) of ACSM organic aerosol mass spectra to further characterize the sources of ambient organic aerosol (OA). Furthermore, absorption Angström exponent (AAE) and scattering Angström exponent (SAE) were calculated.

Non-refractory PM1 consisted of organics (84%, 6.35 μg/m^3 with standard deviation (SD) of 4.00 μg/m^3), nitrate (9%, 0.66 μg/m^3 (SD=0.51 μg/m^3)), ammonium (4%, 0.32 μg/m^3 (SD=0.20 μg/m^3)) and sulphate (3%, 0.20 μg/m^3 (SD=0.12 μg/m^3)). Four types of OA were observed: hydrocarbon-like organic aerosol (HOA), biomass burning organic aerosol (BBOA), more and less oxygenated organic aerosol (OOA1 and OOA2, respectively) (Fig. 1). At the beginning of the measuring campaign domestic heating was a reason of higher BBOA concentrations and its contribution to organics of the entire measuring campaign was 18%. As expected, main contributions to organics were OOA1 and OOA2 and reached 34% and 38%, respectively. A diurnal trend of HOA showed two diurnal peaks at rush hours (5-7 h and 19-21 h). The average value of AAE was 1.0 (with standard deviation of 0.2), indicating the dominance of fossil fuel versus biomass burning. SSA varied between 0.9 and 2.6 indicating a great variation among particles size distribution. To conclude, the undertaken investigation identified the main sources of OA and evaluated optical properties of aerosols. The results of this study can provide additional insights into forecasting the radiative forcing in local and global scale.

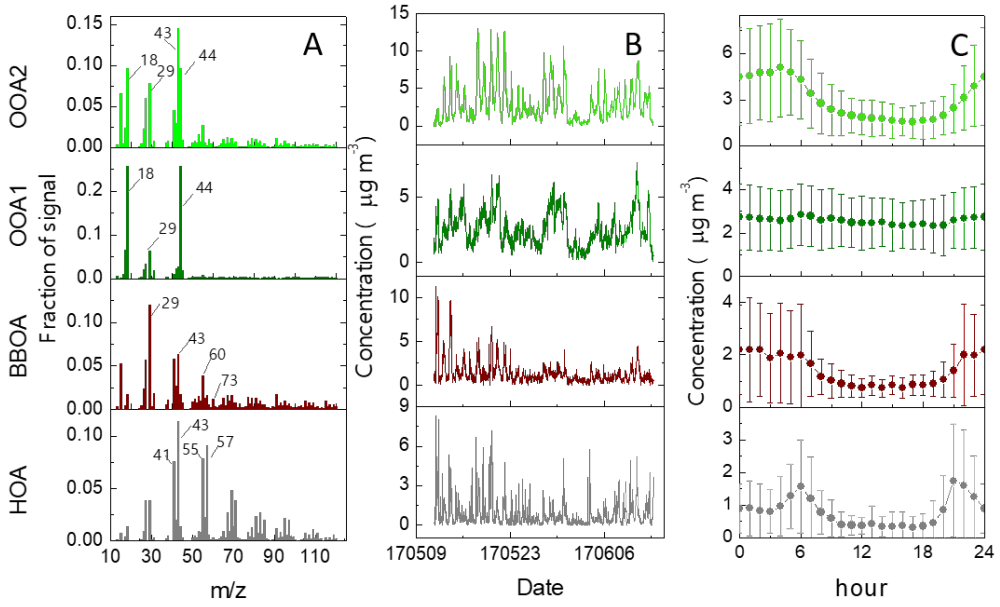

Fig. 1. PMF solutions: (A) mass spectra of OOA2 (green), OOA1 (dark green), BBOA (brown) and HOA (grey) factors, (B) their time series and (C) diurnal time trends.

[1] P. Forster et al., Changes in Atmospheric Constituents and in Radiative Forcing, Condensed Matter and Materials Physics, **77**, 129-234 (2008).

ON THE RELATION OF THE OUTDOOR AND INDOOR AEROSOL PARTICLE CONCENTRATION AT VILNIUS CITY ELEMENTARY SCHOOLS

Vadimas Dudoitis[1], Nina Prokopčiuk[1], Ulrich Franck[2], Nikolaj Tarasiuk[1], Vidmantas Ulevičius[1], Daiva Čepuraitė[3], Kęstutis Štaras[4]

[1]SRI Center for Physical Sciences and Technology, Lithuania
[2]Helmholtz-Centre for Environmental Research, Germany
[3]Centro poliklinika, Lithuania
[4]Vilnius City Municipal Public Health Bureau, Vilnius, Lithuania

vadimas.dudoitis@ftmc.lt

Airborne particles are well known to produce detrimental effects on human health, and children are especially vulnerable to such environmental exposure [1]. During the classes grade-schoolers spend a significant amount of time indoors. The common sources of indoor aerosol are closely related to human personal activity [2, 3]. In order to evaluate indoor aerosol particle exposure among pupils at elementary schools, several schools from different Vilnius county district locations were selected. The aerosol particle number and mass concentrations (PNC and PMC) were measured both inside and outside of the studied buildings. Measurements of outdoor aerosol concentrations were carried out in order to study the influence of the outdoor environment upon the indoors, as well.

A condensation particle counter (CPC, TSI model 3007) was used for measuring aerosol total particle number concentration (PNC^1) up to 10 nm of size. Optical particle sizer (OPS, TSI model 3330) was used for measuring aerosol particle size distribution in the range from 0.3 to 10.0 μm, PNC^2 and PMC. The indoor measurements were conducted in the classrooms during the lessons and in the corridors during the lessons and lesson breaks. The typical measurement duration lasted for 10 min. In order to meet the specific technical requirements for CPC measurement outdoors (air temperature – above 10 ^oC and relative humidity – below 70%), the outdoor air was sucked through an open window into the room up to 3 min. The outdoor aerosol concentration levels were characterised by settling of these extreme values during the induced draught conditions.

During the 2017 autumn measurements, outdoor aerosol $PNCs^1$ (measured by CPC), $PNCs^2$ and PMCs (measured by OPS) varied in the ranges of 2600-17000 cm^{-3}, 30-2890 cm^{-3} and 9-100 $\mu g \cdot m^{-3}$, respectively. Indoor aerosol $PNCs^1$, $PNCs^2$ and PMCs varied in the size range of 1800-24160 cm^{-3}, 13-390 cm^{-3} and 12-274 $\mu g \cdot m^{-3}$, respectively. The levels of indoor aerosol particle concentrations in schools were higher than the outdoor ones and were influenced by the aerosol particle sources inside the building, such as cooking activity in the canteen and school-graders activity in the corridors during the lesson breaks. Measurement areas inside the school can be ranked according to the highest PNC values at the dining room entrances (not in every school) reached up to 70000-77000 cm^{-3}, in the corridors during the lesson breaks – up to 36000-44900 cm^{-3} and in the classrooms – up to 17000-24160 cm^{-3}. The elevated levels of aerosol $PNCs^2$ and PMCs was also depicted in the corridors during the lesson breaks and in the classrooms, equipped with soft furnishing and carpets. Indoor aerosol $PNCs^1$ were more susceptible to the outdoor aerosol concentration increase in the elementary schools, located in the areas, exposed to a comparatively high level of outdoor air pollution.

[1] G. Buonanno, G. B. Marks, L. Morawska, Health effects of daily airborne particle dose in children: Direct association between personal dose and respiratory health effects, Environmental Pollution 180, 246–250 (2013).

[2] H. Guo, L. Morawska, C. He et al., Characterization of particle number concentrations and PM2.5 in a school: influence of outdoor air pollution on indoor air, Environmental Science and Pollution Research 17(6), 1268–1278 (2010).

[3] T. Hussein, T. Glytsos, J. Ondráček et al., Particle size characterization and emission rates during indoor activities in a house, Atmospheric Environment 40(23), 4285–4307 (2006).

VOLUMETRIC DAMAGEABILITY OF TIRE–ASPHALT CONTACT PAIR UNDER VARIOUS LOADS

Gleb Gribovskii

Department of Theoretical and Applied Mechanics, Belarusian State University, Belarus
mmf.gribovskiy@gmail.com

Computer models for describing the three-dimensional stress-strain state of a system tire–asphalt are of great practical importance for determination assessment of volume damageability and wear of the tire tread and the asphalt pavement, which work in conditions of contact, mechanical and sliding fatigue. Today, there are many works dedicated to analytical and computer simulation of stress-strain state of the "rim–tire–asphalt" separate system components [1,2].

The main goal of this work is to use finite-element modeling for the analysis of simultaneous contact interactions of the full multielement system "rim–tire–asphalt" [3], loaded by the various inner pressure P_S (from 0.65 to 0.85 MPa, Δp=0.5 MPa) and radial load F_H (from 6 to 10 kN, Δf=1 kN) on rim, 3D stress-strain state and the state of volumetric damageability. Truck tire geometric model of 22.5″ radius with a simplified rim was taken for the calculation in ANSYS. The following components were added to the model [4] of tire: steel belts, radial ply, wire bead, rubber tread.

Calculation of damageability is based on the model of deformable solid mechanics with dangerous volume. According to this model dangerous volume is the volume where acting stresses are greater than limiting stress [5].

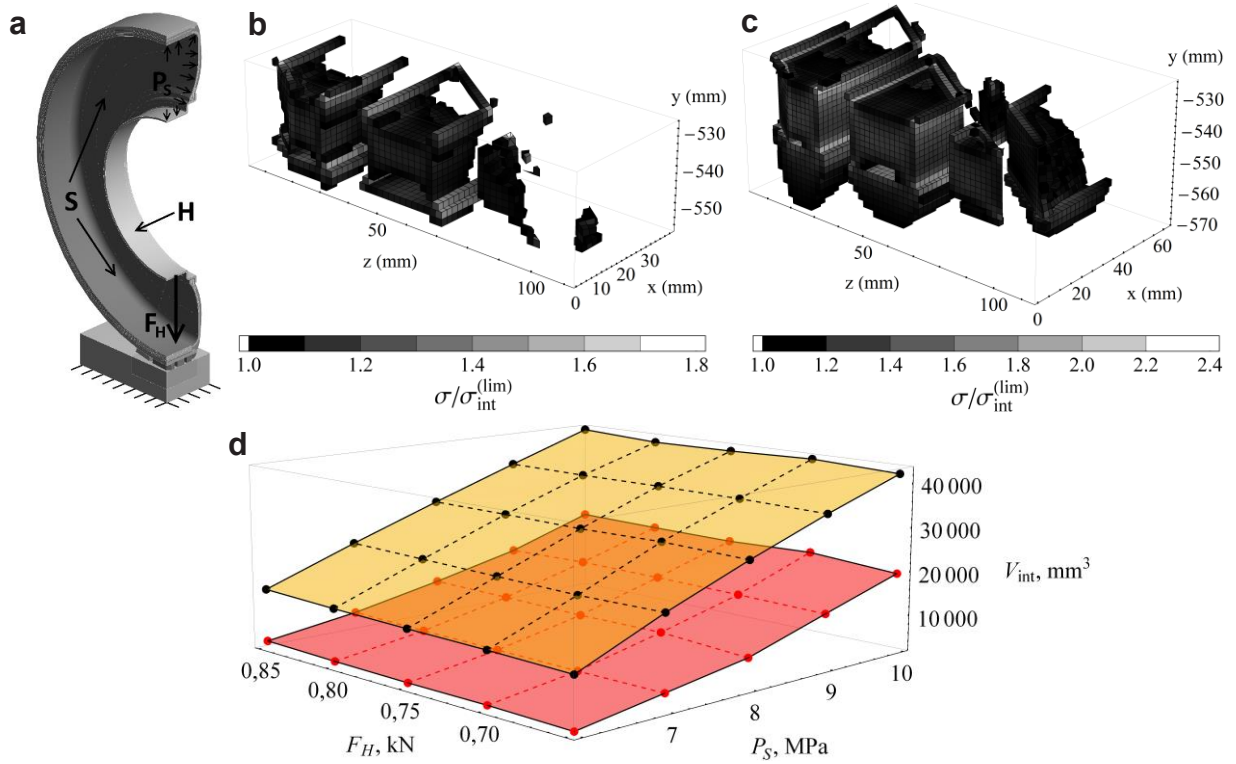

Fig. 1. (a) Model of the system with scheme of loads. (b) Minimum (by P_S = 0.65 MPa, F_H = 6 kN) and (c) maximum (by P_S = 0.85 MPa, F_H = 10 kN) dangerous volume. (d) 3D plot of dangerous volumes values V_{int} by all loads in contact zone: top surface – tire tread; bottom surface – asphalt pavement

Volume damageability by stress intensity ($\sigma_{int}^{(lim)}$ = 0.5 MPa) of tire and asphalt in the contact zone under various loads were calculated (fig. 1-b, 1-c, 1-d). When the radial load on the rim is increased from 6 to 10 kN dangerous volumes in asphalt is also increased 6-7.5 times and in rubber thread increased 2.5-3 times in contact area. If inner pressure is increased from 0.65 to 0.85 MPa than dangerous volumes in tire and asphalt are increased slightly. Minimal value of dangerous volume in asphalt is 2623 mm^3 and in tire is 13883 mm^3 (fig. 1-b). Maximum value of dangerous volume in asphalt is 20722 mm^3 and in tire is 42950 mm^3 (fig. 1-c).

[1] Imad L. Al-Qadi, Hao Wang, Prediction of tire pavement contact stresses and analysis of asphalt pavement responses: a decoupled approach, Journal of the Association of Asphalt Paving Technologists **80**, 289–316 (2011).
[2] S. L. Sokolov, Experimental and computational analysis of stress-strain state of pneumatics in breaker zone under mechanical effects, Journal of Machinery Manufacture and Reliability **40**, 568–572 (2011).
[3] G. V. Gribovskiy, S. S. Sherbakov, Volume damageability of rim–multicomponent tire–asphalt-concrete tribo-fatigue system, International Scientific and Technical Collection Theoretical and Applied Mechanics **32**, 277 – 282 (2017).
[4] G. V. Gribovskii, Three-dimensional stress-strain state and volumetric damageability of tire–asphalt contact pair, 60th scientific conference for young students of physics and natural sciences Open Readings 2017, Vilnius University, 73 (2017).
[5] L. A. Sosnovskiy, TRIBO-FATIGUE: Wear-Fatigue Damage and its Prediction (Springer-Verlag, Berlin, Heidelberg, 2005)

THE IMPACT OF MULDE (WENLOCK: LOWER SILURIAN) MASS EXTINCTION EVENT ON THE ECOLOGICAL DYNAMICS OF OSTRACODES

Simona Rinkevičiūtė[1]

[1]Department of Geology and Minerology, Vilnius University, Lithuania
simona.rinke@gmail.com

The Mulde mass extinction (~428 myr ago) was important geobiological event. Ostracodes - important component of benthic marine communities and allows understanding of the past paleobiological processes [1, 2, 3]. The purpose of this work is to research the impact of the Mulde mass extinction (Lower Silurian) on ostracode ecological dynamics.

In order to achive this goal detailed sampling of the Gėluva-118 core was performed, with later processing of samples, and extraction of ostracod shells. Additionally their taxonomic identification and statistical analyses diversity in the rock samples from Gėluva-118 borehole were accomplished. During this study 58 samples (in 961,5 m - 1041 m depth interval) were taken, which span approximately two million years, - starting from the preextinction phase and the onset of the Mulde biotic event at the beggining of the Gėluva regional stage to the final recovery.

It was determined that immediately after the end of Mulde extinction in concert with a sea levels rise, the increase in abundance of individuals and diversity of taxa began and the maximum ostracode abundance was reached. Statistical analysis shows high abundance of several dominant species, which shows the decrease of complexity of ecosystems in the initial postextinction stage. However, the upper Wenlock is characterized by the decline of dominance and increase in entropy and species evenness. Probably one of the most important factors driving biodiversity and abundance change during this time interval was eustatic sea level change. It should be noted that at the higher sea levels there was higher species richness, and abundanse of their individuals.

[1] Salas M. J., Vannier J., Williams M., 2007. Early Ordovician Ostracods from Argentina: their bearing on the origin of Binodicope and Palaeocope Clades. Journal Paleontology, 81 (6): 1384 – 1395.

[2] Salas M.J., 2011. Early Ordovician (Floian) ostracods from the Cordillera Oriental, Northwest Argentina. Geological Jaurnal, 46: 637 – 650.

[3] Cohen K. M., Finney S.M., Gibbard P.L., and Fan J., 2013. The ICS International Chronostratigraphic Chart. Episodes, 36(3): 199-204.).

DESIGN OF 3-AXIS POSITIONER MECHANICAL DRIVES

Domantas Bartušis[1*], Žilvinas Liaugaudas[1], Andrius Dzedzickis[1], Linas Sinkevičius[1], Vytautas Bučinskas[1], Inga Morkvėnaitė-Vilkončienė[1]

[1] Department of Mechatronic, Robotics, and Digital Manufacturing, Vilnius Gediminas Technical University
domantas.bartusis@vgtu.lt

3-axis positioners are used for objects moving or positioning with high accuracy and can be applied in various fields of applications, for example, machining equipment 3D printers or scanning probe microscopies [1]. For mechanical part of 3D positioning system in scanning probe microscopies, main requirement is positioning accuracy. In similar systems x and y axes have positioning accuracy of 1-3 µm and these two axes are driven by stepper motors. Z axe usually have dual actuators: piezo or electromagnetic for accurate positioning, and stepper motor for coarse positioning and achieves positioning accuracy less than 1 µm [1,2]. Movements of x and y axes are used for scanning point-by-point in the user defined matrix close to surface of interest. The result could be chemical reactivity of the sample (in scanning electrochemical microscope) [1,2], topography (in atomic force microscopy) [3], conductivity (scanning electrochemical impedance microscopy), magnetic properties, etc. The possibility to determine these properties depend on probe's type and on other related equipment. The main problem in this kind of microscopies is positioning of the z-axis. Some of the microscopes can work only in constant-height mode rather than constant-distance. Constant-height mode means that probe is positioned at some distance from surface, and when the probe is moved in x and y axis, z position is constant. Some practical solution of this problem could be controlling of z position by measured signal. However, this method is not accurate and can led to probe crash or surface damage. Also, the goal to determine how the measured signal changes at the same distance from surface, cannot be achieved, since the control system tries to move electrode to the position, where signal is the same – so, the distance is not constant. To work in constant-distance mode, the z axis should be controlled independently on signal from surface of interest, but using another signal for control, for example, shear-force or atomic force microscopy control method. Shear-force method can only be applied when small probes, nanometers in diameter, are used. Two piezo plates are attached to the body of the probe. One piezo plate excites nanoneedle at the frequency, close to resonance, and another plate will measure the response frequency. Atomic force microscopy positioning is based on cantilever's deflection, detected by optical system. The problem in this system is that the fabrication of nano diameter probe is difficult. Therefore, the positioning control systems are based on well-known mechanical principles, and should be designed by mechanical engineers.

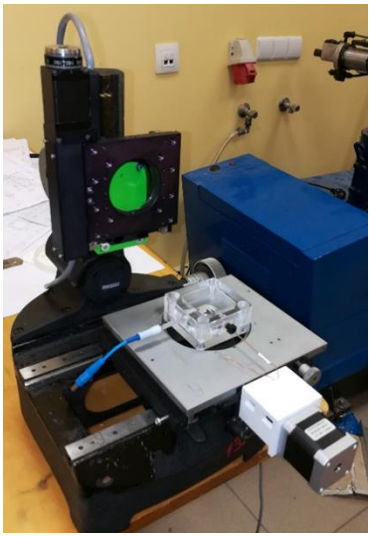

Fig. 1. 3-axis positioner.

The designed 3-axis positioner should meet three requirements: speed, accuracy, and force. The most important parameter is accuracy, when positioner is devoted to positioning of scanning probe. The chosen stepper motors with precise ball screw drives and suitable control system could achieve positioning accuracy of 2.5 µm in x and y axes. It is enough for scanning of biological objects, since it is possible to form a spot with 50 µm diameter and probe (for example, microelectrode) is of 5-10 µm diameter. Chosen drive system, stepper motor and ballscrew are more reliable, less expensive and easy applicable to different needs in comparison with piezo drives or linear motors.

[1] I. Morkvenaite-Vilkonciene, A. Ramanaviciene, and A. Ramanavicius. Sens. Actuat. B, 228 (2016) 200-206.
[2] A. Ramanavicius, I. Morkvenaite-Vilkonciene, A. Kisieliute, J. Petroniene, A. Ramanaviciene. Coll. Surf. B., 149 (2017) 1-6.
[3] I. Morkvenaite-Vilkonciene, A. Ramanavicius, and A. Ramanaviciene. Medicina, 49 (2013). 155-164.

DEGENERATE ANISOTROPY IN HOMOGENEOUS MEDIA: POLAR DECOMPOSITION APPROACH

Roman Kurylenko, Ivan Kolomiets, Sergey Savenkov, Yevgen Oberemok, Alexander Klimov

Faculty of Radio Physics, Electronics and Computer Systems, Taras Shevchenko National University of Kyiv,
64/13, Volodymyrska Str., Kyiv, Ukraine, 01601
romanyson@gmail.com

An important characteristic of any anisotropic medium is its eigenwaves. The main properties of the eigenwaves that are considered in polarimetry are the eigenvalues $V_{e1,2}$ and eigenpolarizations $\chi_{e1,2}$ [1]. To describe the polarization properties of media with a complex anisotropy in polarimetry the Jones and Mueller matrix methods are widely used.

In terms of these matrix methods, there are a number of approaches that allow describing the anisotropy of the medium. The most commonly used method is based on polar decomposition theorem [2]. The essence of this method is that the Jones (Muller) matrix of an arbitrary anisotropic medium can be represented as a product $\mathbf{T}=\mathbf{T}_D\mathbf{T}_R=\mathbf{T}_R\mathbf{T}_D^{/}$. Where Jones matrix $\mathbf{T}_R\left(R,a_1.a_2,a_3\right)$ is unitary polar form which describe the phase anisotropy, R - retardation parameters, a_i - parameters of linear and circular phase anisotropy, and Jones matrices $\mathbf{T}_D\left(D,d_1.d_2,d_3\right)$ or $\mathbf{T}_D^{/}$ describes the amplitude anisotropy, D - diattenuation parameter, d_i parameters of linear and circular amplitude anisotropy. In general case the matrix $\mathbf{T}_R$ and $\mathbf{T}_D$ are not commute, as a result the products $\mathbf{T}_D\mathbf{T}_R$ and $\mathbf{T}_R\mathbf{T}_D^{/}$ (left and right polar forms, respectively) are physically non-equivalent.

One of the interesting case of complex anisotropy is the degenerate anisotropy. This is the case when the eigenvalues and the eigenpolarizations coincide, i.e., $V_{e1}=V_{e2}$ and $\chi_{e1}=\chi_{e2}$, and actually one eigenwave with a certain polarization propagates in the medium [1]. An analysis of degenerate anisotropy features in the terms of methods basing on the generalized equivalence theorem and the differential Jones matrix was made in [1], [2]. In this paper, we investigate the degenerate anisotropy in terms of the polar decomposition. To realize the degenerate anisotropy in a medium their Jones matrix $\mathbf{T}$ must satisfy some conditions [1]. Using these conditions for the right and left polar forms, we obtained the following relation, which has to be fulfilled for an arbitrary homogeneous medium is characterized by the degenerate anisotropy:

$$\left(2C_1C_3+2iC_2C_4\left(R_HD_H+R_{45}D_{45}+R_CD_C\right)\right)^2-4\left(C_1^2+C_2^2R^2\right)\left(C_3^2-C_4^2D^2\right)=0 \qquad (1)$$

where

$$C_1=\cos\left(\frac{R}{2}\right),\ C_2=\frac{\sin\left(\frac{R}{2}\right)}{R},\ C_3=\cosh\left(\frac{\alpha}{2}\right),C_4=\frac{\sinh\left(\frac{\alpha}{2}\right)}{D},\ \alpha=\operatorname{arctanh}\left(D\right) \qquad (2)$$

It can be shown that these conditions are the same for the right and left polar forms.
In this case, the eigenvalues could be written in the following form:

$$V_{e1}=V_{e2}=C_1C_3+iC_2C_4\left(R_HD_H+R_{45}D_{45}+R_CD_C\right) \qquad (3)$$

As it can be seen, the eigenvalues are also the same for the right and left polar forms.
At the same time the singularity conditions Eqs. (1) and (2) give the different eigenpolarizations for different polar forms:

for rigth polar form

$$\chi_{e1}=\chi_{e2}=\frac{C_2C_3R_H-iC_4\left(C_1D_H-C_2D_CR_{45}+C_2D_{45}R_C\right)}{C_1C_4\left(D_C+iD_{45}\right)-C_2\left(C_3-C_4D_H\right)\left(R_{45}-iR_C\right)-C_2C_4R_H\left(D_{45}-iD_C\right)} \qquad (4)$$

for left polar form

$$\chi_{e1}=\chi_{e2}=\frac{C_2C_3R_H-iC_4\left(C_1D_H+C_2D_CR_{45}-C_2D_{45}R_C\right)}{C_1C_4\left(D_C+iD_{45}\right)-C_2\left(C_3+C_4D_H\right)\left(R_{45}-iR_C\right)+C_2C_4R_H\left(D_{45}-iD_C\right)} \qquad (5)$$

In general case, both of the eigenpolarizations Eq. (4) and Eq. (5) are elliptical.

[1] S.N. Savenkov, O.I. Sydoruk, R.S. Muttiah, Eigenanalysis of dichroic, birefringent, and degenerate polarization elements: a Jones-calculus study, App. Opt. **46** No.27, 6700-6709 (2007).
[2] S.Y. Lu, R.A. Chipman, Interpretation of Mueller matrices based on polar decomposition, J. Opt. Soc. Am. A. **13**, 1006-1113 (1996).
[3] I.S. Kolomiets, S.N. Savenkov, Ye.A. Oberemo, Condition for homogeneous anisotropic medium to be characterized by degenerate anisotropy, XII International Young Scientists' Conference On Applied Physics, Kyiv, Ukraine, 14-16 (2012).

POLARIZATION BISTABILITY IN VERTICAL CAVITY SURFACE-EMITTING LASERS

Labatsevich Pavel

[1]Department of Physics, Belarusian State University, Belarus
pavel.lobatsevich@mail.ru

The polarization bistability is essential feature of vertical cavity surface-emitting lasers (VCSEL). It is generally associated with the gain dichroism for two orthogonal polarization modes. But within the framework of our earlier proposed approach to the description of VCSEL polarization [1,2], such mechanism can not be realized in principle, because such modes are not defined. According of our approach the polarization bistability is a result what the duration of polarization evolution is much longer when the intensity evolution one. This effect can be really observed in the polarization instability area, where the duration of polarization evolution becomes significantly longer than the photon lifetime.

The theoretical model, proposed in [2], was used as the based model for bistability investgations. Triangular impulses with linear increase and decrease of current injections were imployed to the laser in order to specific features of polarization bistability. In the modelling both impulse duration and parameters of laser system were varied. The results of numerical calculation can be formulated in the next form.

The influence of process dynamics is shown explicitly by increasing a current rate. An increase in the current rate leads to the expansion of hysteresis regime. It is connected to the fact that at a high speed of current change there is a shift of the polarization switching point to the area of larger currents. And a decrease causes a similar shift to the area of lower currents. However, at a sufficiently high speed of current increase (the reference time is comparable to a photon lifetime in the resonator) there is an essential distortion of a hysteresis curve that compares qualitatively to the results of the paper [3].

The photon lifetime is the essential parameter that affects the formation processes of output radiation polarization in VCSEL. A numerical simulation of polarizable bistability formation process was carried out at a variation of a cavity mirrors reflectivity. Hysteresis curve expanding occurs during increasing the mirror reflectivity that corresponds to the increase in a photon lifetime. At the same time a natural shift of threshold current occurs simultaneously.

The shift of polarization switching point to the area of great current values allows to reduce the level of hysteresis curve distortion at high speeds of current increase, but at the same time, there is a further expansion of a hysteresis curve.

It is also necessary to note that the changing current lifetime affects only threshold current value, and has no practical effect on the character of the polarization hysteresis curve.

Thus, the received results confirm the dynamic nature of polarizable bistability. However, this phenomenon demands a more detailed and comprehensive investigation. What will serve as a task for the subsequent researches.

---

[1] M. Jadan, L.I.Burov, A.S.Gorbatsevich, E.S.Sokolov, Polarization switching in single-mode injection semiconductor laser, Journal of Applied Spectroscopy 76, 717-724 (2009).
[2] L.I.Burov, A.S.Gorbatsevich, P.M.Lobatsevich, Gain dichroism in VCSEL, Journal of BSU, Ser.1, N3, 63-70 (2016)
[3] J.Paul, C.Masoller, P.Mandel, Y.Hong, P.S.Spencer, K.A.Shore, Experimental and theoretical study of dynamical hysteresis and scaling laws in the polarization switching of vertical-cavity surface-emitting lasers, Phys. Rew. A 77,043803 (2008)

INVESTIGATION OF POROUS ANISOTROPIC THIN FILMS FOR ZERO ANGLE POLARIZERS

Lukas Ramalis[1,2], Lina Grinevičiūtė[1], Rytis Buzelis[1] and Tomas Tolenis[1]

[1] State Research Institute Center for Physical Sciences and Technology, Savanorių ave. 231, LT-02300, Vilnius, Lithuania

[2] Department of Physics, Kaunas University of Technology, Studentų St. 50, LT-51368, Kaunas, Lithuania, lukas.ramalis@gmail.com

One of the most used optical elements in laser systems is a polarizer, which main purpose is the separation of light polarizations or controlling the intensity of laser radiation. Regardless of the importance of this element in laser systems, ordinary polarizers have various disadvantages: Brewster angle type polarizers cause deviations of light beam, which requires an additional system calibration, various liquid crystal polarizers have a very small damage threshold or some microsystems require unique solutions.

Solution was developed using anisotropic layers with a columnar structure to form a 0° angle polarizer. Glancing angle deposition method is used to obtain these structures. Anisotropy in these coatings can be obtained by manipulating the position of the substrate during the process. However, in order to form a polarizer, it is necessary first to find out the characteristics of single-layer coatings. In this work, columnar structures of tantalum oxide evaporated on fused quartz glass were investigated.

The evaporation process was performed in a vacuum chamber using physical vapor deposition technique. Nanostructure of thin film was controlled by changing the angle between the substrate and the vapor flux. Material was deposited on the substrate, turned at specific angle with respect to vapor flux [1]. These atoms form shadow areas where following atoms can no longer directly deposit or diffuse due to their low energy. This creates a nano-structural coating, where size and shape of columns depends on the evaporation parameters [2]. There is a wide range of applications for this technology, such as phase plates, antireflection coatings, sensors etc. Varying the inner structure of individual layers in a multilayer coating also allows to form a high reflection mirror, whereas position in the spectral band differs by different polarizations.

These studies have been done to test how laser induced damage threshold depends on thin film band gap and porosity [3]. It is known that after coating formation with columnar structures, voids are also formed. Such layer may absorb heavier particles such as water from environment, which might affect band gap of thin films. In addition, porosity has a significant impact on laser-induced damage threshold [4]. As we can see from Figure 1, porosity increases with an increase of angle of evaporation. Moreover, this figure clearly shows that the porosity in shadowing direction (S pol.) always maintain larger. Thus, the effect of laser induced damage threshold value on porosity and band gap width was investigated. When the linearly polarized light falls perpendicularly to the surface, optical anisotropy is observed in the direction of the shading of the atoms, where the refractive index in S polarization is lower compared with its perpendicular direction P polarization.

After analyzing results, research studies show that due to the highest refractive index differences, the maximum phase delay in the coating has been achieved at an angle of 70°. That makes this angle most suitable to form a polarizer for 0° of incidence. By combining nanostructured and dense isotropic layers, an optical element with a double Bragg's mirror region can be formed, making these thin films suitable for high-power laser applications.

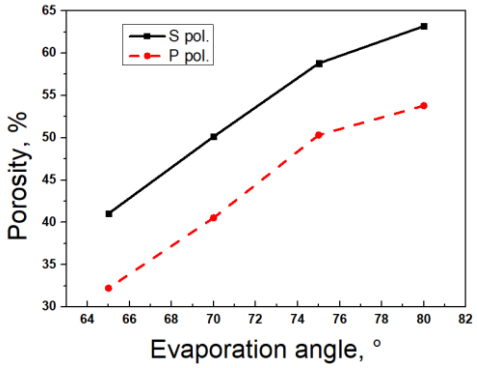

Fig. 1. Dependence of the tantalum oxide porosity on the evaporation angle for S and P polarizations.

[1] K. M. A. Sobahan, Y. J. Park et al., *Effect of Deposition Angle on the Optical and the Structural Properties of Ta2O5 Thin Films Fabricated by Using Glancing Angle Deposition*. Journal of the Korean Physical Society. Vol. 55, No. 3, pp. 12721277, September 2009.

[2] A. Lakhtakia ir R. Messier, Sculptured thin films: nanoengineered morphology and optics. Bellingham, Wash: SPIE Press, 2005

[3] T. Tolenis, M. Gaspariūnas et al., *Assessment of effective-medium theories of ion-beam sputtered Nb_2O_5-SiO_2 and ZrO_2- SiO_2 mixtures*. Lithuanian Journal of Physics, Vol. **54**, No. 2, pp. 99–105 (2014).

[4] H. Shahrokhabadi, M. Vaezzadeh et al., *Band gap energy and refractive index dependence of femtosecond laser induced damage threshold in dielectric thin films*. Elsevier, Thin Solid Films 636, 289–295 (2017).

BESSEL ZONE PLATE DESIGN FOR TERAHERTZ IMAGING

Domas Jokubauskis, Linas Minkevičius, Mindaugas Karaliūnas, Sergejus Orlovas, Gintaras Valušis

Department of Optoelectronics, Center for Physical Sciences and Technology, Lithuania
domas.jokubauskis@ftmc.lt

Terahertz (THz) waves are electromagnetic waves in the frequency range between 0.1 THz and 10 THz. Terahertz radiation is being actively researched for imaging applications in security [1], medical [2] and quality control [3]. Currently, X-ray radiation is used mainly for screening purposes, but because of ionizing nature it is harmful for human beings. For more challenging applications such as detection of low density materials (clothing, plastics, etc.) novel solutions are required. THz radiation, which can penetrate common non-conducting materials can be an optimal solution.

In this work, we present a design THz focusing Bessel zone plate with dimensions of 20 mm x 20 mm x 0.5 mm (WxHxD) fabricated from silicon. It intends to resolve a problem of focusing THz beam into desired areas when the sample is thick.

Bessel zone plate design was calculated to use with 0.6 THz source in transmission geometry. Designed zone plate was simulated employing three-dimensional finite-difference time-domain (3D FDTD) modeling method. The Bessel zone plate produces 10 mm depth of field can be suited for compact solutions in security-oriented THz imaging systems.

---

[1] O. E. Wetter, "Imaging in airport security: Past, present, future, and the link to forensic and clinical radiology," J. Forensic Radiol. Imaging **1**, 152–160 (2013).

[2] X. Yang, X. Zhao, K. Yang, Y. Liu, Y. Liu, W. Fu, and Y. Luo, "Biomedical Applications of Terahertz Spectroscopy and Imaging," Trends Biotechnol. **34**, 810–824 (2016).

[3] F. Destic and C. Bouvet, "Impact damages detection on composite materials by THz imaging," Case Stud. Nondestruct. Test. Eval. **6**, 53–62 (2016).

ULTRASHORT LOW-ENERGY LASER HEATING WITH DONUT-SHAPED PULSES

Yaraslau Okrut[1], Yana Tsitavets [2]

[1] Belarusian State University, Physics Faculty
io.shay@bk.ru

High energy density and coherence of the radiation determined the wide usage of lasers in modern science and industry. Material treatment is considered as one of the main application fields of lasers. In most cases it is based on the heating effect caused by laser beam. To improve the efficiency of these processing types, it is necessary to improve the methods of the temperature field control [1]. The heat transfer simulations are the one of the most useful tools for the study of transient heat conduction for laser-matter interaction problems.

The important property of the laser beam is the shape of pulse (both spatial and temporal). The switch of pulse spatial shape from standard gaussian to the tubular (vortex, Bessel, etc.) will lead to the observable changes in the dynamics of heat generation inside the irradiated sample. The exact knowledge of the pulse spatial shape influence on the temperature field spreading will open up a new class of possibilities: for processing and synthesizing materials [3] in case of high-intensity radiation and for generation of lattice vibrations for the laser acoustics and acoustoplasmonics applications.

We've implemented two versions of 2-temperature model for heating with femtosecond laser pulses (1),(2) with finite-elements commercial software and hand-written finite-difference code.

$$C_e \rho_e \frac{\partial T_e}{\partial t} = \lambda_{T_e} \triangle T_e + Q_s - \gamma (T_e - T_i) \tag{1}$$

$$C_i \rho_i \frac{\partial T_i}{\partial t} = \lambda_{T_i} \triangle T_i + \gamma (T_e - T_i) \tag{2}$$

Here ρ - density, C - heat capasity, T - temperature. The index "e" relates to the electronic subsystem, the index "i" – to the ionic subsystem, parameter γ determines the rate of energy relaxation from electrons to crystalline lattice. The heat source Q_s law is determined by the laser pulse shape [2].

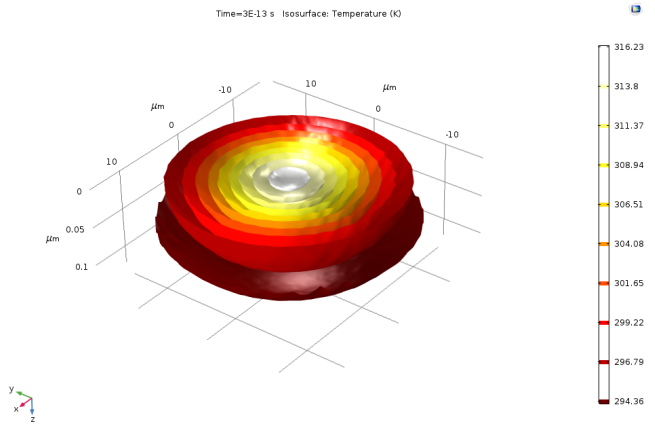

Fig. 1. Isothermal surfaces of electronic temperature T_e (Gauss-shaped pulse)

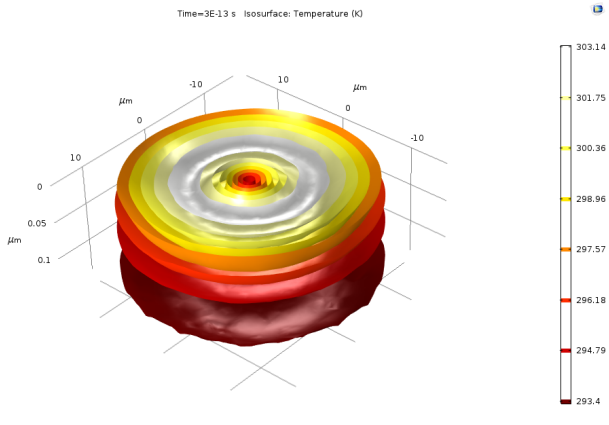

Fig. 2. Isothermal surfaces of electronic temperature T_e (donut-shaped pulse)

It was established that heat energy deposited by donut-shaped pulse does not spread inside the volume directly below the symmetry center of incident pulse for the time $\gtrsim 10\ \tau_p$ (τ_p is the pulse timelength). Examples of isothermal surfaces at time $10\tau_p$ for gaussian and donut pulses are given in Figs. 1 and 2, respectively. Therefore, the presence of non-heated region under the beam center allows a precise preservation of nano-sized areas from the thermal effects during the laser treatment.

[1] O.G. Romanov, G.S. Romanov. Thermomechanical effect of ultrashort laser pulses on single-dimension metallic nanostructures // Bulletin of the Russian Academy of Sciences: Physics, 2014 V. 78, Number 12. P.12991302.

[2] O.I. Baum, G.I. Zheltov, A.I. Omelchenko, G.S. Romanov, O.G. Romanov, E.N. Sobol. Thermomechanical effect of pulse-periodic laser radiation on cartilaginous and eye tissues // Laser Physics, 2013. V.23. 085602 (10pp).

[3] Simulation of Polycrystalline Bismuth Films Transport Properties Based on Experimental Texture Identification / A.S. Fedotov, V. Shepelevich, S. Poznyak, L. Tsybulskaya, A. Mazanik, I. Svito, S. Gusakova, P. Zukowski, T. N. Koltunowicz // Materials of Chemistry and Physics (IF2014=2.259) 2016.

INFLUENCE OF DISPERSION TERMS ON SINGLY RESONANT SYNCHRONOUSLY PUMPED OPTICAL PARAMETRIC OSCILLATOR: THEORETICAL INVESTIGATION

Adomas Gasperaitis[1], Viktorija Tamuliene [1]

[1]Laser Research Center, Vilnius University, Lithuania
adasius@gmail.com

In Ph.D. thesis of K. Ivanauskiene [1], the influence of the dispersion terms on the singly resonant nondegenerate synchronously pumped optical parametric oscillator (SOPO) was investigated experimentally. Adjusting the group velocity dispersion (GVD) coefficient oscillating as well as chaotic behaviour of the spectral components could be observed. Our goal here is to simulate the SOPO numerically and to find the conditions for the oscillating and non-oscillating regimes.

In Ref. [2], the formation of solitons in singly resonant SOPOs was described by the modified complex Ginzburg-Landau equation. This equation was studied in many fields of physics [3] and its solution is called a dissipative soliton. Our study shows that the behaviour of the numerical solutions of the nonlinear coupling equations describing the SOPO are similar to the one of the dissipative solitons. One can obtain oscillating regime. The spectra with one and two maxima were obtained as well. The GVD coefficient as well as the timing mismatch of the resonator were varied and different regimes were obtained. The typical oscillating regime is presented in Fig. 1.

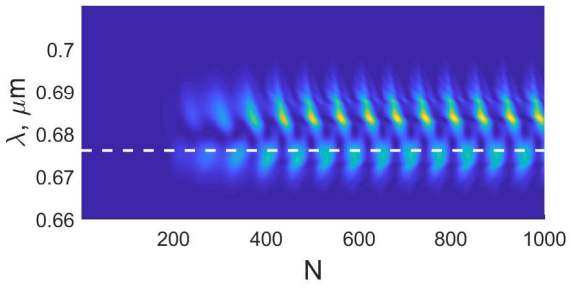

Fig. 1. Dependence of spectral profile on the round-trip number. White dashed line - theoretical wavelength.

When the time mismatch is negative, the spectrum maximum is shifted to the frequency which was found theoretically. It is depicted by the white dashed line in Fig. 1.

The influence of the Kerr nonlinear term was studied, too.

[1] K. Ivanauskiene, Rezonatoriaus komponentu grupinio velinimo dispersijos itaka sinchronikai femtosekundiniais impulsais kaupinamam parametriniam viesos generatoriui, Ph.D. thesis, Vilniaus universitetas, Fiziniu ir technologijos mokslu centras (2017).

[2] P.-S. Jian, W. E. Torruellas, M. Haelterman, S. Trillo, U. Peschel, F. Lederer, Solitons of singly resonant optical parametric oscillators, Opt. Lett. **24**, 400-402 (1999).

[3] N. Akhmediev, A. Ankiewicz, *Dissipative Solitons* (Springer, Berlin, 2005).

How to predict the future of optics?

Robertas Grigutis[1], Andrius Melninkaitis[1]

[1] Laser Research Center, Vilnius University, Lithuania
robertas.grigutis@ff.stud.vu.lt

Optical components used in high power laser systems could be irreversibly damaged due to so-called laser induced damage phenomena. Determining the lifetime of optics is greatly important for applicational purposes. Laser induced damage testing could be a solution to describe the degradation of materials after relatively short periods of time (seconds, minutes, hours), however, this approach might not reflect the real-life situations as the optical elements could be used for many days after being damaged. The aim of this work was to find the mathematical models which best describe femtosecond laser induced damage in single-layer thin-film dielectric optical coatings (Al_2O_3, TiO_2, Ta_2O_5, HfO_2, ZrO_2, Nb_2O_5, SiO_2) and fused silica substrate. The destructive S-on-1 measurements were performed on the samples and then the inspection under Nomarski interference contrast microscope was carried out. The calculated so-called laser survivability curves were fitted with empirical and theoretical models using least square fitting approach. Lastly, fitted curves were extrapolated up to 10^{15} laser pulses. The obtained results from the inspection show that the damages of all tested samples could be classified into two categories: color and catastrophic damage modes, which have different degradation behavior. For the catastrophic damage mode the behavior is more probabilistic, but for the color damage mode - deterministic. Also, the catastrophic mode survivability curves of TiO_2, Ta_2O_5, HfO_2, ZrO_2, Nb_2O_5 and fused silica substrate reach saturation, while color mode survivability curves – continues to decrease. Catastrophic damage mode is best described by type I and II models, when color damage mode – by type III models. We also show that the optical coating process could change the structure of material from the structure of its bulk state. Moreover, we discuss that fitting and extrapolating the material's survivability curve which is determined by both catastrophic and color damage mechanisms with a single model could be misleading. Finally, our results demonstrate that there is no single model that could universally describe catastrophic or color damage mode.

EXPERIMENTAL REALIZATION OF FOCAL LINE WITH CONTROLLED LONGITUDINAL INTENSITY PROFILE

Ernestas Nacius, Sergejus Orlovas, Alfonsas Juršėnas
Center for Physical Sciences and Technology, Industrial Laboratory for Photonic Technologies,
Saulėtekio av. 3, Vilnius, Lithuania.
ernestas.nacius@ftmc.lt

Ideal Bessel beams belong to a family of optical fields with propagation-invariant transverse intensity distribution (also called non-diffracting beams) [1]. The experimental approximation of these beams exhibits long axial intensity line which is useful for many practical applications e.g. microfabrication [2], particle manipulation [3] etc. Such laser beams with high length to width ratio and flat top are called optical needles. One can choose a complex amplitude for each Bessel beam such that the superposition of these beams obeys any chosen axial longitudinal intensity distribution [4]. Furthermore, usage of vector beams, enables one to control also the polarization and transverse localization. As an exotic example can be longitudinally polarized optical needle [5].

First we define a specific longitudinal intensity pattern and compute the corresponding spatial spectra. Then in order to obtain desired beam shape the complex spectral mask is encoded to phase-only mask and displayed on SLM. We investigate the quality of generated optical needle beams by comparing it to the numerical simulation results. We also analyse the limitations of our experimental setup. An example of modeled three beam longitudinal profiles using superposition of zero-order Bessel beams are shown in Fig. 1.

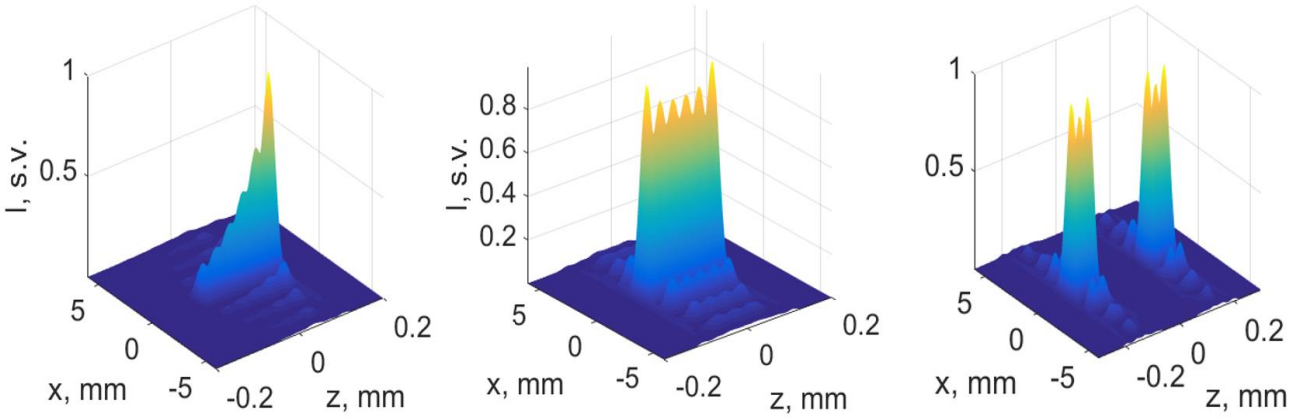

Fig. 1. Examples of modeled longitudinal beam profiles.

[1] J. Durnin, Exact solutions for nondiffracting beams. I. The scalar theory, Journal of the Optical Society of America A **4**, 651 (1987).
[2] M. Duocastella, B. A. Craig, Bessel and annular beams for materials processing, Laser & Photonics Reviews **6**, 607-621 (2012).
[3] R. Yang, L. Renxian, Optical force exerted on a Rayleigh particle by a vector arbitrary-order Bessel beam, Journal of Quantitative Spectroscopy and Radiative Transfer **178**, 230-243 (2016).
[4] M. Zamboni-Rached, Stationary optical wave fields with arbitrary longitudinal shape by superposing equal frequency Bessel beams: Frozen Waves, Optics Express **12**, 4001-4006 (2004).
[5] H. Wang, L. Shi, B. Lukyanchuk, C. Sheppard, C. T. Chong, Creation of a needle of longitudinally polarized light in vacuum using binary optics, Nature Photonics, ***2***, 501 (2008).

EXPERIMENTAL IMPLEMENTATION OF THE FOCAL LINE ENGINEERING WITH WEBER BEAMS USING SPATIAL LIGHT MODULATOR

Justas Baltrukonis[1], Sergej Orlov[1], Pavel Gotovski[1]

[1] Center of Physical Sciences and Technology, Industrial Laboratory for Photonic Technologies, Lithuania
justas.baltrukonis@ftmc.lt

New applications of laser micromachining are emerging from scientific research and industrial needs, for example, faster and more precise cutting of glasses and other transparent materials or even more exotic field like a production of metasurfaces [1]. All this empowers the search for new ways to improve the industrial process of laser microprocessing.

An increasing number of applications for laser beams with a long focal line, also known as Bessel-Gaussian beams [2], can be easily noticed. Due to their elongated profile they can be perceived as ”optical needles” being one of the most prominent member of nondiffracting beams. Another example of the nondiffrating beams is so-called Weber beams [3] that possess parabolic distribution of an electric field in transverse plane. These beams have parabolicity parameter, which provides additional degree of freedom and allows us to control transverse profile - change angle between parabola branches. Furthermore, there is a need within the laser industry not only to change the transverse profile of an optical needle but also to control (engineer) its axial distribution, which is done by superposing many scalar Weber beams [4].

In this work we generate even, odd and traveling Weber beams with initially defined axial intensity profile using phase-only spatial light modulator. We compare experimental results with numerical calculations and analyze the properties of obtained beams. Intensity distribution of Weber beam with axial intensity profile, described as ”two steps”, is shown in Fig 1 (a,b).

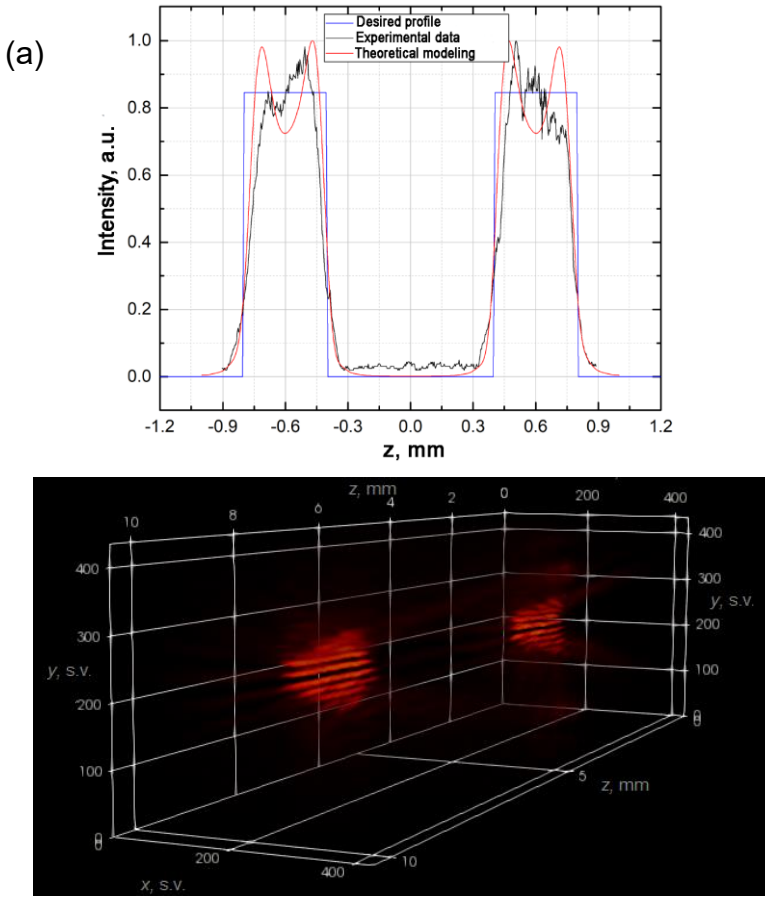

Fig. 1. (a) theoretically modeled and (b) measured three-dimensional distribution of intensity of Weber beam with axial intensity profile described as ”two steps”.

[1] C. Hou-Tong, A. J. Taylor, N. Yu, A review of metasurfaces: physics and applications, Reports on Progress in Physics 79(7) (2016).
[2] J. Durnin, J. Miceli Jr, J. Eberly, Diffraction-free beams, Physical review letters 58(15),1499 (1987).
[3] M. A. Bandres, J. C. Gutirrez-Vega, S. Chavez-Cerda, Parabolic nondiffracting optical wave fields, Optics letters 29(1), 4446 (2004).
[4] M. Zamboni-Rached, E. Recami, H. E. Hernandez-Figueroa, Theory of frozen waves: modeling the shape of stationary wave fields, Journal of the Optical Society of America 22(11), 2465-2475 (2005).

RESEARCH ON LASER–PREFORMED PLASMA INDUCED EFFECTS ON THZ RADIATION GENERATION IN AIR BY BICHROMATIC LASER PULSES

Danas Buožius, Žilvinas Svirskas, Karolis Adomavičius, Maksym Ivanov

Vilnius University Laser Research Center, Saulėtekio Ave. 10, LT-10223 Vilnius, Lithuania
Danas.Buozius@ff.stud.vu.lt

Terahertz (THz) radiation represents the region in the electromagnetic spectrum between far-infrared and microwave radiation and has frequency between 0.1 THz and 10 THz (wavelength varies from 3 mm to 0.03 mm).

As a pump source the Ti:Sapphire laser system (central wavelength about 790 nm) operating at 1 kHz and delivering 9 mJ pulses of 35 fs (FWHM) duration was used. THz radiation and prepulse were generated in ambient air with energies of 5.2 and 1.65 mJ respectively. In the experiment THz radiation was generated by mixing laser and its second harmonic pulses (bichromatic pump [1]) and prepulse was generated using fundamental harmonic only. The prepulse was propagated and focused in the orthogonal direction with respect to the main beam to generate a plasma filament that intercepted the main beam path.

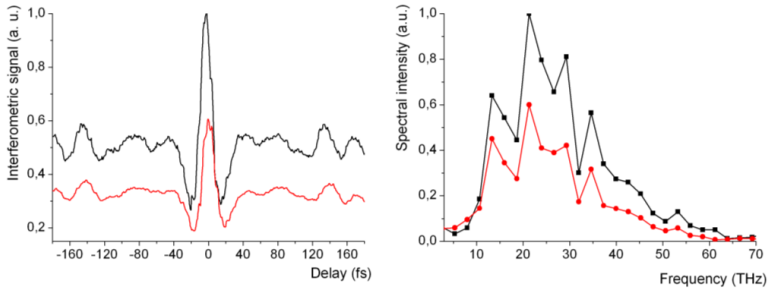

Fig. 1 Interference traces (left) and corresponding THz spectra (right) of generated radiation with (red lines) and without preplasma (black lines). Preplasma filament was created by a 10 cm focal length lens and was located in the focal plane of the pump beam. Energies of the pump and preplasma pulses were 5.2 and 1.65 mJ, respectively.

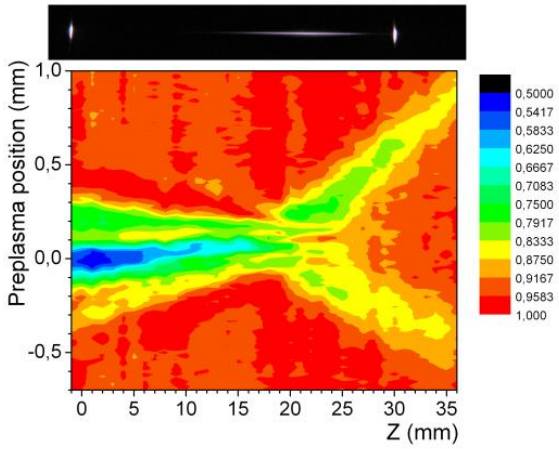

Fig. 2. Dependence of the THz power on the position of the preplasma in respect to the main beam axis and relative distance along the *z* coordinate axis. For the clarity the main plasma filament (seen there as a long string) and preplasma (seen as light points at both ends) at the two exemplary positions of z=-1 mm and z=30 mm are shown above.

The THz signal significantly decreases when the precreated plasma is present in the path of the pump beam. In addition, the dependence of THz attenuation on the mutual position of two plasma filaments have been observed (Fig. 2). Obtained results of preplasma interaction with THz generating filament could be explained by at least two different mechanisms: pump beam diffraction and THz radiation screening induced by preplasma filament [2].

[1] V. Pyragaitė, V. Smilgevičius, K. Steponkevičius, B. Makauskas, and V. Vaičaitis, "Phase shifts in terahertz wave generation by tightly focused bichromatic laser pulses," JOSA B **31**(7) 1430–1435 (2014).
[2] J. Zhao, Zhang, T. Wu, C. Zhang, Y. Zhao, "Terahertz wave absorption via preformed air plasma," Opt. Commun. **380**, 87-90 (2016).

PHASE AND POLARIZATION SINGULARITIES OF VECTOR VORTEX BEAM

Greta Krivickaitė, Aidas Matijošius, Valerijus Smilgevičius, Maksym Ivanov

Vilnius University Laser Research Center, Faculty of Physics, Vilnius University, Lithuania
greta.krivickaite@ff.stud.vu.lt

Light wave with screw dislocation of wave front is referred to as optical vortex. Along the dislocation line in space, the intensity of light is zero and the phase ϕ is undefined (singular). Therefore, a beam that carries an optical vortex has a dark core along the dislocation line in space and its wavefront around the core has a helical form with the complex amplitude proportional to $\exp(il\phi)$, where l – topological charge. Due to special intensity and phase distribution, optical orbital angular momentum (OAM) of $l\hbar$ per photon ($\hbar$ is the reduced Planck constant) rises in the light fields carrying optical vortices. Presence of OAM and "doughnut"-shaped intensity distribution made optical vortices useful in various areas: optical communication, trapping and manipulation and astronomy just to name a few [1].

Besides phase singularity, light beam could carry polarization singularities when orientation of major axis of polarization ellipse is undefined. Radially and azimuthally polarized beams are examples of such polarization singularities with topological index $m = 1$. As it was shown [2], phase front of radially polarized beam also azimuthally modulated. Therefore, question arise, what would be the structure of phase front of a beam carrying both phase and polarization singularities? Note that unlike phase singularity, polarization singularity does not necessary coincide with position of zero intensity.

In this work we track position of singularity upon change of polarization state of a beam. Interferometric methods are, usually, used to detect presence of phase singularities in light fields. Interferogram of optical vortex with a plane wave has a characteristic bifurcation of interference lines ("forked" pattern) centered at the dislocation position. We used a scheme based on a Mach – Zehnder interferometer to detect positions of phase singularities. One arm of interferometer has S-waveplate and quarter wave plate working in tandem. Depending on incoming polarization, S-waveplate generate radially, azimuthally, spirally, circularly or elliptically polarized light. Depending on polarization distribution of generated light beam, position of dislocation appears to be in different places, as shown in fig. 1, b), d). When final polarization state changes from azimuthal through elliptical to circular (fig. 1, c), d)) positions of bifurcation concentrated along Y axes. When final polarization state changes from radial through spiral to azimuthal (fig. 1, a), b)) positions of bifurcation distributed all over the beam, including areas of maximum intensity.

We hypothesize that singularity point localized at the dark core of the vector vortex beam result in ordinary helical wave front of a beam with symmetrically azimuthally distributed orbital angular momentum. However, singularity located at the bright area of the vector beam could result in asymmetric distribution of orbital angular momentum of a cylindrical beam and require further investigation.

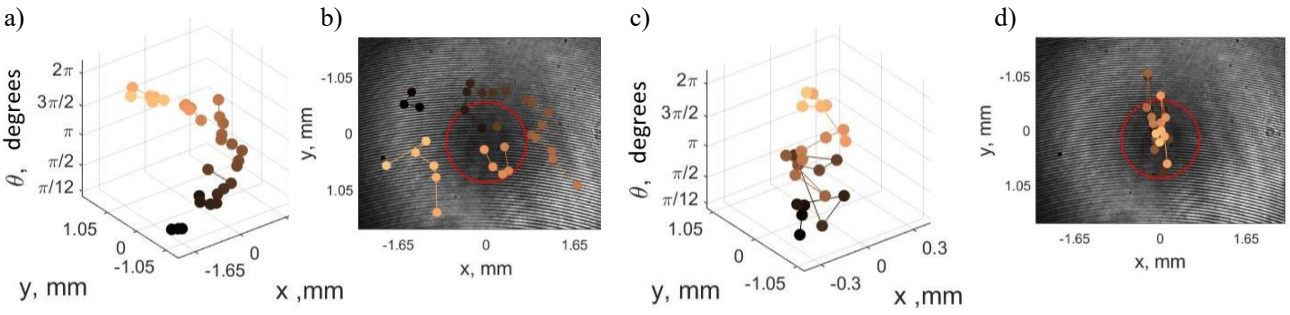

Fig. 1. b), d): Position of singularity point over intensity distribution of the beam. Red circle indicates central (dark) part of the "doughnut". a), c): three-dimensional trajectory of singularity position. a), b): θ is angle of orientation of S-waveplate with respect to incoming vertically (Y-) polarized beam. Final polarization state changes from radial through spiral to azimuthal. c), d): θ is angle of orientation of quarter wave plate with respect to incoming vertically (Y-) polarized beam. Final polarization state changes from azimuthal through elliptical to circular.

[1] Gregory J. Gbur, Singular Optics (Taylor & Francis Group, LLC, 2017).
[2] Q. Zhan, J. R. Leger, Interferometric measurement of the geometric phase in space-variant polarization manipulations, Optics Comm. 213, 241-245 (2002). https://doi.org/10.1016/S0030-4018(02)02123-5.

“OPTICAL KNIVES” – EXPERIMENTAL MATHIEU BEAM ENGINEERING USING SPATIAL LIGHT MODULATOR

Artūras Grabusovas[1], Vitalis Vosylius[1], Sergej Orlov[1]

[1] Center for Physical Sciences and Technology, Industrial Laboratory for Photonic Technologies, Lithuania
arturas.grabusovas@ftmc.lt

In laser material processing applications specific requirements for beam shapes among other properties exist. Hence, methods for generating desired intensity distributions in the transverse plane may serve as door openers for novel approaches and applications. In recent years the optical beams with controllable shape and long focal depth lines have attracted attention for their potential uses in material processing, lithography applications [1, 2].

Mathieu beams have elliptical intensity distribution perceivable as “optical knives” and belong to a family of non-diffracting electromagnetic waves. Here, the beam shape in the transverse plane is retained over a relatively long distance, so that it appears not to be affected by diffraction in free space and can therefore be called propagation invariant.

In contrast to Bessel beam–like shapes the Mathieu beams have asymmetric cross section, which is controlled via order - m and ellipticity - q parameters [1]. The zeroth order beams have the appearance of “optical knives”, where the transverse plane distribution can be altered using ellipticity parameter and the desired axial distribution could be constructed by superposition of multiple beams.

A spatial light modulator (SLM) is a dynamic diffractive optical element which enables experimental generation of a desired beam shape through the manipulation of the incident beam phase distribution. However, an important limitation on the implementable beam parameters are the low and high spatial frequency limits in the beam spatial spectra. This limitation stems from the finite size and resolution of the SLM and therefore requires close attention to the beam spatial spectra.

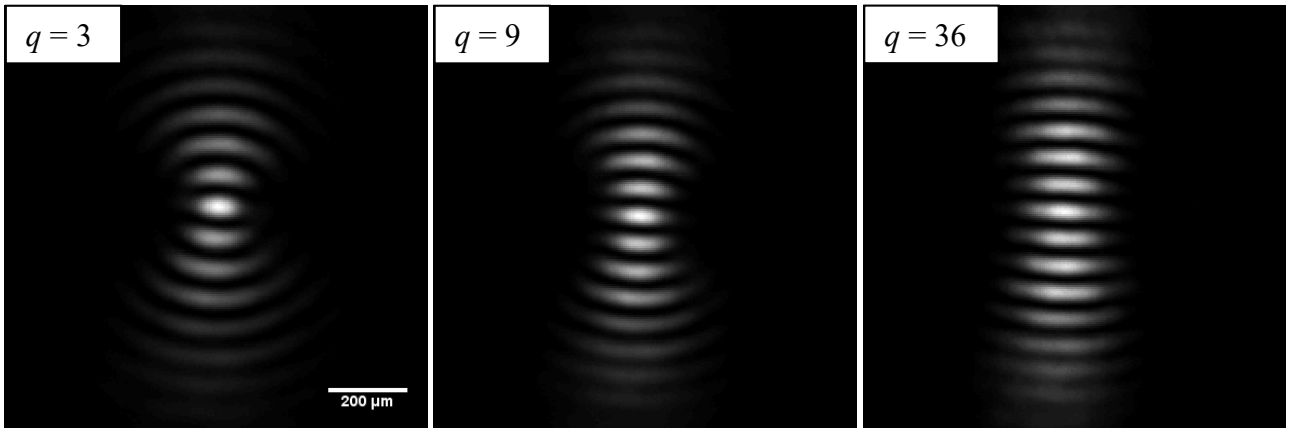

Fig. 1.Measured intensity distributions in the transverse plane of SLM generated Mathieu beams with ellipticity parameters of 3, 9 and 36. Colours representing intensity are normalized to the highest value.

In this work we investigate the transverse plane intensity distributions generated with numerically generated phase masks using SLM. An example of controlling the beam shape is given in Fig. 1 where increasing the ellipticity parameter results in development of wider and flatter “knives”. Similarly the number of parallel “knife” elements can be varied. We report on our achievements in experimentally generating Mathieu beams of different parameter configurations.

[1] C. Alpmann, R. Bowman, M. Woerdemann, M. Padgett, and C. Denz, "Mathieu beams as versatile light moulds for 3D micro particle assemblies" Opt. Express 18, 26084-26091 (2010)
[2] A. Chafiq, Z. Hricha, and A. Belafhal. "Propagation properties of vector Mathieu–Gauss beams." Opt. Commun., 275, 165-169 (2007)

USING LASER INDUCED VOLUME MODIFICATIONS FOR CONROLLING CHEMICAL ETCHING OF THE GLASSES

Kamilė Kasačiūnaitė[1], Antanas Urbas[1, 2], Sergej Orlov[1], Mindaugas Mikutis [2] and Orestas Ulčinas [2]

[1]Center of Physical Sciences and Technology, Industrial Laboratory for Photonic Technologies, Lithuania
[2]Altechna R&D Ltd, Lithuania
kamile.kasaciunaite@ff.stud.vu.lt

Femtosecond laser induced chemical etching (FLICE) technology is a perspective field when applied to fabrication of micro devices. This technology consists out of two steps: 1) modification of the sample with femtosecond laser and 2) etching modified sample in chemicals [1]. FLICE method is being used to obtain various microstructures in glassy materials for micro-/nanofluidics and biofiltering.

Formation of modified surface and volume structures in the glassy materials after irradiation with femtosecond pulses of various parameters was investigated by means of measuring induced retardance in the affected region. Parameters of the laser pulses like fluence, polarisation type, amplitude and phase distribution in the focal zone were varied to achieve modifications of desired size and orientation (Fig. 1).

It is known that etching rate correlates with the density of material, induced-stress and the refractive index [2] that depend on the laser pulse parameters. Based on this, modifications of Type II and Type III were induced to enhance interaction with the etchant. KOH was used to obtain channels or through holes and cuts. Density and temperature of the etchant was optimised to achieve maximal rate of etching.

There was wide set of modification and etching parameters used to achieve highest rate of etching in desired direction to leave unmodified regions as much intact as possible. Influence of combination of laser fluence, polarization and shape of the beam in focal zone was investigated to achieve minimal roughness of the etched channels and cuts.

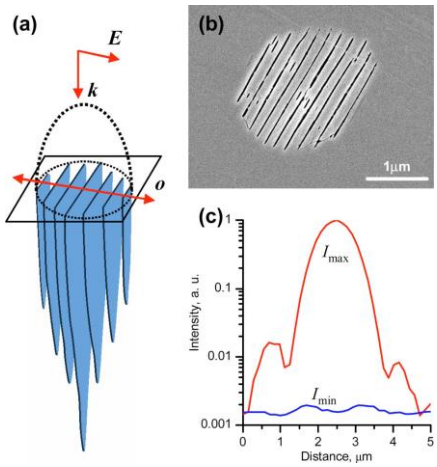

Fig. 1. (Color online) Femtosecond laser-written nanograting voxel. (a) A schematic of a voxel showing the laser light propagation direction k, the orientation of the electric field of the writing laser beam E, and the optical axis o. (b) A SEM image of the cross section of an etched voxel made with 105 laser pulses. (c) Maximum Imax and minimum Imin birefringence signals from a typical voxel (as defined in the text) [3].

[1] V. Stankevič, Formation and characterization of micro- opto-mechanical 3D devices for sensor application in transparent materials, doctoral thesis, Vilnius University, 2017.
[2] A. Said, M. Dugan, P. Bado, Fabrication of high-aspect ratio, micro-fluidic channels and tunnels using femtosecond laser pulses and chemical etching, Optics express, 2120-2129 (2004).
[3] R. S. Taylor, C. Hnatovsky, E. Simova, P. P. Rajeev, D. M. Rayner, and P. B. Corkum, Femtosecond laser erasing and rewriting of self-organized planar nanocracks in fused silica glass, Opt. Lett. 32, 2888-2890 (2007).

OPTICAL PARAMETRIC AMPLIFICATION OF ELLIPTICALLY POLARIZED BEAMS AND SPATIAL DISTRIBUTION OF DEPLETED PUMP BEAM

Maksym Ivanov, Aidas Matijošius, Valerijus Smilgevičius

Vilnius University Laser Research Center, Saulėtekio Ave. 10, LT-10223 Vilnius, Lithuania
maks.ivannov@gmail.com

Linearly polarized beams are traditionally considered in nonlinear experiments of frequency conversion. However, more general case of elliptical polarization (which allows for polarization singularities) is presented in the literature rather poorly. Here we present experimental results of optical parametric amplification of seed beam, which polarization vary from linear through elliptical to circular. Both scalar and vector amplification geometries are considered. Additionally we show that spatial distribution of depleted pump beam depends on spatial distribution and polarization state of the seed.

Fig. 1. demonstrates resulted intensity distributions of parametrically amplified 1064 nm elliptically polarized (orientation of ellipse ψ = -75 deg, ellipticity χ =15 deg) Gaussian seed beam and resulted 1064 nm idler beam. 532 nm vertically polarized Gaussian beam is used as a pump. As it can be inferred from resulting analyzed intensity pattern, polarization of the idler beam is orthogonal to that of the signal beam.

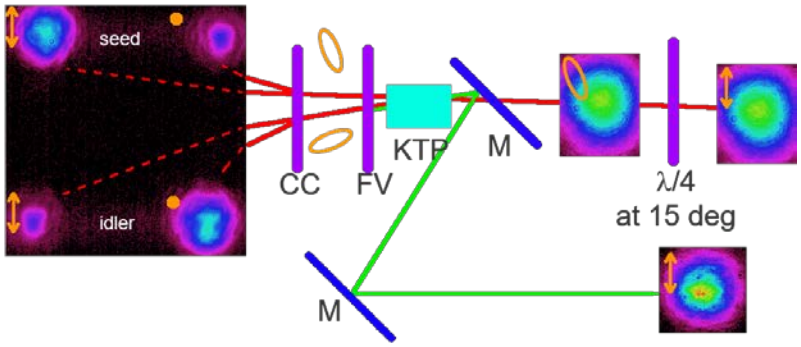

Fig. 1. λ/4 – quarter waveplate oriented at 15 deg with respect to direction of signal beam polarization, M – mirror, KTP – nonlinear crystal, FV – filter blocking 532 nm, CC – calcite crystal analyzer. Insets in the top right – experimentally obtained images of 1064 nm signal beam; bottom right – 532 nm pump beam; left – analyzed 1064 nm signal and idler beams. Orange pictograms indicate polarization state.

As it is seen from Fig. 2, spatial distribution of depleted pump beam resembles inverse of that of signal beam: while signal optical vortex beam has minimum intensity in the center, depleted pump beam has a needle-like pick of intensity in the center of a beam.

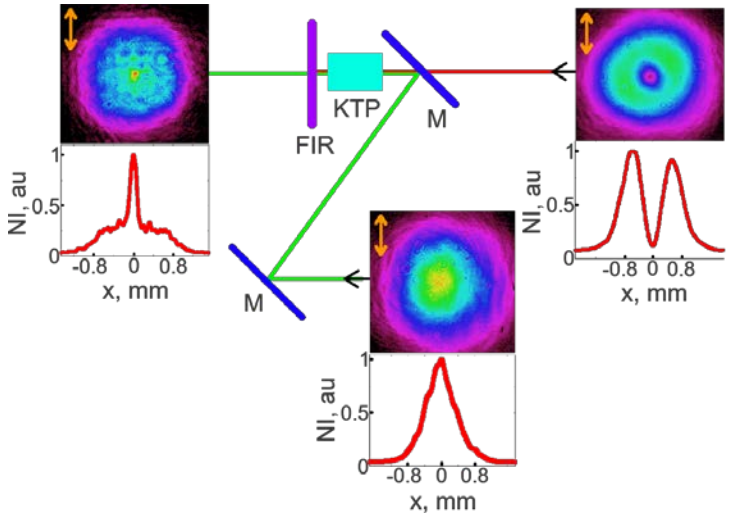

Fig. 2. M – mirror, KTP – nonlinear crystal, FIR – filter blocking 1064 nm. Insets in the top right – experimentally obtained image of 1064 nm optical vortex signal beam and its cross-section; bottom – 532 nm Gaussian pump beam and its cross-section; left – 532 nm depleted pump beam and its cross-section. NI stands for „normalized intensity“. Orange pictograms indicate polarization states.

STUDY OF EFFICIENT COPPER LASER ABLATION

Mantas Gaidys*, Andrius Žemaitis, Paulius Gečys, Mindaugas Gedvilas

Center for Physical Sciences and Technology, Savanorių Ave. 231, LT-02300 Vilnius, Lithuania
mantas.gaidys@ftmc.lt

Machining using nanosecond lasers is commonly used in science, technology and medicine. However, how to use the expensive laser irradiation efficiently is an important and still open question. Many types of materials are used for laser ablation, but few as widely applicable as copper because of high material removal rate and superb processing quality. Using laser irradiation, it is possible to cut, drill and form three-dimensional structures in copper [1]. Laser ablation rate depends on various processing parameters, such as: beam scanning speed, laser power, fluence and pulse repetition rate. In this study, optimal parameters for efficient copper ablation were found experimentally and confirmed theoretically by a commonly-used model.

Rectangular cavities were ablated in a copper sample using a nanosecond laser (Fig. 1).

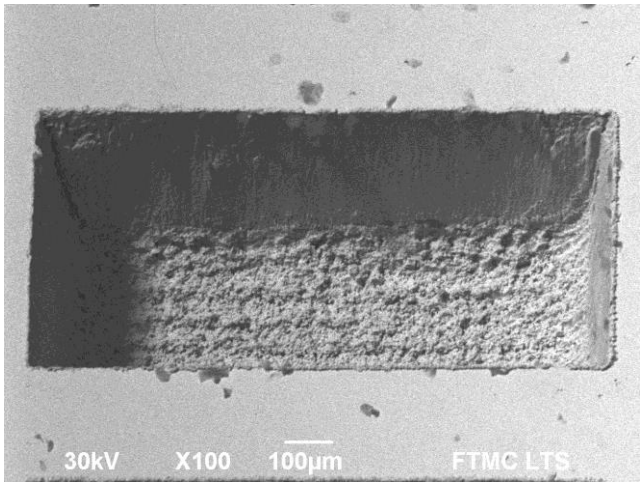

Fig. 1. Scanning electron microscope image of a rectangular cavity ablated in copper using laser processing parameters: pulse repetition rate 40 kHz, beam scanning speed 40 mm/s, laser power 2.72 W.

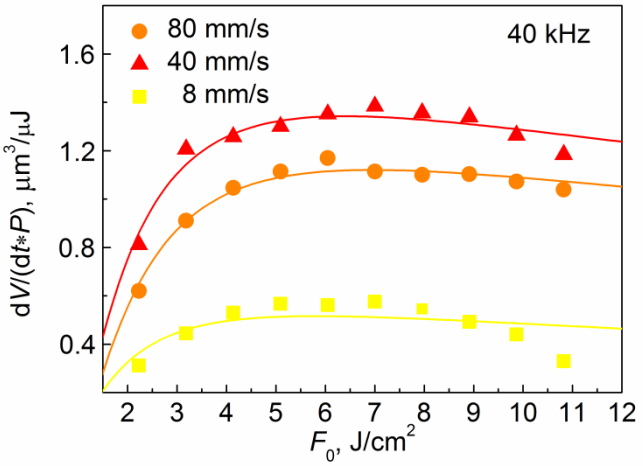

Fig. 2. Ablation efficiency dependence on laser fluence at 40 kHz pulse repetition rate at different beam scanning speeds. Solid points - experimental data, solid lines - fit by Eq. (1).

Experiments were performed at different pulse repetition rates. The beam scanning speed was linearly adjusted to repetition rate in order to keep the distance between laser pulses fixed. The focused beam spot size on the sample was 40 µm. The laser fluence was increased by changing pulse energy. The profiles of laser ablated cavities were measured by a stylus profiler. The surface roughness and the volume ablation rates per average power, also called as specific removal rate or ablation efficiency, were evaluated from profiles at different processing parameters (Fig. 2). The optimal fluence for highest removal rate on copper was found in the 10 – 40 kHz range, which was around 5 - 8 J/cm^2 (Fig. 2). For laser micro machining with a Gaussian beam the volume ablation rate per average power can be described as a function of the laser peak fluence [2]:

$$\frac{\mathrm{d}V}{\mathrm{d}t \cdot P_{\mathrm{av}}} = \frac{1}{2}\frac{\delta}{F_0}\ln\left(\frac{F_0}{F_{\mathrm{th}}}\right)^2 . \qquad (1)$$

Here dV is removed volume of the material, dt – ablation time, P_{av} – average power, F_0 – laser peak fluence, F_{th} - ablation threshold and δ - energy penetration depth. According to the theoretical model mathematically described by Eq. (1) there is an optimal fluence at which material is removed most efficiently (Fig. 2). The optimal scanning speeds for the most efficient ablation at 10, 20, 30 and 40 kHz repetition rates were found 10, 20, 30 and 40 mm/s, respectively.

It was shown, that using the optimal laser fluence and scanning speed not only yields highest ablation rate, but lowest surface roughness as well. This is explained due to the fact, that the chosen speed reduces the ablation threshold but does not allow for saturation of ablation depth. Using this method, two technologically important parameters are optimised at once.

[1] D. Allen, H. Almond, P. Logan, A technical comparison of micro-electrodischarge machining, microdrilling and copper vapour laser machining for the fabrication of ink jet nozzles, Proc. SPIE **4019**, 531–540 (2000).

[2] B. Lauer, B. Jaeggi, Y. Zhang, B. Neuenschwander, Measurement of the Maximum Specific Removal Rate: Unexpected Influence of the Experimental Method and the Spot Size, Proc. ICALEO, 146-154 (2015).

INVESTIGATION OF SIO_2 MIRRORS OPTICAL AND STRUCTURAL PROPERTIES AT HIGH DEPOSITION RATE

Algirdas Jasinskas, Lina Grinevičiūtė and Tomas Tolenis

Center for physical sciences and technology, Savanorių ave. 231, LT-02300 Vilnius, Lithuania
algirdasjas@yahoo.com

Thin films are widely used in laser systems. Rapid development in laser technologies forces an increase in investigations for optical components suitable for high power laser systems. In order to produce high quality thin films, deposition technologies are constantly improved and influence of deposition parameters investigated. The main parameter that represents durability of optical components is laser induced damage threshold (LIDT), which describes the amount of energy that component can withstand without the occurrence of irreversible change. In typical high reflection mirrors, high refractive index material limits LIDT because of low bandgap value.

Glancing angle deposition (GLAD) technology allows to form the so called sculptured thin films (STF) and produce optical components (including mirrors) using only one high band gap material [1]. STFs are formed by directing vapor flux towards the substrate at oblique angle, when substrate itself is rotated around its axis. Because of low adatom mobility and collimated vapor flux, shadowing effect takes place which results in film growth of separate columns and void regions [2]. Various deposition angles and substrate rotation algorithms allow to manipulate thin films inner structure and optical properties. Induced porosity in STFs further increases their laser resistance making them the promising solution for high power laser systems.

The aim of this research is to investigate the influence of deposition parameters for high reflectivity SiO_2 mirrors. The effect of deposition rate and oxygen partial pressure for optical and structural properties of multilayer mirrors was studied.

Two sets of samples were produced using electron beam evaporation plant: five 30 layer mirrors deposited at different rates and three 60 layer mirrors (Fig. 1) deposited at different oxygen partial pressures. Spectroscopic, SEM, AFM and LIDT measurements were performed to determine the influence of these deposition parameters.

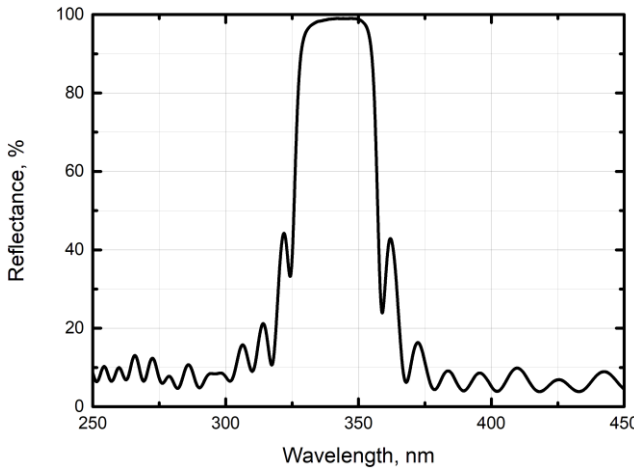

Fig. 1. Reflectance spectrum of 60 layer SiO_2 mirror

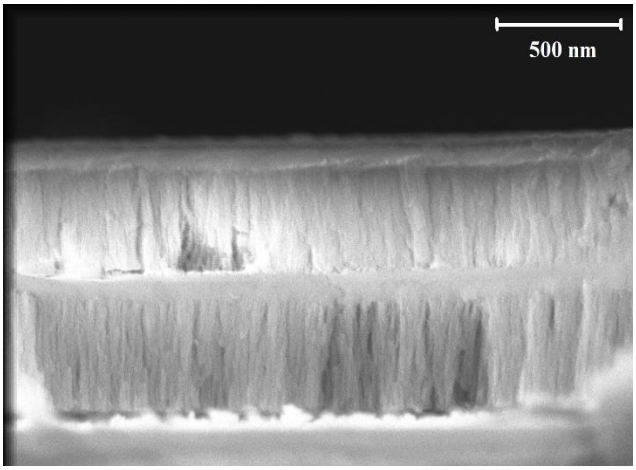

Fig. 2. SEM image of SiO_2 multilayer cross-section deposited at 3 Å/s rate.

Spectroscopic and surface roughness measurements have shown very similar results for all deposition rates. From SEM images (Fig. 2) it was determined that nanostructures of multilayers remain very similar in studied deposition rate interval. The average film column widths for 3 Å/s and 15 Å/s deposition rates were 30.9 nm and 30 nm, respectively. Changing the oxygen partial pressure was shown to have great impact on spectral properties for SiO_2 mirrors. Reflectance bandwidth and spectral region of SiO_2 mirrors were highly dependent on partial pressure. Also, the average surface roughness of 60 layer SiO_2 mirror was found to be nearly 2 times higher (1.46 nm) than 30 layers SiO_2 mirror (0.77 nm).

This study shows that from 3 Å/s to 15 Å/s deposition rate interval spectral properties of SiO_2 high reflectance mirrors remain the same, because of the stability of structural properties. Therefore it is possible to produce SiO_2 mirrors at higher rate without sacrificing quality. Reflectance maxima shift to infrared region with the decrease of oxygen partial pressure, possibly because of scattering of vapor flux. Furthermore, environmental conditions have high infuence for spectral properties of GLAD thin films and should be investigated further.

[1] M. M. Hawkeye, M. T. Taschuk, and M. J. Brett, *Glancing angle deposition of thin films: engineering the nanoscale* (Chichester: Wiley, 2014).
[2] A. Lakhtakia and R. Messier, *Sculptured thin films: nanoengineered morphology and optics,* (Bellingham, Wash: SPIE Press, 2005).

PASSIVELY Q-SWITCHED SUB-NANOSECOND IR LASERS IN CERAMIC MULTILAYERS DEPTH PROFILING BY LIBS METHOD

Ivan Vatlin[1], Ulrich Pacher[2],

[1]Laser Department, Standa Ltd, Lithuania
[2]LIStrat, www.listr.at, Austria
laser42@standa.lt

The very first demonstrations of the Laser-Induced Breakdown Spectroscopy (LIBS) took place in late 60s of the twentieth century [1], nowadays LIBS applications span from handheld metal scrap analyzers [2] to more complex systems for planetary exploration [3]. For the laser sources used in handheld analyzers there are no strict requirements to laser output parameters: beam quality and spatial energy distribution are not specified; there is no need for SLM operation and low timing jitter; the single pulse energy is usually low, about 150 µJ (although there are 5-6 mJ versions on the market); laser pulse energy stability is not specified if the laser peak fluence exceeds the material ablation threshold. At the opposite side, the systems developed for planetary exploration are usually quite expensive and tailored for particular mission requirements. Between these two extremes various applications exist which require compact laser sources with pulse energies of several mJ, excellent beam quality, and stable energetic and temporal characteristics. One such industrial application is the precise and accurate determination of coating thickness and/or fast and reliable detection of chemical and structural irregularities during the surface refinement process.

The present work demonstrates the applicability of Standa's IR passively Q-switched sub-nanosecond lasers for precise, reliable, and reproducible micro-invasive depth profiling of multilayer ceramic coatings. The excitation laser used in the experiments delivered 1mJ, 600 ps laser pulses at 100 Hz with wavelength of 1064 nm. The advanced laser oscillator design ensured SLM operation, high pulse to pulse energy stability, and excellent laser beam quality. The laser beam was expanded by a 10x beam expander and then focused with a f=150 mm lens onto the sample surface. Plasma emission was collected by a two-mirror system and launched into multimode fiber. The opposite fiber tip illuminated the entrance slit of the spectrometer. The typical ablation rates were around 100 nm/pulse. The depth-profile of the Yttria coated Aluminum sample is shown on the image below.

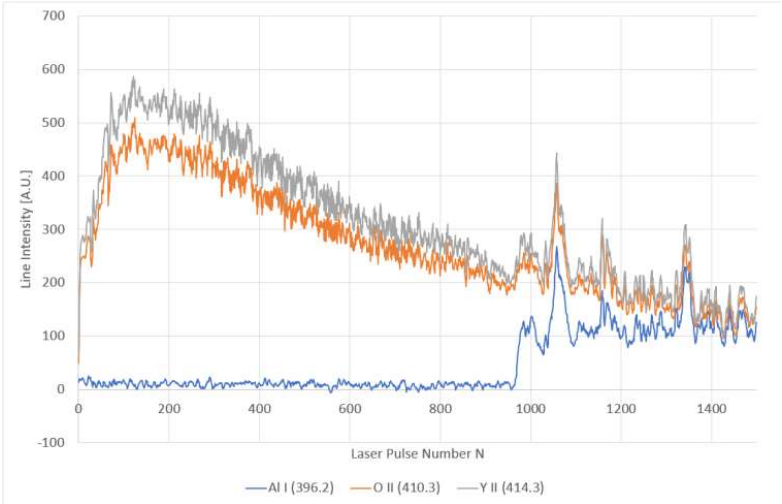

Figure 1 Yttria coated Al sample

In future works we plan to use the developed laser system in analysis of multilayer metal samples to further expand its applications range, and investigate the effect of second harmonic on ablation rates and layers profiling.

[1] Brech and L. Cross, Appl. Spectrosc. 16,59 (1962).
[2] S. Piorek Rapid sorting of aluminum alloys with handheld µLIBS analyzer, Aluminium Two Thousand World Congress and International Conference on Extrusion and Benchmark ICEB 2017
[3] A.K. Knightet al., Characterization of Laser-Induced Breakdown Spectroscopy (LIBS) for Application to Space Exploration, Appl. Spectr. 54(3), 331-340 (2000)

MEASUREMENT OF PHOTONIC CRYSTAL FIBER DISPERSION BY MEANS OF SUPERCONTINUUM GENERATION AND CROSS-CORELLATION FREQUENCY-RESOLVED OPTICAL GATING

Miglė Kuliešaitė, Julius Vengelis, Vygandas Jarutis

Laser Research Center, Faculty of Physics, Vilnius University, Lithuania
migle.kuliesaite@ff.stud.vu.lt

Supercontinuum generation is a phenomenon, when spectrum of a short pulse propagating through nonlinear medium extends hundreds or thousands of times [1]. Photonic crystal fibers (PCFs) are used as a nonlinear medium for generation of supercontinuum. The use of PCFs for supercontinuum generation enabled its use in frequency metrology, spectroscopy, optical coherent tomography, etc. [2] Since physical mechanisms of supercontinuum depend heavily on group velocity dispersion (GVD) of the PCF, it is very important to measure it precisely. Several methods for the measurement of optical fiber GVD are created. One of the methods, which allows to measure GVD in both anomalous and normal regions is called the analysis of geometrical microstructures. The drawback of this method is that it does not take into account that microstructures geometrical parameters throughout the length of the PCF might slightly vary [3]. A new method to estimate PCF GVD using supercontinuum generation and cross-correlation frequency-resolved optical gating (XFROG), recently demonstrated in Vilnius University, will be presented in this report.

To perform measurements of PCF dispersion, an optical setup, in which pump source for supercontinuum generation was Yb:KGW laser oscillator generating 1030 nm wavelength 76 MHz repetition rate and 110 fs duration pulses, was constructed. A beamsplitter was used to divide the radiation with the ratio of energy of 1:3 into two beams. The beam with more energy was used as a reference pulse for XFROG measurements. The other beam with less energy was used for the generation of supercontinuum in PCF. A highly nonlinear solid-core PCF with a core diameter of 4.6μm and a length of 32 cm was used. During XFROG measurement supercontinuum radiation and the reference pulse were non-collinearly focused for sum frequency generation into a 300 μm thickness BBO crystal, cut at φ=0° and θ=30° angles for type II phase matching. By changing the delay of the reference pulse sum frequency spectrum was measured – spectrograms, which show sum frequency dependence from delay of the reference impulse were obtained.

In this report it is shown, that when wavelength of pump radiation for supercontinuum generation is in the region of anomalous PCF dispersion which corresponds to the condition of rapid instantaneous spread of the spectrum, by analyzing the measured spectrograms it is possible to estimate dispersion of the PCF by approximating the XFROG trace with a polynomial function (Fig. 1). The bend point in the XFROG trace corresponds to the zero dispersion wavelength. For our PCF the zero of dispersion was at 1113.2 nm. Several measurements at various pump pulse energies were performed. WE determined that GVD measurement limits are determined by the limits generated supercontinuum spectra – uncertainty interval in Fig.1 right graph increase rapidly when approximation goes to wavelengths were no supercontinuum was generated. The measurement results are in good qualitative agreement with the results provided by the manufacturer, which proves the accuracy and reliability of the novel GVD measurement method.

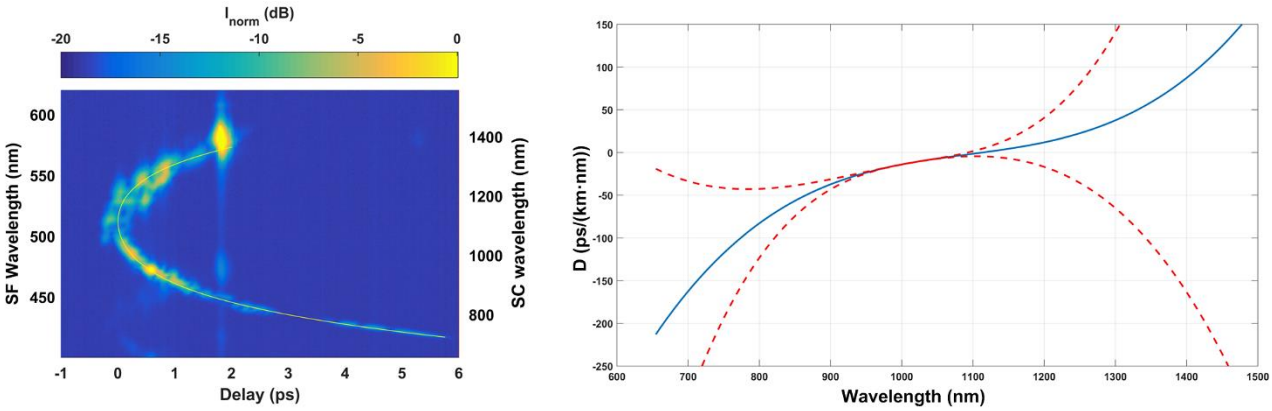

Fig. 1 Left – XFROG trace with fitted polynomial curve (solid line); right – calculated GVD, expressed as dispersion parameter D [2] (solid line). Dashed lines indicate uncertainty interval at confidence level of 95%.

[1] A. Dubietis, *Netiesinė optika*, (Publisher Vilniaus University, Vilnius 2011).
[2] J. Vengelis V. Jerutis V. Sirutkaitis, Estimation of photonic crystal fiber dispersion by means of supercontinuum generation, **42**(9), 1844–184(2017).
[3] K. Saitoh and M. Koshiba, Empirical relations for simple design of photonic crystal fibers, **13**(1), 267–274 (2005).

A COMPARISON OF SINGLE AND MULTIPLE PULSE FEMTOSECOND LASER-INDUCED BREAKDOWN SPECTROSCOPY ANALYSIS

Julius Skruibis, Kotryna Remeikaitė, Ona Balachninaitė
Laser Research Center, Department of Physics, Vilnius University, Lithuania
julius.skruibis@ff.stud.vu.lt

Using femtosecond laser pulses to induce plasma on the surface of the sample allows laser energy to be absorbed before the generation of the plasma has started, which leads to a more effective usage of the laser energy than in the longer pulse case. Because of this reason femtosecond laser pulses allow carrying out laser micromachining, monitoring process and online control with low energy pulses. Double or multiple pulses are used to improve the analytical performance of laser induced breakdown spectroscopy (LIBS) and to increase the rate in laser material processing [1].

In this work we have focused on a comparison of single and multiple pulse femtosecond laser induced breakdown spectroscopy analysis, specifically for femtosecond laser systems. In the experiment we investigated the intensity of the plasma in dependence on a variety of parameters. The total pulse energy was kept equal (with maximum energy of 80 uJ) for plasma excitation by single and multiple pulses. The experiments were carried out using the *CARBIDE* (Light Conversion) laser system with pulse duration 290 fs and power up to 5 W at 1030 nm wavelength, with repetition rate of 60 kHz. We analyzed the plasma spectrums recorded at different scanning speeds, different delays, and their dependence on the number of scans. The collected data allowed us to evaluate the enhancement of the LIBS signal, which was achieved while conducting the experiments with multiple pulse LIBS system.

The enhancement was observed while recording LIBS in multiple pulse mode when compared to the single pulse mode with all different delays in the range of 440 - 760 ps between the multiple pulses. In case of the highest enhancement, the intensity of laser plasma induced by multiple laser pulses were ~3 times greater, than in the case of single laser pulse excitation regime by using the same pulse energy. Thus, the time of plasma observation can be successfully extended when using multiple laser pulses.

Figure 1 shows the comparison between multiple pulse LIBS signals with different delays. All signals were recorded while processing soda-lime glass in dependence on the average laser power. From the picture we can see that LIBS signal can be enhanced up to 3 times by using multiple pulse, instead of single pulse regime.

In essence, the optical system assembled for plasma excitation by multiple femtosecond laser pulses can be applied for the conduction of a precise analysis of material, allowing to detect elements of low concentrations in the sample.

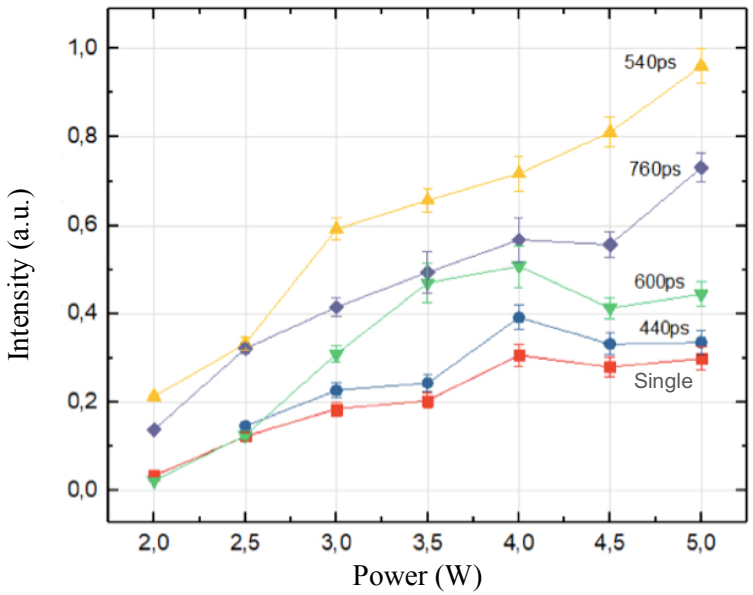

Figure 1 : Na I (589 nm) emission lines intensity comparison of multiple pulses with different delays.

[1] V.I. Babushok, F.C. DeLucia Jr., J.L. Gottfried, C.A. Munson, A.W. Miziolek, Spectrochimica Acta B, Vol. 61, 999–1014(2006).

SYNTHESIS AND OPTICAL PROPERTIES OF $K_2Bi(PO_4)(MoO_4):Pr^{3+}$ PHOSPHORS FOR SECURITY PIGMENT APPLICATIONS

Julija Grigorjevaite[1], Arturas Katelnikovas[1]

[1] Faculty of Chemistry and Geosciences, Vilnius University, Naugarduko 24, LT-03225 Vilnius, Lithuania
julija.grigorjevaite@chf.vu.lt

During past decades, genuine product security has become an important issue for everyone including industry and government bodies. Many anti-counterfeiting techniques are developed for solving this serious problem. For instance, luminescent materials that emit visible light upon excitation with ultraviolet or near infrared radiation have been used as simple luminescent markers [1]. We represent the synthesis and optical properties of Pr^{3+} doped $K_2Bi(PO_4)(MoO_4)$ phosphors which can be successfully used for anti-counterfeiting luminescent pigment applications.

$K_2Bi_{1-x}Pr_x(PO_4)(MoO_4)$ powder samples were prepared by conventional high temperature solid-state reaction. The stoichiometric amounts of high purity starting materials (Bi_2O_3, Pr_6O_{11}, MoO_3, K_2CO_3 and $NH_4H_2PO_4$) were mixed in an agate mortar employing acetone as grinding media. The obtained powder blend was transferred to the porcelain crucible and annealed at 600 °C for 10 h in air. The calcination procedure was repeated another two times [2].

The phase purity was confirmed by powder XRD measurements. Isostructural compounds of $K_2Bi(PO_4)(MoO_4):Pr^{3+}$ are obtained at any Bi^{3+}/Pr^{3+} ratio what is in line with the Vegard's law [3], since the ionic size difference of Bi^{3+} (1.17 Å) and Pr^{3+} (1.126 Å) [4] is less than 15%.

The reflection, excitation and emission spectra of the single phase compounds were measured at room temperature and analyzed. The temperature dependent emission spectra and photoluminescence decay curves in 77–500 K temperature interval were also recorded for the samples doped with 0.5% and 25% Pr^{3+} ions. Thermal quenching activation energies and $TQ_{1/2}$ values were calculated form the obtained data and shall be discussed in great detail.

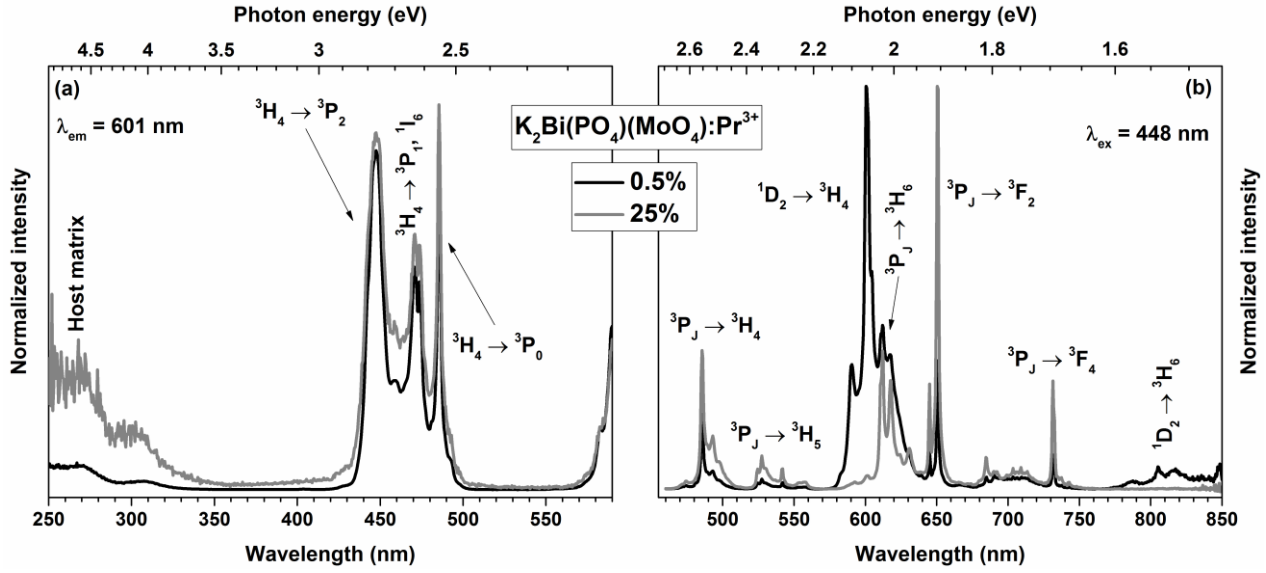

Fig. 1. (a) Excitation (λ_{em} = 601 nm) and (b) emission (λ_{ex} = 448 nm) spectra of samples doped with 0.5% and 25% Pr^{3+}.

Fig. 1a shows normalized excitation spectra of 0.5% and 25% Pr^{3+} doped samples for 601 nm emission. The recorded spectra contain a broad band in the range of 250–350 nm and a set of lines in the range of 430–500 nm that can be assigned to the host matrix and $^3H_4 \rightarrow {}^3P_J + {}^1I_6$ transitions of Pr^{3+} ions, respectively. The normalized emission spectra of $K_2Bi(PO_4)(MoO_4):Pr^{3+}$ phosphors doped with 0.5% and 25% Pr^{3+} under 448 nm excitation are depicted in Fig. 1b. The spectra contain seven sets of emission lines that originate from ^3P_J and $^1D_2$ excited states to the ^3H_J and ^3F_J terminal states. The strongest emission intensity was obtained for the sample doped with 0.5% Pr^{3+}.

It also turned out that the increase of Pr^{3+} concentration leads to a strong concentration quenching due to cross relaxation processes. Besides, the profile of emission spectra could be altered just by changing the Pr^{3+} content in the structure. Samples with higher Pr^{3+} concentration possess rather unique emission spectra and, therefore, could be applied in luminescent security markers, where such properties are highly desired.

[1] P. Kumar, K. Nagpal, B. K. Gupta. ACS. Appl. Mater. Interfaces 9 (2017) 14301-14308.
[2] H. Huang, G. Chen, S. Wang, L. Kang, Z. Lin, Y. Zhang. Mater. Res. Bull., 51 (2014) 455-459.
[3] R.C. Ropp, Luminescence and the solid state, 2nd ed., Elsevier, Amsterdam; Boston, 2004.
[4] R.D. Shannon, Acta Crystallogr., A32 (1976), pp. 751-767.

SYNTHESIS AND CHARACTERIZATION OF NOVEL LUMINESCENT SECURITY PIGMENTS BASED ON $GdBSb_2O_8$ HOST

Indrė Mackevičiūtė[1], Artūras Katelnikovas[1]

[1] Faculty of Chemistry and Geosciences, Vilnius University, Naugarduko 24, LT-03225 Vilnius, Lithuania
indre.mackeviciute@chf.stud.vu.lt

The market of counterfeit goods grows each year. This causes companies that produce the original goods an immense amount of money that were put in product development. Moreover, counterfeit medicine and other chemicals besides the financial damage are also harmful to people and environment and causes thousands of deaths annually [1]. One of the options to recognize the original product is marking it with luminescent security pigments. In this work we present three novel luminescent materials based on $GdBSb_2O_8$ host matrix doped with Tb^{3+}, Sm^{3+}, and Eu^{3+} ions. All of the prepared phosphors possess unique emission spectra that are beneficial for application in luminescent security pigments.

Three sets of $GdBSb_2O_8$ compounds doped with 1%-100% Tb^{3+}, Sm^{3+}, and Eu^{3+} ions were prepared by high temperature solid state synthesis method from high purity Gd_2O_3, H_3BO_3, SbO_2, Tb_4O_7/Sm_2O_3/Eu_2O_3 starting materials. The structural, morphological and optical characteristics of the compounds were investigated by powder X-ray diffraction (XRD), scanning electron microscope (SEM) analysis and UV-Visible spectroscopy. The reflection, excitation and emission spectra as well as photoluminescence (PL) decay curves were measured at room temperature and analysed. Temperature dependent emission spectra and PL decay curves in 77–500 K interval were recorded and thermal quenching activation energies (E_a) calculated. Moreover, room temperature and temperature dependent (77–500 K) colour coordinates for 1931 CIE colour space diagram were calculated from emission spectra and will be discussed.

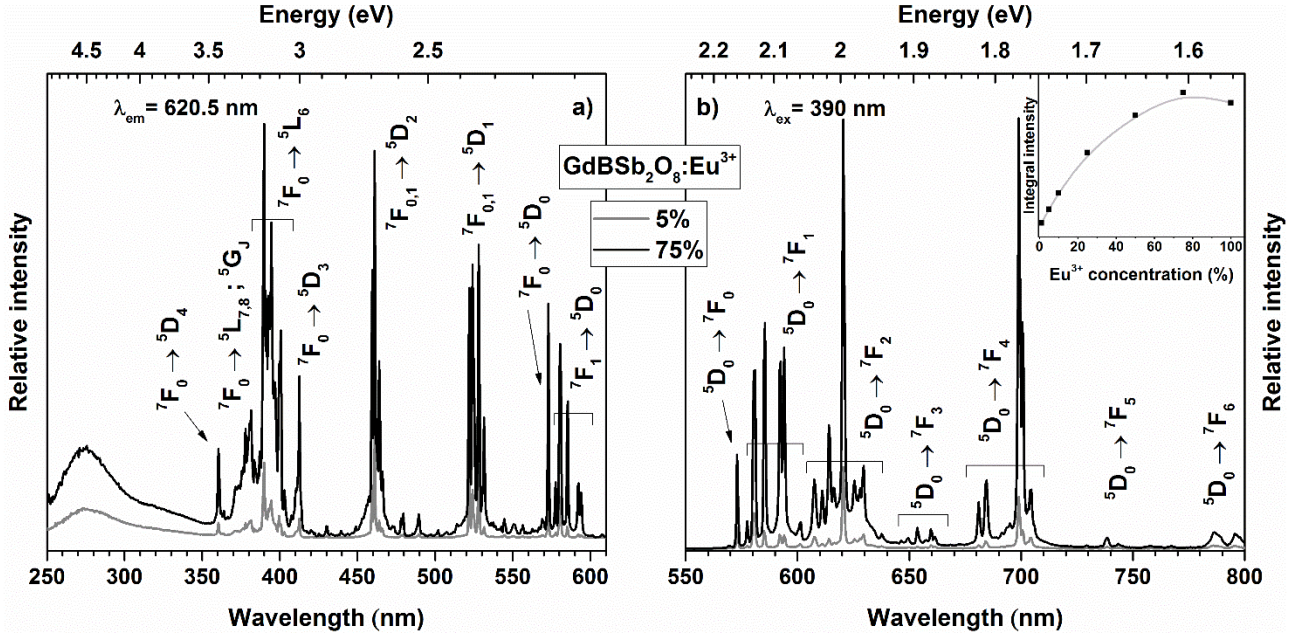

Fig. 1. Excitation (a) and emission (b) spectra of $GdBSb_2O_8$:Eu^{3+} samples. Inset of section (b) shows integrated emission intensity of $GdBSb_2O_8$:Eu^{3+} samples as a function of Eu^{3+} concentration.

The excitation and emission spectra of $GdBSb_2O_8$ doped with 5% and 75% Eu^{3+} are given in Fig. 1. Excitation spectra (Fig. 1a) contain several sets of intensive lines at ca. 390, 460, 525, and 580 nm originating from $^7F_0 \rightarrow {}^5L_J$; ^5G_J, $^7F_{0,1} \rightarrow {}^5D_2$, $^7F_{0,1} \rightarrow {}^5D_1$, and $^7F_{0,1} \rightarrow {}^5D_0$ transitions of Eu^{3+} ions, respectively. Intensive excitation lines indicate that these compounds can be excited in a wide wavelength range. Emission spectra (Fig. 1b) of these compounds, in turn, also possess several sets of intensive emission lines at ca. 580, 620, and 700 nm that are attributed to $^5D_0 \rightarrow {}^7F_{0,1}$, $^5D_0 \rightarrow {}^7F_2$, and $^5D_0 \rightarrow {}^7F_4$ Eu^{3+} transitions, respectively. The integrated emission also indicated (see inset of Fig. 1b) that strongest emission was observed for the sample doped with 75% Eu^{3+} leading to a conclusion that concentration quenching occurs if the activator concentration is further increased.

[1] http://www.oecd.org/industry/global-trade-in-fake-goods-worth-nearly-half-a-trillion-dollars-a-year.htm (accessed on the 23rd of January 2018)

EPR PROBING OF IRRADIATED DIMETHYLAMMONIUM ZINC FORMATE $[(CH_3)_2NH_2][Zn(HCOO)_3]$ HYBRID FRAMEWORK

Lukas Osipovič[1*], Mantas Šimėnas[1], Marius Burkanas[2], Jonas Venius[2,3], Jūras Banys[1]

[1] Faculty of Physics, Vilnius University, Sauletekio 9, LT-10222 Vilnius, Lithuania
[2] Medical Physics Department, National Cancer Institute, Santariskiu 1, LT-08660 Vilnius, Lithuania
[3] Biomedical Physics Laboratory, National Cancer Institute, Baublio 3B, LT-08406 Vilnius, Lithuania
lukas.osipovic@stud.ff.vu.lt

We employ electron paramagnetic resonance (EPR) spectroscopy to study the structural phase transition in irradiated dimethylammonium zinc formate $[(CH_3)_2NH_2][Zn(HCOO)_3]$ (DMAZn), which is considered as a dense metal-organic framework (MOF). This hybrid compound is based on the perovskite AMX_3-type (where A = $(CH_3)_2NH_2^+$, M = Zn^{2+}, X = $HCOO^-$) topology, where the cuboid cavity is occupied by a DMA^+ molecular ion (Fig. 1). The DMA^+ cation is disordered over three positions at $T > T_c$. Here T_c is the temperature of the phase transition. The DMA^+ becomes ordered in one of the three positions below T_c and, as a result, the whole MOF undergoes a structural phase transition when cooled to T_c~160 K. We irradiated $[(CH_3)_2NH_2][Zn(HCOO)_3]$ crystals using 30 keV X-ray source in order to create paramagnetic centers that are necessary for the EPR measurements. The continuous-wave (CW) EPR measurements were performed at X-band microwave frequency using a conventional Bruker E580 EPR spectrometer. After irradiation, we observed an EPR line of a free radical with *g*-factor equal to 2.02. We examined temperature dependence and determined how spin Hamiltonian parameters of the radical change at the phase transition point.

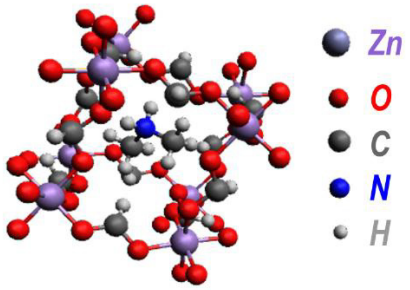

Fig. 1. AMX_3-type perovskite framework in the low-temperature phase. Zn^{2+} and $HCOO^-$ ions form the porous framework. The cuboid cavity is occupied by the DMA^+ ion.

EPR OF METAL-ORGANIC FRAMEWORKS CONTAINING RADICAL LINKERS AND COPPER PADDLE WHEEL UNITS

Marius Navickas[1*], Mantas Šimėnas[1], Eva Gjuzi[2], Frank Hoffman[2], Michael Fröba[2], Jūras Banys[1]

[1]Faculty of Physics, Vilnius University, Sauletekio av. 9, LT-10222 Vilnius, Lithuania
[2]Institute of Inorganic and Applied Chemistry, University of Hamburg, Marin-Luther-King-Platz 6, 20146 Hamburg, Germany
marius.navickas@ff.stud.vu.lt

Metal-organic frameworks (MOF) are hybrid coordination polymers with an open pore system [1]. These coordination networks are formed from the various organic linker molecules and metal centers. The application areas of these highly porous compounds range from the biological imaging to gas storage and separation.

In this work we performed X-band continuous-wave (CW) EPR experiments on MOFs containing different ratio of the paramagnetic radical and diamagnetic linkers. In addition, the investigated compounds consists of so called Cu/Cu dinuclear paddle-wheel (PW) units that are responsible for rich magnetic properties of these materials.

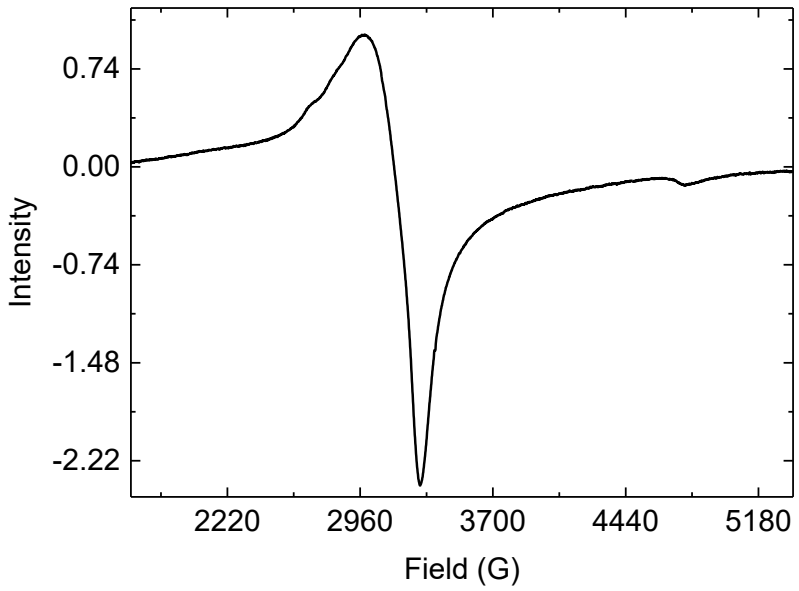

Fig. 1. Room temperature CW EPR spectrum of MOF containing 100% radical linker.

The observed CW EPR spectra are typical for the Cu/Cu PW units with a pronounced inter PW exchange interaction of spin $S = 1$ states (see Fig. 1) [2]. In addition, a signal of Cu^{2+} defect sites can be observed. A small free radical signal was detected only for the compound with 100% of the radical linker. Measurements at different temperatures demonstrate that decreasing temperature signal from intra PW exchange decreases only for the same material.

[1] IUPAC Provisional recommendations on Metal-Organic Framework and coordination polymer terminology.
[2] M. Simenas et. al. J. Phys. Chem. C 2016, 120, 27462-27467.

ELECTRON PARAMAGNETIC RESONANCE OF $[(CH_3)_3NH]_2[KCr(CN)_6]$ AND $[(CH_3)_2NH_2]_2[KCr(CN)_6]$ METAL-ORGANIC FRAMEWORKS

Gediminas Usevičius[1], Mantas Šimėnas[1], Magdalena Rok[2], Grazyna Bator [2], Jūras Banys[1]

[1] Faculty of Physics, Vilnius University, Lithuania
[2] Faculty of Chemistry, University of Wroclaw, Poland
gediminas.usevicius@stud.ff.vu.lt

Metal-organic frameworks (MOFs) are the novel type of porous materal, that have recently emerged and attracted attention of the scientific community [1,2]. These crystalline compounds are unique due to the high degree of porosity which can be utilized for gas adsorption related applications [3]. Additionally, many MOFs containing paramagnetic transition-metal ions exhibit peculiar magnetic properties. The organic part in several of such compounds consists of polar molecules which below a certain phase transition temperature order into a ferroelectric-type phase, making these materials single-phase hybrid multiferroics[4].

Here we present a continuous-wave electron paramagnetic resonance (CW EPR) study of two such hybrid compounds based on the perovskite topology, $[(CH_3)_2NH_2][KCr(CN)_6]$ and $[(CH_3)_3NH][KCr(CN)_6]$. The EPR experiments are performed at the X-band frequency (≈9.5 GHz) on powdered MOF samples in a wide temperature range while cooling. The obtained results indicate that the compound containing trimethylammonium organic cations undergoes two structural phase transitions at T_{c1} = 260 and T_{c2} = 183 K (Fig. 1). A single phase transition at 206 K is observed for the dimethylammonium MOF. These anomalies may be related to the changes of the chromium(III) relaxation times.

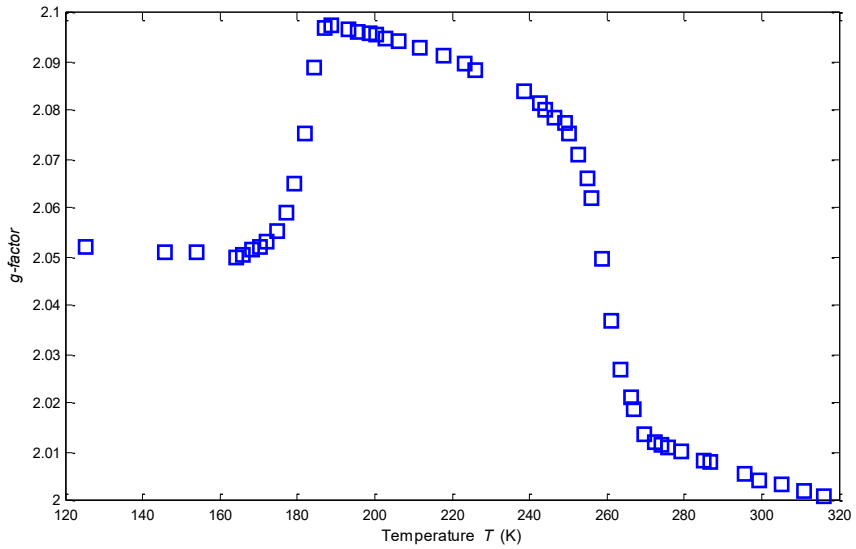

Fig. 1. Temperature dependence of the chromium(III) *g*-factor in $[(CH_3)_3NH][KCr(CN)_6]$.

[1] M. Rosseinsky, Recent Developments in *Metal-Organic Framework Chemistry: Design, Discovery, Permanent Porosity and Flexibility,* Microporous Mesoporous Mater. **73**, 15−30, (2004).
[2] S. T. Meek, J. A. Greathouse, M. D. Allendorf, *Metal-Organic Frameworks: A Rapidly Growing Class of Versatile Nanoporous Materials*, Adv. Mater, **23**, 249−267 (2011).
[3] H.-C. Zhou, J.R. Long, O.M. Yaghi, Chem. Rev. **112**, 673–674 (2012).
[4] R. Ramesh, N. A. Spadin, *Multiferroics: progress and prospects in thin films,* Nature Materials **6,** 21–29 (2007).

FABRICATION AND CHARACTERIZATION OF HIGH EFFICIENCY RED OLED BASED ON THERMALLY ACTIVATED DELAYED FLUORESCENCE

Dovydas Banevičius[1], Domantas Berenis[1], Karolis Kazlauskas[1], Saulius Grigalevičius[2], Saulius Juršėnas[1]

[1]Institute of Photonics and Nanotechnology, Vilnius University, Lithuania

[2]Department of Polymer Chemistry and Technology, Kaunas University of Technology, Lithuania

dovydas@fidi.lt

Organic light emitting diodes, OLEDs, are undergoing a breakthrough due to a recent discovery of a novel emission mechanism employing delayed fluorescence generated by thermal activation (TADF) allowing to reach 100% internal efficiency without implementing heavy metal atoms in emitter molecules. [1] Red TADF OLEDs face two main problems, i.e. rather low external quantum efficiency (EQE) and unsatisfactory colour.

The aim of this work was to fabricate high efficiency red TADF OLEDs as well as evaluate their electrical and optical properties. By using thermal vacuum evaporation technology, we fabricated two series of OLEDs consisting of similar structure and differing by the host material employed: ITO/NPB (60 nm)/TCTA (5 nm)/host:emitter layer (20 nm)/TPBi (30 nm)/LiF (0,8 nm)/Al (100 nm), where ITO – indium tin oxide, NPB (N,N′-Bis(naphthalen-1-yl)-N,N′-bis(phenyl)benzidine) – hole injection layer material, TCTA (Tris(4-carbazoyl-9-ylphenyl)amine) – hole transport and electron blocking layer material, host:emitter layer – emitter-doped host layer, TPBi (2,2′,2"-(1,3,5-Benzinetriyl)-tris(1-phenyl-1-H-benzimidazole)) – electron injection layer material, LiF – lithium fluoride, Al – aluminium cathode. Efficient red-emitting TADF compound TPA-DCPP (7,10-Bis(4-(diphenylamino)phenyl)-2,3 -dicyanopyrazino phenanthrene) was chosen as an emitter. [2] OLED based on neat emitter film expressed EQE of 1.2%. The structure of device is described in Ref.[2]. Such low EQE is attributed to strong aggregation induced quenching of TPA-DCPP. To suppress the quenching, OLEDs based on emitter dispersed in different hosts were fabricated. Novel phenanthroimidazole hosts (Fig. 1) featuring bipolar charge transfer properties and, which previously were successfully utilized as hosts in phosphorescent OLEDs, were employed. [3] OLEDs with emitter concentrations in the hosts ranging from 2% to 20% were fabricated. Commercially available TPBi was used as the reference host yielding 7.2% EQE at 20% doping in optimized device.

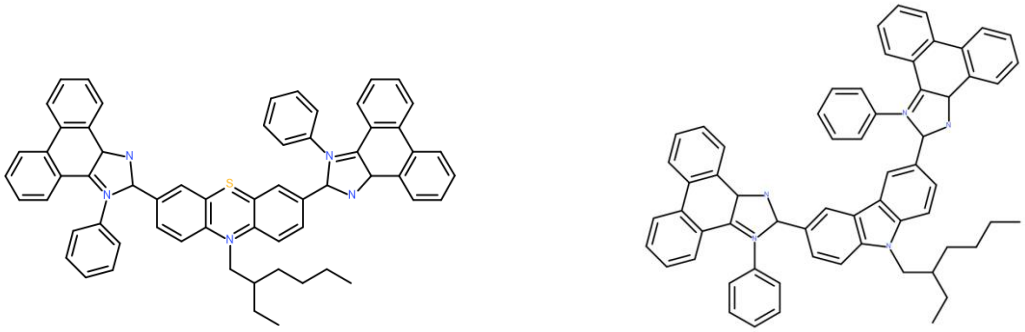

Fig. 1. Chemical structures of phenanthroimidazole host compounds

Non-optimized devices with phenanthroimidazole hosts exhibited up to 2% EQE. Preliminary data based on i-V and L-V characteristics indicate that further layer thickness optimisation is needed to attain charge carriers balance in the devices and attain higher EQE.

[1] H. Uoyama *et al.*, Highly efficient organic light-emitting diodes from delayed fluorescence, *Nature*, **492**, 7428, (2012).

[2] S. Wang *et al.*, Highly Efficient Near-Infrared Delayed Fluorescence Organic Light Emitting Diodes Using a Phenanthrene-Based Charge-Transfer Compound, *Angew. Chemie - Int. Ed.*, **54**, 44, (2015).

[3] D. Tavgeniene *et al.*, Phenanthro[9,10-d]imidazole based new host materials for efficient red phosphorescent OLEDs, *Dye. Pigment.*, **137**, (2017).

IN SEARCH OF EFFICIENT ENERGY TRANSFER HOST FOR RED TADF ORGANIC LIGHT EMITTING DIODES

Edvinas Radiunas[1], Domantas Berenis[1], Dovydas Banevičius[1], Karolis Kazlauskas[1], Saulius Grigalevičius[2], Saulius Juršėnas[1]

[1]Institute of Photonics and Nanotechnology, Vilnius University, Lithuania
[2] Department of Polymer Chemistry and Technology, Kaunas University of Technology, Lithuania
eradiunas@gmail.com

Increasing demand for the organic light emitting diodes (OLEDs) in commercial applications could be associated with the demonstration of novel and attractive photophysical and mechanical properties such as flexibility, tunable fluorescence emission and cheap large area device production. Recently, organic compounds displaying thermally activated delayed fluorescence (TADF) attracted great attention because this class of compounds can harvest both singlet and triplet excited states for luminescence [1]. Although TADF OLEDs exhibit superior performance in the blue and green region the design and synthesis of highly efficient red and near-infrared (NIR) organic TADF materials still remains a great challenge. Furthermore, red and NIR emitting OLEDs offer wide applications in night-vision, telecommunications, sensors and bioimaging [2].

The current work focused on optical and photophysical investigation of phenanthroimidazole derivatives containing various functional groups (phenothiazine, indole, carbazole, triphenylamine). Detailed photophysical measurements were carried out to show that studied compounds exhibited deep ultraviolet absorption (from 329 to 388 nm) and blue-cyan fluorescence (FL) emission (from 410 to 500 nm). Due to the wide band gap and favourable FL emission, the phenanthroimidazole compounds were investigated as a host for energy transfer. Fluorescence energy transfer rate (FRET) was evaluated for efficient red TADF emitter TPA-DCPP (guest). Highest theoretical FRET values were obtained for phenanthroimidazole compounds containing phenothiazine and carbazole fragments. These two host were experimentally examined and compared with commercially-available TPBi host widely used in OLEDs. Guest-host blends were fabricated for different hosts with different TPA-DCPP concentrations (0,1 -10 wt%). Although in theory the compound with phenothiazine fragment exhibited higher FRET rate than a molecule with carbazole moiety, experimentally the later outperformed phenothiazine-phenanthroimidazole compound. The fragment of carbazole between the phenanthroimidazole derivatives provided effective FRET at high levels of TPA-DCPP concentration (10%), and at this point demonstrated superior energy transfer properties compared to well-known TPBi matrix.

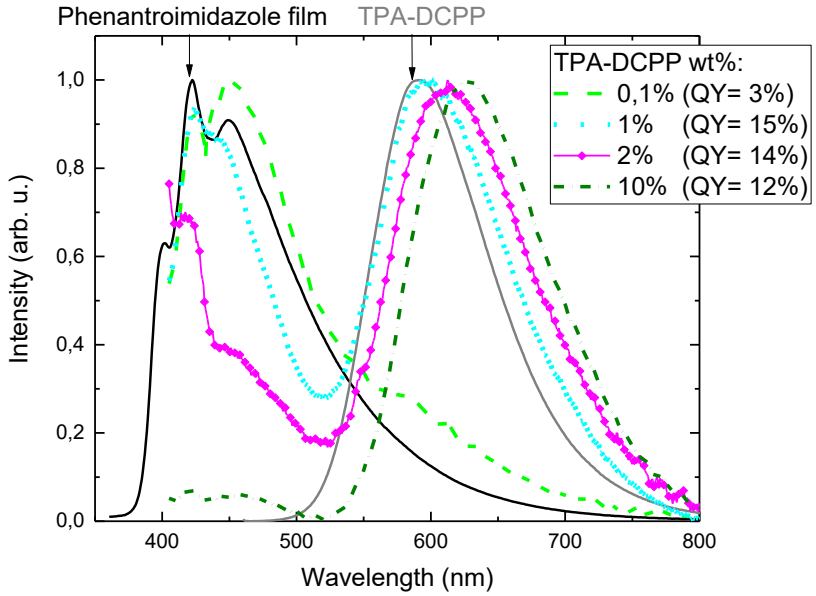

Fig. 1. Fluorescence spectra with corresponding quantum yield (QY) of TPA-DCPP in phenanthroimidazole host dispersed with different TADF emitter concentration.

[1] H. Uoyama, K. Goushi, K. Shizu, H. Nomura, and C. Adachi, 'Highly efficient organic light-emitting diodes from delayed fluorescence', Nature, vol. **492**, 234–238, Dec. (2012).
[2] M. Wang et al., 'One-Compound-Based Highly Efficient Deep-Red to Near-Infrared Thermally Activated Delayed Fluorescence Organic Solid Films and Electroluminescent Devices', Angew. Chem. Int. Ed., **56**, Jul. (2017).

FT-RAMAN SPECTROSCOPIC STUDY OF WATER INFLUENCE ON CONFORMATIONAL EQUILIBRIUM IN IONIC LIQUIDS AND WATER MIXTURES

Edvinas Zacharovas[1], Auksė Naruševičiūtė[1], Lukas Jočionis[1], Jonas Kausteklis[1], Valdemaras Aleksa[1*]

[1]Faculty of Physics, Institute of Chemical Physics, Vilnius University, Saulėtekio ave. 3, LT-10257 Vilnius Vilnius, Lithuania

valdemaras.aleksa@ff.vu.lt

Lately, there has been an increasing need for traditional solvent substitutes, which would be environmentally friendly. For this reason, ionic liquids are of great interest and could be excellent alternative to traditional organic solvents used in industry [1]. The variation of the ionic liquids parameters, as a relatively new class of solvents, provides an opportunity to adapt them to the various chemical processes. The chemical and physical properties could be determined by their structural changes which occurs during the interactions with water molecules. The dependence of the structural transformations of ionic liquids on temperature and pressure has been sufficiently studied by vibrational spectrometry and other methods [1-5]. In the literature there are not so many investigations on conformational equilibrium variations depending on the water content in the system. The aim of this work is to study the structural changes and interactions of three ionic liquids - [C_4mim]OTf, [C_{10}mim]Br, [C_{10}mim]Cl with water molecules while changing the concentration of H_2O in the mixture. The very sensitive method for the monitoring of molecules conformational changes is vibrational spectrometry. It could provide very detailed information of the molecular structures either in neat ionic liquids or in the mixtures with other solvents [2-3]. Raman spectra of ionic liquids and water mixtures in the region 200-3600 cm^{-1} have been registered while water molar ratio in mixtures was changed from $X_W = 0.05$ to $X_W = 0.095$. The ratio of integral intensities I_{gauche}/I_{anti} of corresponding spectral bands of the *gauche* and the *anti* conformers were investigatred (Fig. 1). It was found that the intensity ratio I_{gauche}/I_{anti} is changing with the added water for all studied mixtures, the ammount of mollecules in *gauche* conformation increasing. Another insight to the results could be done when analyzing the ratio of the *gauche* and the *anti* conformers at the low water concentrations. The [C_4mim]OTf has more molecules which formed *gauche* conformers than *anti* and [C_{10}mim]Br, [C_{10}mim]Cl showed the opposite results.

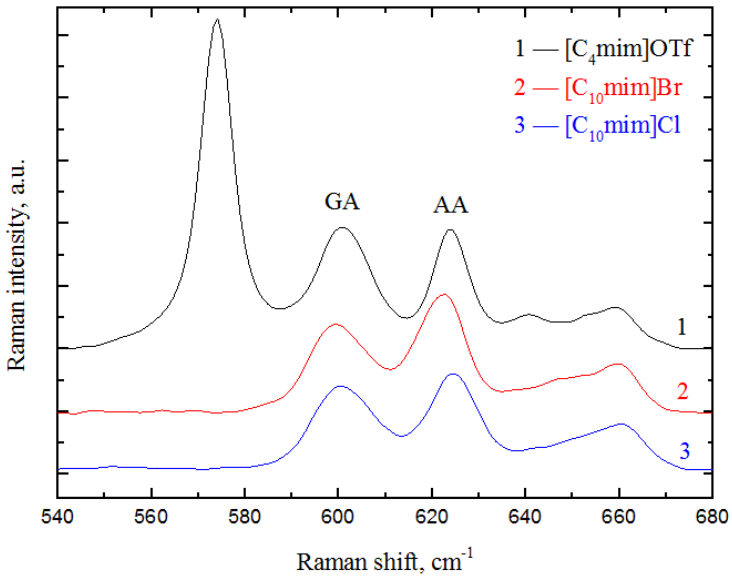

Fig 1. Raman spectra of ionic liquids and water mixtures in the region of *gauche* and *anti* conformations.

[1] Z. Lei, B. Chen, Y-M. Koo, D. R. MacFarlane, Introduction: Ionic Liquids, Chem. Rev., **117** (10), 6633-6635 (2017).
[2] R. W. Berg, Raman Spectroscopy and Ab-Initio Model Calculations on Ionic Liquids, Monatshefte fuer Chemie, **138**, 1045-1075 (2007).
[3] V. H. Paschoal, L. F. O. Faria and M. C. C. Ribeiro, Vibrational Spectroscopy of Ionic Liquids, Chem. Rev. **117**, 7053-7112 (2017).
[4] C. M. O. Le'pori, N. M. Correa, J. J. Silber and R. D. Falcone, How the cation 1-butyl-3-methylimidazolium impacts the interaction between the entrapped water and the reverse micelle interface created with an ionic liquid-like surfactant, Soft matter, **12**, 830-844 (2016).
[5] T. Takamuku, Y. Kyoshoin, T. Shimomura, S. Kittaka, T. Yamaguchi. Effect of Water on Structure of Hydrophilic Imidazolium-Based Ionic Liquid, J. Phys. Chem. B **113** 10817-10824 (2009).

SYNTHESIS AND CHARACTERIZATION OF COPPER OXIDE COMPOSITS FOR PHOTOELECTROCHEMICAL APPLICATIONS

Sergey Zavatski[1], Eugene Chubenko[1], Hanna Bandarenka[1], Vladimir Smirnov[2], Vitaly Bondarenko[1]

[1] Department of Micro- and Nanoelectronics, Belarussian State University of Informatics and Radioelectronics, Belarus
[2] Institute of Energy Research 5 – Photovoltaic, Julich Forschungszentrum, Germany
sergeyzavatski13@gmail.com

Nowadays, the issue of regulating the anthropogenic emissions of greenhouse gases, such as CO_2, CH_4, N_2O, which is mainly associated with the burning of traditional types of hydrocarbon fuels, is acute. One of the solutions to overcome this problem is the implementation and use of alternative clean energy sources. For this reason solar energy and hydrogen economy are promising. The conversion of water into hydrogen using solar energy and semiconductor photocatalytic coatings have attracted much attention due to the use of only water and solar energy, which are abundant, renewable and easily accessible natural resources [1-3].

Therefore, in this work we formed copper oxide (I, II) composites using electrochemical anodization of copper foil and copper thin film deposited on nanostructured silicon surface. Anodization was carried out in aqueous solution of sodium hydroxide at different current densities for 30 min. UV-Vis, photoluminescent and Raman spectroscopy (Fig. 1) were used to study of structural and optical properties. Photoelectrochemical properties of samples was studied using three-electrode cell configuration, where copper oxide composites, silver chloride and ruthenium oxide were as working, reference and counter electrodes, correspondingly.

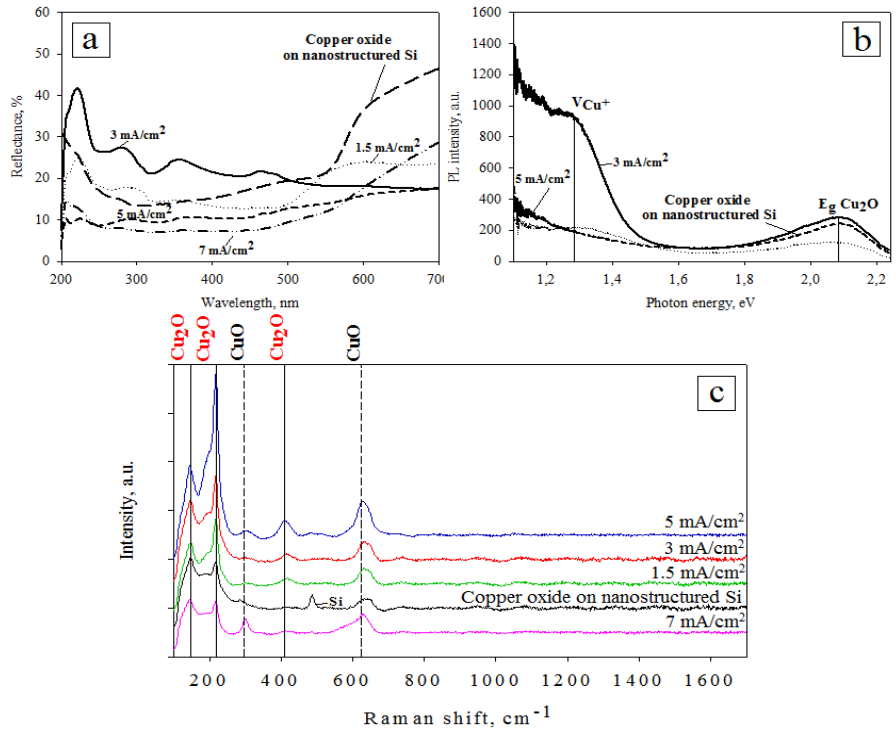

Fig. 1. UV-Vis (a), photoluminescent (b) and Raman (c) spectra of samples prepared at different anodic current densities.

It was found that all of the obtained samples contain both copper oxide (I) (Cu_2O) and copper oxide (II) (CuO). The optical band-gap of Cu_2O calculated from photoluminescence spectra is about 2.1 eV. Reflectance of the samples varied from 10 to 45 % in the 200 – 700 nm spectral range. Voltammetric study of the samples showed the increase of current density in the samples under illumination. Therefore, developed formation method of copper oxide photoelectrodes opens prospects for obtaining high-effective, stable and low-cost photoelectrode for solar water splitting cells.

[1] O. Khaselev, J. A. Turner, A monolithic photovoltaic-photoelectrochemical device for hydrogen production via water splitting, Science **280**, 425-427 (1998).
[2] S. Y. Reece, J. A. Hamel, K. Sung et. al., Wireless solar water splitting using silicon-based semiconductors and earth-abundant catalysts, Science **334**, 645-648 (2011).
[3] T. Faunce, S. Styring, M. R. Wasielewski et. al., Artificial photosynthesis as a frontier technology for energy sustainability, Energy & Environmental Science **6**, 1074-1076 (2013).

LIGHT-EMITTING PROPERTIES OF 4H-PYRAN DERIVATIVES CONTAINING PURE THIN FILMS

Julija Pervenecka[1], Aivars Vembris[1], Elmars Zarins[2], Valdis Kokars[2]

[1]Institute of Solid State Physics, University of Latvia,

[2]Institute of Applied Chemistry, Riga Technical University

julija.pervenecka@inbox.lv

Organic solid-state lasers are one of in nowadays perspective and intensively developing technology in which as laser dyes are widely used different non crystalline structure films forming organic molecules. As all lasers organic solid-state laser should also consists from two main elements: an active medium and resonator. In comparison with traditional inorganic lasers, they would be much cheaper and more easily integrated into photonic devices [1].

However, not all organic compounds could be used for laser active medium preparation. The main requirement for the compound is possibility to excite amplified spontaneous emission (ASE) in their thin films. Only materials, which appropriate to this requirement can be used for preparation of a laser active medium.

In this work were investigated photoluminescence and amplified spontaneous emission properties of two original 4H-pyran derivatives: (E)-5-(2-(4-(bis(2-(trityloxy)ethyl)amino)styryl)-6-methyl-4H-pyran-4-ylidene)-1,3-dimethylpyrimidine-2,4,6(1H,3H,5H)-trione (MWK-1) and (E)-5-(2-(4-(bis(2-(trityloxy)ethyl)amino)styryl)-6-methyl-4H-pyran-4-ylidene)-1,3-diethyl-2-thioxodihydropyrimidine-4,6(1H,5H)-dione (EWK-1), that form amorphous thin films from solution. MWK-1 and EWK-1 are newly synthesised original non-symmetric chromophore molecule that absorbs light in beginning till middle of visible spectral range (~375 nm-570 nm) (MWK-1) and (~388 nm-608 nm) (EWK-1) with maximum at 491 nm (MWK-1), 523 nm (EWK-1) and emits it within red spectral region.

Thin films of investigated compounds on glass substrate were made from chloroform solution by the spin- coating method.

Photoluminescence (PL) was excited at compounds absorption maximum wavelength: 491 nm (MWK-1) and 523 nm (EWK-1). Emitted spectrum was Stokes shifted by ~ 203 nm (MWK-1) and by ~ 181 nm (EWK-1), full width at half maximum of the photoluminescence was ~ 145 nm (MWK-1) and ~ 155 nm (EWK-1), maximum at 694 nm (MWK-1), 704 nm EWK-1). Amplified spontaneous emission was excited by Ekspla 310 series pulse laser at 491 nm (MWK-1) and at 523 nm (EWK-1) wavelength. The irradiation area on the surface of the sample was stripe form with dimension 3x0.4 mm^2. Light emission was collected at the edge of the sample and measured by spectrometer OceanOptics HR4000. As haven't been expected, ASE peak was blue-shifted from PL maximum (approximately by 21 nm (MWK-1) and by 4 nm (EWK-1)). Full width at half maximum of the ASE was ~ 10 nm (MWK-1) and ~ 23 nm (EWK-1) with maximum position at 673 nm (MWK-1) and at 700 nm (EWK-1). Amplified spontaneous emission threshold energy was 65,22 $\mu J/cm^2$ (MWK-1) and 175,42 $\mu J/cm^2$ (EWK-1).

In my presentation I will discussed about photoluminescence and ASE properties of MWK-1 and EWK-1 pure thin films and their perspectives for future use as laser dye in red lasers.

This research was kindly supported by European Regional Development Fund within the Project No. Nr.1.1.1.1/16/A/046 and A.Riekstina SIA "Mikrotīkls" donation, administered by University of Latvia Foundation.

[1] Sebastien Forget, Sebastien Chenais, Organic Solid-State Lasers, Springer-Verlag Berlin Heidelberg 2013, Volume 175, p. 179.

SINGLET EXCITON DIFFUSION IN TRIPHENYLAMINE DERIVATIVES

Karolina Maleckaitė[1], Steponas Raišys[1], Karolis Kazlauskas[1], Saulius Juršėnas[1]

[1] Institute of Photonics and Nanotechnology, Vilnius University, Sauletekio ave 3, LT-10257 Vilnius, Lithuania
kmaleckaite@gmail.com

Exciton diffusion is one of the main processes in operation of organic solar cells as well as other optoelectronic devices, and therefore ways enabling control of exciton diffusion is very important. In the both planar and bulk heterojuction solar cells diffusion of photoexcited singlet excitons towards the heterojunction directly correlates with photocurrent intensity and device efficiency. One way to increase exciton diffusion length (L_D) is based on the control over the molecular separation through the dilution in wide energy gap host material or by chemical structure engineering. [1]

In this work, exciton diffusion in a series of triphenylamine (TPA) derivatives was investigated. The determination of exciton diffusion was based on the evaluation of fluorescence quenching efficiency in the TPA films with randomly distributed quenchers. Monte Carlo simulations of the fluorescence transients in TPA/quencher blends with different quencher concentration (0 – 1.5%) as well as Stern Volmer fluorescence quenching analysis were performed for the evaluation of L_D.[2,3] An increasing number of phenylethenyl sidearms attached to TPA core was found to increase the exciton diffusion length, which is in a good agreement with our previous observations.[4]

It was demonstrated that larger number of sidearms forms a dense molecular network necessary for efficient exciton diffusion and the suggested approach of increasing L_D is attractive for designing new molecules with enhanced exciton diffusivity for application in organic solar cells or other optoelectronic devices.

[1] T. K. Mullenbach, K. A. McGarry, W. A. Luhman, et al., Connecting molecular structure and exciton diffusion length in rubrene derivatives, Adv. Mater. **25**, 3689–3693 (2013).
[2] O. V. Mikhnenko, H. Azimi, M. Scharber et al, Exciton diffusion length in narrow bandgap polymers, Energy Environ. Sci. **5**, 6960–6965 (2012).
[3] H. Y. Hsu, J. H. Vella, J. D. Myers, et al., Triplet Exciton Diffusion in Platinum Polyyne Films, J. Phys. Chem. C 118, 24282 (2014).
[4] S. Raisys, K. Kazlauskas, M. Daskeviciene, et al., Exciton diffusion enhancement in triphenylamines via incorporation of phenylethenyl sidearms, Journal of Materials Chemistry C, **2**, 4792-4798 (2014).

SENSITIZED LIGHT UPCONVERSION IN DIPHENYL ANTHRACENE COMPOUNDS

Greta Bučytė, Steponas Raišys, Karolis Kazlauskas, Saulius Juršėnas
Institute of Photonics and Nanotechnology, Vilnius University, Lithuania
greta@fidi.lt

Light upconversion via sensitized triplet-triplet annihilation (TTA-UC) allows upconverting noncoherent light even at relatively low excitation power densities (~10mW/cm2) [1]. Lower energy photons(near-infrared range) almost non-absorbed by solar cell can be upconverted into higher energy ones which can be easily harvested and contribute to photo current of the solar cell. This feature is very attractive for solar energy harvesting, as the radiation power is sufficient for the process to take place. Light upconversion quantum efficiency in solution is up to 27%, however, in solid polymer films, the efficiency is reduced to 2%. Low efficiency in solid polymer films is mainly determined by emitter aggregation and aggregation induced emission quenching [2]. To this end, to reduce emitter quenching structural modification of diphenyl anthracene (DPA) compounds by steric groups was attempted. Additionally, aggregation was influenced by employing polymers with different glass transition temperature (T_g). To compare, samples were prepared in N_2 and ambient conditions.

For this study, upconverting films based on sensitizer platinum-octaethylporphyrin (PtOEP) and modified DPA compounds (see Fig. 1) in poly(vinyl butyral-co-vinyl alcohol-co-vinyl acetate) (PVBVAVAc) and Tecoflex polymers were fabricated by melt processing technique. The concentration of DPA compounds in polymer matrix was chosen to vary from 1 wt% to 45 wt%. The PtOEP/DPA compound/polymer films were evaluated by measuring fluorescence, phosphorescence and upconversion spectra as well as estimating their emission quantum yields and decay transients.

The obtained data showed that in Tecoflex polymer with lower T_g TTA-UC quantum efficiency decreases with increasing emitter concentration. This decrease occurring due to self-quenching is caused by emitter aggregation at higher concentrations. Conversely, polymer PVBVAVAc featuring higher T_g suppresses emitter aggregation resulting in enhanced TTA-UC quantum efficiency at higher concentrations. Obviously, introduction of complimentary alkyl steric groups in DPA compounds reduced self-quenching effects and enabled fabrication of upconverting polymer films of higher emitter concentrations.

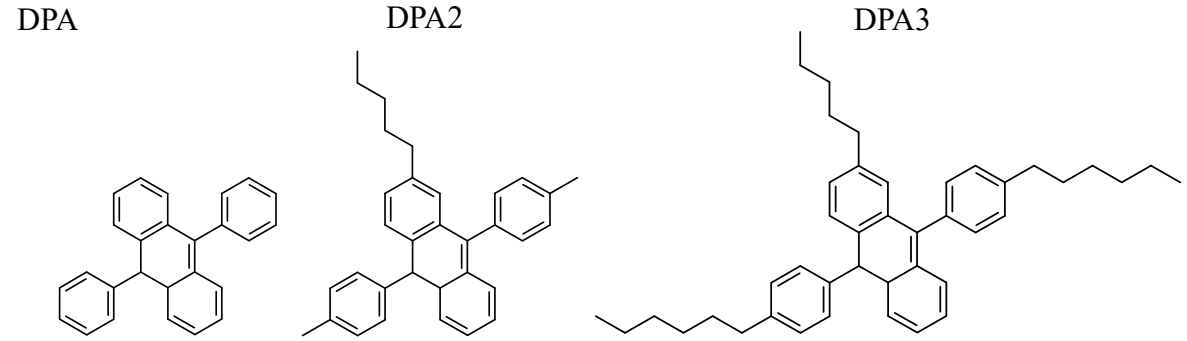

Fig 1 . Molecular structures of DPA compounds modified by steric groups.

[1] S. Baluschev, T. Miteva, V. Yakutkin, G. Nelles, A. Yasuda, and G. Wegner, Phys. Rev. Lett. **97**, 143903 (2006).
[2] S. Raišys, K. Kazlauskas, S. Juršėnas, et al., The role of triplet exciton diffusion in light-upconverting polymer glasses, ACS Applied Materials and Interfaces **8**, 15732–15740 (2016).

OPTICAL AND SURFACE PROPERTIES HFO_2- SIO_2 MIXTURE BASED UV MIRRORS

Giedrius Abromavičius[1], Simonas Kičas[1]

[1] Optical coatings laboratory, Center for Physical Sciences and Technology, Savanorių ave. 231, Vilnius LT-02300, Lithuania
giedrius.abromavicius@ftmc.lt

Strong focus on hafnium oxide as a material for production of high power optical coatings has remained constant within optical coating community for many years [1-3]. Many extensive studies were dedicated to investigate HfO_2 optical and physical properties using almost all common coating technologies like electron beam evaporation, ion plasma ion assisted deposition, beam sputtering, reactive magnetron sputtering, etc. [4-6]. Ion beam sputtering technology is considered as one of the best methods for deposition of advanced optical coatings with very complex spectral and superb optical properties. It also easily allows to produce mixtures of metal oxides with tailored optical and physical properties [7,8].

Important optical properties - absorption, reflectivity, transmittance, as well as optical resistance of formed coatings could be modified and improved using thermal annealing procedure [9]. Deposited material layers could also undergo phase transitions during such post-deposition treatment [10].

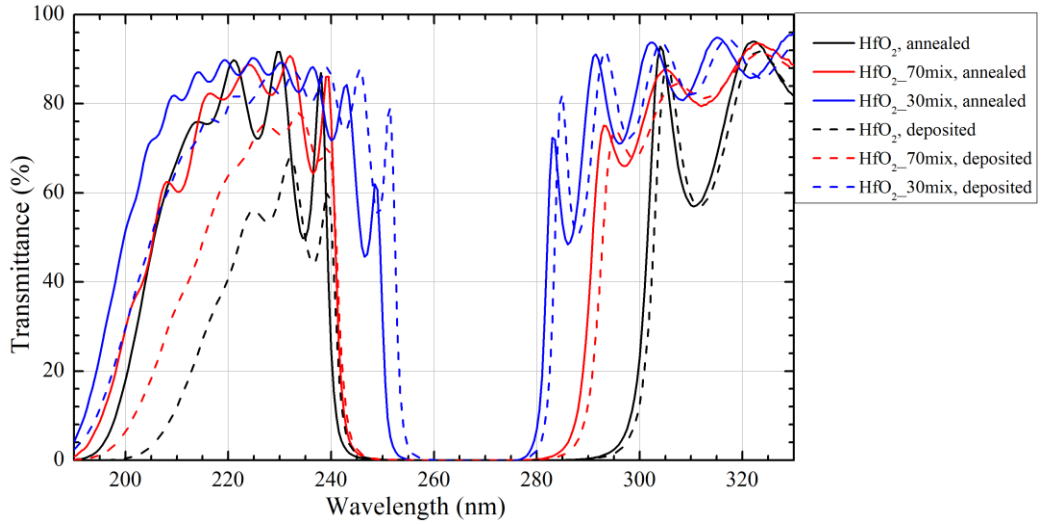

Fig. 1. Transmittance spectra of deposited and annealed dielectric mirrors for 266nm wavelength based on HfO_2 and its mixtures with SiO_2

Presented work investigates optical and surface properties of deposited and annealed dielectric mirrors for 266 nm wavelength based on selected hafnia-silica mixtures. Obtained results demonstrate that thermal annealing minimizes absorption losses and improves reflectivity of the mirrors.

[1] J. B. Oliver, S. Papernov, A. W. Schmid, J. C. Lambropoulos, Optimization of laser-damage resistance of evaporated hafnia films at 351nm, Proc. SPIE 7132, 71320J (2008).
[2] M. Alvisi, M. Di Giulio, S.G. Marrone, M.R. Perrone, M.L. Protopapa, A. Valentini and L. Vasanelli, HfO2 films with high laser damage threshold, Thin Solid Films **358**, 250-258 (2000).
[3] D. Patel, P. Langston, A. Markosyan, E. M. Krous, B. Langdon, F. Furch, B. Reagan, R. Route, M.M. Fejer, J.J. Rocca and C.S. Menoni, SiO2/HfO2 multilayers: impact of process parameters and stack geometry on the optical and structural properties, Proc. of SPIE 7132, 71320L-1 (2008).
[4] R. Thielsch, A. Gatto, J. Heber, N. Kaiser, A comparative study of the UV optical and structural properties of SiO2, Al2O3, and HfO2 single layers deposited by reactive evaporation, ion-assisted deposition and plasma ion-assisted deposition, Thin Solid Films **410**, 86–93 (2002).
[5] A. Hallbauer, D. Huber, G.N. Strauss, S. Schlichtherle, A. Kunz, H.K. Pulker, Overview about the optical properties and mechanical stress of different dielectric thin films produced by reactive-low-voltage-ion-plating, Thin Solid Films **516**, 4587–4592 (2008).
[6] V. Pervak, F. Krausz, A. Apolonski, Hafnium oxide thin films deposited by reactive middle-frequency dual magnetron sputtering, Thin Solid Films **515**, 7984–7989 (2007).
[7] A. Melninkaitis, T. Tolenis, L. Mažulė, J. Mirauskas, V. Sirutkaitis, B. Mangote, X. Fu, M. Zerrad, L. Gallais, M. Commandré, S. Kičas, and R. Drazdys, Characterization of zirconia– and niobia–silica mixture coatings produced by ion-beam sputtering, Applied Optics **50**, C188–C196 (2011).
[8] M. Mende, S. Schrameyer, H. Ehlers, D.Ristau and L.Gallais, Laser damage resistance of ion-beam sputtered Sc2O3/SiO2 mixture optical coatings, Applied Optics **52**, 1368-1376 (2013).
[9] C. Xu, Y. Qiang, Y. Zhu, T. Zhai, L. Guo, Y. Zhao, J. Shao, Z. Fan, Laser-induced damage threshold at different wavelengths of Ta2O5 films annealed over a wide temperature range, Vacuum **84**, 1310-1314 (2010).
[10] C. Xu, Q. Xiao, J. Ma, Y. Jin, J. Shao, Z. Fan, High temperature annealing effect on structure, optical property and laser-induced damage threshold of Ta2O5 films, Applied Surface Science **254**, 6554-6559 (2008).

TITANIUM MONOXIDE THIN FILMS FORMATION BY HYDROTHERMAL OXIDATION

Simonas Ramanavičius[1], Arūnas Jagminas[1]

[1] State Research Institute Center for Physical Sciences and Technology, Vilnius, Lithuania
simonas.ramanavicius@ftmc.lt

Nowadays various titanium oxide layers are widely used for different applications. Solar cells are one of such areas where titanium oxide is especially applicable. Despite this fact there is still a high interest in synthesis of new titanium oxide layers using different methods for new applications in practice. Properties of titanium oxide and its application areas depends on synthesized layer thickness, composition and surface morphology [1,2].

This study is focused on the synthesis and characterization of titanium monoxide layers on a pure titanium foil or titanium layer sputtered on the microscopic glass. Hydrothermal synthesis was selected herein due to simple control of the process. It was observed that physical properties of synthesized titanium oxide layers as well as band gap values depend on the synthesis conditions. Scanning electron microscopy (SEM), X-ray diffraction (XRD), and band gap investigations were employed in this study for the characterization of formed and calcined layers.

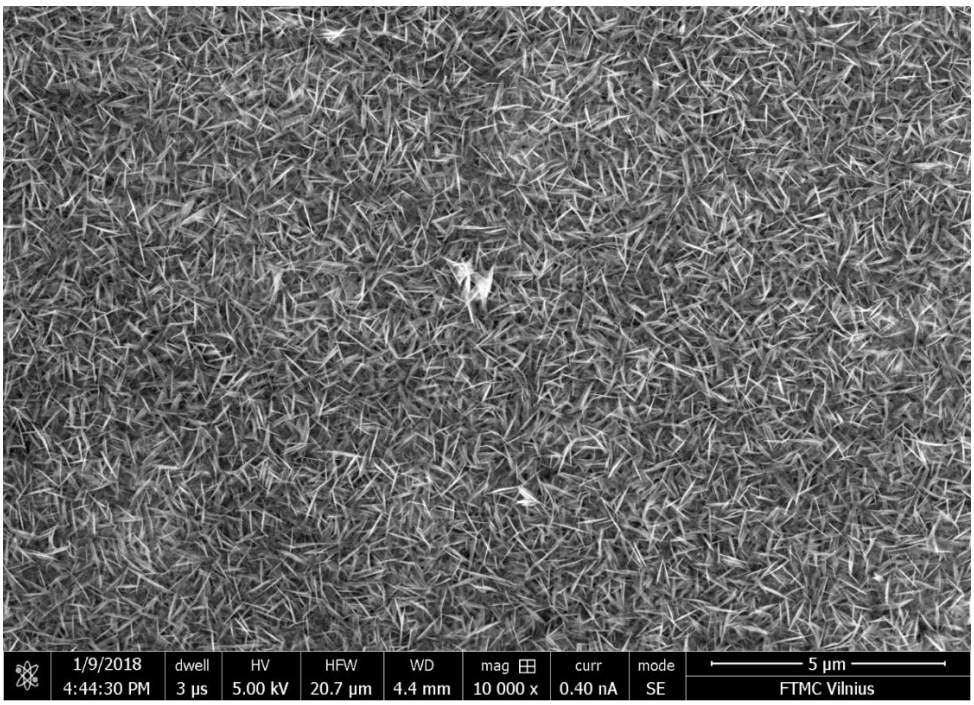

Fig. 1. Top-side SEM image of titanium monoxide film formed by hydrothermal oxidation

It was determined that hydrothermal oxidation is good technique to form high surface area titanium monoxide, $TiO_{0.84}$, thin films (Fig. 1). The main factors determining composition of titanium monoxide thin films are hydrothermal oxidation temperature and pH.

[1] X. Chen, S. S. Mao. Titanium Dioxide Nanomaterials: Synthesis, Properties, Modifications, and Applications. Chemical Reviews 2007, 107(7), 2891-2959. doi: 10.1021/cr0500535
[2] M. Grätzel. Photoelectrochemical Cells. Nature. 2001, 414, 338-344. doi:10.1038/35104607

ELECTRONIC PROPERTIES OF NANOCOMPOSITES FeCoZr-SiO_2

Dzmitry Rusak[1], Anhelina Viazgina[1]

[1]Department of Physics, Belarussian State University,Belarus
fiz.rusakda@bsu.by

Modern investigations of nanocomposites have shown that they are able to demonstrate properties of simple analog elements(resistors,inductive- and capacitive-like). Also, they are more compact and cheaper than traditional ones. In order to develop materials with appropriate properties, it is necessary to understand the factors affecting electronic transport in them. In our work we studied frequency dependences of conductivity σ and phase shift angle θ of samples at the temperatures $20 - 375$ K and in frequency range 50 Hz $-$ 5 Hz.[1]

The study objects were thin films of granular nanocomposites $(FeCoZr)_x(SiO_2)_{1-x}$, obtained by ion-beam sputtering of compound targets. Conductivity and phase shifts angle dependency on frequency and temperature were plotted for interpreting the behavior of the system.[2] Additionally we used admittance and impedance hodographs (Fig.1, Fig.2) for this goal.

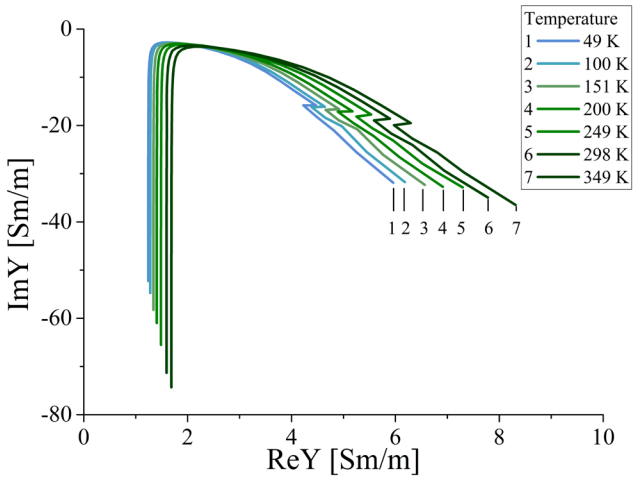

Fig. 1. Admittance hodograph (various temperatures 1-7)

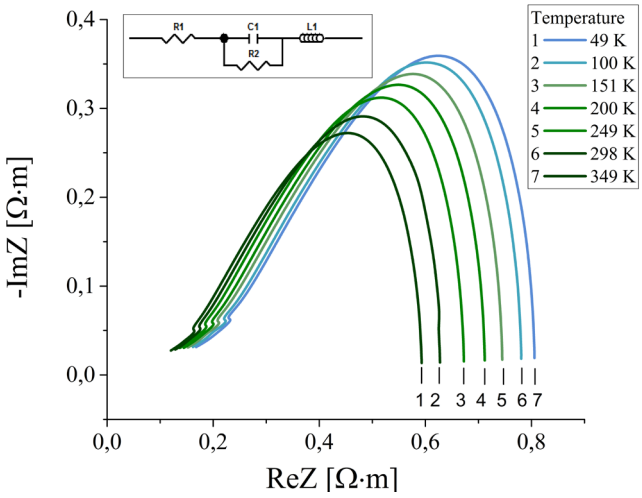

Fig. 2. Impedance hodograph (various temperatures 1-7)

As we can see on the figures, hodograph curvature radius decreases with temperature increasing, and edges shift to the left. Summarizing, we can determine variation of equivant circut parameters (namely:$R_1 \approx 1-4$ kOhm,$C_1 \approx 9-80$ pF, $L_1 \approx 2{,}3-10$ mH, $R_2 \approx 57-80$ kOhm) which describe phase component of the material.

[1] P.Zukowski, T.N.Koltunowicz, O.Boiko, V.Bondariev, K.Czarnacka, J.A.Fedotova, A.K.Fedotov, I.A.Svito . Impedance model of metal-dielectric nanocomposites produced by ion-beam sputtering in vacuum conditions and its experimental verification for thin films of (FeCoZr)x(PZT)(100-x). Vacuum Volume 120, Part B, October 2015,Pages 37-43.

[2] Al doped ZnO films: temperature dependence of electron transport / Svito I.A., Fedotov A.S., Sivakov V., Talkenberg F., Mazanik A.V., Fedotov A.K. // Proceedings of the 9th International Conference New Electrical and Electronic Technology and Their Industrial Implementations NEET-2015 (June 23 - 26, 2015, Zakopane, Poland). - Zakopane. - 2015;

KINETICS OF THE FRICTION FORCE AND LINEAR WEAR CHANGE WHILE TESTING FOR SLIDING FRICTION OF A METAL-POLYMERIC FRICTION PAIR BY THE MULTISTAGE LOADING METHOD

Ihar Dziambouski

Faculty of Mathematics and Mechanics, Belarusian State University, Belarus
igordembovskii@mail.ru

The report contains discussions of the results of tests on sliding friction of a metal-polymeric friction pair by the accelerated multistage loading method. The experiment was carried out at the testing center SZ-01 (the developer is Scientific and Production Group TRIBOFATIGUE Ltd) according to the scheme (Fig. 1).

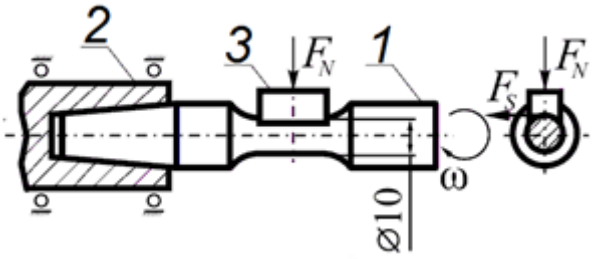

Fig. 1. Scheme of tests for frictional fatigue: 1 - sample; 2 - spindle; 3 - control sample (partial insert).

The cylindrical sample 1, made of steel 30, is fixed in the spindle 2 and rotates at angular velocity ω. Being fixed immovably in the cassette, the control sample 3 (partial insert) with dimensions 10 × 10 × 10 mm made of Poly(methyl methacrylate) is pressed under the action of the contact load F_N to its working area with the diameter d = 10 mm.

In accordance with the proposed method, a step-by-step increase of the contact load F_N is performed during the complete test time. To implement the program, the following are set: the criterion for reaching the limiting state (k_i = const); initial level of contact load F_{N0}; duration (n_i = const) of the loading stage; interval ΔF_{Ni} = const for increment of the contact load. The initial parameters are set depending on the assigned task; the number of cycles ($n_к$) at the last stage of loading is determined by the achievement of the limiting state; the transition from stage to stage is carried out without intermediate pauses; the tests are carried out continuously until the onset of the limiting state. In the described experiment, the initial contact load was F_{N0} = 4 N, the increment step of the load ΔF_{Ni} = 2 N, the duration of the test stage n_i = 9000 cycles. Figure 2 shows the loading program and kinetics of the friction force F_s and linear wear L change of the polymeric insert.

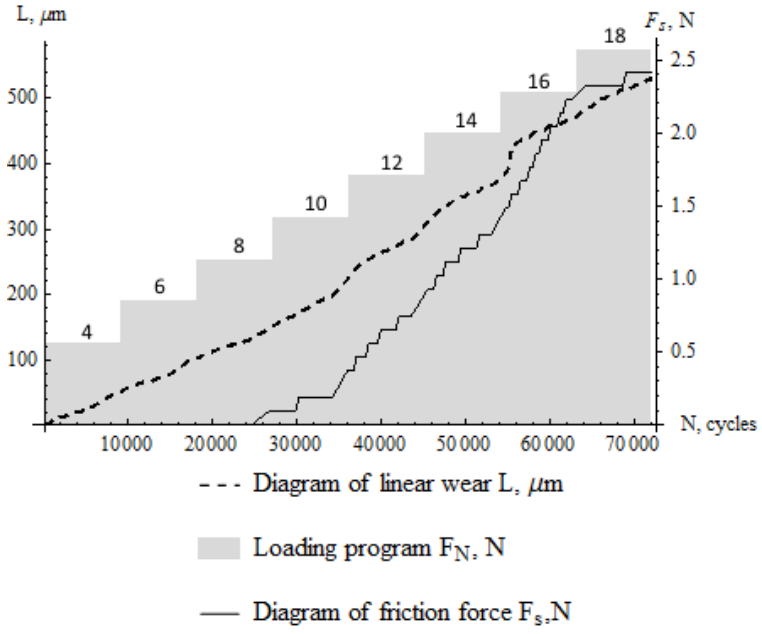

Fig. 2. Diagram of linear wear and friction force dependence on the number of cycles.

From the diagram (see Fig. 2) it is seen that the friction force is subject to oscillations even during one stage of loading; this process is non-stationary, as well as the value of linear wear.

BLUE-LIGHT-EMITTING DERIVATIVES OF BENZOPHENONE AS ELECTROACTIVE MATERIALS

Rasa Keruckienė, Liveta Lapienytė, Juozas Vidas Gražulevičius

Department of Polymer Chemistry and Technology, Kaunas University of Technology, Lithuania
rasa.keruckiene@ktu.edu

Organic luminescent materials have attracted increasing attention for their potential applications in the fields of displays and sensors [1]. To achieve better performance, it is of great importance to have a deep understanding of the inherent light-emitting process and internal mechanism. The employment of thermally activated delayed fluorescence (TADF) in the active layers of organic light emitting diodes has been stated to be very efficient [2]. TADF materials can achieve 100 % of use of excitons through reverse intersystem crossing because of their low energy gap between the lowest singlet excited state S_1 and triplet excited state T_1 [3]. The strategy to achieve such characteristics is to employ both donor and acceptor moieties in a single molecular structure.

In this work, we present benzophenone-based emitters bearing donor-acceptor-donor electronic structure. Benzophenone is known to be a stable acceptor [4]. The donor moieties such as tetrahydrocarbazole, phenoxazine and dihydrodimethyacridine were chosen due to their favourable HOMO orbitals delocalization and electron donating ability [5]. The derivatives were obtained by two-step synthesis procedure. The first step was bromination of the benzophenone and the second step was Pd-catalyzed Buchwald-Hartwig coupling of 3, 3'-dibromobenzophenone with corresponding donor fragments [6].

Thermal, photophysical, electrochemical and photoelectrical properties of the materials will be reported.

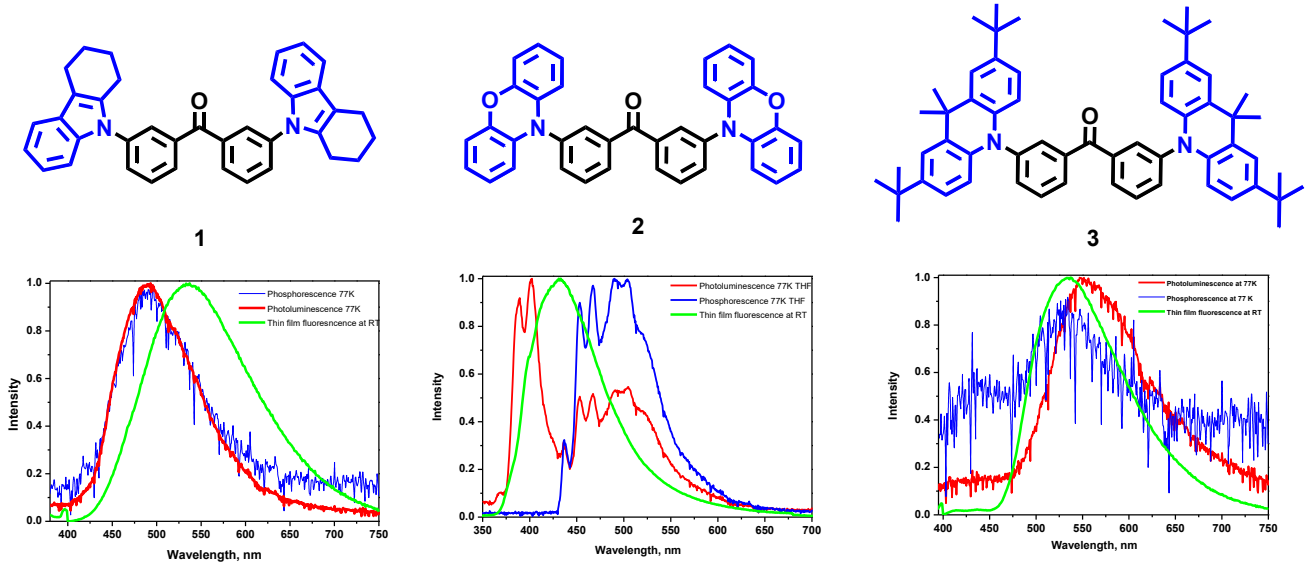

Fig.1. The structures of the electroactive compounds and their photoluminescence and phosphorescence spectra.

Acknowledgment. This research was funded by the European Social Fund according to the activity 'Improvement of researchers' qualification by implementing world-class R&D projects' of Measure No. 09.3.3-LMT-K-712.

---

[1] H. Sasabe, J. Kido, Multifunctional Materials in High-Performance OLEDs: Challenges for Solid-State Lighting, Chemistry of Materials **23**, 621–630 (2011).

[2] S-Y. Lee, T. Yasuda, Y-S. Yang, Q. Zhang, Ch.Adachi, Luminous Butterflies: Efficient Exciton Harvesting by Benzophenone Derivatives for Full-Color Delayed Fluorescence OLEDs, Angewandte Chemie **126**, 6520 –6524 (2014).

[3] T. Komino, H. Nomura, T. Koyanagi and C. Adachi, Suppression of Efficiency Roll-Off Characteristics in Thermally Activated Delayed Fluorescence Based Organic Light-Emitting Diodes Using Randomly Oriented Host Molecules, Chemistry of Materials **25**, 3038–3047 (2013).

[4] S. Aloise, C. Ruckebusch, L. Blanchet, J. Rhaut, G. Buntinx, J.-P. Huvenne, The Benzophenone S1(n,π*) → T1(n,π*) States Intersystem Crossing Reinvestigated by Ultrafast Absorption Spectroscopy and Multivariate Curve Resolution, Journal of Physical Chemistry A **112**, 224 – 231 (2008).

[5] R. Komatsu, H. Sasabe, Y. Seino, K. Nakao and J. Kido, Light-blue thermally activated delayed fluorescent emitters realizing a high external quantum efficiency of 25% and unprecedented low drive voltages in OLEDs, Journal of Materials Chemistry C **4**, 2274–2278 (2016).

[6] G. D. Vo, J. F. Hartwig, Palladium-Catalyzed Coupling of Ammonia with Aryl Chlorides, Bromides, Iodides, and Sulfonates: A General Method for the Preparation of Primary Arylamines, Journal of American Chemical Society **131**, 11049-11061 (2009).

FORMULATION AND PREPARATION OF OPHTALMIC FILMS BY USING NATURAL AND SYNTHETIC POLYMERS

Aiste Kunciute[1], Alisa Palaveniene[1]

[1] Department of Polymer Chemistry and Technology, Kaunas University of Technology, Lithuania
aiste.kunciute@ktu.edu

Development of functional materials, such as polymeric films for wound healing, is an important area of investigation in Europe and beyond. In biomedical applications, the solutions for skin or mucous healing mostly depend on location and cause of injury. One of the specific wound type that attracted this investigation is corneal trauma [1–3].

Most of current solutions for closure of corneal defects, such as Tutoplast® (collagen-based product) and glycerine-preserved corneas, result in temporary poor vision, while ocular adhesives (fibrin-based and cyanoacrylate derivatives) are not suitable for closure of large defects.

Non-invasive protection of cornea by using biocompatible polymeric films is one of a modern solution for corneal injury repair, because it could form a mechanical barrier against external contamination and at the same time enhance cell growth. Moreover, specific physical-chemical parameters, such as appearance and transmittance, equilibrium water content, protein adsorption on a film surface and surface morphology, are highly important and applicable to this invention.

Chitosan-based, chitosan/gelatine-based and acrylate-based films for corneal repair applications were developed and examined. For the preparation of non-soluble chitosan film, prepared chitosan-based hydrogels were immersed in different solutions: (i) 2% NaOH in distilled water, (ii) 2% NaOH in 96% ethanol or (iii) 96% ethanol. For the preparation of crosslinked chitosan/gelatine film, prepared chitosan/gelatine hydrogel was immersed in 0.025% glutaraldehyde for 10, 20 and 30 min. For the preparation of acrylate-based film, 2.7 mL of hydroxyethyl methacrylate (HEMA) was mixed with 2 mL of distilled water and 10 µL of ethylene glycol dimethacrylate (EGDMA) and using diphenyl(2,4,6-trimethylbenzoyl)phosphine oxide as photoinitiator. Optical clarity was characterised by measuring the transmittance spectra using UV-vis spectrophotometer (600 nm). Transmittance of the selected samples was 0.112 ± 0.002, 1.58 ± 0.042 and 0.013 ± 0.001 for chitosan-based film, immersed in 2% NaOH in 96% ethanol solution (Ch-1), chitosan/gelatine film, immersed in 0.025% glutaraldehyde solution for 10 min (ChG-1) and HEMA-based films (HEMA-1), respectively (Fig. 1). Thickness of the prepared samples was 0.797 ± 0.015 mm, 0.980 ± 0.02 mm and 0.205 ± 0.01 mm, respectively. Neutralisation of 1% chitosan hydrogel with 2% NaOH in 96% ethanol mixture contributed to the transparency of chitosan film for corneal trauma application (comparing with chitosan/gelatin crosslinked film), while transparency of acrylate-based film was almost 100%.

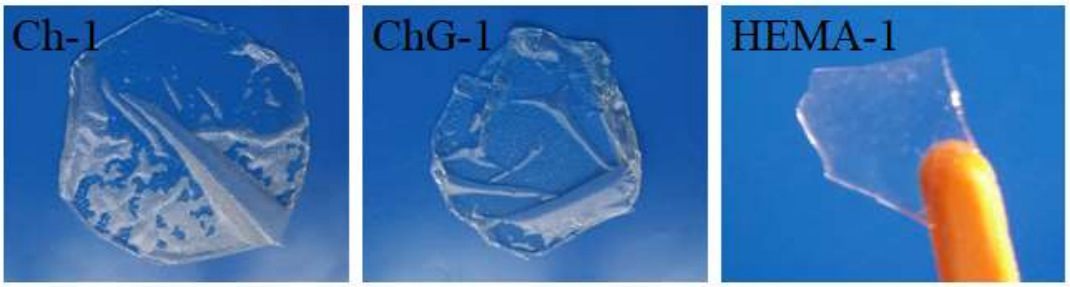

Fig. 1. Macroscopic images of prepared polymeric films

Current research shows that transparent chitosan-based films could be developed. However, further investigation of prepared films is required. Prepared polymer-based films are potential applicants for corneal trauma repair.

2014-2020 EUROPOS SĄJUNGOS FONDŲ INVESTICIJOS LIETUVOJE

The financial support from the Research Council of Lithuania in the form of grant Nr. 09.3.3-LMT-K-712-03-0025 is gratefully acknowledged.

[1] E.Caló, V. V. Khutoryanskiy, Biomedical applications of hydrogels: A review of patents and commercial products, European Polymer Journal **65**, 252-267 (2015).
[2] P. McNutt, T. Hamilton, M. Nelson et al., Pathogenesis of acute and delayed corneal lesions after ocular exposure to sulfur mustard vapor, Cornea **3**, 280-290 (2012).
[3] R. I. Haddadin, G. K. Vora, J. Chodosh, Corneal trauma following keratoplasty, International Ophthalmology Clinics **4**, 23-32 (2013).

Control and diagnosis of low-energy electronic transitions in BiSn systems

Alexander S. Fedotov

Faculty of Physics, Belarusian State University, Belarus
fedotov.alehandro@gmail.com

Semi-metals and narrow-gap semiconductors have found lot of applications in various branches of modern electronics: thermoelectricity, THz generation, infrared emitters, etc. This makes crucial for scientific community to understand the various factors (like temperature and doping) affecting the electronic properties in this class of materials. However, current-day knowledge of temperature, doping and morphology effect on those properties needs further development. With Bi-based alloys as model material we demonstrated how the modern advantages in galvanomagnetic measurements processing allow the better understanding the doping effect on charge carrier parameters.

The modern quantitative mobility spectrum analysis (QMSA) methods use resistivity and Hall data in all available range of magnetic fields and require minimum external input parameters for the computational procedure. This makes QMSA very promising tool for investigation of electronic states in diluted BiSn alloys. The result of QMSA procedure are extracted mobilities and concentrations (the last allow tracking of band extrema on energy scale).

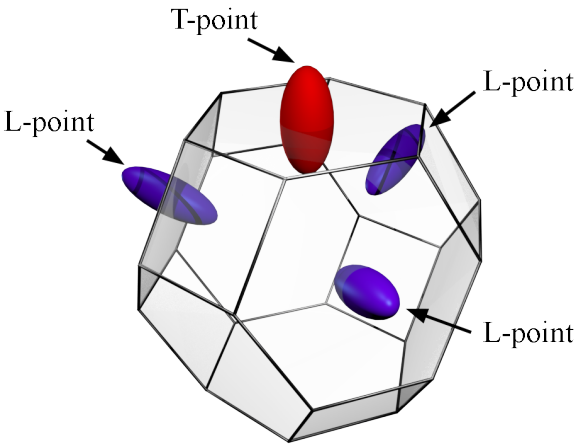

Fig. 1. Fermi surface of Bi-based compound with electronic pockets at L-points and hole pocket at T-point.

The positions of Fermi level relative to extrema of electronic pockets were determined from statistical physics integrals

$$n = \int_0^\infty \frac{8\pi\sqrt{2}}{h^3} m^{3/2} \frac{\sqrt{E}}{e^{\frac{E-\zeta}{k_B T}}+1} dE, \tag{1}$$

where m is the effective mass, ζ is Fermi level position, T is temperature, k_B, h are Boltzmann's and Planck's constants respectively.

It was shown that band overlap E_o decreases in BiSn with the increase of Sn concentration and that E_o for samples with Sn concentration $x \geq 0.02$ at. % reduces with temperature (until zero overlap for $x = 0.08$ at. %, $T = 300$ K). These changes in electronic band structure mean, in fact, the transition of BiSn system from semimetal to the narrow-gap semiconductor.

We acknowledge financial support by the Belarusian Republican Foundation for Fundamental Research in the framework of project F16M-067 "Structure and magnetoresistive characteristics of Bi thin films", as well as by the German Academic Exchange Service (Forschungsstipendien - Kurzstipendien, 2016, nr. 57214227).

[1] J. Antozewski, L. Faraone Quantitative mobility spectrum analysis (QMSA) in multi-layer semiconductor structures, Opto-electronics Review **12(4)**, 347-352 (2004).

FLUCTUATION CONDUCTIVITY, PSEUDOGAP AND THERMO-ELECTRIC POWER IN SINGLE CRYSTAL AND POLYCRYSTALLINE $Ho_{1.4}Ba_{2.4}Cu_{3.4}O_{7-\delta}$ – CeO_2(1wt%) SUPERCONDUCTORS

Eugene V. Petrenko[1], Andrei L. Solovjov[1], Lyudmila V. Omelchenko[1], Victor B. Stepanov[1], Zhang Guo-Ping[2]

[1] B.Verkin Institute for Low Temperature Physics and Engineering of NAS of Ukraine,
47 Nauky Ave., Kharkiv, 61103, Ukraine
[2] Fudan University, Chinese Academy of Sciences, 220 Handan Rd., Yangpu District, Shanghai, China
petrenko@ilt.kharkov.ua

Superconductivity in high-temperature superconductors (HTSC's or cuprates) can be understood by studying their properties in the normal state, which are well known to be very peculiar. The most intriguing property is a pseudogap (PG) observed mostly in oxygen deficient cuprates below any representative temperature $T^* >> T_c$ [1]. At present, it is believed that the proper understanding of PG physics has to offer the possibility to decipher the basic pairing mechanism in the HTSC's which still remains uncertain.

For the first time, temperature dependences of the fluctuation conductivity $\sigma'(T)$, pseudogap parameter $\Delta^*(T)$ and thermoelectric power S(T) have been studied both for the single crystal and the polycrystalline $Ho_{1.4}Ba_{2.4}Cu_{3.4}O_{7-\delta}$ – CeO_2(1wt%) superconductors.

It is shown that in the single crystal near T_c $\sigma'(T)$ is well described by the 3D Aslamasov–Larkin (AL) and 2D Maki–Thompson (MT) fluctuation theories. At the same time, in the polycrystalline sample above the 3D-2D crossover temperature T0 $\sigma'(T)$ is solely described by the 2D-AL equation. The result points out the presence of fluctuating Cooper pairs (FCPs) in the samples, which are believed to be responsible for the PG formation.

PG analysis allows us to trace the peculiarities on $\Delta^*(T)$ both in single crystal and polycrystalline samples. Moreover, obtained $\Delta^*(T)$ parameters are found to correlate with results of the S(T) measurements. In the single crystal, $\Delta^*(T)$ exhibits the maximum around $T_{max} \approx 227$ K, below which $\Delta^*(T)$ demonstrates descending linear region. Interestingly, such $\Delta^*(T)$ behavior is typical for all magnetic superconductors [2]. Finally, below $T_{pair} \approx 156$ K $\Delta^*(T)$ acquires a shape usually observed in cuprate HTSC's. Accordingly, S(T) expectedly changes its character at $T = T^*$ and begins to decrease. After further cooling it demonstrates the plateau at (172−156) K. Below Tpair, where FCPs have to appear, S(T) starts to decrease more rapidly. Finally, S(T) descends more intensively below T_0, where FCP behave like quasi-SC pairs.

In the polycrystalline sample, $\Delta^*(T)$ has a shape, typical for nonmagnetic superconductors, with a wide maximum at T_{pair} ~120 K, and S(T) shows no peculiarities T^*. Down to T_{pair}, S(T) increases linearly, which is typical for cuprates. Below T_{pair}, S(T) unexpectedly increases, showing a maximum at about T_{01}. But, like in the case of the single crystal, below T_{01} S(T) rapidly decreases most likely due to formation of the SC fluctuations in the sample.

[1] A. L. Solovjov, V. M. Dmitriev, Low Temp. Phys. 35, 169 (2009).
[2] A. L. Solovjov, L. V. Omelchenko, A. V. Terekhov, K. Rogacki, R. V. Vovk, E. P. Khlybov and A. Chroneos, Materials Research Express 3, 076001 (1-13) (2016).

STUDY OF CARRIER DRIFT TRANSIENTS IN ORGANIC COMPOUND BF-10 LAYERS

Kornelijus Pūkas, Tomas Čeponis, Eugenijus Gaubas

Vilnius University, Faculty of Physics, Institute of Photonics and Nanotechnology, Lithuania
kornelijus.pukas@ff.stud.vu.lt

Transient current technique (TCT) is based on the analysis of the current pulse durations and shapes which arise from the non-equilibrium carrier capture and drift processes within the electric field region inside the material. Considerations of TCT, based on Shockley-Ramo theorem (SRT) model, are widely applied for direct evaluation of the excess carrier drift mobility [1].

In this work, carrier drift mobility in the bifluorene BF-10 organic compound layers of 1 μm thickness have been investigated by recording of current transients using parallel (with the same oriented electric field and impinging laser beam) profiling regime and optical injection of carrier domains. The capacitor type device structures were formed by deploying indium-tin oxide (ITO) electrodes, transparent for excitation light. Profiling of the capacitor type organic device has been performed by varying applied voltage in the range from 10 to 60 V. Ultraviolet (354 nm) laser pulses of 400 ps duration were used to inject excess carrier sheets within inter-electrode gap.

Changing polarity of voltage on electrodes enabled us to separate the packet of drifting carriers, - either holes or electrons (Fig. 1). The initial component of a current transient is ascribed to a bipolar drift (Fig. 1b). Here, a sub-domain of the excess spatially separated carriers, which polarity is relevant to be attracted to a front electrode, rapidly moves to this electrode and induces charge on electrodes, according to SRT. This induced charge modifies a drift of the second sub-domain by slowing it. While the current variations in the tail stage of a transient are associated with the monopolar drift of a sub-domain of carriers which are attracted to a rear electrode (Fig. 1a). The current, determined by this monopolar drift of a slow sub-domain, decreases due to carrier capture to traps, and this carrier density reduction can be partially compensated by field enhanced re-emission (Poole-Frenkel effect) of trapped carriers. Nevertheless, current pulse ends when the slow domain reaches a rear electrode, and this instant can be clarified from the rear kink within current variation curve (Fig. 1a). Both components of a current pulse, associated with the hole and electron drift, have been clearly observed for the bias voltage values close to 60 V, as illustrated in Fig. 1.

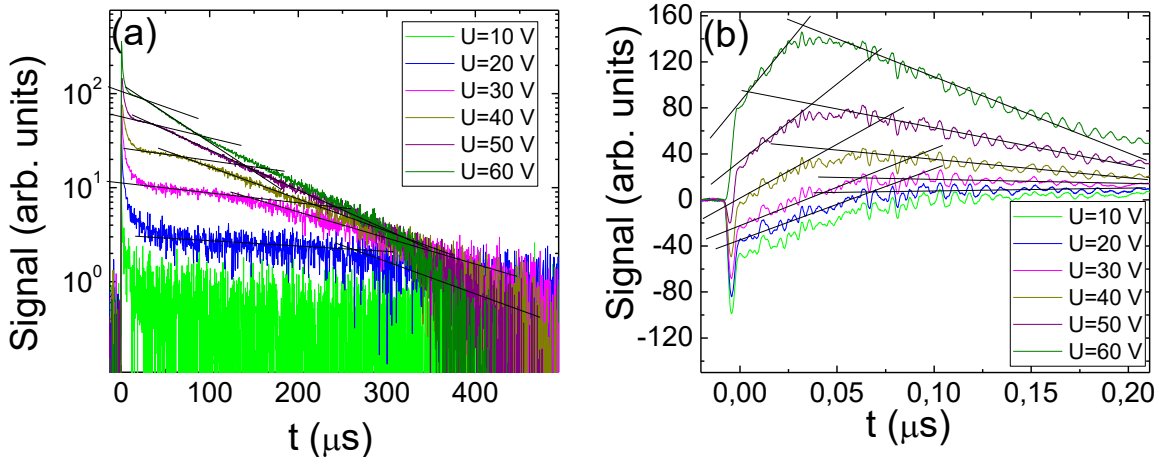

Fig. 1. Variations of current transients recorded by changing bias voltage (a) and the initial component (b) of current transients ascribed to the bipolar drift of the excess carrier packets where holes drag electrons.

The characteristic transit times of holes and electrons have been extracted from these current transients. The acting fields can be estimated from simulations of these transients using the SRT model. Then, the drift mobility and carrier lifetime parameters have been evaluated. Field dependent variations of these parameters in BF-10 capacitor-type structure will be discussed.

[1] E. Gaubas, T. Ceponis, D. Meskauskaite and N. Kazuchits, Profiling of current transients in capacitor type diamond sensors, Sensors **15**, 13424-13458 (2015).

PSEUDOGAP IN THE OPTIMALLY DOPED $YBa_2Cu_3O_{7-\delta}$ SINGLE CRYSTALS UNDER PRESSURE UP TO 1 GPA

Lyudmila Omelchenko[1], Andrei Solovjov[1], Eugene Petrenko[1], Ruslan Vovk[2]

[1]B.Verkin Institute for Low Temperature Physics and Engineering of NAS of Ukraine,
Nauky Ave., 47, Kharkiv 61103, Ukraine
[2]Physics Department, V. Karazin National University, 4 Svoboda Sq., 61077 Kharkiv, Ukraine
omelchenko@ilt.kharkov.ua

One of the most intriguing properties of cuprates is the pseudogap [1] which is opening at some characteristic temperature $T^* >> T_c$. By definition, pseudogap is a state of matter characterized by a reduced (but nonzero) density of electronic states at the Fermi level [2]. It should be stressed that the fundamental difference of the pseudogap state from the superconducting one is that in the latter the superconducting gap is opening and density of electronic states is equal to zero. It is expected that the correct understanding of the PG nature will allow one to shed light on the superconducting pairing mechanism in high temperature superconductors which remains debatable so far. In particular, this is important for searching for novel superconductors with yet higher T_c's.

The influence of the hydrostatic pressure P up to 0.95 GPa on the excess conductivity $\sigma'(T)$ and the pseudogap $\Delta^*(T)$ in optimally doped $YBa_2Cu_3O_{7-\delta}$ single crystals (T_c = 91.1 K at ambient pressure) is investigated by electrical resistivity measurements. A pronounced enhancement of the pseudogap under pressure of $d\ln\Delta^*/dP = 0.32$, which is only a factor of 1.12 smaller than in slightly doped single crystals, is revealed for the first time. This implies a somewhat more moderate increase of the coupling strength in optimally doped cuprates with increasing pressure. Simultaneously, the ratio $2\Delta^*(T_c)/k_BT_c = 5$ at P j 0 GPa, which is typical for high temperature superconductors with strong coupling, increases by 16% with increasing pressure. At the same time, the pressure effect on T_c is minor: $dT_c/dP = +0.73$ K·GPa^{-1}, whereas $d\ln\rho/dP = (-17 \pm 0.2)$ %GPa^{-1} is comparable with that in lightly doped YBCO single crystals. This suggests that the mechanisms of the pressure effect on $\rho(T)$ and T_c are noticeably different. Independently of pressure, near T_c, $\sigma'(T)$ is well described by the Aslamazov - Larkin (3D - AL) and 2D Hikami - Larkin fluctuation theories, exhibiting a 3D - 2D crossover with increasing temperature [1, 3]. However, the temperature interval $T_c < T < T_{01}$, in which $\sigma'(T)$ obeys the classical fluctuation theories, is exceptionally narrow (≈1.16 K). Nevertheless, a peculiarity at the temperature T_{01}, up to which the wave function phase stiffness in the superconductor is maintained, is clearly observed in the dependence $\Delta^*(T)$. Below T_{01} a fast growth of $\Delta^*(T)$ is revealed for the first time [3]. It can be associated with a sudden increase of the superfluid density, ns, that is the density of fluctuating Cooper pairs (short-range phase correlations) forming in the sample when T approaches T_c.

[1] A. L. Solovjov, Fluctuation conductivity and pseudogap in high-temperature YBCO superconductors, Low Temp. Phys. **35**, 227 – 264 (2009).
[2] A. L. Solovjov Superconductors - Materials, Properties and Applications. Chapter 7: Pseudogap and local pairs in high-T_c superconductors, Rijeka.,137 (2012).
[3] A.L. Solovjov, L.V. Omelchenko, R.V. Vovk et al, Hydrostatic-pressure effect on the pseudogap in slightly doped $YBa_2Cu_3O_{7-\delta}$ single crystals, Physica **B**., 493, 58 – 67 (2016).

LUMINESCENCE IN TWO-COMPONENT SILICATE GLASS DOPED WITH RARE EARTH IONS FOR SOLID-STATE WHITE LIGHT SOURCES

Vaida Marčiulionytė[1], Augustas Vaitkevičius[1], Yevgeny Tratsiak[2], Ekaterina Trusova[3], Mikhail Korjik[3], Gintautas Tamulaitis[1]

[1] Institute of Photonics and Nanotechnology and Semiconductor Physics Department, Vilnius University, Lithuania
[2] Research Institute for Physical Chemical Problems, Belarusian State University, Belarus
[3] Research Institute for Nuclear Problems, Belarusian State University, Belarus
vaida.marciulionyte@ff.stud.vu.lt

Reliable and more efficient solid-state light source technologies are increasingly in demand, especially for cost-sensitive applications. So far, blue LED chip and down converting phosphor emitting in green-yellow range is the most common approch for white light generation with LEDs. However, thermal degradation enhanced at high emission power and poor color rendering limits the use of the phosphor-converted white LEDs in more widespread lighting applications. Fortunately, silicate glass phosphors exhibit superior thermal performance and can take advantage of mature glass processing technologies significantly reducing their cost. The color rendering properties of glass phosphors can be improved by altering the composition as well as doping of the glass host. As a result, glass phoshors in combination with blue LEDs are a suitable solution in comercial production of high brightness solid-state white light sources.

We investigated heat treated two-component silicate glasses with composition $BaO\text{-}2SiO_2$ and $SrO\text{-}2SiO_2$ doped with Ce, Dy, Eu, and Tb activators. After glass production, $BaO\text{-}2SiO_2$ was further treated at 850 °C, 900 °C and 950 °C for 1 hour. $SrO\text{-}2SiO_2$ glass was heat treated at 800 °C, 850 °C and 900 °C for 1 hour. The samples were produced in Belarusian State Technical University.

The light emission properties of the samples under study were investigated by measuring their photoluminescence (PL) spectra. The measurements were performed using microscope system WITec Alpha 300 S operated in confocal mode. The PL spectra were recorded using a spectrometer with a thermoelectrically cooled CCD camera. CW laser diode emitting at 405 nm (*ALPHALAS*) was exploited for excitation. All measurements were performed at room temperature.

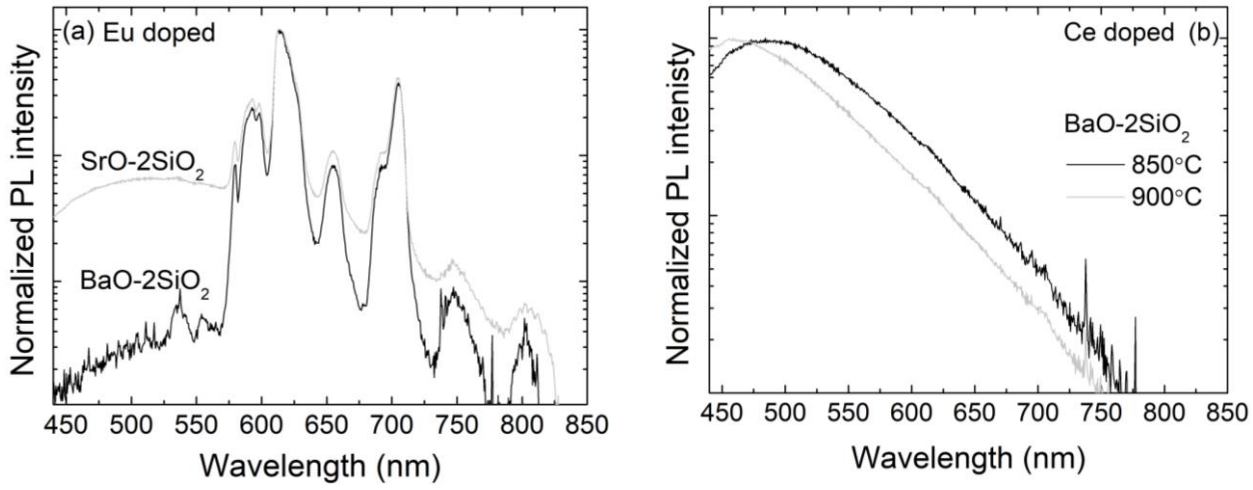

Fig. 1 Spatially averaged photoluminescence spectra of $BaO\text{-}2SiO_2$ and $SrO\text{-}2SiO_2$ glasses doped with Eu (a) and of Ce doped $BaO\text{-}2SiO_2$ glasses after thermal treatment at different temperatures (indicated) (b).

Our results show that PL emission from two-component silicate glasses doped with rare earth ions is affected by glass composition and thermal treatment conditions. As seen in Fig. 1 (a), where the characteristic spectra from Ba and Sr glasses doped with Eu are presented, the ratio of emission from Eu^{2+} and Eu^{3+} ions can be controlled by changing the composition of the glass matrix. This is probably caused by Eu ions undergoing additional reduction during the annealing process. The PL spectra presented in Fig. 1 (b) show that the temperature during thermal treatment can cause different internal structure of the glass resulting in different emission spectra when comparing with that in the untreated glass. We also performed rapid aging experiments showing that the glass composition and the annealing temperature have an affect on long term stability of the silicate glass. Color coordinates calculations have also been performed.

The results show that the PL spectrum is tunable by varying the glass composition, controlled doping, and thermal treatment. This confirms that two component silicate glasses are prospective candidates for improved phosphor-based white LEDs.

INFLUENCE OF A LOW GAMMA-RADIATION FLUX ON ELECTRICAL POLARIZATION OF CdZnTe CRYSTALS

Oleksii Poluboiarov[1], Oleg Chugai[2], Oleksii Voloshin[2]

[1] Department for Nonlinear Optical Crystals, Institute for Single Crystals of NAS of Ukraine, Ukraine
[2] Faculty of Aircraft Radio Systems, N.E. Zhukovsky Kharkiv National Aerospace University, Ukraine
alexei.poluboyarov@gmail.com

Earlier [1], we ascertained that exposure to ultra-low exposure doses (D = 10–100 R) of gamma-radiation can cause a significant change in low-frequency values of the real ε′ and imaginary ε″ parts of the complex dielectric permittivity ε* of cadmium-zinc telluride crystals grown from the melt. Therefore, in the present work we have investigated the variation of ε′ and ε″ for the same crystals under the exposure of a low gamma-ray flux.

$Cd_{1-x}Zn_xTe$ (x = 0,1–0,2) crystals were grown from the melt by high-pressure Bridgman method (HPB). Specimens with orthogonal faces (5×5×5 mm^3 in size) were made from different parts of crystalline ingots. Real and imaginary parts of specimens' complex dielectric permittivity ε* were measured in the frequency range of 10^1–10^4 Hz. ^{137}Cs isotope with the activity of 1 μCi was used as the source of gamma-radiation, the exposure dose rate of radiation was nearly 700 μR/h.

It is ascertained that under the exposure of gamma-radiation with the indicated dose rate, significant changes (up to 30%) in the both parts of the complex dielectric permittivity are often observed. Changes in the quantities were observed of both positive and negative signs. The regularities of the changes in the investigated quantities without taking into account their sign are revealed.

The change in crystals electrical polarization under the exposure of a low gamma-ray flux is explained involving the concepts of the metastable point defects reconstruction. Moreover, the initial state of the entire system of point defects is determined by the deviation of the crystal composition from the stoichiometric. These conclusions are confirmed by the results of a study of the localized states energy spectrum by scanning photodielectric spectroscopy method [2].

[1] V.K. Komar, S.V. Sulima, O.N. Chugai et al. Effect of ionizing radiation in ultrasmall doses on dielectric properties of CdZnTe crystals with anomalously high polarizability. Tech. Phys. Lett. **37**, 589-596 (2011).

[2] V. K. Komar, V. P. Migal, O. N. Chugai et al. Investigation of localized states in cadmium zinc telluride crystals by scanning photodielectric spectroscopy. Appl. Phys. Lett. **81**, 4195-4197 (2002).

TCAD SIMULATIONS OF FUNCTIONAL CHARACTERISTICS FOR SILICON LOW GAIN AVALANCHE DETECTORS

Kornelijus Pūkas[1], Lukas Dundulis[2], Juozas Vyšniauskas[2], Eugenijus Gaubas[1]

[1]Vilnius University, Faculty of Physics, Institute of Photonics and Nanotechnology, Lithuania
[2]Vilnius University, Faculty of Physics, Institute of Applied Electrodynamics and Telecommunications
kornelijus.pukas@ff.stud.vu.lt

Silicon sensors with charge multiplication layer, known as Low Gain Avalanche Detectors (LGAD), are anticipated to be the functional particle detectors after heavy irradiations by hadrons. The concept of internal gain due to charge multiplication is addressed to an enhancement of the signal-to-noise ratio (SNR). The LGAD detectors become the most promising devices for applications in high energy physics experiments where harsh radiation environments, such as the inner detectors of Large Hadron Collider (LHC), are met.

Conventional a P-type LGAD consists of $N^+PP^-P^+$ layers with P-well formed by deep diffusion of boron (B) into P^- layer. However, it was shown that an effect of the "acceptor removal" occurs in irradiated LGAD sensors which causes the loss of internal gain [1]. Radiation damage partially removes a boron from the multiplication layer, thereby reducing the effective doping concentration. Acceptor removal is consistently described by relation:

$$N(\Phi) = N_0 \cdot e^{-b\Phi}, \quad (1)$$

where N is the dopant concentration (acceptor density), Φ is the irradiation fluence, and the parameter b which is a function of N_0. This detrimental effect might be partially suppressed by forming the N-well ($P^+NN^-N^+$) Si structure with the phosphorus doped an epitaxial (N-well) layer. In this work, the results of simulations of the operation characteristics for the P-type and N-type LGAD devices are reported.

A functionality of LGAD device has been validated by digital experiments performed using of Technology Computer-Aided Design (TCAD) algorithms and the Drift-Diffusion (DD) approach. Simulations have been carried out employing a Sentaurus Device software platform. It has been obtained that the shape and duration of current pulses is quite different (Fig. 1) in N- and P-type Si LGAD's mainly due to the difference of the ionization coefficients. These coefficients are approximately 10 times greater for electrons than for holes ($\alpha_e \cong 10 \cdot \alpha_h$). Nevertheless, the collected charge is almost the same for P-type (Fig. 1a) and N-type (Fig. 1b) Si devices if radiation traps are ignored in simulations.

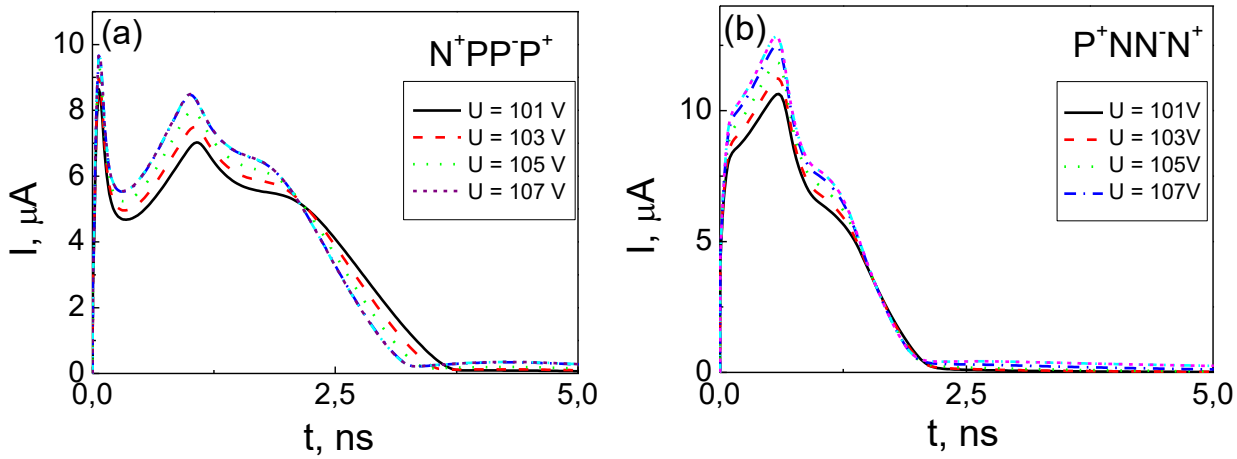

Fig. 1. Variations of current transients simulated by changing a bias voltage for P-type (a) and N-type (b) Si LGAD structures.

A probability of carrier trapping during their drift increases with irradiation fluences assumed in simulations. It has been shown that thickness of the active layer within a sensor plays an important role in charge collection. Nevertheless, the rather thin (~50 μm) modelled LGAD sensors appear to be functional and exhibit a proper charge collection efficiency due to the carrier density increase through the internal amplification, proportional to the radiation injected secondary carrier pairs. It has been demonstrated that the rather low bias voltage, applied to LGAD, is sufficient to get proper charge collection. The impact of radiation induced traps which affect the detector current and charge collection efficiency will be discussed.

[1] G. Kramberger, et al, Radiation effects in Low Gain Avalanche Detectors after hadron irradiations, Journal of Instrumentation **10**, P07006 (2015).

INVESTIGATION OF ELECTRICAL PROPERTIES IN THE MAGNETIC FIELD OF CERAMICS BASED ON ZnO DERIVED BY IRON

Aliaksei Pashkevich[1,2], Krystsina Kirylchyk[2], Viktoryia Halauchuk[2]

[1]Institute for Nuclear Problems of Belarusian State University, Republic of Belarus
[2]Faculty of Physics, Belarusian State University, Republic of Belarus
alexei.paschckevich@yandex.by

Nowadays, great attention is paid to the search for new materials based on wide-gap oxides, as well as to studying their structure and properties for the purpose of application in various areas of the radioengineering, electronics and optoelectronics [1,2]. Even compounds based on such studied oxide as ZnO, obtained by ceramic technology, are not fully understood. The aim of this work is to study the electrical properties of ZnO-based ceramics when they are doped with iron using various types of Fe_xO_y iron oxide alloying agents.

Samples based on ZnO prepared by the two-stage synthesis method were obtained by conventional ceramic technology. ZnO and Fe_xO_y (FeO, Fe_2O_3, Fe_3O_4) powders were used as initial components. In the ceramics studied, we used the stoichiometric relation $(Fe_xO_y)_{10}(ZnO)_{90}$, where the mass of the iron oxide powders corresponded to 10 wt. %.

Electronic transport properties of ceramics in a magnetic field were studied by measurements of electrical conductivity and Hall effect that allowed to evaluated concentrations and Hall mobility of charge carriers. The character of temperature and field dependences pointed to strong inhomogeneity of the ceramics and large-scale potential fluctuations contribution to charge transfer [3-5].

The decrease in the concentration and change of temperature slop of n(T) (Fig.1a) indicated that main charge carriers in doped samples were originated from the deeper donor level than in non-doped ZnO.

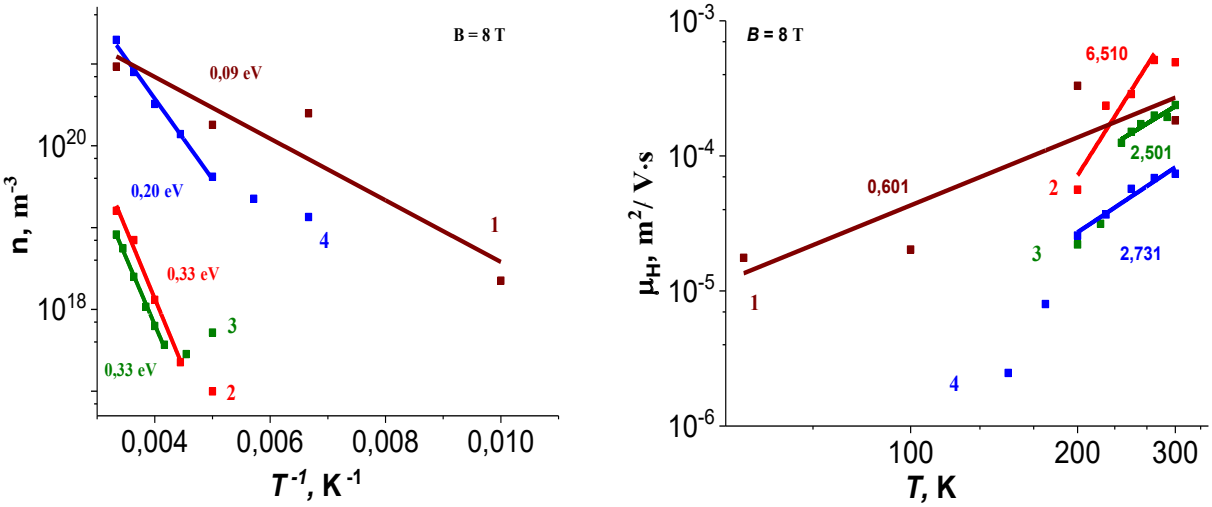

(a) (b)

Fig. 1. Temperature dependences of the (a) concentration n of charge carriers in the Arrhenius coordinates and (b) Hall mobility μ_H in the temperature range 150-300 K of ZnO (1) and $(Fe_xO_y)_{10}(ZnO)_{90}$ (2-4) ceramics: 2 - $(FeO)_{10}(ZnO)_{90}$; 3- $(Fe_2O_3)_{10}(ZnO)_{90}$; 4 - $(Fe_3O_4)_{10}(ZnO)_{90}$ under the action of a magnetic field.

The Hall mobility μ_H(T) in doped ceramics (Fig. 1b) exponentially rises with temperature. The slope of μ_H(T) in logarithmic coordinates (Fig.1b) rises with the increase of inhomogeneity. These observations indicate a power-law character of the Hall mobility temperature dependence typical for stronglyinhomogeneous materials [3].

[1] *Ayman Sawalha, M.Abu-Abdeen, A. Sedky*, Electrical conductivity study in pure and doped ZnO ceramic system, Physica B **404** (2009).
[2] A.S. Fedotov, V. Shepelevich, S. Poznyak, L. Tsybulskaya, A. Mazanik, I. Svito, S. Gusakova, P. Zukowski, T.N. Koltunowicz, Simulation of polycrystalline bismuth films Seebeck coefficient based on experimental texture identification, Materials Chemistry and Physics **177**, 413 – 416, (2016).
[3] A. Ya. Shik, Kinetic phenomena in inhomogeneous semiconductors, Non-homogeneous and impurity semiconductors in external fields, 22-40 (Chisinau: Shtiintsa, 1979).
[4] N. Mott, E. Davis, Electronic processes in non-crystalline substances (Moscow: Nauka, 1982).
[5] *B.I. Shklovskii, A.L. Efros.*Electronic Properties of Doped Semiconductors (Berlin, Springer, 1984).

RAMAN SPECTROSCOPY OF EPITAXIAL SiC FILMS GROWN ON SiGe/Si SUBSTRATES

Mikhail Lobanok, Mikalai Piatrou, Andrei Novikau, Stanislau Prakopyeu, Peter Gaiduk

Department of Physical electronics and nanotechnology, Belarusian State University, Minsk
mishalobanok@gmail.com

Silicon carbide (SiC) is a semiconducting material with a number of unique characteristics, such as chemical, thermal and radiation resistance, optically favorable band structure, elevated electron mobility and high break-down voltage. SiC has been intensively investigated all over the world for a long time, however till now it has too narrow range of applications in electronics. This is mainly due to a range of problems connected to defect-free growth of bulk SiC and production of wafers; as a result, the electronic-grade SiC substrates are too expensive for commercial mass-production. Epitaxial SiC films on silicon substrates have better prospects for electronic applications, however the growth of SiC/Si structures faces the problems of large lattice mismatch and very different thermal expansion constants which result in formation of dislocations, twins and stacking faults. Raman scattering yilds the information on crystalline phases and structural quality of solids and can therefore be used for routine examination of thin SiC films and SiC/Si interfaces. In the present work we applied Raman scattering for investigation of epitaxial SiC thin films, grown on a Si substrate with thin SiGe buffer layer on the surface.

The Si-wafes of (100) surface orientation with and without surface-located $Si_{0,75}Ge_{0,25}$ bufer layers are used in this study. The samples are chemically cleaned and the surface is refreshed in 5% $HF+H_2O$ solution just before carbonization. The growth of SiC layer is proceeded in a tungsten-foil-based heating cell. The cell is constructed in a vacuum chamber and is equiped with a thermocouple and two gas inputs. The growth of SiC layers is carried out in a vacuum better then $1 \cdot 10^{-3}$Pa at the temperature of 1100°C during 10 min. The structural properties were investigated by Raman spectroscopy in backscattering configuration at room temperature with a Raman confocal microscope Nanofinder High End (Lotis TII, Belarus–Japan). Solid-state lasers at 473 or 532 nm were used for spectra excitation.Using chemical etching from the back side, the samples are prepared as thin SiC foils: This procedure allows to exlude influence of the substrate and to improve resolution of Raman spectra.

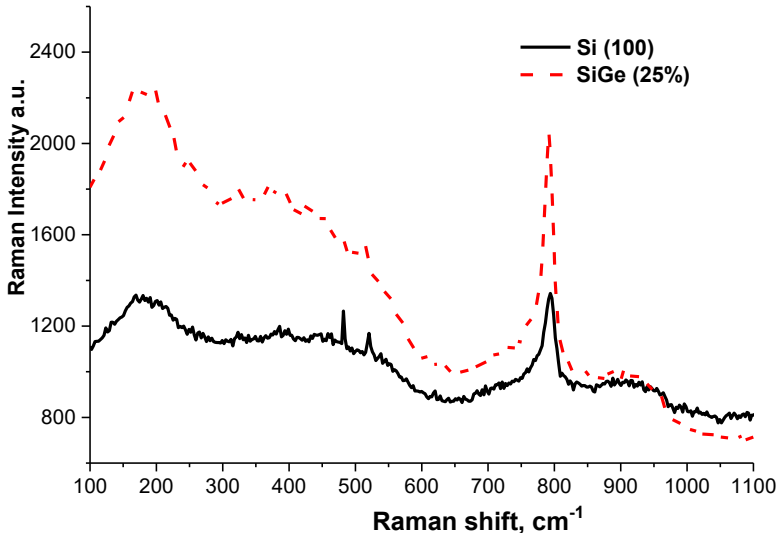

Fig. 1. Raman spectrum of epitaxial grown silicon carbide on top of SiGe\Si and Si substrate.

Analysis of raman spectroscopy spectra shows the presense of two silicon carbide phases which are 3C and 6H polytypes. It could be concluded that thermal treatment of the Si / SiGe buffer structure at 1100 ° C in a carbon atmosphere is accompanied by epitaxial growth of thin silicon carbide layers.

[1] S.A. Kukushkin, A.V. Osipov FTT (2008) V. 50, P. 1188-1195.
[2] Ferro G., "3C-SiC Heteroepitaxial Growth on Silicon: The Quest for Holy Grail"// Critical Reviews in Solid State and Materials Sciences, 40:56–76, 2015
[3] *I.G. Aksyanov, M.E. Kompan, I.V. Kulkova* FTT (2009) V. 52, P. 1724-1728.

RAMAN SPECTROSCOPIC STUDY ON THE STRUCTURE OF $La_{2-x}Dy_xMo_2O_9$

Giedrė Gaidamavičienė[1], Jonas Gadeikis[1], Tomas Murauskas[1], Žilvinas Tokarevas[2], Valdemaras Aleksa[2], Artūras Žalga[1*]

[1] Faculty of Chemistry and Geosciences, Institute of Chemistry, Vilnius University, Naugarduko Str. 24, LT-03225 Vilnius, Lithuania

[2]Faculty of Physics, Institute of Chemical Physics, Vilnius University, Saulėtekio ave. 3, LT-10257 Vilnius Vilnius, Lithuania

arturas.zalga@chf.vu.lt

In the past decades, fast oxygen-ion conductors attracted considerable attention of many scientists due to their unique properties and many relevant applications in solid oxide fuel cells, oxygen sensors and oxygen pumping devices [1]. One of the main requirements for such devices is to obtain high ionic conductivity. Nowadays, the most popular materials used as solid electrolytes are yttria-stabilized zirconia (YSZ), scandia stabilized zirconia (ScSZ) and gadolinium doped ceria (GDC). However, these electrolytes works at high temperatures (operating temperature 1,073 – 1,273 K) and limits the commercialization. Laccore et al. reported a promising LAMOX family materials, which exhibits high oxide-ion conductivity at intermediate operating temperature (873 – 973 K). Unfortunately, $La_2Mo_2O_9$ has some disadvantages, poor ionic conductivity at low temperatures and degradation in reducing environments [2].

$La_2Mo_2O_9$ exists in two crystalline forms: monoclinic α phase ($P2_1$) that occurs at room temperature with a very low conductivity and cubic β phase ($P2_13$), which is stabile above 853 K [3]. After phase transition the oxide-ion conductivity increases sharply reaching values higher than those of YSZ (0,06 S/m at 800°C) [4]. In order to stabilize β-phase of the lanthanum molybdate in low temperature and decrease the degradation in reducing environments, K^+, Sr^{2+}, Ba^{2+},Ca^{2+}, Bi^{3+}, V^{5+}, S^{6+}, Cr^{6+}, W^{6+}, and other ions can be used to suppress the phase transition to the α-phase.

In this paper, we report the environment friendly synthesis method to synthesize $La_{2-x}Dy_xMo_2O_9$. All La–Dy–Mo–O tartrate gel precursors for $La_{2-x}Dy_xMo_2O_9$ ceramics (x=0.005, 0.01, 0.025, 0.05, 0.1, 0.2) were prepared by an aqueous sol-gel technique in the sol-gel process using tartaric acid as a ligand. The obtained La–Dy–Mo–O tartrate gels were dried at 393 K and heat treated at 473 K, 673 K, 873 K, 1,073 K, 1,273 K and 1,473 K of temperatures, respectively. Raman spectroscopy and X-Ray diffraction were applied for the detailed investigation of the phase transition from the meta-stabile high-temperature cubic α-phase to the room-temperature α-crystalline modification. In addition, the suppression of the phase transition by addition of the dysprosium amount according to the vibrational, rotational, and other low-frequency modes in the $La_2Mo_2O_9$ was also studied.

[1] C. Tealdi, G. Chiodelli, L. Malavasi, G. Flor, Effect of alkaline-doping on the properties of La2Mo2O9 fast oxygen ion conductor, Journal of Materials Chemistry **14**, 3553-3557 (2004).

[2] L. Ge, K. Guo, L. Guo, Sinterability, reducibility, and electrical conductivity of fast oxide-ion conductors $La_{1.8}R_{0.2}MoWO_9$ (R=Pr, Nd, Gd and Y), Ceramics International **41**, 10208–10215 (2015).

[3] V. I. Voronkova, E. P. Kharitonova, and A. E. Krasil'nikova, Specific Features of Phase Transitions and the Conduction of $La_2Mo_2O_9$ Oxide-Ion Conducting Compound Doped with Vanadium, Crystallography Reports **55**, 276-282 (2010).

[4] A. Kežionis, D. Petrulionis, E. Kazakevičius, S. Kazlauskas, A. Žalga, R. Juškėnas, Charge carrier relaxation phenomena and phase transition in $La_2Mo_2O_9$ ceramics investigated by broadband impedance spectroscopy, Electrochimica Acta **213**, 306-313 (2016).

RAMAN AND INFRARED STUDY OF $La_{2-x}Y_xMo_2O_9$

Giedrė Gaidamavičienė[1], Žygimantas Gricius[1], Tomas Murauskas[1], Martynas Smolianskis[2], Valdemaras Aleksa[2], Artūras Žalga[1*]

[1]Faculty of Chemistry and Geosciences, Institute of Chemistry, Vilnius University, Naugarduko Str. 24, LT-03225 Vilnius, Lithuania

[2]Faculty of Physics, Institute of Chemical Physics, Vilnius University, Saulėtekio ave. 3, LT-10257 Vilnius Vilnius, Lithuania

arturas.zalga@chf.vu.lt

Oxide-ion conductors are used extensively for the electrochemical applications, such as oxygen separation, oxygen sensors, and the fuel cell component as electrolytes. As a new generation of power system, solid oxide fuel cells (SOFCs) have gained considerable attention due to their high efficiency of energy conversion and environmental compatibility [1]. Lately, the discovery of high ionic conductivity in a new family of oxides based on the parent compound lanthanum molybdate, $La_2Mo_2O_9$, known as LAMOX, has given a new and important input to the research in this field. To avoid the ionic conductivity decrease, induced by the phase transition, various types of substitutions on La site (K^+, Ca^{2+}, Sr^{2+}, Ba^{2+}, Pb^{2+}, Pr^{3+}, Y^{3+}, Dy^{3+}, Sm^{3+}, Eu^{3+}, Nd^{3+}, Gd^{3+}, Bi^{3+}) or Mo site (W^{6+}, Cr^{6+}, V^{5+}, Nb^{5+}, P^{5+}, S^{6+}) have been devoted to the stabilization of high conductive β-phase [1].

In this study the $La_{2-x}Y_xMo_2O_9$ (x=0.2; 0.1; 0.05; 0.01; 0.005) compounds from La–Y–Mo–O tartrate gel precursors by heat treatment were synthesized via aqueous sol-gel method. The substituted double oxides were additionally investigated by thermogravimetry (TG) and differential scanning calorimetry (DSC), X-ray diffraction (XRD), scanning electron microscopy (SEM), Fourier transform infrared (FT–IR) and Raman spectroscopy (RS) techniques. The TG/DSC analysis revealed both the possible decomposition processes of volatile organic parts in the La–Y–Mo–O tartrate gel precursors and the crystallization of cubic β-phase of the final material above 813 K of temperature. XRD results confirmed the formation of crystalline phases. SEM analysis showed the dependency of the surface morphology from the amount of yttrium substitution on La site in the final ceramics. Meanwhile, the FT–IR and RS investigations revealed possible vibrational, rotational, and other low-frequency modes in the analyzed oxides. Additionally, these techniques allowed to evaluate the substitution effect not only in the crystalline phases, but also in amorphous gels and their intermediate decomposition products.

[1] X. Liu, H. Fan, J. Shi, G. Dong, Q. Li, High oxide ion conducting solid electrolytes of bismuth and niobium co-substituted $La_2Mo_2O_9$, International Journal of Hydrogen Energy **39**, 17819-17827 (2014).

AQUEOUS SOL-GEL SYNTHESIS AND CHARACTERIZATION OF BARIUM DOPED LAMOX MATERIALS

Giedrė Gaidamavičienė, Emilija Užpurvytė, Artūras Žalga*

Faculty of Chemistry and Geosciences, Institute of Chemistry, Vilnius University, Naugarduko Str. 24, 03225 Vilnius, Lithuania

arturas.zalga@chf.vu.lt

The mixed oxides composed of lanthanum and transition metals still attract a great interest because of their interesting physico-chemical properties fundamentally and technologically [1]. Lanthanum molibdate $La_2Mo_2O_9$ and the doped compounds on its basis (LAMOX) attract much attention because of the high oxygen conductivity ($6 \cdot 10^{-2}$ Sm/cm), which was found by Lacorre group in 2000 year [2].

Fully crystalline and monophasic $La_{2-x}Ba_xMo_2O_{9-\delta}$ (x = 0.01, 0.1, 0.5, 0.1) materials were prepared by an aqueous tartaric acid-assisted sol-gel method after heat treatment at 823 K of temperature. Fully crystalline and monophasic materials were prepared after heat treatment at 823 K of temperature. In order to estimate the stability of obtained ceramics all samples were additionally sintered at 1273 K and 1473 K temperatures, respectively. The thermogravimetric analysis and differential scanning calorimetry (TG-DSC) were also used for both the investigation of decomposition processes of the synthesized gels and estimation of $La_2Mo_2O_9$ crystal phase formation, which is directly related with the phase transition at about 813 K of temperature. Besides, X-ray diffraction analysis was applied to confirm the presence of the target phases, while the surface morphology of the synthesized materials was analyzed by scanning electron microscopy (SEM).

[1] A. Khaled, J. J. Pireaux, S. Khelili., Synthesis and Characterization of Ca and Ba Doped LAMOX Materials and Surface Study by X-ray Photoelectron Spectroscopy, Acta Chimica Slovenica **59**, 766–778 (2012).

[2] P Lacorre, F Goutenoire, O Bohnke, R Retoux, Y. Laligant, Designing fast oxide-ion conductors based on $La_2Mo_2O_9$, Nature **404**, 856–858 (2000).

SYNTHESIS AND CHARACTERIZATION OF SAMARIUM DOPED CERIA CERAMICS

Eglė Venslauskaitė, Giedrė Gaidamavičienė, Žygimantas Gricius, Artūras Žalga*

Faculty of Chemistry and Geosciences, Institute of Chemistry, Vilnius University, Naugarduko Str. 24, 03225 Vilnius, Lithuania

arturas.zalga@chf.vu.lt

Doped ceria has been widely studied as electrolyte materials for intermediate temperature solid oxide fuel cells (IT-SOFCs). Solid oxide fuel cells (SOFCs) are high-temperature devices that have ceramic electrolytes and all solid components. They have good modality and accept a wide range of fuels, including hydrogen and other, more accessible chemicals like methane, gasoline and coal. It is believed that SOFCs are ideal for future clean power generation [1].

Advantage of using ceria-based electrolytes is well known as higher ionic conductivity. Thus, it is expected, with a similar power output, to lower the operation temperature for SOFC stacks from 1,173 – 1,273 K currently for zirconia-based cells to 973– 1,073 K for ceria-based cells. This advantage makes the fuel cell using ceria-based electrolyte competitive with other types of fuel cells operating at lower temperature. In addition, the reduction in operation temperature would avoid high temperature interaction and inter-diffusion that take place between cell components and thus increase the stack life time. It also relieves materials constraints and allows more flexibility in regard to the choice of stack materials (e.g., the use of metallic rather than ceramic separators) and thus lowers the fabrication costs [2].

In this work, $Ce_{1-x}Sm_xO_{2-x/2}$ (x = 0.1, 0.2, 0.3 and 0.4) compounds has been prepared by an aqueous sol-gel synthesis method using tartaric acid as a complexing agent in the sol-gel processing. In order to explain and better understand the possible thermal decomposition behavior of the synthesized precursors and crystallization process of the final materials, the thermal analysis (TG/DSC) of the as-prepared Ce–Sm–O tartrate gel precursors for $Ce_{0.9}Sm_{0.1}O_{1.95}$, $Ce_{0.8}Sm_{0.2}O_{1.9}$, $Ce_{0.7}Sm_{0.3}O_{1.85}$ and $Ce_{0.6}Sm_{0.4}O_{1.8}$ ceramics was performed. Moreover, the crystal phase structures and surface morphology of the as-prepared compounds were investigated by X-ray diffraction (XRD) and scanning electron microscopy (SEM).

[1] Y. Lin, C. Su, C. Huang, J. S. Kim, C. Kwak, Z. Shao, A new symmetric solid oxide fuel cell with a samaria-doped ceria framework and a silver-infiltrated electrocatalyst, Journal of Power Sources **197**, 57-64 (2012).

[2] G. B. Jung, T. J. Huang, M. H. Huang, C. L. Chang, Preparation of samaria-doped ceria for solid-oxide fuel cell electrolyte by a modified sol-gel method, Journal of Materials Science **36**, 5839-5844 (2001).

SPECTROSCOPIC STUDY OF La–R–Mo–O TARTRATE PRECURSORS AND $La_{2-x}RE_xMo_2O_9$ (RE=Nd, Sm, Eu, Dy) CERAMICS OBTAINED BY SOL-GEL METHOD

Giedrė Gaidamavičienė[1], Tomas Murauskas[1], Paulius Normantas[2], Valdemaras Aleksa[2], Artūras Žalga[1*]

[1] Faculty of Chemistry and Geosciences, Institute of Chemistry, Vilnius University, Naugarduko Str. 24, LT-03225 Vilnius, Lithuania
[2]Faculty of Physics, Institute of Chemical Physics, Vilnius University, Saulėtekio ave. 3, LT-10257 Vilnius Vilnius, Lithuania
arturas.zalga@chf.vu.lt

Lacorre et al. discovered one of the most promising solid oxide fuel cells (SOFC) electrolyte $La_2Mo_2O_9$ that contains intrinsic oxygen vacancies [1]. Two main properties that solid electrolyte must have is high ion conductivity and thermal expansion coefficient. These two characteristics can be increased by substituting lanthanum molybdate by rare-earth elements such as Ce, Nd, Sm, Gd, Dy, Er, and Yb [2]. The essential task to produce good electrolyte for SOFC is to stabilize lanthanum molybdate β cubic phase at room temperature. After phase transition from α to β phase the anionic conductivity increases sharply by two orders of magnitude. $La_2Mo_2O_9$ substitution by alkali or alkaline earth metals can suppress the phase transition to the monoclinic α phase. Besides, there is some literature, that monoclinic phase can be also suppressed by substituting lanthanum molybdate by rare-earth elements.

Moreover, it is well-known that transport properties of the material strongly depend on the preparation technique that is used for the synthesis of final multicomponent oxides. Such effect like porosity, impurities and low connectivity between the grains [3] can be easy eliminated choosing right synthesis method that overcomes conventional solid-state reaction. In this case, a sol-gel synthesis helps to avoid the use of high temperatures, several heating times and grinding procedures of starting materials in order to be able to produce high-homogeneity, single-phase final compounds.

In this work, the influence of substitution effect of the lanthanide to the vibrational, rotational, and other low-frequency modes of both La–RE–Mo–O tartrate gel precursor heat treated at different temperatures and the final $La_{1.8}Eu_{0.2}Mo_2O_9$ ceramics (where, RE=Nd, Sm, Eu and Dy) was investigated in detail.

[1] P. Lacorre, F. Goutenoire, O. Bohnke, R. Retoux and Y. Laligant, Designing fast oxide-ion conductors based on $La_2Mo_2O_9$, Nature **404**, 856-858 (2000).
[2] D. S. Tsai, M. J. Hsieh, J. C. Tseng, H. Y. Lee, onic conductivities and phase transitions of lanthanide rare-earth substituted $La_2Mo_2O_9$, Journal of the European Ceramic Society **25**, 481–487 (2005).
[3] D. Marrero-López, J. Pena-Martinez, D. Pérez-Coll and P. Nunez, Effects of preparation method on the microstructure and transport properties of $La_2Mo_2O_9$ based materials, Journal of alloys and compounds, **422**, 249-257 (2006).
[4] H. Gocmez, O. Ozcan, Low temperature synthesis of nanocrystalline α-Al_2O_3 by a tartaric acid gel method, Materials Science and Engineering A **475**, 20–22 (2008).

ULTRAFAST EXCITED STATE RELAXATION DYNAMICS OF MONO AND MULTILAYER GRAPHENE

Erika Rajackaitė[1], Domantas Peckus[1], Asta Tamulevičienė[1,2], Tomas Tamulevičius[1,2], Rimas Gudaitis[1], Šarūnas Meškinis[1], Sigitas Tamulevičius[1,2]

[1] Institute of Materials Science of Kaunas University of Technology, K. Baršausko Str. 59, Kaunas LT-51423, Lithuania
[2] Department of Physics, Kaunas University of Technology, Studentų Str. 50, Kaunas LT-51368, Lithuania
erika.rajackaite@ktu.edu

Graphene has rapidly established himself as intriguing building block for various optoelectronic applications. Graphene is an appealing material for photonics and optoelectronics because it offers several advantages compared with other materials. First, graphene is gapless. This enables charge carrier generation by light absorption over a very wide energy spectrum, unmatched by any other material. Furthermore, graphene exhibits ultrafast carrier dynamics, wavelength-independent absorption, tunable optical properties via electrostatic doping, low dissipation rates and high mobility, and the ability to confine electromagnetic energy to unprecedented small volumes [1].

In the current research, graphene films were synthesized on single and double copper foils (catalyst) by novel microwave plasma enhanced chemical vapor deposition technique (IPLAS, Germany). Methane and hydrogen gases mixture was used as a working gas at 30 mbar pressure, substrate temperature was 600 °C. For versatile inspections, in the sequel the transfer of formed graphene layers on different substrates (amorphous glass, quartz, PMMA, SiO_2/Si) was performed by etching copper foil in different etchants at room temperature. Raman scattering spectroscopy (532 nm, inVia, Renishaw, UK) was used to control the technological process and the Raman scattering spectra confirmed successful transfer of the graphene films in a controllable way in the form of mono or multilayers. The transmittance measurements were carried out by means of UV/VIS spectrometer. Atomic force microscope (NanoWizard, Germany) analysis indicated the changes of graphene films morphology and integrity before and after the transfer.

Ultrafast excited state relaxation dynamics in graphene was studied by means of transient absorption spectroscopy (TAS). HARPIA spectrometer was used for TAS measurements. The samples were excited using a Pharos ultrafast Yb:KGW laser (Light Conversion) with a regenerative amplifier at a 66.7 kHz repetition rate and 290 fs duration pulses at 1030 nm wavelength. The pump beam wavelength was tuned with an Orpheus collinear optical parametric generator and harmonic generator Lyra (Light Conversion) to 350 nm and an energy density of 20.8 μJ/cm^2. The samples were probed with a white light supercontinuum generated using a 2 mm thickness sapphire plate excited with a fundamental laser wavelength (1030 nm). The spectral range of the supercontinuum probe as well as the detection range of the TAS dynamics spanned wavelengths from 365 to 700 nm. The excitation beam was focused to an ~700 μm diameter spot, while the diameter of the supercontinuum probe was ~500 μm.

The samples of graphene transferred on PMMA substrate have shown the best quality TAS signal (Fig. 1).

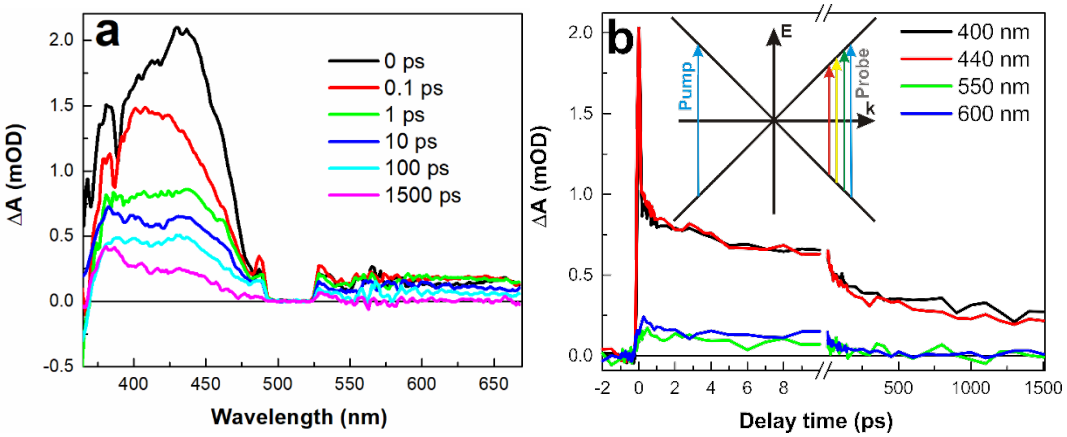

Fig. 1. TAS spectra (**a**) and traces (**b**) of graphene on PMMA substrate. The inset shows energy diagram of graphene.

The data received during these measurements have indicated that ultrafast TAS relaxation traces consist of two parts the fast one (~1 ps) and slower one (~100 ps). The first duration of decay can be attributed to electron cooling by thermal equilibration with the lattice, while the second one to cooling of the lattice [2].

[1] F. H. L. Koppens, T. Mueller, Ph. Avouris et al., Photodetectors based on graphene, other two-dimensional materials and hybrid systems, Nature Nanotech. **9,** 780-793 (2014).
[2] K. J. Tielrooij, L. Piatkowski, M. Massicotte et al., Generation of photovoltage in graphene on a femtosecond timescale through efficient carrier heating, Nature Nanotech. **10**, 437-443 (2015).

MAGNETRON-SPUTTERED COPPER FILMS GROWTH INVESTIGATION

Naglis Kyžas[1], Alexandr Belosludtsev[1]

[1]Optical Coatings Laboratory, Center for Physical Sciences and Technology, Lithuania
nkyzas@gmail.com

Ultrathin metal films play an important role in the nowadays micro- and nanoelectronics, optoelectronics and photonics. Cu thin films are well known because of two important characterizations: high electrical conductivity and high electro-migration resistance. Nevertheless, in recent years due to nonlinear optical properties change some new applications in optics appear. The reason is that copper may represent discontinuous, island-like structures that exhibit excitation of localized plasmon–polaritons under light illumination.

It is essential to find optimized deposition conditions and be able to tune effectively optical properties of prepared material. For this reason in this work, copper films growth is investigated in details. Copper, as other noble metals (gold, silver and etc.), has distinctive growth stages when growing on dielectric substrates (3D Volmer-Weber growth mechanism). Optical properties of during such growth highly depend on the structure of the film.

Copper films were prepared by magnetron sputtering technique. In-situ real-time measurements of transmittance spectra change during growth of the film were done (Fig. 1). Three stages of copper film growth depending on layer thickness were determined from these measurements.

Moreover, five samples of different thickness were prepared, their transmittance, reflectance spectra were measured and losses values were calculated. Measured and calculated data were compared with theoretical values for continuous copper films.

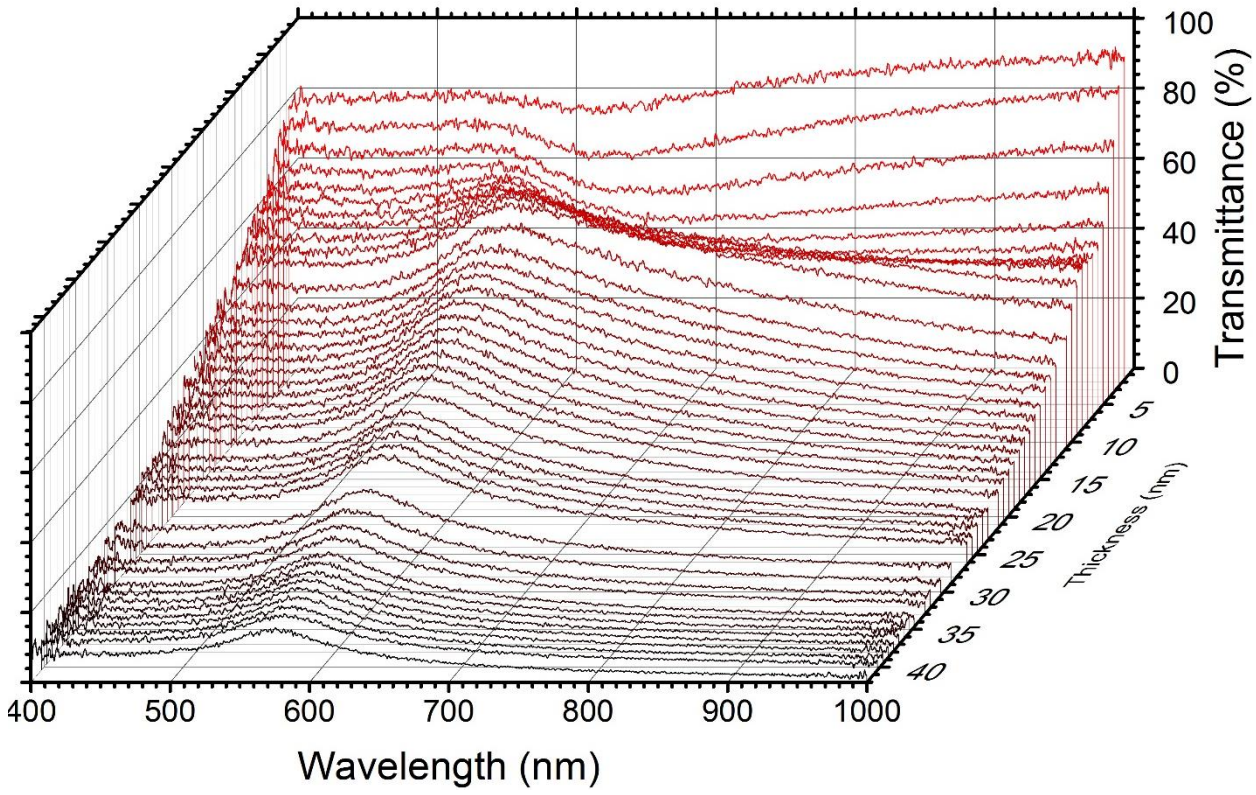

Fig. 1. Transmittance spectra evolution during copper film growth. Recorded in-situ real-time.

PI-MOCVD DEPOSITION AND INVESTIGATION OF UNDOPED BARIUM STANATE THIN FILMS

Tomas Murauskas, Valentina Plaušinaitienė

[1] Department of Inorganic Chemistry, Vilnius University, Lithuania
tomas.murauskas@chgf.vu.lt

In search of novel and cost-effective transparent conductive oxide (TCO) materials to replace Sn-doped In2O3 (ITO) , alkaline-earth stannate family MSnO3 is being widely investigated. La-doped Barium stannate (BaSnO3) as n-type perovskite semiconductor has been reported to exhibit good visible light transparency and high charge carrier mobility. Unlike common TCO materials barium stannate is perovskite type material and is a good match with various ferroelectric piezoelectric and other active materials. Due its properties BaSnO3 could prove to be a perfect candidate as electrode layer in wide range of applications. In recent years single-phase film deposition has been achieved by physical methods such as Molecular beam epitaxy (MBE)[1] or Pulsed laser deposition (PLD)[2]. The aim of this work was to deposit crystalline single-phase barium stannate thin films by Pulsed injection metal organic chemical vapor deposition (PI-MOCVD) method which allows much easier and wider compositional control. MOCVD is most desirable and widely used technology in mico- and optoelectronics fabrication. Although this type of deposition has so far not been successfully used for the deposition of such materials.

Barium stannate depositions were carried out using solution containing Sn(thd)2 and Ba(thd)2 precursors in dimethoxyethane. Layers were deposited in Ar:O2 (8:2 v/v) atmosphere. Due to low film/substrate lattice mismatch, cubic LaAlO3 was selected as a substrate. Effects of deposition temperature and precursor ratio on thin film were investigated. In order to determine layer composition and morphology Scanning Electron Microscopy (SEM) and Energy Dispersive X-ray Spectroscopy (EDX) were used. Film phase composition and crystal orientation were characterized using X-ray Diffractometry technique.

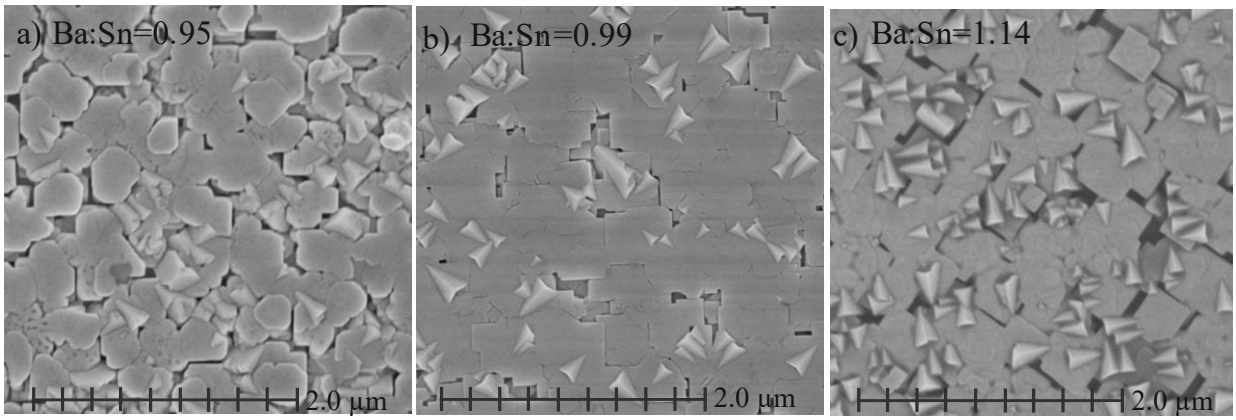

Fig 1. SEM images of thin $BaSnO_3$ layers surfaces deposited on (100) $LaAlO_3$ substrate using 850°C temperature. Barium and tin (Ba:Sn) elemental ratio of thin films determined by EDX: a) 0,95; b) 0,99 c) 1,14.

For the first time thin epitaxial barium stannate films (200-250 nm) have been obtained using PI-MOCVD method on $LaAlO_3$ (100) substrates (Fig.1). It was observed that changing precursor ratio in the solution, Ba/Sn ratio of the layer could easily be controlled whilst using 850 °C deposition temperature. To achieve stoichiometric thin films a surplus amount or $Ba(thd)_2$ was necessary. In addition, no other phases were detected even if layer composition slightly deviated from stoichiometric composition. It was also discovered that surface morphology was greatly dependant on precursor ratio, thus allowing us to control and obtain smoother surfaces.

[1] Woong-Jhae Lee, Hyung Joon Kim et al., Transparent Perovskite Barium Stannate with High Electron Mobility and Thermal Stability, Annual Review of Materials Research, **47**, 391-423 (2017).
[2] K.K. James, P.S.Krishnaprasad et al., Structural and optical properties of La-doped BaSnO3 thin films grown by PLD, Journal of Physics and Chemistry of Solids, **76**, 64-69 (2014).

SYNTHESIS AND PROPERTIES OF ACRIDANE-BASED COMPOUNDS

Naveen Masimukku, Deividas Paliulis, Dalius Gudeika

Department of Polymer Chemistry and Technology, Kaunas University of Technology, Radvilenu pl. 19, LT-50254 Kaunas, Lithuania
mentinas@gmail.com

Acridine derivatives as matrix materials in a light-emitting layer of OLEDs in a blocking layer for electrons in OLEDs. This invention further leads to a light-emitting layer which comprises at least one emitter material and at least one matrix material [1], OLED displays shows many advantages over LCD including wider viewing angles, higher contrast ratio, access to flexible panels, high luminous efficiency, improved fluorescent and phosphorescent emitters for the devices [2]. In this report synthesis and properties of acridine based derivatives (**4-7**) will be presented (Scheme 1) and all these materials synthesized by Suzuki-coupling method [3] with 2,7-dibromo-9,9-dimethyl-9,10-dihydroacridine and different aromatic boronic acid compounds.

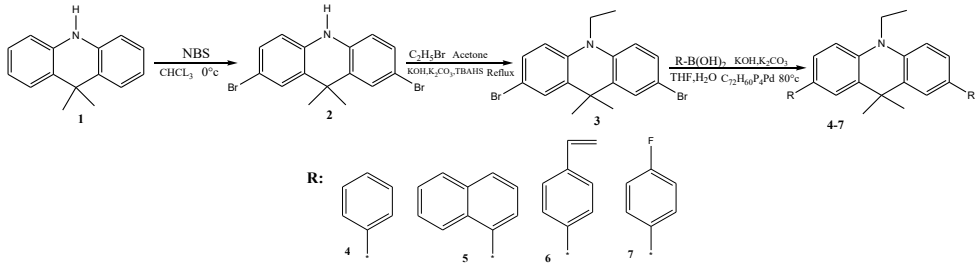

Scheme 1. Synthesis of **4-7**.

The synthesized compounds were proven by H^1, C^{13} NMR, IR, and mass spectrometry. The ionization potential of materials was estimated by cyclic voltammetry, they are ranged from 5.4-5. 6 eV.Thermal and Photo physical properties of materials were investigated. All materials show high thermal stability, the glass transition temperatures are observed in the range.

Acknowledgement. This research was funded by the European Social Fund under the No 09.3.3-LMT-K-712 "Development of Competences of Scientists, other Researchers and Students through Practical Research Activities" measure.

---

[1] Klaus kahle,Patent US **2010**/0219406 A1, P.001.
[2] Müllen, K., Scherf, U. Organic Light-Emitting Devices: Synthesis Properties and Applications; Eds.; Wiley-VCH: Weinheim, **2006**.
[3] B. Huang et al. Journal of Luminescence **2016,** 8, 172.

SYNTHESIS AND PROPERTIES OF PHENOTHIAZINE-BASED DERIVATIVES

Donatas Jurkus, Dalius Gudeika

Department of Polymer Chemistry and Technology, Kaunas University of Technology, Radvilenu pl. 19, LT-50254 Kaunas, Lithuania
ktultu@gmail.com

The aim of this work was to create low-molar mass compounds which could be as potential organic semiconductors. It was chosen to synthesize two derivatives of triphenylamine containing cyclohexane and non-conjugated fluorene moieties and explore their thermal, optical, photophysical and photoelectrical properties.

Two new derivatives, 1,1-bis[4-(N,N-diphenyl)aminophenyl]cyclohexane and 9,9-bis[4-(N,N-diphenyl)aminophenyl]fluorene, were obtained via modified Ullmann coupling reaction using powdered copper alloy as a catalyst at high temperature. The products were obtained in sufficient yields. Their chemical structure was proven by nuclear magnetic resonance and infra-red spectroscopy and mass-spectrometry methods.

As confirmed by differential scanning calorimetry, cyclohexane containing compound is capable of glass formation with its glass transition temperature of 68°C, but the amorphous state of this material is not stable and it crystallizes after some short time. Thermogravimetric analysis showed quite high thermal stability of cyclohexane containing compound. Its thermal degradation starts only near 400°C.

The electronic spectra (absorption and emission of radiation) and ionization potential measurements (by electron photoemission) of these compounds showed their very similar energetic structure and electric properties. They both show intensive absorption at c.a. 305 nm and emission at c.a. 365 nm and their ionization potential values are very cloce, c.a. 5.6 eV.

Also the hole-drift mobility of cyclohexane moiety containing compound film with inert polymer (bisphenol-Z polycarbonate) was explored. It reaches 2×10^{-6} cm^2/Vs in the electric field of 10^6 V/cm.

SYNTHESIS OF GLASSY ANALOGS OF ALLUAUDITE-TYPE CATHODE MATERIALS FOR SODIUM BATTERIES

Adrianna Chamryga[1], Tomasz K. Pietrzak[1]

[1] Faculty of Physics, Warsaw University of Technology, Poland
ada.chamryga@gmail.com

At our faculty, a phenomenon of thermal nanocrystallization in amorphous analogs of crystalline cathode materials for lithium and sodium batteries – e. g. $LiFePO_4$, $Li_3V_2(PO_4)_3$, $Na_3V_2(PO_4)_3$ or $Na_3V_2(PO_4)_3F_3$ – have been studied for many years [1]. In most cases, a gigantic increase in the conductivity was observed, as a result of a proper thermal treatment of the materials. This effect was due to a growth of nanocrystallites (ca 10 nm) in a glassy matrix. Well-developed surfaces of the nanograins provide favorable conditions for electron hopping which is the mechanism of charge carrier transport in glasses containing transition metal oxides (e.g. V_2O_3, Fe_2O_3, Mn_2O_3).

Recently, other interesting candidates for cathode materials in sodium batteries were developed, i.e. $Na_2M_3(PO_4)_3$ (where M = Fe, V, Mn) with so-called alluaudite structure. Their theoretical gravimetric capacity is as high as 170 mAh/g [2]. Even though different transition metals M were tested, experimental values of gravimetric capacity reported in the literature for alluaudite-type cathode materials remain disappointing [3, 4]. Nanocrystallization of glassy analogs of alluaudites might be a solution for this issue.

In this work, we attempted to synthesize glassy samples of general composition $Na_2M_3(PO_4)_3$ (where M = Fe, V, Mn). Appropriate amounts of reagents – the first sample: Na_2CO_3 + $FePO_4{\cdot}2H_2O$ / $FeC_2O_4{\cdot}2H_2O$ / V_2O_5 / $Mn(CH_3COO)_2{\cdot}4H_2O$ + $NH_4H_2PO_4$ – were mixed and homogenized in a mortar. The batches were put in porcelain crucibles, placed in a furnace preheated to 600 °C and melted at 1300 °C. A double crucible method was used to provide a non-oxidizing atmosphere. The melts were poured onto a stainless steel plate and immediately pressed with another one plate. In this technique – called melt-quenching – a cooling rate can be approximately 1000 °C/s.

The amorphousness of the samples was investigated with an X-ray diffractometry (XRD) using Philips X'pert Pro apparatus with copper anode and a nickel filter. The temperatures of thermal events occurring in the samples upon heating were determined from differential thermal analysis (DTA) measurements in argon flow using TA Instruments SDT Q600 apparatus.

The results presented in this poster are the first stage of our experiments, in which we expect to synthesize highly-conductive alluaudite-type nanocrystalline cathode materials for sodium batteries.

[1] T.K. Pietrzak, M. Wasiucionek, P.P. Michalski, A. Kaleta, J.E. Garbarczyk, Highly conductive cathode materials for Li-ion batteries prepared by thermal nanocrystallization of selected oxide glasses, Materials Science and Engineering B **213**, 140–147 (2016).

[2] K. Trad, D. Carlier, L. Croguennec, A. Wattiaux, M.B. Amara, C. Delmas, $NaMnFe_2(PO_4)_3$ Alluaudite Phase: Synthesis, Structure, and Electrochemical Properties As Positive Electrode in Lithium and Sodium Batteries, Chemistry of Materials **22**, 5554–5562 (2010).

[3] W. Huang, B. Li, M.F. Saleem, X. Wu, J. Li, J. Lin, D. Xia, W. Chu, Z. Wu, Self-Assembled Alluaudite $Na_2Fe_{3-x}Mn_x(PO_4)_3$ Micro/Nanocompounds for Sodium-Ion Battery Electrodes: A New Insight into Their Electronic and Geometric Structure, Chemistry – A European Journal **21**, 851–860 (2015).

[4] M. Wen, X. Liu, Y. Zhao, Sh. Liu, H. Liu, Y. Dong, Q. Kuang, Q. Fan, Synthesis of alluaudite-type $Na_2VFe_2(PO_4)_3$/C and its electrochemical performance as cathode material for sodium-ion battery, Journal of Solid State Electrochemistry (2017), available on-line.

SYNTHESIS OF DOUBLE SILICATES OF POTASSIUM AND RARE-EARTH METALS WITH APATITE STRUCTURE

Anastasiia I. Kashuba [1], Ekaterina V. Borisova [2]

[1] Vasyl' Stus Donetsk National University, Vinnytsia, vul, 600-richchia, 21, Ukraine.
E-mail: kashuba.a@donnu.edu.ua
[2] KU Leuven, Oude Markt 13, 3000 Leuven, Belgium. E-mail: kateryna.borysova@kuleuven.be

Silicates with apatite structure are used in various fields of science and technology. In medicine the injection of silicate apatite into the structure significantly increase biocompatibility and bioactivity of materials [1]. These compounds found application as the materials for lasers, phosphors and catalysts [2,3,4]. In recent years, attracted the attention of researchers silicates of rare earth elements (REE) as promising materials for fuel cells, which are highly efficient and environmentally friendly source of electricity [5,6].

There are several methods of the synthesis of double silicates: solid-phase method, method of coprecipitation, sol-gel method and hydrothermal method. The first was the solid-phase method of synthesis. However, this process requires the high temperatures (from 1200°C up to about 1900°C) – for the synthesis of silicates without an alkali metal ,so there is interest in the study of double silicates potassium and REE, which require much lower temperatures. The solid-phase synthesis was used to prepare a samples of $KPr_9(SiO_4)_6O_2$, $KSm_9(SiO_4)_6O_2$, $KNd_9(SiO_4)_6O_2$. The temperature of synthesis of double silicates was of 800°C, 900°C, and 1000°C. Selected temperature conditions prevented the sublimation of potassium oxide.

Silicates potassium and REE were studied by X-ray diffraction (XRD), scanning electron microscopy (SEM) and infrared spectroscopy (IR).

XRD results confirmed that the structure of apatite begins to form at a baking temperature of 800°C. Calcination at 900°C, and 1000°C leads to the full interaction of all components, as a result in the presence of only the peaks of the phase on the X-ray. Further temperature increase does not cause any changes. According to electron microscopy for a samples with potassium, elements uniformly distributed over the surface of the particles, which indicates a uniformity of samples.

[1] Chen X., Wu T., Wang Q and Shen J.W. Shield effect of silicate on adsorption of proteins o.nto silicon-doped hydroxyapatite // Biomatirials.- 2008. V. -29, №15.- P. 2423-2432.
[2] E. Kendrick, M.S. Islam, P.R. Slater, Journal of Material Chemistry 17 (2007), 3104 P
[3] Leon-Reina, E.R. Losilla, M. Martinez-Lara, S. Bruque, M.A.G. Aranda J.Mater.Chem. 14 (2004), 1142 P.
[4] Xue Lu, Haitao Liu, Xinyu Yang. A single-phase white-emitting $La_{10}(SiO_4)_6O_3$: Eu^{2+}/Eu^{3+} phosphor for near-UV LED-based application. //Ceramics International. – 2017. – Vol-. 43 (15).
[5] A.J. Jacobson. Materials for Solid Oxide Fuel Cells.//Chem. Mater. -2010.- V-.22. P.660–674.
[6] Higuchi, Y.; Sugawara, M.; Hawazaki, K.; Uewatsu, K.; Nakayama,S. U.S. Patent 2004/0161651 A1.

DIELECTRIC PROPERTIES OF ZIF-90 AND UIO-66 METAL-ORGANIC FRAMEWORKS

Diana Pavlovaitė[1], Sergėjus Balčiūnas[1], Robertas Grigalaitis[1], Mantas Šimėnas[1], Jūras Banys[1], Martynas Kinka[1], Fa-Kuen Shieh[2], Kevin C.-W. Wu[3]

[1]Faculty of Physics, Vilnius University, Sauletekio 9/3, LT10222 Vilnius, Lithuania.
[2] Department of Chemistry, National Central University, Chung-Li 32001, Taiwan
[3] Department of Chemical Engineering, National Taiwan University No. 1, Sec. 4, Roosevelt Road, Taipei 10617, Taiwan
pavlovaited@gmail.com

Metal-organic frameworks (MOFs) have emerged in the recent years as promising materials as their physical properties suggest variety of applications in gas absorption and storage containers, microreactors, etc.[1] due to their porous structure. In this research two MOF materials were studied: ZIF-90 and UIO-66.

UIO-66 and ZIF-90 powders were prepared for dielectric studies by compressing them into cylindrical pellets and evaporating silver electrodes on their flat surfaces to obtain an ohmic contact with the measurement cell. Dielectric properties were measured at five different atmospheres: N_2, CO_2, H_2O, C_2H_5OH and vacuum, in 100 K – 400 K temperature region sweeping the measurement frequency in 100 Hz – 1 MHz range.

In this presentation data obtained during dielectric studies of UIO-66 and ZIF-90 in various atmospheres will be presented. From Figure 1 we can observe that in humid conditions ZIF - 90 experiences anomaly at room temperature. As temperature increases dielectric permittivity increases in all frequencies and experiences maximum at 300K, as temperature further increases permittivity drops, similar results were obtained with UIO-66 as well. No significant anomalies of dielectric permittivity were observed for measurements in non-polar gas (nitrogen and carbon dioxide) atmosphere.

Experimental data of both UIO-66 and ZIF-90 were approximated by Cole-Cole equation [2] which helped to distinguish Maxwell-Wagner relaxation due to absorption of water molecules into the structure.

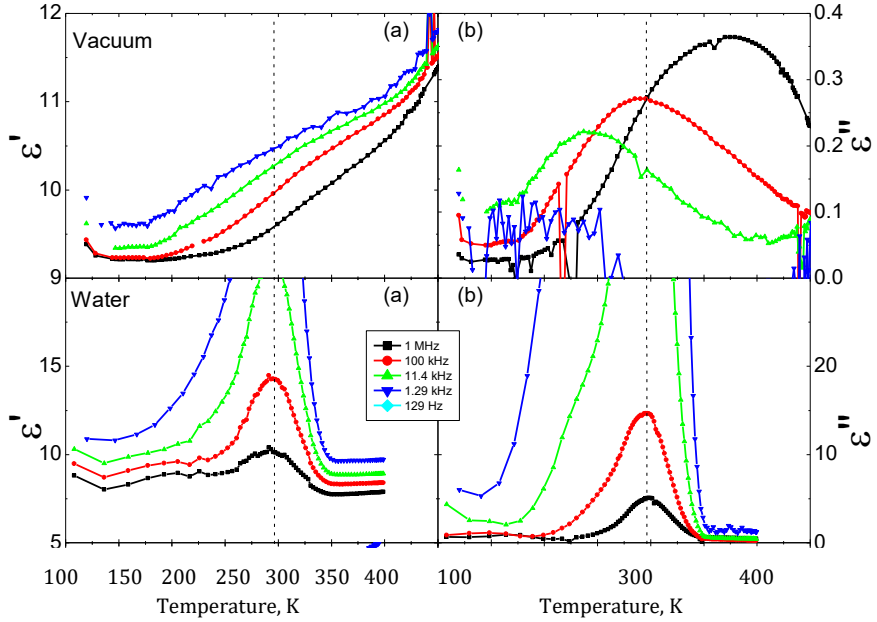

Fig. 1: Temperature dependence of the real (left) and imaginary (right) parts of dielectric permittivity of ZIF-90 in vacuum and water respectively.

[1] I. Ahmed, S.H. Jhung, Composites of metal–organic frameworks: Preparation and application in adsorption, Mater. Today. 17 (2014) 136–146. doi:10.1016/j.mattod.2014.03.002.
[2] A. R. V. Hippel, *Dielectrics and waves*. Wiley, 1954.

MAGNETIC PROPERTIES AND MAGNETOCALORIC EFFECT ON $GdCo_{1.8}M_{0.2}$ with M=Al, Cu, Ni

Ruxandra Anca Cotop[1], Dragos Farcas[2], Gabriela Souca[1], Roxana Dudric[1], Romulus Tetean[1]

[1] Faculty of Physics, Babes-Bolyai University, Cluj Napoca, Romania
ruxicotop@gmail.com
[2]Nicolae Balcescu National College, Cluj Napoca, Romania

In this work, the structural, magnetic properties and magnetocaloric effect of $GdCo_{1.8}M_{0.2}$ with M = Al, Cu, Ni, and Si were investigated. The X-ray analysis showed that all these compounds are single phase and crystallize in the cubic $MgCu_2$ (C15) structure. The Gd occupies -43m sites while Co and Ni are distributed in -3m positions.

The magnetic properties were studied in external magnetic fields up to 12 T and a large temperature range 4.2 – 650 K. All of the samples are ferromagnetically, ordered, the Gd and Co magnetic moments being antiparallel oriented. The ferromagnetic-paramagnetic transition temperatures are a few tens of degrees above room temperature. As example, the Curie temperatures, T_C, are 378 K for M=Cu, 384 K (M=Al) and 332 K (M=Ni). The saturation magnetizations are higher than in the parent compound, being 5.24 μ_B/f.u. in the compound with copper and 5.29 μ_B/f.u for M =Ni. Assuming that the magnetic moment of gadolinium is 7 μ_B/atom, we have determined the cobalt magnetic moments, M_{Co}, at 4.2 K. The M_{Co} are little dependent on composition, M_{Co} = 0.94 ± 0.3 μ_B/atom. It was shown that in $GdNi_2$ compound Ni atoms show a very weak or null magnetic contribution. Band structure calculations performed on $GdNi_2$ show that there is a small magnetic moment of 0.12 μ_B/atom on Ni while from magnetic measurements a null magnetic moment is suggested [1]. The replacement of Co by M atoms modified the exchange interactions. When cobalt is substituted by M atoms a p-d type hybridization appear. Due to this hybridization the electronic configuration of cobalt d band is modified and consequently the magnetic moment.

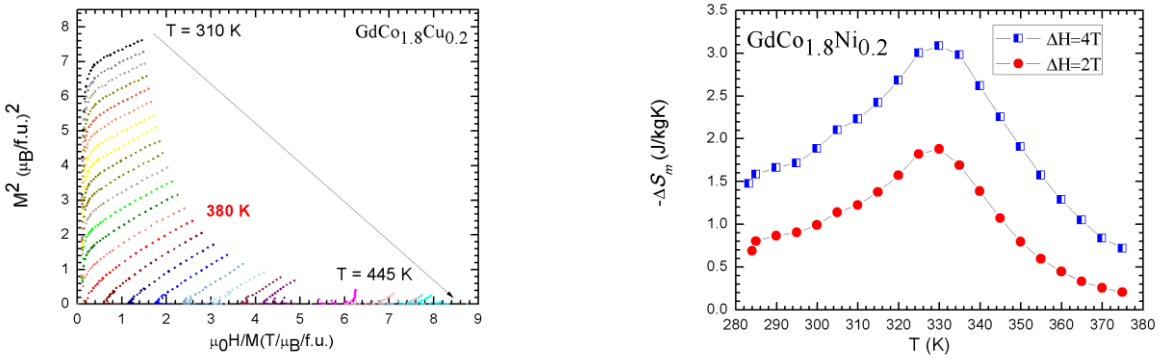

Fig. 1. Honda Arrot plots and the temperature dependences of magnetic entropy change for $GdCo_{1.}Cu_{0.2}$.

The magnetization isotherms and Arrot plots for the samples with M = Cu measured around the transition temperatures are shown in Fig.1. From the Arrot plots we can see that these compounds undergo a second-order magnetic phase transition at the Curie temperature. Similar behaviours were found for all of the investigated samples. The magnetocaloric effect was also studied. Fig.1. show the magnetic entropy change, ΔS_M, as a function of temperature for different magnetic field changes for the compounds with M = Ni. The $\Delta S_M(T)$ peaks are broad and have a symmetrical shape, a behavior which is characteristic for materials exhibiting a second-order magnetic phase transition [2]. As example, for a magnetic field change from 0 to 4 T, the obtained maximum entropy change values are 2.81 J/kgK for (M = Cu) to 3.08 J/kgK (M = Ni). The magnetic entropy changes versus temperature plots in applied field changes of 0-4 T and 0-2 T respectively for M = Ni sample are presented in Fig.1. The relative cooling power are rather high, being 157.36 J/kg for M = Cu and 215.6 J/kg for M = Ni. Due to their high RCP values these compounds are promising candidates for applications in magnetic refrigeration devices just above room temperature range.

[1] E. Burzo, A. Chelkovski, H. R. Kirchmayr, Landolt Börnstein handbuch, Vol. 19 d2, Springer Verlag, Berlin, 1990.
[2] J. Lyubina, O. Gutfleisch, M. D. Kuz'min, and M. Richter. J. Magn. Magn. Mater., 320 (18):2252 - 2258, 2008.

THE EFFECT OF AU NANOPARTICLES ADDITION ON THE LUMINESCENT PROPERTIES OF BaI_2:Eu FINE POWDERS

Solomakha Tatsiana[1], Tret'yak Yauhen[1]

[1] Research Institute for Physical Chemical Problems, Belarusian State University, Belarus
solomakha.tanja@gmail.com

Nowadays scintillation materials are widely used in a variety of practical applications such as energy physics, nuclear physics, medicine, national security, exploration and etc. Iodides of alkaline earth elements, activated with Eu^{2+} ions, are attractive compounds for use as scintillation materials (they have high light output (up to 120000 photons/MeV) and energy resolution (up to 3% at 662 keV)). In this area the most promising is $BaI_2:Eu^{2+}$ that has high Z_{ef}, is not radioactive and has the smallest band gap among the halides of alkaline earth elements [1,2].

From literature it is known that doping of materials with metal nanoparticles allows to influence significantly on their optical, electrical and mechanical properties. For instance, injection of Au nanoparticles in TiO_2 allowed to detect an anodic photocurrent generated by visible-light illumination (TiO_2 has the wide bandgap (3.3 eV) and is able to generate photocurrents only when illuminated with ultraviolet light). Injection of indium tin oxide and Au nanoantennas in CaF_2 allowed to use this material for surface-enhanced infrared spectroscopy [3,4]. In accordance with the foregoing, the effect of Au nanoparticles addition on luminescent, structural and morphological properties of $BaI_2:Eu^{2+}$ powders has been studied. As $BaI_2:Eu^{2+}$ powders synthesis method the approach described in [5] has been used. The Au nanoparticles in the amount of 0.1 at. % were added to the precursor ($BaCO_3:Eu^{3+}$) on the first stage of synthesis.

On X-ray diffraction patterns for $BaI_2:Eu^{2+}$ samples with Au nanoparticles addition intensive reflexes of BaI_2 hydrates phases and low-intensive reflexes of AuI phase [Powder Diffraction File № 15–0521] have been observed. Formation of AuI can be explained by reaction of Au nanoparticles with iodine, which is released on the second stage of the synthesis. According to luminescence data one can observe that luminescence intensity of $BaI_2:Eu^{2+}$ sample without Au nanoparticles addition is higher than that of $BaI_2:Eu^{2+}$ sample with Au nanoparticles addition. Moreover luminescence intensity of $BaI_2:Eu^{2+}$ sample without Au nanoparticles addition increases in first days and then gradually decreases throughout 2 weeks, while luminescence intensity of $BaI_2:Eu^{2+}$ sample with Au nanoparticles addition increases in first days and then saves its value throughout 2 weeks. This effect is probably connected with low solubility and photostability of AuI, what perhaps prevents destruction of BaI_2.

---

[1] M. Nikl, A. Yoshikawa, Recent R&D Trends in Inorganic Single-Crystal Scintillator Materials for Radiation Detection, Advanced Optical Materials **3**, 463-481 (2015).
[2] E. V. van Loef, C. M. Wilson, N. J. Cherepy et al., Crystal growth and scintillation properties of strontium iodide scintillators, IEEE Transactions on Nuclear Science **56**, 869-872 (2009).
[3] C. Clavero, Plasmon-induced hot-electron generation at nanoparticle/metal-oxide interfaces for photovoltaic and photocatalytic devices, Nature Photonics **8**, 95-103 (2014).
[4] M. Abb, Y. Wang, N. Papasimakis et al., Surface-enhanced infrared spectroscopy using metal oxide plasmonic antenna arrays, Nano letters **14**, 346-352 (2013).
[5] E. V. Tret'yak, G. P. Shevchenko, T. A. Solomakha, M. V. Korzhik, Effect of precursor morphology on the structural properties, optical absorption, and luminescence of $BaI_2:Eu^{2+},Eu^{3+}$, Inorganic Materials **53**, 307-312 (2017).

Nuclear Gamma Resonance Study of Electrodeposited Fe – W coatings

Karolina Varsockaja[1,2], Jonas Reklaitis [1], Aliona Nicolenco [3],
Natalia Tsyntsaru[3,4], Henrikas Cesiulis[3]

[1]Center for Physical Sciences and Technology, Savanorių av. 231, Vilnius, Lithuania
[2]Faculty of Physics, Vilnius University, Saulėtekio av. 9, Bld. III, Vilnius, Lithuania
[3]Faculty of Chemistry and Geosciences, Vilnius University, Naugarduko str. 24, Vilnius, Lithuania
[4]Institute of Applied Physics of ASM, Chisinau, Academiei str. 5, Chisinau, Republic of Moldova
karolina.varsockaja@ff.stud.vu.lt

Recently, tungsten alloys have attracted extensive research attention as appealing alternative materials for versatile applications. It has been shown that addition of tungsten to iron group metals improves their mechanical, tribological, magnetic and electrical properties [1]. They could also be used for the manufacturing of ultra large-scale devices (ULSI) and micro/nano -electro -mechanical systems (MEMS/NEMS) [2]. The investigations on Fe – W alloys have lately been gaining importance as the use of both Co – W and Ni – W alloys is discouraged because of health issues. The most convenient known way to obtain Fe – W alloys is electrodeposition [3]. By fine tuning of deposition parameters one can control the structure and composition of the deposits

In this study, Fe – W coatings were electrodeposited from Fe(III) based glycolate-citrate bath in the pulse current mode. The average cathodic current density was kept constant at 15 $mA \cdot cm^{-2}$, while the duty cycle (d.c.) was changed from 16 % to 100 %. The structural changes were investigated by nuclear gamma resonance. This precise method provides information about the structure and composition as well as magnetic and electrical properties of deposits. The measurements were carried out with Wissenschaftliche electronik GmbH Mössbauer spectrometer using a ^{57}Co in Rh matrix as a source.

The structural composition of Fe – W alloys deposited under various plating conditions is shown in Fig.1. Spectral lines corresponding to α – Fe, Fe(W) and Fe_2W phases were found for alloy deposited with the lower W content (obtained at d.c. 100 %), while the coatings with the higher tungsten content (obtained at d.c. 50 %) consist of Fe(W), Fe_2W and W(Fe) phases. Apparently, these structural changes could be related to the mechanical and magnetic properties of the investigated coatings.

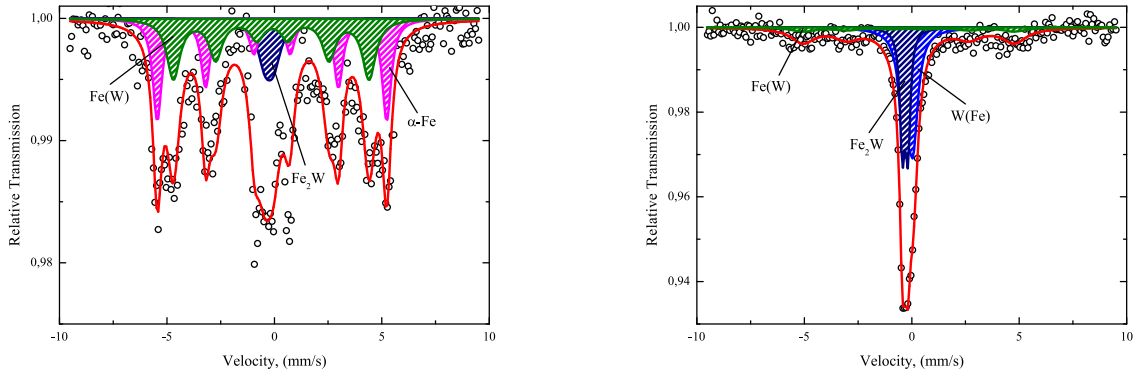

Figure 1. Mössbauer spectras of Fe-W coatings with different plating conditions. a) d.c. 100 %, b) d.c. 50 %.

Acknowledgements. Authors acknowledge funding from H2020 (project SELECTA 642642), and the Moldavian national project (15.817.02.05A).

[1] A. Nicolenco, N. Tsyntsaru, J. Fornell, E. Pellicer, J. Reklaitis, D. Baltrunas, H. Cesiulis, and J. Sort. Mapping of magnetic and mechanical properties of Fe-W alloys electrodeposited from Fe(III)-based glycolate-citrate bath, Materials & Design **139**, 429–438 (2018).
[2] N. Tsyntsaru, H. Cesiulis, M. Donten, J. Sort, E. Pellicer, and E.J. Podlaha-Murphy. Modern trends in tungsten alloys electrodeposition with iron group metals, Surface Engineering and Applied Electrochemistry **48**(**6**), 491–520 (2012).
[3] Y. Nishi, Y. Mogi, K. Oguri, and T. Watanabe. Preparation of FeW amorphous films by an electroplating method, Journal of Materials Science Letters **14**(**1**), 1–3 (1995).

STUDY OF DSB: Ce^{3+} SCINTILLATION GLASS CERAMICS FOR CALORIMETRY

Pavel Orsich[1], Vitaly Mechinski[1], Mikhail Korjik[1], Valera Dormenev[2], Hans-Georg Zaunick[2]

[1] Research Institute for Nuclear Problems, Minsk, Belarus
[2] Justus Liebig University,2nd Physics Institute, Giessen, Germany
lovetreygolnik@gmail.com

Application of crystalline materials in detectors for ionizing radiation detectors has played a crucial role in the discovery of the properties of matter and promoted a continuous progress in the detecting technique. Future detector concepts at high-energy physics (HEP) experiments will require a tolerable level of radiation damage in particular caused by electromagnetic part of ionizing radiation and energetic hadrons: minor deterioration of the optical transmission, low level of afterglow and radio-luminescence. Heavy materials demonstrate sufficient damage under the hadronic part of the ionizing radiation [1, 2] excluding consideration for high energy experiments at future particle colliders.

The disilicate of barium ($BaO_2 - SiO_2$) doped with Ce (DSB:Ce) is one of the new scintillation materials made from binary composition and obtained by standard glass production technology with a successive thermal annealing. It can be produced in bulk and fiber shapes. DSB:Ce glass has a slightly lower stopping power. Its density is 3.8 g/cm^3, its effective Z is 51 and its radiation length (X_0) is 3.3 cm [3]. Therefore applications of DSB:Ce in calorimetry will most probably require an additional absorber. On the other hand, on the contrary to crystalline materials, the production of large quantities is relatively easy and the production costs are rather low.

For the present study, nine large piece of DSB:Ce ($20 \times 20 \times 100\,mm^3$) were provided by Radiation Instruments and New Components (Belarus) to evaluate their scintillation properties and radiation hardness to gamma-irradiation.

The non-uniformity of light output of each of the DSB:Ce samples was measured with γ-rays of 1.17 MeV and 1.33 MeV generated by respectively an 60 Co radioactive source. We estimate the light output for the best DSB:Ce sample to be around 40 phe/MeV, thus two times larger than the one of a PWO crystal at room temperature [4]. We also investigated the temperature dependence of the light output from -25 °C to +20 °C. [4]. The temperature dependence of the light yield LY(T) is on the level of 0.05 % which is 40 times less than in case of $PbWO_4$.

Several samples were irradiated at the Radiation Center (Justus-Liebig-University Giessen, Germany) using a strong ^{60}Co source at a dose rate of 2Gy/min. The transmission was subsequently measured again and compared with transmission before the radiation.

DSB:Ce has a very small temperature dependence of the light output. The radiation damage of new DSB: Ce scintillating glass quantified by the change of the optical transmission was investigated. Preliminary results indicate that by optimizing the raw material purity and the production parameter improvement of radiation damage could be obtained. Further optimization of raw material and production conditions are currently investigated.

Therefore, DSB: Ce can be considered to be a prospective material for application in calorimetry.

[1] E. Auffray, A. Barysevich, A. Fedorov, M. Korjik, M. Koschan, M. Lucchini, V. Mechinski, C.L. Melcher, A. Voitovich, Radiation damage of LSO crystals under γ- and 24 GeV protons irradiation. Nuclear Instr. and Meth. in Physics Res. A721 (2013) pp.76-82.

[2] E. Auffray , M. Korjik, A. , Experimental Study of Lead Tungstate Scintillator Proton-Induced Damage and Recovery. IEEE Trans. on Nucl. Sci, 59 (2012) pp. 2219-2223.

[3] R. W. Novotny, K.-T. Brinkmann, A. Borisevich, V. Dormenev, M. Korjik, D. Kozlov, P. Orsich, H.-G. Zaunick, S. Zimmermann, Study of the Glass and Glass Ceramic Stoichiometric and Gd^{3+} Heavy Loaded $BaO_2 - SiO_2$ (DSB:Ce) Scintillation Materials for Calorimetry Application, Conference Record N3D1-3, Nuclear Science Symposium-Medical Imaging Conference 2015, 1-7 November, San Diego, USA.

[4] E. Auffray, N. Akchurin, A. Benaglia, A. Borisevich, C. Cowden, J. Damgov, V. Dormenev, C. Dragoiu, P. Dudero, M. Korjik, D. Kozlov, S. Kunori, P. Lecoq, S. W. Lee, M. Lucchini, V. Mechinsky, K. Pauwels, " DSB:Ce3+ scintillation glass for future, Journal of Physics: Conference Series 587 (2015) 012062.

SUPERPARAMAGNETIC RESONANCE OF IRON-OXIDE NANOPARTICLES

Laisvydas Giriūnas[1], Andreja Bužan Bobnar[2], Denis Arčon[2]

[1] Faculty of Physics, Vilnius University, Saulėtekio al. 9, 10222 Vilnius, Lithuania
[2] Jožef Stefan Institute, Jamova cesta 39, 1000 Ljubljana, Slovenia
laisvydas.giriunas@ff.stud.vu.lt

The purpose of this work is to study different samples of magnetite (Fe_3O_4) and maghemite with cobalt-oxide ($CoO{\cdot}Fe_2O_3$) nanoparticles by X-band (9.37 GHz) electron paramagnetic resonance (EPR). Under the influence of temperature the orientation of total magnetization of these ferromagnetic nanoparticles can flip randomly despite being below the Curie temperature, which, in other words, means, they are superparamagnetic. We can orient the direction of magnetization of these nanoparticles with the external magnetic field and measure the energy between the magnetization states using the EPR method.

In this study we observe a correlation between the apparent linewidth in the EPR spectrum and the temperature of the samples, which ranges from 300 K to 5 K. As a result, we see that EPR spectra at around 300 K show a relatively narrow resonance line, but as the temperature lowers to 5 K, the apparent resonance field decreases and the linewidth considerably increases.

To help us better understand the experimental data we use computer simulations. The theoretical formalism for the simulations is based on the insight, that the distributions of particle volumes are well described with a lognormal function [1]. With this in mind, it has been shown [2] that the two following assumptions are appropriate. Firstly, we assume that the particles are magnetically ordered ellipsoidal domains with magnetic moments equal to $M_S V$, where M_S is the spontaneous magnetization and V is the volume of the particle. Secondly, we assumed that the resonance field is not only comprised of static external magnetic field, but it should also include anisotropic contributions: the magnocrystalline anisotropy field and the demagnetising field.

With all the considerations, the line shape function is derived from the damped precession equation of Landau–Lifshitz [3]. As it was already shown before [2], the volume and temperature dependence of the individual nanoparticle linewidth can be well described with a Langevin function ($L(x) = \coth(x) - 1/x$) as:

$$\Delta_B = \Delta_T L\left(\frac{M_S V B_{res}}{kT}\right),$$

where Δ_T – the saturation linewidth at temperature T, which corresponds to the largest particles in the sample, B_{res} is the resonance field, k – Boltzmann constant.

In this work, the results from the experimental data and computer simulations are presented and discussed.

[1] R. Berger, et. al., Journal of Magnetism and Magnetic Materials **234**, 535-544 (2001).
[2] R. Berger, J. Kliava, J.-C. Bissey, J. Appl. Phys. **87**, 7389-7396 (2000).
[3] R. Berger, J.-C. Bissey, J. Kliava, J. Phys.: Condens. Matter **12**, 9347-9360 (2000).

THE DIRECT ACTION AND INTERACTION COEFFICIENTS FOR X-RAY SPECTROMETRIC DETERMINATION OF THE QUANTITATIVE COMPOSITION OF CLAYS

Anna Trubača-Boginska[1*], Andris Actiņš[1], Ruta Švinka[2], Visvaldis Švinka[2]

[1] Faculty of Chemistry, University of Latvia, Latvia
[2] Institute of Silicate Materials, Riga Technical University, Latvia
anna.trubaca-boginska@lu.lv

Clays are sedimentary rocks with a very diverse elemental composition which is mainly dependent on the mineral content. In Latvia, the typical clay mainly consists of SiO_2, Al_2O_3, Fe_2O_3, K_2O, MgO, TiO_2, CaO un Na_2O (if the composition of the elements is expressed in oxide formulas). For determination of chemical composition more often are used X-ray fluorescence spectrometry (XRFS). The method is non-destructive and can analyze a large number of samples relatively quickly. However, previous studies [1] have shown that analysis of samples with such a complex elemental matrix by XRFS is difficult. It is estimated that the elements in the sample matrix can mutually affect the X-ray fluorescence analytical signal either strengthening or weakening it.

The aim of this study was to evaluate direct action and interaction coefficients using the standard additive method. Mathematical processing is performed assuming that the expected linear relationship between the amount of the additive and the analytical signal. The direct action coefficient shows the effect of the added element oxide on the analytical signal of the same element. In turn, interaction coefficients show the added element oxide effect on the other elements analytical signals. The additives of Al_2O_3, Fe_2O_3, K_2CO_3, MgO, TiO_2, CaO and NaF were used to determine the initial composition of the element oxides of the clay. It should be noted that the SiO_2 content in the clay sample is higher than 50%, so its determination by the standard additive method will not give accurate results. Therefore, the silicon dioxide is calculated by taking into account previously determined element oxides in combination with thermogravimetric analysis of the sample.

Based on the interaction results, it was found that the addition of Al_2O_3 reduces the analytical signal of K_2O. Reduction of the analytical signal was also observed for Al_2O_3 and MgO using Fe_2O_3 and TiO_2 as additives. Therefore, the resulting direct action and interaction coefficients were used to develop a multi-parameter optimization method that would allow recalculating element oxide content from XRF data without implementing the additive method in the future. It should be noted that such calculations will be possible for clay samples with a similar composition. Comparison of XRFS, standard additive, and multi-parameter optimization methods are summarized in Table 1. Standard additive and multi-parameter optimization methods give very similar results.

Table 1.

Comparison of methods

Element oxide	Method		
	XRFS data	Standard additive	Multi-parameter optimization
		W, %	
SiO_2	57 ± 2	51.6 ± 1.9	51 ± 2
Al_2O_3	19.3 ± 1.2	22.0 ± 1.5	22.6 ± 1.8
Fe_2O_3	7.16 ± 0.19	7.23 ± 0.19	7.09 ± 0.17
K_2O	4.5 ± 0.3	4.1 ± 0.4	4.1 ± 0.4
CaO	4.34 ± 0.15	4.48 ± 0.13	4.45 ± 0.16
Na_2O	2.29 ± 0.17	3.72 ± 0.15	3.65 ± 0.15
MgO	1.6 ± 0.4	1.15 ± 0.03	1.11 ± 0.03
TiO_2	0.90 ± 0.07	0.77 ±0.05	0.78 ± 0.04

This work was supported by the European Regional Development Fund within the Project 1.1.1.1/16/A/077 «Mineral and synthetic nanopowders for obtaining of porous ceramics and modification of ceramic materials».

[1] A. Palaša, X-ray spectrometrical determination of glass fibre composition with addition method. Bachelor thesis. Riga: University of Latvia, 2010. 67. p.

PHOTOLUMINENCE PROPERTIES OF YAG:Ce^{3+}/BN PHOSPHORS AND THEIR THERMAL CHARACTERISTICS

Justina Aglinskaitė[1], Akvilė Zabiliūtė-Karaliūnė[1], Greta Inkrataitė[2], Andrija Valaitytė[2], Ramūnas Skaudžius[2], Pranciškus Vitta[1]

[1] Institute of Photonics and Nanotechnology, Vilnius University, Lithuania
[2] Institute of Chemistry, Vilnius University, Lithuania
justinaaglin@gmail.com

Laser diodes (LDs) based lighting is expected to become the main high power Solid-State-Lighting technology as it provides efficient and colour-stable white light [1]. Luminairy is usually made of a blue or UV laser diode and a remote yellow phosphor which converts part of LD's light to yellow (Fig. 1). LDs based lighting has a higher light intensity per area which is needed in some quasi-point source applications such as car headlamps, projectors and narrow beam outdoor torches. The main challenge of LDs based luminairies is stable operating at high temperatures. Temperature of phosphors rises because of energy loses due to nonradiative photoluminescence (PL) decay and Stokes shift. Huge amount of not dissipated heat can cause the increase of temperature which leads to the degradation of phosphor and the changed colour of luminairy. For this reason it is important for a phosphor to have as good thermal stability and conductivity as possible [2]. To solve this task scientists are developing new materials and techniques. One way to increase thermal conductivity of phosphor is to change media in which phosphor powder is dispersed. While commercial LED luminaries are usually made of phosphors which are dispersed in silicon, holding media can be changed to glass or other high thermal conductivity transparent material. Steady temperature can also be maintained by using rotating phosphor wheel. Finally, ceramic or bulk phosphors can be used for even higher thermal stability but it requires more complicated phosphor production technologies and therefore are more expensive [3, 4].

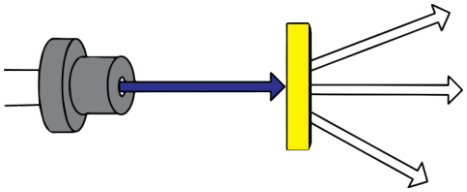

Fig. 1. Source of white light based on blue laser diode and yellow phosphor plate which converts part of the blue light into yellow.

In this work the photoluminescence properties of the group of samples made of YAG:Ce^{3+} phosphor and boron nitride (BN) powders are presented. Some of the samples also contain two types of polymers (M280 ir M600) which were used for better mechanical properties. Different samples contain different concentrations of phosphor, BN and polymer. Photoluminescence emission spectra have been measured for all samples under 450 nm excitation, PL quantum yields have been measured in integrating sphere while PL lifetimes have been measured using frequency domain method using 450 nm laser diode excitation. Samples thermal properties were also evaluated.

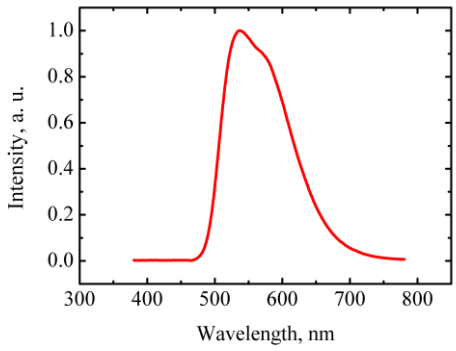

Fig. 2. Photoluminescence spectra of selected sample.

The results have shown that photoluminescence emission spectra do not depend on sample's composition (Fig. 2.) while PL quantum yield strongly varies between different samples. It is also shown that YAG:Ce^{3+}/BN samples have a good thermal conductivity and thermal stability of photoluminescence properties.

[1] Denault, Kristin A., et al. "Efficient and stable laser-driven white lighting." Aip Advances 3.7 (2013): 072107.
[2] Trivellin, Nicola, et al. "Laser-Based Lighting: Experimental Analysis and Perspectives." Materials 10.10 (2017): 1166.
[3] Lenef, Alan, et al. "Laser-activated remote phosphor conversion with ceramic phosphors." Thirteenth International Conference on Solid State Lighting. Vol. 9190. International Society for Optics and Photonics, 2014.
[4] Cantore, Michael, et al. "High luminous flux from single crystal phosphor-converted laser-based white lighting system." Optics Express 24.2 (2016): A215-A221.

ULTRATHIN COPPER FILMS OPTICAL AND STRUCTURAL CHARACTERISTICS DEPENDENCIES ON DEPOSITION PARAMETERS

Audrius Valavičius[1], Povilas Jurkšaitis[1,2], Alexandr Belosludtsev[1]

[1] Optical coatings laboratory, Center for Physical Sciences and Technology, Savanorių ave. 231, Vilnius LT-02300, Lithuania

[2] Department of Physics, Vilnius University, Saulėtekio ave. 9, LT-10222, Vilnius, Lithuania

audrius.valavicius@ftmc.lt

During the recent decades, thin film coatings appeared in many fields of industry, including such industries like semiconductors, optoelectronics, optics and even aerospace. Manufacturing of laser optics often take advantage of dielectric layers, which are used for production of high reflection mirrors, antireflective coatings, filters, polarizers, etc. However the production of non polarizing beam splitters, used in various laser experiments, can get very complicated using only the dielectric structure [1]. For this reason, ultrathin metal layers are introduced in the structure, for better performance of the coating. Due to the specific features of metals, interest in ultrathin metal films is growing rapidly among scientist. These films are used not only for production of non polarizing beam splitters [2], but also for development of superlenses [3], for a more detailed imaging, or transparent conductive electrodes, which could be used with applications in solar cells and OLED screens [4].

The research was made on ultrathin copper films. Their optical properties and morphology were evaluated. The dependencies on deposition rate, deposition temperature and film thickness were studied. Optical loss of all samples was calculated from the transmittance and reflectance spectra. Morphology was measured using atomic force microscope. Copper samples were made by electron beam evaporation technology at temperatures from 50 ºC to 200 ºC degrees, deposition rates from 1 Å/s to 11 Å/s and thicknesses from 6 to 32 nanometers.

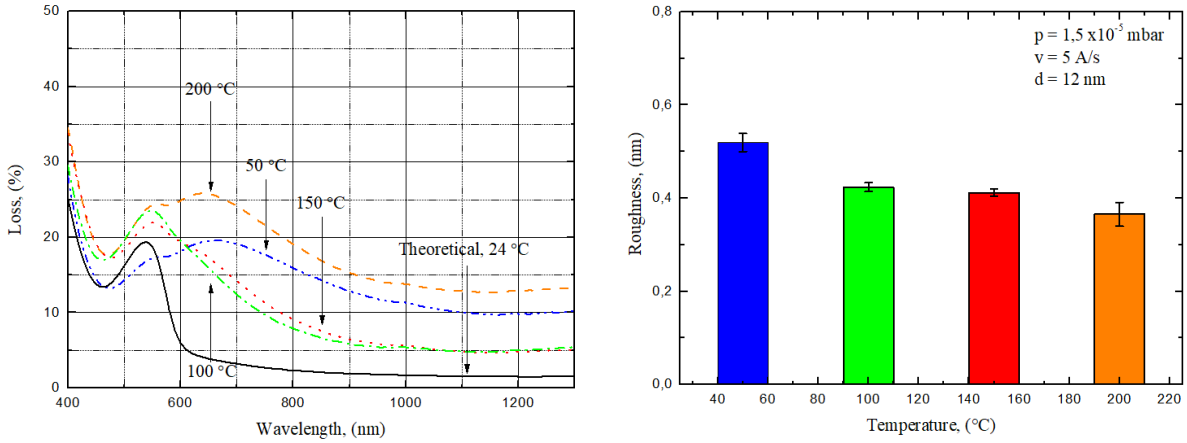

1 pav. Optical loss and surface roughness of ultrathin copper films (12 nm) for samples prepared with different deposition temperatures.

Depending on evaporation process parameters, ultrathin copper films exhibit different optical properties and morphology. It has been shown that, depending on deposition temperature, ultrathin films show different initial stage growth mechanism, therefore some of the samples did not form a continuous metal layer and the absorption of those layers increased substantially (*1 pav.*).

Dependence on deposition rate of copper material showed that, using higher layer deposition rate results in more dense copper films, which exhibits lower absorption of infrared radiation. At low deposition rate (1 Å/s), continuous film was not observed. In this case, ultrathin copper films grow in form of separated metal islands with gaps between them. Furthermore, these islands interact with electromagnetic radiation and localized surface plasmon (LSP) resonance occurs. During LSP resonance, optical absorbtion in the material can be enhanced by up to 15 %. Increase in layer thickness results in more continuous layer, however surface roughness can be increased drastically near percolation threshold.

Ultrathin copper films exhibit tendencies of their growth mechanisms depending on deposition parameters such as temperature, rate and thickness. This allows to better control continuous copper films for variety of applications.

[1] J. Ciosek, J. A. Dobrowolski, G. A. Clarke, ir G. Laframboise, „Design and manufacture of all-dielectric nonpolarizing beam splitters“, *Appl. Opt.*, t. 38, nr. 7, p. 1244, kovo 1999.

[2] J. H. Shi ir Z. P. Wang, „Designs of infrared nonpolarizing beam splitters with a Ag layer in a glass cube“, *Appl. Opt.*, t. 47, nr. 14, p. 2619–2622, geg. 2008.

[3] X. Zhang ir Z. Liu, „Superlenses to overcome the diffraction limit“, *Nat. Mater.*, t. 7, nr. 6, p. 435–441, birž. 2008.

[4] L. Martinez, D. S. Ghosh, S. Giurgola, P. Vergani, ir V. Pruneri, „Ultrathin metal film:An emerging transparent electrode for the optoelectronics industry“, 2008, p. 15–17.

PATTERNING OF ERBIUM OXIDE LAYERS ON SILICON USING PHOTOLITOGRAPHY AND WET ETCHING

Tomas Drunga, Tomas Grinys

Institute of Photonics and Nanotechnology, Vilnius University, Lithuania
drungatomas@gmail.com

The wide band gap Gallium nitride is an excellent semiconductor for the production of high power, high speed transistors [1] as well as semiconductor lasers [2] and light emitting diodes (LEDs) [3]. While GaN bulk substrates are still too expensive for practical use, much attention is drawn towards GaN on Si technology. However, in case of heteroepitaxy, technical difficulties arise due to the difference of crystal lattice types and constants together with thermal expansion coefficients between these two substances. In order to grow high quality GaN, an interlayer of Er_2O_3 could be used to reduce the lattice and thermal mismatch between Si and GaN [4]. Moreover, to avoid the cracking of GaN, it can be grown on a patterned substrate [3].

In this work the wet etching process was investigated in order to perform patterning of Er_2O_3 films on Si using photolithography. Etching rates and activation energies in H_2SO_4 and HCl were evaluated. The layers of Er_2O_3 were patterned as well as the size of the etched structures was determined. Finally, the influence of diffusion and the anisotropy of etching speed are discussed.

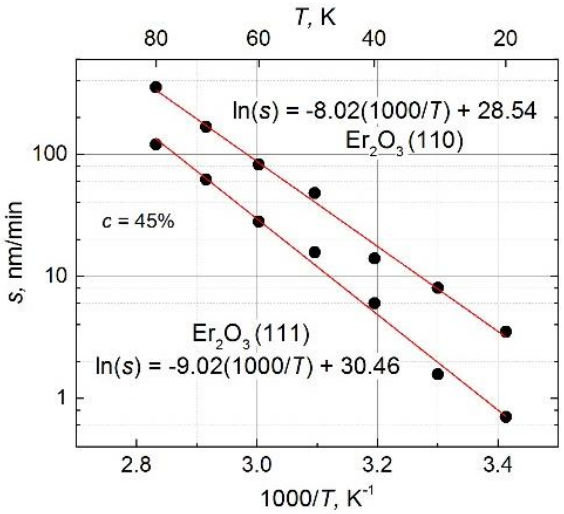

Fig. 1. Etching activation energies of Er_2O_3 in H_2SO_4

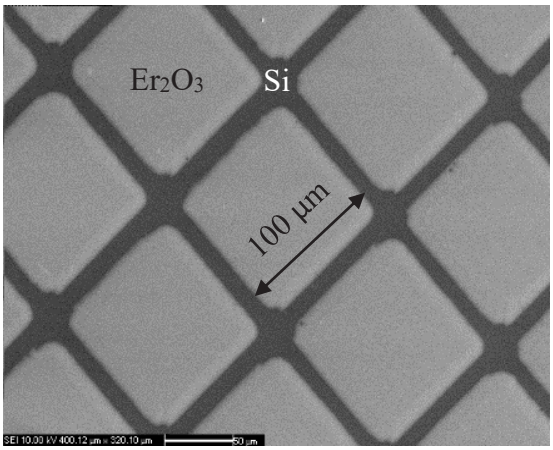

Fig. 2. SEM image of a patterned Er_2O_3 layer on Si

[1] Stephen L. Colino and Robert A. Beach, Ph.D., "Fundamentals of Gallium Nitride Power Transistors", 2009.
[2] Tanya Paskova, Drew A. Hanser, Keith R. Evans, "GaN Substrates for III-Nitride Devices", Proceedings of the IEEE, Volume: 98, Issue: 7, July 2010.
[3] Zhu D, Wallis DJ, Humphreys CJ, "Prospects of III-nitride optoelectronics grown on Si", Reg Prog Phys, 2013.
[4] F. Erdem Arkun, Rytis Dargis, Andrew Clark, Robin S. Smith, Michael Lebby, "Growth of GaN by MOCVD on Rare Earth Oxide on Si(111)", Abstract #1953, 224th ECS Meeting, The Electrochemical Society, 2013.

BORON DOPED DIAMOND MICROELECTRODE ARRAY FOR NEUROTRANSMITTER MONITORING

Kornelija Vitkute[1,2], Jessica Koehne[1]

[1]Center for Nanotechnology, NASA Ames Research Center, United States of America
[2]Department of Neurobiology and Biophysics, Vilnius University, Lithuania
kornelijavitkute@gmail.com

Boron doped diamond (BDD) microelectrode biosensors have been widely implemented for health and environment monitoring because of their unique properties. High resistance to surface biofouling and chemical degradation, stability, robustness, and a relatively wide potential window among other are only a couple of reasons for their superiority to traditional electrodes [1]. Coupled with its inherent biocompatibility, BDD is an ideal candidate electrode for human brain neurotransmitter monitoring *in vivo* [2]. A 3 x 3 array of BDD microelectrode pads has been designed, fabricated and used for the electrochemical detection of dopamine and serotonin in presence of excess ascorbic acid. Similar chemical structure of these neurotransmitters often results in overlapping reduction signals, therefore differential pulse voltammetry has been employed for differentiating between the respective neurotransmitter peaks. Experiments were performed with BDD as the working electrode, Ag/AgCl as the reference electrode and Pt as the counter electrode. Increasing scan rate measurements were made in order to define adsorption/diffusion controlled charge transfer kinetics. AFM, SEM and Raman spectroscopy have been used to characterize the structure and composition of the BDD material. A comparison between the BDD macroelectrode and microelectrode biosensors has been made to distinguish the effects of the electrode's surface area on the data obtained. The results support that BDD is a strong candidate for the detection of neurotransmitters in the brain.

[1] Suzuki, A. *et al.* Fabrication, characterization, and application of boron-doped diamond microelectrodes for in vivo dopamine detection. *Anal. Chem.* **79,** 8608–8615 (2007).
[2] Alcaide, M., Taylor, A., Fjorback, M., Zachar, V. & Pennisi, C. P. Boron-doped nanocrystalline diamond electrodes for neural interfaces: In vivo biocompatibility evaluation. *Front. Neurosci.* **10,** 1–9 (2016).

INVESTIGATION OF BIPOLAR SMALL ORGANIC MOLECULES AS ACTIVE MATERIAL IN ELECTROCHROMIC DEVICES

Valentinas Andrulis[1], Erika Rajackaitė[2], Tomas Matulaitis[3], Asta Dabulienė[3], Audrius Bučinskas[3], Dalius Gudeika[3], Asta Tamulevičienė[1,2]

[1] Department of Physics, Kaunas University of Technology, Studentų Str. 50, Kaunas, Lithuania
[2] Institute of Materials Science of Kaunas University of Technology, K. Baršausko Str. 59, Kaunas, Lithuania
[3]Department of Polymer Chemistry and Technology, Kaunas University of Technology, Radvilėnų Av. 19, Kaunas, Lithuania
valentinas.andrulis@ktu.edu

Electrochromic materials (ECMs) possess the ability to change their optical properties as reversible responses through the alternation of the applied potential or current. ECMs are employed in numerous practical applications, such as electronic paper, smart windows and optical memory devices [1]. In most cases, the inorganic oxides based on W, Mo, Ir or Ni are used [2]. Organic ECMs have unique advantages over their inorganic counterparts, which include fast response time, flexible device fabrication, a relatively narrow absorption band in displaying diverse and clear colours and large-scale processability [1].

In the present study different type small organic molecules were investigated as active materials in electrochromic devices (ECD). The changes of structure during the device performance were investigated employing Raman scattering (inVia, 532 nm, Renishaw, UK) and FTIR (Vertex 70, Bruker, Germany) spectroscopies. The change of transmittance under the impact of applied voltage was registered using UV/VIS spectrometer. The ECD containing ion-conducting liquid with active organic material was sandwiched between two electrode surfaces using a spacer of ~1 mm. An indium tin oxide (ITO)-coated glass/PET (Solaronix, Switzerland) was used as electrodes in the device. The electrolyte solution was prepared by dissolving organic molecules (10^{-3} M) and tetrabutylammonium hexafluorophosphate $TBAPF_6$ (0.1M) in acetonitrile. Then, electrolyte was injected into the electrochromic device with the use of a syringe.

The FTIR spectrum of starting material in powder form is presented in Fig. 1. The inset in Fig. 1 shows the chemical structure of the compound used in ECD. The investigated compound was dissolved in acetonitrile with $TBAPF_6$ and injected between two ITO-glass electrodes. At the starting point (no applied voltage), the absorption around 440 nm was observed as shown in Fig. 2. The influence of the applied voltage on the transmittance of the system was tested. It was shown that under the applied voltage of 3 V the absorption peak at 440 nm disappeared, and the overall transmittance of the sample decreased.

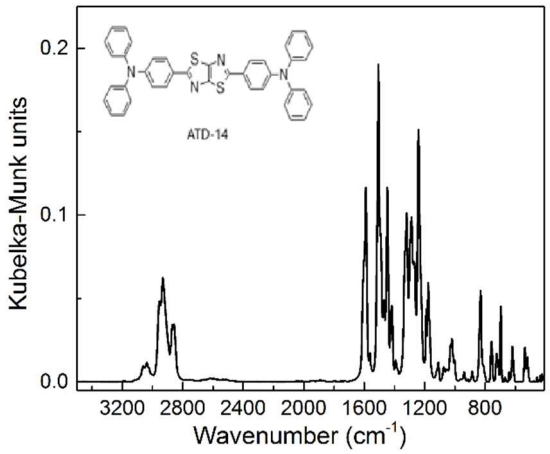

Fig. 1. FTIR spectrum of ATD-14 compound measured in diffuse reflectance configuration

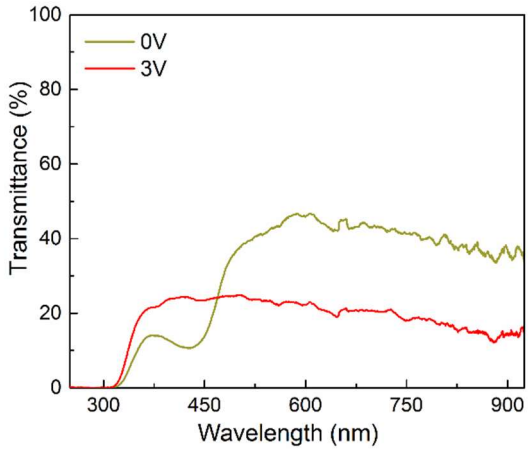

Fig. 2. Transmittance variation of the thin liquid film of ATD-14 in an ITO device with the switch of voltage from 0 V to 3 V.

Acknowledgement. This research was supported by the Research, Development and Innovation Fund of Kaunas University of Technology (grant No. MTEPI-P-17022).

[1] L.-h. He, G.-m. Wang, Q. Tang, et al., Synthesis and characterization of novel electrochromic and photoresponsive materials based on azobenzene-4,4'-dicarboxylic acid dialkyl ester, J. Mater. Chem. C **2**, 8162-8169 (2014).
[2] C. G. Granqvist, Oxide electrochromics: An introduction to devices and materials, Sol. Energy Mater Sol. Cells 99, 1-13 (2012).

STRESS-STRAIN AND DAMAGEABILITY STATES OF THE BORING BAR FRONT-END STRUCTURE OF HEAVY-DUTY HORIZONTAL BORING LATHE

PhD, DSc [1]Sherbakov Sergei S., PhD [2]Shi Wu, PhD [2]Junpeng Shao, [1]Nasan Aleh A., [1]Padhaiskaya Daria A.

[1]Belarusian State University, Minsk, Republic of Belarus
[2]Harbin University of Science and Technology, Harbin, China
oleg.nasan@gmail.com

Multi-element tribo-fatigue boring bar front-end structure, which is one of the most critical components of heavy-duty horizontal boring lathe (see Fig. 1a) is studied in this work. The structure contains contact interactions with friction between its various elements and a non-contact bending.

The aim of the work was to improve cutting process on the existing super heavy-duty horizontal boring lathe by carrying out computer simulations for determining stress-strain state of front-end structure of new design. Another aim of this work was to determine the positions of the system elements for minimizing damageability of the system while increasing the boring radius.

For that purpose computer finite-element models considering two phases of loading: bolts pretension and cutting process in spatial static statement were created [1]. All elements of the system consist from the 18HGT steel.

Firstly, it was shown that if motion of only two upper bases is considered then there is no reason to model full front-end structure with the boring bar. After that, several calculations of the front-end structure were made from which boundary conditions for the submodel, shown in Fig. 1b, were applied for the cutting edges.

During submodeling, elementary classical analysis based on the distributions of the stress tensor components was held for every part of the system (see Fig. 1c). Then for obtaining more precise results the analysis of dangerous volumes (see Fig. 1d) and volumetric integral damageability was performed [2].

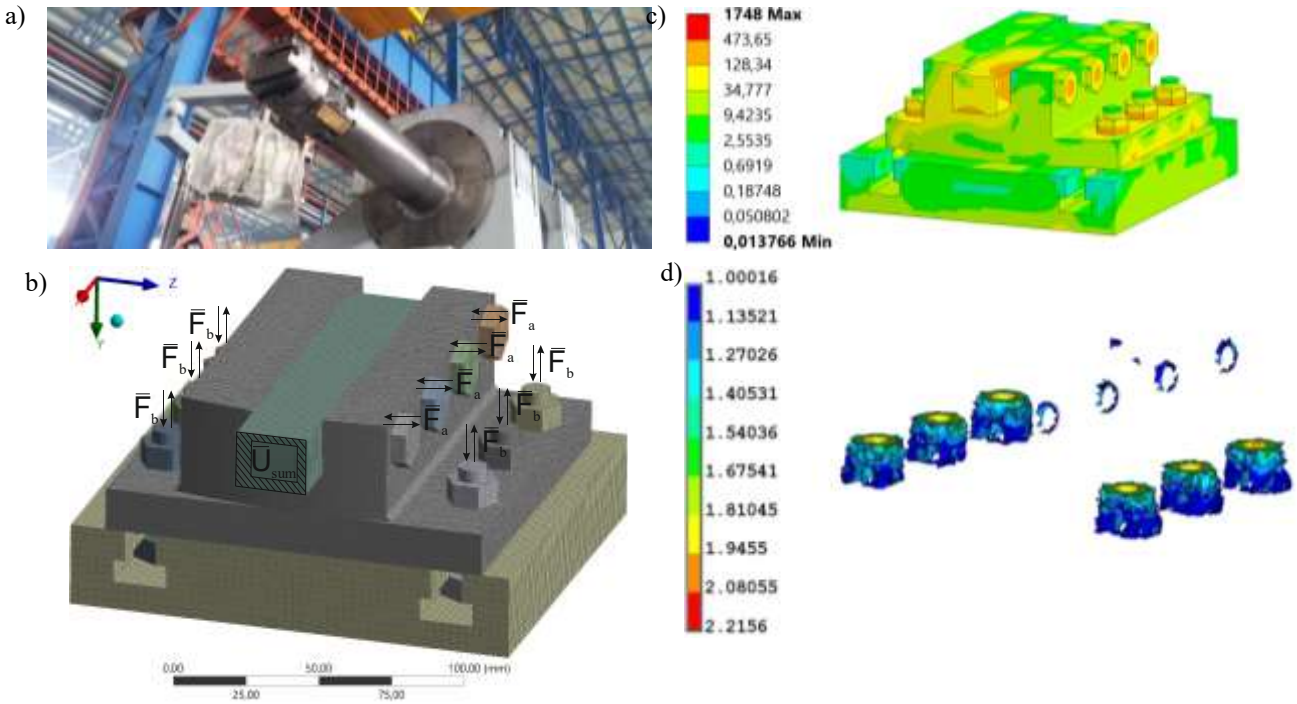

Fig. 1. General views of a) front-end structure; b) FEM mesh with loading scheme of submodeled front-end structure; c) distribution of equivalent stress σ_{eqv} during boring process in the submodel; d) dangerous volumes in the upper base

According to the results of the research, it is recommended to apply rigid fixing of the upper base in the position closest to the center of the middle base in order to minimize the volumetric damageability of the system.

This work was supported by National special project for international scientific and technological cooperation of the People's Republic of China (2012DFR70840).

[1] S.S. Sherbakov, Wu Shi, Shao Junpeng, A.A. Nasan, Spatial stress-strain state of the boring bar front-end structure of heavy-duty horizontal boring lathe depending on the boring radius, Theoretical and Applied Mechanics **33**, 130–136 (2018).
[2] L.A. Sosnovskiy, S.S. Sherbakov, *Mechanothermodynamics* (Springer, 2016).

ALL-PRINTED GAS SENSOR FOR SPACE MANUFACTURING

Kazimieras Badokas[1,2], Dong-Il Moon[2], Meyya Meyyappan[2]

[1] Vilnius University, Sauletekio Ave 9, Bld. III, Vilnius, LT-10222, Lithuania
[2] Center for Nanotechnology, NASA Ames Research Center, Moffett Field, CA 94035, USA
badokas.k@gmail.com

Technologies that enable humans to live and work more securely in space will be an important determinant for future missions. In this regard, printed electronics offer a great advantage for space exploration by providing the ability to easily augment, replace or repair system components after mission deployment. Gas sensors are extremely important for monitoring air quality in crew cabin as well as locating gas leaks, if any. Compared to other electronics, gas sensors have inherently short lifetime, and malfunction could cause serious situations. Accordingly, gas sensors may be considered as consumable requiring periodic replacement. To solve these problems, we propose printed gas sensors in the International Space Station (ISS) for future missions.

In this background, we developed printed gas sensors using a single-walled carbon nanotubes (SWNTs) ink and a single-input and multiple-output (SIMO) design. The prototype sensors were fabricated fully by printing techniques on a flexible substrate; therefore, the printed gas sensor could be useful for various applications. Furthermore, the sensor response, i.e., SIMO scheme that refers to a single gas concentration and the collection of multiple terminal responses, is defined by a statistical Gaussian measure to overcome the variation issues from printing techniques and nanotechnology. Arduino system with Bluetooth module was also implemented in the printed sensor platform for control of proposed SIMO scheme, data acquisition and wireless data transfer. We demonstrate the ammonia sensor as a proof of concept, although target gases could be extended upon necessity to be evolved as a form of e-nose.

EUROPIUM COORDINATION COMPOUNDS BASED NANODIMENSION THIN FILMS FOR LIGHT-EMITTING DEVICES

Olena Litsis[1], Nataliia S. Kariaka[1], Tatiana Yu. Sliva[1], Yu.V. Kolomzarov[2], I.E. Minakova[2], Vladimir M. Amirkhanov[1]

[1] Department of chemistry, Taras Shevchenko National University of Kyiv, 12, Lva Tolstogo Str., Kyiv, 01033, Ukraine
[2] V.E. Lashkaryov Institute of Semiconductor Physics, National Academy of Sciences of Ukraine, Kyiv, Ukraine
olitsis@ukr.net

Light emitting diodes employing heavy-metal complexes are very attractive since the electroluminescence (EL) efficiency, which is limited by the radiative recombination of singlet excitons and can be increased by the addition of the phosphorescent emission from the triplet excitons of the complexes. In order to obtain efficient emission from the complexes, they are usually dispersed in a suitable host displaying the two main properties of: 1) providing efficient energy/charge transfer to the phosphorescent dopants and 2) avoiding concentration quenching effects of the complexes. The use of an electroluminescent polymer as host for the phosphorescent complexes has the further advantage that its own fluorescent component can be exploited for multicolor emission, provided that the energy transfer (ET) from polymer to phosphorescent guest is incomplete and that no direct charge trapping at the dopant site occurs. Thanks to their narrow red emission, Eu^{3+}-complexes have attracted considerable interest in designing organic light emitting diodes (OLEDs) for full color displays. In the last few years, many reports appeared where blends of Eu^{3+}-diketonates in fluorescent π-conjugated polymers polyfluorenes type have been used. Förster resonant energy transfer (FRET) takes place in such blends because of overlap between the polymer emission and complex absorption.

In this paper, we report on a simple and promising approach to realize EL heterostructures using a blend film of blue and red-orange Eu^{3+} complex. Bright blue emission in the 410-450 nm range is characteristic of the **PFD** (poly(9,9-di-*n*-dodecylfluorenyl-2,7-diyl). The overlapping absorption was shown for $EuWi_3 \cdot 2KM$ complex (where Wi^- – carbacylamidophosphate ligand $PhC(O)N^-P(O)(OCH_3)_2$; KM - Michler's ketone $[(CH_3)_2NC_6H_4]_2CO$) in the range 390-440 nm. Also $EuWi_3Phen$ (Phen = 1,10 – phenantroline) complex with absorption in the range 275-350 nm was used. Both complexes under investigation, being excited by UV light, show intensive photoluminescence with maxima at 612.5 nm, observed for $^5D_0 - {}^7F_2$ transition.

The strong correlation between frequency of the spin coating process and film thickness is confirmed by AFM images of $EuWi_3Phen$ films deposited at different resolutions (frequencies of rotation) and concentrations, as shown in Fig. 1. Absolute measurement of the film thickness was made. It can be easily observed that the homogeneity of the film is enhanced when the frequency of the spin coating process rises (Table 1).

Table 1. Thickness of $EuWi_3Phen$ thin films, deposited on the glass substrate (volume of solution 250 µl, time of rotation 15 min)

Deposition parameters		**Thickness, nm**
C, mol/l	*Freqquency of rotation, rpm*	
0,01	500	47
0,001	1000	10
0,01	500	4,5
0,001	1000	10

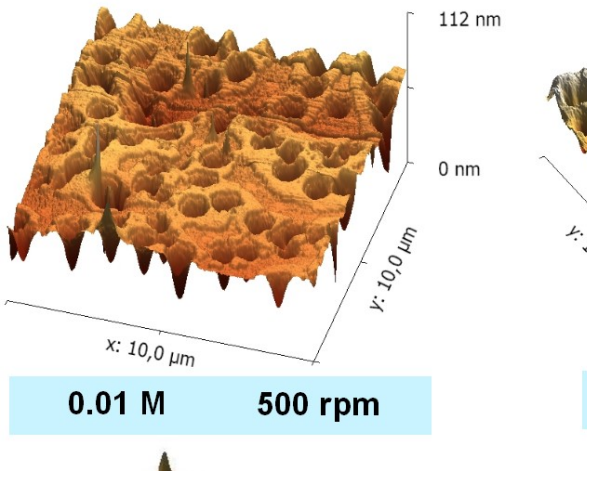

Fig.1. AFM images of $EuWi_3Phen$ thin films deposited at several frequencies of rotation by spin coating of toluene solutions

The polymer-based planar light-emitting heterostructures fabricated in this work have the ITO/PEDOT:PSS/**PFD**/Ca+Al (**1**) structure. Samples of different solution concentration have been created by spin coating and their current-voltage (A-V) characteristics have been investigated. The best A-V values of EL starting and puncture voltage were demonstrated for 5 mg/ml PFD solution. Wherefore this concentration was used for fabrication of polymer-blend-based EL devices. They have the structures ITO/PEDOT:PSS/PFD+$EuWi_3 \cdot 2KM$/Al+Ca (**2**) and ITO/PEDOT:PSS/PFD+$EuWi_3Phen$/Al+Ca (**3**). Diodes prepared with thinner organic films allow higher currents at lower voltages; this can be achieved either by increasing the frequency of the spin coater rotation or by using concentrations of Complex:Toluene lower than 10% weight (the best values was demonstrated for 5%). Fig. 2 shows the I-V characteristics of **1**-**3** heterostructures. The PFD and PFD-Complex layers were deposited at the same spin coater frequencies of rotation (2500 rpm). Bright electroluminescence in all heterostructures was observed. In general, the best performance of the devices made with europium complexes was observed.

CYCLODEXTRIN GLUCANOTRANSFERASE PRODUCTION BY ALKALIPHILIC BACTERIA ISOLATED FROM POTATO SOIL

Robertas Sičiovas, Nicola Tiso, Audrius Maruška

Instrumental Analysis Open Access Center, Faculty of Natural Sciences, Vytautas Magnus University, Vileikos 8, LT-44404 Kaunas, Lithuania
robertas.siciovas@stud.vdu.lt

Raw starch degradation pathway via cyclodextrins is usually carried out by alkaliphilic bacteria by producing cyclodextrin glucanotransferase (CGTase) enzyme. Alkaliphilic bacteria most commonly found in starch sources or alkaline saline environment. Bacteria require an alkaline pH and have an optimal growth at ca. pH 10. CGTase convert starch and other 1, 4-linked α-glucans to cyclodextrins (CD), which are featured by hydrophilic outside and hydrophobic central cavity. Because of the ability to form inclusion complexes with various organic and inorganic compounds, CD can be used to modify the physicochemical characteristics of low polarity drugs or used as chiral selectors in capillary electrophoresis and chromatography [1, 2].

The objective of our study was to optimize the cultivation conditions and growth medium composition for CGTase production from alkaliphilic bacteria isolated from local sources and use the enzyme for cyclodextrins synthesis from starch. Effective CD production from raw sources would allow to reduce high production costs and extend the uses of these cyclic polysaccharides in analytical chemistry, pharmaceutical and food industries. To authors knowledge, no such studies were carried out in Lithuania up-to date.

18 soil samples from the fields of growing and storage places of potato and other starch sources in Lithuania were collected and used for the isolation of CGTase producing bacteria on starch-agar plates. After 24 hours of incubation on starch-agar medium at 37 °C, the plates were stained with 0.02% (w/v) iodine in 0.2% (w/v) KI solution. Colonies that showed clear zones were considered as a starch hydrolyzing enzyme producer and were sub-cultured on Horikoshi-II agar plates. After 24-48 hours of incubation on Horikoshi-II medium at 37 °C, yellowish colored zones were detected around the bacteria colonies, suggesting possibility of CGTase production by those strains [3]. However, agar plate methods are sensitive for some of glycoside hydrolase family enzymes. Therefore, positive isolates were cultivated in alkaline liquid medium and CGTase activity was measured in the cultures supernatants. Enzymatic activity was evaluated spectrophotometrically by phenolphthalein assay measuring the quantitative ability to produce CD [4]. One unit of the CGTase activity was defined as the amount of enzyme that catalyzes the production of 1 μmol of β-CD per minute under the reaction conditions. Sample with the biggest enzymatic activity was selected for the optimization of culture conditions for the production of CGTase. The enzyme production was optimized using several growth conditions. These included the different carbon sources substituting soluble starch (pea starch, wheat starch, corn starch, potato starch), main carbon source concentration (0-3% (w/v)), sodium carbonate concentration (pH) (0-2% (w/v)), magnesium sulfate concentration (0.02-0.2% (w/v)), different inorganic salts additives (NaH_2PO_4, Na_2HPO_4, KH_2PO_4, K_2HPO_4, $NH_4H_2PO_4$, NaCl), inoculum size (0.25-3% (v/v)), medium volume (25-150 ml), temperature (25-42 °C) and harvesting time (0-54 hours).

A total number of 18 samples were processed for isolation of CGTase producing bacteria of which all (100%) showed starch hydrolyzing activity and 10 isolates (56 %) showed qualitative cyclization activity. Bacteria isolated from potato soil (Raseiniai District 55º24'2" N 22º53'14" E) showed the biggest enzymatic activity after 48 hours of incubation in Horikoshi-II medium at 37 °C. The optimal conditions for CGTase production was consisted of 3% (w/v) soluble starch, 0.5% (w/v) soya peptone, 0.5% (w/v) yeast extract, 1.5% (w/v) sodium carbonate (pH 10.5), 0.02% (w/v) magnesium sulfate, 0.1% (w/v) ammonium dihydrogen phosphate and 2.5% (v/v) inoculum size. It was also determined that isolated bacteria produce the highest concentration of CGTase at 37 °C temperature after 30 hours of cultivation in 100 ml of growth medium. During the study, enzymatic activity varied from 2.56 ± 0.84 mU/ml to 175.09 ± 3.74 mU/ml.

---

[1] K. Horikoshi, Microbiology and Molecular Biology Reviews **63(4)**, 735-750 (1999).
[2] A. Rocco, A. Maruška, S. Fanali, Analytical and Bioanalytical Chemistry **402(9)**, 2935-2943 (2012).
[3] A. F. Elbaz, A. Sobhi, A. ElMekawy, Bioprocess and Biosystems Engineering **38(4)**, 767-776 (2015).
[4] R. R. Panchal and K. N. Rajput, International Journal of Pharma and Bio Sciences **8(1)**, 333-338 (2017).

Acknowledgement: The research funding was granted by Research Council of Lithuania project 09.3.3-LMT-K-712-03-0128.

CHLOROPHYLLIN-BASED PHOTOSENSITIZATION FOR MICROBIAL CONTROL OF FOODS

Eglė Paškevičiūtė[1], Bernadeta Žudytė[1], Živilė Lukšienė[1]

[1] Institute of Applied Research, Vilnius University, Lithuania
bernadetazud@gmail.com

In recent years fruits and vegetables have been increasingly implicated as 2nd leading cause of foodborne illnesses [1]. Thus, existing decontamination technologies for microbial control are not enough effective.

In this context photosensitization seems promising. It employs a photosensitizer which preferentially associates with microorganism and after activation with visible light of appropriate wavelength generates around reactive oxygen species (ROS) which induce lethal damage of microorganism [2].

The present investigation was undertaken to evaluate the effectiveness of Chlorophyllin-based photosensitization for microbial control of fresh produce, i.e. cocktail tomatoes.

Data presented in Fig. 1A indicated that after illumination of Chl-soaked tomatoes with LED-based light (405 nm (light dose 3 J/cm^2) microbial contamination reduced by 2.4 log (99%), whereas the population of *Listeria* reduced by 1.5 log (95 %) (Fig. 1B).

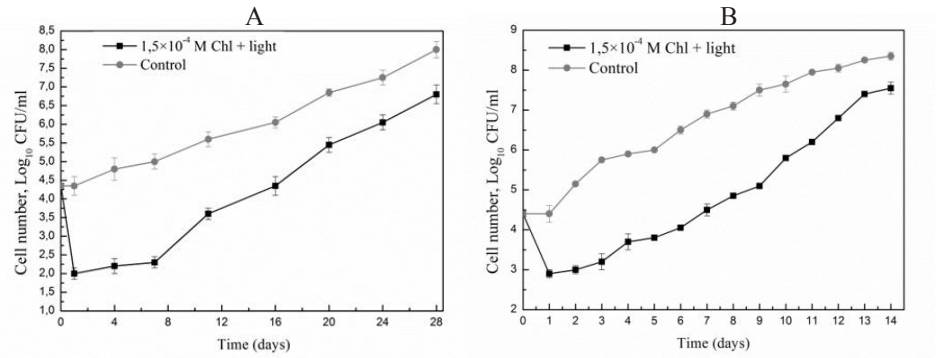

Fig. 1 A - Regrowth of mesophilic bacteria on cherry tomatoes after photosensitization treatment: 1.5x10^{-4}M, 5 min illumination, light dose 3 J/cm^2; B - Regrowth of thermoresistant pathogen *Listeria monocytogenes* 56Ly.

During treatment temperature on the surface of tomatoes changed only from 23 °C to 28.5 °C what means that treatment is not dangerous to food matrix.

Nutritional quality of treated tomatoes was tested evaluating total antioxidant activity. No statistically significant changes of the antioxidant activity of treated tomatoes have been found.

Comparing the decontamination efficiency of Chl-based photosensitization with conventional preservation treatments showed that that Chl-based photosensitization was most effective (Fig. 2).

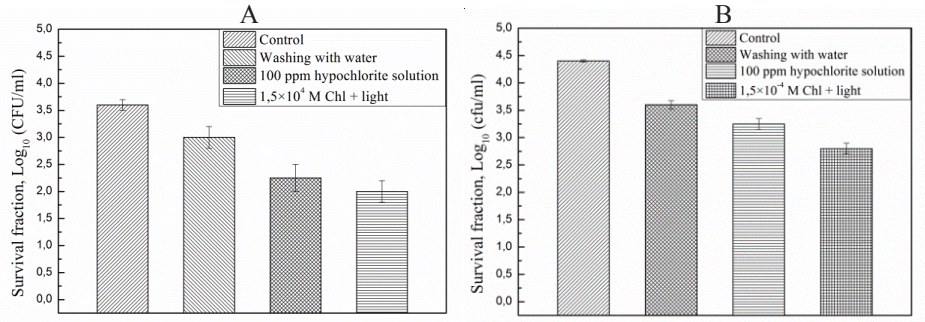

Fig. 2 A - Inactivation of termoresistant *Listeria monocytogenes* 56Ly; B - termoresistant *Bacillus cereus* SV60 inoculated on tomatoes by Chl-based photosensitization in comparison with conventional treatments.

Chl-based photosensitization drastically reduced the population of naturally distributed surface attached mesophilic bacteria and inoculated termoresistant strains of *B. cereus* and L. *monocytogenes*. Moreover, it did not induce harmful effects on nutritional quality of tomatoes, acted nonthermally and prolonged the shelf-life of tomatoes by 4 days. In our opinion, chlorophyllin-based photosensitization has a huge potential as alternative not-chemical, light-based fruit and vegetable preservation technology.

[1] I. Castro-Ibáñez, M.I. Gil, A. Allende, Ready-to-eat vegetables: Current problems and potential solutions to reduce microbial risk in the production chain, LWT - Food Sci. Technol. 85, 284–292 (2017).

[2] Z. Luksiene, E. Paskeviciute, Novel approach to decontaminate food-packaging from pathogens in non-thermal and not chemical way: Chlorophyllin-based photosensitization, in: J. Food Eng., Elsevier Ltd, 317-323 (2012).

BIODEGRADATION OF CROSS-LINKED EPOXIDIZED LINSEED OIL-BASED POLYMERS AND THEIR COMPOSITES

Egle Surkaite, Justina Vaicekauskaite, Jolita Ostrauskaite

Department of Polymer Chemistry and Technology, Kaunas University of Technology, Lithuania
jolita.ostrauskaite@ktu.lt

Recently increased environmental consciousness and the search of new renewable raw materials has led to the increased interest of both polymer research and industry. For the production of polymers it is desired that polymer would have properties similar to those of petroleum-derived polymers and be able to decompose into harmless substances after use.

Natural oils have become the center of attraction for their potential use as starting materials for the preparation of polymers due to ready availability, inherent biodegradability, limited toxicity, and existence of modifiable functional groups.[1,2] Natural oils possess unique characteristics of biodegradation, biocompatibility and structure versatility which make it possible to develop a variety of novel polymeric materials.[3,4]

The aim of this study was to investigate the biodegradability of the cross-linked linseeed oil-based photopolymers and polyphosphates synthesized with and without reactive diluent bis[4-(glycidyloxy)phenyl]methane as well as their composites with industrial waste materials of natural origin (horn meal, pine needles, pine bark and mix of grain waste and weeds). Utilization of renewable resources instead of petroleum sources and their biodegradability in different environments enable such polymers and polymer composites to be more easily acceptable than the conventional plastics. [5]

Biodegradation of the cross-linked linseeed oil-based photopolymers, polyphosphates and their composites was investigated by the respirometric method. This method is based on changes in pressure following oxygen consumption in a hermetically closed bottle containing the sample. This apparatus measures the oxygen consumption almost continuously over the incubation period. The measurement of biochemical oxygen demand with OxiTop® respirometric measuring system was carried out according to the standardized procedure ISO 14851.

Fig. 1. OxiTop® respirometric measuring system

It was determined that the biodegradation rate of all linseeed oil-based cross-linked polymers was lower than that of cellulose which was used an internal standard. The biodegradability of the investigated cross-linked polymers depended on amount and chemical structure of the used reactive diluent. The higher amount of aromatic reactive diluent was used in the reaction mixture for the synthesis of photopolymers the lower biodegradation rate was determined. The higher amount of aromatic reactive diluent was used in the reaction mixture for the synthesis of polyphosphate the higher biodegradation rate was determined. The biodegradability of the linseeed oil-based polyphosphate composites depended on the amount and nature of industrial waste filler. The highest biodegradation value was determined for the polymer composites filled with mix of grain waste and weeds. The lowest biodegradation value was determined for the polymer composites filled with horn meal.

Acknowledgements. Financial support from the Research Council of Lithuania (project No. MIP-066/2015) is gratefully acknowledged.

[1] Biermann U., Bornscheuer U., Meier M. A. R., Metzger J. O., Schafer H. J., Oils and fats as renewable raw materials in chemistry, Angewandte Chemie International Edition, 2011, 50, 3854–3871.
[2] Montero de Espinosa L., Meier M. A. R., Plant oils: The perfect renewable resource for polymer science?!, European Polymer Journal 2011, 47, 837–852.
[3] Huang S. W., Zhuo R. X., Recent Advances in Polyphosphoester and Polyphosphoramidate-Based Biomaterials, Phosphorus Sulfur and Silicon and the Related Elements, 2008, 183, 340–348.
[4]Wang Y. C., Yuan Y.Y., Du J. Z., Yang X. Z., Wang J., Recent progress in polyphosphoesters: from controlled synthesis to biomedical applications, Macromolecular Bioscience, 2009, 9, 1154–1164.
[5]Emadian S. M., Onay T. T., Demirel B., Biodegradation of bioplastics in natural environments, Waste Management, 2017, 59, 526-536.

DETECTION OF HYPOCHLOROUS ACID-PRODUCING ACTIVITY OF NEUTROPHILS IN RESPONSE TO PLANT LECTINS USING CELESTINE BLUE B

Veronika Lutsenko[1], Daria Grigorieva[1], Irina Gorudko[1], Alexey Sokolov[2,3,4]

[1] Department of Physics, Belarusian State University, Belarus
[2] Department of Molecular Genetics, Research Institute of Experimental Medicine, Saint-Petersburg, Russia
[3] Department of Biophysics, Research Institute of Physico-Chemical Medicine, Moscow, Russia
[4] Department of Fundamental Problems of Medicine and Medical
nika.lutsenko@tut.by

Lectins are proteins of non-immune origin, which reversibly and selectively bind to carbohydrates and carbohydrate components of glycoconjugates of different nature. The presence of various types of carbohydrate-binding proteins has been identified in tissues, biological fluids and on the surface of human and animal cells. The role of endogenous lectins and carbohydrate-binding proteins in the body is associated with functioning of the immune system and regulation of biorecognition processes that can trigger the effector cells functions [1]. It has been shown that many plant lectins, along with physiological stimulants (chemotactic peptides, cytokines) and endogenous lectins cause a neutrophils activation, inducing secretory degranulation and production of reactive oxygen species (superoxide and H_2O_2) by these cells [1-4]. It is also known that reactive halogen species (RHS), which are formed in reactions catalyzed by myeloperoxidase (MPO) in the presence of H_2O_2 and halogen ions, play an important role in the regulation of various physiological and pathological processes (antimicrobial protection, cytotoxicity, redox regulation and others). However, the role of lectins in stimulating RHS production by neutrophils is not well understood.

Nowadays a problem of searching for a specific and sensitive probe for hypochlorous acid (HOCl) detection is being actively studied. Recently it was proposed a spectrophotometric method of measuring the kinetics of HOCl production by monitoring the oxidation of the dye Celestine blue B – C.I.51050 (CB) in the presence of taurine [5]. It was shown that CB selectively reacts with HOCl and becomes oxidized to glycol, which which results in a color change of CB from blue to pink and in emergence of fluorescence at 578 nm (excitation at 488 nm). Using the new method, we studied the ability of plant lectins with different carbohydrate specificity to stimulate formation of HOCl by neutrophils.

For neutrophil activation were used plant lectins of different carbohydrate specificity: WGA *(Triticum vulgaris* agglutinin) – GlcNAc-specific lectin of wheat germ, CABA (*Caragana arborescens* agglutinin) – a lectin of the caracane tree, specific to GalNAc residues, Con A (*Canavalia ensiformis* agglutinin) – mannose-binding lectin of cannulae seeds, GalNAc/galactose-specific lectin of bean seeds PHA-L (*Phaseolus vulgaris* agglutinin), SNA (*Sambucus nigra* agglutinin) – lectin of blackberry cortex, specific for galactose and sialic acid residues, as well as SBA (*Glycine hispida* agglutinin) – galactose-specific soy lectin.

It was shown that WGA, CABA, Con A and PHA-L (0.05-0.1 g/L) along with the well-known agonists – N-formylmethionyl-leucyl-phenylalanine (fMLP) and phorbol 12-myristate 13-acetate (PMA) activate neutrophils judged by the increasing fluorescence intensity due to CB oxidation by HOCl, while SNA and SBA were inactive in this regards. It is note that active lectins, as well as fMLP, caused a fluorescence signal only in the presence of cytochalasin b (5 mg/L). This fact is consistent with literature data that inhibition of actin polymerization promotes the release into the extracellular space of MPO, stored in azurophilic granules [4].

The ability of lectins to stimulate the formation of HOCl by neutrophils depends on their carbohydrate specificity. The use of lectins for estimation of hypochlorous acid-producing activity of neutrophils using CB can be important both in the study of the pathogenesis of various inflammatory diseases associated with neutrophil dysfunction, and for development on the base of lectins drugs with immunomodulatory action aimed at enhancing the functional activity of neutrophils. This study was supported by grants Russian Scientific Foundation Grant 18-515-00004, Belarusian Republican Foundation for Fundamental Research (B16P-015) and MD-5133.2018.4.

[1] A. V. Timoshenko, The use of endogenous lectins in clinical diagnostics, Medical news, **4**, 16-20 (1997).
[2] I. V. Gorudko, A. V. Mukhortava, B. Caraher et al., Lectin-induced activation of plasma membrane NADPH oxidase in cholesterol-depleted human neutrophils, Archives of biochemistry and biophysics, **516**, 173-181 (2011).
[3] G. Pereira-da-Silva, C. F. Carvalho, C. M. Roque-Barreira, Neutrophil activation induced by plant lectines: modulation of inflammatory processes, Inflammation & Allergy-Drug Targets, **11**, 433-441 (2012).
[4] A. V. Timoshenko, K. Kayser, H. J. Gabius, Lectin-triggered superoxide/H_2O_2 and granule enzyme release from cells, Methods in Molecular Medicine, 441-445 (1998).
[5] A. V. Sokolov, V. A. Kostevich, S. O. Kozlov et al., Kinetic method for assaying the halogenating activity of myeloperoxidase based on reaction of celestine blue B with taurine halogenamines, Free Radical Research, **49**, 777-789 (2015).

REGULATION OF NEUTROPHIL ACTIVITY BY REACTIVE OXYGEN, NITROGEN AND CLORINE SPECIES

Alena Kavalenka, Elizaveta Kavalenka, Alexandra Zayko

Department of Biophysics, Faculty of Physics, Belarusian State University
ai0628k@gmail.com

Neutrophils are immune cells which provide intracellular or extracellular capture of different particles and cells destroying them by oxygen-independent and oxygen-dependent enzyme mechanisms. Oxygen-dependent mechanisms include activation of myeloperoxidase (MPO), NADPH-oxidase, NO-synthase and generation the reactive oxygen, nitrogen and chlorine species (RONCS), in particularly, $\cdot O_2^-$, H_2O_2, OCl^-, $ONOO^-$ and free-radical products. Intracellular destruction is associated with endocytosis. Extracellular destruction is due to neutrophil extracellular "traps" (NETs) formation from DNA strands with enzymes localized on them. Pathogen microorganisms as well as erythrocytes, platelets can be captured in these NETs [1,2]. It is assumed that RONCS released outside neutrophils can influence the cells on the principle of feedback and change their activity. Accumulation of NO_2^- in medium can occur due to processes not associated with neutrophils, but NO_2^- interactes with neutrophil products that leads to additional RONCS yield. The aim of the work was to investigate the effects of H_2O_2, OCl^-, $ONOO^-$, NO_2^- on neutrophil activity.

Neutrophils were isolated from donor blood by density gradient centrifugation. Cells were resuspended in Earle's medium at pH 7.3. The cell activity was assessed by chemiluminescent method under the action of fMLP (10 μM), PMA (8 μM) and during adhesion to glass. The cell structure was studied by nephelometry and light microscopy.

It was established that the kinetics of RONCS generation were changed as a result of the incubation of cells in the presence of NO_2^- (in a concentration of 0.02 to 1 mM), H_2O_2 (from 10 to 80 μM), $ONOO^-$ (7-12 μM), OCl^- (5 μM). When cells were activated with fMLP or PMA, an increase in the ability of neutrophils to generate RONCS was revealed during the first minutes, then a decrease in the RONCS yield can be observed compared to cells incubated without adding extracellular RONCS. The cell ability to generate RONCS and secrete MPO in the extracellular medium upon activation during adhesion to glass increased in neutrophils incubated in the presence of NO_2^-, $ONOO^-$ and OCl^- and decreased in neutrophils subjected to H_2O_2. Alteration of RONCS formation in neutrophils treated by combination of "NO_2^- + OCl^-" was corresponded to the sum of the effects observed at separate action of NO_2^- and OCl^-. The effects of combined action of "NO_2^- + H_2O_2", "NO_2^- + H_2O_2 + OCl^-" on cell activity were not additive indicating the different mechanisms of RONCS action on neutrophils (fig.1).

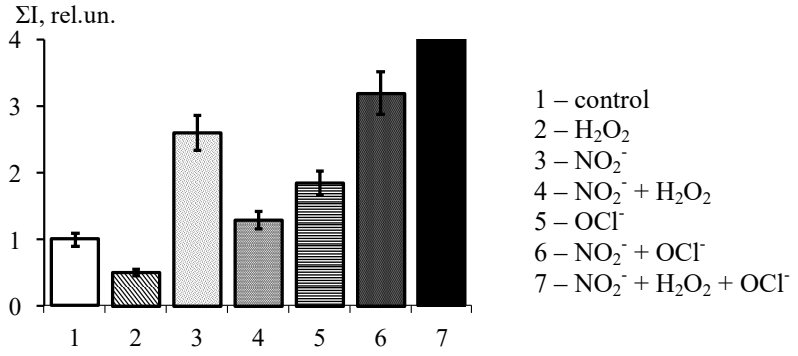

Fig. 1. Influence of RONCS on luminol-dependent chemiluminescence integral intensity of neutrophils activated during adhesion to glass

Colchicine is inhibitor of tubulin microtubule assembly required for intracellular transport of granules. Cytochalasin B a is blocker of the actin filament assembly. Inhibition of H_2O_2, $ONOO^-$ and lidocaine action was detected when neutrophils treated by cytochalasin B. Colchicine and lidocaine induced effects similar to the effect of H_2O_2 on neutrophil ability to generate RONCS. Previously, it was shown that exposure of neutrophils to H_2O_2 and $ONOO^-$ at low concentrations (1-100 μM) causes the increase of RONCS generation ability during phagocytosis of latex particles and the change of ability to secrete MPO [3,4]. The obtained data indicate the important role of cytoskeleton elements (microtubules and actin filaments) and enzymes which regulate granule movement in cells and secretion of oxygen-activating enzymes in realization of RONCS influence on neutrophils. The prolonged action of "NO_2^- + H_2O_2", $ONOO^-$, PMA (but not H_2O_2) on neutrophils induced a change in cell sizes and formation of NETs, particularly at higher concentration of the substances. These effects can be blocked by the treatment of cells with cytochalasin B, lidocaine, inhibitors of oxygenases and NO-synthase.

[1] D.S.A. Abdallah, et al. *Toxoplasma gondii* triggers release of human and mouse neutrophil extracellular traps, Infect. Immun. **8**,768–777 (2012).
[2] V.J. Papayannopoulos, et al. Neutrophil elastase and MPO regulate formation of neutrophil extracellular traps, J.Cell.Biol. **191**, 677–691 (2010).
[3] A.I. Kavalenka, et al. Effects of H_2O_2 on neutrophil ability to generate ROCS and to secrete MPO in vitro,Cell Tissue Biol. **1**, 551–559 (2007).
[4] M.N. Starodubtseva, A.I. Kavalenka, et al. Peroxynitrite regulates exocytosis of neutrophil granules, Biol. Membrane **27**, 459–470 (2010).)

ALTERATION OF FUNCTIONAL ACTIVITY OF HUMAN BLOOD NEUTROPHILS AFTER EXPOSURE TO CONSTANT ELECTRIC FIELD WITH STRENGTH UP TO 1 V/SM

Elizaveta Kavalenka, Artemiy Yushkevich, Alena Kavalenka

Department of Biophysics, Belarusian State University
ai0628k@gmail.com

Electromagnetic fields are increasingly used in medicine, physiotherapy, technologies for growing biological tissues, in cellular technologies for controlling the movement, functioning of cells and permeability of their membranes. Blood cells can be target cells to which the effect is directed, and they can be "companions" of other target cells in some tissues. Aim of the work was to study the change of morphological and functional characteristics of neutrophils after application of constant electric field with strength up to 1 V/sm.

Neutrophils were isolated from human blood by gradient centrifugation. Red blood cells were deleted by hypotonic lysis. Cells were suspended in Earle's salt balanced solution at pH 7,3.

Constant electric field was formed by parallel wire still electrodes using software controlled measurement stand which was developed in department of biophysics in BSU. It is necessary to note, that electric current in cell suspensions was not more than 10 mA at voltage 1 V between electrodes placed one from another at a distance of 1 sm. Cells were incubated under electric field during different time periods up to 1 hour.

Ability of cells to reactive oxygen (ROS) generation and secretion of enzymes were studied by chemiluminescence methods. The count and size of cells and cellular aggregates were investigated by light microscopy and light scattering methods. Activity of neutrophils was stimulated under adhesion of the cells to glass surface, action of chemoattractant fMLP and at phagocytosis of latex particles at 37 °C.

It was revealed that exposure of neutrophils to constant electric field with strength of 1 V/sm leads to the amplification of cell aggregation and release of myeloperoxidase from cells in extracellular medium. The significant cell destruction was not found. ROS generation at activation of the cells at adhesion, fMLP action and latex particles was strong altered after electric field exposure. The changes of kinetics of cell activation were established. Effects of constant electric field action on neutrophils depend on duration and strength of impact.

So, constant electric field with strength up to 1 V/sm is not cause strong destructive action on human blood neutrophils and leads to modulation of functional activity of the cells.

Alterations in rat brain mitochondria phosphoproteome induced by psychoemotional stress

Maria Trawkina, Alexander Ivanchyk, Aliaksey Yantsevich[1]

[1] Institute of Bioorganic Chemistry, National Academy of Sciences of Belarus, Belarus
mtrawkina@gmail.com

Stress is a nonspecific reaction of organism to external influence that leads to the alterations in processes of free radical oxidation, ion homeostasis and cellular metabolism [1]. Nervous tissue is especially sensitive to the stress impact. As energy demands of nervous tissue cells are quiet high, they contain a significant quantity of mitochondria; dysfunction of the latter may lead to a number of neurological diseases, such as Alzheimer's, Parkinson's, Huntington's diseases etc. [2]. Unfortunately

exact molecular mechanisms of stress are not fully characterized nowadays.

Post-translational modifications of proteins (PTM) are understood as any differences between functional protein and linear amino acid sequence. Phosphorylation, acetylation, methylation, sulfation and glycosylation are considered as the most important covalent PTMs. The latter may play an important role in the fast regulation of protein activity [3]. Changes in post-translational modification status of proteins may be associated with pathologic states and diseases [4].

The aim of this work was to study the changes in phosphoproteome of rat brain mitochondria induced by psychoemotional stress. The whole protein fraction was extracted by chloroform-methanol method and underwent trypsin digestion, the mixture of peptides was separated by high-performance liquid chromatography (1290 Infinity, Agilent) and detected mass-spectrometrically (Q-TOF 6550 series, Agilent). Data analysis was conducted in Spectrum Mill software (Agilent), the data were compared manually and validated with GPS web-server; methabolic and signaling pathways analysis was performed with PANTHER, SwissProt, Reactome and KEGG Pathways databases.

It was found that under stress conditions significant changes in rat brain mitochondria phosphoproteome occur. In particular, changes of phosphoryation status of proteins involved in pathways of immune, endocrine, nervous, sensory systems and such signaling pathways as cGMP-PKG, cAMP, Hippo, HIF-1, PI3K-Akt, Jak-STAT, MAPK, AMPK, Rap1, calcium signaling were detected. Besides alterations in phosphorylation status of proteins involved in metabolism of carbohydrates (TCA cycle, inositol phosphate metabolism), amino acids (glycine, serine, threonine, lysine metabolism), nucleotides (purine metabolism), cofactors and vitamins (porphyrin, chlorophyll, thiamine metabolism) took place. Moreover phoshorylation status alterations were also found for proteins involved in pathways of neurodegenerative diseases (Alzheimer's, Parkinson's, Huntington's disease), endocrine and metabolic diseases and cancer pathways.

[1] Z. Kuchukashvili, G. Burjanadze, K. Menabde et al., Long-lasting stress, quantitative changes in nitric oxide concentration and functional state of brain mitochondria, Acta Neurobiol Exp 72, 40–50 (2012).

[2] A. K. Reeve, E. M. Simcox, M. R. Duchen et al., Mitochondrial Dysfunction in Neurogenerative Disorders (Springer International Publishing, Switzerland, 2016).

[3] M. Aguiar, R. Masse, B. F. Gibbs, REGULATION OF CYTOCHROME P450 BY POSTTRANSLATIONAL MODIFICATION, Drug Metabolism Review, 37, 379 – 404, 2005.

[4] A. Hofer, T. Wenz, Post-translational modification of mitochondria as a novel mode of regulation, Experimental Gerontology 56, 202 – 220 (2014).

METHYLENE BLUE ACTS AS AMYLOID REMODELLING AGENT ON SUPEROXIDE DISMUTASE I AGGREGATION

Greta Musteikytė, Vytautas Smirnovas

Institute of Biotechnology, Life Sciences Center, Vilnius University, Lithuania
gretamus@gmail.com

Amyotrophic lateral sclerosis (ALS) is a neurodegenerative disease that results in motor neuron death and has no approved treatment yet. Around 20% of ALS cases are caused by Cu, Zn human superoxide dismutase (SOD1) aggregation into amyloid fibrils. First step of potential strategies to combat the disease could be finding an effective aggregation inhibitor *in vitro*. However, only a few studies for SOD1 protein have been done in this field for now. They involve *in vitro* screening of 640 FDA approved drugs [1], several flavonoids[2] and curcumin[3] only. Our goal was to test inhibitory effect of a small molecule methylene blue, which has been shown to inhibit Alzheimer's disease-linked amyloid beta oligomerization[4].

Recombinant SOD1 was purified from *E. Coli* by Ni^{2+} affinity chromatography. Aggregation experiments were carried out in 10 mM potassium phosphate, 0.5 M GuHCl and 5 mM DTT buffer solution, pH 7.4. Kinetics of aggregation was monitored using Thioflavin T (ThT) fluorescence assay. Morphology of aggregates was visualised by atomic force microscopy and secondary structure was tested by infrared spectroscopy.

The presence of methylene blue leads to reduced ThT fluorescence intensity and results in different morphology as well as secondary structure of aggregated protein. Seeded aggregation kinetics suggests that methylene blue possibly modulates surface properties of pre-added fibrils without affecting stability of protein monomer, but further investigation is needed to reveal the exact methylene blue mode of action.

[1]I. Anzai, K. Toichi, E. Tokuda, A. Mukaiyama, S. Akiyama and Y. Furukawa, Screening of Drugs Inhibiting In vitro Oligomerization of Cu/Zn-Superoxide Dismutase with a Mutation Causing Amyotrophic Lateral Sclerosis, *Frontiers in Molecular Biosciences*, vol. 3, no. 40, (2016).

[2]X. Zhuang, B. Zhao, S. Liu, F. Song, F. Cui, Z. Liu and Y. Li, Noncovalent Interactions between Superoxide Dismutase and Flavonoids Studied by Native Mass Spectrometry Combined with Molecular Simulations, *Analytical Chemistry*, vol. 88, no. 23, pp. 11720-11726, (2016).

[3]N. Bhatia, A. Srivastava, N. Katyal, N. Jain, M. Khan, B. Kundu and S. Deep, Curcumin binds to the pre-fibrillar aggregates of Cu/Zn superoxide dismutase (SOD1) and alters its amyloidogenic pathway resulting in reduced cytotoxicity, *Biochimica et Biophysica Acta (BBA) - Proteins and Proteomics*, vol. 1854, no. 5, pp. 426-436, (2015).

[4]M. Necula, L. Breydo, S. Milton, R. Kayed, W. van der Veer, P. Tone and C. Glabe, Methylene Blue Inhibits Amyloid Aβ Oligomerization by Promoting Fibrillization, *Biochemistry*, vol. 46, no. 30, pp. 8850-8860, (2007).

Cloning, expression and purification of *Toxoplasma gondii* Hsp90 N domain

Dovilė Daunoraitė, Marius Gedgaudas, Aurelija Mickevičiūtė,
Daumantas Matulis, Egidijus Kazlauskas

Department of Biothermodynamics and Drug Design, Institute of Biotechnology, Vilnius University, Vilnius, Lithuania
dovile.daunoraite@gf.stud.vu.lt

Parasitic protozoan diseases affect millions of people worldwide causing severe morbidity and mortality. These diseases include malaria, leishmaniasis, toxoplasmosis and cause over a million deaths every year. It is estimated that billions of people may be infected with some form of protozoan parasite. As parasites quickly develop resistance mechanisms, many drugs have become ineffective. Furthermore, many of the current drugs have unacceptable side effects. Therefore there is an urgent need to develop novel treatments against parasitic protozoan diseases [1]. *Toxoplasma gondii*, which is the main subject of our research, causes oportunistic infection to immunocompromised hosts such as HIV patients. The most acute form of the disease is toxoplasmic encephalitis that often lead to fatal outcome [2].

Heat shock protein 90 (Hsp90) is a highly conserved dimeric molecular chaperone. It is essential for eukaryotic cells and is involved in various key pathways ensuring correct folding, maturation and degradation of select client proteins. Healthy human cells are significantly less sensitive to partial Hsp90 inhibition than parasitic protozoa, which depend on the chaperone to adapt to stressful conditions during infection. This makes Hsp90 an attractive drug target against these diseases [2, 3].

Our aim is to develop drugs based on Hsp90 inhibition to treat protozoan diseases. One of the first challenges is the acquisition of a viable target protein model for ligand binding experiments. As full length proteins are often hard to obtain and are unsuitable for some of the experimental techniques, we chose to work with the isolated N-terminal domain of Hsp90 (Hsp90N), which binds ATP and most of the Hsp90-selective inhibitors [4]. However, protozoan Hsp90N tend to misfold. Here we suggest that addition of a short (4-5 aa long) complementary β-sheet is necessary for the correct folding of *Toxoplasma gondii* Hsp90N, when expressed in *Escherichia coli*. This β-sheet can be successfully adopted from homologous Hsp90N of *Plasmodium falciparum* [5]. Protein stability was assessed using fluorescence thermal shift assay and correct active site folding was confirmed by binding studies with Hsp90N ligands.

[1] Fletcher, Stephanie M., et al. "Enteric protozoa in the developed world: a public health perspective." Clinical microbiology reviews 25.3 (2012): 420-449.
[2] Addmore, et al. "Intracellular protozoan parasites of humans: the role of molecular chaperones in development and pathogenesis." Protein and peptide letters 18.2 (2011): 143-157.
[3] Schopf, Florian H., Maximilian M. Biebl, and Johannes Buchner. "The HSP90 chaperone machinery." Nature Reviews Molecular Cell Biology (2017).
[4] Gewirth, Daniel T. "Paralog specific Hsp90 Inhibitors–a brief history and a bright future." Current topics in medicinal chemistry 16.25 (2016): 2779.
[5] Corbett, Kevin D., and James M. Berger. "Structure of the ATP-binding domain of Plasmodium falciparum Hsp90." Proteins: Structure, Function, and Bioinformatics 78.13 (2010): 2738-2744.

IMPACT OF ENVIRONMENTAL FACTORS ON INSULIN AGGREGATION KINETICS

Romuald Stanilko[1], Tomas Šneideris[2], Vytautas Smirnovas[2]

[1]Faculty of Fundamental Sciences, Vilnius Gediminas Technical University, Lithuania
[2]Department of Thermodynamics and Drug Design, Institute of Biotechnology, Lithuania
rs.stanilko@gmail.com

Amyloid fibrillation is directly implicated in several degenerative pathologies such as Alzheimer and Parkinson diseases. Recent studies have demonstrated that the epigallocatechin-3-gallate (EGCG), the main and most significant polyphenol in green tea, potently inhibits the formation of amyloid fibrils [1]. However, epidemiological inferences are sometimes conflicting and in vitro and in vivo studies may seem discrepant [2]. In this study, we have investigated the influence of EGCG at different environmental conditions on insulin fibril formation. Because of insulin's ease of access, insulin fibrillation has been the subject of intense biochemical studies and has emerged as a major model for the formation of amyloid aggregates. Fibrillation of insulin are meaningful not only for the quality control of pharmaceutical insulin batches but also to gain a deeper understanding of the amyloid fibrillation process.

In this work the effect of 2 non-identical forms of EGCG (oxidized and reduced) were observed. Our results confirmed that oxidized EGCG is a more potent inhibitor against the formation of recombinant human insulin amyloid fibril than reduced EGCG [3]. In addition, oxidized form of EGCG shows noticeably stronger inhibition behavior to the fibril formation in the phosphatic buffer (pH=2.4) than in acetic acid buffer (pH=1.85). The results of the present study may provide a new guide on finding novel anti-amyloidogenic agents.

---

[1] D. E. Ehrnhoefer, J. Bieschke, A. Boeddrich, M. Herbst, L. Masino, R. Lurz, S. Engemann, A. Pastore, and E. E. Wanker, "EGCG redirects amyloidogenic polypeptides into unstructured, off-pathway oligomers," *Nat. Struct. Mol. Biol.*, vol. 15, no. 6, pp. 558–566, 2008.

[2] M. Cascella, S. Bimonte, M. R. Muzio, V. Schiavone, and A. Cuomo, "The efficacy of Epigallocatechin-3-gallate (green tea) in the treatment of Alzheimer's disease: An overview of pre-clinical studies and translational perspectives in clinical practice," *Infect. Agent. Cancer*, vol. 12, no. 1, pp. 1–7, 2017.

[3] T. T. An, S. Feng, and C. M. Zeng, "Oxidized epigallocatechin gallate inhibited lysozyme fibrillation more strongly than the native form," *Redox Biol.*, vol. 11, no. December 2016, pp. 315–321, 2017.

EFFECT OF TEMPERATURE AND DENATURANT CONCENTRATION ON ELONGATION OF DISTINCT MOUSE PRION PROTEIN FIBRIL STRAINS

Tomas Šneideris, Vytautas Smirnovas

Institute of Biotechnology, Life Sciences Center, Vilnius University, Lithuania
sneideris.t@gmail.com

Prion diseases is a group of fatal neurodegenerative disorders that affect many mammalian species. These diseases have three distinct causes: in the most of cases (85%) occurrence of these diseases in humans is spontaneous, less likely (10%) it is a result of mutations in the PrP gene *PRNP* and in a rare cases (5%) it is an infection due to exposure to prions via medical procedures, prion-contaminated food or cannibalism [1]. One of the most interesting aspects of prion diseases is existence of multiple "strains", which lead to different disease phenotypes that are distinguished by distinct clinical signs, incubation time and neuropathology. However, it is still not clear what factors lead to polymorphism of prions or how many polymorphs can be formed. The main causative agent of prion diseases is thought to be the aggregated form of native prion protein (PrP^{C}), known as PrP^{Sc}. The infectivity of prion diseases is based on PrP^{Sc} ability to self-propagate by binding to PrP^{C} and inducing its conformational conversion to the PrP^{Sc} state [2]. One of the possible mechanisms by which PrP^{Sc} self-replicates is the elongation of amyloid fibrils [3].

The aim of this study is to determine and compare the effect of temperature and denaturant concentration on elongation kinetics of distinct mouse prion fibril strains. Results of this research could contribute to the deeper understanding of amyloid polymorphism and self-propagation.

Distinct strains of mouse prion protein fibrils display different profiles of elongation kinetics under various environmental conditions. In some cases, unusual profile of elongation kinetics point to possible remodeling of existent amyloid fibrils or presence of multiple polymorphs in a sample, however, due to complexity of the aggregation process it is difficult to determine the real cause and deeper investigation is needed.

[1] J. Collinge, "Mammalian prions and their wider relevance in neurodegenerative diseases," *Nature*, vol. 539, no. 7628, pp. 217–226, 2016.
[2] N. J. Cobb, M. I. Apostol, S. Chen, V. Smirnovas, and W. K. Surewicz, "Conformational Stability of Mammalian Prion Protein Amyloid Fibrils Is Dictated by a Packing Polymorphism within the Core Region," *J. Biol. Chem.*, vol. 289, no. 5, pp. 2643–2650, 2014.
[3] K. Milto, K. Michailova, and V. Smirnovas, "Elongation of mouse prion protein amyloid-like fibrils: Effect of temperature and denaturant concentration," *PLoS One*, vol. 9, no. 4, pp. 1–5, 2014.

THE ASSOCIATION BETWEEN HALOGENATIVE STRESS-INDUCED LACTOFERRIN AND CALCIUM SIGNALING IN NEUTROPHILS

Maria Terekhova[1], Anatoly Kokhan[1], Daria Grigorieva[1], Irina Gorudko[1], Semak Igor[2], Alexey Sokolov[3,4]

[1] Department of Physics, Belarussian State University, Belarus
[2] Department of Biology, Belarussian State University, Belarus
[3] Institute of Experimental Medicine, Saint-Petersburg, Russia
[4] Federal Research and Clinical Center of Physical-Chemical Medicine, Moscow, Russia
autumn_frost@mail.ru

The topical problem of present-day biology and medicine is the drug-design and the development of medical strategy aimed to increase of human lifespan. One of the promising protein is lactoferrin (Lf), a member of the transferrin family of iron-binding glycoproteins, contained in exocrine secretions, in milk and in the secondary granules of mature neutrophils [1,2]. Lf has a vast number of useful properties, such as antiviral, antifungal, and even some anticancer activities [1]. It was raised a herd of transgenic goats in Belarus in order to produce recombinant human lactoferrin (rhLf), which is indistinguishable in biochemical and biological properties from Lf, purified from human milk [2].

By now it was shown the ability of Lf to bind to a specific receptor of different immune, epithelial and endothelial cells [1]. Neutrophils are the most abundant white blood cells in circulation and play the key role in host defense. Recently we have shown [3], that rhLf stimulates dose-dependent release of elastase from neutrophils. Because calcium signaling modulates critical neutrophil functions, including degranulation, cellular proliferation, respiratory burst, so it is important to study the influence of rhLf on calcium response of neutrophils.

The stimulation of neutrophils in inflammatory focus is accompanied by production of reactive oxygen and halogen species (ROS and RHS) leading to development of oxidative and halogenative stress [4]. ROS and RHS are able to modify various biomolecules such as lipids, proteins, nucleic acids resulting in alteration their physicochemical properties and biological activity. Whereas Lf can be affected by ROS and RHS in inflammatory focus it is unknown whether its structure and functional properties will change or not. Therefore, this work aims to study structural changes of rhLf under the halogenative stress and features of Ca^{2+}-signaling in neutrophils in response to native and halogenated rhLf.

Changes in physicochemical properties of rhLf were determined using fluorescence analysis. Modification of amino acid content of rhLf and its conformation was examined by monitoring changes in the intrinsic fluorescence due to the destruction of tryptophan residue in protein (λ_{ex}=285 nm, λ_{em}=340 nm) and in the fluorescence spectra of the added external probe ANS (λ_{ex}=350 nm, λ_{em}=475 nm). The halogenative stress was caused by addition hypochlorous acid (HOCl) in a molar ratio protein:HOCl 1:100. It was showed that there are a significant modification of protein tryptophan residues (a reduction of 77% in the intensity of tryptophan fluorescence intensity) and protein tertiary structure changes (a decrease to 38% in ANS fluorescence intensity) after HOCl action.

Measurement of intracellular free calcium ion concentration ($[Ca^{2+}]_i$) in neutrophils under rhLf action was measured by fluorescent method using fura 2, AM (λ_{ex1}=340 nm, λ_{ex2}=380 nm, λ_{em}=510 nm). It was determined that rhLf is able to initiate a dose-dependent increase in $[Ca^{2+}]_i$ in the cytosol of neutrophils. The maximum effect is observed on addition of 250-500 μg/ml of protein. The magnitude of the effect was comparable to that of the chemotactic peptide fMLP, which is a potent inducer of Ca^{2+}-signalling in neutrophils. The addition of the modified rhLf to neutrophils causes a much smaller increase in $[Ca^{2+}]_i$ compared with the effect of native rhLf.

Thus, in this research we showed that rhLf is able to regulate Ca^{2+}-signaling in neutrophils. The modification of rhLf under RHS leads to such structural changes in the molecule that the protein loses its ability to stimulate Ca^{2+}-response. This study was supported by Russian Scientific Foundation Grant 18-515-00004.

[1] D Legrand, E Elass, M Carpentier, J Mazurier . Lactoferrin: a modulator of immune and inflammatory responses, Cell. Mol. Life Sci. **62 (22)**, 2549-2559 (2005).
[2] J Zhang, L Li, Y Cai [et al.] Expression of active recombinant human lactoferrin in the milk of transgenic goats, Protein Expression and Purification **57**, 127-135 (2008).
[3] D Grigorieva, A Sokolov, I Goruko Recombinant human lactoferrin modulates neutrophil degranulation and H2O2 production via increase of intracellular free calcium ion concentration and tyrosine phosphorylation, XIII Intern. Conf. on Lactoferrin Struc., Func. & Appl., 49 (2017)
[4] P Lacy Mechanisms of Degranulation in Neutrophils, Allergy Asthma Clin Immunol. **2(3)**, 98-108 (2006).

ANALYSIS OF ANCHOR MOLECULES FOR TETHERED BILAYER LIPID MEMBRANE FORMATION ON NOVEL SERS ACTIVE BIOSENSOR

Indre Aleknaviciene[1], Gintaras Valincius[1]

[1] Vilnius university Life Sciences Center, Institute of Biochemistry, Vilnius, Lithuania
*indre.aleknaviciene@gmail.com

Surface enhanced Raman spectroscopy (SERS) is a powerful vibrational spectroscopy technique that allows highly sensitive structural detection of low concentration analytes and is applicable for studies of model systems on roughened electrodes [1]. The active area of our SERS substrates is formed using an ultra-short pulse laser on a soda-lime glass substrate. The resulting surface structure features stochastic nanopattern, which meets good resonance characteristics for various excitation wavelengths and adsorbed analyte molecules. The tethered lipid bilayers (tBLMs) (Fig 1.) are considered as perspective experimental platforms for membrane biosensors and may be suitable for a broad spectrum of biophysical experiments such as peptide/membrane interactions, protein/membrane interactions, lipid phase transitions and others. Attached to a SERS active surface, tBLMs may allow monitoring of biologically relevant events with Raman spectroscopy. It is known that structure of the self-assembled monolayers (SAMs) used to anchor phospholipid bilayers to surfaces affects the functional properties of the tethered bilayer membranes (tBLMs) [2].

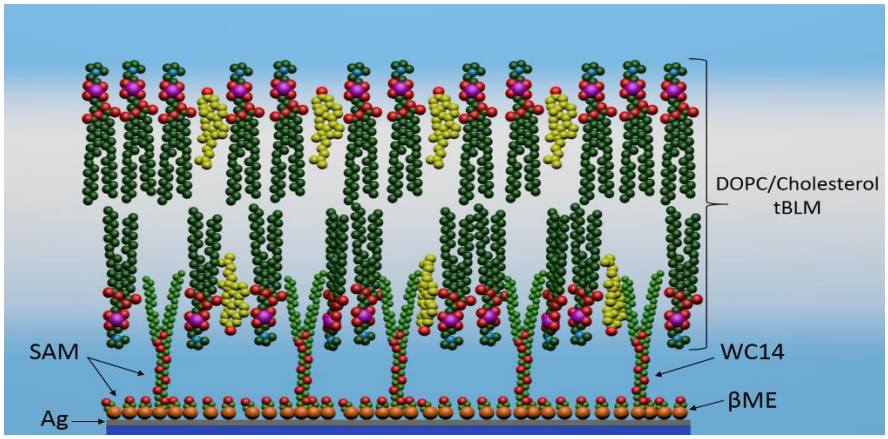

Fig.1 Schematic representation of tethered bilayer lipid membrane (tBLM) on a silver surface.

The aims of this study are to test new surface enhanced Raman scattering (SERS) substrates coated with silver to determine their suitability to analyse self-assembled monolayer (SAM) of anchor molecules for tBLM formation on roughed surface. Two types of anchor molecules were chosen to form SAMs on nanostructured silver surface - long strand thiolipid Wilma's compound (WC14) and different short strand back fillers - 2-mercaptoethanol (2-ME), 3-mercapto-1-propanol, 4-mercapto-1-butanol. We received a good quality SERS spectra form SAM of anchor molecules before and after tBLM formation.

[1] Mosier-Boss PA. Review of SERS Substrates for Chemical Sensing. Nanomaterials. 2017;7(6):142. doi:10.3390/nano7060142.
[2] Rakovska B, Ragaliauskas T, Mickevicius M, Jankunec M, Niaura G, Vanderah DJ, Valincius G. Structure and Function of the Membrane Anchoring Self-Assembled Monolayers. Langmuir, 2015, 31 (2), pp 846–857 doi: 10.1021/la503715b.

BINDING AND INHIBITION OF CATALYTICALLY ACTIVE HUMAN CARBONIC ANHYDRASES BY THIAZOLE-SUBSTITUTED BENZENESULFONAMIDES

Vaida Paketurytė, Edita Čapkauskaitė, Asta Zubrienė, Daumantas Matulis

Department of Biothermodynamics and Drug Design, Institute of Biotechnology, Vilnius University, Saulėtekio al. 7, Vilnius LT-10257, Lithuania

vaidapaketuryte@gmail.com

Studies of the interaction between proteins and small molecules are important due to two main reasons: first, this research is helpful for rational drug design and, second, it is necessary to deepen the understanding about molecular interactions, which are still relatively poorly understood. In this study, target proteins are human catalytically active carbonic anhydrase (CA) isoforms. These proteins are zinc containing metalloenzymes, which have high similarity of the active site and participate in many physiological processes. On the other hand, CAs have different tissue, subcellular localization and this causes that each isozyme is associated with different pathology or disease [1]. Thus, controlling the catalytic activity of only one, desease associated, enzyme would help to avoid side effects, which are inherent to many drugs.

It is well know that sulfonamides bind to the zinc ion in the active site of CA and inhibit its catalytic activity [2]. Furthermore, different substitutions of benzenesulfonamides (or other suflonamides) have different affinity to CAs. Tracking the changes of the chemical structures of compounds (inhibitors) and selectivity or affinity for CAs could be useful for the lead compound (potential drug) optimization.

Scientists have tested the CA binding affinities of various nitrogen-containing heterocycles (such as pyrrole, oxazole, furazane, etc.) attached to benzenesulfonamide, but there were no studies about thiazolylbenzenesulfonamides and their affinity to CAs. Thus, in this study, *para* and *meta* - substituted thiazolylbenzenesulfonamides with chlorine atom in *ortho* position were synthesized, observed affinities to all 12 catalytically active recombinant human CA isoforms were determined by the fluorescent thermal shift assay (Fig. 1B) and the pH-independent (intrinsic) affinities were calculated. Moreover, several other methods (stopped-flow CO_2 hydration assay (Fig. 1A) and X-ray crystallography) were used to prove that these thiazole-substituted benzenesulfonamides act as CA inhibitors. The correlation between chemical structures of compounds and intrinsic affinities to CAs was determined and the conclusions about the energetic contributions of the thiazole ring and its substituents were made.

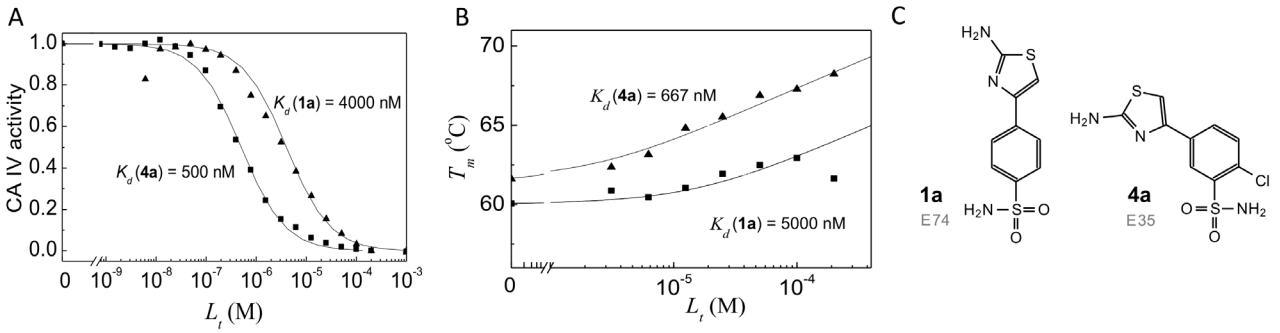

Figure 1. Binding and inhibition of human carbonic anhydrase IV with compounds **1a** and **4a** determined by (Panel A) the stopped-flow CO_2 hydration (25 °C, pH 7.5) and (Panel B) fluorescent thermal shift (37 °C, pH 7.0) assays. Panel C shows chemical structures of compound **1a** and **4a**.

[1] Alterio, V., Di Fiore, A., D'Ambrosio, K., Supuran, C. T. & De Simone, G. Multiple Binding Modes of Inhibitors to Carbonic Anhydrases: How to Design Specific Drugs Targeting 15 Different Isoforms? Chem. Rev. 112, 4421–4468 (2012).

[2] Supuran CT. How Many Carbonic Anhydrase Inhibition Mechanisms Exist? Journal of Enzyme Inhibition and Medicinal Chemistry. 2016;31(3):345–360.

EPITOPE MAPPING OF MONOCLONAL ANTIBODIES AGAINST HUMAN CARBONIC ANHYDRASE XII

Aistė Imbrasaitė, Dovilė Stravinskienė and Aurelija Žvirblienė

Institute of Biotechnology, Life Sciences Center, Vilnius University, Vilnius, Lithuania.
aisteim@gmail.com

Human carbonic anhydrase XII (CA XII) is a single-pass transmembrane protein with an extracellular catalytic domain [1]. This enzyme is being recognized as a potential biomarker for different tumors [2]. Monoclonal antibodies (MAbs) are widely used as diagnostic, research and therapeutic reagents in oncology [3]. An important step in the characterization of MAbs, especially those used in therapeutic strategies, is the identification of the binding sites (epitopes) of these antibodies on their target antigens [4].

The aim of our study was to construct overlapping CA XII protein fragments to identify the epitopes of MAbs raised against recombinant CA XII.

Eight hexahistidine-fused overlapping fragments (fragment # 1 (aa 1–94), fragment # 2 (aa 41–175), fragment # 3 (aa 166–264), fragment # 4 (aa 75–264), fragment # 5 (aa 9–195), fragment # 6 (aa 17–184), fragment # 7 (aa 24–207) and fragment # 8 (aa 33–196)) of CA XII protein (Fig. 1) were constructed to identify the epitopes of MAbs raised against recombinant CA XII. All CA XII fragments were efficiently expressed in transformed *E. coli* cells. MAbs against CA XII were generated by hybridoma technology and characterized previously [2]. In total, 10 MAbs (1D5, 4A6, 5D2, 8C9, 9A8, 13F5, 15A4, 6G5, 14D6, 20G7) recognized the extracellular domain of CA XII protein by Western blot. Specific binding of the MAbs with the constructed CA XII fragments was observed. The accurate aa sequence of the epitope recognized by the MAb 14D6 was determined (Fig. 1). It was shown, that the MAb 14D6 binds near the active center of CA XII, which explains the inhibitory properties of this antibody.

This study provides new data on the CA XII-specific MAbs, that are promising diagnostic and therapeutic tools which can be applied for the diagnostics and therapy of various types of cancers.

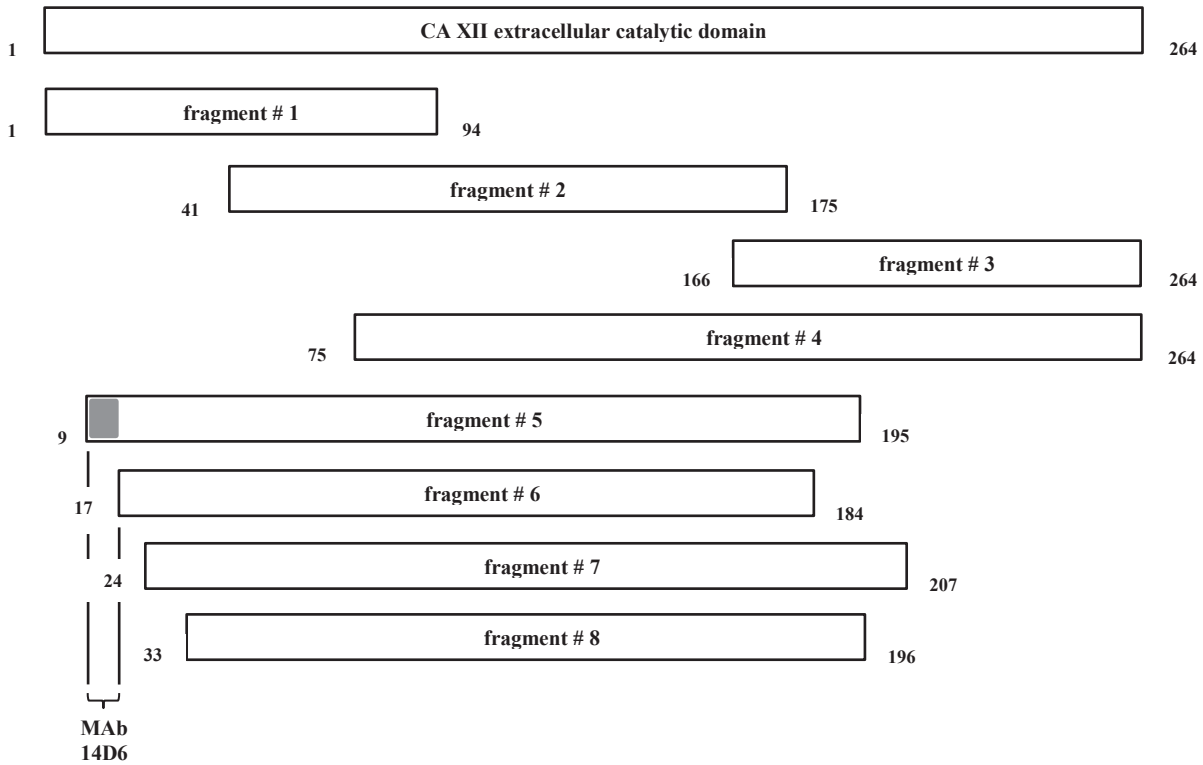

Fig. 1. Scheme of eight overlapping CA XII protein fragments and epitope of MAb 14D6.

[1] D.A. Whittington, A. Waheed, B. Ulmasov, et al., Crystal structure of the dimeric extracellular domain of human carbonic anhydrase XII, a bitopic membrane protein overexpressed in certain cancer tumor cells, Proceedings of the National Academy of Sciences of the United States of America **98** (17), 9545-9550 (2001).

[2] D. Dekaminaviciute, R. Lasickiene, S. Parkkila, et al., Development and Characterization of New Monoclonal Antibodies against Human Recombinant CA XII, BioMed Research International, (2014).

[3] Q. Zhang, G. Chen, X. Liu and Q. Qian, Monoclonal antibodies as therapeutic agents in oncology and antibody gene therapy, Cell Research **17**, 89–99 (2007).

[4] P. N. Nelson, G. M. Reynolds, E. E. Waldron EE, et al., Demystified …: Monoclonal antibodies, Molecular Pathology **53** (3), 111-117 (2000).

AB INITIO METHOD APPLICATION FOR ANALYSIS OF ELECTRON AND PROTON TRANSFER AT LACCASE T1 CU SITE

Justinas Babinskas[1*], Visvaldas Kairys[2], Inga Matijošytė[1]

[1] Sector of Applied Biocatalysis, Institute of Biotechnology, Life Sciences Center, Vilnius University, Lithuania
[2] Department of Bioinformatics, Institute of Biotechnology, Life Sciences Center, Vilnius University, Lithuania
justinas.babinskas@gmail.com

Laccases are multi-copper oxidases (EC 1.10.3.2), capable of oxidizing phenolic and aromatic primary and secondary amine substrates. [1] They are well-known in the field of biocatalysis and have a wide range of application: from food industry to organic synthesis [2,3]. However, researchers recognize that laccases still have untapped potential due to lacking knowledge of their catalysis mechanisms.

The basic catalysis mechanism of laccases consists of three phases: i) substrate one-electron oxidation at T1 site ii) one-electron transfer from T1 to T2/T3 Cu cluster iii) four-electron and four-proton oxygen molecule reduction to water at T2/T3 cluster. By this work, we investigated the substrate oxidation at T1 Cu site by quantum chemistry methods. By reducing T1 Cu site – $[Cu(His)_2(Cys)(Met)(Substrate)]^+$ to $[Cu(Imidazole)_2(SCH_3)(Substrate)]^+$, we computed the most likely mechanism of substrate oxidation (Scheme 1):

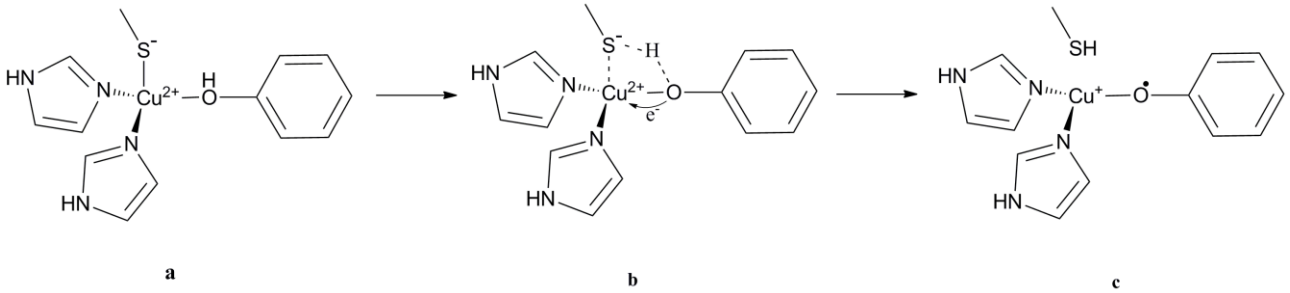

Scheme 1. Reaction mechanism with phenol as the substrate. **a** – Enzyme-Substrate complex [E-S]; **b** – Transition state [TS]; **c** – Reduced enzyme-Product complex [E'-P].

Calculations of transition state [TS] provided profound understanding of the reaction:

- importance of simultaneous electron and proton transfer;
- deformation of lone pair atomic orbitals on substrate O or N and Cys S atoms, due to proton transfer;
- dependence of activation energy on electron correlation;
- importance of conjugation between aromatic ring, HO- or HN- and Cu.

More details of the study will be provided during the poster presentation.

[1] S. M. Jones, E. I. Solomon, Electron transfer and reaction mechanism of laccases, Cellular and Molecular Life Sciences **72**, 869-883, (2015).
[2] J. F. Osma, J. L. Toca-Herrera, S. Rodríguez-Couto, Uses of laccases in the food industry, Enzyme Research 2010, 1–8, (2010).
[3] R. Luque, Ed., Green Chemistry, Nova Science Publishers, Hauppauge, N.Y, (2012).

THE EFFECT OF HYDRATION ON NANOMECHANICAL RESPONSE OF PORCINE SKIN

Viktorija Zaranko[1], Marija Jankunec[1]

[1] Institute of Biochemistry, Life Sciences Center, Vilnius University, Lithuania
viktorija.zaranko@chf.stud.vu.lt

Skin is a barrier that protects organism from external factors/pathogens and prevents water loss. Various skin properties depend on the humidity of external environment. Knowledge of how humidity affects nanomechanical properties of the skin could be of great interest to pharmacy, medicine and cosmetology. The aim of this project is to develop a protocol for the use of atomic force microscopy (AFM) in a personalized health care system.

In literature there are several approaches to describe the use of unique technique as AFM either for the structural changes or for skin disease detection [1]. Previous studies characterizing the mechanics of stratum corneum have used macroscopic testing equipment designed for homogenous materials. Such measurements ignore the tissue's rich topography and heterogeneous structure, and cannot describe the underlying mechanistic process of tissue failure. It was already shown that skin tissue is highly dependable on ambient humidity to which samples are equilibrated [2].

In this work, AFM was used to investigate the changes in topography and elasticity of the dermatomed porcine ear skin due to different water activity (a_w) in ambient environment. Water activity is the partial vapor pressure of water in a substance divided by the standard state partial vapor pressure of water. In the other words, a_w is the indicator of water capacity in the sample of interest. Nanomechanical and viscoelastic properties of the superficial skin layer, stratum corneum, may vary with the water content. And the response to water loss may indicate the state of skin – healthy intact or damaged (either unhealthy or treated, scarred) skin tissue.

The frozen samples of dermatomed porcine ear (~500 µm in the thickness) were thawed and incubated for 24 hours in three solutions with different water activity, a_w: phosphate buffer (PBS) pH 7,4, a_w=0,992; phosphate buffer/propylene glycol (PBS/PG) 8/2, a_w=0,936; phosphate buffer/polyethylene glycol 1500 (PBS/PEG1500) 55/45, a_w=0,946.

After incubation, surface topography maps (Fig. 1, A) and force-distance curves (Fig. 1, B) of samples were obtained either in the plain PBS or in the solution of interest. Mean elastic (Young's) moduli of the samples was calculated from force curves according Hertz model (spherical indenter):

$$F = \frac{4}{3}\frac{E}{(1-\nu^2)}\sqrt{R}\delta^{3/2} \qquad \text{(Eq. 1)}$$

where F = force (from force curve), E = Young's modulus (fit parameter), ν = Poisson's ratio (sample dependent, typically 0.2 - 0.5), R = radius of the indenter (tip), δ = indentation.

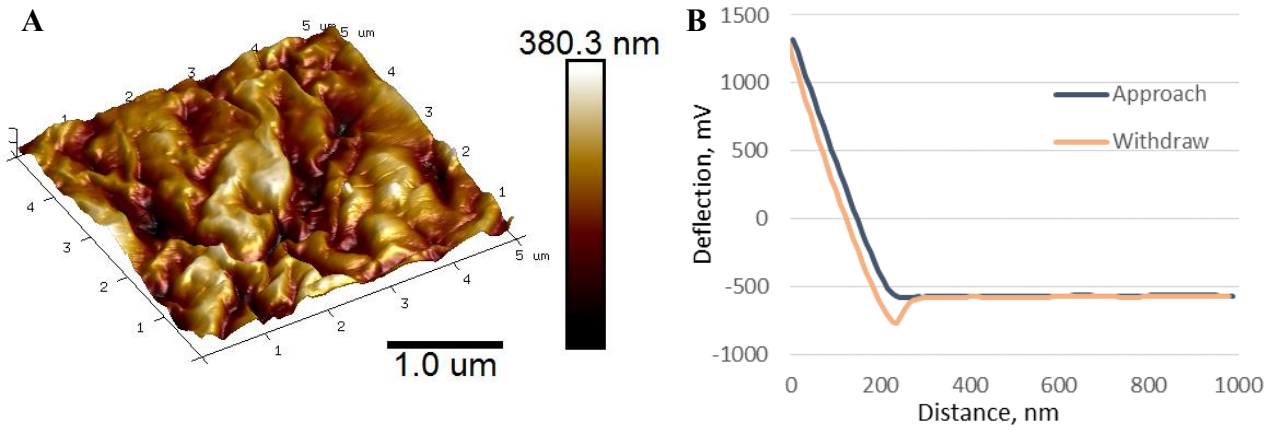

Fig. 1. (**A**) Representative topography image of porcine skin surface. (**B**) Force-distance curve.

Calculated elastic moduli for skin samples, incubated in PBS, PBS/PG and PBS/PEG1500 were 1,23±0,86 MPa, 1.75±0,82 MPa and 1,81±0,70 MPa, respectively. Results show that even small changes in water activity significantly affect stiffness of the skin – with decreasing water activity elastic modulus increases, i.e., skin becomes stiffer.

[1] A. Olejnik and I. Nowak, 'Application of atomic force microscopy in skin related research', in *Microscopy and imaging science: practical approaches to applied research and education*, A. Méndez-Vilas, Ed. Formatex Research Center, 2017, pp. 27–33.

[2] X. Liu, J. Cleary and G.K. German, 'The global mechanical properties and multi-scale failure mechanics of heterogeneous stratum corneum'. Acta Biomaterialia, 2016 (43), pp. 78-87.

DIRECTION OF CELL GROWTH UNDER LONG-TERM ELECTRICAL STIMULATION

Yuliya Kunitskaya, Tatiana Kochetkova, Elizaveta Kavalenka, Elena Golubewa, Pavel Bulai

Department of Biophysics, Belarusian State University
yuliya.kunitskaya@gmail.com

Regulation of the cell functioning by means of electric field has already been described in a variety of works. However, the result of such studies is of interest as not only a basis for creating methods of tissue engineering, but also in the field of regenerative medicine [1]. Restoration of the damaged area of the cell monolayer is possible not only by regulating the proliferative activity of cells, but also by changing the direction of the cell growth. Thus, this work is aimed at studying the effect of long-term electrical stimulation (ES) on the direction of the cell growth.

Rat glioma C6 cells were used as the object of the study. The cells were incubated at 37°C in a humidified atmosphere of 5% CO_2. A uniform alternating electric field was used for the long-term electrical stimulation of cells. The parameters of the applied electric stimuli were as follows: electric field strength – 50 V/m, the number of stimulating pulses in the train – 1, 5 and 10, the frequency of the trains – 10 Hz. The formation of the damaged area of the cells' monolayer was implemented with a pipet tip [2].

Earlier it was shown that the anisotropic growth of cells occurs when both the number of pulses in the train and the field strength was varied. However at a lower field strengths the fraction of cells oriented at an angle between 31°-60° increases with an increment of the total duration of the train [3]. The observed effect reduces with an increase of the field strength. As a result, an electric field strength of 50 V/m was chosen to study the restoration of damaged area of the cell monolayer.

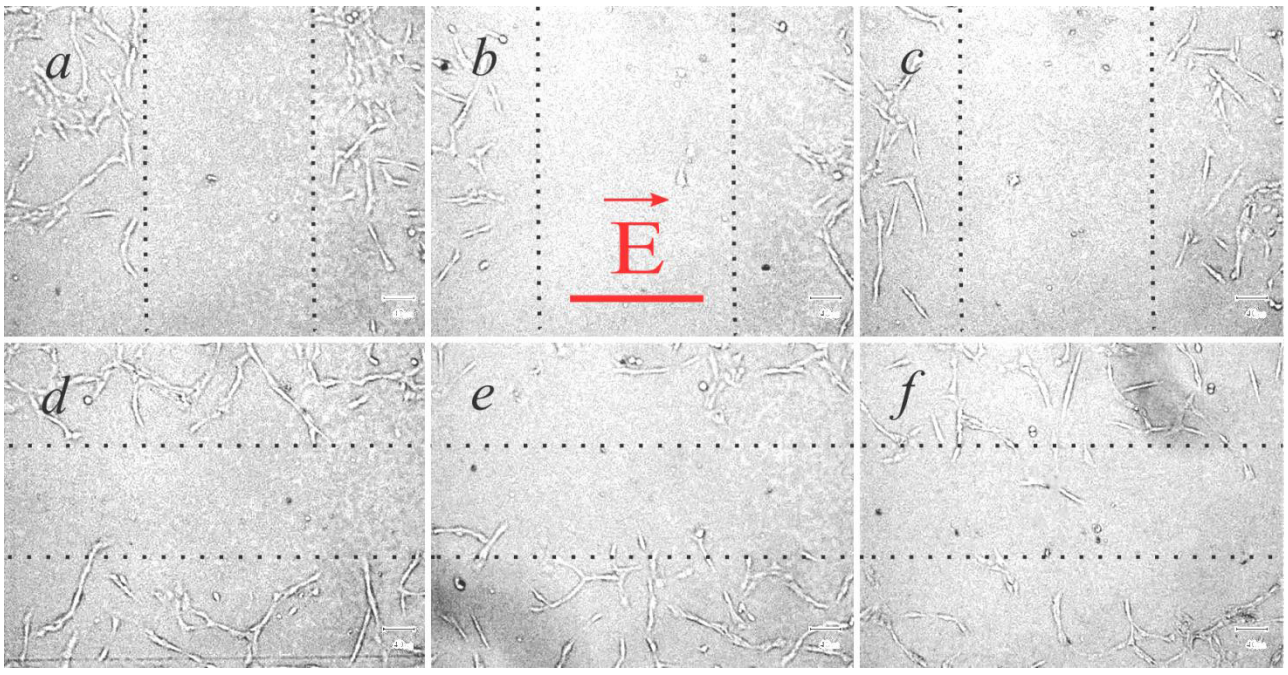

Fig. 1. The damaged area of C6 cell monolayer:
a,d –control; b,e – control after 12 h; c,f – monolayer after 12 h of ES

The anisotropic growth of cells was observed after the long-term electrical stimulation. Large fraction of cells was oriented orthogonally to the electric field vector, while in the control sample no significant changes in the growth direction was observed. The maximum effect of cell reorientation was discovered at 10 stimulating pulses in the train. It was found that the fraction of cells increased in the damaged area parallel to the electric field vector (Fig. 1f). On the contrary, no cells were found in the damaged area orthogonal to the electric field vector (Fig. 1c). Therefore, it was shown that due to the orthogonal reorientation of cells in accordance with the electric field, the fastest restoration of the damaged area is possible.

[1] L. C. Kloth, Electrical Stimulation Technologies for Wound Healing, Advances in Wound Care, 3(2): 81-90 (2014).
[2] C.C. Liang, A.Y. Park, J.L. Guan, In vitro scratch assay: a convenient and inexpensive method for analysis of cell migration in vitro, Nature Protocols 2 (2) 329-333 (2007).
[3] Y. Kunitskaya, E. Golubeva, T. Kochetkova, E. Kavalenka, P. Bulai, Dependence of the spatial orientation of the outgrowths of the C6 cell line on the number of stimulating pulses in the train upon prolonged exposure to an external electric field, The 22th Russian Scientific Conference of Students of Physics and Young scientists, Yekaterinburg – Rostov-on-Don, 335 – 336 (2016).

TEMPORAL REGULATION OF TYPE III CRISPR-CAS EFFECTOR COMPLEX ACTIVITY

Irmantas Mogila[1], Brighton Samatanga[2], Ralf Seidel[2], Virginijus Siksnys[1], Gintautas Tamulaitis[1]

[1] Institute of Biotechnology, Life Sciences Center, Vilnius University, Lithuania
[2] Institute of Experimental Physics I, University of Leipzig, Germany
mogirmantas@gmail.com

CRISPR-Cas is a unique defence system providing bacteria and archaea with adaptive immunity against viruses and foreign plasmids [1]. Short CRISPR RNA (crRNA) molecules assemble with Cas proteins to form effector complexes which monitor for foreign nucleic acids and destroy them. CRISPR-Cas employ variety of effector complexes which differ greatly in composition and interference mechanisms. Type III CRISPR-Cas systems utilize multisubunit Csm and Cmr complexes which bind crRNR complementary foreign transcripts and degrade them [2]. Upon complex binding to target RNA the Cas10 subunit is activated. This induce Cas10 DNA nucleolytic activity for invading DNA degradation and polymerase-cyclase activity for signalling molecule synthesis for altruistic suicide pathway [3, 4, 5, 6]. Since Cas10 activity could result in imprudent host nucleic acid degradation, it must be temporally regulated. Indeed, although bound RNA is fully cleaved in several seconds, the induced Cas10 activities slowly diminish over an hour [4, 6]. We hypothesized that RNA cleavage products stimulate the Cas10 protein of Type III effectors until they dissociate.

Therefore the aim of this study was to determine the rate of RNA cleavage products dissociation from *Streptococcus thermophilus* Csm complex (StCsm). To evaluate dissociation dynamics we used biochemical assay and fluorescence cross-correlation spectroscopy (FCCS), which allows the quantitative analysis of fluorescently labelled molecules co-diffusion in the sample [7]. Our data show that during cleavage reaction 5'- and 3'-products of activating RNA dissociate gradually with half-time of ~10-20 minutes, thus supporting our hypothesis.

[1] E. V. Koonin, K. S. Makarova, F. Zhang, Diversity, classification and evolution of CRISPR-Cas systems. Current Opinion in Microbiology 37, 67–78 (2017).

[2] G. Tamulaitis, M. Kazlauskiene, E. Manakova, Č. Venclovas, A. O. Nwokeoji, M. J. Dickman, P. Horvath, V. Siksnys, Programmable RNA shredding by the type III-A CRISPR-Cas system of *Streptococcus thermophilus*, Mol Cell **56**, 506-517, (2014).

[3] G. Tamulaitis, Č. Venclovas, V. Siksnys, Type III CRISPR-Cas Immunity: Major Differences Brushed Aside. Trends Microbiol. 25, 49–61 (2017).

[4] M. Kazlauskiene, G. Kostiuk, Č. Venclovas, G. Tamulaitis, V. Siksnys, A cyclic oligonucleotide signaling pathway in type III CRISPR-Cas systems. Science 357, 605–609 (2017).

[5] O. Niewoehner, C. Garcia-Doval, J. T. Rostøl et al. Type III CRISPR-Cas systems produce cyclic oligoadenylate second messengers. Nature 548, 543–548 (2017).

[6] M. Kazlauskiene, G. Tamulaitis, G. Kostiuk, Č. Venclovas, V. Siksnys. Spatiotemporal Control of Type III-A CRISPR-Cas Immunity: Coupling DNA Degradation with the Target RNA Recognition. Mol Cell **62**, 295–306, (2016).

[7] K. Bacia, S. A. Kim, P. Schwille, Fluorescence cross-correlation spectroscopy in living cells. Nat. Methods 3, 83–89 (2006).

QUENCHER PROCEDURE FOR ANALYSIS OF BIOLOGICALLY ACTIVE COMPOUNDS OF HOP (*HUMULUS LUPULUS* L.) LEAVES AND CONES

Mantas Dūdėnas[1], Žydrūnas Stanius[1], Vilma Kaškonienė[1], Tomas Drevinskas[1], Audrius Sigitas Maruška[1], Ona Ragažinskienė[2], Kęstutis Obelevičius[2]

[1] Instrumental Analysis Open Access Centre, Faculty of Natural Sciences, Vytautas Magnus University, Lithuania
[2] Sector of Medicinal Plants of Kaunas Botanical Garden of Vytautas Magnus University, Kaunas, Lithuania
mantas.dudenas@gmail.com

Hop (*Humulus lupulus* L.) is a plant, which is probably the best known for being used in brewery for bittering. Bitter α- and β-acids found in cones of hops have antibacterial and antioxidant properties. However, it is known that hops contain other biologically active compounds (i.e. xanthohumol, 8-prenylnaringenin and others) that have anti-cancer, radical scavenging, peroxide reducing and antioxidant properties [1, 2]. It is very likely, that biologically active compounds can be found in different proportions across the whole plant. It is also possible that various parts of hop plant contain biologically active compounds that are insoluble in some solvents. There is lack of information about biologically active compounds of the leaves of hops.

The QUENCHER procedure, standing for QUick, Easy, New, CHEap and Reproducible, is the method, which relies on the surface reaction phenomenon between solid (bound or trapped antioxidant compounds) and dissolved materials [3]. The purpose of this study was to apply QUENCHER procedure for determination of phenolic compounds, flavonoid compounds and radical scavenging activity of hop leaves and cones as well as to compare the results with that obtained using extract of raw material, which prepared by conventional liquid extraction. Five different Lithuanian hop varieties (*Raudoniai, Fredos taurieji, Fredos derlingieji, Kauno ankstyvieji, Kauno gražieji*) growing in Kaunas Botanical Garden of Vytautas Magnus University were analyzed. To our knowledge, it is the first study on the application of QUENCHER procedure for the analysis of phenolic compounds of different parts of hops. The total amount of phenolic compounds, the amount of flavonoids and radical scavenging activity using DPPH (1,1-diphenyl-2-picrylhydrazyl) were determined using spectrophotometric methods [4]. Results were expressed as rutin equivalents mg/g of plant.

The analysis has shown that the total content of phenolic compounds using QUENCHER procedure was higher compared to the methanol extracts. The concentration of phenolic compounds in methanol extracts varied from 31.4 mg/g (leaves of *Kauno gražieji*) to 78.2 mg/g (cones of *Fredos taurieji*). In contrast, the total content of phenolic compounds using QUENCHER procedure varied from 91.7 mg/g (cones of *Kauno ankstyvieji*) to 168.5 mg/g (leaves of *Fredos taurieji*). It is interesting to note, that the total content of phenolic compounds was higher in the samples of leaves than the cones, whereas methanol extracts have shown opposite results. Phenolic compounds that are insoluble in methanol may be the reason of higher content of phenolic compounds using QUENCHER procedure. Also, higher content of such compounds in leaves using QUENCHER could be the consequence of various compounds that are insoluble in methanol. When comparing the total content of flavonoids, there was no big difference between two methods. The highest content of flavonoids (23.3 mg/g) was in the methanol extract of cones of *Kauno gražieji* whereas the lowest concentration of flavonoids was of the leaves of the same variety (11.0 mg/g). However, the correlation between the total content of phenolic compounds and radical scavenging activity using QUENCHER procedure is notably lower ($r = 0.661$) than in methanol extracts ($r = 0.928$). Such results may have occurred because there are some phenolic compounds that have lower or no radical scavenging activity. The radical scavenging activity in methanol extracts varied from 34.4 mg/g (leaves of *Kauno ankstyvieji*) to 87.2 mg/g (cones of *Fredos taurieji*). In contrast, radical scavenging activity using QUENCHER procedure varied from 48.4 mg/g (leaves of *Kauno gražieji*) to 121.0 mg/g (leaves of *Fredos taurieji*). It is worth noticing that the QUENCHER procedure usually provides higher errors because of inhomogeneity of the samples (RSD <9.6 % and 4.0 % for phenolic compounds using QUENCHER and traditional extraction respectively, RSD <13.3 % and 3.8 % for flavonoids using QUENCHER and methanol extracts respectively and RSD <10.0 % and 2.4 % for radical scavenging activity using QUENCHER procedure and traditional extraction respectively).

In conclusion, the QUENCHER procedure was successfully applied for the determination of phenolic compounds, flavonoids and radical scavenging activity in different parts of hop plant. The total content of phenolic compounds using QUENCHER procedure was higher compared to methanol extracts, while there was small differences in total content of flavonoids between two methods. The radical scavenging activity of different parts of hops varies between two methods. The QUENCHER procedure results in higher errors.

Acknowledgements:
This project was financed by Research Council of Lithuania project No. 09.3.3-LMT-K-712-03-0133.

[1] P. Allsopp, S. Possemiers, D. Campbell, C. Gill, I. Rowland, A cComparison of the anticancer properties of isoxanthohumol and 8-prenylnaringenin using *in vitro* models of colon cancer, BioFactors, **39**, 441–447 (2013).
[2] W. Hardwick, *Handbook of Brewing*, 2nd Ed. (Boca Raton: CRC Press, USA, 2006).
[3] M. Henrion, M. Servaes, F. Thielecke, V. Fogliano, Application of the QUENCHER methodology to the food industry, Food Chemistry, **240**, 951–958 (2018).
[4] V. Kaškonienė, G. Ruočkuvienė, P. Kaškonas, I. Akuneca, A. Maruška, Chemometric analysis of bee pollen based on volatile and phenolic compound compositions and antioxidant properties, Food Analytical Methods, **8**, 1150–1163 (2015).

POLYMORPHISM OF MOUSE PRION PROTEIN

Elžbieta Kulicka[1], Tomas Šneideris[2], Vytautas Smirnovas[2]

[1]Faculty of Fundamental Sciences, Vilnius Gediminas Technical University, Lithuania
[2]Department of Thermodynamics and Drug Design, Institute of Biotechnology, Lithuania
elzbietka.kulicka@gmail.com

Prion diseases, also known as the transmissible spongiform encephalopathies (TSEs), are a group of fatal neurodegenerative disorders that affect humans and animals. These diseases are associated with conformational conversion of the cellular prion protein, PrP^{C}, into an oligomeric β-sheet rich form, PrP^{Sc}. A growing number of observations support the once heretical hypothesis that transmission of TSE diseases does not require nucleic acids, and that PrP^{Sc} alone can act as an infectious agent. One of the most intriguing features of prions is their ability to form different strains, leading to distinct phenotypes of TSE diseases. [1] However it is still not clear what factors lead to polymorphism of prions or how many polymorphs can be formed. The aim of this research is to study aggregation of mouse prion protein under various environmental conditions that could possibly induce formation of distinct amyloid aggregates (strains) *in vitro*. Results of this research could contribute to the deeper understanding of amyloid polymorphism.

The mouse prion protein (MoPrP 89-230) was expressed in E. *coli* and purified by Ni^{+} affinity chromatography. To prepare fibrils, monomeric prion protein was diluted to concentration of 0,5 mg/mL in 50 mM phosphate buffer (pH 6) containing 2 M GuHCl and incubated under variuos environmental conditions. The morphology and secondary structure of formed fibrils were determined by atomic force microscopy and infrared spectroscopy respectively. The resistence to denaturant (GuSCN) were observed by platereader, measuring the Thioflavin T fluorescence. Fractional loss of signal at increasing denaturant concentrations corresponds to the fraction of MoPrP dissociated from amyloid fibrils. Different temperature and agitation conditions lead to formations of distinct strains of mouse prion protein. Currently four distinct strains were propagated that displayed different structural, morphological aspects and resistance to chemical denaturation.

---

[1] N. J. Cobb, W. K. Surewicz. "Prion diseases and their biochemical mechanisms". *Biochemistry*. vol. 48, no. 12, pp. 2574–2585, 2009

IDENTIFICATION AND EVALUATION OF ANTIBACTERIAL AGENTS PRODUCED BY MICROORGANISMS IN LOCAL RAW BIOPRODUCTS

Domantas Armonavičius[1], Audrius Maruška[1], Vilma Kaškonienė[1], Rūta Mickienė[1]

[1]Instumental Analysis Open Access Centre, Department of Biology, Vytautas Magnus University, Lithuania
domantas.armonavicius@stud.vdu.lt

Microorganisms with a wide range of antibacterial activity can be an effective tool dealing with pathogenic and food spoilage bacteria. Depending on the environment, microorganisms adapt, resulting in different strains that can produce antibacterial substances with different properties. Such substances are bacteriocins, produced by lactic acid bacteria and killer toxins, produced by yeast [1, 2]. These materials are widely investigated in medicine and veterinary medicine as narrow-spectrum antibiotics. Bacteriocins and killer toxins are also important in food industry because microorganisms which produce them are non-pathogenic and normally colonize the human body [3].

The aim of this work is to find lactic acid bacteria and yeast which have antibacterial activity in local raw materials such as sour milk, whey and bee bread. All isolated bacteria were preliminary identified based on their staining by Gram and catalase test. The antibacterial activity of all isolated microorganisms using *S. aureus*, *E. coli*, *M. luteus* and *P. vulgaris* strains was determined by agar well diffusion method. Lactic acid bacteria which were isolated from sour milk showed antibacterial activity against all tested pathogenic bacteria and bacteria isolated from whey showed antibacterial activity against *P. vulgaris* and *M. luteus.* Detailed results of the work will be presented during the conference.

[1] Kaškonienė V., Stankevičius M., Bimbiraitė-Survilienė K., Naujokaitytė G., Šernienė L., Mulkytė K., Malakauskas M., Maruška A., Current State of Purification, Isolation and Analysis of Bacteriocins Produced by Lactic Acid Bacteria, Applied Microbiology and Biotechnology 101, 1323-1335 (2017).

[2] Buyuksirit T., Kuleasan H., Antimicrobial Agents Produced by Yeasts, *Int*ernational Journal of Biological, Biomolecular, Agricultural, Food and Biotechnological Engineering 8, 1114-1117 (2014)

[3] Oliveira T., Ramalhosa E., Nunes L., Pereira J. A., Colla E., Pereira E. L., Probiotic potential of indigenous yeasts isolated during the fermentation of table olives from Northeast of Portugal, Innovative Food Science and Emerging Technologies 44, 167-172 (2017)

SMALL NON-CODING RNA MEDIATED ANTIMICROBIAL RESISTANCE IN LACTIC ACID BACTERIA

Sigita Grigaitytė[1], Raminta Mineikaitė[1], Gabrielė Trečiokaitė[1], Milda Mickutė[1], Giedrius Vilkaitis[1]

[1] Department of Biological DNA Modification, Institute of Biotechnology, Vilnius University, Vilnius, Lithuania
sigita.grigaityte@gmc.vu.lt, raminta.mineikaite@gf.stud.vu.lt, gabriele.treciokaite@gf.stud.vu.lt

Non-pathogenic lactic acid bacteria (LAB) such as *Lactococcus lactis* and *Lactobacillus casei* have a long history of use for food production such as cheese and yogurt fermentation. In recent years much interest has been shown in their potential in medicine as live drug delivery tools and probiotics. Since bacterial cell wall is a major barrier between the bacterial cell and its environment, it is of utmost importance to determine how the bacterial cell wall forms and changes under stress conditions in order to enhance both the properties of these microorganisms and their viability. Many studies have already been performed in order to understand protein function in bacterial cell wall formation, however, only little is known about the role of bacterial small non-coding RNAs (sRNAs). These 40-500 nt molecules are considered major post-transcriptional regulators of gene expression in bacteria. This study covers novel sRNA identification and analysis of *L. lactis* and *L. casei* possibly responsible for antimicrobial stress mediated cell wall adaptation.

In order to obtain deep insight in novel sRNAs of *L. casei* BL23 and *L. lactis* MG1363 sequencing analysis was performed. The results of bioinformatic analysis showed the bulk of identified sequences are potential sRNAs.

In parallel to sequencing, functional analysis for the identification of sRNA of *L. casei* BL23 was performed. After inserting 50-500 bp sheared genomic fragments of these microorganisms to a shuttle vector, *L. casei* genomic library was constructed. Following the selection of bacteria that are resistant to antimicrobials, more than 40 unique non-protein coding *L. casei* BL23 genome sequences were found to be responsible for ampicillin and penicillin G resistance. After combining data from functional analysis and sRNA sequencing we confirmed *L. casei* genome sequences that conferred to the highest resistance of ampicillin and penicillin G were found to be coding sRNAs. In *L. lactis* sRNAs potentially responsible for antimicrobial resistance were detected by differential analysis of sequencing results. sRNAs with different expression levels after exposure to lysozyme or penicillin G were identified and their function was experimentally confirmed.

Since all of the tested antimicrobials trigger cell wall formation, peptidoglycan composition analysis of *L. lactis* and *L. casei* clones with overexpressed sRNAs was performed. Significant differences identified in peptidoglycan composition suggest that the bacterial sRNA may have a major role in bacterial cell wall formation.

The work was supported by a grant from the Research Council of Lithuania MIP-059/2015.

ION CHANNEL POPULATIONS DISTINGUISHED IN THE TONOPLAST OF *NITELLOPSIS OBTUSA* USING PATCH CLAMP TECHNIQUE

Vilmantas Pupkis, Indrė Lapeikaitė, Vilma Kisnierienė

Institute of Biosciences, Life Sciences Center, Vilnius University, Lithuania
vilmantas.pupkis@gmail.com

Historically giant internodal cells of macroalgae *Characeae* have been extensively used as a convenient experimental system in plant electrophysiology, including ion channel research. Ion channel activity is crucial to maintenance of cell membrane electrochemical potential, osmoregulation, and morphogenesis. Ion channels also determine characteristics of action potentials, therefore research on a molecular level provides fundamental knowledge as well as insights into cellular plant signaling events [1].

Patch clamp technique provides an excellent means to research ion channel characteristics on a single channel level under near-physiological conditions. A microelectrode is pushed against a desirable membrane forming a high resistance (usually larger than 1 GΩ) seal. Currents passing through ion channels in the sealed area can be easily detected in high resolution. Thus patch clamp method enables analysis of electrical activity of ion channels that represents conformational changes of single molecules in real time [2].

It is difficult to patch plant plasma membrane due to the cell wall. This obstacle in Characeaen algae may be overcome by using cytoplasmic droplet technique – in this way an easy access to the vacuolar membrane (tonoplast) is provided. Characeaen cell is placed vertically in a solution approximately isotonic with the cell sap and "decapitated". The cell sap then flows out of the cell, in a bath solution spontaneously forming cytoplasmic droplets [3]. The spherical droplets consist of cytoplasm covered by the tonoplast.

Our conducted experiments indicate at least three different ion channel populations in the tonoplast of a freshwater Characeaen algae *Nitellopsis obtusa*, easily distinguished by their conductances (Fig. 1) and densities in the membrane. In accordance with previous investigations [4], it is postulated that the highest conductance ion channels should be K^+ channels while the middle conductance channels are responsible for Cl^- transport.

The results suggest a complex ion channel system in the tonoplast of *N. obtusa* that may be employed to execute various physiological functions. Further investigations will shed more light on the properties of found ion channel populations and their possible roles in plant signaling.

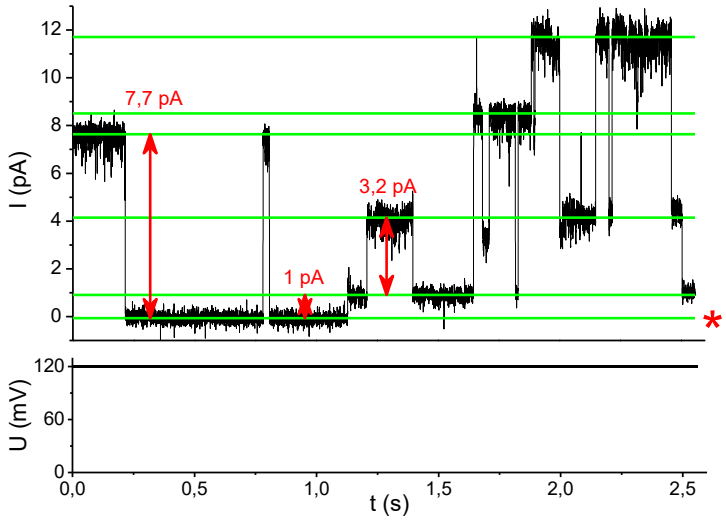

Fig. 1 A recording of three types of ion channel activity at 120 mV in tonoplast-attached configuration. Current amplitudes are denoted by arrows, vertical lines signify various amplitude levels, the asterisk represents closed state of all the ion channels.

[1] M. J. Beilby, M. T. Casanova. *The physiology of characean cells* (Springer Science & Business Media, 2014).
[2] B. Sakmann, E. Neher, *Single-channel recording* (Springer Science & Business Media, 2009).
[3] N. Kamiya, K. Kuroda. Cell Operation in Nitella: I. Cell Amputation and Effusion of the Endoplasm, Proceedings of the Japan Academy **33** (3), 149-152 (1957).
[4] M. Katsuhara, T. Mimura, M. Tazawa. Patch-clamp study on ion channels in the tonoplast of Nitellopsis obtusa, Plant and cell physiology **32** (2), 179-184 (1991).

THE EFFECTS OF NANOSECOND PULSED ELECTRIC FIELDS ON *SACCHAROMYCES CEREVISIAE* CELLS

Povilas Simonis[1], Skirmantas Kersulis[2], Voitech Stankevich[2], Vytautas Kaseta[3,1], Egle Lastauskiene[4,1] and Arunas Stirke[1, 4]

[1] Laboratory of Bioelectrochemistry, State Research Institute, Center for Physical Sciences and Technology, Sauletekio ave. 3, LT-10257, Vilnius, Lithuania
[2] High Power Pulse Laboratory, State Research Institute, Center for Physical Sciences and Technology, Sauletekio ave. 3, LT-10257, Vilnius, Lithuania
[3] State Research Institute Center for Innovative Medicine, Santariškių 5, LT-08406, Vilnius, Lithuania
[4] BioScience Institute, Life Sciences Center, Vilnius University, Sauletekio ave. 7, LT-10257, Vilnius, Lithuania
simonis.povilas@gmail.lt

Saccharomyces cerevisiae is one of the most well-studied and understood eukaryotic organisms. The studies of yeast cell allow to reconstitute a possible molecular mechanisms of various abiotic effects.

Pulsed electric field is one of the most intensively investigated abiotic effects on biological tissues and cell suspensions for past decade. It has been previously shown that a nanosecond pulsed electric field (nsPEF) permeabilize the plasma membrane, alter gene expression, cause phosphatidylserine translocation, affect the distribution of intracellular ions and even lead to the death of mammalian cells. There is still a lack of sufficient data related to the effects of nsPEF on yeast cells yet.

In our study we analyzed the effects of square shaped electrical pulses of different duration (τ= 10-90 ns) and pulse number (pn= 1-5) with electric field strength (E) up to 220 kV/cm and showed that nanosecond pulses can induce the yeast cell death, which in turn is dependent on the electric field pulse parameters and increase with the rise in E, τ and pulse number. Exposure of yeast cells to nsPEFs was accompanied by metacaspase activation (Fig. 1), membrane permeability to propidium iodide and the externalisation of phosphatidylserine [1].

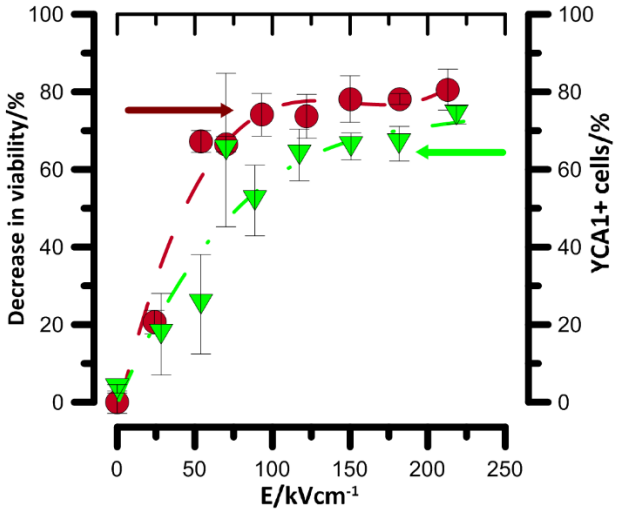

Fig. 1 Decrease in viability and YCA1+ activation dependence on the electric field strength after exposure to 5 pulses with durations of 90 ns.

Furthermore, the investigation of yeast cells permeabilization to tetraphenylphosphonium ions (TPP^+), which was induced by high power nanosecond duration electrical pulses, had demonstrated the following features: (i) The study of TPP^+ ions absorption rate by yeast cells is an effective method for detection of short duration electric pulse influence on yeast cell wall properties; (ii) Shortening of the electric pulse duration makes it possible to achieve more homogeneous electrical treatment of yeast cell clusters and by this way to increase the effectiveness of single cell permeabilization; (iii) The significant acceleration of TPP^+ ions absorption rate (up to 65 times) can be achieved without any influence on the vitality of the cells [2].

We conclude that square shaped electric field pulses with nanosecond durations induce wide variety of effects including caspase-dependent apoptosis, oxidative stress, cell wall permeabilization, and that such abiotic treatment can be used in various fields starting from food safety and ending in medicine.

[1] P. Simonis, S. Kersulis, V. Stankevich et al., Caspase dependent apoptosis induced in yeast cells by nanosecond pulsed electric fields, Bioelectrochemistry **115**, 19–25 (2017).
[2] A.Stirke, A. Zimkus, S. Balevicius et al., Permeabilization of yeast Saccharomyces cerevisiae cell walls using nanosecond high power electrical pulses, Applied Physics Letters **105**, 1–4 (2014).

MECHANISMS OF INHIBITION OF MIELOPEROXIDASE BY CATECHOL DERIVATIVES

Shishkanova Polina, Sharshunovich Darya, Semenkova Galina, Sorokin Victor, Faletrov Yaroslav, Ksendzowa Galina, Shadyro Oleg

Department of Radiation Chemistry and Chemical-Pharmaceutical Technology, Belarusian State University, Minsk
pavlina.shishkanova@gmail.com

Myeloperoxidase (MPO, EC 1.11.1.7) is a heme-based peroxidase enzyme responsible for antimicrobial activity against a wide range of organisms. This enzyme is copiously expressed in stimulated neutrophil granulocytes, where it catalyzes the production of hypohalous acids, from hydrogen peroxide (H_2O_2) and halides (Cl^-, Br^-, I^-). Hypochlorous acid (HOCl or in less extent HOBr and HOI) generated by MPO and also reactive oxygen species (ROS) are involved in the microbicidal activity of neutrophils, contributing to innate host defenses [1]. But increased level of MPO in neutrophils and in blood may be accompanied by the hyperproduction of hypochlorous acid and ROS, which leads to the development of halogenating stress in the organism. This can cause inflammation and subsequently leads to various pathologies, such as Alzheimer's disease, cardiovascular disease, diabetes, malignant tumors, etc. [2]. Therefore, the search for drugs that regulate the oxygen-activating function of neutrophils and the development of new approaches aimed at preventing the occurrence of halogenating stress in the body are very important at present.

Previously we studied influence of catechol derivatives on ROS generation by neutrophils stimulated to phagocytosis. It was shown that 4,6-di-tert-butyl-3-(((2-mercaptophenyl)imino)methyl) benzene-1,2-diol (S1), 4,6-di-tert-butyl-3-(((2-mercaptoethyl)imino)methyl)benzene-1,2-diol (S2), 4,6-di-tert-butyl-3-((2-phenylhydrazineyli-dene)methyl)benzene-1,2-diol (S3) and N'-(2,3-dihydroxybenzylidene) isonicotinohydrazide (S4) cells in micromolar concentrations effectively decrease ROS production of due to MPO inhibition, but not NADPH oxidase inhibition. No one of analyzed compounds has cytotoxic effect on neutrophils [3].

The purpose of our study was to find out the mechanism of MPO inhibition by catechol derivatives.

Neutrophils were allocated from blood of healthy people on the basis of a standard method. Cells were destroyed in three cycles of freezing and thawing. The resulting mixture was centrifuged. The supernatant containing free MPO was used for the analysis. The enzyme activity was determined by its ability to generate HOCl and ROS. The formation of ROS and HOCl was registered by chemiluminescent method at the temperature of 37°C in Earl's solution containing H_2O_2 and luminol. Measurements were conducted using biochemiluminometer BHL-1 (BSU, Belarus). The concentration of catechol derivatives in the analyzed probe was equal to 4 μM.

Kinetic curves of ROS and HOCl production in the system «MPO–H_2O_2–luminol» with analyzed compounds and without them in reversed Lineweaver–Burk plot were obtained. It was found that S1 inhibits the enzyme by uncompetitive way while S2, S3, S4 decrease enzyme activity by mixed inhibition.

Also computer modeling was used to estimate ability of the compounds under consideration to act as MPO ligands (substrates or inhibitors). Affinity of the compounds was assessed using Autodock 4.2 and AutoDockTools software. Human MPO three-dimensional structures were downloaded from www.pdb.org database (PDB ids: 4dl1, 4c1m and 1dnw). The calculations demonstrated that S3 and S1 have the highest affinity to MPO active site among compounds tested (Table 1).

Table 1. The theoretically-calculated inhibition constants (Ki) for complexes of myeloperoxidase with the catechol derivatives

Ligand	Ki, M
S1	$2.67 \cdot 10^{-7} – 4.26 \cdot 10^{-7}$
S3	$3.27 \cdot 10^{-7} – 6.05 \cdot 10^{-7}$
S4	$1.07 \cdot 10^{-6} – 2.68 \cdot 10^{-6}$
S2	$1.28 \cdot 10^{-6} – 2.90 \cdot 10^{-5}$

The values of the inhibition constants (Ki) obtained in mathematical modeling correlate with the previously obtained experimental data [3].

The data altogether indicate that the compounds might affect MPO activity via interaction with MPO at not only catalytic site, giving us promising starting point for further research of catechol derivatives as potential medicines for inhibiting myeloperoxidase and preventing halogenating stress in the organism.

[1] Spalteholz, H. // Arch. Biochem. Biophys. - 2006. - V. 445. (2). P. 225-234.
[2] Malle, E. //Br. J. Phaemacol. - 2007. - V. 152 (6). P. 838–854.
[3] Shishkanova, P. // «Open Readings 2017», Vilnius. - 2017. P. 366.

THE IMPACT OF STERILIZATION PROCESS ON BEE POLLEN ANTIOXIDANT ACTIVITY

Vaida Adaškevičiūtė, Vilma Kaškonienė, Rūta Mickienė, Audrius Maruška

Instrumental Analysis Open Access Centre, Vytautas Magnus University, Vileikos str. 8, LT – 44404 Kaunas, Lithuania
vaida.adaskeviciute@stud.vdu.lt

Since ancient times, bee pollen has been used as a food additive or a medicament for several diseases in traditional medicine. Over the past few years, interest in the study of this appreciated natural bee product has increased greatly, mainly due to their chemical composition and biological properties, especially antioxidant activity. High amount of phenolic compounds, mainly flavonoids, are responsible for the antioxidant activity of bee pollen [1]. Sterilization of pollen could help to create new products with bee pollen, when the usage of bacteria is necessary for the further production process. Moreover, sterilized products could be used for the preparation of safer medicaments. The aim of this research was to determine the effect of sterilization process of bee pollen on its antiradical activity and total phenolic compounds content. Lithuanian bee pollen sample was homogenized and sterilized by different thermal processes: in water bath, for 20 and 40 minutes, using 72℃, 80℃, 90℃ temperatures, and in thermostat, for 10, 20 and 40 minutes, using 72℃, 80℃, 95℃ temperatures.

The impact of different sterilization methods on total phenolic compounds content, total flavonoid content and antioxidant activity of bee pollen was determined by spectrophotometric methods [2]. The total content of phenolic compounds was measured using Folin–Ciocalteu reagent. The flavonoid content analysis was carried out by colorimetric reaction with aluminum chloride. Antiradical activity was characterized by the total radical scavenging activity which was measured using 2,2-diphenyl-1-picrylhydrazyl (DPPH) free radical.

The results showed that the microbial growth in bee pollen samples was inhibited, after heat treatment of samples in thermostat at 95℃ temperature for 10, 20 or 40 minutes. The water bath samples and samples, when the sterilization was carried out in thermostat at 72℃ or 80℃ temperatures were not successful in decontaminating: the growth of microbiological organisms, mainly molds, was observed. The sterilization caused a significantly higher total phenolic compounds content, which changed from 18.98±0.04 to 36.44±0.73 mg rutin equivalent/g sample. Unfortunately, sterilized and not sterilized pollen samples did not show relatively high significant difference between the total flavonoid content: it ranged from 7.92±0.11 to 11.54±0.11 mg rutin equivalent/g sample. Although, the total antioxidant activity has increased from 9.81±0.26 to 35.60±0.23 mg rutin equivalent/g sample, which allow to assume that despite the sterilization process and high temperature pollen do not lose their antioxidant properties, but only improves them.

Acknowledgements:
This project was financed by Research Council of Lithuania project No. 09.3.3-LMT-K-712-03-0127

[1] R. Guiné, Bee Pollen: Chemical Composition and Potential Beneficial Effects on Health, Current Nutrition & Food Science, 11, 301-308 (2015).
[2] V. Kaškonienė, G. Ruočkuvienė, P. Kaškonas, I. Akuneca, A. Maruška, Chemometric analysis of bee pollen based on volatile and phenolic compound compositions and antioxidant properties, Food Analytical Methods, 8(5), 1150-1163 (2015).

GD-95RM lipase – new synthetic *Geobacillus* lipase variant with beneficial physicochemical properties

Gytis Druteika, Renata Gudiukaitė

Department of Microbiology and Biotechnology, Institute of Biosciences, Life Sciences Center, Vilnius University, Sauletekio avenue 7, LT-10257 Vilnius, Lithuania
gytis.druteika@gf.stud.vu.lt

The lipases from *Geobacillus* bacteria are lipolytic enzymes which can be active at extreme conditions (alkaline pH, high temperature, organic solvents or detergents in reaction environment) and have a great potential for application in bioconversion and ecotechnology [1].

In this study the new *Geobacillus* lipase variant GD-95RM was designed through random mutagenesis using *Taq* polymerase together with GD-95 lipase gene as a template. We showed that this new lipase displayed ability to work under the industrially attractive conditions mentioned before. The mutated GD-95RM lipase was active at broad temperature range (5 – 85 °C) (Fig. 1a), was able to hydrolyze *p*-NP esters with various acyl chain length (Fig. 1b), worked at pH interval from pH 6 to pH 11and retained lipolytic activity after incubation with methanol for 30 minutes. Several mutations obtained by the GD-95RM lipase had a positive effect on the lipolytic activity compared to GD-95 lipase. The specific lipolytic activity of new mutated lipase was more than twice higher than parental enzyme (950 U/mg versus 400 U/mg). It is important to mention the possibility of long term storage of a GD-95RM lipase in cold environment. This enzyme has not experienced the loss of lipolytic activity even after incubation at 4 °C for over 3 months.

The ability to hydrolyze long acyl chain substrates, which are also common in natural fats combined with long term storage, low requirements for the production and high lipolytic activity makes the GD-95RM lipase an industrially attractive biocatalyst.

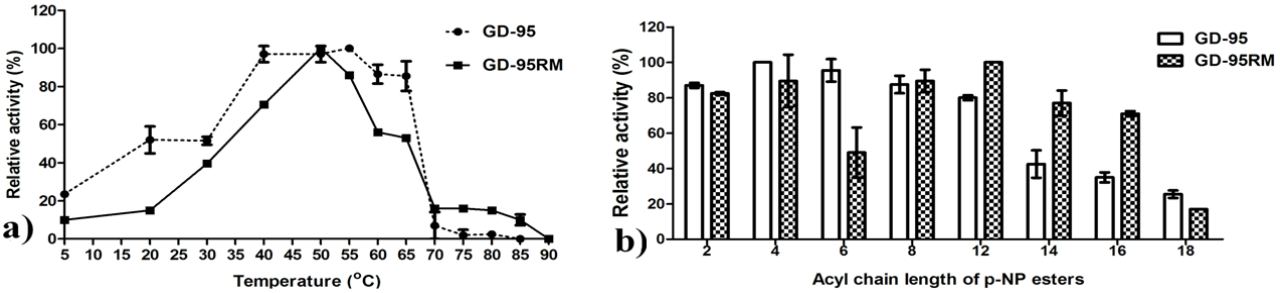

Fig. 1 Analysis of physicochemical properties of GD-95RM and parental GD-95 lipases. Effect of temperature on the activity of recombinant lipases (a); activity of mutated GD-95RM and GD-95 lipases toward various *p*-NP esters (b). The results of GD-95 were adapted based on the Gudiukaite et al. [2]

[1] M. Guncheva, D, Zhiryakova, Catalytic properties and potential applications of *Bacillus* lipases, J Mol Catal B Enzym **68**:1–21 (2011).
[2] R. Gudiukaite, A. Gegeckas, D. Kazlauskas, D. Citavicius, Influence of N- and C- terminal regions on activity, expression, characteristics and structure of lipase from *Geobacillus* sp. 95, Extremophiles **18**:131-45 (2014).

ELECTROCHEMICAL ACTIVITY OF POLYPYRROLE MODIFIED SACCHAROMYCES CEREVISIAE

Vilius Aukscionis[1], Antanas Zinovicius[2,4], Aura Kisieliute[1,3], Jurate Petroniene[1], Lina Mikoliunaite[1], Inga Vilkonciene-Morkvenaite[2,3], Arunas Ramanavicius[1,3]

[1] Vilnius University, Faculty of Chemistry, Department of Physical Chemistry, Vilnius, Lithuania
[2] Vilnius Gediminas Technical University, Faculty of Mechanics, J. Basanavičiaus g. 28, 03224 Vilnius, Lithuania
[3] Center for Physical Sciences and Technology, Saulėtekio 3, 10257 Vilnius, Lithuania
[4] Kaunas University of Technology, Faculty of Chemical technology, Radvilėnų pl. 19, 50299 Kaunas, Lithuania
vilius.aukscionis@gmail.com

As we strive to find new ecologically friendlier sources of energy, alternative sources such as Microbial Fuel Cells (MFC) have grown in interest. Biofuel cells are bioelectrochemical systems which convert chemical energy into an electric current by using biological components e.g. living cells.

In this research, we examine the effects of modifying Saccharomyces cerevisiae (S.cerevisiae) with a conducting polymer - polypyrrole [1] for the use in electrochemical systems e.g. biosensors, MFC.

The synthesis of polypyrrole was induced by biochemical processes present in living S. cerevisiae and formed a layer within the cell's wall. A double mediator system with a hydrophilic and a lipophilic substance [2] ensured the charge transfer between the cell's cytoplasm and the extracellular medium. For investigating the changes due to encapsulation three techniques were employed: firstly, amperometric measurements at constant potential, secondly, scanning electrochemical microscopy [3] and finally atomic force microscopy. The last technique provided insight about the morphological changes and physical properties of S.cerevisiae, the other two techniques contributed to the bioelectrochemical activity evaluation.

The conductive polymer layer around the cells facilitates redox potential and microorganism generated current charge transfer in the direction of the electrode thus converting into an electrical current.

By comparing the control group and the modified group we found that there is a difference in cell morphology and the electrochemical signal. The changes could be appointed to the difference in the cell's wall electrical conductivity, surface area, transport of mediators. These findings could help in the development of MFC, biosensors or other electrochemical systems.

This research is/was funded by the European Regional Development Fund according to the supported activity 'Research Projects Implemented by World-class Researcher Groups' under Measure No. 01.2.2-LMT-K-718 and by the European Social Fund under the No 09.3.3-LMT-K-712 "Development of Competences of Scientists, other Researchers and Students through Practical Research Activities" measure.

[1] A. Ramanavicius, E. Andriukonis, A. Stirke, L. Mikoliunaite, Z. Balevicius and A. Ramanaviciene, Enzyme and Microbial Technology, 2016, 83, 40-47.
[2] I. Morkvenaite-Vilkonciene, A. Ramanaviciene, and A. Ramanavicius, 9,10-Phenanthrenequinone as a redox mediator for the imaging of yeast cells by scanning electrochemical microscopy. Sensors and Actuators B: Chemical, 2016. 228, 200-206.
[3] A. Ramanavicius, I. Morkvenaite-Vilkonciene, A. Kisieliute, J.Petroniene, A.Ramanaviciene. Scanning electrochemical microscopy based evaluation of influence of pH on bioelectrochemical activity of yeast cells − Saccharomyces cerevisiae Colloids and Surfaces B: Biointerfaces.Amsterdam 2017, 149, 1-6.

ULTRA-SMALL GOLD NANOPARTICLES AGAINST CLINICALLY ISOLATED PATHOGENS

Kotryna Semėnaitė[1], Rokas Žalnėravičius[1], Arūnas Jagminas[1]

[1] State Research Institute Center for Physical Sciences and Technology, Vilnius, Lithuania
rzalneravicius@gmail.com.

Over the years, natural and chemically synthesized antibiotics have been used to control infections resulting from community environments. Currently, there is a growing demand for the synthesis of nanomaterials that would replace widely applied antibiotics due to their antimicrobial properties. Available reports show that metal nanoparticles (NPs) such as Ag, Au, Cu, Zn, Si [1] and metal oxide nanoparticles including TiO_{2-x}, ZnO, CuO, Cu_2O, Co_3O_4, MgO, ZrO_2, Ni_2O_3 or normal spinel structure ferrites $[M^{2+}][Fe^{3+}]O_4$ where M^{2+} is the metal ion as Zn^{2+}, Mn^{2+}, Cu^{2+}, Co^{2+} [2] were identified to exhibit antimicrobial activity against multi-drug resistance pathogens. The molecular mechanisms for antibacterial effect of nanoparticles are still being investigated, but there are two more popular proposed possibilities in this regard: (a), free metal ion toxicity arising from dissolution of the metals from the surface of nanoparticles and (b), oxidative stress *via* generation of reactive oxygen species (ROS) on the surfaces of nanoparticles [3]. We also suspect that this effect could be attributed to amino acid-induced generation of negative curvature at the surface of membrane due to a specific interaction, where the cationic amine groups induce negative curvature wrapping of anionic membranes leading to micellization/vesiculation and disrupt of membrane integrity causing the thinning of membranes (Fig. 1).

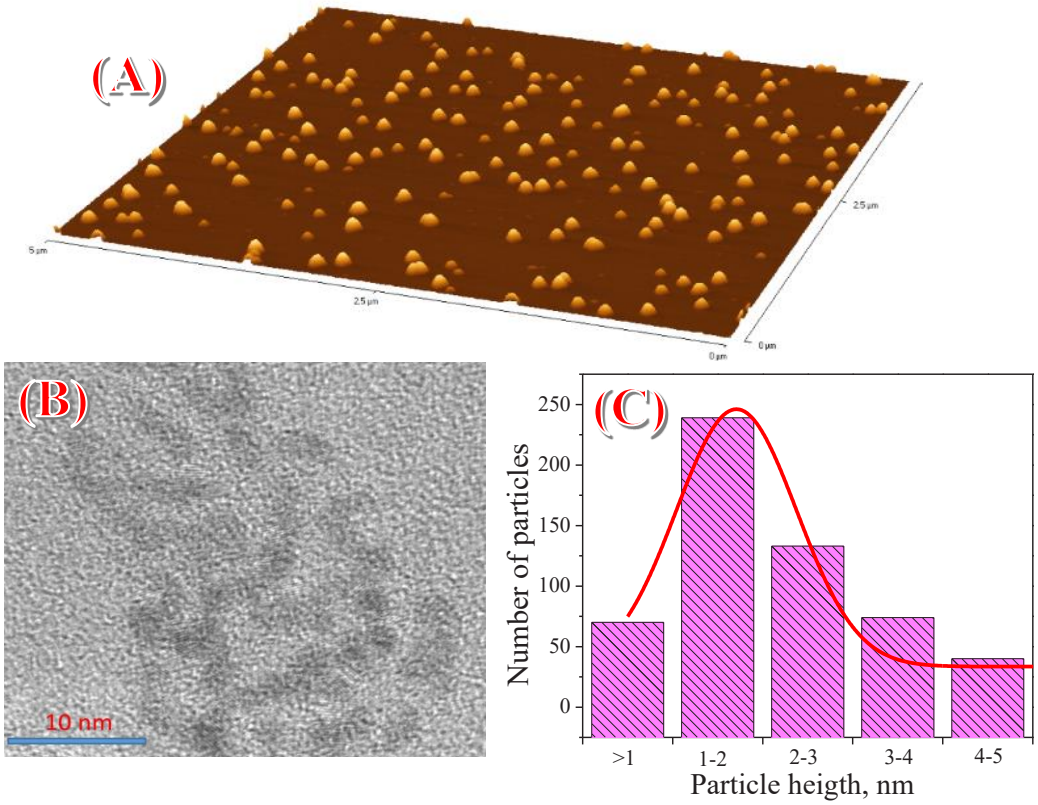

Fig. 1. AFM 3D view (a) TEM image (b) and size distribution histogram (c) of gold nanoparticles detached from magnetite nanoparticles.

Identifying previously published papers of our research group, it is worth mentioning that we have synthesized quite different antimicrobial agents such as ultra-small gold NPs and nanoclusters. The antibacterial activities of these nanomaterials were tested *in vitro* against gram-negative *Acinetobacter baumannii*, *Salmonella enterica* and gram-positive *Micrococcus luteus,* methicillin-resistant *Staphylococcus aureus* bacteria.

[1] S.M. Dizaj, F. Lotfipour, M. Barzegar-Jalali, M.H. Zarrintan, K. Adibkia, Antimicrobial activity of the metals and metal oxide nanoparticles, Materials Science and Engineering C, 44 (2014) 278-284.
[2] E. Hoseinzadeh, P. Makhdoumi, P. Taha, et. al. A Review on Nano-Antimicrobials: Metal Nanoparticles, Methods and Mechanisms, Current Drug Metabolism, 18 (2017) 120–128.
[3] A. Besinis, T.D. Peralta, R.D. Handy, The antibacterial effects of silver, titanium dioxide and silica dioxide nanoparticles compared to the dental disinfectant chlorhexidine on *Streptococcus mutans* using a suite of bioassays, Nanotoxicology 8 (2014) 1–16.

SIMULATION OF NOISE INFLUENCE ON LEARNING PROCESS IN TWO-DIMENSIONAL BIOLOGICAL NEURAL NETWORKS

Tatsiana Pyzhyk, Andrey Denisov

Department of Physics, Belarusian State University, Belarus
Tatsiana.pyzhyk@gmail.com

An understanding of brain processes mechanisms has a great importance for formation of general ideas about a brain and for the possibility of treatment and prevention of neuropathology [1]. Learning is the one of the most important process which takes place in the mammalian brain. Just the ability to learn is the basis for survival in the ever-changing environment. Each pyramidal neuron in a brain has thousands of synaptic contacts in cortex and approximately 80% of them are excitatory and 20% are inhibitory. The balance of excitation and inhibition signals is a very important factor [2]. This phenomenon is based on neuroplasticity and is realized due to homeostatic tuning of synaptic contacts strength [3]. In addition, an important feature of a biological network is that cortical neurons *in vivo* are subjected to an ongoing stimulation by input synaptic activity which is the main source of a low-intensity noise and sustains membrane potentials of cortical neurons in a noisy and depolarized state [4-6]. The computer model of neural network with similar to biological parameters was developed to investigate the influence of noise and inhibition on the learning process.

The model is realized in the Neural Simulation Tool (NEST) simulation software. The model network consists of the 100×100 nodal grid of excitatory neurons and the 50×50 nodal grid of inhibitory neurons, which are superimposed on each other. Neurons are simulated on the basis of integrate-and-fire (IAF) model. Excitatory synaptic contacts are based on the spike time dependent plasticity (STDP) rule, and inhibitory contacts are implemented as stationary constant strength connections whose value equal to half of the maximum of excitatory connections strength. Initial values of excitatory connections are distributed evenly within minimal and maximal strengths. Connections in the model are of each-to-each type with constant probability. Delay of propagation depends on a distance between cells linearly. A noise component is included as high frequency Poisson generators connected to each neuron. It is similar to uniform background subliminal activity in biological networks. The resulting model has important properties of biological neural network, such as dense local recurrent connections [2]. The training signals are represented as repetitive simultaneous activations of cells groups. Two training signals are set in opposite quarters of network with different time intervals.

The effect of learning is estimated as the ratio of average membrane potential of two learning zones in an inter-stimuli period. Both zones are in opposite quarter to last presented signal. The first one includes neurons on which other stimulus was set before. The second one consists of other cells in the same quarter. Learning is observed in case when the coefficient of learning is greater than one. In this case, learning is defined as more strong response of previously trained cells under the influence of excitation waves which propagate from the place of delivery of another stimulus.

It was shown that a noise impact and/or a high intensity of the training signal could lead the network to the state with a maintained epileptic activity in case of the absence or weak inhibition. The introduction of inhibition makes it possible to observe training at those values of noise and/or signal intensity at which training was impossible earlier. It also leads to suppression of an epileptic activity if such activity arises. However, large values of the inhibiting weights strength lead to the conditions when most of the neurons are in the state with a membrane potential well below the threshold potential. It makes learning impossible. A positive effect of noise exposure is that a subthreshold activation of neurons throughout the network is caused by a wave of induced activity propagating from the first training signal, but the most significant changes in the membrane potential occur in the region corresponding to the second training signal. Over-threshold activation occurs at a certain ratio of excitation and noise in the region corresponding to the second training signal. It leads to the fixation of previously learned signals (because of STDP). Therefore, the network-learning coefficient depends on ratio of such parameters as strength of excitatory and inhibitory synaptic contacts, intensity of noise and training signal. The proposed model can be extended by introducing plasticity of inhibitory neurons.

[1] G. Neves, S. F. Cooke, T. V. P. Bliss., Synaptic plasticity, memory and the hippocampus: a neural network approach to causality, Nature Reviews Neuroscience **9**, 65-75 (2008).
[2] A. Renart., J. De La Rocha, P. Bartho et al., The asynchronous state in cortical circuits, Science **327**, 587-590 (2010).
[3] J. Barral, Al. D. Reyes, Synaptic scaling rule preserves excitatory-inhibitory balance and salient neuronal network dynamics, Nature neuroscience **19**, 1690-1696 (2016).
[4] N. Fourcaud, N. Brunel, Dynamics of the firing probability of noisy integrate-and-fire neurons, Neural computation **14**, 2057-2110 (2002).
[5] B. Haider, A. Duque, A. R. Hasenstaub et al., Neocortical network activity in vivo is generated through a dynamic balance of excitation and inhibition, Journal of Neuroscience **26**, 4535-4545 (2006).
[6] N. Brunel, Dynamics of sparsely connected networks of excitatory and inhibitory spiking neurons, Journal of computational neuroscience **8**, 183-208 (2000).

ANTIOXIDANT PROPERTIES OF SUPPLEMENTARY PHYTOCOMPLEXES FOR MEAT FOODS

Sharshunovich Darya[1], Shishkanova Polina[1], Semenkova Galina[1], Tsarik Galina[1], Madzievskaya Tatyana[2], Mikhnova Svetlana[3].

[1] Department of Radiation Chemistry and Chemical-Pharmaceutical Technology, Belarusian State University, Minsk
[2] Center of food technologies of Unitechprom BSU, Minsk
[3] Local fund «Scientific and Technological park of BSU», Minsk
shershunovichd@mail.ru

ROS (reactive oxygen species) and RHS (reactive halogen species) production in human body is a very important process that takes place in biological systems in normal and pathological state. Normally ROS and RHS act as microbicidal agents that utilize pathogenic microorganisms by phagocytosis. They also take part in multiple metabolic transformations by activation of enzymes and signal cascades in cells [1]. ROS and RHS concentration should be sustained at optimal level because their accumulation leads to oxidation and damage of biologically important molecules and cell structures. ROS and RHS hyperproduction (oxidating and halogenating stress) leads to development of various pathologies such as atherosclerosis and other vascular diseases [2]. Due to this, it is urgent to design profilactic food products containing natural antioxidants [3]. Another important way to decrease the risk of cardiovascular diseases is to reduce salt consumption.

In the Local fund «Scientific and Technological park of BSU» and in the Center of food technologies of Unitechprom BSU supplementary phytocomplexes supposed to be used in profilactic meat foods with decreased content of salt were developed. All the phytocomplexes are made of natural spicy-aromatic plants (Allium sativum, Coriandrum sativum, Anethum graveolens, Ocimum basiliicum, Piper nigrum, Pimpinella anisum, etc.) with addition of B group vitamines and minerals.

In this work influence of water extracts of three phytocomplexes («FC-6-1», «FC-16U-4», «FC-Tonus-U») on ROS and RHS that make important contribution to oxidation and halogenation stress was studied.

Neutrophils were allocated from blood of healthy people on the basis of a standard method. For MPO release cells were destroyed in three cycles of freezing and thawing. Influence of water extracts of the phytocomplexes on free radical processes in model systems «Luminol-NaOCl» where luminol is oxidized by NaOCl and «MPO-luminol-H_2O_2» where luminol is oxidized by H_2O_2 in presence of MPO and in neutrophils stimulated with fMLP was studied using method of chemiluminescence. Measurements were conducted with biochemiluminometer BHL-1 (BSU, Belarus). Water extracts were prepared by heating 5g of phytocomplex with 55 g of water to 100 °C for 1 hour.

It was found that all the analyzed extracts express antioxidant activity in studied systems. Extract of «FC-6-1» has the brightest antioxidant properties. It effectively inhibits neutrophils ability to produce ROS, halogenating activity of MPO and can utilize NaOCl without producing free radicals.

Table. – The degree of chemiluminescence inhibition (%) in cell and model systems under influence of «FC-6-1» water extract

Water extract dilution rate	**«Luminol-NaOCl»**	**«MPO-luminol-H_2O_2»**	**«Neutrophil-luminol-fMLP»**
1:20	99,74±1,16	99,77±0,04	99,87±1,32
1:200	90,39±4,35	93,57±0,16	64,45±1,08
1:1000	92,22±2,87	—	18,84±0,59
1:2000	93,82±2,52	67,58±3,50	—

Thus, all the analyzed phytocomplexes with antioxidant activity have potential ability to protect body tissues from halogenating stress and can be used in profilactic meat foods production.

[1] Panasenko O.I., Gorudko I. V., Sokolov A. V. // Uspekhi Biologicheskoi Khimii – 2013 – V. 53 – P. 195-244;
[2] Zhang R., Brennan M.L., Fu X. // JAMA. - 2001 - V. 286. P. 2136.
[3] Volkov V.C., Romanova N.P., Poselyugina O.B. // Cardiology. – 2003. –V. 11. – P. 36-37

PERCHLORATE ANION INFLUENCE ON THE INHIBITION AND LIGAND BINDING OF HUMAN CARBONIC ANHYDRASE VII

Ona Marija Vaitkevičienė[1], Asta Zubrienė[1], Daumantas Matulis[1]

[1] Department of Biothermodynamics and Drug Design, Institute of Biotechnology, Vilnius University, Vilnius, Lithuania
ona.vaitkeviciene@chf.stud.vu.lt

Human carbonic anhydrases (CA) are often studied as potential targets for drug design [1]. The goal of this study was to prepare a recombinant human CA VII protein and to demonstrate the influence of perchlorate (ClO_4^-) to the binding of CA inhibitors.

The main methods used for the study were thermal shift assay (TSA) and isothermal titration calorimetry (ITC) [2]. CA VII was purified using imobilised metal affinity chromatography (IMAC) or by use of a solid phase with covalently-linked carbonic anhydrase-specific inhibitors (sulfonamides) and a ClO_4^- gradient. The protein-ligand dissociation constants, obtained from TSA and ITC experiments using CA inhibitor acetazolamide (AZM), were compared between the different protein purification methods. Furthermore, IMAC-purified CA VII protein-ligand dissociation constant was obtained during ITC experiments in presence of ClO_4^- and using AZM as a ligand. The main result of the study showed that the use of ClO_4^- during the protein purification process affected the dissociation constants and the free energy of the CA VII-inhibitor interaction.

[1] Talibov, V. O., Linkuvienė, V., Matulis, D., & Danielson, U. H. (2016). Kinetically Selective Inhibitors of Human Carbonic Anhydrase Isozymes I, II, VII, IX, XII, and XIII. Journal of Medicinal Chemistry, 59(5), 2083–2093.

[2] Matulis, D. (2008). Baltymų fizikinė chemija. Kaunas: Technologija.

Modelling of Solid-Liquid Interface in Accord with the Electronic Continuum Correction: Rutile (110) Surfaces

Denys Biriukov[1], Milan Předota[1], Ondřej Kroutil[1,2]

[1] Institute of Physics and Biophysics, Faculty of Science, University of South Bohemia, České Budějovice, Czech Republic
[2] Faculty of Chemistry, Materials Research Centre, Brno University of Technology, Brno, Czech Republic
dbiriukov@prf.jcu.cz

Interactions between mineral surfaces and aqueous solutions play an important role in a wide range of natural and industrial phenomena. Over the last years, a lot of scientific attention has been devoted to the exploring of structural and dynamical properties of various compounds in the interfacial and bulk regions. For such purpose, many experimental techniques like non-linear spectroscopy and X-ray reflectivity have been applied to investigate the origin of processes occurring at the mineral-fluid interface. With that, well-known theoretical approaches such as quantum chemical calculations and classical molecular dynamics (CMD) have allowed us to explain these interactions at the atomic and molecular level.

Recently developed theoretical method known as electronic continuum correction (ECC) [1] has been introduced to improve the accuracy of CMD simulations. The idea of ECC lies in the scaling of atomic charges to solve a problem of overestimated pairwise interactions in nonpolarizable force fields. The scaling factor must be equal to an inverse square root of the electronic part of the dielectric constant of the solvent (in the case of water, it is roughly 0.75). At the same time, Lennard-Jones parameters should be refined to provide reasonable interatomic distances. Therefore, so-called ECC-R (electronic continuum correction with rescaling) method combining both charges and van der Waals parameters rescaling has appeared. The importance and success of this technique was already shown for systems with ions [2], simple organic molecules [3], and proteins [4].

In our work, we applied ECCR method to model rutile (TiO_2) surfaces (110) interacting with water and ions, namely, Na^+, Rb^+, Sr^{2+}, representing small monovalent, large monovalent, and large divalent cations, respectively, and Cl^- as counter-anion in the solution. The simulation setups were prepared in a similar way as in our previous works [5] with parameters modified according to the ECCR concept. We performed a set of simulations over a range of surface charge densities corresponding to different pH conditions. The output data (density profiles, interatomic interactions, adsorption sites, dynamical properties) were obtained and discussed. The results were compared against X-ray scattering experimental data [6], outcomes from the same system without applying ECC-R, and our previously published results (see Fig. 1 as an example). This comparison will allow assessing the benefits of the ECC-R method for studying similar systems.

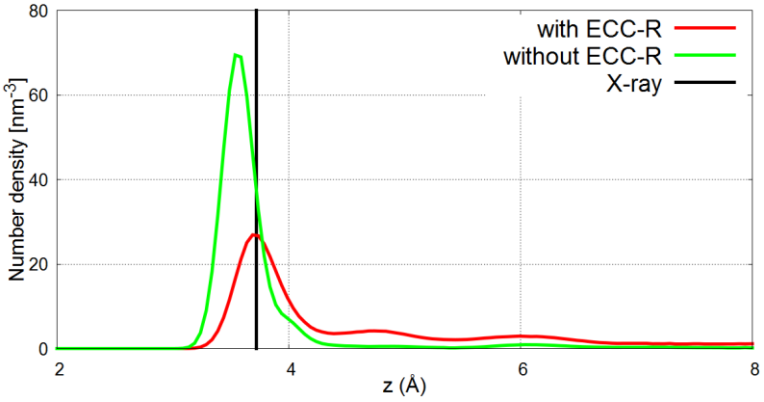

Fig. 1. Axial number density profiles of Rb^+ for the most negatively charged hydroxylated rutile surface (σ = -0.4 C/m^2, pH around 11) in comparison with experimental data.

[1] Leontyev, I., Stuchebrukhov, A. Accounting for Electronic Polarization in Non-Polarizable Force Fields. *Phys. Chem. Chem. Phys.* **13**, 2613−2626 (2011).
[2] Kohagen, M., Mason, P. E., Jungwirth, P. Accounting for Electronic Polarization Effects in Aqueous Sodium Chloride via Molecular Dynamics Aided by Neutron Scattering. *J. Phys. Chem. B* **120**, 1454-1460 (2015).
[3] Kroutil, O., Předota, M., Kabeláč, M., 2017. Force Field Parametrization of Hydrogenoxalate and Oxalate Anions with Scaled Charges. *J. Mol. Model*, **23**:327 (2017).
[4] Kohagen, M., Lepsik, M., Jungwirth, P. Calcium Binding to Calmodulin by Molecular Dynamics with Effective Polarization. *J. Phys. Chem. Lett.* **5**, 3464−3469 (2014).
[5] Předota, M., Machesky, M. L., Wesolowski, D. J., Cummings, P. T. Electric Double Layer at the Rutile (110) Surface. 4. Effect of Temperature and pH on the Adsorption and Dynamics of Ions. *J. Phys. Chem. C* **117 (44)**, 22852−22866 (2013).
[6] Kohli, V., Zhang, Z., Park, C., Fenter, P. Rb^+ and Sr^{2+} Adsorption at the TiO_2 (110)−Electrolyte Interface Observed with Resonant Anomalous X-ray Reflectivity. *Langmuir* **26 (2)**, 950–958 (2009).

THE OPTICAL DAMAGE THRESHOLD OF FEMTOSECOND 3D NANOLITHOGRAPHY PRODUCED MICROSTRUCTURES UNDER INTENSE FEMTOSECOND IRRADIATION

Laurynas Čekanavičius, Linas Jonušauskas, Mangirdas Malinauskas

Vilnius University, Laser Research Center, Saulėtekio Ave. 10, Vilnius, Lithuania
laurynas.cekanavicius@ff.stud.vu.lt

Femtosecond 3D nanolithography, commonly referred as direct laser writing, is keeping the pace by its' rapid development employing nonlinear light–matter interaction and in recent years has got significantly closer from its academical origins to industrial applications. It has been demonstrated that femtosecond 3D nanolithography is a suitable technique for 3D fabrication of biodegradable tissue scaffolds, chip-scale interconnects, lab-on-a-chip microdevices and other functional elements as micro-optical elements urging the technique's lab-to-fab transfer [1].

Functional 3D printed micro-optics can be used in various applications [2], yet further spread is limited by the uncertainty of optical resiliency (i.e. degradation in intense light) of available photopolymers. In this work we have chosen five variant polymers differing in their origin (commercial and experimental), composition (purely organic and hybrid organic-inorganic) and performed quantitative study of their optical resiliency. Tested materials include common in lithography SU8, OrmoClear oriented to optical applications, Ember PR48 used in stereolithography, SZ2080 hybrid organic-inorganic material [3] suitable for diverse use, which was also tested both, photosensitized and pure.

Our femtosecond 3D nanolithography produced microstructures research for optical damage threshold comparison was performed for volume micro-optical elements as for this day closest experiments are performed only with photopolymer thin-films [4]. Tests were performed using S-on-1 laser induced damage threshold (LIDT) evaluation method. It relies on statistical data using linear approximation of the characteristic damage curve for LIDT determination. Microstructures were irradiated for 60 s with 1030 nm, 100 kHz, 300 fs laser pulses using f = 10cm focusing lens considering that experienced fatigue would allow finding close to practical daily use polymer LIDT value. Carried out optical damage threshold measurements suggest, that photoinitiator presence in the photopolymer plays crucial role for its' optical resilience. Even after standard error evaluation [5], SZ2080 without photoinitiator LIDT exceeded all other materials by several times [Fig. 1].

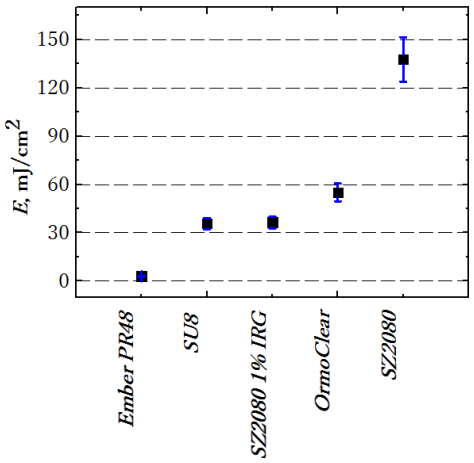

Fig. 1. Direct comparison of optical damage threshold of different photopolymers under intense femtosecond laser irradiation lasting for 60 seconds. Photoinitiator-free material shows the highest LIDT exceeding other tested polymers.

[1] M. Malinauskas, A. Žukauskas, S. Hasegawa, Y. Hayasaki, V. Mizeikis, R. Buividas, S. Juodkazis, Ultrafast laser processing of materials: from science to industry, Light Sci. Appl 5(8), e16133–e16133 (2016).
[2] A. Žukauskas, V. Melissinaki, D. Kaškelytė, M. Farsari, M. Malinauskas, Improvement of the fabrication accuracy of fiber tip microoptical components via mode field expansion, J. Laser Micro/Nanoeng. 9(1), 68–72 (2014).
[3] A. Ovsianikov, J. Viertl, B. Chichkov, M. Oubaha, B. MacCraith, I. Sakellari, A. Giakoumaki, D. Gray, M. Vamvakaki, M. Farsari, C. Fotakis, Ultra-low shrinkage hybrid photosensitive material for two-photon polymerization microfabrication, ACS Nano 2(11), 2257–2262 (2008).
[4] A. Žukauskas, G. Batavičiūtė, M. Ščiuka, T. Jukna, A. Melninkaitis, M. Malinauskas, Characterization of photopolymers used in laser 3D micro/nanolithography by means of laser-induced damage threshold (LIDT), Opt. Mater. Express 4(8), 1601 (2014).
[5] G. Batavičiutė, P. Grigas, L. Smalakys, A. Melninkaitis, Revision of laser-induced damage threshold evaluation from damage probability data, Rev. Sci. Instrum. 84(4), 045108 (2013).

ENHACED THERMAL STABILITY OF CrN/SiN$_X$ NANOSTRUCTURED MULTILAYER COATING DEPOSITED BY MAGNETRON SPUTTERING TECHNIQUE

Alexander Malashevich[1], Sergey Zlotski[1], Gregory Abadias[2]

[1] Physics Faculty, Belarusian State University, Belarus
[2] Institut Pprime, Université de Poitiers, France
Malashevich@bsu.by

Thin multilayer coatings based on nitrides of transitional metals (TM) are widely used as hard protective coatings in the industry for hardening of the cutting instruments, punches, the frictional surfaces of the machine parts and so on.

One of the most important properties of the coatings for their practical application in many fields of the industry is their resistance to harsh environments exposure, in particular, to high temperature oxidation, influence of corrosive medium (for example, saline or acid solutions) and ion irradiation damage.

One of the promising approach of both improvement of mechanical characteristics and increase in a resistance to high-temperature oxidation is the formation of multilayered film structures. Multilayers consisting of alternate stacking of TM nitride and SiNx layers are characterized by very low intermixing that promotes their thermal stability and oxidation resistance.

CrN/SiN$_x$ multilayer coatings with different thickness of CrN and SiNx layers were deposited on (001) Si substrate by a reactive magnetron sputtering under Ar + N_2 plasma discharges at the temperatures of 300-450°C. Multilayer coatings were synthesized via sequential sputtering from elemental Cr and Si_3N_4 targets .

According to transmission electron microscopy (TEM) and X-ray diffraction (XRD) analysis the multilayer coating consist of nanocrystalline (200)-oriented CrN and amorphous SiNx layers. Reducing the CrN layer thickness fraction with respect to bilayer thickness leads to decrease in crystallite size and increase in the lattice parameter of CrN phase due to higher compressive stress.

The oxidation resistance under air using in situ XRD, in the temperature range from 400 to 950°C was studied, as well as by WDS and SEM methods after air annealing procedure. Fig. 1 shows XRD analysis results of CrN/SiNx nanostructured multilayer coating and CrN monolayer coating.

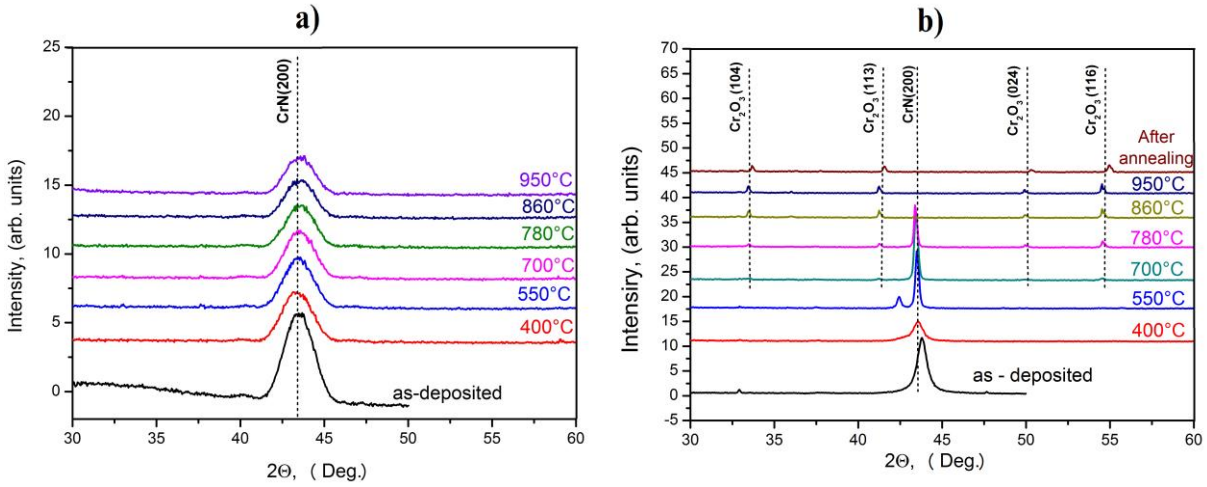

Fig. 1. XRD analysis results of a) CrN / SiNx (5 nm / 5 nm – CrN and SiNx layer thickness respectively) multilayer nanostructured coating (total thickness~ 256 nm) b) CrN monolayer coating (total thickness~259 nm)

According to XRD analysis results, CrN/SiNx nanostructured multilayer coating possess a greater thermal stability then CrN monolayer coating. Fig. 1 b) shows that the chromium oxide begins to form at a temperature of about 700℃, but in case of multilayer coatings, oxides at a temperature of 950 ˚C weren't detected.

[1] P.H. Mayrhofer, C. Mitterer, L. Hultman, H.Clemens, Microstructural design of hard coatings, Prog. Mater. Sci. 51, 1032 (2006)
[2]S.Veprek, M. Veprek-Heijman, P. Karvankova, Ja. Prochazka, Different approaches to superhard coatings and nanocomposites, Thin Solid Films 476, 1 (2005)
[3]A. Raveh, I. Zukerman, R. Shneck, R. Avni, I. Fried, Thermal stability of nanostructured superhard coatings: A review, Surf. Coat. Technol. 201, 6136 (2007)

UPCONVERSION LUMINESCENCE AND ENERGY TRANSFER IN $NaGdF_4:Nd^{3+}$, Yb^{3+}, Er^{3+} HEXAGONAL NANOPARTICLES UNDER 808 nm LASER EXCITATION

Gintarė Plečkaitytė[1], Ieva Mikalauskaitė[1], Arturas Katelnikovas[1], Aldona Beganskienė[1]

[1] Institute of Chemistry, Faculty of Chemistry and Geosciences, Vilnius University, Naugarduko st. 24, 03225, Vilnius, Lithuania
gintare.pleckaityte@chf.stud.vu.lt

The 808 nm excited lanthanide doped upconverting nanoparticles (UCNPs) have received much attention in recent years due to minimized heating effect, improved tissue penetrability and lower water absorption if compared to the conventional excitation with 980 nm laser. These UCNPs are more appropriate for in vitro/in vivo biomedical diagnostic and theranostic applications [1]. Nd^{3+} ions are considered as good energy donor candidate because of its high absorption cross-section around 800 nm which is about one order of magnitude larger than its Yb^{3+} counterpart at ca. 980 nm. Further energy transfer to bridging Yb^{3+} ions with transfer to energy acceptor-activator ions (Er^{3+}, Tm^{3+}, Ho^{3+}, Pr^{3+}) [2] would be the cause of emission in visible (VIS) and near-infrared (NIR) regions.

In the present study single phase hexagonal $NaGdF_4:Nd^{3+}$ (0-10%), Yb^{3+} (20%), Er^{3+} (2%) and $NaGdF_4:Nd^{3+}$ (0-40%), Yb^{3+} (20%) nanoparticles with size range of 36-58 nm were synthesized by the thermal decomposition of trifluoroacetates method. Typical emission lines originating from the intraconfigurational transitions of Yb^{3+}, Er^{3+} and Nd^{3+} ions were observed in VIS and NIR regions. The acquired data showed that the ratio of integrated intensity of green and red emission bands of Er^{3+} ions decrease if doping concentration of Nd^{3+} ions increases.

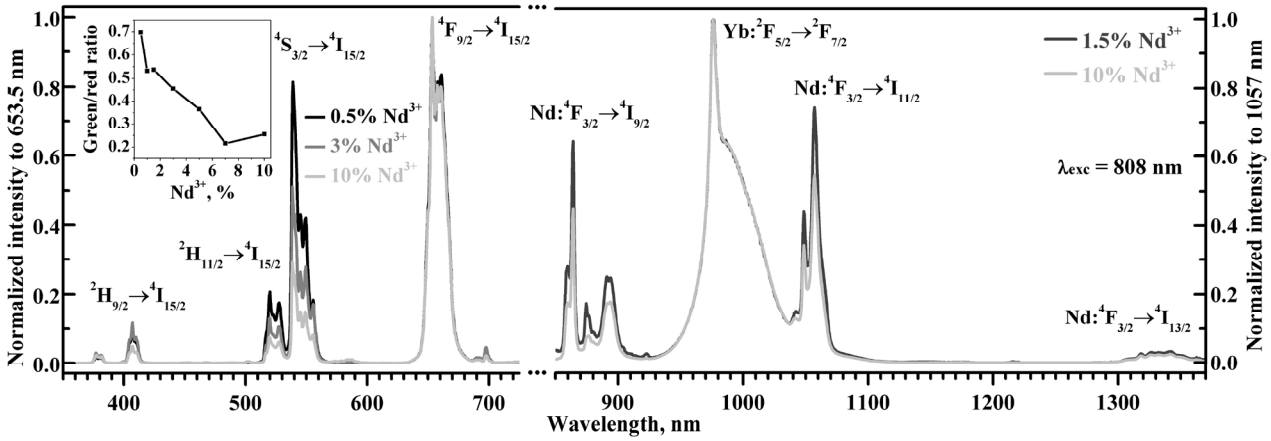

Fig.1. Upconversion emission spectra of $NaGdF_4:Yb^{3+}$ (20%), Er^{3+} (2%), Nd^{3+} (0,5-10%)

A typical optical limitation of lanthanide doped nanostructures is emission quenching which occurs as a result of cross-relaxations between dopant ions leading to energy loss through non-radiative processes [3]. Unfortunately, the literature on the $Nd^{3+} \rightarrow Yb^{3+}$ energy transfer and the optimal Nd^{3+} and Yb^{3+} concentrations is rather scarce. Therefore, the aim of this work is to investigate the $Nd^{3+} \rightarrow Yb^{3+}$ energy transfer in single phase $NaGdF_4$ hexagonal nanoparticles with particular focus on finding optimal concentration of these ions when the energy transfer is the strongest and cross-relaxation processes are the weakest. The energy transfer and cross-relaxation processes were investigated by exciting the synthesized nanoparticles with 808 nm laser radiation and measuring their room temperature emission spectra in the VIS and NIR range. This data was supported by recording the photoluminescence decay curves for Nd^{3+}, Yb^{3+}, and Er^{3+} emission and calculating their emission lifetime values. Furthermore, the temperature dependent emission spectra and photoluminescence decay curves in the range of 77 – 500 K were also recorded and will be discussed in great detail.

[1] B. Liu, C. Li, P. Yang, Z. Hou, J. Lin, 808-nm-Light-Excited Lanthanide-Doped Nanoparticles: Rational Design, Luminescence Control and Theranostic Applications, Adv Mater, 29 (2017).
[2] X. Li, R. Wang, F. Zhang, L. Zhou, D. Shen, C. Yao, D. Zhao, Nd^{3+} sensitized up/down converting dual-mode nanomaterials for efficient in-vitro and in-vivo bioimaging excited at 800 nm, Sci Rep, 3 (2013) 3536.
[3] F.J. Pedraza, C. Rightsell, G.A. Kumar, J. Giuliani, C. Monton, D.K. Sardar, Emission enhancement through Nd^{3+}-Yb^{3+} energy transfer in multifunctional $NaGdF_4$ nanocrystals, Appl Phys Lett, 110 (2017) 223107.

LITHIUM/SODIUM/MAGNESIUM VANADATE-PHOSPHATE GLASSES AS POTENTIAL CATHODE MATERIALS

Wiktoria Zajkowska[1], Tomasz K. Pietrzak[1]

[1]Faculty of Physics, Warsaw University of Technology, Poland
w.zajkowska@onet.pl

Most of vanadium oxides have layered structure, what makes them interesting for potential cathode materials applications. Intercalation is a reversible process of ion inclusion into layered-structured material. Lithium batteries have been examined for 40 years and Li^+ plays its role, but today's world needs even better batteries working analogously to Li-ion batteries. Due to fact that deposits of lithium are mostly localized in China, there is substantial need for finding a new replacement for energy storage materials. The idea for replacing lithium in batteries is using sodium [1] or magnesium [2]. Nanocrystallization of glassy analogs of crystalline cathode materials is a very effective method to improve electrical properties of the material, what was proven also in case of vanadate-phosphate glasses. ([3], [4])

M_xO-V_2O_5-P_2O_5 , M = Li, Na, Mg samples were prepared by melt-quenching technique. Weighted chemicals (Li_2CO_3, Na_2CO_3, MgO, V_2O_5, $(NH_4)H_2PO_4$) were mixed and milled carefully in a mortar and put into alumina crucibles. The precursors were heated at 1300°C for 30 minutes in an induction furnace. Afterwards, the molten compound was poured onto a stainless-steel plate and rapidly covered with the same one. XRD (X-ray diffractometry) measurements were carried out to identify presence of crystalline phases and to check the amorphousness. Philips X'pert apparatus was used. The analysis of the DSC (differential scanning calorimetry) could give information on glass transition and crystallization temperature, those measurements were carried out by Q200 setup (TA Instruments). The conductivity was improved by thermal nanocrystallization process and its results were presented in Arrhenius plots. The conductivity was measured by DC (Direct Current) and IS (Impedance Spectroscopy) methods. The sample was kept in a tubular furnace Czylok while temperature controller (Eurotherm 2404) was constantly stabilizing. The parameters of the sample (temperature and resistance) were measured by thermocouple, Adam 4011 and Keithley 2001.

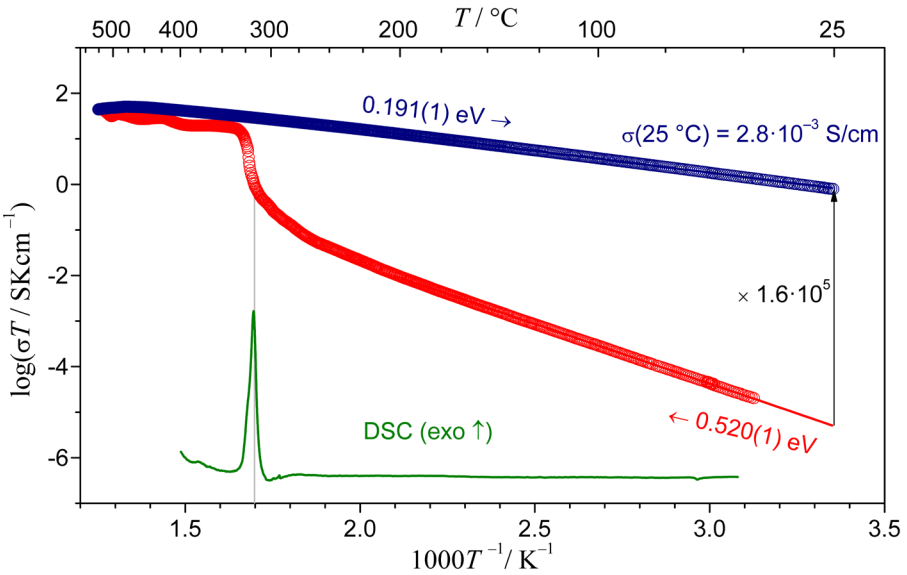

Figure 1. Arrhenius plot of $90NaV_2O_5{\cdot}10P_2O_5$ sample. Red points (lowers ones) correspond to a heating ramp and blue points (higher ones) indicate on cooling ramp. The irreversible increase of conductivity caused by nanocrystallization process is clearly visible.

An example of conductivity dependencies in the sample as function of a temperature is presented in Arrhenius plot. The plot consists of two ramps: heating (red points) ramp and cooling one (blue points). The nanocrystallization process included heating up to 515°C. As expected, due to nanocrystallization process, the conductivity increased irreversibly. In the future, there are plans to carry out the electrochemical measurements of L, N, M samples.

[1] S. Tepavcevic, H. Xiong, V. Stamenkovic, X. Zuo, M. Balasubramanian, V. Prakapenka, Ch. Johnson, T. Rajh, Nanostructured Bilayered Vanadium Oxide Electrodes for Rechargeable Sodium-Ion Batteries, ACSnano **6**, 530–538 (2012)

[2] P. Liu, D. Zhou, K. Zhu, Q. Wu, Y. Wang, G. Tai, W. Zhang, Q. Gu, The Intercalation Phase Diagram of Mg in V_2O_5 from First-Principles, Chemistry of materials **27**, 3733–3742 (2015)

[3] T. Pietrzak, L. Pawliszak, P. Michalski, M. Wasiucionek, J. Garbarczyk, Highly conductive $90V_2O_5{\cdot}10P_2O_5$ nanocrystalline cathode materials for lithium-ion batteries, Procedia Engineering **98**, 28–35 (2014)

[4] T. Pietrzak, J. Garbarczyk, M. Wasiucionek, I. Gorzkowska, J. Nowiski, S. Gierlotka, Electrical properties vs. microstructure of nanocrystallized V_2O_5 P_2O_5 glasses, An extended temperature range study, Solid State Ionics **192**, 210 – 215 (2010)

THE RATE OF GOLD NANOPARTICLE FORMATION AS AN INDIRECT SIGNAL FOR REDUCING SUGAR CONCENTRATION IN THE SAMPLE

Benediktas Brasiūnas[1,2], Anton Popov[1,2], Almira Ramanavičienė[1,2]

[1]Department of Analytical and Environmental Chemistry, Faculty of Chemistry and Geosciences, Vilnius University, Lithuania

[2]NanoTechnas - Center of Nanotechnology and Materials Science, Faculty of Chemistry and Geosciences, Vilnius University, Lithuania

benas.brasiunas@gmail.com

Nanoparticles are a unique group of materials with exceptional features and broad application in various fields [1]. Gold nanoparticles (AuNPs) exhibit unique optical and physical properties. Various types of solution focused approaches have been developed in the past few decades to improve the control over the size, shape and surface functionality of AuNPs while the formation and growth of AuNPs can be used as analytical signal for designing sensors and biosensors [2]. Optical methods are useful for the AuNPs formation monitoring due to the color and absorbance band changes in the visible region, which can be measured by UV-Vis spectroscopy. Furthermore, such method is fast and nondestructive for the sample. Reducing carbohydrates are of a high importance due to their influence to human health and due to their possible application for AuNPs and AuNPs-based analytical systems development [3].

The main aim of this study was to develop a rapid and simple method for the detection of reducing sugars in real samples. AuNPs were formed in a redox reaction between tetrachloroauric acid ($HAuCl_4$) and reducing sugars. Cetyltrimethylammonium bromide (CTAB) was added as a surfactant to stabilize already formed AuNPs. The redox reaction takes place in basic medium at room temperature at optimal $HAuCl_4$, CTAB and NaOH concentrations without the need of AuNP seeds. The formation of AuNP was observed using UV-Vis spectroscopy method while the size of AuNP was determined from dynamic light scattering measurements and SEM or TEM images. Linear calibration curves were obtained for various reducing sugars in modelling and real samples, however the main attention was directed towards the optimization of the developed method for lactose detection in milk.

Acknowledgments

This research was funded by the European Social Fund under the No 09.3.3-LMT-K-712-03-0090 “Development of Competences of Scientists, other Researchers and Students through Practical Research Activities” measure.

[1] R. Geethalakshmi, D. Sarada, Gold and silver nanoparticles from Trianthema decandra: synthesis, characterization, and antimicrobial properties, Int J Nanomedicine, **7**, 5375-5384 (2012).

[2] A. Ramanaviciene, J. Voronovic, A. Popov, R. Drevinskas, A. Kausaite-Minkstimiene, A. Ramanavicius, Investigation of biocatalytic enlargement of gold nanoparticles using dynamic light scattering and atomic force microscopy, Colloids Surf. A Physicochem Eng Asp, **510**, 183–189 (2016)

[3] K. Ilaslana, I. H. Boyaci, A. Topcu, Rapid analysis of glucose, fructose and sucrose contents of commercial soft drinks using raman spectroscopy, Food Control, **48**, 56-61 (2015)

AL FOIL AS A PROMISING SUBSTRATE FOR SERS OF MICROCRYSTALS

Yauheniya Korza, Anna Matsukovich, Elena Shabunya-Klychkovskaya

B.I. Stepanov Institute of Physics, National Academy of Sciences of Belarus, Belarus
korza_ev@list.ru

Aluminum (Al) is a promising material for applications in plasmonics. Nowadays, SERS substrates based on plasmonic Al have primarily focused on nanostructures fabricated using e-beam lithography, such as nanoparticle or nanohole arrays and bowtie structures, along with roughened films and gratings [1, 2].

This work shows the investigation of microcrystals of lead (II) oxide (PbO) and lead (II) chromate ($PbCrO_4$) by SERS. The samples were prepared as the thin layers on the glass and aluminum foil. The size of microcrystals is about 10 μm. Raman scattering (RS) spectra were registered by spectrometer NanoFlex (Solar LS, Belarus) with Ar^+ laser (488 nm). Raman spectra exposure time was 60 s.

Aluminum foil is charecterized by roughnesses with height about 150-200 nm and diameter from 1 to 10 μm. Reflectance spectrum of Al foil has peaks at 615 and 670 nm.

Raman spectrum of PbO (Fig.1a) has bands at 138, 284, 382 and 419 cm^{-1}. SERS spectrum of lead (II) oxide is characterized by enhancement of intensity of the bands at 138 cm^{-1} and 284 cm^{-1} on 1 order of magnitude. Also SERS spectrum has new bands at 477 and 550 cm^{-1} corresponding to α-PbO [3].

Raman spectrum of $PbCrO_4$ on the glass (Fig.1b) has a peak at 843 cm^{-1}. The using Al foil gives Raman scattering enhancement of this peak up to 8 times. In the case of lead (II) chromate adsorbed on Al foil the new bands at 335, 360, 375 and 403 cm^{-1} appear. The obtained spectra are characterized with a high signal-to-noise ratio and low luminescence background.

Thus we conclude, the using Al foil allow to essentialy increase the sensitivity of RS for microcrystals study and could be a promising substitute for gold (Au) and silver (Ag) in plasmonics research due to its lower cost and simplicity of sample preparation.

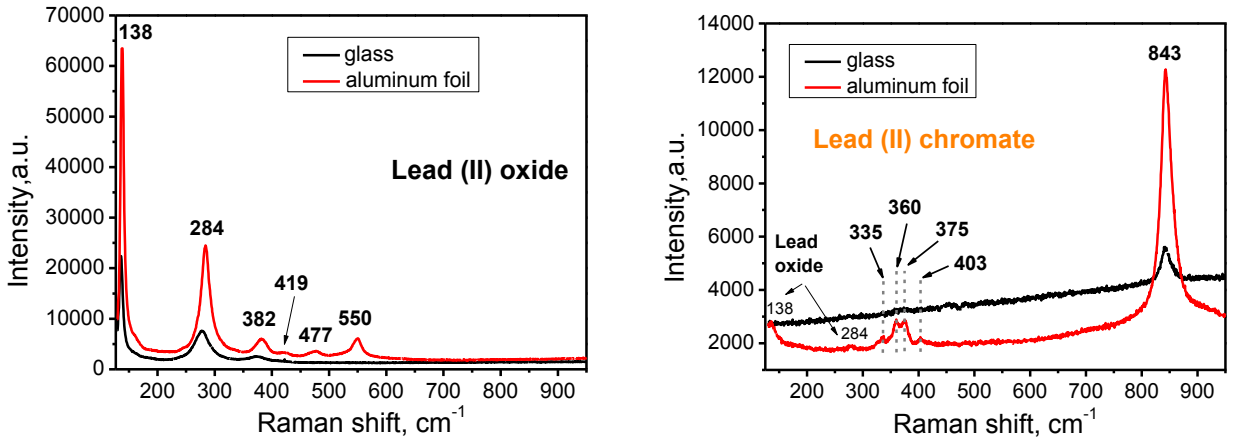

a) b)

Fig. 1. Raman spectra of microcrystals: a) lead (II) oxide and b) lead (II) chromate.

[1] S. Tian et al., Aluminum Nanocrystals: a sustainable substrate for quantitative SERS-based DNA detection. Nano Lett. 17(8). 5071-5077 (2017).
[2] C. L. Lay et al., Aluminum nanostructures with strong visible-range SERS activity for versatile micropatterning of molecular security labels. Nanoscale. 10. 575-581 (2018).
[3] M. Cortez-Valadez et al., Additional active Raman modes in α-PbO nanoplates. Physica. E 53. 146–149 (2013).

HELIUM ION MICROSCOPY OF 1D STRUCTURES ABLATED EMPLOYING FEMTOSECOND LASER INTERFERENCE FIELD

Aušrinė Jurkevičiūtė[1], Mindaugas Juodėnas[1], Vadzim Adashkevich[2], Andrius Vasiliauskas[1], Tomas Tamulevičius[1,3], Jacek Fiutowski[2], Sigitas Tamulevičius[1,3], Horst-Günter Rubahn[2]

[1]Institute of Materials Science, Kaunas University of Technology, K. Baršausko St. 59, LT-51423 Kaunas, Lithuania
[2]Mads Clausen Institute, University of Southern Denmark, Alsion 2, DK-6400 Sonderborg, Denmark
[3]Department of Physics, Kaunas University of Technology, Studentų St. 50, LT-51368 Kaunas, Lithuania
ausrine.jurkeviciute@ktu.lt

Development of technologies for organised nanoscale structures are demanding due to applications in fluid dynamics, sensors or optical devices. Periodic structures in noble metal films are particularly interesting due to their plasmonic properties [1]. Silver nanoparticles based plasmonic structures can be fabricated in many different approaches, e.g. evaporation, sputtering, ion implantation [2]. Another approach is laser irradiation, which leads to formation of nanoislands, beads, nanoparticles or self-organised patterns [3]. In order to further control optical properties of plasmonic material, it can be embedded in dielectric or semiconducting matrix. This is also beneficial for protecting nanoparticles from unwanted degradation in environment [4].

In this work, we present laser interference field ablation of amorphous diamond-like carbon (DLC), silver (Ag) and nanocomposite (DLC:Ag) thin films on silicon and quartz substrates. DLC and DLC:Ag films were fabricated employing magnetron sputtering in a mixture of acetylene and argon gas using carbon and silver targets, respectively. Ag films were fabricated by e-beam evaporation. The thickness of deposited films was 60 nm.

One-dimensional (1D) periodic structures in thin films were ablated using Yb:KGW femtosecond laser pulses (second harmonic wavelength 515 nm, pulse duration 290 fs). The laser beam was separated into two using diffractive optical element (DOE) and then overlapped with 4f lens system into one spot on the surface of the sample to create the interference pattern. The pitch of the pattern was altered by changing the angle of the incidence, i.e. changing the pitch of the DOE. To find best parameters of microfabrication the laser fluence was varied from 1 mJ/cm^2 to 226 mJ/cm^2 and the number of applied pulses was varied from 1,000 to 125,000. The total area of ablated pattern was 300 $\times$ 300 μm^2. For each pitch, the total of 25 patterns with different micromachining parameters were created.

The ablated structures were investigated using scanning electron microscope (SEM, Hitachi S-4800) and helium ion microscope (HIM, Zeiss ORION NanoFab) (Fig. 1). The determined pitches of 1D structures are 1.26 μm and 0.56 μm.

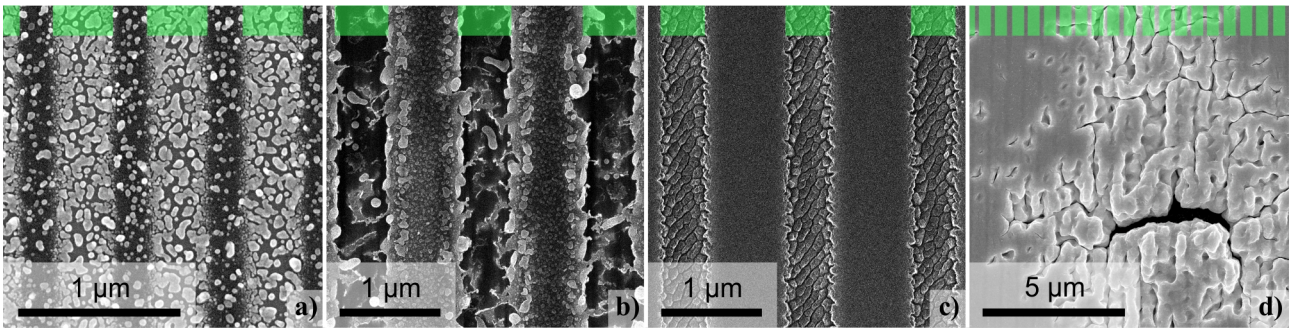

Fig. 1. Microscope images of 1D structures in thin films: a) SEM of DLC:Ag (15.3 at.% Ag) on silicon substrate, 27 mJ/cm^2, 8,000 pulses; b) HIM of DLC:Ag (6.5 at.% Ag) on quartz substrate, 27 mJ/cm^2, 1,000 pulses; c) HIM of DLC on quartz substrate, 27 mJ/cm^2, 125,000 pulses; d) SEM of Ag on silicon substrate, 145 mJ/cm^2, 64,000 pulses. Green-shaded areas (colour online) indicate the bright fringes of interference maxima (ablated parts of the material).

From the microscopy characterisation it was determined that ablation threshold is lower for composite DLC:Ag materials than pure DLC or Ag. For DLC:Ag with higher silver content the laser fluence should be at least 10 mJ/cm^2 together with 64,000 pulses, while for lower silver content the structure is already present with 27,000 pulses at the same fluence. For DLC the fluence should be at least 27 mJ/cm^2 with 8,000 pulses. For Ag the fluence should be at least 145 mJ/cm^2 with 64,000 pulses, however this results in a damage of the film rather than 1D structure. In all cases, for higher fluences the number of pulses can be decreased. Only for pure Ag increasing the fluence even more results in the peeling off of the film. In conclusion, femtosecond laser interference field ablation is convenient tool for fabrication of 1D periodical structures in various materials, if the laser parameters are carefully selected.

[1] R.J. Peláez, C.N. Afonso, M. ŠkereÅĹ et al., Density patterns in metal films produced by laser interference, Nanotechnology **26** (2015).
[2] S.M. Novikov, V.N. Popok, A.B. Evlyukhin et al., Highly Stable Monocrystalline Silver Clusters for Plasmonic Applications, Langmuir. **33** (2017).
[3] C.E. Rodríguez, R.J. Peláez, C.N. Afonso et al., Plasmonic response and transformation mechanism upon single laser exposure of metal discontinuous films, Appl. Surf. Sci. **302** (2014).
[4] S. Tamulevičius, Š. Meškinis, T. Tamulevičius et al., Diamond like carbon nanocomposites with embedded metallic nanoparticles, Rep. Prog. Phys. **81** (2018).

SYNTHESIS OF CORE–SHELL UPCONVERTING NANOPARTICLES, THEIR CHARACTERIZATION AND APPLICATION

Dovile Baziulyte-Paulaviciene[1], Greta Jarockyte[2], Ricardas Rotomskis[2], Vitalijus Karabanovas[2], Simonas Varapnickas[3], Mangirdas Malinauskas[3], Simas Sakirzanovas[1]

[1] Institute of Chemistry, Vilnius University, Naugarduko str. 24, LT-03225, Vilnius, Lithuania
[2] National Cancer Institute, P. Baublio 3b, Vilnius LT-08406, Lithuania
[3] Physics Faculty, Vilnius University, Sauletekio Ave. 10, LT-10223, Vilnius, Lithuania

dovile.baziulyte@chf.vu.lt

Lanthanide (Ln^{3+}) ions doped fluorides nanoparticles have been extensively investigated due to the advantages associated with their unique optical properties. Hexagonal phase β-$NaGdF_4$ is a promising matrix for the creation optical/magnetic dual-modal bioprobes, but upconversion luminescence (UCL) efficiency of this host material is still low and needs to be improved. A major method to enhance the UCL intensity is to use a core–shell structure, where the inert shell protects the luminescent rare earth ions in the core by passivating the surface lattice defects and shielding the core from the surrounding environment [1]

In this work, we present the thermal decomposition synthesis and surface functionalization of Ln^{3+}-doped core-shell upconverting nanoparticles (UCNPs) and demonstrate how they can be used in biological applications and temperature sensing [2]. Yb^{3+} and Er^{3+}-doped $NaGdF_4$ core-shell nanoparticles with various shell thicknesses of $NaGdF_4$ were successfully prepared. The effect of shell thickness on luminesce intensity and decay kinetics will be presented. X-ray diffraction (XRD), scanning electron microscopy (SEM) and photoluminescence (PL) spectroscopy were used to characterize UCNPs (Fig. 1). The studies show that size and shell thickness have effects on photo-physical properties of core-shell upconverting nanoparticles.

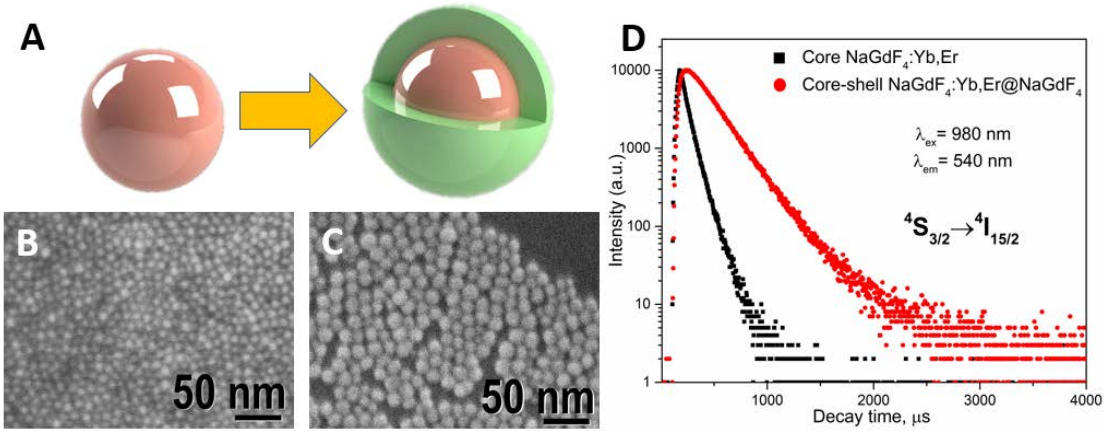

Fig. 1. Schematic illustration of core and core-shell UCNPs (A). SEM images of core (B), core-shell (C) UCNPs and their luminescence decay curves of the $^4S_{3/2}$ energy level of Er^{3+} ions (D).

Acknowlegments: This work was supported by Lithuanian Science Council grant S-LAT-17-2 „Optical 3D micro-/nano-processing (OPTIBIOFORM)".

[1] D. Baziulyte-Paulaviciene, V. Karabanovas, M. Stasys, et al. Synthesis and functionalization of $NaGdF_4$:Yb,Er@$NaGdF_4$ core–shell nanoparticles for possible application as multimodal contrast agents. Beilstein Journal of Nanotechnology **8**, 1815-1824 (2017).

[2] S. Varapnickas, D. Baziulytė-Paulavičienė, S. Šakirzanovas, M. Malinauskas, Upconverting nanocrystals as luminescent temperature probes for local-heating imaging during direct laser writing 3D nanolithography, Proc. SPIE 10456 (2018).

RESISTIVITY AND LOW FREQUENCY NOISE CHARACTERISTICS OF VITREOUS CARBON FOAMS

Marina Tretjak

Institute of Applied Electrodynamics and Telecommunications, Vilnius University, Sauletekio 3, 10257 Vilnius, Lithuania

marina.tretjak@ff.stud.vu.lt

The rigid foams which are porous have a good compromise between lightness and performances. Therefore their employment in the different technical sectors is growing. But beyond the lightness, foams can be optimized, depending on the foreseen applications. In some articles we can see, how rigid foams can be used in transportation sector [1, 2]. They can be good thermal or acoustic insulators, shock absorbers. Also there are a lot investigations how to use rigid foams in high-temperature insulation, electromagnetic shielding and catalysis or energy conversion sectors [3]. The cellular vitreous carbon foams of controlled structure are started to fabricate [1, 2]. Development of rigid foams opens door for new investigations of the carbon foams. In some cases cellular vitreous carbon foams distinguish by lager cells' size for lower bulk density. Ratio between physical properties, cell size, total porosity and other parameter of cellular vitreous carbon foams is not clear [3].

Cellular vitreous carbon foams were produced from phenolicfuranic resins, condensed tannins co-reacted with furfuryl alcohol in the present case [3]. The foams which are investigated in this work are made of vitreous carbon therefore they are electrically conducting. The samples differ by bulk density and cell size which are not correlated with each other. These features says that we need more detail studies of physical properties of carbon foams as a function of their porous structure. Mechanical, acoustic and electromagnetic properties were already analyzed [4-6]. Low frequency noise spectroscopy is an informative method for investigation of the charge carrier transport and conduction mechanisms in various materials [7, 8]. On the other hand, $1/f$ noise is an important consideration in assessing the potential vitreous carbon foams in different electronic devices. Therefore, aim of this work was to investigate the noise and electrical transport properties of vitreous carbon foams and characteristics' dependence on their density.

Vitreous carbon foams of different density were investigated. The samples density was from 0,064 g/m^3 to 0,075 g/m^3. Resistance and low frequency (10 Hz – 20 kHz) noise characteristics have been carried out in temperature range from 73 K to 380 K.

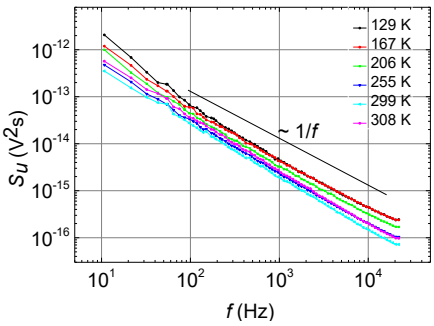

Fig. 1. Dependences of voltage fluctuation spectral density on frequency at different temperatures (carbon foam density is 0,067 g/m^3)

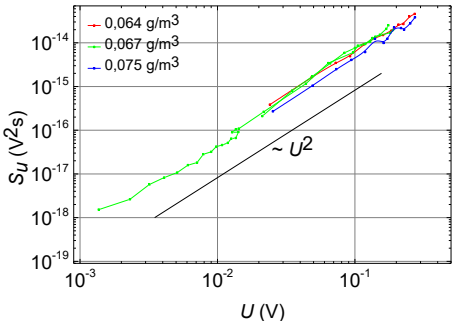

Fig. 2. Dependences of voltage fluctuation spectral density on voltage for different dencity foams (at 86 Hz and 290 K).

Low frequency noise spectra of investigated materials comprises of $1/f^{\alpha}$ type components (Fig. 1). $1/f^{\alpha}$ type fluctuations show that Mott's hopping and charge carrier capture and release processes in localized states dominate in the charge carrier transport in the investigated materials. In (Fig. 2) we can see that noise spectral density can be approximated by sample voltage square. Therefore, noise is originated from the resistance fluctuations. The fluctuation spectral density does not depend on vitreous carbon foam density.

[1] L.J. Gibson, M.F. Ashby, Cellular Solids: Structure and Properties, second ed., Cambridge University Press, 1999.
[2] M. Inagaki, J. Qiu, Q. Guo, Carbon foam: preparation and application, Carbon **87,** 128-152 (2015).
[3] M. Letellier, A. Szczurek, M.C. Basso, A. Pizzi, V. Fierro, O. Ferry, et al., Preparation and structural characterisation of model cellular vitreous carbon foams, Carbon **112,** 208-218 (2017).
[4] M. Letellier, C. Delgado-Sanchez, M. Khelifa, V. Fierro, A. Celzard, Mechanical properties of model vitreous carbon foams, Carbon **116**, 562-571 (2017).
[5] M. Letellier, S. Ghaffari Mosanenzadeh, H. Naguib, V. Fierro, A. Celzard, Acoustic properties of model cellular vitreous carbon foams, Carbon **119,** 241-250 (2017).
[6] M. Letellier, J. Macutkevic, P. Kuzhir, J. Banys, V. Fierro, A. Celzard, Electromagnetic properties of model vitreous carbon foams, Carbon **122**, 217-227 (2017).
[7] C. Barone, G. Landi, C. Mauro, H. C. Neitzert, and S. Pagano, Universal crossover of the charge carrier fluctuation mechanism in different polymer/carbon nanotubes composites, Appl. Phys. Lett. **107**, 143106, (2015).
[8] M. Arjmand, M. Mahmoodi, G. A. Gelves, S. Park, U. Sundararaj, Electrical and electromagnetic interference shielding properties of flow induced oriented carbon nanotubes in polycarbonate, Carbon **49**, 3430 (2011).

RESONANCE ENERGY TRANSFER BETWEEN SILVER NANOPARTICLES AND ORGANIC DYE MOLECULES

Austėja Bukauskytė[1,2], Marius Franckevičius[2], Vidmantas Gulbinas[2]

[1] Faculty of Physics, Vilnius University, Saulėtekio Ave. 9-III, LT-10222 Vilnius, Lithuania
[2] Center for Physical Sciences and Technology, Saulėtekio Ave. 3, LT-10257 Vilnius, Lithuania
bukauskyte.austeja@gmail.com

Noble metal nanocrystals exhibit rich surface plasmon resonance properties. This effect gives metal nanoparticles a number of unusual useful optical properties, that can be applied in many fields, such as surface enhanced Raman spectroscopy [1], metal enhanced fluorescence spectroscopy [2], optical biosensors, optoelectronics etc.

Due to the interesting influence of metal nanoparticles on spectroscopic properties of nearby organic molecules, the metal nanoparticle – organic molecule systems have been widely investigated, manly focusing on the plasmon-induced fluorescence enhancement. Another effect, molecule fluorescence quenching by resonance excitation energy transfer to metal nanoparticles, was also widely investigated. On the other hand, much less is known about opposite energy transfer from photoexcited nanoparticle to organic molecules. Very short excited state lifetimes of metal nanoparticles and a lack of Stokes shift make this process inefficient and difficult for experimental investigation. Wang et al. have recently reported blue-shifted molecular fluorescence created by the plasmon-induced resonance energy transfer [3].

In our work we investigate the resonance energy transfer from silver nanoparticles to organic dye DODCI molecules. Spherical silver nanoparticles were formed using thermal evaporation and annealing method. Organic dye DODCI was used as an energy acceptor.

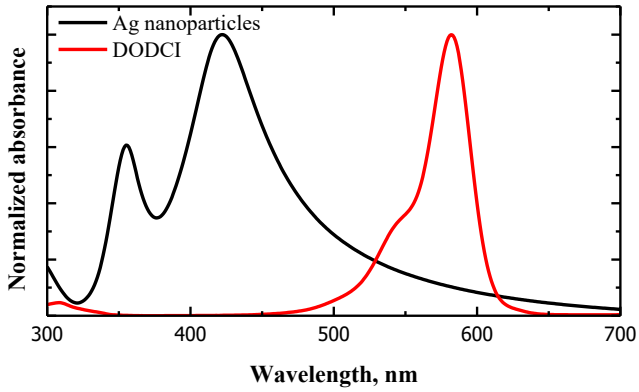

Fig. 1. Absorption spectra of silver nanoparticles (black line) and DODCI molecules (red line).

Measured fluorescence excitation spectrum of DODCI molecules adsorbed on silver nanoparticles showed resonance energy transfer from silver nanoparticles to DODCI molecules. DODCI fluorescence has been observed under excitation of the nanoparticle-dye system to the plasmon resonance band located at the short wavelength side from the dye absorption band where dye absorbance was negligible.

[1] J. R. Lakowicz et al., Plasmon-controlled fluorescence: a new paradigm in fluorescence spectroscopy, Analyst, 133, 1308–1346, (2008).
[2] W. Xie and S. Schlücker, Rationally designed multifunctional plasmonic nanostructures for surface-enhanced Raman spectroscopy: a review, Reports on Progress in Physics, 77, 116502, (2014).
[3] M. Wang et al., Molecular-Fluorescence Enhancement via Blue-Shifted Plasmon-Induced Resonance Energy Transfer, J. Phys. Chem. C, 120, 14820−14827, (2016).

INVESTIGATION OF THE INFLUENCE OF IRON CONTENT IN $LiFe_xMn_{1-x}BO_3$ THERMALLY NANOCRYSTALLIZED GLASSES

Jakub Szymon Otrębski, Przemysław Piotr Michalski, Tomasz Karol Pietrzak, Jerzy Edward Garbarczyk

Faculty of Physics, Warsaw University of Technology, Poland
jakub1@wp.eu

Despite the increasing energy efficiency of modern electronic devices, the batteries are still the relevant part and determine the usefulness of the entire device. The investigated compound of $LiFe_xMn_{1-x}BO_3$ is proposed to be applied as cathode material in the most common kind of batteries – Li-ions. It is motivated by high value of theoretical gravimetric capacity 220–222 $mAhg^{-1}$ (depending on the composition) and satysfying conductivity taking into account an ease in synthesizing.

Previous studies in the Solid State Ionics Division showed gigantic increase of specific conductivity after thermal nanocrystallization comparing to the initial glassy sample [1]. The process consist in creating nanomaterial from glass through isothermal annealing at strictly determined temperature. The temperature must be choosen in the way to nucleation process of new crystal grains will be the highest. The nanometric crystalline grains are formed in the sample, which are responsible for observed conductivity enhancemnet. Investigations of $LiFeBO_3$ subjected to nanocrystallization showed increase of conductivity by more than 6 orders of magnitude vs glass. Nevertheless, the difficulties appeared in obtaining the sample in a glassy state [2], which is required for further process. The $LiMnBO_3$ admixture should have solved mentioned issue, because of its' good glass-forming properties [3]. The aim of this mixed compound was to combine satysfying conductivity with an ease of obtaining the sample in a glassy form.

Glassy compositions of $LiFe_xMn_{1-x}BO_3$ for $x = 0.25, 0.5, 0.75$ were obtained using melt-quenching method. Thermal (DTA), structural (XRD) and electrical (IS) reseraches were employed to characterize as-prepared glasses.

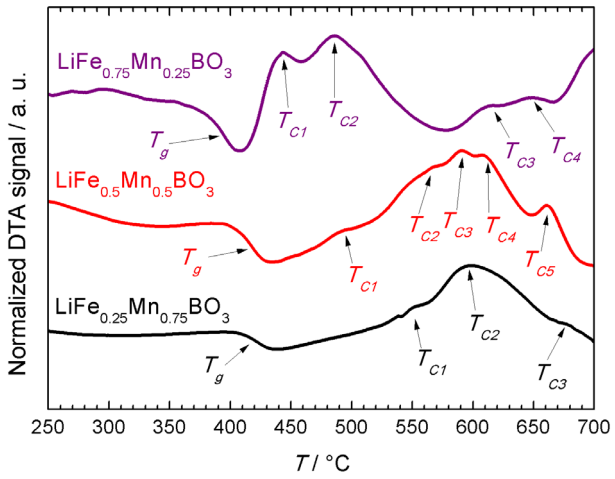

(a) DTA curves of analyzed materials for heating rate 10 °Cmin^{-1}.

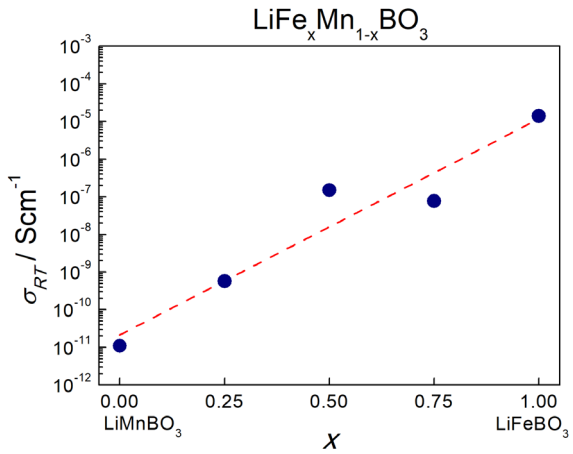

(b) Dependences of specific conductivity at room temperature after nanocrystallization on x in compositions. The results for $x = 1$ and $x = 0$ were taken from [2] and [3], respectively.

Determining the temperatures of essential (from the viepoint of this work) thermal events, showed translation into side of higher temperatures for the samples with higher content of manganese (a). Glass transitions were registered in the range 395–421 °C depending on composition. First peaks of crystallizations appeared at 551, 489, 443 °C for samples with $x = 0.25, 0.5, 0.75$, respectively. Structural measurements showed that ideally amorphous phase was obtained for samples with $x = 0.25, 0.5$ only, whereas, for $x = 0.75$ visible was slight content of Fe_3O_4 phase. For the all three compositions characteristic was lack of changes in the structure till 400 °C. Above this temperature mainly the phases of $FeBO_3$, $LiMnBO_3$ appeared.

For different samples, the most beneficial was different temperature of nanocrystallization, considering increase of conductivity. The best result was registered for $LiFe_{0.5}Mn_{0.5}BO_3$ ($x = 0.5$) sample, where the increase of specific conductivity was by a factor $5 \cdot 10^7$ after annealing at 450 °C versus initial glass. The dependence of conductivity on content of iron in composition was also determined (b). This relation has an exponential character with increasing amount of iron in the sample.

[1] PIETRZAK T.K.: *Nowe nanomateriały oparte na szkłach wanadanowo-fosforanowych i żelazowo-fosforanowych*. PhD Thesis, Warsaw University of Technology, 2012.
[2] MICHALSKI P.P., PIETRZAK T.K., NOWIŃSKI J.L., WASIUCIONEK M., GARBARCZYK J.E.: *Novel nanocrystalline mixed conductors based on $LiFeBO_3$ glass*. Solid State Ionics **302** (2017) 40–44.
[3] GOŁĘBIEWSKA A.: *Investigation of glass-forming properties of $LiMnBO_3$*. Bachelor's Thesis, Warsaw University of Technology, 2017.

POLARIZATION DEPENDENCE IN GOLD NANOROD FILMS

Liudmila Trotsiuk, Andrey Ramanenka, Leonid Gurinovich

B.I.Stepanov Institute of Physics, National Academy of Sciences, Belarus
l.trotsiuk@ifanbel.bas-net.by

Polarized light emission find wide applications in particularly in liquid crystal displays and different nanophotonic devices [1]. Therefore, the obtaining polarized light emission devices is of great scientific and practical interest.

Gold nanorods (AuNRs) are of current interest because of their anisotropic shape and unique optical properties. The presence of two plasmon (transverse and tunable longitudinal) bands with high absorption coefficients and good photostability determine the prospects of their application for the production of polarizing filters [2]. Polarized light with the electric field oriented parallel or perpendicular to the AuNRs can excite the longitudinal or the transverse surface plasmon band.

The aim of this work was to fabricate the polarized film containing gold nanorods and demonstrate its polarization-dependent optical properties.

old nanorods were synthesized via seed-mediated growth method [3]. The polarization film was prepared by adding gold nanorods to a 5% poly(vinyl alcohol) (PVA) solution. The film was stretched in 4 times at 30 ° C.

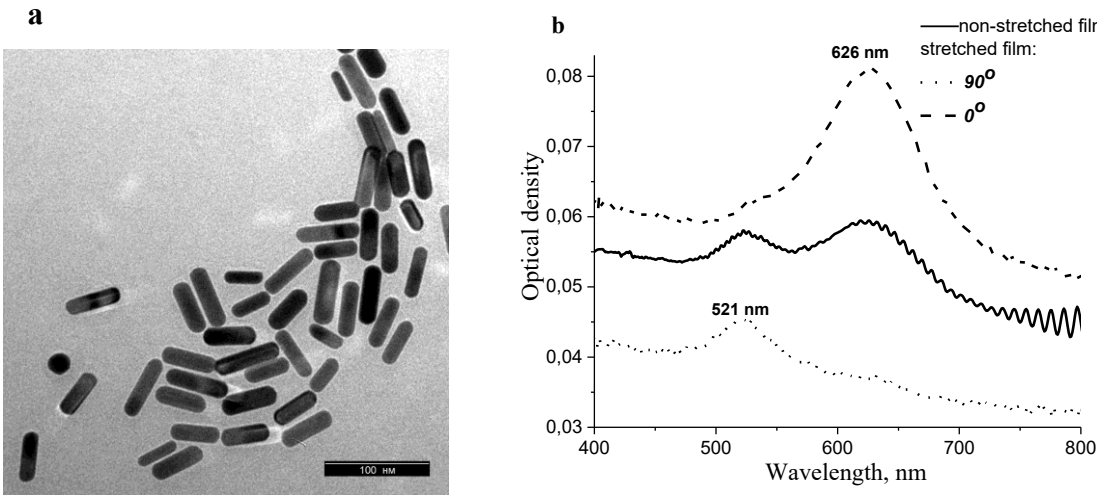

Fig. 1. a) TEM image of AuNRs; b) UV-vis-NIR spectra of non-stretched AuNR-PVA film and stretched film for 0° and 90° polarization angles.

Figure 1a demonstrate TEM image of synthesized AuNRs. Figure 1b shows UV-vis-NIR spectra of non-stretched AuNR-PVA film and stretched film for 0° and 90° polarization angles. The non-strechted film has two extinction peaks irrespective of the light polarization directions. While the stretched AuNR-PVA film has only one extinction peak upon each polarized excitation, which corresponds to the longitudinal at 0° and transverse at 90° bands of AuNRs.

[1] S. Liu, L. Jiafang and L. Zhi-Yuan, Macroscopic polarized emission from aligned hybrid gold nanorods embedded in a polyvinyl alcohol film, Advanced Optical Materials **1**, 227-231 (2013).

[2] J. Pérez-Juste, Jorge, et al., Optical Control and Patterning of Gold-Nanorod–Poly (vinyl alcohol) Nanocomposite Films, *Advanced Functional Materials* **15,** 1065-1071 (2005).

[3] B. Nikoobakht, M. A. El-Sayed, Surface-enhanced Raman scattering studies on aggregated gold nanorods, J. Phys. Chem. A 107, 3372 (2003).

POLARIZATION DEPENDANT ULTRAFAST PLASMON RELAXATION DYNAMICS IN GOLD NANOWIRES

Mindaugas Juodėnas[1], Adrien Chauvin[2], Domantas Peckus[1], Tomas Tamulevičius[1,3], Abdel-Aziz El Mel[2], Pierre-Yves Tessier[2], Sigitas Tamulevičius[2,3]

[1]Institute of Materials Science of Kaunas University of Technology, K. Baršausko Str. 59, Kaunas LT-51423, Lithuania
[2] Institut des Matériaux Jean Rouxel, Université de Nantes, CNRS, 2 rue de la Houssinière B.P. 32229, 44322 Nantes cedex 3, France
[3]Department of Physics, Kaunas University of Technology, Studentų Str. 50, LT-51368 Kaunas, Lithuania
Mindaugas.Juodenas@ktu.lt

Since few years, nanoporous materials are of great interest for various applications including sensors based on surface-enhanced Raman scattering, catalysis, and biotechnology. Currently, tremendous efforts are dedicated to the development of nanoporous nanowires materials [1]. A new strategy to prepare highly ordered ultralong porous gold nanowires with a tunable porosity was recently reported [1]. This two-step approach is based on the growth of Au−Cu alloy nanowires by magnetron sputtering over a nanograted substrate serving as a physical template followed by electrochemical dealloying allowing creation of nanoporous nanowires [1].

In order to explain the great plasmonic properties of nanoporous material, study of plasmonic effects in porous and nonporous Au nanowires was performed by means of transient absorption spectroscopy (TAS). The samples were excited at 435 nm, the power of excitation was 2 mW, frequency of pulses was 200/3 kHz. The signal of TAS was registered not in the casual transparent mode but in the reflection one. The TAS setup was arranged that reflection angle from the sample would be as small as possible because reflection angle may have the additional impact on TAS signal. The grating template used determines the geometry of the nanowires studied and as one can see (Fig. 1a and 1b) the neighboring lines with subwavelength spacing are parallel. This fact is very important owing polarization dependent TAS signal. The polarization of pump and probe pulses used for the TAS measurements were parallel, perpendicular or mixed with respect to the alignment of porous and nonporous Au nanowires.

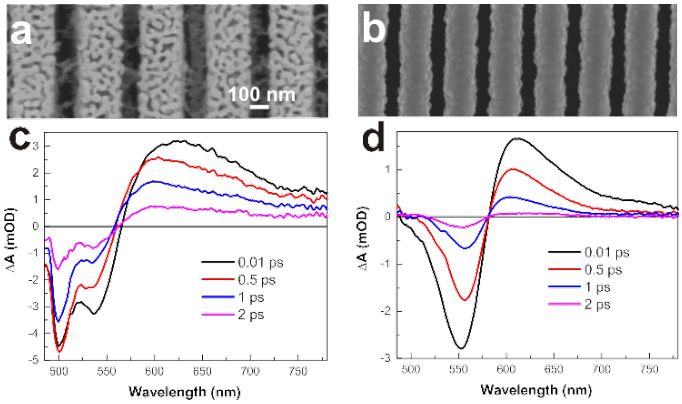

Fig. 1. SEM images of porous (**a**) and nonporous (**b**) Au nanowires. TAS spectra of porous (c) and nonporous Au nanowires (d) when polarizations of pump and probe pulses are parallel to the nanowires.

There is a clear difference in TAS signal between the porous and nonporous Au nanowires (Fig 1c and 1d). TAS signal (spectra and traces) shows that localized surface plasmon resonance (LSPR) was excited during the measurements. We suggest that TAS signal appears because of LSPR in nanoparticles [2,3], i.e. because of the nanometric width of the gold lines where transversal LSPR mode is excited.

The LSPR relaxation typically consists of several steps: electron-electron (e-e) scattering, electron-phonon (e-p) coupling and phonon-phonon (p-p) coupling [3]. In our case, we can presumably observe e-p coupling and p-p coupling. The process of e-e scattering creates hot electrons. The hot electrons during the e-p coupling process transfer their energy to the lattice of Au nanowires and the material heats up during ~1 ps. The hot lattice transfers energy to the environment by p-p coupling that happens during ~100 ps. We can observe both processes like a negative TAS signal.

TAS spectra of nonporous Au nanowires show no evidential dependence on polarization of pump and probe beams while porous Au nanowires show clear dependence.

[1] A. Chauvin, C. Delacôte, L. Molina-Luna et al., Planar arrays of nanoporous gold nanowires: when electrochemical dealloying meets nanopatterning, ACS Appl. Mater. Interfaces **8**, 6611–6620 (2016).
[2] M. Kauranen, A. Zayats, Nonlinear plasmonics, Nature Photon. **6**, 737-748 (2012).
[3] D. Peckus, H. Rong, L. Stankevičius et al., Hot electron emission can lead to damping of optomechanical modes in core−shell Ag@TiO_2 nanocubes, J. Phys. Chem. C **121**, 24159-24167 (2017).

SERS and fluorescence-based ultrasensitive detection of organic dye using combination of gold colloid and silvered porous silicon

Nadia Khinevich [1], Sergey Zavatski[1], Hanna Bandarenka[2], Asta Tamuleviciene[2], Sigitas Tamulevicius[2], Iuliia Mukha[3]

[1] Department of Micro-and Nanoelectronics, Belarusian State University of Informatics and Radiolectronics, Belarus

[2] Institute of Materials Science, Kaunas University of Technology, Lithuania

[3]Chuiko Institute of Surface Chemistry of NAS of Ukraine, Ukraine

khinevichnadia@gmail.com

Fluorescence microscopy is a well-known imaging technique that shows specific protein distribution in cells. In recent years, combination of fluorescence microscopy and Raman spectroscopy is also used to provide both finding and identification of different organic molecules. However, the most currently available fluorescent organic dyes are characterized by relatively weak emission, rapid photo-bleaching and tendency to hide Raman signal. Alternatively, metallic nanoparticles have also been extensively applied for cellular imaging and biomedical diagnostics. For example, inorganic metallic nanocrystals known as quantum dots (QDs) are often used as fluorescence labeling agents for biological cells and tissues. QDs offer significant advantages over conventional organic dyes such as brighter fluorescence and higher resistance to photo-bleaching that make them suitable for ultra-sensitive imaging [1]. What is more nanoparticles of noble metals demonstrate activity in surface-enhanced Raman scattering (SERS) spectroscopy which opens prospects of a detection sensitivity of 16 orders of magnitude higher than that of ordinary Raman spectroscopy [2]. As a result, recovery of Raman signal from fluorescence background is observed. In this paper, we report on visualization and SERS-detection of organic dye R6G that is mixed with gold colloids and adsorbed on the SERS-active substrate based on the silvered porous silicon.

SERS-active substrates were formed by electrochemical etching of highly-doped n-Si wafers in HF-based solution that resulted in fabrication of mesoporous silicon layer of 5 μm thickness and following electroless deposition of silver nanoparticles of 10 – 150 nm diameters. The concentration of gold nanoparticles in colloid was 4×10^{-4} mol per liter of water while their diameters varied from 10 to 20 nm. An analyte for the SERS and fluorescence measurements was prepared by mixing water solution of 10^{-9} M R6G and gold colloid in 1 : 9 volume ratio. As a result, total concentration of R6G was 1×10^{-10} M. This mixture was drop-deposited on the porous silicon coated with silver nanoparticles and dried in the air. Optical microscope equipped with filter provided transmission in the range of 330 – 385 nm was used for the fluorescence imaging. SERS measurements were performed using 532 nm laser.

The analyte drop formed so-called “coffee ring” on the substrate after complete drying because of agglomeration of gold nanoparticles. Fig. 1 shows fluorescence image and SERS spectrum of R6G drop-deposited on the silvered porous silicon from its mixture with gold colloid.

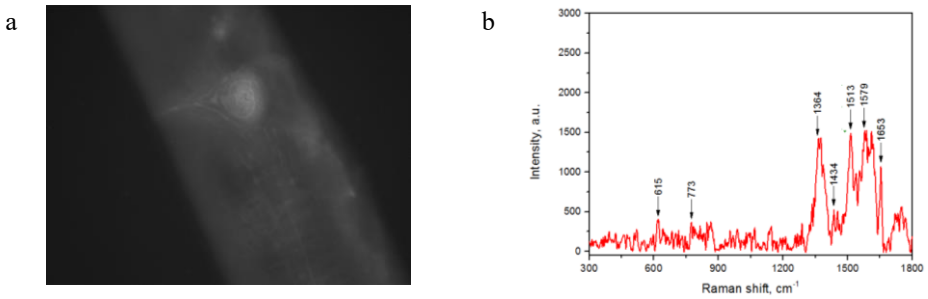

Fig. 1. (a) Fluorescence image and (b) SERS spectrum of 1×10^{-10} M R6G drop-deposited from its mixture with gold colloid on silvered nanoparticles porous silicon.

Following Fig. 1, we can observe the highest fluorescence in the area of “coffee ring”. Despite the SERS spectrum (Fig. 1, b) is a little bit noisy, typical bands of R6G (615 cm^{-1}; 773 cm^{-1}; 1364 cm^{-1}; 1434 cm^{-1}; 1513 cm^{-1}; 1579 cm^{-1}; 1653 cm^{-1}) are distinguished. The ability to register SERS spectrum is caused by the rough surface of the silvered porous silicon that provides absorption between 370 nm and 800 nm due to an arrangement of surface plasmon resonance in this range [3]. The most intensive absorption is in near UV region. That is why, SERS spectrum is not completely hidden in fluorescence background.

Summarizing, the combination of fluorescence and SERS techniques allowed us to find and identify organic dye R6G drop-deposited from the solution of 1×10^{-10} M. This opens an opportunity of ultrasensitive bioimaging and molecules identification.

[1] A. M. Smith, H. W. Duan, A. M. Mohs and S. M. Nie, Bioconjugated quantum dots for in vivo molecular and cellular imaging, Advanced Drug Delivery Reviews **60**, 1226-1240 (2008).

[2] N. Uzunbajakava, A. Lenferink, Y. Kraan, B. Willekens, G. Vrensen, J. Greve and C. Otto, Nonresonant Raman imaging of protein distribution in single human cells, Biopolymers 72, 1-9 (2003).

[3] A. M. Smith, H. W. Duan, A. M. Mohs And S. M. Nie, Formation regularities of plasmonic silver nanostructures on porous silicon for effective surface-enhanced Raman scattering, Nanoscale Research Letters **11**, 262 (2016).

SYNTHESIS OF $NaGdF_4:Yb^{3+},Er^{3+}@NaGdF_4$ UPCONVERTING NANOPARTICLES AND CHARACTERIZATION OF OPTICAL PROPERTIES

Rokas Vargalis, Dovile Baziulyte-Paulaviciene, Simas Sakirzanovas

Department of Applied Chemistry, Faculty of Chemistry and Geosience, Vilnius University, Lithuania
rokas.vargalis@chf.stud.vu.lt

Lanthanide ions exhibit unique luminescent properties, including the ability to convert of two or more photons near infrared long-wavelength excitation radiation into shorter visible wavelengths through a process known as photon upconversion [1]. Upconverting nanoparticles (UCNPs) can be used for different applications varying from biological imaging to targeted drug delivery. $NaGdF_4$: Yb^{3+},Er^{3+} exhibits excellent upconversion fluorescence peaks in blue, green and red spectral areas under 980 nm IR laser excitation [2].

The main purpose of this work was to synthesize $NaGdF_4:Yb^{3+},Er^{3+}@NaGdF_4$ core-shell upconverting nanoparticles using thermal decomposition method and to find out optimum temperature and time for synthesis, to get monodispersed UCNPs, which have the most intense photoluminescence properties. We investigated two groups of particles with different time of synthesis: 60/90 min by changing temperatures from 280˚C to 320˚C.

The results received show that synthesis time and synthesis temperature influences photoluminescence intensity, size and agglomeration of UCNPs. The upconversion photoluminescence spectra *(figure 1.c.)* and SEM images *(figure 1.a.b.)* of $NaGdF_4:Yb^{3+},Er^{3+}@NaGdF_4$ obtained at different synthesis time show varying photoluminescence intensity and nanoparticles morphology, accordingly. Scanning electron microscopy (SEM), powder X-ray diffraction (XRD), and photoluminescence (PL) spectra have been employed to characterize the size, crystal structure and emission intensity of the samples, respectively.

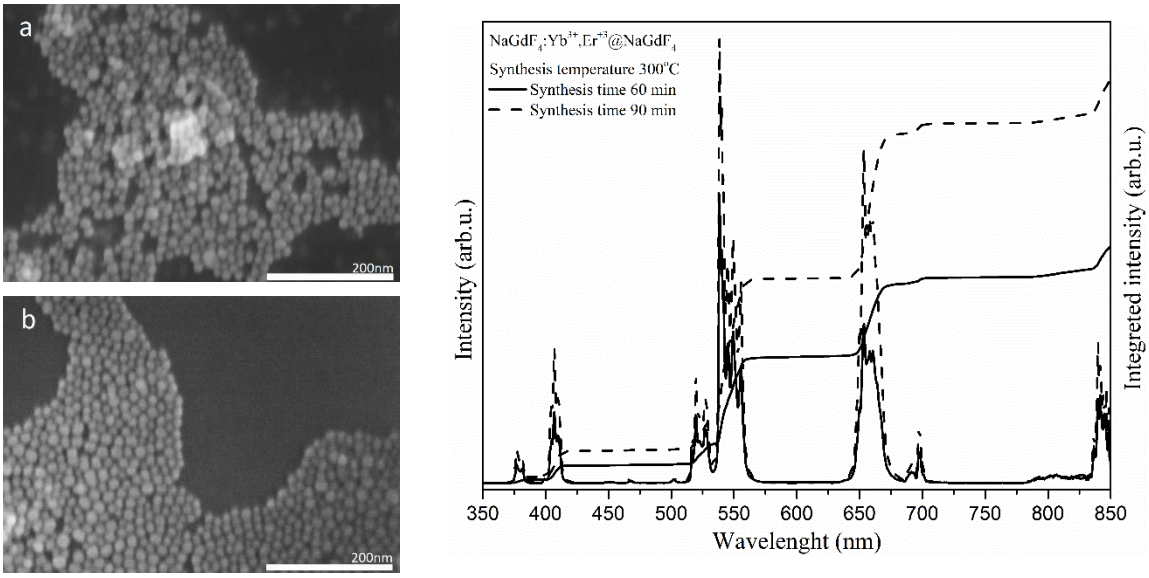

Figure 1. SEM images of $NaGdF_4:Yb^{3+},Er^{3+}@NaGdF_4$ nanoparticles synthesis temperature 300 °C and synthesis time a) 60 minutes, b) 90 minutes, c) photoluminescence intensity dependence on synthesis time .

[1] Baziulyte-Paulaviciene, D., et al., *Synthesis and functionalization of NaGdF(4):Yb,Er@NaGdF(4) core–shell nanoparticles for possible application as multimodal contrast agents.* Beilstein Journal of Nanotechnology, 2017. **8**: p. 1815-1824.

[2] Zhou, J., et al., *Dual-modality in vivo imaging using rare-earth nanocrystals with near-infrared to near-infrared (NIR-to-NIR) upconversion luminescence and magnetic resonance properties.* Biomaterials, 2010. **31**(12): p. 3287-3295.

Impact of presythesis on electrical and structural properties of samples with composition $LiFe_{0.85}V_{0.10}PO_4$ nanocrystalised from glassy phase.

Piotr Pasza Storożenko[1]

[1] Faculty of Physics, Warsaw University of Technology, Poland
piotr.pasza.storozenko@gmail.com

Problem and motivation: all olivine-like materials synthesized in our laboratory went through the presynthesis process. This process takes a lot of time and it wasn't measured what's the actual impact of presynthesis on materials final properties.

Proccess of presynthesis consists of heating sample for 2 hours in 300°C and then for another 2 hours in 570°C in pure (99.999%) nitrogen atmosphere before actual synthesis. Synthesis was done by melt-quenching method after melting sample in 1300°C. Sample IG65A of material went under presynthesis before actual synthesis. Sample IG65N was synthesised without a presythesis.

Synthesised materials were measured with the follwing methods:

- differential thermal analysis (DTA) - temperatures of thermal events where obtained. Observation of a glass transition confirmed that amorphous materials were obtained;
- X-ray diffractometry (XRD) - it was confirmed that both samples were obtained in~an amorphous phase.
  Sample IG65A crystallized in a NASICON phase with addition of Fe2O3.
  Sample IG65N crystallized as a mixture of tryphilit, NASICON, LiP, Fe2O3 phases.
  Average size of grains in sample IG65A was between 70 and 76 nm.
  Average size of grains in sample IG65N was between 62 and 73 nm;
- impedance spectroscopy (IS) - during nanocrystallization, conductivity of sample IG65A increased by over three orders of magnitude to the value $8 \cdot 10^{-6}$ Scm^{-1}, conductivity of sample IG65N increased by almost five orders of magnitude to the value $2.4 \cdot 10^{-3}$ Scm^{-1};
- thermoelectric power measurements (TEP) - both samples, before and after, nanocrystallization process showed electron conductivity.
  Probably nanocrystallization process improved holes conductivity.
  Glassy phase samples had very high value of Seebeck coefficient.

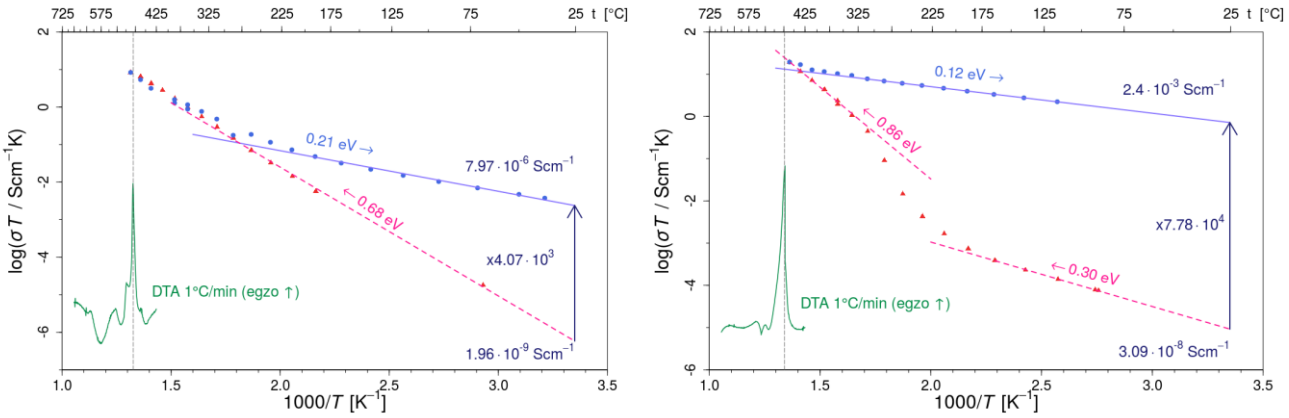

Fig. 1. Arrhenius plots with DTA curve. They present change of samples conductivity during heating (triangles) and cooling (circle). Sample IG65A is on the left and IG65N on the right.

Sample that was synthesized without presynthesis process - IG65N - had better electrical properties after nanocrystallization then sample IG65A. Sample IG65N also nanocrystallized in a desirable structure (tryphilit) with smaller average grains sizes. Presynthesis is not necessary to obtain high conductivity of nanocrystallized materials.

RECONSTRUCTION OF THE MR-IMAGES BY PARTIALLY INTERPOLATED SIGNAL DATA

Andrii Netreba, Yriy Kyiashko, Andrii Komarov

Department of Radiophysics, Electronics and Computer Systems, Taras Shevchenko National University of Kyiv, Ukraine
avn@univ.kiev.ua

Magnetic resonance imaging today is a powerful method of studying the internal structures of the human body. Its wide application it received due to diagnostic woes and virtually no harmful effect on the patient. In connection with a wide range of applications, the actual tasks that physicists and engineers are working on are improving the accuracy of diagnostics, reducing measurement time, obtaining data on biophysical and biochemical processes. The characteristics of the magnetic fields used have a significant effect on the solution of the above problems, among which it is important to note the magnitude of the constant magnetic field, the parameters of spatial instability or inhomogeneity. The solution of the problem of compensating the instability of magnetic fields remains relevant in the tomography. An example of such studies is the research on the correction of distortions caused by the heterogeneity of the magnetic fields [1].

The work is devoted to the development of a technique for reconstruction of images from partially incomplete data of measured signals. This technique is useful in solving problems of reducing the time of measurement. During the measurements, the patient is in the measuring area of the tomograph and must be as much as possible immobile. His movement leads to the appearance of artifacts. In addition, some of the measured data can be distorted by electromagnetic processes in the receiving system. These distortions can be cased by random significant amplitude fluctuations of the signal. In this work, we simulate the recording of signals based on the processing of a real tomographical image (Fig.1,a). For simulation we considered the free-induction decay signal, Eq. (1) for constructing tomograms weighted by spine density $\rho(x,y)$ in gradient k-space (k_x,k_y).

$$S(k_{xl},k_{ym}) = \widehat{S}\sum_{a,b}\rho(x_a,y_b)\cdot e^{i\left(k_{xl}x_a+k_{ym}y_b\right)}, \quad (1)$$

where $\widehat{S}$ is a constant, $k_{x,y}=\gamma G_{x,y}\tau_{1,2}$ (γ - hydrogen gyromagnetic ratio; $G_{x,y}$ - magnetic fields transverse gradients; $\tau_{1,2}$ - MR pulse sequences delay time characteristics).

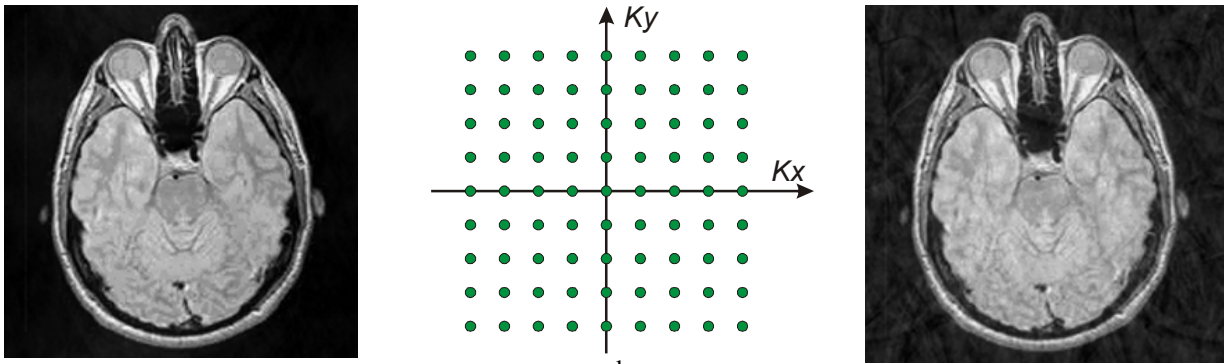

a b c

Fig. 1. MR-images reconstructed for different measurement conditions (a-full set of signal measurements, b-grid in the gradient magnetic k-space, c-reconstruction by 90 percent of signal measurements).

To carry out the reconstruction a complete set of signals is necessary in the corresponding to the space-frequency two-dimensional spectrum (K-space, Fig.1,b). We considered the array of the signals with fullness from 50 to 90 percent with 10 percent increments. The reconstructed image for completeness of 90 percent is shown in Fig.1,c. Missing data on the gradient grid in K-space were calculated by interpolation over available nearest points [2]. This image can be measured in a real tomograph for 10 percent of the time faster, and this is a few minutes. During this time, it is possible, that the patient will not make a significant movement, then the quality benefits will be even more obvious. It should be noted that such measurements can be carried out when it is known in advance that the quality requirements can be reduced. A second option for applying the method can be the processing of already available data that have the above described inaccuracies. The third application of the proposed approach is the development or calibration of tomographical systems.

[1] S. P. M. Crijns, B. W. Raaymakers and J. J. W. Lagendijk, Real-time correction of magnetic field in homogeneity-induced image distortions for MRI-guided conventional and proton radiotherapy, Phys. Med. Biol. **56**, 289 (2010).

[2] Gavrilyuk V.S., Netreba, A.V., Radchenko, S.P., MR image reconstruction from data acquired on an irregular k-space trajectory,. - IEEE 36th International Conference on Electronics and Nanotechnology, 183-186(2016).

Modelling the side-chains of amino acids using robotics-inspired methods

Algirdas Grybauskas[1], Saulius Gražulis[1]

[1]Vilnius University Institute of Biotechnology, Lithuania
algirdas.grybauskas@bti.stud.vu.lt

Understanding the conformations of amino acids is a deciding factor when predicting the interactions between a protein and the ligand. The misidentification of such interactions might produce false computation results due to inaccurate models. Consequently, constructing the robust library of rotational isomers, also known as rotamers, is a key factor in predicting the consequences of a point mutation in a protein, binding energies with a designed molecule or protein surface.

Various rotamer libraries that differ both in strategies and quantity or quality of initial data has been developed. Most of the widely used libraries are generated first by carefully selecting high-resolution protein structures from Protein Data Bank archive (PDB), then grouping amino acids by their type and calculating the frequency of the most occurring dihedral angles in that group [1]. Depending on the library, groups can be further divided by structure of the main chain atom, solvent accessibility or other criteria [2].

Using general pre-calculated libraries is very favourable, because it requires almost no computational-time when determining correct conformations. However, libraries are dependent on the initial structures and lack both diversity of side-chain rotamers and the interaction with surrounding atoms [1].

In this study, we are developing the program that generates the rotamer library that can be constructed using only the structure of the investigated protein. The core principle of the approach is a limited movement of side-chains imposed by the fixed number of degrees of freedom (Fig.1). A position of the side-chain atom can vary due to the bond torsion, stretching and angle bending.

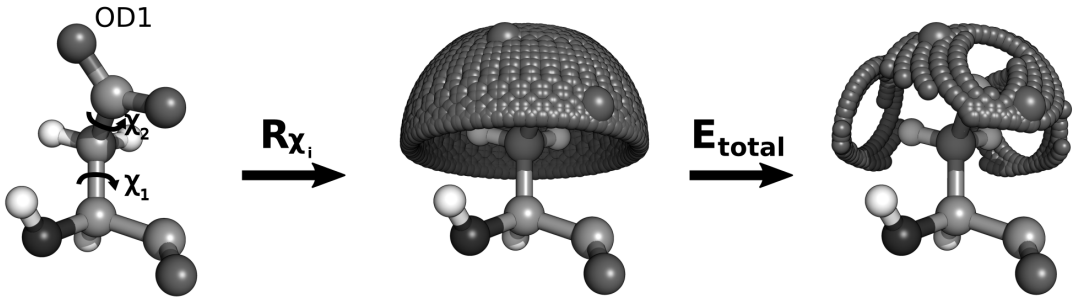

Fig. 1. The simplified diagram of the search of conformational space for oxygen in the aspartic acid

The dihedral angle was chosen as the variable for constructing a simple rotamer model, because rotation around the bond produces the most extreme changes on the positions of atoms. The possible atom position of the specific side-chain is determined by first changing the dihedral angles for all bonds. It can be achieved by using matrix multiplication of the rotation matrices:

$$\boldsymbol{p}^{0\prime} = \boldsymbol{T}^0_n(\prod_{i=1}^{n}\boldsymbol{R}_{\chi_i}\boldsymbol{T}^i_{i-1})\boldsymbol{p}^0 \tag{1}$$

where $\boldsymbol{p}$ is the vector describing the position of the atom, $\boldsymbol{T}$ - the transformation matrix for changing the frame of reference and $\boldsymbol{R}$ - the rotation matrix. Matrix multiplication is calculated analytically for greater computational efficiency.

Then potential energy of each side-chain atom is calculated and high-energy rotamers are excluded (2). Combinatorial explosion is avoided by using dead-end elimination and cell-list neighbour search while calculating potential energy. The bond stretching and angle bending are planned to be included in the model in the future.

$$E_{total} = \sum_{i}^{n} E_{Leonard-Jones} + E_{Coulomb} + E_{H-bond} \tag{2}$$

Building such dynamic library could increase likelihood of detecting rare rotamers and reveal broader picture on the impact of side-chain positions.

[1] Miao, Zhichao, and Yang Cao. "Quantifying side-chain conformational variations in protein structure." Scientific reports 6 (2016): 37024.
[2] Dunbrack Jr, Roland L. "Rotamer libraries in the 21st century." Current opinion in structural biology 12, no. 4 (2002): 431-440.

DEVELOPMENT AND VALIDATION OF MIXED-MODE SOLID PHASE EXTRACTION METHOD FOR THE DETERMINATION OF MEDICINE DRUGS IN BIOLOGICAL MATRICES

Nerijus Karlonas

The State Forensic Medicine Service, Toxicology Laboratory, Didlaukio 86E, LT-08303 Vilnius, Lithuania
nerijuskarlonas@yahoo.com

Benzodiazepines belong to a group of substances well known for their sedative, hypnotic and anticonvulsant properties and they are used worldwide for the therapy of anxiety, sleep disorders and convulsive attacks [1]. Benzodiazepines are among the most commonly drugs today and are often found in a combination with other drugs in drug-related fatalities [1, 2]. Therefore, it is essential for a laboratory to develop a rapid method for the detection of this class compounds.

Gas chromatography with negative ion chemical ionization mass spectrometry (GC/NICI-MS) is a sensitive and selective technique for the analysis of benzodiazepines [3, 4]. The mechanism of NICI is characterized as a "soft" ionization technique, whereby NICI spectra exhibit information about prominent molecular anions and therefore about their molecular weight. This method enables to reach the highest specificity for these analytes and meet the requirements of good laboratory practice.

Therefore, the main aim of study was to develop and validate a new sensitive and specific method based on GC/NICI-MS using mixed-mode solid phase extraction for the determination of these drugs in whole blood. To the best of my knowledge, this method has been used for the first time for the optimization of sample preparation at pH 1.0. Analytical methods in clinical and forensic toxicology may either be used for screening and identification of benzodiazepines in biological fluids or for their quantification in these matrices, or in both cases. For the quantitative bioanalytical procedures there is a general agreement that at least the following validation parameters should be evaluated: the limit of detection (LOD) and quantification (LOQ), selectivity, calibration model (linearity), accuracy, precision (RSD), recovery, robustness and stability [3, 5, 6, 7]. The reliability of this method was certified by means of an exhaustive validation study.

The presented method has several advantages when compared with other previously published data [3, 4, 8, 9]. The LOD and LOQ for 15 benzodiazepines in whole blood samples for the developed method were in the range of 0.24 – 0.62 ng mL^{-1} and 0.72 – 1.89 ng mL^{-1}, respectively. The linear relationships with the coefficient of determination (r2) were in the range from 0.9961 to 0.9997.

Furthermore, no interferences were observed from the tested substances at the retention times of 15 benzodiazepines. The results of intraday and interday accuracy test for three different concentrations of analyte were in the range of 89.5 – 110.5 %, while all RSDs (precision) for replicate determinations were in the range of 4.08 - 9.52 %. Moreover, it was determined that extraction efficiency ranged from 82.9 (±6.2) % to 94.6 (±3.4) %. The absolute recoveries for most of the analytes ranged from 80.6 to 91.4 %, except for oxazepam (70.8 %), lorazepam (62.2 %), clonazepam (61.8 %) and α-OH-alprazolam (61.1 %). It was shown that conservation at ambient temperature (22.5 ± 0.5 °C) up to 50 h did not significantly alter analytical results. The stability of tested samples ranged from 84.6 to 115.5 %, and the precision was less than 12.4 %. Moreover, this method has several advantages: elimination of interferences, low-volume of samples (0.2 mL), a multi-residue analysis, and very fast chromatographic separation of fifteen analytes. Sensitive and specific NICI-MS detection combined with various characteristic fast GC parameters resulted in sharp and symmetric peaks shape of the analytes in chromatographic separation lasting for 3.9 min, while still maintaining sufficient resolution.

Obtained results showed, that the developed mixed-mode solid phase extraction method is accurate, sensitive, selective and specific enough to detect analytes after a long time of a single oral administration of some drugs using GC/NICI-MS. Finally, it was demonstrated, that this method is applicable for the determination of trace concentrations of benzodiazepines in real whole blood samples. The developed method can be applied in routine toxicological analysis during the investigations of both clinical and forensic cases.

[1] T. Blencowe, K. Raaska, P. Lillsunde. Therapeutic Drug Monitoring **33**, 64-71 (2011).
[2] C. M. Cunningham, G. E. Hanley, S. Morgan. Health Policy **97**, 122-129 (2010).
[3] N. Karlonas, A. Padarauskas, A. Ramanavicius, Z. Minkuviene, A. Ramanaviciene. Chemija **23**, 91-99 (2012).
[4] T. Gunnar, K. Ariniemi, P. Lillsund. Journal of Mass Spectrometry **41**, 741-754 (2006).
[5] F. T. Peters, O. H. Drummer, F. Musshoff. Forensic Science International **165**, 216-224 (2007).
[6] N. Karlonas, A. Padarauskas, A. Ramanavicius, A. Ramanaviciene. Journal of Separation Science **36**, 1437-1445 (2013).
[7] N. Karlonas, A. Ramanavicius, A. Ramanaviciene. Journal of Separation Science **37**, 551-557 (2014).
[8] V. F. Samanidou, M. N. Uddin, I. N. Papadoyannis. Bioanalysis **1**, 755-784 (2009).
[9] R. Kaartama, P. Jarho, J. Savolainen, H. Kokki, M. Lehtonen. Journal of Chromatography B **879**, 1668-1676 (2011).

ANALYSIS OF VALUE OF C REACTIVE PROTEIN IN COMPARISON TO BISAP SCORE IN PREDICTING THE SEVERITY OF NEWLY PRESENT ACUTE PANCREATITIS

Tomas Kairys[1], Artautas Mickevičius[2]

[1] Vilnius Univeristy, Faculty of Medicine, Lithuania
[2] Vilnius Univeristy Santaros Clinics, Lithuania
Tomas.kairys@mf.stud.vu.lt

Introduction: Pancreatitis is an inflammatory process in which pancreatic enzymes autodigest the gland. The gland heals without any impairment of function or any morphologic changes. Management depends largely on severity. Medical treatment of mild acute pancreatitis is relatively straightforward. Treatment of severe acute pancreatitis involves intensive care; the goals of medical management are to provide aggressive supportive care, to decrease inflammation, to limit infection or superinfection, and to identify and treat complications as appropriate. Worldwide, the incidence of acute pancreatitis ranges between 5 and 80 per 100,000[1], so the disease is rather common, necessitating the means to differentiate between mild and severe forms, due to both health related end economic reasons

Goals: To determine the possible applications of C reactive protein (CRP) and Bisap score in determining the severity of accute pancreatitis.

Means and Methods: A retrospective analysis of 130 case histories of patiens, treated in Vilnius Univeristy Santaros clinics, from year 2014 to 2015, with a diagnosed and confirmed accute pancreatitis.The patien were grouped according to Atlanta[2] classification into 3 groups of severity.The formed database was analysed, comparing the correlation cooficient and median scores of CRP in comparison to Ranson scale.

Results: Ranson score was significantly higher in Atlanta 3 group, compared to Atlanta 1 and 2 (1,32 ± 1,18 vs 1,53±1,08 vs 3±1,53).A weak/ intermediate correlation between CRP and severity of acute pancreatitis was determined.Correlation coefficient of Ranson score was 0,619, compared to CRP's correlation coefficient of 0,373

Conclusions: Ranson score proved unable to distinguish between Atlanta 1 and 2 groups, but proved to be valuable in identifying Atlanta 3 severity group. CRP showed to weakly correlate with the grade of severity of acute pancreatitis, so although it might provide some usefull information on first presentation of disease, its value is rather limited.

[1] Epidemiology, natural history, and predictors of disease outcome in acute and chronic pancreatitis
Banks, Peter A.
Gastrointestinal Endoscopy , Volume 56 , Issue 6 , S226 - S230
[2] Banks PA, Bollen TL, Dervenis C*, et al*
Classification of acute pancreatitis—2012: revision of the Atlanta classification and definitions by international consensus
Gut 2013;**62:**102-111.
[3] Ranson JH, Rifkind KM, Roses DF, Fink SD, Eng K, Spencer FC (1974). "Prognostic signs and the role of operative management in acute pancreatitis". *Surgery, Gynecology & Obstetrics*. **139** (1): 69–81

MICROBIAL DIVERSITY OF INVASIVE *FABACEAE* PLANTS

Čepukoit Dovilė [1], Putramentaitė Aurelija [2], Burokienė Daiva [1]

[1] Nature Research Centre, Žaliųjų Ežerų Str. 49, LT-08406 Vilnius, Lithuania
[2]Vilnius University, Faculty of Nature Science, Department of Microbiology and Biotechnology, Vilnius, Lithuania
dovile.cepukoit@gamtostyrimai.lt

Over the past few decades, invasive plant species are spreading to new territories due to human activity as a consequence of international trade. This resulted in tremendous expansion of invasive organisms. They threaten biological diversity of native flora, they are able to replace them resulting in enormous economic and ecological losses.

The *Fabaceae* family is widely spread in the world and belongs to the third largest family of flowering plants. But only few representatives of this family are found in Lithuania which are included in the lists of invasive plants. Microorganisms found in these plants may have influence on plants grown in natural ecosystems, but this kind of impact is not clear till now. Thus, fungal and bacterial microorganisms were isolated from invasive plants which belong to the genera *Robinia*, *Sarothamnus* (*Cytisus*) and *Caragana* and three genera of native herbaceous plants: *Trifolium*, *Astragalus* and *Securigera*.

The collection of microscopic fungi (approx. 200 isolates) and bacteria (approx. 168 isolates) was gathered. Investigations on pathogenic, morphological, biochemical, genetic features of isolated microorganisms are pursued due to further identification and characterization of obtained isolates.

THE IMPACT OF 3D PRINTED PLA SCAFFOLDS MICROSTRUCTURIZATION ON RAT'S DPSC OSTEOGENIC DIFFERENTIATION

Miglė Kalvaitytė[1], Egidijus Šimoliūnas[1], Milda Alksnė[1], Virginija Bukelskienė[1]

[1] Department of Biological models, Institute of Biochemistry, Life Sciences center, Vilnius University, Lithuania
miglekal@yahoo.com

The main purpose of tissue engineering is to develop artificial tissue or organ which could be used for treatment [1]. This study was focused on artificial bone tissue development, because of its necessity in medicine and odontology. The aim of this work was to evaluate the impact of polylactic acid (PLA) scaffolds microstructurization on rat's dental pulp stem cells (DPSC) osteogenic differentiation *in vitro*.

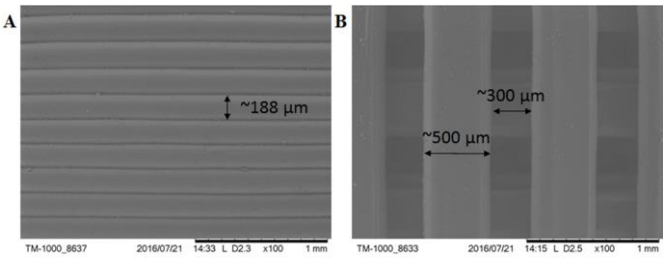

Fig. 2. SEM images of wavy (A) and porous (B) PLA scaffols.

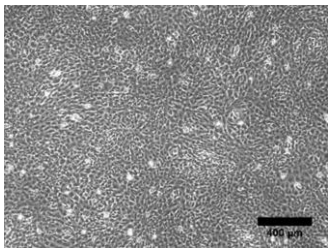

Fig. 1 Rat's dental pulp stem cell (DPSC).

Stem cells were isolated from rat's dental pulp by outgrowth from intact tissue and purified with magnetic beads coated with antibodies against cell surface marker CD44. These cells were immunologically characterized by flow cytometry and their multipotency was examined by osteogenic, myogenic and adipogenic differentiations. PLA scaffolds with two different microstructures were created by 3D printing. Wavy topography consisted of 188 µm wide joined threads, while porous micro-woodpile geometry PLA scaffolds had 300 µm diameter pores. For successful cell number evaluation, new method was established which rely on DAPI fluorescence when it is bound to DNA. This method was used for DPSC proliferation evaluation on PLA scaffolds. Results showed that both microstructurised 3D PLA scaffolds enhanced DPSC proliferation, compared to flat tissue culture polystyrene surface. Osteogenic differentiation results indicated that wavy PLA scaffolds were more suitable for matrix mineralization; however, alkaline phosphatase activity increased the most in the cells, seeded on porous scaffolds. The expression of three osteogenic differentiation genes - Runx2, osteopontin (OPN) and osteocalcin (OCN), were evaluated at different time points using reverse transcription and qPCR. Results showed that Runx2 gene transcription is better activated at beginning stages on wavy scaffold. OPN gene expression is earlier activated on wavy scaffold, however, later on, no difference has been found between two analysed scaffolds. OCN gene expression, which indicates late osteogenic differentiation, wasn't detected. Moreover, it was showed, that cell's environment and scaffolds microstructurization is sufficient enough to induce DPSC osteogenic differentiation.

All things considered, PLA scaffolds are suitable for rat's DPSC proliferation and osteogenic differentiation. Moreover, surface topography influenced DPSC osteogenic differentiation capacity. Ordered scaffolds can be successfully applied as templates for cell proliferation and differentiation.

[1] R. Langer, J.P. Vacanti, Tissue Engineering, Science 260, (1993)|.

ACCUMULATION OF CHEMOTHERAPEUTIC AGENTS IN 3D SPHEROID CELL CULTURES

Iveta Mikalajūnaitė[1], Greta Jarockytė[1], Ričardas Rotomskis[1,2]

[1] Biomedical Physics Laboratory of National Cancer Institute, Baublio 3B, LT08406, Vilnius, Lithuania.
[2] Biophotonics group of Laser Research Centre, Vilnius University, Saulėtekio 9, c.3, LT-10222, Vilnius, Lithuania

iveta.mikalajunaite@gmail.com

The development of safe, effective and patient-acceptable chemotherapeutic agents for cancer treatment is an expensive and lengthy process [1]. There is a risk of failure during development because of lack of clinical efficacy and/or unacceptable toxicity. It is necessary to improve *in vitro* testing methods for more precise investigation of drug candidates. In drug development it is essential to choose in vitro assays that would be most relevant model to *in vivo* tissues [2]. Nowadays most commonly cells are grown as monolayers. Unfortunately, cells grown as monolayers have some limitations, cells lose their tissue specific functions and morphology. Cells that are grown in 3D cell cultures correspond to the processes occurring in the natural environment *in vivo* more accurately compared to cell monolayers because of the lack of cell–cell and cell–extracellular matrix signalling [3].

The aim of this study was to investigate the effects of chemotherapeutic agents for 3D cells culture spheroids, their viability and accumulation in the cells.

In this study micro-sized cellular aggregates called 3D spheroid cell culture were used to assemble *in vitro* avascular cancer models. 3D spheroids of MDA-MB-231 breast cancer cells were formed using a hanging drop method. Spheroids were growing in 3D Perfecta 96-Well Hanging Drop Plate (Biomatrix, USA). Full formed spheroids were analyzed after 24 h, 48 h and 72 h of incubation with 10 mM ciplatin and 20 mM doxorubicin. Spheroids with cisplatin were stained with LIVE/DEAD viability assays (ThermoFisher, USA) and spheroids with doxorubicin were stained with Hoechst 33258 (Sigma, Germany). Viability of spheroids with cisplatin and accumulation of doxorubicin in spheroids with doxorubicin were observed after 24 h, 48 h, 72 h using Nikon Eclipse Te2000-U confocal microscope (Nikon, Japan).

Chemotherapeutic agents induced changes of structure of 3D spheroids cell culture. It has been found that doxorubicin effectively accumulates in the cells after 24 h. However, distribution of doxorubicin was heterogeneous: in some cells doxorubicin accumulated only in cytoplasm, in others both in cytoplasm and nucleus and small amount of cells do not have any doxorubicin accumulated at all. By increasing of incubation time to 72 h, most of the cells accumulate doxorubicin in nucleus. Also this study reveals that cisplatin has negative influence already after 24 h of incubation. By increasing of incubation time to 48 h and 72 h have been observed decreases of cells viability.

These results indicate possibility to use 3D cells culture spheroids for drugs testing.

[1] Fitzgerald KA, Malhotra M, Curtin CM., O'Brien FJ, O'Driscoll CM.. Life in 3D is never flat: 3D models to optimise drug delivery. Journal of Controlled Release. 2015; 215, 39–54.
[2] Breslin S, O'Driscoll L. Three-dimensional cell culture: The missing link in drug discovery. Drug Discovery Today. 2013; 18(5–6), 240–249.
[3] Edmondson R, Broglie JJ, Adcock AF, Yang L. Three-Dimensional Cell Culture Systems and Their Applications in Drug Discovery and Cell-Based Biosensors. ASSAY and Drug Development Technologies. 2014; 12(4), 207–218.

GERANIUM ROBERTIANUM L. INTRODUCTION, BIOLOGICALLY ACTIVE COMPOUNDS IN OVERGROUND

Sandra Saunoriūtė[1], Ona Ragažinskienė[1], Audrius Maruška[2], Erika Šeinauskienė[1]

[1]*Sector of Medicinal Plants, Kaunas Botanical Garden of Vytautas Magnus University, Ž.E. Žilibero str. 6, LT- 46324 Kaunas, Lithuania*
[2]*Centre of Environmental Research, Vytautas Magnus University, Vileikos str. 8, LT-44404, Kaunas, Lithuania*

sandra.saunoriute@vdu.lt

The introduction of the medicinal (aromatic) plants, their diversity are increased and the genetic medicinal plant resources are accumulated. It is important to determine the regularity of the accumulation of biologically active compounds in different stages of vegetation, introduced in medicinal, spice (aromatic) plants. The dynamics of their qualitative and quantitative indicators of their biologically active compounds determines the shelf life of the medicinal plant raw material and its quality [4].

The aim of these chemical analyses is to determinate total content of phenolic compounds, total content of flavonoid compounds and radical scavenging activity of *Geranium robertianum L*. methanolic extracts in the different vegetation periods: intense growth, flower buds, start blossoming, massive blossoming, end of blossoming.

The object of these analyses is *G. robertianum L*. It is a annual, sometimes biennial herbaceous plant of *Geraniaceae* family can be found widely in Europe, with the exception of the far north, in temperate parts of Asia, North Africa, Atlantic area of North America, and temperate parts of South America [1]. In Lithuania *G. robertianum* L. grows in humid deciduous or mixed forests, bushes, ash, roadsides. The metanolic extracts studied come from Sector of Medicinal Plants, Kaunas Botanical Garden of Vytautas Magnus University were harvested during the year 2016.

According to the literature, *G. robertianum* L. has been used for a long time in the folk medicine of several countries in different preparations, for a multitude of therapeutic purposes [3]. Its anti-inflammatory, haemostatic, antidiabetic, antibacterial, antidiarrhoeic, antiallergic, anti-cancer, antihepatotoxic, diuretic and tonic properties, as well as its suitability for the treatment of digestive system ailments has made this species very appreciated in herbal medicine [2].

In this study, the amount of non-volatiles compounds was performed using spectrophotometry methods. The amount of phenolic compounds was evaluated using Folin–Ciocalteu reagent spectrophotometry method. Colorimetric aluminium chloride method was carried out to determinate the total content of flavonoid compounds. Lastly, the radical scavenging activity was estimated by DPPH (2,2-diphenyl-1-picrylhydrazyl).

[1] D. E. Allen, G. Hatfield, Medicinal plants in folk tradition: an ethnobotany of Britain & Ireland. Timber Press, Portland, Cambridge (2004).
[2] J. B. Harborne, C. A. Williams, Phytochemistry of the genus *Geranium*, in: Lis-Balchin, M. (Ed.), *Geranium* and *Pelargonium* - The genera *Geranium* and *Pelargonium*, Taylor & Francis, London, 20–29 (2002).
[3] N. Radulović, M. Dekic, Z. Stojanovic–Radic, Chemical composition and antimicrobial activity of the volatile oils of *Geranium sanguineum* L. and *G. robertianum* L. (*Geraniaceae*). Med. Chem. Res. 21, 601–615 (2012).
[4] O. Ragažinskienė, A. Maruška, Perspektyvių vaistinių augalų cheminės sudėties mokslinių tyrimų raida Vytauto Didžiojo universitete. Vytauto Didžiojo universiteto Botanikos sodo raštai, 15: 82–94 (2011).

TARGETED RNA KNOCKDOWN BY TYPE III-A CRISPR-CAS EFFECTOR COMPLEX IN ZEBRAFISH

Dalia Smalakyte[1], Thomas Fricke[2], Michal Pastor[3], Agnieszka Kolano[2], Gintautas Tamulaitis[1], Virginijus Siksnys[1], Matthias Bochtler[2,3]

[1]Institute of Biotechnology, Vilnius University, Saulėtekio av. 7, 10257 Vilnius, Lithuania
[2]International Institute of Molecular and Cell Biology, Trojdena 4, 02-109 Warsaw, Poland
[3]Institute of Biochemistry and Biophysics PAS, Pawinskiego 5a, 02-106 Warsaw, Poland
daliasmalakyte@gmail.com

RNA knockdown is a powerful experimental technique to study gene function and is commonly mediated through RNA interference (RNAi). However, some organisms such as zebrafish cannot tolerate the additional load on their interfering RNA machinery. As an alternative way for RNA knockdown in this useful model organism we propose the use of type III-A CRISPR-Cas effector complex Csm from *Streptococcus thermophilus* (StCsm) as programmable endoribonuclease. We have targeted a transgenic EGFP, expressed from a variety of promoters, with StCsm loaded with crRNA, complementary to the EGFP transcript. StCsm was injected into zebrafish embryos at one cell stage afterwards RNA knockdown was evaluated by monitoring EGFP fluorescence by imaging and FACS analysis of digested embryos. Efficacious knockdown was observed for strains expressing EGFP under early promoters for both maternally and zygotically expressed EGFP. Our results suggest that StCsm mediated RNA knockdown has a potential to overcome the technical limitation of RNA knockdown in zebrafish.

DNA METHYLATION ANALYSIS OF METALLOTHIONEIN CODING GENES IN RENAL AND PROSTATE TUMORS

Rūta Maleckaitė[1], Kristina Daniūnaitė[1,2], Sonata Jarmalaitė[1,2].

[1]Human Genome Research Group, Institute of Biosciences, Life Sciences Center, Vilnius University, Vilnius, Lithuania;
[2]National Cancer Institute, Vilnius, Lithuania.
ruta.maleckaite@gmail.com

In recent years, mortality of renal cancer (RCa) has been increasing in Lithuania because there are no symptoms about oncologic changes in organism. According to statistical data, about 50% of RCa cases are determined accidentally, e.g. during ultrasound examinations. Prostate cancer (PCa) is the most frequent oncologic disease of men in Lithuania and the second one worldwide. Increased levels of prostate–specific antigen (PSA) in blood are used as a diagnostic indicator of PCa. However, PSA screening has relatively high rates of false-positive and false-negative results, thus, it lacks specificity. Nowadays, epigenetic tools such as DNA methylation analysis could be used as effective measure to investigate early changes in renal and prostate tissues. Our aim was to investigate promoter methylation status of metallothionein coding genes as potential new biomarkers for renal and prostate cancer diagnosis.

In total, 80 samples – 40 RCa, 10 peritumoral (PRT), and 30 noncancerous renal tissues (NRT) – from 30 RCa patients and 202 samples – 151 PCa and 51 noncancerous prostate tissues (NPT) – from 176 PCa patients were analyzed in the present study. Extracted genomic DNA was modified by bisulfite treatment and methylation–specific PCR (MSP) was used to analyze the promoter hypermethylation status of selected metallothionein genes: *MT1E*, *MT1F*, and *MT1G*. Adenomatous polyposis coli gene (*APC*), a widely studied tumor suppressor, was included for comparison.

In RCa cases, promoters of the *MT1E*, *MT1F*, and *MT1G* genes were methylated in 33%, 0% and 10% of tumors, respectively (Fig. 1A). Only methylation of *MT1E* gene was significantly more frequent in RCa as compared to NRT samples (P = 0.0059). The differences of methylation frequencies between RCa and PRT were not statistically significant for all three genes. *MT1E* was also more frequently methylated in RCa cases with larger tumor size and smaller patient's waist circumference (P = 0.0110 and P = 0.0195, respectively). No associations were observed between promoter methylation status and RCa patients' age, sex, tumor stage, or Fuhrmann grade.

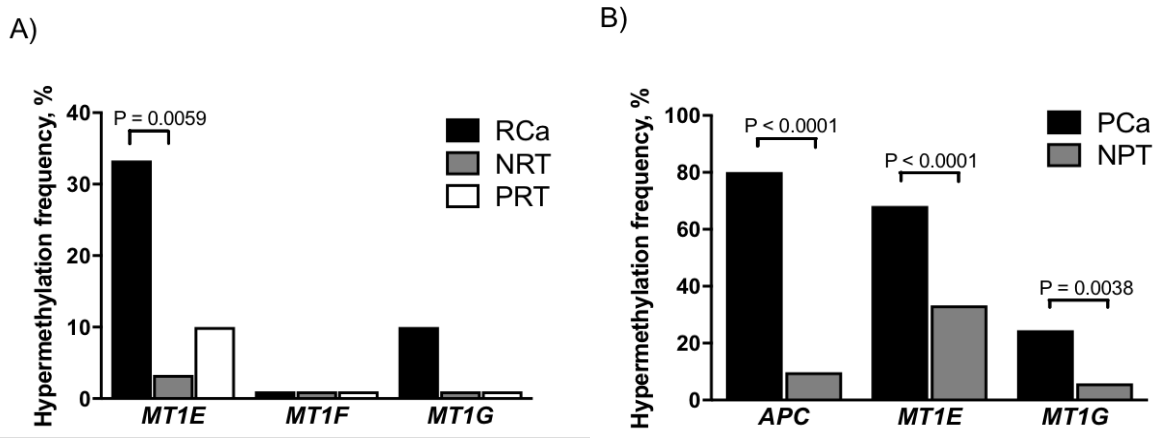

Fig. 1. Hypermethylation frequencies of metallothionein coding genes and *APC* in renal (A) and prostate (B) cancer samples. RCa/ PCa – renal/ prostate cancer, PRT – peritumoral renal tissues, NRT/ NPT – noncancerous renal/ prostate tissues.

In PCa cases, promoters of the *APC*, *MT1E*, and *MT1G* genes were methylated in 80%, 68%, and 25% of tumors and in 10%, 33%, and 6% of NPT, respectively (Fig. 1B). The differences of methylation frequencies between PCa and NPT were statistically significant for all three genes (P < 0.0001, P < 0.0001, and P = 0.0038, respectively). *APC* and *MT1G* were frequently methylated in PCa of advanced tumor stage (≥pT3 vs. pT2; P = 0.0117 and P = 0.0054, respectively) and in cases with biochemical disease recurrence (P = 0.0144 and P = 0.0073, respectively). Moreover, PCa patients with methylated *MT1G* status had significantly larger prostate mass (P = 0.0024). No correlations were determined between promoter hypermethylation and patients' age, preoperative PSA level, or Gleason grade groups, defined according to International Society of Urological Pathology.

In conclusion, our study identified promoter methylation of *MT1E* as a novel biomarker for diagnostics of RCa or PCa, while methylation of *APC* and *MT1G* could be exploited as potential prognostic biomarkers of PCa progression.

TP53 MUTATION ANALYSIS IN THE ETIOLOGY OF BREAST CANCER

Ieva Sadzevičienė[1], Kristina Daniūnaitė[1,2], Rasa Sabaliauskaitė[2], Valerijus Ostapenko[2], Sonata Jarmalaitė[1,2]

[1]Human Genome Research Group, Institute of Biosciences, Life Sciences Center
Vilnius University, Vilnius, Lithuania;
[2]National Cancer Institute, Vilnius, Lithuania
ieva.sadzeviciene@gf.vu.lt

Breast cancer (BC) is the most common malignant disease among women in the world. Mutations of various cancer-related genes is commonly associated with BC. Tumor protein 53 gene (*TP53*) mutations has been found in about 30% inherited and 20% sporadic BC cases [1]. Tumors with mutated *TP53* has a higher rate of pathological response to cytotoxic chemotherapy than wild-type (wt) *TP53* tumors. Furthermore, *TP53* mutations are more frequent in BC cases of advanced stage, with affected lymph nodes, positive for Ki67 expression, and in tumors showing aggressive behavior, like triple negative BC (TNBC) [2]. Therefore, the aim of the present study was to evaluate *TP53* mutation status in BC and examine associations with clinical-pathological and immunological parameters.

Tissue samples were collected from 116 BC cases during 2007-2009 at National Cancer Institute. *TP53* mutation analysis was performed using Sanger sequencing, single-strand conformation polymorphism (SSCP), and next-generation sequencing methods.

At least one *TP53* mutation was identified in 29% (34 of 116) BC cases. The vast majority of mutations were detected within DNA binding domain (75%, 21 of 28), particularly in exon 8 (25%, 7 of 28). Single nucleotide substitutions were the most common type of alterations (86%, 24 of 28), whereas deletions of various length (up to 23 bp) comprised 11% (3 of 28) as well as 2 bp inversion (3%, 1 of 28). *TP53* mutations were more frequently detected in poorly differentiated tumors (G3) as compared to moderately differentiated ones (58% and 9%, respectively; $P < 0.0001$). Moreover, high mutation frequency was significantly associated with TNBC subtype (81%, 13 of 16) in comparison to luminal A (9%, 5 of 54, $P = 0.0001$), luminal B (38%, 9 of 23; $P = 0.0201$), and HER2+ BC subtypes (30%, 7 of 23; $P = 0.0031$) (Fig.1.). Particularly, *TP53* mutations were more common in estrogen receptor-negative, progesterone receptor-negative, and Ki67-positive tumors ($P < 0.0001$, $P = 0.0039$, and $P < 0.0001$, respectively).

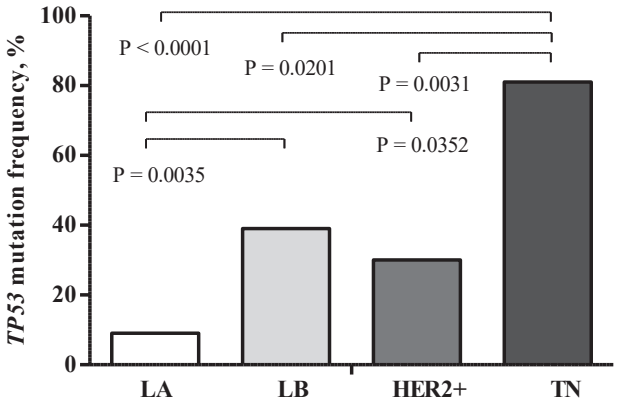

Fig.1. Distribution of *TP53* mutation frequencies among breast cancer (BC) subtypes. LA – luminal A, LB – luminal B, HER2+ – luminal or nonluminal BC subtype with HER2 receptor expression, TNBC - triple-negative BC.

In conclusion, our study revealed differences in *TP53* mutation rate among various BC subtypes, which might facilitate tumor differentiation at diagnosis and assist in treatment decision making, which is currently based on hormone receptor status.

[1] L. Bouaoun, D. Sonkin, M Ardin, M Hollstein, G Byrnes, J Zavadil, M Olivier. *TP53* Variations in Human Cancers: New Lessons from the IARC *TP53* Database and Genomics Data. Hum Mutat. 2016 Sep;37(9):865-76.

[2] P. Bertheau, J. Lehmann-Che, M. Varna, A. Dumay, B. Poirot, R. Porcher, E. Turpin, L.F. Plassa, A. Roquancourt, E. Bourstyn, P. Cremoux, A. Janin, S.Giacchetti, M. Espie, H. The. *P53* in breast cancer subtypes and new insights into response to chemotherapy. The Breast. 2013; 22: S27eS29.

INVESTIGATION OF INTERACTIONS BETWEEN CHITOSAN AND CAFFEOYLQUINIC ACID DERIVATIVES OF ARTICHOKE EXTRACT

Deimante Simanaviciute[1], Ramune Rutkaite[1], Rima Klimaviciute[1], Valdas Jakstas[2], Liudas Ivanauskas[3]

[1] Department of Polymer Chemistry and Technology, Kaunas University of Technology, Lithuania
[2] Department of Pharmacognosy, Lithuanian University of Health Sciences, Lithuania
[3] Department of Analytical and Toxicological Chemistry, Lithuanian University of Health Sciences, Lithuania
deimante.simanaviciute@ktu.lt

Chlorogenic acid, an ester of caffeic and quinic acids, is the most abundant polyphenol that is known to prevent diseases associated with oxidative stress and its related complications. It can exist in the form of three different isomers, namely, i.e. 3-*O*-caffeoylquinic acid, 5-*O*-caffeoylquinic acid and 4-*O*-caffeoylquinic acid [1, 2]. However, the application of caffeoylquinic acid derivatives (CQ) is restricted because of their readily oxidation, low bioavailability, sensitivity to heat and light and high hydrophilicity. In order to overcome these disadvantages those anionic phenolics could be immobilized on cationic polymers such as chitosan (ChS). Nevertheless, the immobilization of pure phenolic acids is expensive and irrational. The appliance of natural extracts instead of pure compounds is more convenient way to achieve desirable results.

In the present study, the formation of water insoluble complexes between ChS and phenolic compounds such as CQ, present in the artichoke extract (AE) has been investigated and the adsorption/desorption of AE on/from ChS has been studied. The Langmuir adsorption model has been used to describe the equilibrium adsorption of AE components from the initial aqueous solution on ChS at different temperatures (Fig. 1).

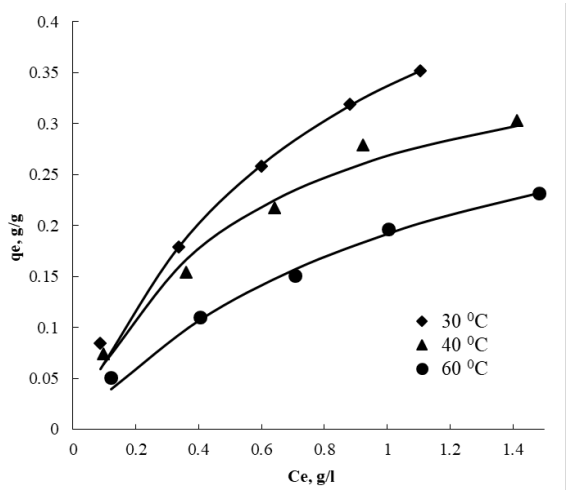

Fig. 1. Adsorption isotherms of AE on ChS at different temperatures. Symbols represent experimental data and lines represent fitted curves of the Langmuir adsorption model.

The UPLC and HPLC procedures were used to determine the composition of AE as well as to estimate the amounts of individual components adsorbed on ChS. The chromatographic analysis results clearly proved that not only CQ, but also various other phenolic compounds were adsorbed on ChS.

The antioxidant activity of the formed AE/ChS complexes was studied. It was demonstrated that the immobilization of active components of the natural extract effectively prevented the rapid loss of antioxidant activity over the time.

Acknowledgment. The authors are grateful to the Research Council of Lithuania for the financial support of the project MIP-055/2015.

[1] D. Bagdas, N. Cinkilic, H.Y. Ozboluk, M.O. Ozyigit, M.S. Gurun, Antihyperalgesic activity of chlorogenic acid in experimental neuropathic pain, Journal of Natural Medicines **67** 698-704 (2013).
[2] N. Nakatani, S.I. Kayano, H. Kikuzaki, K. Sumino, K. Katagiri, T. Mitani, Identification, quantitative determination, and antioxidative activities of chlorogenic acid isomers in prune (*Prunus domestica L.*), Journal of Agricultural and Food Chemistry **48** 5512-5516 (2000).

Demographic characteristcs of patents with pulmonary embolism in Lithuania

Vetra Markeviciute[1], Medeine-Silene Markeviciute[1], Pranas Serpytis[2]

[1] Faculty of Medicine, Vilnius University, Lithuania
[2] Santaros Clinic`s of Vilnius University Hospital, Lithuania
vetramarkeviciute@gmail.com

Pulmonary embolism is a sudden blockage in a lung artery [1]. The blockage usually is caused by a blood clot that travels to the lung from a vein in the leg [1]. Pulmonary embolism is a relatively common acute cardiovascular disorder with high early mortality rates that, despite advances in diagnosis and treatment over the past 30 years, have not changed significantly [2]. Pulmonary embolism is responsible for approximately 100,000 to 200,000 deaths in the United States each year. [3]

This study was collected in Vilnius university hospital Santaros clinic`s retrospectively, from case reports of pacients, treated from 2015 to 2016. All data of patients with pulmonary thromboembolism treated in VUH SC from 2015 to 2016 was collected and analyzed.

In the period from 2015 to 2016, 570 patients with pulmonary thromboembolism were treated in VUL SK. 21-98 years of age (M=71.19, SD=14.23). 309 women (54.2%, N=570) and 261 men (45.8%, N=570). 52 patients died during treatment (9.1%, N=570). 109 patients had/have an oncologic disease (19.1%, N=570). 214 patients were treated in an intensive care department (37.5%, N=570). 89 patients had a sudden drop in blood pressure (15.6%, N=570). Right ventricular dysfunction (57.7%, N=570) was observed in 329 patients.

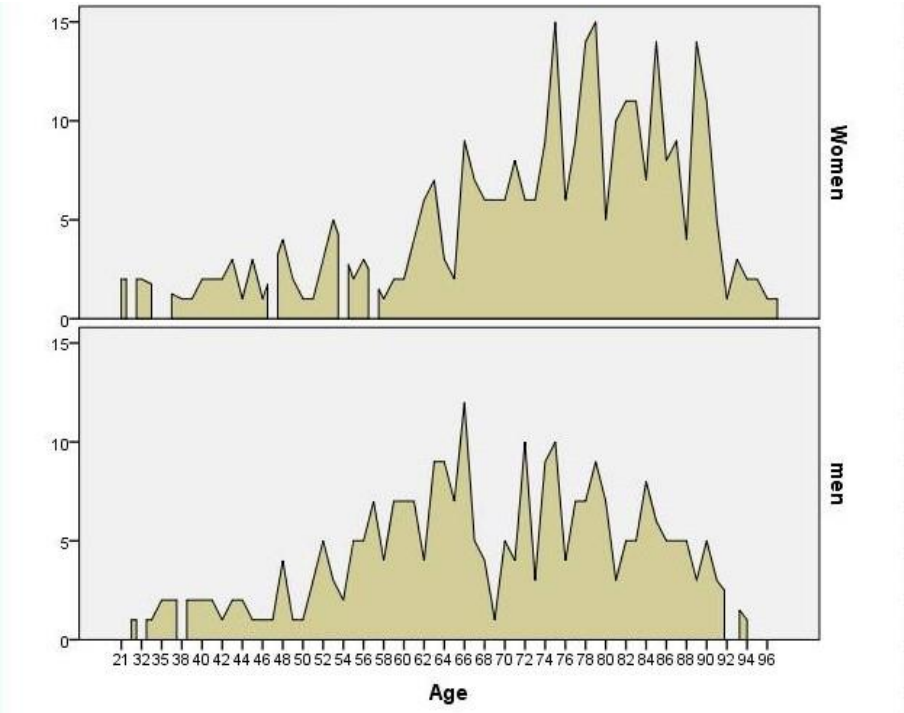

Fig. 1. Distribution of patients with pulmonary embolism by age and sex.

Pulmonary embolism is increasingly prevalent among elderly patients, yet the diagnosis is missed more often in these patients than in younger ones because respiratory symptoms often are dismissed as being chronic. [4] In one retrospective study of 1023 patients with PE, the five-year cumulative mortality rate was 32 percent [5]. Mortality was only 9.1% in Lithuania.

[1] https://www.ncbi.nlm.nih.gov/pubmedhealth/PMHT0022020/
[2] Jan Bělohlávek, Vladimír Dytrych, Aleš Linhart. Pulmonary embolism, part I: Epidemiology, risk factors and risk stratification, pathophysiology, clinical presentation, diagnosis and nonthrombotic pulmonary embolism. Exp Clin Cardiol. 2013 Spring; 18(2): 129–138.
[3] Abigail K. Tarbox, Mamta Swaroop. Pulmonary embolism. Int J Crit Illn Inj Sci. 2013 Jan-Mar; 3(1): 69–72. doi: 10.4103/2229-5151.109427
[4] https://emedicine.medscape.com/article/300901-overview#a6
[5] https://www.uptodate.com/contents/treatment-prognosis-and-follow-up-of-acute-pulmonary-embolism-in-adults

BRACHIAL PLEXUS TRACK IN THE INTERSCALENE GAP: ANATOMICAL VARIATIONS AND THEIR CLINICAL SIGNIFICANCE

Dovile Majauskyte[1], MD, PhD Egle Kontrimaviciute[2], MD Giedrius Volbekas[3]

[1] Vilnius University, Faculty of Medicine, Vilnius, Lithuania
[2] Chief of the Anesthesiology and Intensive Care Unite of Vilnius University Hospital Santaros Clinics, Assoc. Prof. of Vilnius University
[3] Vilnius University Hospital Santaros Clinics
dovile.majauskyte@mf.stud.vu.lt

Keywords: Brachial plexus, anatomical variations, ultrasound guided examination.

Introduction: Brachial plexus anatomical variations is important to anesthesiologist who administer regional anesthetic blocs[1]. The cognition of these variations helps in clinical practice.

Aim: The goal of this study was to scan posterior triangles of the neck by ultrasound and identify the relationship between brachial plexus and scalene muscles, compare results with scientific literature data and evaluate anatomical variations prevalence depending on age and sex.

Materials and methods: 100 participants (38 men, 62 women) were examined by ultrasound. Scanned 200 brachial plexus altogether. All anatomical variations have been classified. Age and sex were noted and relation between anatomical variations were checked.

Results: The mean of age of participants were 33.63 (SD 12.4) years. Only 3.5% (n=200) of brachial plexus were not identified, (bilateral 6%). C5 and C6 roots tracked the interscalene gap (ISG) 76% of all cases, bilateral 63% and it is the commonly described anatomical position. C5 root tracked anterior to anterior scalene muscle (ASM) 10% (bilateral 4%), C5 only pierce ASM 7% (bilateral 2%), C5 pierce ASM and root anterior 3% (bilateral 2%), C5 and C6 pierce ASM together 0.5% (bilateral 0%) of all cases (Fig. 1.). No statistically significant correlation was found between sex, age and distribution of anatomical variations. However, some findings showed that older participants had the same anatomical variants bilateral more often (p=0.048).

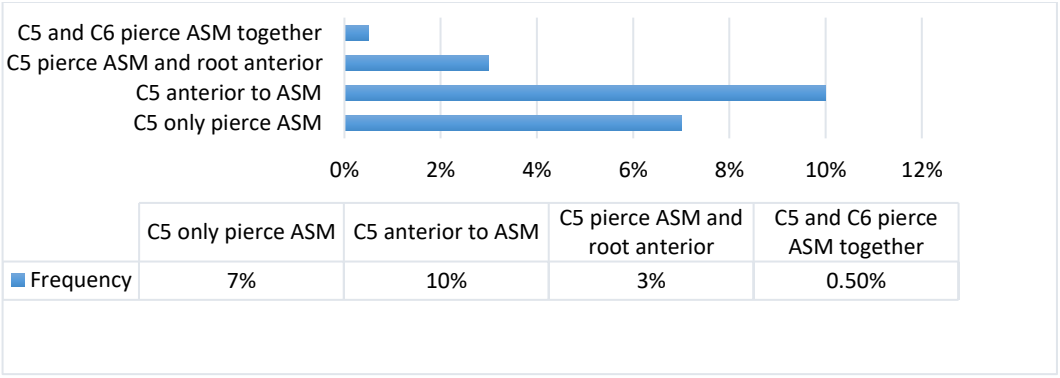

Fig. 1. Brachial plexus anatomical variations frequency

Conclusion: Ultrasound guided examination of posterior triangles of the neck is relatively onefold, because the structures are superficial and easily visualized. Anatomical variations described as normal have been reported more often (76%) than published in literature and abnormal cases have been found less (0.5-20.5%) respectively[1-3]. There was no statistically significant value between sex, age and distribution of anatomical variations.

[1] Harry WG, Bennett JD, Guha SC. Scalene muscles and the brachial plexus: Anatomical variations and their clinical signifi cance. Clin Anat 1997;10:250-2.
[2] Kessler J, Gray AT. Sonography of scalene muscle anomalies for brachial plexus block. Reg Anesth Pain Med 2007;32: 172-3.
[3] Natsis K, Totlis T, Tsikaras P, Anastasopoulos N, Skandalakis P, Koebke J. Variations of the course of the upper trunk of the brachial plexus and their clinical signifi cance for the thoracic outlet syndrome: A study on 93 cadavers. Am Surg 2006;72:188-92.

FABRICATION OF FLEXIBLE MICROPOROUS 3D SCAFFOLDS VIA STEREOLITHOGRAPHY AND OPTIMIZATION OF THEIR BIOCOMPATIBILITY

Giedrė Grigalevičiūtė[1], Daiva Baltriukienė[2], Evaldas Balčiūnas[2], Linas Jonušauskas[1], Mangirdas Malinauskas[1]

[1] Laser Research Center, Vilnius University, Saulėtekio ave. 10, Vilnius, Lithuania
[2] Life Sciences Center, Vilnius University, Saulėtekio ave. 7, Vilnius, Lithuania
giedre.grigaleviciute@gmail.com

Recently 3D printing technologies have received a lot of attention in the areas of science and industry. Differently from traditional processes of manufacturing, 3D printing allows fabrication of arbitrary geometry objects, using computer aided design and spatial formation of the structures layer by layer. It can be applied in various fields. One of them is medicine, where 3D printed objects have already made a great influence in such areas as orthopedics [1], face and skull reconstruction [2], plastic surgeries [3], teeth and mouth operations [4], etc.

Cells can be seeded into 3D printer-formed structures and artificial tissue or organ can be grown and implanted into human body. Currently, there is a lack of elastomeric photostructurable resins that would fit for tissue engineering requirements for scaffolds: non-degradable, but also biocompatible; permeable to low molecular weight molecules, gases and nutrients, avoiding waste accumulation; pore size should be appropriate for cell to cell interaction and migration [5]. However, optimizing biocompatibility of existing commercial resin would make a great influence. Application of new materials would open the door for new tissue engineering possibilities, enabling fabrication of the scaffolds with different mechanical, physical, biochemical and electrical properties that are needed for different types of tissues [6].

In this work the principles of fabrication of 3D scaffolds via stereolithography and scaffolds' biocompalibilty are investigated. In this research the requirements of reproducing the original environment of cells in such bioscaffolds are used in order to create and test mechanically flexible microporous structures. The scaffolds were fabricated using the tabletop 3D printer *Autodesk Ember*. Commercial photoresin *Formlabs Flexible* was used for this task. Optimization steps presented in this paper allowed to increase the biocompabaility of the scaffolds by 48% in comparison to unoptimized ones.

Sample Nr.	Temperature, °C	Duration in methanol	Duration in isopropanol
1	22-25	0	20 min
2	22-25	1 h	1 h
3	37-40	1 h	1 h
4	22-25	72 h	72 h
5	37-40	72 h	72 h

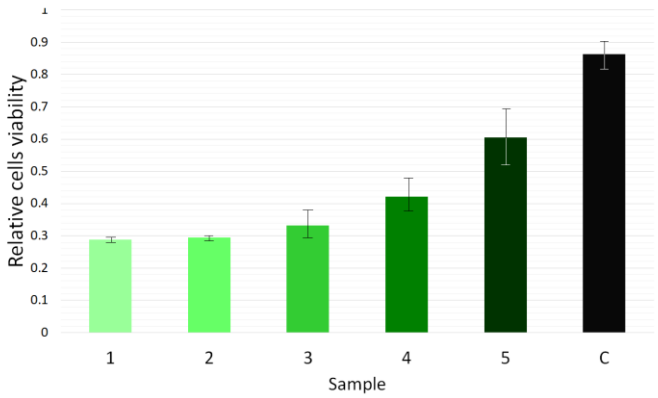

Fig. 1. Improved biocompatibility by applying various post-processings, C –control.

[1] F. Auricchio, S. Marconi, 3D printing: clinical applications in orthopaedics and traumatology, EFORT Open Reviews **1**(5), 121–127 (2016).
[2] A. Sutradhar, J. Park, D. Carrau, T. H. Nguyen, M. J. Miller, G. H. Paulino, Designing patient-specific 3D printed craniofacial implants using a novel topology optimization method, Med. Biol. Eng. Comput. **54**(7), 1123–1135 (2015).
[3] P. Kamali, D. Dean, R. Skoracki, P. G. L. Koolen, M. A. Paul, A. M. S. Ibrahim, S. J. Lin, The current role of three-dimensional printing in plastic surgery, Plast. Reconstr. Surg. **137**(3), 1045–1055 (2016).
[4] Y. Wang, J. Yu, L. Lo, P. Hsu, C. Lin, Developing customized dental miniscrew surgical template from thermoplastic polymer material using image superimposition, CAD system, and 3D printing, Biomed. Res. Int. **2017**, 1–8 (2017).
[5] P.S. Timashev, M. V. Vedunova, D. Guseva, E. Ponimaskin, A. Deiwick, T. A. Mishchenko, E. V. Mitroshina, A.V. Koroleva, A. S. Pimashkin, I. V.Mukhina, V. Y. Panchenko, B. N. Chichkov, V. N. Bagratashvili, 3D *in vitro* platform produced by two-photon polymerization for the analysis of neural network formation and function, *Biomed. Phys. Eng. Express* **2**(3), 035001 (2016).
[6] A. E. Jakus, A. L. Rutz, R. N. Shah, Advancing the field of 3D biomaterial printing, Biomed. Mater. **11**(1), 014102 (2016).

DETECTION OF MENINGITIS BACTERIA IN THE SPINAL FLUID VIA RAMAN SPECTROSCOPY

Arsenii Orlov[1], Tatiana Baikova[1], Sergey Gonchukov[1], Alexander Sundukov[2], Tatiana Svistunova[3]

[1]National Research Nuclear University (Moscow Engineering Physics Institute), Russia
[2]A.I. Yevdokimov Moscow State University of Medicine and Dentistry, Russia
[3]Moscow Infectious Clinical Hospital № 2, Russia
orlov.arseneey@gmail.com

Unlike other biological fluids spinal fluid (SF) is much less often used to diagnostics of diseases. Anyway, despite the certain difficulties of SF sampling its biomedical research is the only reliable approach for diagnosing meningitis Traditional cytological, bacteriological, virological, and serological techniques are complex, expensive, require a lot of time and not always reliable. Raman spectroscopy (RS) undoubtedly is the most prospective way to SF researching because it is fast and non-invasive as well as provides reliable information about changes at the molecular level.

Researches to identify specific lines of bacteria which are the causative agents of meningitis were carried out. These lines can be used to efficiently detect and identify bacteria in the spinal fluid. Studies were carried out via Raman spectrometers Nicolet Almega XR and DXR2 with laser radiation at 532 nm and 785 nm wavelengths. Stokes components were registered in the range from 400 to 3100 cm^{-1}. The measurements were carried out both by the traditional RS method and by the methods of surface-enhanced and resonant RS.

It is shown that the characteristic lines which can be used to detect bacteria are mainly due to the amide, protein, and DNA vibrations. For example, Staphylococcus aureus bacteria characteristic lines are associated with fluctuations of carotenoids (1528 and 1152 cm^{-1}).

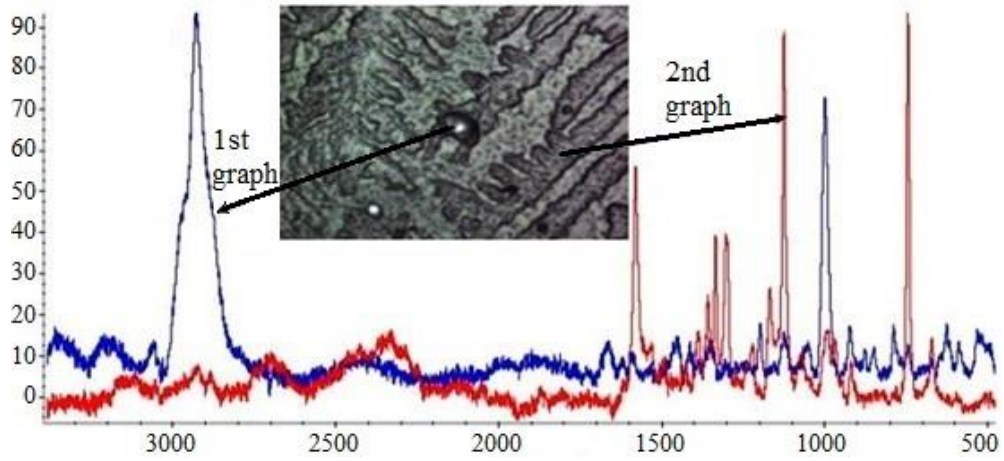

Fig. 1. Raman shift (cm^{-1})

Fig. 1. Raman spectra of the dried spinal fluid drop taken from a patient with a bacterial form of meningitis. Spectrum of bacteria (1st graph), spectrum of spinal fluid dendritic structure (2nd graph).

Thus, Raman spectroscopy of spinal fluid is quite useful way which could allow to quickly establish the cause of the meningitis in order to appoint the right treatment as soon as possible.

[1] T.V. Baikova, S.A. Minaeva et al., Detection of single bacteria – causative agents of meningitis using Raman microscopy. Journal of Physics: Conference Series 594 (2015).
[2] Cheng et al., Rapid identification of bacteria utilizing amplified dielectrophoretic force-assisted nanoparticle-induced surface-enhanced Raman spectroscopy, Nanoscale Research Letters 2014, 9:324.
[3] Pamela A. Mosier-Boss, Review on SERS of Bacteria, Biosensors 2017, 7(4), 51.

SOCIODEMOGRAPHIC RISK FACTORS CONNECTION WITH HIGH-SENSITIVITY C- REACTIVE PROTEIN AND FIBRINOGEN

Julija Mažeikaitė[1], doc. Viktorija Andrejevaitė[2]

[1]Faculty of Medicine, Vilnius University, Lithuania
[2]Clinic of Internal Diseases, Family Medicine and Oncology, Vilnius University, Lithuania
julija.fausta@gmail.com

Introduction: It is known that socioeconomic status is linked with health outcomes. Inflammation is one of the most important factors in cardiovascular disease pathophysiology. The main leading cause of death in the United States in 2016 was heart disease (23.1%). Nowadays it is important to indicate health correlation with various social-demographic factors in order to know where to tease out the effects on health out- comes.

Aim: Identify sociodemographic risk factors such as living place, family status, education, monthly incomes connection with inflammatory marks (high- sensitivity CRP and fibrinogen) between smoking 40-55 age man.

Materials and methods: Accomplished retrospective analysis that investigated 257 smoking man between 40 and 55 years. This research includes 245 respondents, which were grouped by living place (urban, sub- urban and rural), family status (single, married, living with a person in a conjugal relationship outside marriage), education (secondary and below, professional, tertiary education), incomes (until 434euro/month, 435-724euro/month, under 725euro/ month). Furthermore, blood inflammation markers- serum high sensitivity- CRP and fibrinogen concentration were analysed. Statistic analysis of data was made by SPSS 20.0 pro- gram. Statistic accuracy mark <0,05.

Results: There are no statistical correlation between hs- CRP concentration and living place (p=0,881), family status (p=0,590), education (p=0,729 and incomes (p=0,488). Correlation between fibrinogen concentration and all measured sociodemographic risk factors: living place (p=0,442), family status (p=0,421), education (p=0,744) and in- comes (p=0,665) also is statistically insignificant.

Conclusions: During this research I did not found any statistical correlation of blood inflammatory marks and sociodemographic risk factors among smoking men population.

SPECTROSCOPIC PROPERTIES AND ACTIVITY OF GLUCOSE OXIDASE

Raminta Mazėtytė[1,2], Urtė Bubnienė[3], Arūnas Ramanavičius[2,3], Renata Karpič[2]

[1] Faculty of Physics, Vilnius University, Saulėtekio Ave. 9-III, LT-10222 Vilnius, Lithuania
[2] Institute of Physics, Center for Physical Sciences and Technology, Saulėtekio av. 3, LT-10257 Vilnius, Lithuania.
[3] Department of Physical Chemistry, Faculty of Chemistry, Vilnius University, Naugarduko Str. 24, LT-03225 Vilnius, Lithuania
raminta.mazetyte@gmail.com

The usage of biosensing systems is promising - rapid and accurate method for detection and analysis of various compounds. Nowadays one of the best-known and the most common biosensors are the glucose biosensors. They can accurately detect concentration of glucose in blood during a short period of time – it is very important to people with diabetes [1]. The active part of the biosensor is a glucose oxidase (GOx) enzyme immobilized on the surface of the electrode. When constructing an enzymatic biosensor, one of the most important aims is to determine properties of an enzyme under different environmental conditions. Despite the increasing number of studies on GOx, there is little information about the properties of the enzyme at different pH conditions [2].

Spectroscopic properties of glucose oxidase (GOx) and flavin adenine dinucleotide (FAD) were investigated in different acidity environments. The purpose of this research was to evaluate absorption and fluorescence spectra changes and to associate them with changes of GOx activity. The study of the absorption and fluorescence spectra and the measurements of relaxation times were carried out using a citric acid sodium phosphate buffer with pH values from 2 to 8.

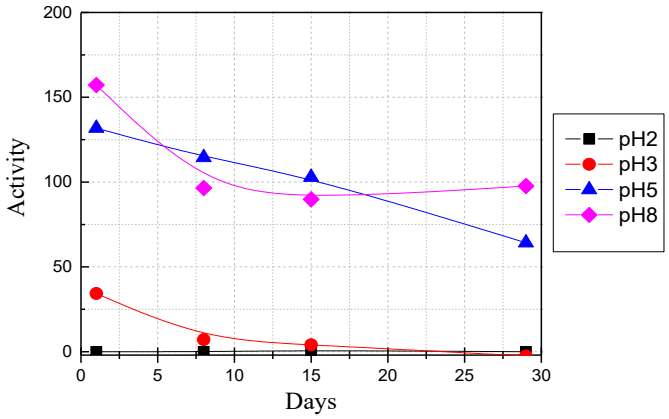

Fig.1. Changes of GOx activity during the 29-day period.

GOx is a flavin adenine dinucleotide (FAD) containing glycoprotein. FAD is involved in enzymatic redox reactions and determines the enzyme's activity. GOx will lose its activity if FAD dissociates from the enzyme active site.

A. Ciucu described a fast spectrometric method of determining the activity of glucose oxidase [3]. The determination of GOx activity based on enzymatic reduction of benzoquinone to hydroquinone and on the measurement of the rate of increase of hydroquinone absorbance at 290 nm. Calculated changes of GOx activity during the 29-day period are shown in Fig.1.

The data analysis showed that at pH 2-3 solution acidity, the fluorescence intensities of FAD and GOx at 530 nm were the most intense. At pH 2, the GOx enzyme is completely inactive throughout the 29-day period. At the first day, the fluorescence intensity of GOx at the optimum pH (6) was the lowest and the activity of GOx was the highest compared to other pH solutions.

During this study, GOx activity trend was found: over time GOx's activity is decreasing. The increased intensity of the fluorescence band of GOx at 530 nm is associated with a decreased activity of an enzyme. The changes of fluorescence intensity band are associated with dissociation of FAD from the enzyme. However, the process is not reversible and the decrease of fluorescence intensity is associated with structural changes in the FAD: reduction of FAD, organic molecule aging process.

[1] Eun-Hyung Yoo, Soo-Youn Lee, Glucose Biosensors: An Overview of Use in Clinical Practice, Sensors (2010), 10, 4558-4576.
[2] L. Dumitrascu, N. Stanciuc, G. E. Bahrim, A. Ciumac and I.Aprodu, pH and heat-dependent behaviour of glucose oxidase down to singlemolecule level by combined fluorescence spectroscopy and molecular modelling, J Sci Food Agric 2016; 96: 1906–1914.
[3]A. Ciucu, C. Pâtroescu, Fast Spectrometric Method of Determining the Activity of Glucose Oxidase, Analytical Letters, 17:12, 1417-1427, (1984).

INVESTIGATION OF CHARGE CARRIER TRANSIT VIA THE FREQUENCY DOMAIN

[1]Džiugas Litvinas, [2]Akvilė Zabiliūtė-Karaliūnė, [2]Pranciškus Vitta

[1]Vilnius University, Faculty of Physics, Saulėtekio al. 9, LT-10222 Vilnius
[2]National Center for Physical and Technology Sciences, Saulėtekio al. 3, LT-10257 Vilnius
dziugas.litvinas@ff.stud.vu.lt

In this work we seek to utilize the Frequency-Domain (FD) method [1] for the investigation of charge carrier transit in organic optoelectronic devices and to show that this technique is financially more appealing than other currently utilized methods, i.e. Time-of-Flight (TOF) [2] or Carrier Extraction by Linearly Increasing Voltage (CELIV) [3], both of which need expensive equipment capable of generating short impulses of light – lasers – as a prerequisite.

The TOF method is often called upon for determining charge carrier mobility and relaxation times in materials of small conductivity and mobility, solar cells. TOF's basis is applying a constant voltage U to a sample, exciting a layer of thickness d with a light impulse and then measuring the drift time τ of photogenerated charge carriers. The kinetics of the former frequently follows an exponential decay law, Eq. (1) and the carrier mobility μ can be determined appropriately, Eq. (2):

$$n(t) = n_0 e^{-t/\tau}, \qquad (1) \qquad \mu = d^2/U\tau. \qquad (2)$$

where t – time, n_0 – concentration of carriers at $t = 0$. Still, the small density of injected carriers leads to a low signal-to-noise ratio; this can be improved by using samples, which are grown in substrates of silicon, indium tin oxide (ITO) and etc. [4]

Knowledge about TOF is necessary to change parameters from FD into ones that describe a solar cell. These methods are bound by an inverse Fourier transform: in an FD procedure, the sample signal (i.e., photovoltage) decay time τ for an arbitrary frequency f is determined by knowing the phase shift φ between two modulated excitation (modulation depth M) and sample response (mod. depth m) harmonic signals. For example, during mono-exponential decay:

$$\tan\varphi = 2\pi f\tau, \quad \mu = m/M = (1+\tan^2\varphi)^{-0.5}. \qquad (3)$$

In a more general case, whence decay is a weighted sum of several exponents, the FD method allows us to evaluate several different decay times τ_i that are influenced by the sample's structure specifics (having found the correct coefficients a_i):

$$\tan\varphi = \frac{N_\omega}{D_\omega}, \ \mu = \frac{m}{M} = \sqrt{N_\omega^2 + D_\omega^2}, \ N_\omega = \sum_i \frac{a_i\omega\tau_i^2}{1+\omega^2\tau_i^2} \Big/ \sum_i a_i\tau_i, \ D_\omega = \sum_i \frac{a_i\tau_i}{1+\omega^2\tau_i^2} \Big/ \sum_i a_i\tau_i, \ \sum_i a_i = 1, \omega = 2\pi f. \quad (4)$$

A block diagram regarding our experimental setup is presented in Fig. 1. We used a bulk heterojunction poly(3-hexilthiophene-2,5-diil)/[6,6]-phenil-C61 butyric acid (P3HT/PCBM) based photovoltaic material with transparent ZnO and Ag_2O paste electrodes as the sample. This we expect slow drift times of orders 10^{-3} – 10^0 s. For the excitation we used a 3 mW 400 nm LED. The generator creates two identical phase-aligned harmonic signals, changing from 1.6 to 2 V, directed to a phase analyzer and the LED. The voltage range was chosen to not saturate the excitation or photovoltaic response signals and maintain their sinusoidal shape. The solar cell's contacts are connected to the phase analyzer: this way both the excitation and the modulated phase-shifted response signals are provided for comparison. The mentioned apparatus and generator are connected to a PC via USB; software controls the signals' frequency and executes logarithmic stepping over an arbitrary frequency interval. The final isolated (after removing system environmental noises) phase shift φ between the excitation and photovoltaic response signals vs harmonic signal frequency f is shown in Fig. 2. Applying a tri-exponential decay fit to our sample yielded the following decay durations τ_i and their appropriate weights a_i: $\tau_1 = 0.002$ s, $a_1 = 0.91$; $\tau_2 = 0.012$ s, $a_2 = 0.08$ and $\tau_3 = 0.112$ s, $a_3 = 0.01$. It is evident that our calculated values fall within the expected time range of 10^{-3} – 10^0 s and the most prominent time is 0.002 s, which is likely to play the most significant role when determining the charge carrier's mobility.

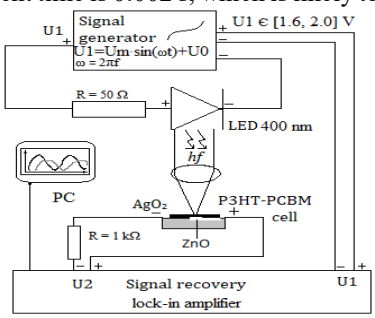

Fig. 1. Block diagram of the experimental setup for P3HT/PCBM cell investigation via FD method.

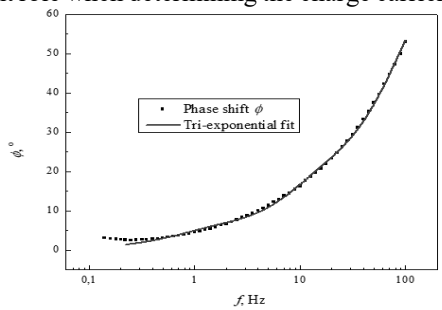

Fig. 2. Phase shift between the excitation and photovoltaic response signals φ vs harmonic signal frequency f.

Aknowledgement. This research was funded by a grant (No. 09.3.3.-LMT-K-712-03-0069/LSS-14900-1607) from the Research Council of Lithuania.

[1] J. R. Lakowicz, TrAC Trends in Analytical Chemistry, vol. 5, no. 10, p. 257-263, 1986.
[2] R. G. Kepler, B. P. M., S. J. Jacobs, R. A. Anderson and M. B. Sinclair, Applied Physics Letters, vol. 66, no. 26, p. 3618-3620, 1995.
[3] G. Juška, Physical Review Letters, vol. 84, no. 21, p. 4946-4949, 2000.
[4] B. Chen, Japanese Journal of Applied Physics, vol. 39, no. 2000, p. 1190-1192, 2000.

Computer Assisted Identification of Cancerous Kidney Tissue by Means of FTIR Spectroscopy

Rimantė Bandzevičiūtė[1], Vidita Urbonienė[1], Feliksas Jankevičius[2,3], Valdas Šablinskas[1]

[1]Chemical Physics Institute, Faculty of Physics, Vilnius University, Saulėtekio Ave. 3, LT-10257 Vilnius, Lithuania
[2]Faculty of Medicine, Vilnius University, Santariškių str. 2, LT-08661 Vilnius, Lithuania
[3]Lithuanian National Cancer Institute, Santariškių str. 1, LT-08660 Vilnius, Lithuania
rimante.bandzeviciute@ff.vu.lt

Cancer is one of the most common causes of death in the world [1]. In some cases tumor can be treated by removing it while functional tissue around it is stored. The determination of the exact margin between normal and cancerous tissues during a surgery is one of the most important factors for a successful treatment, favorable prognosis and reduced risk of recurrences of cancer.

During the last decade, various methods of infrared spectroscopy were applied for the tissue analysis of different types of human cancer. The methods showed good results for the identification of the removed cancerous tissues [2-4]. During the process of cancer development, the changes of chemical content of the cells are observed in the biological tissue. These changes on the molecular level can be determined by analyzing the infrared spectra of the tissue. In this work, the technique of an attenuated total reflection of infrared radiation (ATR IR) is applied for the analysis of the extracellular fluid (ECF) of the normal and tumorous human kidney tissue containing single cells. This technique allows examining the ECF of the tissue immediately after the surgery directly in OR since this method does not require any special preparation of the specimen. When this technique is applied for the tissue recognition *in vivo*, there is the need of special software for determination of cancerous tissues.

In this study, there were analyzed the ATR IR absorption spectra of ECF of the normal and tumorous human kidney tissue of 115 patients undergoing partial or radical nefrectomy.

The main differences between ATR IR absorption spectra of ECF of the normal and cancerous human kidney tissue are observed in the spectral region 1200 – 950 cm^{-1} where spectral bands of the υ (C-O), υ (C-C) and δ (C-O-H) vibrations of glycogen are located (Figure 1). In this region, there are observed two spectral bands in the case of normal and three bands in the case of cancerous kidney tissue.

In this work, there was created an algorithm and written a computer program for automatically identification of normal and cancerous human kidney tissues by analyzing the ATR IR absorption spectra. The program compares the spectrum that is being analyzed with the spectra from the spectral library, which is built from previous studies. The library contains the ATR IR absorption spectra of ECF of the normal and cancerous human kidney tissue, water and ethanol. The program is capable to recognize the tissue type immediately after registration of the spectrum. Due to the fact that the most frequently diagnosed type of human kidney malignant tumor is a clear cell renal cell carcinoma (86 %), the best results are achieved for the identification of cancerous tissue of this type of the tumor. The program identifies the cancerous tissue with 90 % accuracy, while the normal tissue is identified with 94 % accuracy. After evaluation of the validity of this method for the cancerous tissue diagnosis, it was established that the tissue type can be identified with 90 % sensitivity and 94 % specificity, while the positive and negative predictive values reached 93 % and 92 % respectively. It is possible that the normal human kidney tissue could be recognized with better accuracy according to the probable differences between ATR IR absorption spectra of ECF of the different kidney tissue areas.

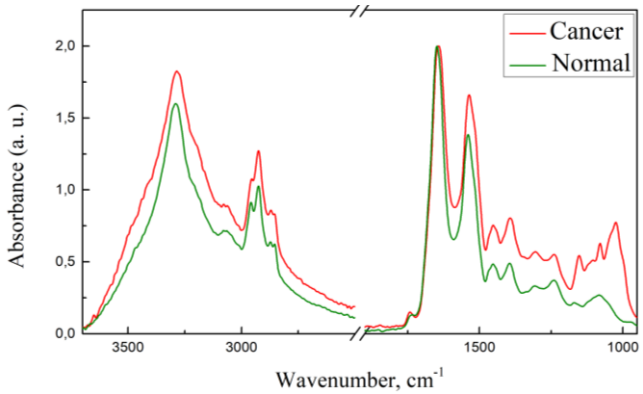

Fig. 1. The ATR IR absorption spectra of ECF of the normal (green) and cancerous (red) human kidney tissue.

[1] L. A. Torre et al., CA Cancer J Clin **65**, 87–108 (2015)
[2] P. Tian et al., Int J Clin Exp Med **8**, 972-981 (2015)
[3] N. Wald et al., Biochimica et Biophysica Acta, **1862**, 202–212 (2016)
[4] A. Benard et al., Analyst, **139**, 1044–1056 (2014)

DO THE $H^+_5O_2$+X COMPLEXES (X=Ar,Ne,He) WITH C_2 SYMMETRY REALLY EXIST?

Anton Paltsev[1], George Pitsevich[1], Elena Shalamberidze[1], Vitas Balevicius[2]

[1] Department of Physical Optics, Belarusian State University, Minsk, Belarus
[2] Vilnius University, Vilnius, Lithuania
danny.mad@yandex.ru

Protonated water dimer ($H^+_5O_2$) attracts researchers' attention as one of the simplest protonated water clusters, investigations of which are interesting both for better understanding of proton transfer mechanisms and hydrogen bond properties. Our recent investigations [1,2] shed some light on the dynamics of the shared proton stretching vibrations. The problem is that we have to compare calculated IR spectra with experimental IR spectra of the $H^+_5O_2$+X complexes, where X=Ar,Ne,He acts like a carrier. According to [3] these complexes exist in only one configuration where protonated water dimer loses C_2 symmetry. This fact was confirmed both by the data of calculations represented in work [4] and by our calculations performed in frame of standard DFT methods. At the same time it is clear that due to dipole moment of free $H^+_5O_2$ directed along C_2 symmetry axis the most strong interaction between protonated water dimer and inert gases is expected when the last two are accommodated on C_2 axis.

We assumed that the failure of standard DFT methods to locate $H^+_5O_2$+X complexes with C_2 symmetry is because of the lack of dispersion interaction accounting. Based on these considerations, we used wB97XD density functional which takes in account dispersion interaction [4]. Using wB97XD/acc-pVTZ level of theory we were able to find configurations of the $H^+_5O_2$+X complexes with C_2 symmetry for all X= Ar,Ne,He. Equilibrium configuration of the $H^+_5O_2$+Ar complex with and without C_2 symmetry represented on Fig.1.

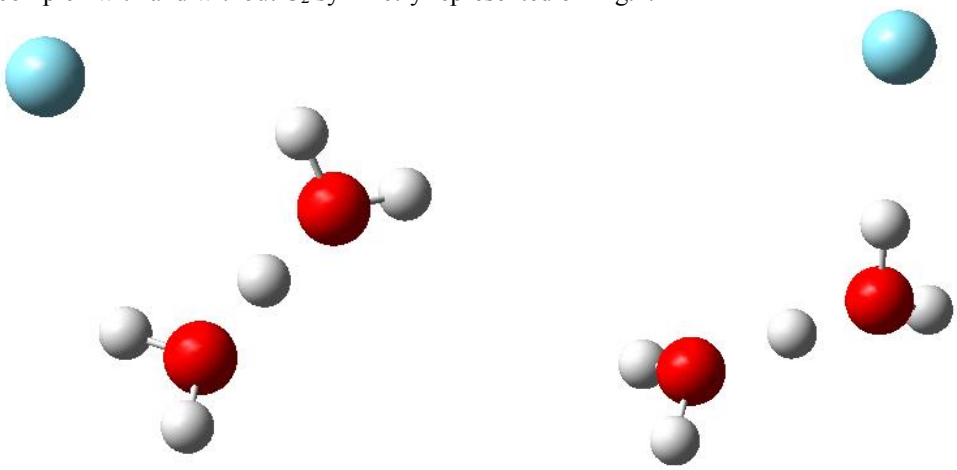

Figure 1 Equilibrium structure of the $H^+_5O_2$+Ar complex with (left) and without (right) C_2 symmetry calculated at wB97XD/acc-pVTZ level of theory.

According to the calculations it was found that for all inert atoms complexes with C_2 symmetry posses much smaller distorted geometry and IR spectra of free protonated water complex and shared proton remains at the centrum of the hydrogen bridge. A different situation appears in complexes without C_2 symmetry. The shared proton tends to move towards the water molecule that is closer to Ar/Ne/He. Calculated IR spectra of such complexes differ strongly from the free complex ones. In case of Ar atom this shift is more significant. So we can assume that addition of the Ar/Ne/He atom to the PWD molecule stabilizes the H_3O+ fragment of the PWD. Our calculations confirm the deformation of the C_2 configuration, but for both complexes ($H^+_5O_2$+Ar, $H^+_5O_2$+Ne, $H^+_5O_2$+He) the water molecules are still oriented with respect to each other similarly as in the case of the C_2 configuration, i.e. only the proton shifts towards one of the monomers without relative rotation of the water molecules; the shift in the case of $H^+_5O_2$+Ar is significantly bigger than in the case of $H^+_5O_2$+Ne and $H^+_5O_2$+He but the O_1O_5 distance is in neither case hardly affected compared to the case without carrier gas. At the same time existence of the $H^+_5O_2$+X complexes with C_2 symmetry still questionable in spite of the fact that experimental spectra rather say in favor of their existence. The further investigations are needed.

[1] G. Pitsevich, A. Malevich, E. Kozlovskaya, E. Mahnach, I. Doroshenko, V. Pogorelov, L. Pettersson, V. Sablinskas, V. Balevicius, MP4 study of the anharmonic coupling of the shared proton stretching vibration of the protonated water dimer in equilibrium and transition states, J. Phys. Chem. A**, 121**, 2151 (2017).

[2] G. Pitsevich, A. Malevich, E. Kozlovskaya, E. Shalamberidze, I. Doroshenko, V. Pogorelov, E. Mahnach, V. Sapeshko, V. Balevicius, MP4 study of the multimode coupling in protonated water dimer, J. Mol. Struct. **1139**, 328 (2017).

[3] N.I. Hammer, E.G. Diken, J.R. Roscioli, M.A. Johnson, E.M. Myshkin, K.D. Jordan, A.B. McCoy, X. Huang, J.M. Bowman, S. Stuart, The vibrational predissociation spectra of the H_5O_2 $^+$RGn(RG = Ar,Ne) clusters: correlation of the solvent perturbations in the free OH and shared proton transitions of the Zundel ion, J. Chem. Phys. **122**, 244301 (2005).

[4] J.-D. Chai, M. Head-Gordon, Long-range corrected hybrid density functionals with damped atom-atom dispersion corrections, Phys.Chem.Chem.Phys. **10**, 6615 (2008).

EFFECT OF THE HALOGEN SUBSTITUTION ON STRENGTH OF THE INTRAMOLECULAR H-BOND AND SPECTRAL PARAMETERS OF THE ACETHYLACETONE MOLECULE.

Uliana Peretolchina[1], George Pitsevich[1], Elena Shalamberidze[1], Valdas Sablinskas[2]

[1] Department of Physical Optics, Belarusian State University, Minsk, Belarus
[2] Vilnius University, Vilnius, Lithuania
danny.mad@yandex.com

Acetylacetone (AA) molecule is interesting due to the intramolecular H-bond formation as well as proton tunneling. To study the effect of halogen substitution on H-bond strength were performed calculations of the equilibrium structures and IR spectra of the next few molecules, represented on Fig.1.

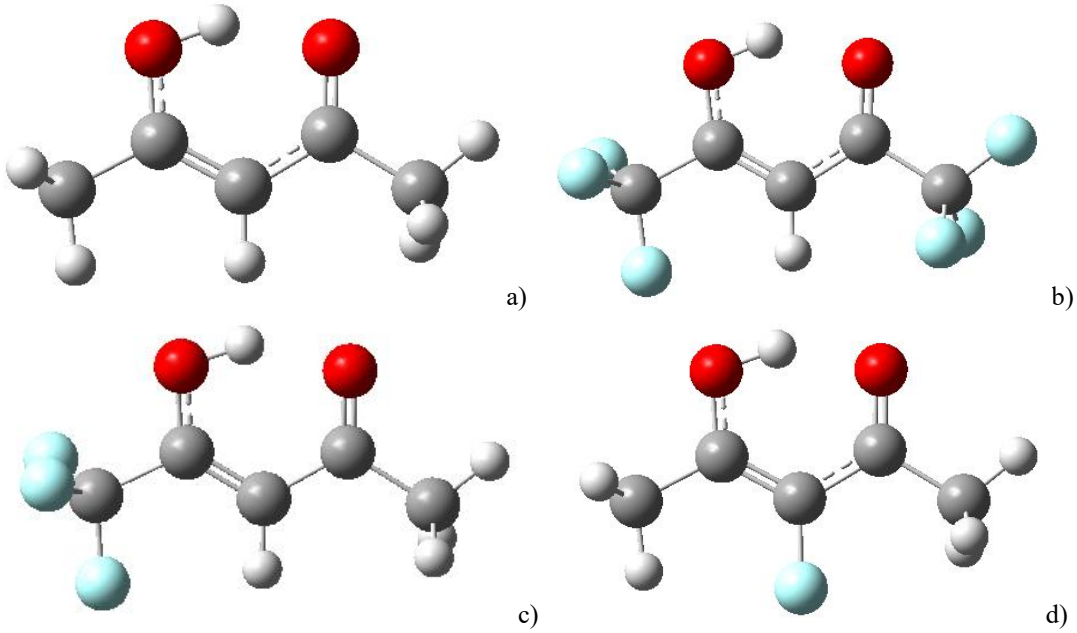

Figure 1 Equilibrium structure of the AA (a) and its halogen substituted analogies (b,c,d) where the blue atom is Br, Cl, and F.

All calculations were performed using wB97XD/cc-pVTZ and B3LYP/cc-pVTZ level of theory. Some structural data of the hydrogen bridge of the molecules in hand collected in Table 1.

Table 1 Some structural and spectral parameters of the AA and its halogen substituted analogies obtained on B3LYP/cc-pVTZ level of theory

Molecule	Structural and spectral parameters of hydrogen bridge			
	$l_{O\cdots O}$ [Å]	$l_{O\cdots H}$ [Å]	$\delta_{O-H\cdots H}$ [deg]	ω_{O-H} [cm^{-1}]
AA	2.53302	1.61394	149.56	2997
AA-Br_6	2.54906	1.65570	146.97	3175
AA-Cl_6	2.55650	1.66595	146.58	3183
AA-F_6	2.57490	1.69249	145.41	3197
AA-Br_3	2.53311	1.61411	148.78	3009
AA-Cl_3	2.53454	1.62001	148.17	3012
AA-F_3	2.53607	1.62890	147.68	3022

As one can see substitution by halogen atoms leads to the weakness of the H-bond in AA. The length of the hydrogen bridge increase in sequence Br, Cl, F. Simultaneously, in accordance with this sequence the frequency of the stretching O-H vibration, is rising. To analyze more careful O-H group vibrations some anharmonic calculations, as well as calculations with potential energy surface, were made too.

MULTIPULSE TRANSIENT ABSORPTION SPECTROSCOPY OF FUCOXANTHIN: REVELATIONS THROUGH PERTURBATIONS

Robert G. West[1], Marcel Fuciman[1], David Bína[2], Hristina Staleva[1], Radek Litvín[2], Tomáš Polívka[1,2]

[1]Faculty of Science, University of South Bohemia, Czech Republic
[2]Institute of Plant Molecular Biology, Czech Academy of Sciences, Czech Republic
rwest@prf.jcu.cz

Without carotenoids as spectral sensitizers and photoprotectors, light harvesting systems of plants, alga, and other photosynthetic organisms would not survive in the light conditions in which we see them thrive. Primarily, these pigments efficiently transfer energy of absorbed light to nearby pigments, such as chlorophylls, in the first step of most photosynthetic processes. In some systems this efficiency is achieved through a frequently-debated S_1/ICT state which recently has been revealed to be two coupled states.[1] The mystery is how these coupled states are involved in the energy transfer process and how to quantify their equilibration process. Multipulse transient absorption spectroscopy makes it possible to perturb the equilibrium by prematurely removing a population of one state in order to observe hidden and concomitant processes as well as energy transfer pathways. Featured here are pump-dump-probe studies on fucoxanthin in various environments and in Fucoxanthin Chlorophyll-a Protein (FCP) antenna, revealing their effects on equilibration dynamics between S_1 and ICT states. Quantification of these processes as well as hints toward preferred donor state in FCP was revealed by global analyses and a Monte-Carlo approach to kinetic trace analysis.

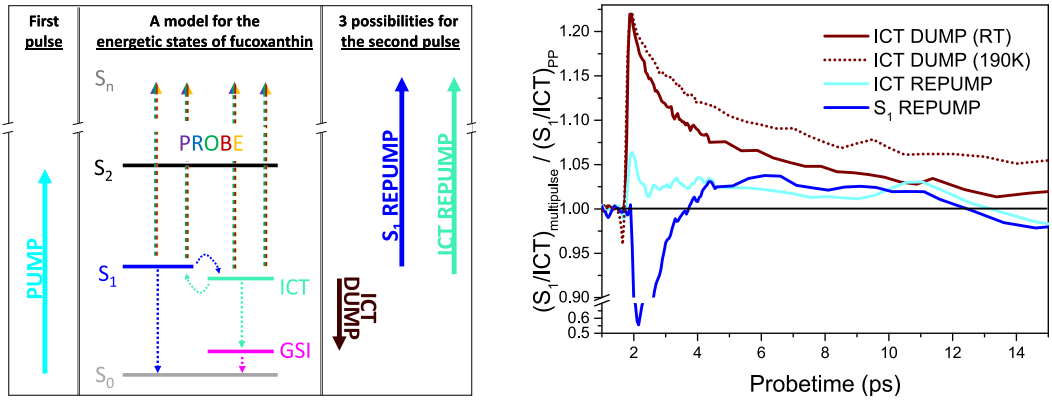

Fig. 1. A schematic of the energetic states of a carbonyl carotenoid at the time of the perturbation (left). Manipulation of kinetic traces of the S_1 and Intramolecular Charge Transfer (ICT) state signature bands in Fucoxanthin in methanol. The ratio of the ratio of S_1 to ICT state band traces, multipulse regime to pump-probe regime (right). The 190 K data is normalized to RT data.

[1] K. Redeckas, V. Voiciuk, M. vengris, Investigation of the S1/ICT Equilibrium in Fucoxanthin by Ultrafast Pumpdumpprobe and Femtosecond Stimulated Raman Scattering Spectroscopy, Spectroscopy. Photosynth. Res. (2016).

MOLECULAR SPECTRA FROM FIRST PRINCIPLES FOR ACCURATE ATMOSPHERIC AND PLANETARY STUDIES

Nikodem Stolarczyk

Institute of Physics, Faculty of Physics, Astronomy and Informatics, Nicolaus Copernicus University, Torun, Poland
280301@stud.umk.pl

Molecular collisions at microscale are manifested in molecular spectroscopy as a perturbation of the shapes of optical resonances. Analysis of the line shapes constitutes an important tool for studying quantum scattering and testing ab initio molecule-molecule and molecule-atom interactions [1]. A proper treatment of collisional perturbations of the molecular line shapes is necessary for achieving high accuracy in optical metrology, e.g. determination of the Boltzmann constant [2] or exact tests of QED [3]. Furthermore, accuracy of atmospheric measurements of the Earth (e.g. controlling the concentration of greeenhouse gases) and other planets, particullary gas giants, or even opacity of exoplanetary atmospheres requires proper description of the molecular collisional line-shape effects.

To achieve the above goals, recently a new relational structure has been introduced to the most popular line-by-line spectroscopic database HITRAN [4,5], that enables the collisional, beyond-Voight, line-shape effects to be represented properly. It is, however, extremelly challenging to populate the entire database with purely experimental data for enormous ammount of molecular tansitions and thermodynamical conditions (i.e. all the bands, branches, temperature ranges etc.). In my talk I will present the way, the theoretical quantum-scattering calculations are implemented into the flexible structure of modern spectroscopical databases. This approach demonstrated here for the benchmark system of helium-perturbed H_2 lines is applicable to many other molecular systems. The results are also validated on the ultra-accurate experimental data of the H_2-He system [6].

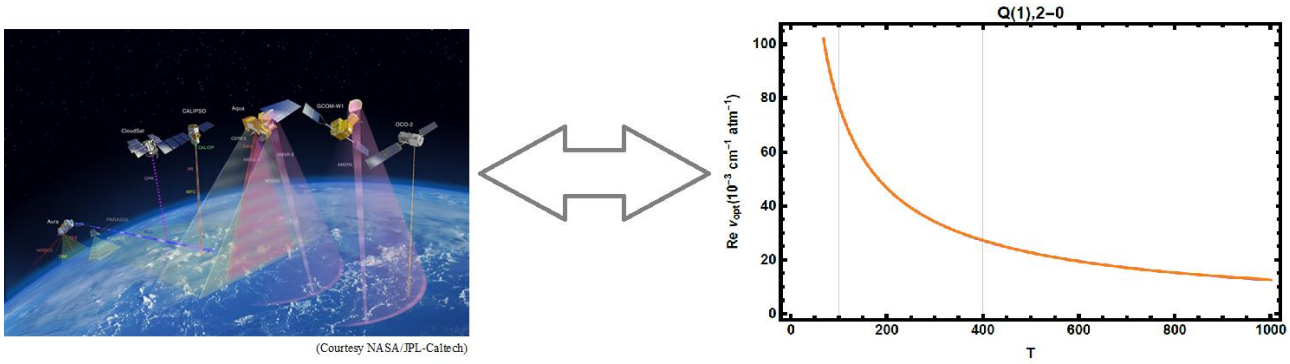

Fig. 1. Accurate reference molecular spectra are required for remote atmospheric studies.

[1] P. Wcisło, F. Thibault, H. Cybulski, and R. Ciuryło, Phys. Rev.A 91, 052505 (2015).
[2] L. Moretti, A. Castrillo, E. Fasci, M. D. De Vizia, G. Casa, G.Galzerano, A. Merlone, P. Laporta, and L. Gianfrani, Phys. Rev. Lett. 111, 060803 (2013).
[3] P. Wcisło et al. , Phys. Rev.A 93.022501(2016).
[4] P. Wcisło, I. E. Gordon, H. Tran, Y. Tan, S.-M. Hu, A.Campargue, S. Kassi, D. Romanini, C. Hill, R. V. Kochanov,and L. S. Rothman, J. Quant Spectrosc. Radiat. Transfer 177, pages 75-91 (2016).
[5] I.E. Gordon et al. J. Quant. Spectrosc. Radiat. Transfer 203, pages 3 - 69 (2017).
[6] P. Wcisło et al. , in preparation.

COMBINED EXPOSURE LASER RADIATION AND MAGNETIC FIELD FOR OXYGENATION OF BIOLOGICAL TISSUE

Anastasia Tabolich [1*], Mustafo Asimov[2]

[1] Department of laser physics and spectroscopy, Belarus State University, Minsk.Belarus
[2] Institute of physics named after B. I. Stepanov of NAN Belarus, Minsk, Belarus
nastya.tabolich@mail.ru

Biophotonics at low intensity laser radiation are scientifically interesting because of several reasons: 1) in recent years, has grown interest professionals to the problems of minimizing the negative impact on the human body in the treatment of cancer; 2) there is no single comprehensive study on exposure to optical radiation and magnetic field in conjunction with acoustic waves to accelerate the metabolism of cells when they are hypoxic; 3) With the accelerated growth of technological progress, the urgent need is study use and combine different techniques to achieve a specific goal.

In this work we will presentasemi the combined technology of tissue oxygenation to investigate elimination of local hypoxia and the modification of the intratumoral transport of oxygen via photodissociation complex oxyhemoglobin (HbO_2).

In recent years more and more attention is paid to physical methods of treatment in spite of the fact that as T.I. Grushina (2013) fairly emphasized, "the physiotherapy and an oncology were the incompatible fields of medicine until recently". Now the situation began to change radically as evidential works in which it is convincingly shown that physical methods at the combined application with radio - and a chemotherapy improve results of treatment of tumors and quality of life of patients with malignant new growths began to appear. One of such physiotherapeutic methods is magnetotherapy which in various options and technologies already finds application or is actively approved as a component of complex therapy of tumoral processes. [1]

From the literature it is known that the widely held clinical-physiological studies of the effects of electromagnetic fields on humans, and that magnetic therapy increases blood flow and as a consequence of the oxygenation of biological tissue. [2] But despite extensive study of magnetic therapy at this stage studies of its impact on the oxygenation havn't. It was therefore decided to conduct the study and to determine the contribution of the magnetic field on the saturation of cells with oxygen. It was shown that after ten minutes of exposure to a biological tissue (hand) the amount of oxygen increased in 1.85 times. This suggests that the experimental data are fully consistent with the theory. It was found that in the transition from a wavelength of λ =670 nm to the infrared region of reduced therapeutic effect. From which it follows that for efficient photodissociation of oxyhemoglobin is necessary to choose the wavelength of radiation in the absorption bands.

According to the currently available literary data, it can be argued that the proposed method will be essential in the treatment of cancer diseases Advantage the proposed method is the locality of the impact.

The results obtained in this study are significantly new in comparison with the data available to us according to the known sources.

[1] A. Pletnev,V.Ulaschik, Magnetic fields in experimental and clinical oncology (Belarus,2016)

[2] C. L.Mackall et al. A pilot study of consolidative immunotherapy in patients with high-risk pediatric sarcomas, Clinical Cancer Research **14**, 4850-4585 (2008).

STATISTICAL INSIGHTS INTO THE CHEMICAL BONDING IN CRYSTAL STRUCTURES

Andrius Merkys[1,2], Antanas Vaitkus[1], Saulius Gražulis[1,2]

[1]Vilnius University Institute of Biotechnology, Saulėtekio 7, LT-10257 Vilnius, Lithuania
[2]Vilnius University Faculty of Mathematics and Informatics, Naugarduko 24, LT-03225 Vilnius, Lithuania
andrius.merkys@gmail.com

Methods of crystal structure determination, most prominent of them being X-ray crystallography, provide exact 3D coordinates of the atoms that constitute crystal structures. Chemical bonding, which is usually of interest to the chemists, is not captured by crystal structure determination methods and has to be inferred from the coordinates of the atoms. Usually, two atoms are assumed to be connected by a chemical bond if the distance between them is shorter than the sum of their element-specific bonding radii, typically covalent radii, that is an usual radius of an atom in a covalent bond. This method has been known at least since the publications of William Lawrence Bragg [1]. However, there is no one univocal table of covalent radii as the methodologies for defining and deriving them differ strongly. It has been noted that clear distinctions exist in the distance distributions of atom pairs, allowing to differentiate between bonded and non-bonded interactions. Unpopulated ranges correspond to the so-called van der Waals gap, a region of energetically unfavourable interatomic distances, which may in some cases be contaminated due to the presence of non-covalent interactions. Furthermore, distance distributions of some elements, such as alkaline elements, copper, silver, mercury, iron, tin to name a few, do not have such a clear van der Waals gap and pose a difficulty in fitting them to the aforementioned approach [2]. Nevertheless, distance criterion for connectivity is widely used, and covalent radii for problematic elements have been approximated. We have made an attempt to investigate the bonding radii of atoms using a statistical approach. Distances between nearest neighbouring atoms, as established by 3D Voronoi tessellation of the crystal [3], were measured in each of the 380 000 crystal structures in the Crystallography Open Database (COD, http://www.crystallography.net) [4] and pooled together for analysis. Limiting observations to those of the neighbouring cells of Voronoi tessellation allowed to curb the most of the non-informative random distribution of long distances without the need of artificial cut-offs. Visual analysis of the resulting histograms reveal clearly separated high density regions corresponding to the covalent and van der Waals interactions as well as other features with chemical meaning. To identify these features, automatic unsupervised statistical methods [5] could be harnessed.

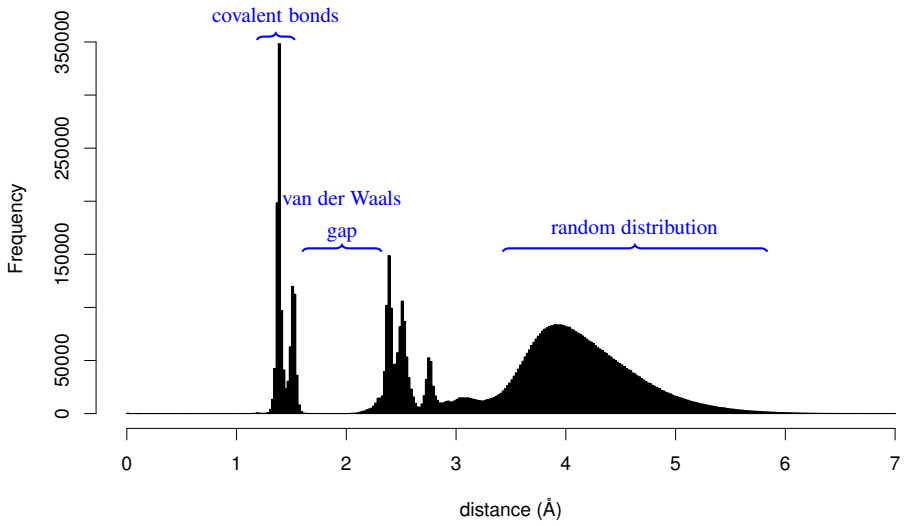

Fig. 1. Histogram of carbon–carbon distances in the COD

[1] Cordero, B.; Gómez, V.; Platero-Prats, A. E.; Revés, M.; Echeverra, J.; Cremades, E.; Barragán, F. & Alvarez, S. Covalent radii revisited Dalton Transactions, 2008, 2832-2838
[2] Alvarez, S. A cartography of the van der Waals territories Dalton Transactions, 2013, 42, 8617-8636
[3] Olechnovič, K. & Venclovas, Č. Voronota: A Fast and Reliable Tool for Computing the Vertices of the Voronoi Diagram of Atomic Balls Journal of Computational Chemistry, 2014, 35, 672-681
[4] Gražulis, S.; Daškevič, A.; Merkys, A.; Chateigner, D.; Lutterotti, L.; Quirós, M.; Serebryanaya, N. R.; Moeck, P.; Downs, R. T. & Le Bail, A. Crystallography Open Database (COD): an open-access collection of crystal structures and platform for world-wide collaboration. Nucleic Acids Research, 2012, 40, D420-D427, http://nar.oxfordjournals.org/content/40/D1/D420.abstract
[5] Merkys, A.; Long, F.; Murshudov, G. N. & Gražulis, S. Stereochemical statistics in Crystallography Open Database. Acta Crystallographica Section A, 2013, 69, s388-s389, http://scripts.iucr.org/cgi-bin/paper?S0108767313096621

SCANNING ELECTROCHEMICAL MICROSCOPY FOR THE INVESTIGATION OF MUSCLE-DERIVED MESENCHYMAL STEM CELLS

Jurate Petroniene[1], Daiva Bironaite[2], Rokas Miksiunas[2], Lina Mikoliunaite[1], Arunas Ramanavicius[1,3]

[1] Vilnius University, Faculty of Chemistry, Department of Physical Chemistry, Vilnius, Lithuania
[2] Department of Regenerative medicine, State Research Institute Centre for Innovative Medicine, Sauletekio 5, LT08406 Vilnius, Lithuania
[3] State Research Institute Centre for Physical Sciences and Technology, Laboratory of Bio-nanotechnology, Vilnius, Lithuania
E-mail:jurate.petroniene@chf.vu.lt; arunas.ramanavicius@chf.vu.lt

Scanning electrochemical microscopy (SECM) is a electroanalytical technique investigating enzymatic reactions, occurring in enzyme-based biosensors or living cells [1,2]. SECM can be used for the investigations of redox measurements and/or electrical stimulations of the cells. In this study we investigated human skeletal muscle-derived mesenchymal stem cells (MDMSC) and different their populations using SECM. Measurements confirmed that menadione can be a suitable mediator for the MDMSC redox measurements since generate low levels of reactive oxygen species preserving cell viability.

Additionally, vertical cell scan by SECM showed that cells differently responded to various concentrations of menadione by moving the microelectrode vertically approaching the surface of the immobilized on conductive and nonconductive surfaces.

Finally, the MDMSC were exposed to alternating and constant currents on conducting and not conducting surfaces and myogenic differentiation have been investigated.

All together our investigations show that SECM can be applied not only for the investigation of redox processes but also for the stimulation of cell the cells and regulation of differentiation processes. Information about the cell shape was registered by atomic force microscopy [3].

This research is/was funded by the European Regional Development Fund according to the supported activity 'Research Projects Implemented by World-class Researcher Groups' under Measure No. 01.2.2-LMT-K-718 and by S-MIP-17-13

[1] Morkvenaite-Vilkonciene, I., A. Ramanaviciene, and A. Ramanavicius, *9,10-Phenanthrenequinone as a redox mediator for the imaging of yeast cells by scanning electrochemical microscopy.* Sensors and Actuators B: Chemical, 2016. **228**: p. 200-206.

[2] A.Ramanavicius, I. Morkvenaite-Vilkonciene, A. Kisieliute, J.Petroniene, A.Ramanaviciene. Scanning electrochemical microscopy based evaluation of influence of pH on bioelectrochemical activity of yeast cells − Saccharomyces cerevisiae Colloids and Surfaces B: Biointerfaces.Amsterdam : Elsevier Science BV Vol. 149 (2017). p. 1-6. ISSN: **0927-7765;** DOI: **10.1016/j.colsurfb.2016.09.039**

[3] L. Mikoliūnaitė, A. Ramanavičius Functionalised atomic force microscopy for the protein modified surface analysis Advanced materials and technologies: book of abstracts of the 16-th international conference-school, Palanga, Lithuania, 27-31 August 2014. Kaunas: Technologija, 2014. p. 34.ISSN: **1822-7759.**

DETERMINATION OF TRACE ELEMENTS IN ADIPOSE TISSUE OF OBESE PEOPLE BY INDUCTIVELY COUPLED PLASMA OPTICAL EMISSION SPECTROMETRY

Agne Kizalaite*, Aivaras Kareiva, Aleksej Zarkov

Institute of Chemistry, Vilnius University, Naugarduko 24, LT-03225 Vilnius, Lithuania
agne.kizalaite@chgf.stud.vu.lt

There is now a large volume of evidence showing that obesity is strongly associated specifically with a range of comorbid diseases, such as diabetes mellitus, dyslipidemia, cardiovascular disease, hypertension, sexual dysfunction, respiratory diseases and certain cancers. These diseases are very associated with dangerous pathologic changes – metabolic syndrome. The etiology, diagnostic criteria and treatment of metabolic syndrome is still unclear. So metabolic syndrome pathogenesis, diagnostic criteria and treatment still remains relevant medical and scientific problem.

It is well known that metal ions are essential for normal functioning of human organism. Lack of certain microelements can lead to some disorders and diseases. At the same time overdose of metals may lead to the toxic effect and negative influence on human health. Determination of metals in human body tissues and physiological fluids is widely used in medicine with an aim to find the link between metal concentrations and various diseases and to monitor human health [1-3].

Inductively coupled plasma optical emission spectrometry (ICP-OES) is a powerful tool for elemental analysis, which is widely used for the determination of metals in biological and clinical samples [4]. ICP-OES allows determination of about 70 elements with detection limits in ppb range.

The motivation of this work was to try to find some differences in content of trace elements in adipose tissue of obese people with and without metabolic syndrome. Moreover, different layers of adipose tissue were analyzed separately in order to investigate distribution of metals between these layers.

Analyzed adipose tissue samples were digested using microwave reaction system with a mixture of nitric acid (HNO_3) and hydrogen peroxide (H_2O_2). Al, Ba, Ca, Co, Cu, Cr, Fe, K, Li, Mg, Mn, Na, Ni, Sr and Zn were selected for the quantitative determination. Optimization procedure for chosen analytes was performed prior to measurements by ICP-OES. Influence of such parameters as power, plasma gas flow, nebulizer gas flow, auxiliary gas flow and plasma viewing position on analytical signal strength were investigated. Selection of emission line from the point of view of signal intensity and potential spectral interferences was also performed. For the determination procedure optimal conditions were set for each analyzed element.

The main aim of this work was to develop analytical method for the determination of trace elements in adipose tissue. Comparison of metal content in different layers of adipose tissue of people with and without metabolic syndrome will be discussed in the present work.

[1] J.M. Harrington, D.J. Young, A.S. Essader, et al., Analysis of human serum and whole blood for mineral content by ICP-MS and ICP-OES: Development of a mineralomics method, Biological Trace Element Research **160**, 132-142 (2014).

[2] M.P. Chantada-Vázquez, A. Moreda-Piñeiro, M.C. Barciela-Alonso, P. Bermejo-Barrera, Spectrometric-based techniques for metal-binding protein assessment in clinical, environmental, and food samples, Applied Spectroscopy Reviews **52,** 145-174 (2017).

[3] N.B. Ivanenko, A.A. Ivanenko, N.D. Solovyev, et al., Biomonitoring of 20 trace elements in blood and urine of occupationally exposed workers by sector field inductively coupled plasma mass spectrometry, Talanta **116**, 764-769 (2013).

[4] A. Hanć, I. Komorowicz, M. Iskra, et al., Application of spectroscopic techniques: ICP-OES, LA-ICP-MS and chemometric methods for studying the relationships between trace elements in clinical samples from patients with atherosclerosis obliterans, Analytical and Bioanalytical Chemistry **399,** 3221-3231 (2011).

SYNTHESIS AND CHARACTERIZATION OF UV-CURABLE SOYBEAN OIL AND MYRCENE BASED POLYMERS

Miglė Lebedevaitė[1], Jolita Ostrauskaitė

[1] Department of Polymer Chemistry and Technology, Kaunas University of Technology, Radvilenu Rd. 19, LT-50254 Kaunas, Lithuania
migle.lebedevaite@ktu.lt

UV-curing allows fast, almost instant, transformation of liquid resin into solid material. Thus it is commonly used for curing of thin polymer films in application such as fast drying of varnishes, paints, printing inks and adhesives, as well as in the stereolithographic process.[1]

Bio-based polymeric materials have emerged as an environmentally friendly alternative to petrochemical ones due to their sustainability, lower carbon footprint and often lower cost. Epoxidized soybean oil acrylate (ESOA) resin is an attractive alternative to petroleum-based resins, because it is inexpensive, possess good mechanical and chemical properties, and is derived from renewable resources. ESOA can be cured through its reactive acrylate groups using any appropriate free radical polymerization initiators, including ultraviolet initiators, electron beam curing, high-energy radiation, etc. [2]

Terpenes and terpenoids, synthesized by plants and fungi, constitute a valuable and cheap biomass resource and are easily accessible in large scale from various essential oils or as byproducts from diverse industrial processes.[3,4] Myrcene is an oily liquid extracted from the essential oils of many plants. In industry it is mainly obtained from the pyrolysis of β-pinene [5], which is produced from the distillation of pine tree oil and is already used in many industrial processes. The chemical structure of myrcene contains three highly reactive double bonds, including one conjugated double bond and a single one which act as reactive sites in the applications. [6]

UV-curing of monomer mixtures consisting of ESOA, myrcene and aromatic comonomers, divinylbenzene or vanillin dimethacrylate, in different ratios was carried out using photoinitiator 2,2-dimethoxy-2-phenylacetophenone. The influence of the amount of aromatic comonomer to the reaction kinetics, mechanical and thermal properties of the resulted cross-linked polymers was investigated.

Chemical structure of the cross-linked polymers was confirmed by IR spectroscopy. The insoluble fraction of the photocross-linked polymers was determined by Soxhlet extraction. Mechanical testing of the cross-linked polymer specimens was performed by compression test on a BDO-FB0.5TH (Zwick/Roell) testing machine and by three-point bending test with TA Instruments RSA-G2 Solids Analyzer. Thermogravimetrical analysis was conducted on a Perkin Elmer TGA 4000 instrument. Differential scanning calorimetry analysis was performed on TA Universal DSC Q2000 V24.10 Build 122 instrument.

It was determined that the rate of photocross-linking, mechanical and thermal properties of the photocross-linked polymers strongly depended on aromatic comonomer structure and their amount in reaction mixture. Polymers with bio-based vanillin dimethacrylate showed better mechanical properties, higher amount of insoluble fraction and higher glass transition temperatures than those of polymers with synthetic divinylbenzene. The better mechanical and thermal properties of polymers were obtained when higher amounts of vanillin dimethacrylate were used.

Acknowledgement. Financial support from the Research Council of Lithuania (project No. S-LAT-17-2) is gratefully acknowledged.

[1] A. Javadi, H.S. Mehr, M. Sobani, M.D. Soucek Cure-on-command technology: A review of the current state of the art, Process in Organic Coatings **100** 2016, 2–31.

[2] Behera D., Banthia A. K., Synthesis, Characterization, and Kinetics Study of Thermal Decomposition of Epoxidized Soybean Oil Acrylate, Journal of Applied Polymer Science, **Vol. 109**, 2583-2590 (2008).

[3] A. Corma, S. Iborra, A. Velty Chemical Routes for the Transformation of Biomass into Chemicals, American Chemicals Society **107,** 2007, 2411–2502.

[4] F. R. Marin, C. Soler-Rivas, O. Benavente-Garcia, Z. Castillo, J. A. Perez- Alvarez, By-products from different citrus processes as a source of customized functional fibres, Food Chemistry **100**, 2007, 736–741.

[5] M.B. Kolicheskia, L. C. Coccob, D. A. Mitchellc, M. J. Kaminski Anal, Applied Pyrolysis. **80** 2007, 92-100.

[6] P. A. Robles-Dutenhefner, M. G. Speziali, E. M. B. Sousa, E. N. dos Santos, E. V. Gusevskaya, Selective hydrogenation of myrcene catalyzed by sol–gel Pd/SiO2 Applied Catalysis A: General. **295**, 2005, 52-58.

INFLUENCE OF MOBILE PHASE COMPOSITION ON RETENTION AND EFFICIENCY IN HYDROPHILIC INTERACTION CHROMATOGRAPHY

Inga Baškirova*, Vilma Olšauskaitė, Audrius Padarauskas

Department of Analytical and Environmental Chemistry, Vilnius University, Lithuania
inga.baskirova@chf.stud.vu.lt

Hydrophilic interaction chromatography (HILIC) is a feasible alternative for the analysis of highly polar and ionized compounds that are poorly or even not retained in reversed-phase chromatography [1]. This separation technique uses a polar stationary phase (for example, unmodified silica or a polar bonded phase) in conjunction with a polar mobile phase containing more than 60-70% organic solvent (typically acetonitrile) in aqueous buffer. Although HILIC has been widely applied, the retention mechanism in this separation mode is still under debate [2]. The primary retention mechanism is believed to be partitioning of the analytes between a water layer adsorbed on the surface of the hydrophilic stationary phase and the less polar bulk mobile phase. However, secondary interactions such as hydrogen bonding, ionic and even hydrophobic can also occur depending on the nature of the analyte, stationary and mobile phases [3]. If the sample contains a large number of the analytes having different properties then it becomes difficult to predict their chromatographic behaviour.

The aim of the current work was to investigate the effect of mobile phase composition on the chromatographic behaviour of anionic, cationic and neutral compounds under hydrophilic interaction chromatography conditions using bare silica stationary phase.

HILIC separations were performed on a Waters Acquity UPLC system (Waters, Milford MA, USA) equipped with an Acquity UPLC photodiode array detector (PDA). Acquity UPLC BEH HILIC column (2.1×100 mm, 1.7 μm, Waters) was used in the experiments. We selected six compounds (acetylsalicylic acid, creatinine, nicotine, nicotinic acid, acetaminophen and uracil) as model analytes to examine the retention and efficiency properties of the mobile phases.

The effect of three organic solvents, namely acetonitrile (ACN), methanol (MeOH) and isopropanol (IPA) on the chromatographic behaviour of the analytes was investigated. For all analytes the eluting strength follows the order: ACN < IPA < MeOH, which is correlated with the different hydrogen bonding abilities of the solvents. Polar protic solvents (MeOH and IPA) can be both donor and acceptor of hydrogen bonds and aprotic ACN can be only hydrogen bond acceptor. Consequently, protic solvents can more effectively compete for polar active sites on the surface of stationary phase, replacing water molecules and thus producing a more hydrophobic surface. For all analytes acetonitrile provided the highest peak efficiency.

As expected, all coumpounds exhibited typical HILIC behaviour of increasing retention with increasing ACN content in the mobile phase. The retention for the charged analytes were much more strongly affected by ACN concentration than for the neutral compounds. This is possibly due to enhanced secondary analyte/stationary phase interactions (e.g., hydrogen bonding and electrostatic interactions) which may become predominant as water content decreases.

Minimal changes in retention and efficiency of neutral compounds were observed upon changing pH (3-7) and ammonium acetate buffer concentration (0-10 mmol/L). The efficiency of charged analytes significantly increased with increasing pH and buffer concentration. The changes in retention for cationic and anionic compounds with increasing pH and buffer concentration were in the opposite direction. The retention of anions increased, whereas an opposite trend was observed for cationic analytes.

Obtained results showed that the three mobile phase parameters (concentration of organic solvent, pH and buffer concentration) enabled manipulation of the retention and efficiency of analytes with different charge state and should be useful for optimization of mobile phase during HILIC method development.

[1] B. Buszewski, S. Noga, Hydrophilic interaction liquid chromatography (HILIC) - a powerful separation technique, Anal. Bioanal. Chem. **402**, 231-247 (2012).
[2] P. Hemstrom, K. Irgum, Hydrophilic interaction chromatography, J. Sep. Sci. **29**, 1784-1821 (2006).
[3] A. E. Karatapanis, Y. C. Fiamegos, C. D. Stalikas, A revisit to the retention mechanism of hydrophilic interaction liquid chromatography using model organic compounds. J. Chromatogr. A **1218**, 2871-2879 (2011).

ELECTROCATALYTIC HYDROGEN EVOLUTION ON ELECTRODEPOSITED MOLYBDENUM ALLOYS

Edita Vernickaitė[1], Oksana Bersirova[2], Natalia Tsyntsaru[1,3], Henrikas Cesiulis[1]

[1] Department of Chemistry and Geosciences, Vilnius University, Lithuania
[2] V.I. Vernadskii Institute of General & Inorganic Chemistry, Ukraine
[3]Institute of Applied Physics of ASM, Moldova
edita.vernickaite@chf.stud.vu.lt

Hydrogen evolution technology is considered as a key element for a sustainable economic growth and generation of a clean energy [1]. As usually precious platinum is typically applied in electrocatalytic systems for hydrogen evolution reaction (HER), the development of new cost effective and durable materials, which possess high catalytic activity for HER, is necessary. The metallic Mo or its alloys can be used as active electrodes for hydrogen evolution [2-4]. This kind of electrodeposits can be obtained by using non-aqueous and molten salt electrolytes [5]. Unfortunately, the pure Mo deposits cannot be obtained from aqueous molybdate solutions. Only by induced co-deposition process with iron group metals (Ni, Co, Fe) the Mo alloys with high content of refractory metal in the alloy can be obtained [6].

In this study Mo-rich Ni-Mo, Co-Mo, Fe-Mo alloys were electrodeposited onto copper substrates from highly concentrated acetic electrolyte and characterized in terms of their morphology and composition in the view of possible application for HER in alkaline solution. Smooth, globular and crack-free coatings containing ~ 52 at.% Mo in their composition were obtained under galvanostatic mode at 30 mA/cm^2 at 30 °C. At the higher current densities the cathodic current efficiency decreases dramatically and extremelly high percentage of oxygen is incorporated into alloys' composition.

Electrocatalytic activity towards cathodic hydrogen evolution in 30 % NaOH solution at the temperature range of 25÷65 °C on the electrodeposited Co-52at.%Mo, Fe-54at.%Mo and Ni-54at.%Mo alloy coatings was evaluated by means of voltammetry technique. It was found that the exchange current density of hydrogen evolution reaction for Co-52at.%Mo and Fe-54at.%Mo deposits was considerably higher than for Ni-54at.%Mo alloy coatings. A significant improvement of catalytic activity for all tested coatings with increasing of the temperature was noticed (Fig.1).

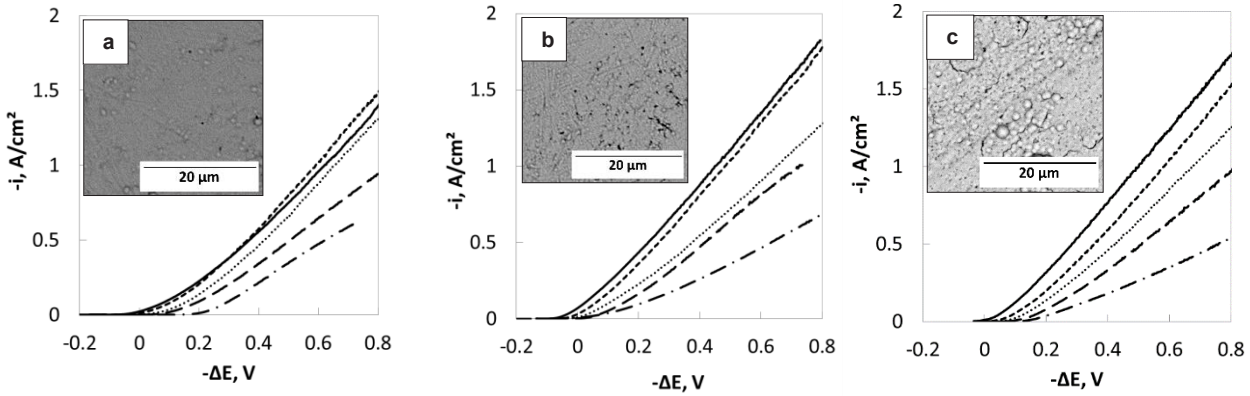

Fig. 1. Effect of temperature on cathodic polarization curves for (a) Ni-54at.%Mo, (b) Co-52at.%Mo, (c) Fe-54at.%Mo electrodes in 30 wt.% NaOH, scan rate 2 mV/s.

- - 25 °C, --- 35 °C, ····· 45 °C, ····· 55 °C, — 65 °C.

Extrapolation of the polarization curves obtained at different temperatures, in the coordinates ln$i$ - ΔE to value ΔE=0 makes it possible to determine the exchange currents densities (ECD) that describe the ability of electrode to reduce hydrogen ions from electrolyte. In this study, the highest calculated ECD value for HER at 65 °C (~ 0.45 A/cm^2) was demonstrated for Co-52Mo and Fe-54Mo alloy coatings. Moreover, Fe-54at.%Mo and Co-52at.%Mo electrodes are characterized by slightly lower activation energy, respectively 26.5 and 27.0 kJ/mol, compared to Ni-54at.%Mo coating (29.9 kJ/mol).

Acknowledgments. Authors acknowledge funding from H2020 project SMARTELECTRODES (No.778357) and the Moldavian national project (15.817.02.05A).

[1] A. Züttel, A. Borgschulte, L. Schlapbach, *Hydrogen as a future energy carrier* (Wiley-VCH Verlag GmbH&Co, KGaA, Weinheim, 2008).
[2] L. S. Sanches, S. H. Domingues, C. E. B. Marino, L. H. Mascaro, Characterisation of electrochemically deposited Ni–Mo alloy coatings, Electrochemistry Communications **6**, 543–548 (2004).
[3] J. M. Jakšic, M. V. Vojnovic, N. V. Krstajic, Kinetic analysis of hydrogen evolution at Ni-Mo alloy electrodes, Electrochimica Acta **45** 4151-4158 (2000).
[4] N. R. Elezovic, V. D. Jovic, N. V. Krstajic, Kinetics of the hydrogen evolution reaction on Fe–Mo film deposited on mild steel support in alkaline solution, Electrochimica Acta **50** 5594–5601 (2005).
[5] N. Ene, C. Donath, Texture of electrolytic Mo deposition from molten alkali halide, Journal of Optoelectronics and Advanced Materials **8** (2) 708-711 (2006).
[6] A. Brenner, *Electrodeposition of Alloys* (Academic Press Inc., New York, 1963).

PHOTORHEOMETRICAL STUDY OF CROSS-LINKING KINETICS OF ACRYLATED SOYBEAN OIL AND SQUALENE HEXATHIOL

Deimantė Valaitytė, Sigita Kašėtaitė, Jolita Ostrauskaitė*

Department of Polymer Chemistry and Technology, Kaunas University of Technology, Kaunas, Lithuania
E-mail: *jolita.ostrauskaite@ktu.lt

The recent development of polymeric materials derived from renewable raw materials attracts the attention of both scientists and manufacturers due to the continuous rise of consumer needs for plastics and rapidly depleting oil reserves. Vegetable oils are potential starting materials for the preparation of polymers due to their ready availability, inherent biodegradability, limited toxicity, and existence of modifiable functional groups [1]. Thiol-ene addition reaction was selected for the synthesis of acrylated soybean oil-based polymers due to its high conversion, fast reaction rates, low oxygen inhibition, and good tunability of the resulting polymer networks [2]. Hexathiol derived from squalene was selected as a curing agent in this reaction. Squalene is a triterpenoid found in shark liver, in wheat germ, and in olive oil. It is produced industrially from the olive oil. Polyunsaturation of this compound make it a very attractive candidate to use it in the preparation of biobased polymers [3].

The aim of this work was the investigation of cross-linking kinetics of acrylated soybean oil (ASO) with squalene hexathiol (SH6) by real-time photorheometry. Photorheometry allows to monitor typical rheological properties such as viscosity and shear modulus while a material is irradiated with UV and/or visible light. Rheometric evaluation of photocuring kinetics provides a more physical complement to traditional chemical kinetics measurement techniques such as photo-DSC or real-time IR spectroscopy [4].

Two photoinitiators, 2-hydroxy-2-methylpropiophenone (HMP) and ethylphenyl (2,4,6-trimethylbenzoyl) phosphinate (TPOL) in different quantities were monitored in photocross-linking of acrylated soybean oil with squalene hexathiol by a MCR302 rheometer from Anton Paar equipped with UV/Visible spot curing system OmniCure S2000 and the plate/plate measuring system.

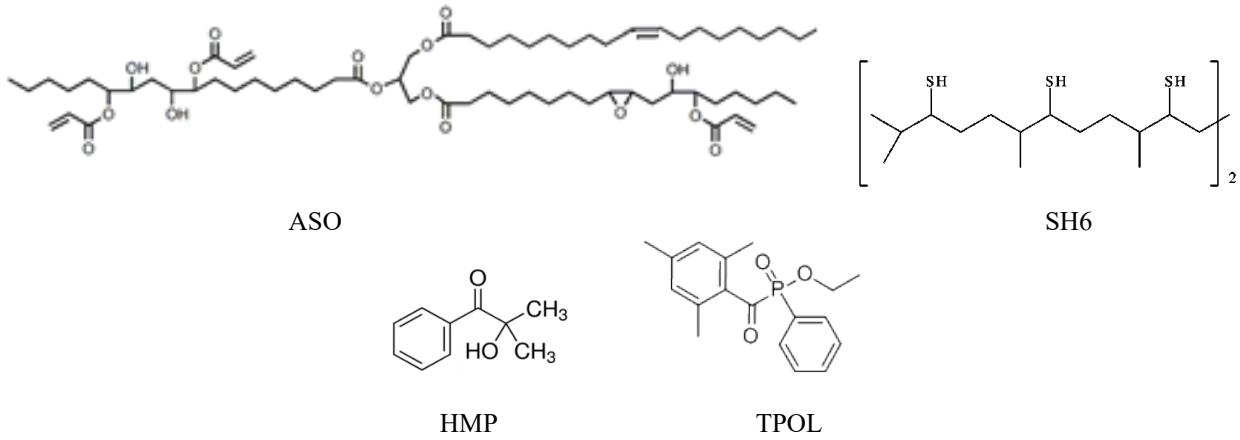

Fig. 1. Chemical structure of monomers and photoinitiators used in this study.

It was determined that photocross-linking of both studied systems was faster when the amount of photoinitiator was higher. The values of storage modulus G‘ and loss modulus G“ depended on the concentration of photoinitiator. The higher concentration of photoinitiator caused the higher values of modules G‘ and G“ and thus the more rigid cross-linked polymers were obtained. The rate of photocross-linking was higher when TPOL was used as photoinitiator.

Acknowledgement. Financial support from the Research Council of Lithuania (project No. S-LAT-17-2) is gratefully acknowledged.

[1] L.Fertier, H. Koleilat, M. Stemmelen et al., The use of renewable feedstock in UV-curable materials - a new age for polymers and green chemistry, Progress in Polymer Science **38**, 932-962 (2013).
[2] C.E. Hoyle, C.N. Bowman, Thiol–Ene Click Chemistry, Angewandte Chemie **49**, 1540-1573 (2010).
[3] R. Acosta Ortiz, E.A. Obregón Blandón, R. Guerrero Santos, Synthesis of novel hexathiolated squalene and its thiol-ene photopolymerization with unsaturated monomers, Green and Sustainable Chemistry **2** (2012), Article ID: 19003, DOI:10.4236/gsc.2012.22011.
[4] J.D. Schall, A.F. Jacobine, J.G. Woods et al., Photorheometry: A tool for characterizing high-performance adhesives and coatings, Abstracts of Papers of the American Chemical Society **97**, 941-942 (2007).

MIGRATION OF ADDITIVES FROM COMMERCIAL POLYPROPYLENE PACKAGES

Toma Petrulionienė[1], Evaldas Naujalis[1]

[1] Department of Metrology, State research institute Center for Physical Sciences and Technology, Lithuania
toma.petrulioniene@ftmc.lt

Recently there has been growing interest in plastics research. Because of the excellent chemical and physical properties plastics are used in many fields. Polypropylene (PP) is one of the most extensively used polymer as it exhibits excellent chemical resistance, high tensile strength and low density. In order to improve the properties of the plastics, during the manufacture process, additives such as plasticizers, stabilizers, antioxidants, pigments and other are required to be added. However, all the additives can migrate from the plastics into the food and contaminate it during production or storage.

An objective of this study was to investigate commercial PP packages in order to find out what kind of additives are used most often to manufacture the packages. The PP samples (films for food packaging, candy trays, food preservation bags, plastic jars and etc.) were analyzed by thermal desorption GC/MS. Approximately 0.1 g of PP that was cut in to small pieces was inserted into a glass thermal desorption tube. Plugs of glass wool were inserted into the thermal desorption tubes to hold the PP material in the tube. The tubes were sealed with caps made of Teflon, loaded into autosampler and analysed.

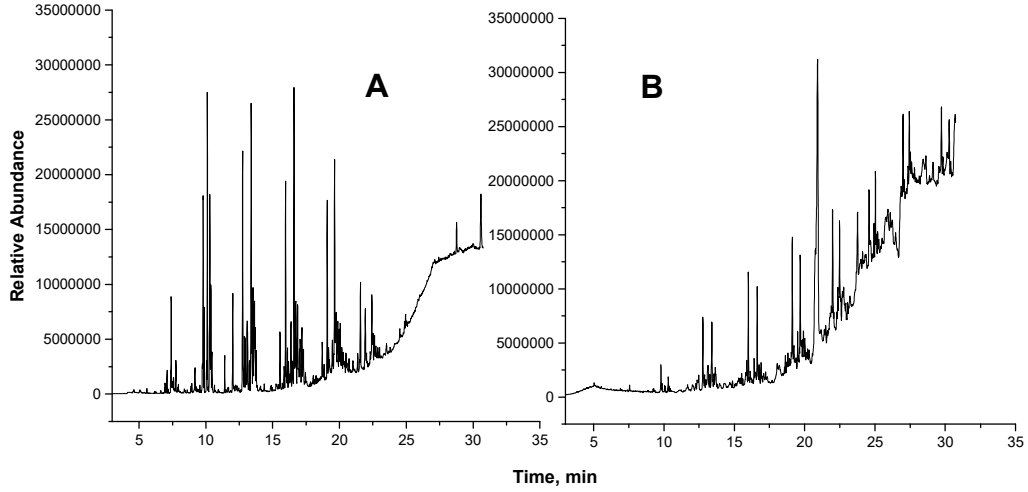

Fig. 1. TD-GC/MS total ion chromatogram of dark colored (A) and light (B) PP packages.

In order to compare the difference between the colored PP packages, it was chosen to analyze light and dark colored packages. Figure 1 shows clear difference between GC-MS chromatograms of different colored PP packages. The potential migrants were identified using *NIST MS Search 2.0* spectra library and were sorted by groups of compound classes such as acids, alcohols, aldehydes, halogenated compounds, hydrocarbons and etc. The most striking result to emerge from the data comparison was that dark colored PP packages release more migrants than light colored PP packages, but it seems that the main migrants are the same. The reason for this is not clear yet but it might be related to the pigments that are used during the manufacture process of dark plastic packages.

However, more research on this topic needs to be undertaken before the association between the migrants and their source of origin could be more clearly understood.

MOLECULAR DIMER ABSORPTION SPECTRA AND EXCITED STATE RELAXATION IN VIBRONIC MODEL

Vytautas Bubilaitis, Olga Rancova, Darius Abramavicius

Institute of Chemical Physics, Faculty of Physics, Vilnius University, Lithuania
vytautasbubilaitis@gmail.com

Nonlinear spectroscopic methods, that were developed in recent decades, enable to observe and analyze the excitation transfer and relaxation in molecular aggregates. For the description of these systems the theoretical models are needed that could help to discern the origin of these effects. Molecular aggregates are interesting because they exhibit properties of both solid state and single molecule. In these aggregates the optical excitation can spread across several molecules or localize. Excitation dynamics in these objects can be described quite well by Frenkel exciton and Redfield relaxation theories.

In some cases, though, such description can be insufficient, particularly, when the molecular aggregate exhibits a resonant oscillation, when frequency of oscillation is close to energy of electronic levels. The vibronic model enables us to account for these oscillations explicitly. Usually molecular aggregate Hamiltonian is divided into parts: system, bath, and system-bath interaction. Then all oscillations are taken as a part of the bath, and are accounted by assuming that the system-bath interaction is weak and second order perturbation theory is applied in relation to this interaction. Vibronic approach expands this description by including the oscillation into the system Hamiltonian explicitly as a harmonic quantum oscillator. The eigenstates of this system Hamiltonian are vibronic states - the excitations that are spread across electronic and vibrational states.

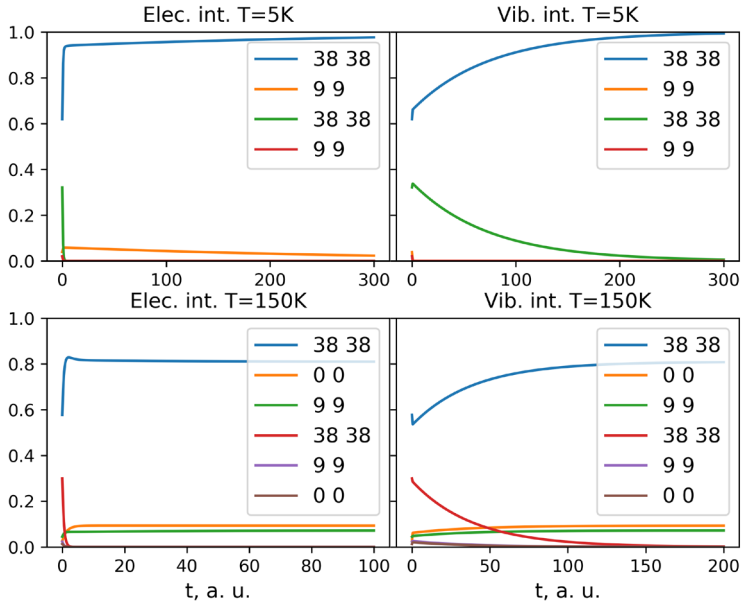

Fig. 1. The relaxation of excited state in dimer with vibronic model. Columns show different kinds of interaction with bath (electronic and vibrational), row show different temperatures. Interaction between molecules J is 600 cm^{-1}, and explicit bath oscillator frequency is 250 cm^{-1}. Legends show what part of state is made of electronic states in percentages, first number first molecule, second number - second.

Vibronic model theory was developed in [1]. In this work this model was applied to calculate absorption spectra for molecular dimer with vibronic model for different parameters. Also the relaxation of excited state in vibronic model was analyzed for molecular dimer. These calculations were made for two cases: when there is only electronic or vibrational interaction with bath.

The results show that the vibronic model is most useful in cases, when the energy gap between electronic excitations is similar to a bath oscillator frequency 1, also that there are two modes of excited state population relaxation: fast and slow, when there is only one type of interaction with the bath (electronic or vibrational).

[1] V. Butkus, L. Valkunas, D. Abramavicius, Vibronic phenomena and exciton-vibrational interference in two-dimensional spectra of molecular aggregates, J. Chem. Phys. 140, 034306 (2014).

MIXTURES OF WATER AND IONIC LIQUIDS: INSIGHTS FROM MOLECULAR DYNAMICS SIMULATIONS

Sonata Kvedaravičiūtė[1], Kęstutis Aidas[1]

[1] Institute of Chemical Physics, Vilnius University, Lithuania
sonata.kvedaraviciute@stud.chf.vu.lt

Room-temperature ionic liquids (IL's), also called liquid salts, are considered to be a promising alternative to conventional organic solvents due to their appealing features such as low vapor pressure, thermal stability, high ionic conductivity. However, due to their high hygroscopicity, it is very difficult to synthesize and maintain pure ionic liquids, therefore it is relevant to study the influence of water on the properties of ionic liquids. Ionic liquids based on 1-butyl-3-methylimidazolium cation, [C4mim], and tetrafluorborate, [BF_4], or chloride, [Cl], anions are highly hygroscopic. Water affects various properties of these ionic liquids, including structural and dynamical parameters on the molecular level [1, 2]. The structure of ionic liquids is not easy to study experimentally as these systems obviously do not possess a periodic lattice. Molecular dynamics (MD) simulations on the other hand is a promising method to determine structural properties of ionic liquid and water mixtures. The main purpose of this study is to analyze structural changes of ionic liquids based on 1-butyl-3-methylimidazolium (Fig. 1) with the increasing water content in these systems. We are thus simulating early stages of the formation of the so called water pockets the existence of which has been earlier predicted theoretically using MD simulations and recently confirmed experimentally [2].

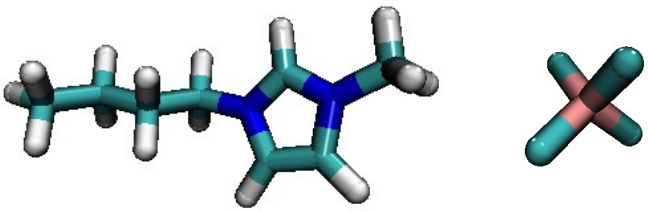

Fig. 1. Ionic pair of 1-butyl-3-methylimidazolium and tetrafluorborate [C4mim][BF_4]

Classical MD simulations of pure ionic liquids [C4mim][BF_4] and [C4mim][Cl] as well as their mixtures with water were conducted using AMBER type of force fields. The force field parameters used for 1-butyl-3-methylimidazolium and the anions were proposed by Liu et al. [3]. Water was represented by a standard TIP3P model. After proper equilibration in the NPT ensemble, final sampling of the trajectory for the duration of a few nanoseconds was performed in the NVT ensemble. AMBER program was used to conduct all the simulations in this work.

Analysis of the recorded trajectories allowed us to investigate structural changes in the local structure of IL with the rising size of the water droplets. Radial and angular distribution functions as well as relevant coordination numbers were obtained, e.g. coordination number for H2 varies from 1.6 (to chlorine) in [C4mim][Cl] to 1.7 for boron atoms in [C4mim][BF_4] for pure ionic liquids. The local structure around the H2 proton in the imidazolium ring of the 1-butyl-3-methylimidazolium as well as around the water molecules was under particular scrutiny.

The authors are grateful to the High Performance Computing Center “HPC Sauletekis” at Faculty of Physics of Vilnius University for computational resources.

[1] A. A. Niazi, B. Rabideau D. & A. E. Ismail. Effects of water concentration on the structural and diffusion properties of imidazolium-based ionic liquid–water mixtures. The Journal of Physical Chemistry B, **117(5)**, 1378-1388 (2013).
[2] K. Saihara,Y. Yoshimura, S. Ohta, A. Shimizu. Properties of water confined in ionic liquids. Scientific reports, **5,** 1-9 (2015).
[3] Z. Liu, S. Huang, W. Wang. A refined force field for molecular simulation of imidazolium-based ionic liquids, The Journal of Physical Chemistry B, **108(34)**, 12978-12989 (2004).

THERMOANALYTICAL AND STRUCTURAL STUDIES ON ALKALINE EARTH METALS SUBSTITUTED $La_2Mo_2O_9$ MATERIALS

Giedrė Gaidamavičienė, Tomas Murauskas, Artūras Žalga

Faculty of Chemistry and Geosciences, Institute of Chemistry, Vilnius University, Naugarduko Str. 24, LT-03225 Vilnius, Lithuania

giedre.prievelyte@chf.vu.lt

Ionic conductors have been attracting considerable attention since they were discovered by Faraday over 200 years ago. Devices such as the solid oxide fuel cell (SOFC) take an interest as the critical step in hydrogen economy. To be technologically viable these oxide electrolytes must exhibit high oxide-ion mobility and low operating temperatures [1–3]. Since Laccore at el. reported $La_2Mo_2O_9$ high ionic conductivity, it has attracted much attention because of its potential application as solid electrolyte (0.06 S/cm at 1073 K) [2].

$La_2Mo_2O_9$ exists in two different crystallographic modifications: monoclinic α phase (P21) that occurs at room temperature with a very low conductivity and cubic β phase (P213), which is stabile above 853 K. After phase transition the anionic conductivity increases sharply by two orders of magnitude. In order to stabilize β-phase of the lanthanum molybdate in low temperatures, K^+, Sr^{2+}, Ba^{2+},Ca^{2+}, Bi^{3+}, V^{5+}, S^{6+}, Cr^{6+}, W^{6+} and other ions can be used to suppress the phase transition to the α-phase. The substitution with lower valence cation (Ca^{2+}, Sr^{2+}) could stabilize the cubic structure of β-phase and increase oxygen-vacancy concentration. This action may lead to higher ionic conductivity and better stability of final ceramic [4–6].

Moreover, it is well-known that transport properties strongly depend on the preparation methods, which are used for the synthesis of polycrystalline powders. Negative effect of these properties can be caused by porosity, impurities and low connectivity between the grains [7], which usually occurs using traditional synthesis technique like solid-state reaction. Meanwhile, using aqueous sol-gel synthesis it is possible both to avoid the limitations described above, and to enhance homogeneity, purity and density of the final ceramics. This method also allows to synthesize different ceramic materials in relatively low temperatures. Besides, using this technology, chemical reaction takes place either in an atomic or molecular levels and long diffusion paths is not necessary. Furthermore, in the sol-gel process using tartaric acid as a ligand it is possible to reduce interactions between the individual components, thus avoiding the formation of precipitates during the gelation process.

In this study, we report environmentally benign and simple method, which is successfully applied for the synthesis of $La_{2-x}M_xMo_2O_{9-\gamma}$ (where, M = Ca and Sr). Besides, in order to investigate both the thermal decomposition of La–M–Mo–O tartrate gel precursors and crystallization temperature of the final double oxide the thermogravimetric analysis and differential scanning calorimetry (TGA-DSC) were performed. The obtained results clearly showed that calcium and strontium doping in the lanthanum site stabilizes cubic β phase of $La_2Mo_2O_9$ at room temperature and no phase transition from meta-stable cubic phase to monoclinic was observed. Additionally, all synthesized materials were analyzed by X-Ray diffraction (XRD) analysis and Raman spectroscopy in order to show the highest doping amount of alkaline earth metal in lanthanum molybdate without secondary phase formation. Furthermore, the morphology of different doped ceramics were investigated by scanning electron microscopy (SEM), which revealed the dense surface formation with individual micrometer sized particles of the samples sintered at 1473 K of temperature.

[1] S. J. Skinner and J. A. Kilner, Oxygen ion conductors, Materials Today, **6,** 30-37 (2003).

[2] P. Lacorre, F. Goutenoire, O. Bohnke, R. Retoux and Y. Laligant, Designing fast oxide-ion conductors based on $La_2Mo_2O_9$, Nature, **404**, 856-858 (2000).

[3] S. Basu, P. Sujatha Devi, and H. S. Maiti, Nb-Doped $La_2Mo_2O_9$: A New Material with High Ionic Conductivity, Journal of The Electrochemical Society, **152**, A2143-A2147 (2005).

[4] A. Khaled, J. J. Pireaux and S. Khelili, Synthesis and Characterization of Ca and Ba Doped LAMOX Materials and Surface Study by X-ray Photoelectron Spectroscopy, Acta Chimica Slovenica, **59**, 766-778 (2012).

[5] A. Kežionis, D. Petrulionis, E. Kazakevičius, S. Kazlauskas, A. Žalga, R. Juškėnas, Charge carrier relaxation phenomena and phase transition in $La_2Mo_2O_9$ ceramics investigated by broadband impedance spectroscopy, Electrochimica Acta, **213**, 306-313 (2016).

[6] Santanu Basu, P.Sujatha Devi, N.R. Bandyopadhyay, Sintering and densification behavior of pure and alkaline earth (Ba^{2+}, Sr^{2+} and Ca^{2+}) substituted $La_2Mo_2O_9$, Journal of the European Ceramic Society, **33**, 79-85 (2013).

[7] D. Marrero-López, J. Pena-Martinez, D. Pérez-Coll and P. Nunez, Effects of preparation method on the microstructure and transport properties of $La_2Mo_2O_9$ based materials, Journal of alloys and compounds, **422**, 249-257 (2006).

PRIMARY AMINES ADDITION TO TRIPLE BOND LEADING TO PRODUCTION OF FUNCTIONALIZED 1,3-DIENES

Lukas Šteinys, Aurelija Urbanaitė, Inga Čikotienė*

Department of Organic Chemistry, Institute of Chemistry, Faculty of Chemistry and Geosciences, Vilnius University, Naugarduko 24, LT-03225, Vilnius, Lithuania
lukas.steinys@chf.stud.vu.lt

2-(1-Alkynyl)-2-alken-1-ones are electron-deficient 1,3-conjugated compounds being able to undergo catalyst-free or catalytic nucleophilic addition reactions [1]. Usually 2-(1-alkynyl)-2-alken-1-ones participate in transition metal-catalyzed or electrophile mediated tandem nucleophilic addition-cyclization or cycloaddition-cyclization reactions to produce polysubstituted furan derivatives [2]. In the literature, there are only several examples about the metal-catalyzed synthesis of polysubstituted pyrroles from 2-(1-alkynyl)-2-alken-1-one oximes [3] or *in situ* generated imines of 2-(1-alkynyl)-alken-1-ales [4].

As a result, our group decided to synthesize several imines of 2-(1-alkynyl)-2-alken-1-ones and investigate their cyclization reactions to corresponding polyfunctional pyrrole derivatives. However, unexpectedly we found that earlier mentioned electron-deficient 1,3-conjugated compounds react with aliphatic primary amines in a highly unusual isomerization-addition manner.

Herein, we describe mild and atom-efficient, regio- and stereoselective addition of aliphatic primary amines to 2-(1-alkynyl)-2-alken-1-ones to obtain polysubstituted (Z)-β-enaminones having cycloalkane rings [5]. The reaction proceeds via double bond migration.

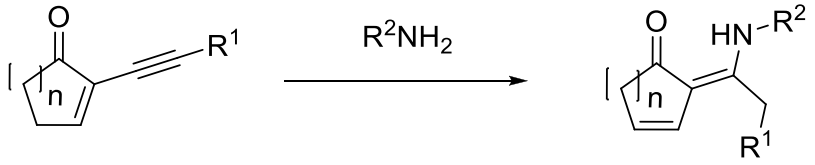

n = 1, 2

R^1 = Ph; 4-$MeOC_6H_4$; 4-FC_6H_4; 4-ClC_6H_4; *n*-Bu

R^2 = *c*-Hex; *t*-Bu; *n*-Bu; *i*-Bu; *i*-Pr; *c*-Pr; Bn; $HC{\equiv}CCH_2$; $H_2C{=}CHCH_2$

Fig. 1. Reaction between 2-(1-alkynyl)-2-alken-1-one and aliphatic primary amine.

[1] a) X. Yu, H. Ren, Y. Xiao, J. Zhang, Chem. Eur. J. **14**, 8481-8485 (2008); b) X. Yu, J. Zhang, Adv. Synth. Catal. **353**, 1265-1268 (2011).
[2] a) T. Yao, X. Zhang, R. C. Larock, J. Org. Chem. **70**, 7679-7685 (2005); b) C.-H. Cho, F. Shi, D.-I. Jung, B. Neuenswander, G. H. Lushington, R. C. Larock, ACS Comb. Sci. **14**, 403-414 (2012).
[3] M. Zhang, J. Zhang, Chem. Commun. **48**, 6399-6401 (2012).
[4] W.-L. Chen, J. Li, Y.-H. Zhu, L.-T. Ye, W. Hu, W.-M. Mo, ARKIVOC **9**, 381-392 (2011).
[5] A. Urbanaitė, L. Šteinys, A. Brukštus, I. Čikotienė, Eur. J. Org. Chem. **2017**, 1624-1627 (2017)

QUANTITATION OF SODIUM DODECYL SULFATE IN THE PRESENCE OF PROTEINS

Andrius Žilionis[1]

[1] Faculty of Chemistry and Geosciences, Vilnius University, Lithuania
andrius.zilionis@chf.vu.lt

Sodium dodecyl sulfate (SDS) is one of the most commonly used detergents in protein chemistry. It has shown benefits for sample preparation, including protein solubilization and denaturation. SDS is typically used at concentrations between 0,1 % and 2 %, but application of 4 % SDS was also reported [1]. However, application of SDS in sample preparation for liquid chromatographic – mass spectrometric (LC-MS) analysis is limited, because SDS is recognized to cause significant chromatographic peak broadening in reversed phase liquid chromatography and signal suppression in electrospray ionization mass spectrometry. Given the advantages of using SDS for protein sample preparation, detergent removal prior to LC-MS analysis is often performed.

It was clearly reported that threshold tolerance of SDS in LC-MS experiments is 0,01 % [2]. Several different strategies can be applied to lower SDS concentration below this level. In order to compare the effectiveness of different SDS removal methods for a given protein sample, a simple and accurate SDS determination method is required. Mukerjee suggested photometric SDS determination method based on organic dye methylene blue and dodecyl sulfate ion pair extraction from aqueous solution to chloroform [3]. This strategy was reported being compatible with a number of biochemical reagents, nucleic acids and proteins [4]. However, our results show that high concentration of protein prevents methylene blue extraction to organic phase (see Fig. 1).

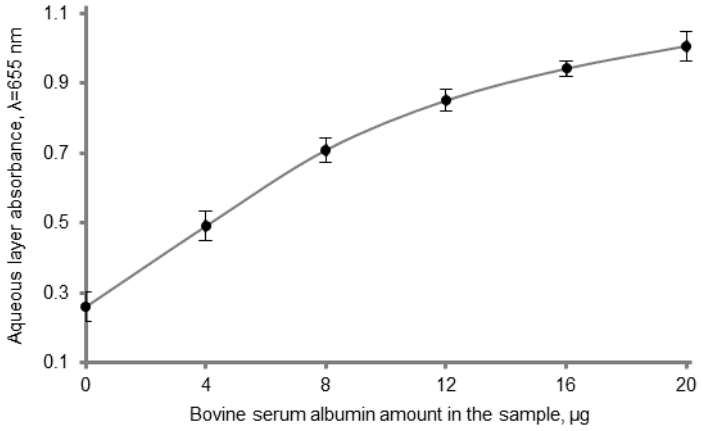

Fig. 1. Influence of bovine serum albumin on methylene blue – dodecyl sulfate ion pair extraction from aqueous solution to chloroform. The standard deviation is indicated by error bars (n=3).

In this work we present a simple modification of Mukerjee's method, which enables SDS concentration measurement in samples initially containing 1.8 mg/ml bovine serum albumin. Our modified method includes cold acetone protein precipitation procedure, which is applied to both protein samples and calibration curve SDS standards before methylene blue – dodecyl sulfate extraction. Protein removal prevents precipitate formation between aqueous and chloroform layers, thus ensuring efficient ion pair extraction. Moreover, we measured absorbance of the aqueous layer instead of measuring absorbance of organic phase. This is in contrast to reported procedures, but aqueous layer is compatible with disposable polystyrene cuvettes while chloroform requires cuvettes made of glass. The method reported is accurate (relative error < 7 %) and relative standard deviation is less than 5 % (n = 8). The concentrations and the volumes of reagents were optimized so that the method is suitable for monitoring of SDS at concentrations between 0.002 % and 0.025 %. The method was successfully used for comparison of different SDS removal strategies.

[1] J. R Wisniewski, A. Zougman, N. Nagaraj, M. Mann, Universal sample preparation method for proteome analysis, Nature Methods **6**, 359-362 (2009).
[2] D. Botelho, M. J. Wall, D. B. Vieira, S. Fitzsimmons, Fang Liu, A. Doucette, Top-down and bottom-up proteomics of SDS-containing solutions following mass-based separation, Journal of Proteome Research **9**, 2863-2870 (2010).
[3] P. Mukerjee, Use of ionic dyes in the analysis of ionic surfactants and other ionic organic compounds, Analytical Chemistry **28**, 870-873 (1956).
[4] M. Arand, T. Friedberg, F. Oesch, Colorimetric quantitation of trace amounts of sodium lauryl sulfate in the presence of nucleic acids and proteins, Analytical Biochemistry **207**, 73-75 (1992).

ADSORPTION OF CAFFEIC ACID ON CHITOSAN MICROGRANULES

Greta Zambzickaite, Dovile Liudvinaviciute

Department of Polymer Chemistry and Technology, Kaunas University of Technology, Lithuania
greta.zambzickaite@yahoo.com

Caffeic acid (CA), a phenolic acid present in numerous dietary plants, was shown to exhibit antioxidant, anti-inflammatory, and anticancer activities [1]. Being hydroxycinnamic acid derivative CA has a high antioxidant activity due to the presence of conjugated double bonds in the side chain. However, the presence of unsaturated bonds in the molecule also determines the instability of CA. Different methods are used to protect bioactive phenolic compounds from oxidative damage. One of them is the formation of complexes with natural polysaccharides, such as chitosan (CH). In acidic medium CH amino groups are protonated, and can form ionic complexes with negatively charged compounds.

The purpose of the present investigation was to evaluate the equilibrium adsorption of CA onto CH microgranules at different temperatures, as well as to assess the antioxidant properties of obtained complexes.

In the adsorption study aqueous CA solution at pH equal to 3.20 ± 0.1 was poured over CH microgranules, flask was stoppered and shaken for 120 min at different temperatures. Then the mixture was filtered through a paper filter, and UV absorbance intensity of the filtrate at λ_{max}=316 nm was measured for the determination of CA concentration by using calibration curve.

The obtained adsorption isotherms of CA onto CH at different temperatures are presented in Fig. 1, and show that amount of adsorbed CA decreased with an increase of the adsorption temperature. The mathematical adsorption models have been used to assess the adsorption data, and the thermodynamic characteristics have been determined.

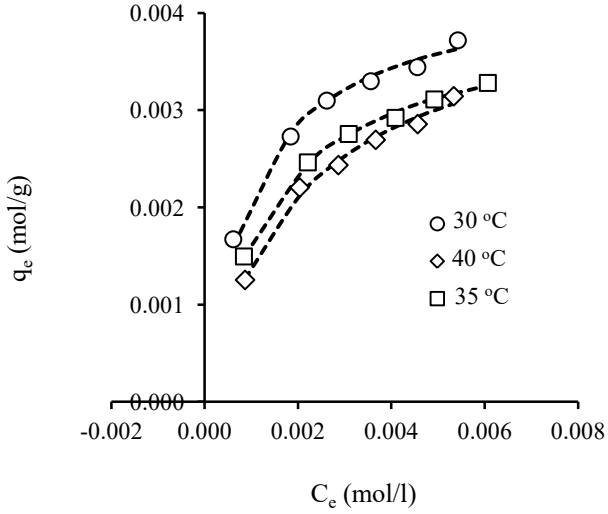

Fig. 2. Adsorption isotherms of CA onto CH microgranules at different temperatures. Symbols represent experimental data and dashed lines represent fitted curves of the Langmuir adsorption model.

Analysis of the Langmuir, Freundlich, Dubinin-Radushkevich and Temkin adsorption models parameters demonstrated that CA is adsorbed on the ionized amino groups of CH due to electrostatic interactions between the latter groups and the carboxylic group of CA. Adsorption proceeded moderately difficult and the physical forces also played a role in the adsorption process. Analysis of thermodynamic parameters of adsorption showed that CA adsorption on CH was spontaneous. However, the negative values of changes in Gibbs free energy decreased with an increase of adsorption temperature. The negative values of the changes of enthalpy and entropy implied that adsorption was endothermic process, and the order of systems during the course of adsorption increased.

The adsorption of CA onto CH microgranules was confirmed by FT-IR spectroscopy. Desorption of CA from CA-CH microgranules as well as antioxidant activity of complexes were also investigated.

Acknowledgment. The authors are grateful to the Research Council of Lithuania for the financial support of the project MIP-055/2015.

[1] F. Natella, M. Nardini, M. Di Felice, C. Scaccini, Benzoic and cinnamic acid derivatives as antioxidants; structure-activity relation, Journal of Agriculture and Food Chemistry, **47**, 1453–1459 (1999).

THE INVESTIGATION OF AMYLOID AGGREGATES USING VIBRATIONAL SUM-FREQUENCY GENERTION SPECTROSCOPY

Edvinas Navakauskas[1], Simona Strazdaitė[1], Rima Budvytytė[2], Ilja Ignatjev[1], Gintaras Valinčius[2], Gediminas Niaura[1]

[1]Fizinių ir technologijos mokslų centras, Saulėtekio al. 3, LT-10257 Vilnius

[2]Vilniaus universitetas Gyvybės mokslų centras, Saulėtekio al. 7, 10223 Vilnius

Edvinas.Navakauskas@gmail.com

The formation of amyloid fibrils in cells and/or an intercellular net from primary disordered proteins is associated with more than 40 different clinical conditions such as Alzheimer's disease, Parkinson's disease, and type II diabetes. Amyloid β-protein (Aβ) is a normal product of cellular metabolism derived from the amyloid precursor protein (APP) by the successive action of the β- and γ-secretases [1]. Its elimination processes operating in parallel usually counterbalance this production of Aβ. When these production and elimination processes are disbalanced, proteins form different aggregates: small soluble oligomers and insoluble polymeric fibrils. All these aggregates are accumulating in brains and causing inflammatory processes, cell death, and tissue degradation.

The goal of our study is to investigate the aggregation process of protein on a molecular level. The most relevant question we aim to answer is how does the phospholipidic membrane of the cell influence the structure of the aggregates? It is believed that this interaction greatly affects the aggregation process therefore, it is important to understand how the molecular structure of aggregates changes at each stage of the formation due to the interaction with the membrane. To answer this questions a surface-sensitive spectroscopic method, which would allow probing molecules only in contact with lipid membrane is needed.

Vibrational sum frequency generation (VSFG) spectroscopy is a surface sensitive and molecular specific technique. It is widely recognized non-linear optical spectroscopic tool for studying the conformation and orientation of various adsorbed molecules at diverse interfaces. It is a second-order nonlinear optical process where two pulsed laser beams, one of fixed visible frequency and the other of tunable infrared frequency overlap spatially and temporally at an interface to generate a sum-frequency signal (schematics at fig. 1). The frequency of the generated VSFG signal is the sum of the two incident field frequencies and it is enhanced when the infrared frequency matches the vibrational frequency of the probed molecules. Moreover, VSFG can be used to unambiguously determine the chirality of the molecules. We applied SFG technique to study the structure of Aβ fibrils. We measured the chiral SFG spectrum of Aβ fibrils in Amide I band and NH vibration region. Our results confirmed NMR experiment [2] and showed that these fibrils are formed from parallel β-sheets.

In addition, we use Fourier transform IR (FTIR) spectroscopy to observe a protein aggregation process in the bulk solution. The repeat units in proteins give rise to nine characteristic IR absorption bands (amides A, B and I–VII) [3]. Amide I bands (1600-1700 cm^{-1}) are the most prominent and sensitive vibrational bands of the protein backbone, and they relate to protein secondary structural components.

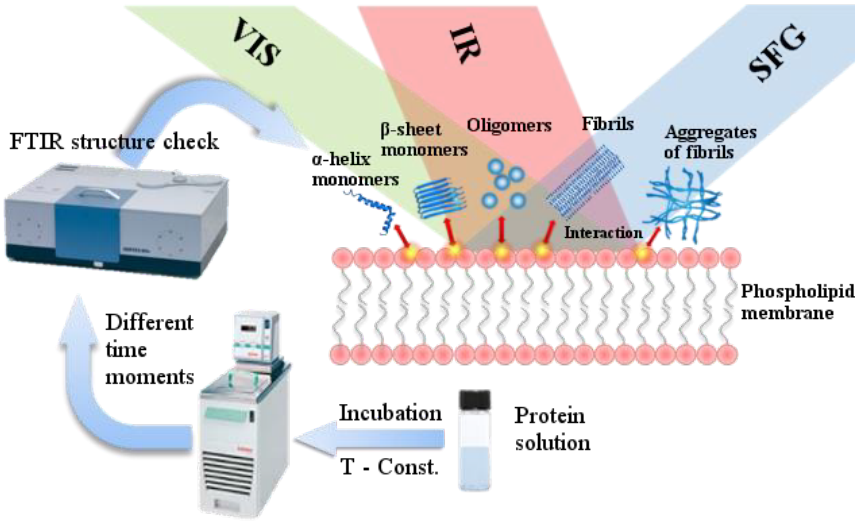

Fig. 1. Schematics showing the protein aggregation and investigation of these aggregates using FTIR and VSFG spectroscopies.

[1] T. Saido , M. A. Leissring. Proteolytic Degradation of Amyloid β-Protein, Cold Spring Harb Perspect Med, 1-13 (2012).
[2] R. Tycko. Solid State NMR Studies of Amyloid Fibril Structure, Annu Rev Phys Chem. 62, 279–299, (2011).
[3] H. Yang, S. Yang, J. Kong, A. Dong, S. Yu. Obtaining information about protein secondary structures in aqueous solution using Fourier transform IR spectroscopy, Nature protocols Vol. 10 No. 3, 382-395, (2015).

SILVER-COATED MONOLITHIC SILICA COLUMN FOR SEPARATION OF TRANS FATTY ACIDS

Vilius Poškus, Vida Vičkačkaitė

Department of Analytical and Environmental Chemistry, Vilnius University, Naugarduko St. 24,LT-03225 Vilnius, Lithuania

poskus.vilius@gmail.com

There is a growing demand from both the industry and academy to increase the performance, reliability and speed of analytical processes for fatty acids determination. The fatty acids contained in fat sample are most commonly measured by gas chromatography after their extraction and conversion into methyl esters derivatives. However, even with the use of long and efficient capillary columns cis/trans isomers of fatty acids are hardly separated and their peaks often overlap. To separate these cis/trans isomers, a pre-separation by silica based silver-ion solid phase extraction (Ag^+ -SPE) can be employed [1]. Monolithic silica columns have greater (through-pore size)/(skeleton size) ratios than conventional silica particle-packed columns (1–2 versus 0.25–0.4), resulting in higher permeability in comparison with particulate columns with a similar number of theoretical plates [2]. The potential of silver ion chromatography in combination with monolithic HPLC columns for the separation and concentration of ω3 long-chain polyunsaturated fatty acids esters have been studied [3]. However, in its ionic state, silver is not stable for a long period of time, especially under the exposure of light. Nevertheless, only a limited number of studies have been reported on the application of metallic Ag nanoparticles (Ag NPs) for separations of unsaturated organic compounds [4].

We have successfully synthesized monolithic silica SPE column by employing the one-pot acid−base two-step reaction catalyzed by acetic acid and hydrolysis of urea. The slow hydrolysis of urea into carbon dioxide and ammonia at 60 °C leads to the base-catalyzed polycondensation. The morphology of the obtained silica monolith was characterized by a scanning electron microscopy. Further, the modification of monolithic silica with aminopropyl groups was achieved by the reaction of (3-aminopropyl)triethoxysilane and silanol groups on the silica surface. Thermogravimetric analysis demonstrated a resolved exothermic peak between 300 and 350 °C due to the pyrolysis of aminopropyl groups. Various techniques of Ag NPs formations on the functionalized monolithic silica surface were applied and investigated. Prepared sorbents were tested for fractionation of rape seed oil fatty acids methyl esters.

[1] V. Poskus, V. Vickackaite, G. Brimas, *Chemija*, **27**(3), 179 (2016).
[2] T. Ikegami, N. Takana, *Annu. Rev. Anal. Chem.*.**9**, 317 (2016).
[3] P. Fagan, C. Wijesundera, *J. Sep. Sci*., **36**, 1743 (2013).
[4] Y. Zhu, K. Morisato, G. Hasegawa, N. Moitra, T. Kiyomura, H. Kurata, K. Kanamori, K. Nakanishi, *J. Sep. Sci*. **38**, 2841 (2015).

FORMATION OF COPPER SULPHIDES ON POLYPROPYLENE MATRIX USING VARIOUS REDUCING AGENTS

Kamilė Vonžodaitė, Eglė Balčiūnaitė, Rasa Alaburdaitė, Edita Paluckienė

Department of Physical and Inorganic Chemistry, Kaunas University of Technology, Lithuania
egle.balciunaite@ktu.lt

Copper sulphides mark a big variety of valuable physical properties. One of the most valuable physical properties that determine wide usage of these compounds is electrical conductivity. Depending on stoichiometric composition, these copper sulphides can be isolators, semiconductors, conductors, and superconductors. They are widely used in advanced technologies, like gas sensors, as polarizers of infrared radiation, galvanic and solar cells, catalysts and other.

Polypropylene (PP) is a chemically resistant, stiff constructive plastic, which is characterized by good dielectric properties. In comparison to other plastics it is one of the lightest and cheapest.

Usage of polymer films, coated with electroconductive layers, has been increasing in the past years due to their elasticity, resistance against corrosion, and low toxicity. Electrically conductive Cu_xS layers on polymers can be prepared by the sorption-diffusion method **Error! Reference source not found.**. By this method, the surface of a polymer is initially treated by a different sulphurization agent and, subsequently, aqueous Cu (I/II) salt solution.

The aim of this study was to form copper sulfide layers on polypropylene films and investigate their properties. The process of forming copper sulfide layers consisted of five stages: surface pre-treatment, oxidation, sulfurization, treatment with Cu(I/II) salt solution, and thermal treatment.

Firstly, PP films were cleaned with ethanol and acetone ultrasonically and were held in an oxidizing solution of $KMnO_4$ for 2–4 h to enhance their adhesive properties [2]. Oxidized samples were sulfurized in an acidic solution of thiourea with ammonium persulfate additive for 1–5 h and treated with $CuSO_4$, using hydroquinone or hydroxylammonium sulfate as a reducing agents. Finally, all samples were thermally treated in an electric oven. Formed copper sulfide layers were investigated by measuring electrical resistivity, using X-ray diffraction, UV spectroscopy, and contact angle measurements.

Based on the experimental' data, the highest UV absorption and the most intense color on the polypropylene film was observed for the samples that were treated with Cu(I-II) for the longest time. X-ray diffraction analysis has revealed that there are traces of Cu_xS and sulphur on the polypropylene films. Additionally, surface wettability changed depending on the treating stage.

[1] R. Alaburdaitė, E. Paluckienė, S. Grevys, Investigation of Cu_xS layers on polypropylene film formed by using different sulfuring agents, Chalcogenide Lett. **13**(12), 529-536 (2016).

[2] J. Wang, Y. Zhu, Y. Fu, Fabrication and properties of $KMnO_4$-treated functionalized biaxially oriented polypropylene (BOPP) films coated with a hybrid material, J Sol-Gel Sci Technol **71,** 176-183 (2014).

MOLECULAR DYNAMICS SIMULATIONS OF DIFFUSION COEFFICIENT OF SEVERAL IMIDAZOLIUM BASED IONIC LIQUIDS

Milda Koreivaitė[1], Kęstutis Aidas[2]

[1]Faculty of Chemistry and Geosciences, Vilnius University, Lithuania
[2]Institute of Chemical Physics, Faculty of Physics, Vilnius University, Lithuania
milda.koreivaite@chf.stud.vu.lt

Ionic liquids are organic salts composed of relatively large asymmetric organic cations and weakly coordinated organic or inorganic anions, and they are characterized by a relatively low melting point. Due to their unique properties, ionic liquids are promising materials for many applications in bio-nanotechnology or chemical industry. They are already now used as nontoxic solvents or electrolytes in high-performance lithium-ion batteries, fuel and solar cells. Large number of ionic liquids with desirable properties can in principle be created by combining different cations and anions. The rational design of ionic liquids can only be achieved if accurate prediction of its properties based solely on the knowledge of the constituent ions is possible. This would open the door for control and optimization of the properties of the newly developed ionic liquids. To this end, the understanding of the structure and dynamics of the ions at the molecular level is indispensable. The main task of present work is to evaluate the temperature dependence of the self-diffusion coefficient of several imidazolium based ionic liquids using classical molecular dynamics (MD) simulations. Our computational predictions are compared to available experimental data.

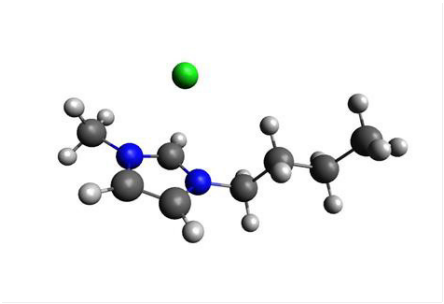

Fig. 1. Ionic pair of 1-butyl-3-methyl-imidazolium and chloride.

We have considered the ionic liquids composed of 1-butyl-3-methyl-imidazolium, C4mim, and four different anions including chloride, iodide, bromide and tetrafluoroborate, BF_4, see Fig. 1 for the structure of [C4mim][Cl] ionic pair. The molecular dynamics simulations are based on classical equations of the motion, and the potential energy function of the system is to be considered in order to solve those equations. We have adopted Amber type force fields for the molecular systems we simulate. The MD simulations were carried out using the AMBER program. The diffusion coefficients were evaluated using the Einstein equation, and the mean-square displacement function was obtained by sampling the trajectory of the simulated system for the duration of 1 ns. Charge reductions scheme was utilized to account for charge transfer intermolecular. We have also applied reduced charge scheme in order to effectively take the intermolecular charge transfer interactions into account. Self-diffusion coefficients of the cations were considered for the temperatures in the range of 283 to 343 K.

We thank the High Performance Computing Center „HPC Sauletekis“ of Vilnius University for providing computational recourses.

SYNTHESIS AND UPCONVERSION PHENOMENON OF $NaYF_4$ MICROPARTICLES DOPED WITH VARIOUS LANTHANIDES

Iveta Jasmantaite, Simas Sakirzanovas

Department of Applied Chemistry, Faculty of Chemistry and Geosciences, Vilnius University, Lithuania
iveta.jasmantaite@chf.stud.vu.lt

Upconversion (UC) is an anti-stokes process when long-wavelength radiation is converted to short-wavelength light employing two or more low energy photons [1]. Today the biggest focus is on upconverting particles which are characterized by luminescence mechanism – opposite from organic dyes and quantum dots. Also, these particles are used in bioassays, biosensors, solar cells [2]. Performing this work it was expected to synthesize upconverting microparticles which will give at least the same luminescence signal.

The main purpose was to synthesize upconverting microparticles using co-precipitation method. Excitation, photoluminescence and upconversion emission spectra were obtained to verify upconversion phenomenon of synthesized particles *(Fig. 1, d)*. Scanning electron microscope (SEM) was used to measure size and evaluate morphology of microparticles. It was noticed that varying different molar amounts of trivalent rare-earth lanthanide ions (Er^{3+}, Yb^{3+}, Tm^{3+}, Ho^{3+}) or their combinations, the morphology remains similar *(Fig. 1, b-c)* as the undoped $NaYF_4$ *(Fig. 1, a)*.

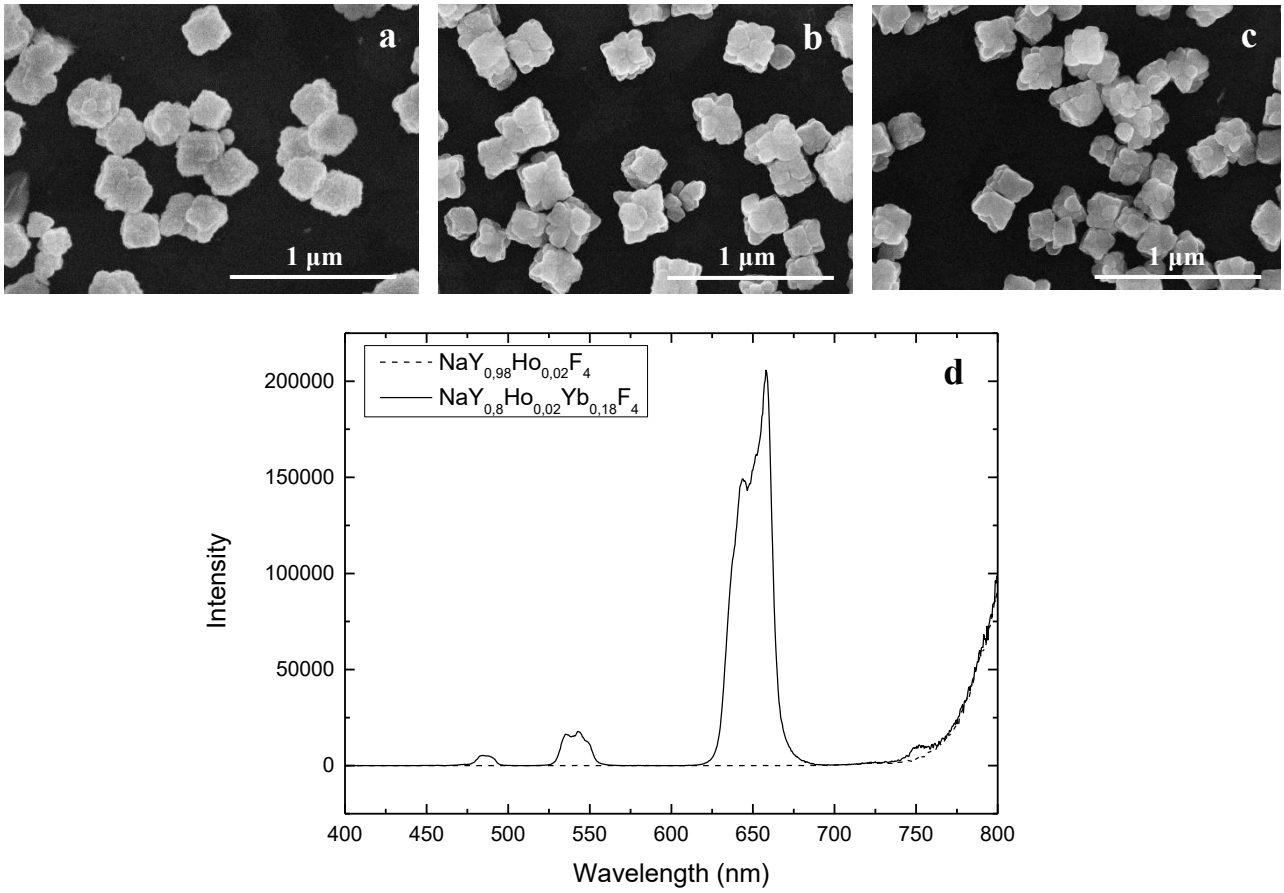

Fig. 1. SEM images of microparticles: (a) $NaYF_4$, (b) $NaY_{0,98}Er_{0,02}F_4$, (c) $NaY_{0,8}Er_{0,02}Yb_{0,18}F_4$, (d) upconversion emission spectra of $NaY_{0,98}Ho_{0,02}F_4$ and $NaY_{0,8}Ho_{0,02}Yb_{0,18}F_4$

---

[1] Chen, H., Zhai, X., Li, D., Wang, L., Zhao, D., Qin, W. (2012). Water-soluble Yb^{3+}, Tm^{3+} codoped $NaYF_4$ nanoparticles: Synthesis, characteristics and bioimaging. *Journal of Alloys and Compounds*, 511(1), pp. 70-73

[2] DaCosta, M. V., Doughan, S., Han, Y., Krull, U. J. (2014). Lanthanide upconversion nanoparticles and applications in bioassays and bioimaging: A review. *Analytica Chimica Acta*, 832, pp. 1-33

YTTRIA-STABILIZED ZIRCONIA AND LITHIUM DISILICATE BIOCERAMIC COATINGS PREPARED VIA SOL-GEL METHOD FOR ODONTOLOGICAL USES

Edvinas Staisiunas[1], Gytis Baranovas[1], Jurgis Pilipavicius[1]

[1] Department of Inorganic Chemistry, Faculty of Chemistry and Geosciences, Vilnius University, Lithuania
edvinas.staisiunas@gmail.com

Titanium and its alloys are successfully applied as an implant material in dentistry. However, one of the common problems associated with this metal is inflammation of the soft tissues due to allergic reaction to Ti and V ions. Another concern is that titanium alloys are prone to low tissue formation in the immediate vicinity of the implant surface resulting in voids for possible bacterial activity [1]. Enhancements and protection of the surface of titanium is needed in order to improve the growth of the tissues while limiting the growth of bacteria. Yttria-stabilized zirconia (YSZ) and lithium disilicate ceramics due to its good mechanical, chemical stability and biocompatibility are most common materials used in dentistry. These ceramics are used as the base material for dental crowns and partial fixed dental prostheses in account of its functional and aesthetic properties [2]. Coatings of YSZ and lithium disilicate ceramics on titanium implants might be a promising approach to augment mechanical and biocompatibility properties of titanium [3].

The aim of this work is to obtain monophase, uniform, crack-free YSZ and lithium disilicate ceramic coatings via sol-gel process distinguishing high biocompatibility and low bacterial activity.

A stable YSZ sol was prepared by mixing zirconium acetate and yttrium nitrate with complexing agent acetylacetone diluted in isopropyl alcohol. After obtaining stable tetragonal phase YSZ sol was coated on silicon, titanium and titanium nitride (TiN) coated titanium by spin coating method. The optimal concentration of YSZ sol for homogenous coatings was researched to be 3%. The first coatings on silicon were annealed in argon atmosphere at 800 °C. Nonetheless, heating coatings on titanium to such temperature resulted in formation of oxide layer even in inert atmosphere heating conditions, which was observed to be negligible and tetragonal phase of YSZ was still obtained when annealing temperature was changed to 650 °C. The surface of coatings was characterized by scanning electron microscopy (SEM) and X-ray diffraction (XRD). Coatings on titanium with vapor deposited titanium nitride layer in comparison to coatings on silicon or titanium resulted in less cracked surface (figure 1). The cell growth proved the biocompatibility of YSZ coatings to be independent of a number of deposited layers. Withal, improvements in uniformity of coatings are hoped to be made by changing sol composition.

In case of lithium disilicate synthesis from lithium dissolved in ethanol and then combined with tetraethyl orthosilicate (TEOS) led to mixture of two different yet stable phases: orthorhombic lithium metasilicate Li_2SiO_3 and orthorhombic lithium disilicate $Li_2Si_2O_5$ [4]. In synthesis, where lithium methoxide was mixed with TEOS without any additional solvents, pure phase of lithium disilicate was achieved (figure 2). Nevertheless, solvent suitable to sustain lithium disilicate phase is needed to be found in order to start using these sols for coating purposes.

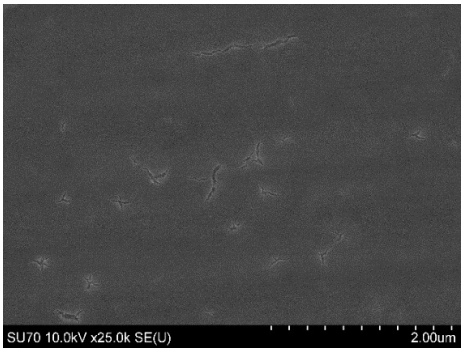

Fig. 1. SEM image of YSZ deposited on Ti/TiN substrate

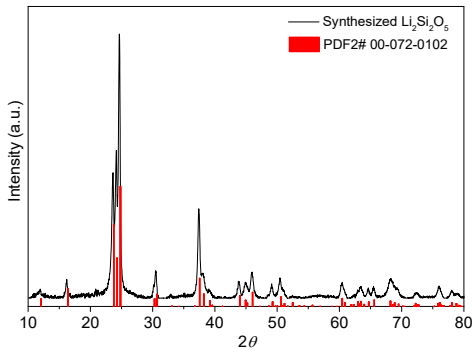

Fig. 2. XRD graph of obtained pure orthorhombic lithium disilicate phase

Acknowledgement: This research was funded by the European Social Fund under the No 09.3.3-LMT-K-712 "Development of Competences of Scientists, other Researchers and Students through Practical Research Activities" measure.

[1] Shi, X., et al. Hydrothermal treatment for TiN as abrasion resistant dental implant coating and its fibroblast response. Materials Science and Engineering: C **49**, 1-6 (2015).

[2] Pieger, S., et al. Clinical outcomes of lithium disilicate single crowns and partial fixed dental prostheses: a systematic review. J Prosthet Dent **112** , 22-30 (2014).

[3] Aragón-Duarte, M. C., et al. Nanomechanical properties of zirconia- yttria and alumina zirconia- yttria biomedical ceramics, subjected to low temperature aging. Ceramics International **43**, 3931-3939 (2017).

[4] P. Li, B. A. Ferguson, L. F. Francis. Sol-gel processing of lithium disilicate Part I Crystalline phase development of gel-derived powders. Journal of Materials Science: Volume **30**, Issue **16**, 4076–4086 (1995).

STUDY OF 3-METHYL-ACETYLACETONE STRUCTURE AND INTERACTION WITH WATER

Rasa Platakytė[1], Justinas Čeponkus[1], Valdas Šablinskas[1]

[1]Vilnius university, Institute of Chemical Physics, Lithuania
rasa.platakyte@gmail.com

Hydrogen bond is crucially important in every biochemical system where it can form both inside and between molecules. Its relationship with molecular structure is mutually dependent and it can greatly influence energy and charge transfer processes. Through those, various macroscopic properties of the system may be modified. One of the most common hydrogen bonds are of O-H…O type – this is also the case in β-diketone type of molecules. The simplest molecule of this class is acetylacetone (AcAc) and it has been studied by various theoretical and experimental methods for quite some time now. However, to better understand hydrogen bonding and intermolecular interactions with water, it is important to also analyze molecules with modified structure. The replacement atom or group can influence molecular dynamics due to its different size (steric effect) or alter charge distribution due to its greater or lesser electronegativity. In this study, the alpha hydrogen in acetylacetone was changed to a methyl group, resulting in 3-methyl-acetylacetone ($AcAcCH_3$) molecule.

Experiments were performed using infrared absorption spectroscopy combined with low-temperature matrix isolation. The spectra of both pure substances (AcAc, $AcAcCH_3$, water) and their mixtures were registered. Density functional theory (DFT) at the B3LYP/6-311++G(3df,3dp) level was used to perform calculations in order to obtain optimal geometries and harmonic frequencies of the molecules and their complexes with water.

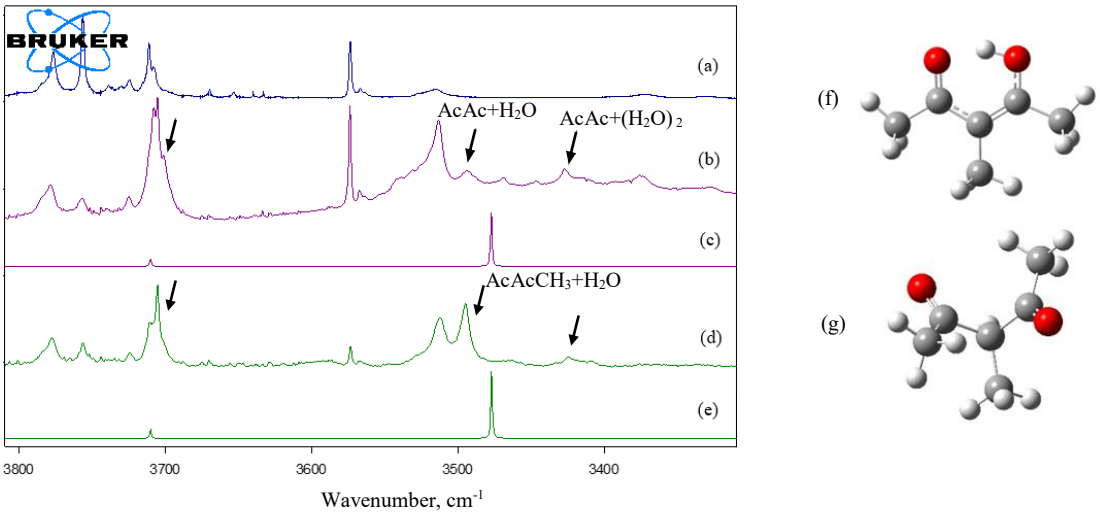

Fig. 1. (a) H_2O in argon [Ar] experimental, (b) $AcAcCH_3$ + H_2O in Ar (1:2:500) experimental and (c) calculated, (d) AcAc + H_2O in Ar (1:1:500) experimental and (e) calculated spectra. The scaling coefficient for calculated spectra was 0.96. Two possible tautomers of AcAcCH3 are shown in (f) and (g).

The evaluation of internal hydrogen bond is a little complicated as there is no observable band for stretching OH vibration due to proton tunneling. Theoretical results indicate a stronger bond for $AcAcCH_3$ (O…H distance is 1.54 Å and the out of plane γOH vibrational band is calculated to be at 1036 cm^{-1}) than for AcAc (O…H distance – 1.61 Å, γOH band at 1010 cm^{-1}). Possible explanation for the decreased distance upon addition of a methyl group is steric effect. In addition, the region between 1800 cm^{-1} and 1600 cm^{-1} (the C=C and C-O stretching region) exhibits more spectral bands for $AcAcCH_3$ which indicates a possibility of coexistence of at least two different tautomers.

In the spectra of mixtures (fig. 1) we can see new bands appear upon complex formation. One of the bands, attributed to water's free OH stretching vibration is observed at 3700 cm^{-1} not only for $AcAcCH_3$ but for other, i.e. halogenated, acetylacetone derivatives as well [1]. The bound OH stretching vibration band and its shift from the monomer band is a good way to evaluate intermolecular hydrogen bond strength. Comparing the results for AcAc and $AcAcCH_3$, we see that theory predicts no change in band positions and we can indeed assign the band at 3490 cm^{-1} to molecule-water associates. Calculations also give very similar results regarding complex formation energy (23.5 kJ/mol for AcAc-water and 23.7 kJ/mol for $AcAcCH_3$-water) and $H_w…O_{AcAc}$ distance (1.9 Å for both). Again, there are several additional spectral bands in the $AcAcCH_3$ spectrum, some of which can be explained by tautomer coexistence. The band at 3430 cm^{-1}, observed for both AcAc and $AcAcCH_3$, might be a result of larger molecular complexes – ones acetylacetone forms with two water molecules instead of one.

[1] L. B. Favero, L.Evangelisti, B.Velino, W. Caminati, Morphing the internal dynamics of acetylacetone by CF3→CH3 substitutions. The rotational spectra of trifluoroacetylacetone, J. Phys. Chem. A **118**, 4243-4248 (2014).

SYNTHESIS AND PROPERTIES OF AMPHOTERIC HYDROXYETHYL STARCHES

Migle Babelyte, Ramune Rutkaite

Department of Polymer Chemistry and Technology, Kaunas University of Technology, Lithuania
migle.babelyte@ktu.edu

Amphoteric starch contains both cationic and anionic groups in the same molecule. Generally, cationic starch derivatives are starch ethers prepared by using tertiary amino or quaternary ammonium groups containing reagents. Meanwhile, anionic starches can be synthesized by introducing phosphate, phosphonate, sulfate, sulfonate or carboxyl groups into starch molecules. The synthesis of amphoteric starches might be achieved by applying two different approaches, namely, firstly anionic modification and thereafter cationic modification or firstly introduction of positively charged groups and then anionic modification. The main applications of amphoteric starches are in the paper industry as wet-end additives and viscosity modifiers in construction industry [1]. Also amphoteric starches can be used in cosmetic industry as thickeners or emulsion stabilizers.

The aim of the present work to prepare amphoteric hydroxyethyl starches (CHES/AHES) of different composition and to investigate their polyelectrolyte complexes formation in water by using anionic and cationic compounds.

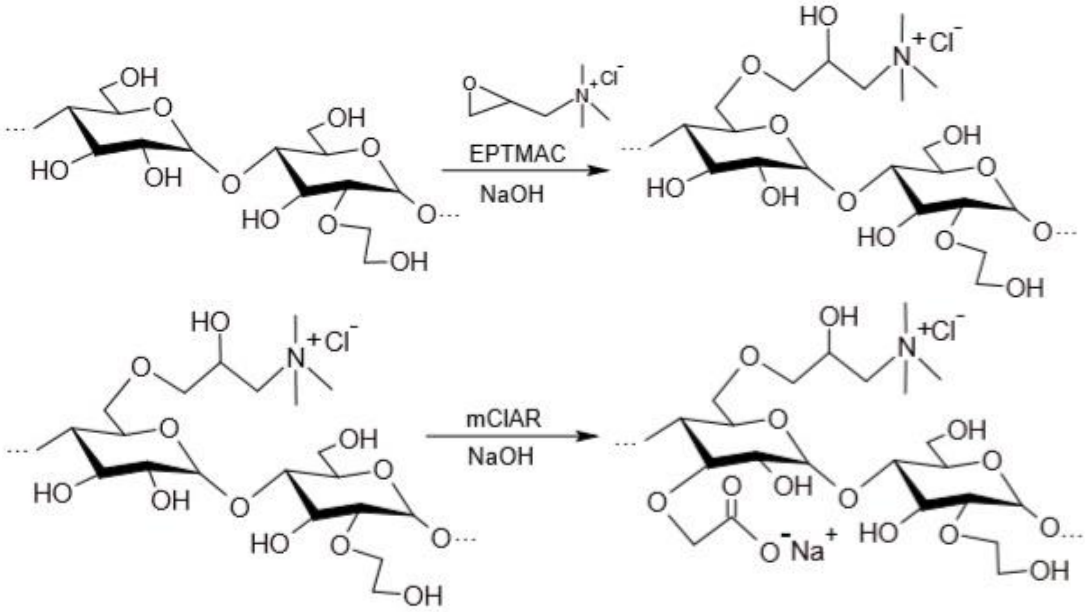

Fig. 1. Two – step amphoteric starch synthesis scheme

Preparation of CHES/AHES has been achieved by using cationic and anionic modifying reagents by two - step reaction as demonstrated in the synthesis scheme in Fig. 1. Firstly, cationic hydroxyethyl starches (CHES) were prepared by the reaction of hydroxyethyl starch (HES) with (2,3-epoxypropyl)trimethylammonium chloride (EPTMAC) in the presence of sodium hydroxide at 45°C for 24 h [2]. The molar ratio of the HES : EPTMAC : NaOH : H_2O was 1 : 0.35-1.02 : 0.04 : 3-8.2. Synthesized CHES then were reacted with monochloroacetic acid (mClAA) in alkaline solution at 55 °C for 48 h. The molar ratio of the CHES : mClAA : NaOH : H_2O was 1 : 1-1.5 : 2.4-3.6 : 90. By changing the amounts of the cationic and anionic reagents amphoteric starches with different degree of substitution of cationic and anionic groups were synthesized.

Several different types of polyelectrolyte complexes in water were formed by employing positively and negatively charged groups of CHES/AHES. The polyelectrolyte complexes were prepared by ionotropic gelation between cationic groups of amphoteric starches and anionic phosphate groups of sodium tripolyphosphate (NaTPP). The polyelectrolyte complexes of other kind were prepared by interacting anionic groups of amphoteric starches and cationic groups of poly(dialyldimethylammonium chloride) (PDADMACl). The formation of the polyelectrolyte complexes was explored by changing the concentrations and ratio of complex forming components as well as pH of the medium. The obtained water insoluble polyelectrolyte complexes were characterized by using FTIR spectroscopy and light scattering techniques.

Acknowledgement. This research was funded by the European Social Fund under the measure No 09.3.3-LMT-K-712 “Development of Competences of Scientists, other Researchers and Students through Practical Research Activities”.

[1] O. B. Wurzburg (1986). Modified starches: properties and uses. CRC Press, Inc., Boca Raton, Florida, p. 277.

[2] R. Rutkaitė, J. Bendoraitienė, R. Klimavičiūtė, E. Lekniutė, I. Narmontaitė, V. Šinkūnaitė (2012). Charged starch nanoparticles prepared by polyelectrolyte complex formation, Chemija, Vol. 23. No. 4, 328 – 335.

FORMATION AND PROPERTIES OF ROSMARINIC ACID AND CHITOSAN COMPLEXES

Karolina Almonaityte, Dovile Liudvinaviciute

Department of Polymer Chemistry and Technology, Kaunas University of Technology, Lithuania
karolinaalmo@gmail.com

Rosmarinic acid (RA) is an ester of caffeic acid and 3,4-dihydroxyphenyllactic acid which is a second of the most frequently occurring caffeic acid esters in the plant kingdom after chlorogenic acid. The conjugated double bond in the side chain of RA molecule enhances its antioxidant activity, however, makes RA vulnerable to heat, oxygen, light and moisture, and, consequently, influences the instability of RA [1]. Chitosan (CH) is a naturally occurring polymer derived from chitin by deacetylation reaction. It is soluble in acidic aqueous solution, in which the protonation of amino groups occurs. After protonation D-glucosamino units of CH are positively charged, and therefore CH can be regarded as a natural pseudo cationic biopolymer, which could form polyelectrolyte complexes with negatively charged polymers and low molecular compounds [2].

The aim of the present investigation was to obtain RA and CH complexes (RA-CH) by adsorbing RA onto CH microgranules, to evaluate formed complexes by FT-IR and fluorescence spectroscopy, TG analysis, as well as, to assess the stability of RA-CH complexes in different media.

To obtain RA-CH complexes, RA aqueous solution was poured over CH microgranules, stirred with a magnetic stirrer at room temperature (22±1 °C) for 60 min, and then filtered. RA-CH microgranules were washed twice with distilled water and dried at room temperature. To obtain the RA-CH complexes with higher amounts of RA, the procedure described above was repeated with the RA-CH microgranules obtained in the previous step. The RA-CH complexes were characterized by RA to CH molar ratio. The formation of RA-CH complexes was also confirmed by FT-IR spectroscopy.

The RA-CH complexes with RA to CH molar ratio ranging from 0.11 to 0.86 were evaluated by using fluorescence spectroscopy and TG analysis. Furthermore, desorption experiments were performed by using various media such as distilled water, ethanol, phosphate buffer solution (pH=6.8) and 0.5 % aqueous acetic solution. The TGA thermograms of RA, CH and RA-CH complexes microgranules are presented in Fig. 1, a. The fluorescence spectra of RA, CH ethanol solutions, and RA-CH complexes dispersions in ethanol are presented in Fig. 1, b.

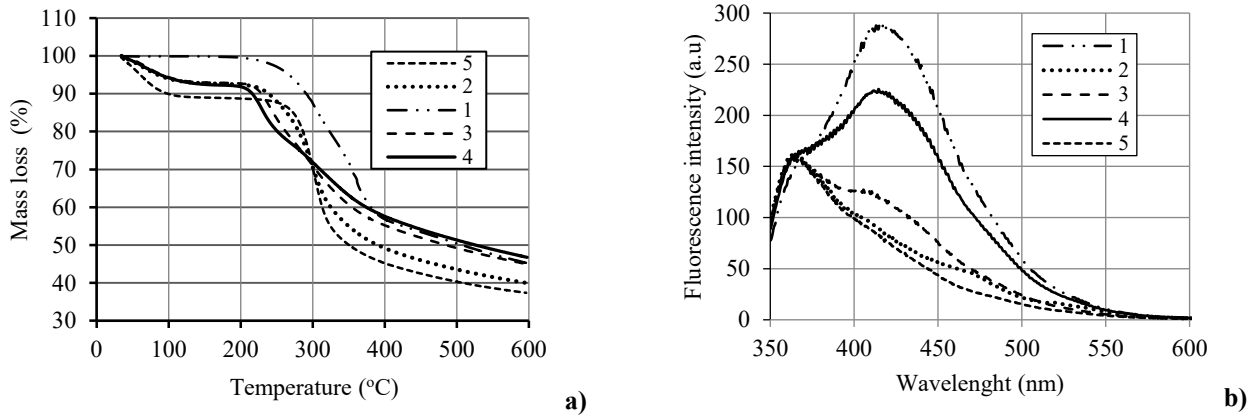

Fig. 1. TGA thermograms (a) and fluorescence spectra (b) of RA (1), CH (5) and RA-CH complexes with RA to CH molar ratio: 2– 0.11; 3 – 0.39; 4 – 0.86.

The thermal degradation of RA-CH complexes occurred at temperatures lower than that of CH alone (Fig.1, a). It can be suggested that by the formation of ionic bonds between chitosan and RA during the adsorption the loss of polymer organization can occur.

The amount of RA released from RA-CH complexes microgranules depended both on the complex composition and desorption medium. The fluorescence intensity of complexes dispersions in ethanol (Fig. 1, b) increased with the increasing amount of RA in complexes and it is related with the amount of RA released into the desorption medium.

Acknowledgment. The authors are grateful to the Research Council of Lithuania for the financial support of the project MIP-055/2015.

[1] H. Cao, W.X. Cheng, C. Li et al., DFT study on the antioxidant activity of rosmarinic acid, Journal of Molecular Structure: THEOCHEM, **719**, 177–183 (2005).
[2] Y. Luo, Q. Wang, Q., Recent development of chitosan-based polyelectrolyte complexes with natural polysaccharides for drug delivery, International Journal of Biological Macromolecules, **64**, 353–367 (2014).

A STUDY OF ELECTRODEPOSITED MOLYBDENUM SULFIDE AS A HYDROGEN EVOLUTION REACTION CATALYST

Ramūnas Levinas[1], Natalia Tsyntsaru[1,2], Henrikas Cesiulis[1]

[1]Vilnius University, Naugarduko 24, Vilnius, Lithuania
[2] Institute of Applied Physics of ASM, 5 Academy str., Chisinau, Moldova
ramunas.levinas@chf.vu.lt

Molybdenum sulfide is a low-cost hydrogen evolution reaction (HER) catalyst that has gained considerable attention in the field of renewable energy during recent years. Edge sites, grain boundaries, and sulfur vacancies in the crystal lattice all exhibit HER catalytic activity [1], but the basal plane does not [2]. Therefore, a lot of research is currently focused on distribution of MoS_2 on various substrates with large surface areas to expose more edge sites. MoS_2 can be obtained in various ways, including chemical (chemical vapour deposition, hydrothermal synthesis) and electrochemical methods. Electrodeposition is comparatively simple and cheap, but the deposited films typically are amorphous and thus, it is more difficult to obtain the desired film morphology.

In this study, we investigated the electrodeposition of non-stoichiometric MoS_x films from an electrolyte containing a common sulfur and molybdenum ion precursor – tetra thiomolybdate (MoS_4^{2-}). A strong dependence on the solution pH was observed. Linear sweep voltammetry measurements showed that current densities increase significantly in more acidic solutions, leading to changes in the surface morphology as well. Thus, at pH 9 the surface is smooth and has no noticeable structures, but when deposition is carried out at pH 6 the surface is covered with molybdenum sulfide crystallites (Fig. 1) of up to ~ 1 μm size. EDS analysis confirmed film stoichiometry as MoS_{2+x} (where x = 0,5 to 1).

The electrodeposited MoS_{2+x} films were tested for their electrocatalytic activity in acidic solution (0.5 M H_2SO_4). Electrode polarization was carried out from open circuit potential (OCP) at a rate of 2 mV s^{-1} until a cut-off current density of 40 mA cm^{-2} was reached. The films showed good HER activity, reaching 10 mA cm^{-2} at -0.275 V (Fig. 2). Tafel slopes for different samples fell within the 50 – 60 mV dec^{-1} range, suggesting that H^+ adsorption is not the rate-determining step of the hydrogen evolution reaction occurring on a MoS_{2+x} catalyst. Film stability, however, remains an issue, as the catalytic performance of some films degrades noticeably over several measurements.

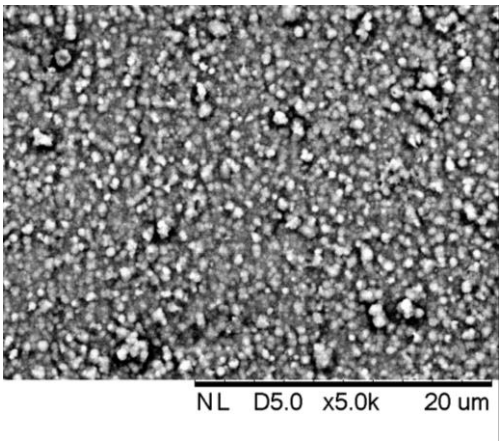

Fig. 1. SEM image of MoS_{2+x} film. Deposition time – 1600 s.

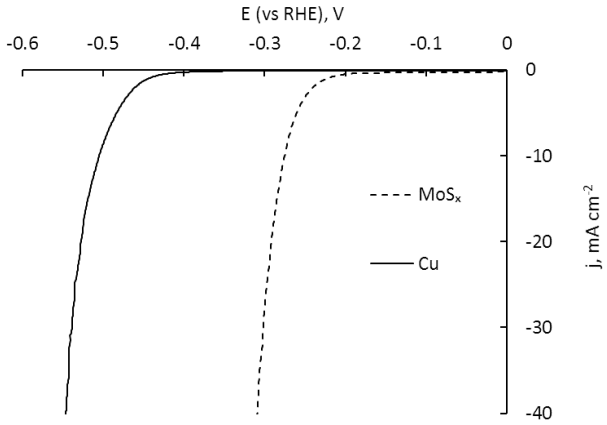

Fig. 2. HER polarization curves of uncoated copper substrate and electrodeposited MoS_{2+x} film.

Acknowledgement: authors acknowledge funding from H2020 project SMARTELECTRODES (No.778357) and the Moldavian national project (15.817.02.05A).

[1] Guoqing Li et al, All The Catalytic Active Sites of MoS2 for Hydrogen Evolution, J. Am. Chem. Soc., 138 (51), 16632–16638 (2016).
[2] T. F. Jaramillo et al, Identification of Active Edge Sites for Electrochemical H_2 Evolution from MoS_2 Nanocatalysts, Science (2007).

ELECTROCHEMICAL DEPOSITION OF COBALT FOAMS AND INVESTIGATION OF DEPOSITION CONDITIONS

Modestas Vainoris[1], Natalia Tsyntsaru[1, 2], Henrikas Cesiulis[1]

[1] Department of Physical Chemistry, Vilnius University, Lithuania
[2] Insitute of Applied Physics of ASM, Chisinau, Moldova
modestas.vainoris@chgf.vu.lt

Cobalt, its alloys and its many different complexes are being applied in very versatile fields, like anticorrosion, anti-wear coatings, magnetic alloys [1], many different sensors, catalysts and even as cancer drugs [2]. Metal foams provide big surface area, that can be easily accessed by solution, therefore give its morphology metal foams are good candidates to use as sensors or catalysts, or simply as a template for them. Aim of this work was to produce cobalt foams and to investigate influence of different additives and deposition conditions on porosity and surface area of cobalt metal foams. Foams were formed via electrodeposition, using hydrogen bubble template method.

Cobalt foams have been deposited using both galvanostatic and pulse deposition modes, using sizeable cathodic current densities (0.6-2.5A/cm²). Influence of current density, deposition time and pulse duration on porosity and surface area have been investigated. Copper plates were chosen as substrate onto which cobalt foam was deposited. In order to examine the effects on metal foams deposition, different ions and additives were used in making of acidic solutions containing 0.2M either $CoCl_2$ or $CoSO_4$, and additives (2M NH_4Cl or 1M $(NH_4)_2SO_4$). Morphology of Co foams was investigated using Scanning Electron Microscopy (SEM) coupled with Energy Dispersive Spectroscopy (EDS), and X-ray diffraction (XRD). Surface area was evaluated using Electrochemical Impedance Spectroscopy (EIS), by calculating Double Layer Capacitance and from it true surface area has been estimated.

Cobalt coatings obtained from solutions that didn't contain ammonium ions proved to be poorly attached to copper surface, and powder like in appearance. Upon addition of ammonium ions, the adhesion improved significantly, the surface was riddled with unevenly distributed cylindrical pores. While using galvanostatic deposition conditions there did not seem to be significant relation between pore radius, density and current density with deposition time. However, using pulse deposition mode pores density, diameter and length can be easier to control.

In order to further increase surface area of cobalt foams 2M of isopropyl alcohol was added to solutions. This has substantially decreased surface tension, and in turn increased porosity of Co foams. This worked with both sulfate and chloride containing solutions.

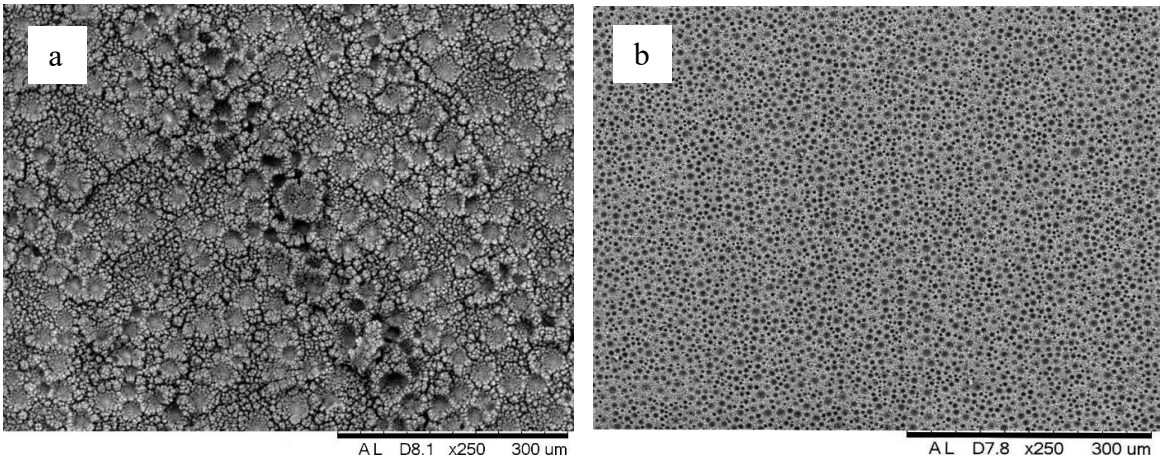

Fig. 1. SEM images of Co foams obtained at these conditions a) 0.2M $CoCl_2$ and 2M NH_4Cl j=1.8A/cm² 60s, b) 0,2M $CoSO_4$ and 1M $(NH_4)_2SO_4$ 100ms j=2.5A/cm², 1s j=0.6A/cm², 10 cycles

Acknowledgements: authors acknowledge funding from H2020 project SMARTELECTRODES (No.778357) and the Moldavian national project (15.817.02.05A).

[1] Inoue, A., Shen, B., Koshiba, H., Kato, H., & Yavari, A. R. (2003). Cobalt-based bulk glassy alloy with ultrahigh strength and soft magnetic properties. *Nature Materials*, *2*(10), 661–663.

[2] Ott, I., Schmidt, K., Kircher, B., Schumacher, P., Wiglenda, T., & Gust, R. (2005). Antitumor-active cobalt-alkyne complexes derived from acetylsalicylic acid: Studies on the mode of drug action. *Journal of Medicinal Chemistry*, *48*(2), 622–629.

[3] Chin, P., Sun, X., Roberts, G. W., & Spivey, J. J. (2006). Preferential oxidation of carbon monoxide with iron-promoted platinum catalysts supported on metal foams. *Applied Catalysis A: General*, *302*(1), 22–31. http://doi.org/10.1016/j.apcata.2005.11.030

INVESTIGATION AND POSSIBLE APPLICATIONS OF Eu^{3+} LUMINESCENCE IN $K_2LaNb_5O_{15}$ MATRIX

Ignatij Mackevic, Arturas Katelnikovas

Faculty of Chemistry and Geosciences, Vilnius University, Naugarduko 24, LT-03225 Vilnius, Lithuania
ignatij.mackevic@chf.stud.vu.lt arturas.katelnikovas@chf.vu.lt

The poor correlated color temperature (CCT) and color rendering index (CRI) values together with thermal degradation upon long term operation time at elevated temperatures of commonly known blue emitting LED-chip coated with yellow $Y_3Al_5O_{12}$:Ce (YAG) phosphor forces white-LED manufacturers to search for alternative ways to produce good quality white light in LEDs [1]. The suggested solution to this problem is combining near-UV excited red, blue and green phosphors into one system that creates white light of desired quality [2]. Due to the lack of red light emitting phosphors meeting the requirements on the market, an attempt to synthesize such phosphor for possible application in white-LEDs was carried out. $K_2LaNb_5O_{15}:Eu^{3+}$ appeared to be promising candidate. Even though investigations proved $K_2LaNb_5O_{15}:Eu^{3+}$ to have relatively low thermal quenching temperature ($TQ_{1/2}$) a larger amount of this phosphor could be introduced to LED devices and obtain even input of each phosphor's emitted different color light to compensate this drawback.

Even more promising area of use of synthesized $K_2LaNb_5O_{15}:Eu^{3+}$ is fluorescent security pigments in printing inks. These pigments have rather unique ability to restrain invisible under normal daylight, while upon excitation with appropriate wavelengths they emit corresponding light with distinctive color which helps recognize genuine money, documents, valuable papers etc. and distinguish them from forgery products.

$K_2La_{1-x}EuxNb_5O_{15}$ (x=0.01-1.00) were synthesized using high-temperature solid-state reaction. Precursory materials used for synthesis were K_2CO_3, Eu_2O_3, La_2O_3 and Nb_2O_5 of high purity. All materials were weighted and mixed in stoichiometric amounts in agate mortar using acetone as media. Obtained powders were then transferred to alumina crucibles and annealed at 1300 °C for 10 h.

XRD analysis of undoped, 50% doped, 100% doped and reference powder samples match well together proving that isostructural compounds are obtained at any Eu^{3+} doping concentration.

Excitation, emission, reflection spectra and photoluminescence (PL) decay curves of $K_2LaNb_5O_{15}:Eu^{3+}$ samples with different Eu^{3+} concentrations were recorded at room temperature and CIE 1931 colour coordinates and decay times were calculated.

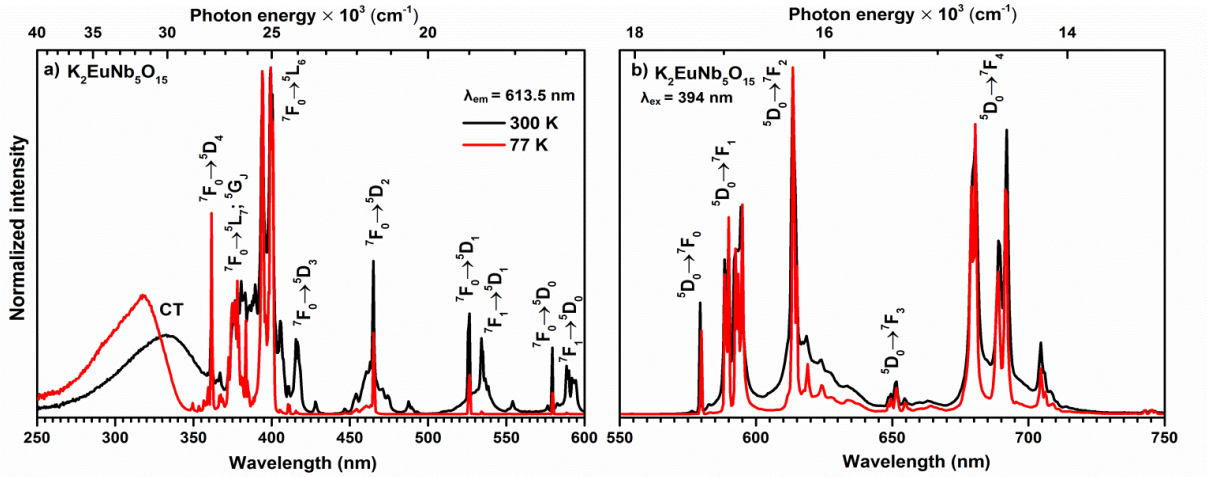

Fig. 1. Excitation (λ_{em}=613.5 nm) (a) and emission (λ_{ex}=394 nm) (b) spectra of $K_2EuNb_5O_{15}$ phosphor at 77 and 300 K.

Moreover, the temperature dependent excitation and emission spectra, and PL decay curves were recorded in the 77–500 K range in order to investigate the thermal quenching processes in this structure. Excitation spectra of $K_2EuNb_5O_{15}$ sample (Fig. 1a) possessed broad band in 250–400 nm range which belongs to the host lattice charge transfer (CT) band and many typical $^7F_J \rightarrow {}^5L_J$; ^5G_J; ^5D_J narrow excitation lines of Eu^{3+} ions at the rest of the investigated spectra interval. Emission spectra (Fig. 1b) contained several sets of intensive emission lines in the orange – deep-red spectral region originating from the $^5D_0 \rightarrow {}^7F_J$ transitions of Eu^{3+} ions.

Furthermore, from the obtained data, thermal quenching activation energies (E_a) and $TQ_{1/2}$ values were calculated and will be discussed. Finally, room temperature quantum yield measurements under 335, 394, and 465 nm excitation revealed that phosphors possess ca. 70% efficiency what is very promising for practical application.

[1] M. R. Krames, O. B. Shchekin, R. Mueller-Mach, et al., Status and Future of High-Power Light-Emitting Diodes for Solid-State Lighting, Journal of Display Technology **3**, 160-175 (2007).
[2] M. Bessho, M. Shimizu, Latest trends in LED lighting, Electronics and Communications in Japan **95**, 1-7 (2012).

BIOACTIVE ADDITIVES IN COMPOUND FERTILIZERS

Austėja Eimontaitė, Rasa Šlinkšienė

Department of Physical and Inorganic Chemistry, Kaunas University of Technology, Lithuania
austeja.eimontaite@ktu.edu

Nowadays, as many diverse fields of bioactive additives that can be used in the fertilizer industry as fertilizer catalysts. The literature contains information on molasses [1], asches [2], amino acid [3] and others additives used in fertilizer production. The object of our research is algae and their use in fertilizer production.

There are many ways in which algae can be used today, but the most relevant and widely explored are bioenergy and biofuels, biomedical, cosmetic products, fertilizers and pigments. As a biomedical use macroalgae produce a variety of natural bioactive compounds and metabolites, such as polysaccharides, polyunsaturated fatty acids, and phlorotannins [4]. Some types of brown and red macroalgae are used in cosmetics due to the presence of vitamins, minerals, amino acids, sugars, lipids, and other biologically active compounds [5]. Algae based fuels are considered to be the most sustainable, renewable, effective and environment friendly response to climate change and food security, as well as only renewable energy resource that has the capacity to meet the global demand for fuels in the long-term [6]. The microalgae biomass is used as a source of carotenoids, also known as pigments. In photosynthetic organisms like plants and algae, carotenoids are associated with the light harvesting complex photosynthesis, functioning as accessory pigments and are also known for their photoprotective effect of photosystems from oxidative damage [7].

The most important parameters for algae cultivation are light, nutrients, aeration, temperature and pH, which determine the efficiency of biomass utilization and chemical composition. For comparison we had algae (Clorela) from Aleksandras Stulginskis University (ASU) and from Buxtrade GmbH (BG), which were analysed in different methods. As we can see below in the table 1 and figure 1 chemical composition and structure is different.

Table 1. Some chemical elements concertation in the algae

Elements concentration, %	K	P	Ca	S	Fe	Cu	Na	Mg	Mn	Si
ASU	1,41	1,90	7,92	1,28	1,11	0,46	1,20	0,43	0,41	0,07
BG	3,34	2,63	0,58	1,89	0,73	0,0	0,0	0,27	0,04	0,25

The results presented in Table 1 show that algae can be used in the production of fertilizers because they contain different nutrients without heavy metals. As the particle size and surface of the raw material are very important for the granulation of the fertilizer, SEM analysis was performed and the results are presented in Figure 1.

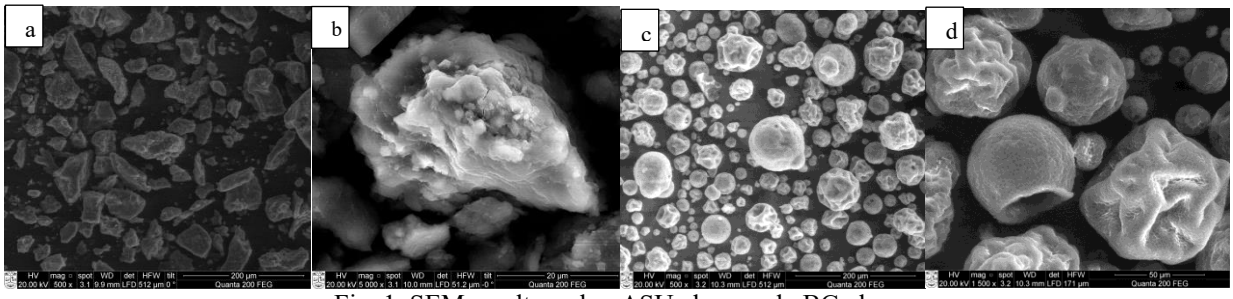

Fig. 1. SEM results: a, b – ASU algae; c,d– BG algae

To determine the agglomeration and plasticity of algae, they were granulated in drum granulator using water and aqueous solutions of various concentrations of molasses.

[1] G. Paškevičienė, R. Paleckienė, A.M. Sviklas, R. Šlinkšienė. Molasses influence on ash granulation process and quality parameters. Materials Science / KTU. Kaunas: Technologija. ISSN: 1392-1320. 2010, Vol. 16, no. 4, p. 373-379.
[2] R. Paleckienė, A. M. Sviklas, R. Šlinkšienė, V. Štreimikis. Processing of rape straw ash into compound fertilizers using sugar factory waste // Polish journal of environmental studies. Olsztyn: HARD Publishing Company. ISSN 1230-1485. 2012, Vol. 21, 4, p. 993-999.
[3] R. Paleckienė, A. M. Sviklas, R. Šlinkšienė. Physicochemical properties of a microelement fertilizer with amino acids // Russian Journal of Applied Chemistry. New York: Maik Nauka/Interperiodica/Springer. ISSN: 1070-4272. 2007, Vol. 80, no. 3, p. 352-357.
[4] J.S. Chang, C. X. Li, D. J. Lee, H. M. Wang. Potential biomedical applications of marine algae. Elsevier. https://doi.org/10.1016/j.biortech.2017.05.198. 2017, Vol. 244, p. 1407-1415.
[5] Ariede M. B., Baby A. R. and others. Cosmetic attributes of algae – a review. Elsevier. http://dx.doi.org/10.1016/j.algal.2017.05.019. 2017, Vol. 25, p. 483-487.
[6] Vassilev C. G., Vassilev S. V., (2016) Composition, properties and challenges of algae biomass for biofuel application: an review. Elsevier. http://dx.doi.org/10.1016/j.fuel.2016.04.106. 2016, Vol. 181, p. 1-33.
[7] J.S Chang, J. Hu, D.J. Lee, D. Nagarajan, Q. Zhang. Heterotrophic cultivation of microalgae for pigment production: a review. Elsevier. http://dx.doi.org/10.1016/j.biotechadv.2017.09.009. 2017, in Press.

SYNTHESIS AND ANALYSIS OF 2,5-SUBSTITUTED BENZENESULFONAMIDES AS INHIBITORS OF CARBONIC ANHYDRASES

A. Jankūnaitė[1,2], V. Paketurytė[2], A. Zakšauskas[2], D. Matulis[2]

[1] Department of Organic Chemistry, Vilnius University, Lithuania
[2] Department of Biothermodynamics and Drug Design, Vilnius University, Lithuania
alberta.jankunaite@chf.stud.vu.lt

Carbonic anhydrases (CA) are zinc-containing metalloenzymes that catalyze the reversible hydration of carbon dioxide and are present in prokaryotes and eukaryotes. The majority of CA research is concentrated on the human CA isoforms that are studied as targets for the treatment of various diseases. Twelve human CA isoforms have been descirbed, which all possess very different subcellular localization, tissue distribution and catalytic activity. Inhibition of these isozymes has phamacological applications in the scope of antiglaucoma, anticonvulsant or antitumor drugs[1]. The most common and well-studied class of CA inhibitors for this matter is aromatic/heterocyclic sulfonamides. Unfortunately, many sulfonamides posses a lack of selectivity, therefore a great need of potent and selective CA inhibitors remains.

The significant conservation within the active site of the enzymes make it difficult to design compounds that only bind a single target isoform. Investigation of various substitutes in the sulfonamide scaffold and their influence on the inhibition selectivity is essential designing new CA inhibitors.

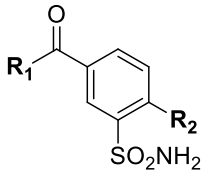

1: R_1=OMe	**a**: R_2=Cl	**e**: R_2=S-cyclohexyl	**i**: R_2=SO_2-cyclohexyl
2: R_1=NHBu	**b**: R_2=SPh	**f**: R_2=SO_2Ph	**j**: R_2=$NHCH_2$Ph
3: R_1=$NH(CH_2)_2OH$	**c**: R_2=SCH_2Ph	**g**: R_2=SO_2CH_2Ph	**k**: R_2=NH-cyclooctyl
4: R_1=$NH(CH_2)_3OH$	**d**: R_2=$S(CH_2)_2$Ph	**h**: R_2=$SO_2(CH_2)_2$Ph	**l**: R_2=NH-cyclohexyl

A series of 2,5-substituted benzenesulfonamides were synthesized and their binding to carbonic anhydrase isozymes were determined by the fluorescent thermal shift assay (FTSA). The results will be presented in a poster.

[1] C. Lomelino, R. McKenna, Carbonic anhydrase inhibitors: a review on the progress of patent literature (2011–2016), Expert. Opin. Ther. Pat., **26**, 947-956 (2016).

SOL-GEL SYNTHESIS, CHARACTERIZATION AND LUMINESCENCE OF $Li_{0.05}Eu_{0.05}Ca_{0.9}MoO_4$

Gytautas Janulevičius, Artūras Žalga*

Faculty of Chemistry and Geosciences, Institute of Chemistry, Vilnius University, Naugarduko Str. 24, LT-03225 Vilnius, Lithuania
gytautas.janulevicius@chf.stud.vu.lt

Calcium molibdate is an important material for its unique properties as luminescent [1-12], optical fiber [5, 10], magnetic [10], catalytic [3, 6, 10, 12], scintilating [6, 7, 10, 12] material. By doping the molybdate with europium (Eu^{3+}), it is possible to produce strong red luminescence [9]. Luminescence can be improved by co-doping with an alkali metal (Li^+, Na^+, K^+) [9].

The preparation and characterization of the Li–Eu–Ca–Mo–O tartrate gel precursor, which was produced by the simple aqueous sol–gel method and calcined at 673 K, 773 K and 873 K temperatures are reported. The crystalline lithium and europium substituted calcium molybdate ($Li_{0.05}Eu_{0.05}Ca_{0.9}MoO_4$) and as-prepared Li–Eu– Ca–Mo–O tartrate gel investigated by thermal analysis (TG/DSC), X-ray diffraction (XRD), scanning electron microscopy (SEM) and photoluminescence spectroscopy (PL). TG/DSC analysis showed the possible decomposition mechanism of synthesized gel precursor. XRD studies allowed the identification of main type of crystalline structure in the $Li_{0.05}Eu_{0.05}Ca_{0.9}MoO_4$ system. SEM analysis revealed the changes of surface morphology of the final compound depending on sintering temperature. Moreover, PL measurements enabled the estimation the electronic structure of synthesized material.

[1] G.-K. Choi, J.-R. Kim, S.H. Yoon, K.S. Hong, Microwave dielectric properties of scheelite (A=Ca, Sr, Ba) and wolframite (A=Mg, Zn, Mn) $AMoO_4$ compounds, J. Eur. Ceram. Soc. **27**, 3063–3067 (2007).
[2] Y. Wang, J. Ma, J. Tao, X. Zhu, J. Zhou, Z. Zhao, L. Xie, H. Tian, Low temperature synthesis of $CaMoO_4$ nanoparticles, Ceram. Int. **33**, 693–695 (2007).
[3] T. Thongtem, S. Kungwankunakorn, B. Kuntalue, A. Phuruangrat, S. Thongtem, Luminescence and absorbance of highly crystalline $CaMoO_4$, $SrMoO_4$, $CaWO_4$ and $SrWO_4$ nanoparticles synthesized by co-precipitation method at room temperature, J. Alloys Compd. **506**, 475–481 (2010).
[4] J. Zhang, L. Wang, Y. Jin, X. Zhang, Z. Hao, X. Wang, Energy transfer in $Y_3Al_5O_{12}:Ce^{3+}$, Pr^{3+} and $CaMoO_4:Sm^{3+}$, Eu^{3+} phosphors, J. Lumin. **131**, 429–432 (2011).
[5] D. Gao, X. Lai, C. Cui, P. Cheng, J. Bi, D. Lin, Oxidant-assisted preparation of $CaMoO_4$ thin film using an irreversible galvanic cell method, Thin Solid Films. **518**, 3151–3155 (2010).
[6] Y. Sun, J. Ma, X. Jiang, J. Fang, Z. Song, C. Gao, Z. Liu, Ethylene glycol-assisted electrochemical synthesis of $CaMoO_4$ crystallites with different morphology and their luminescent properties, Solid State Sci. **12**, 1283–1286 (2010).
[7] Y. Yin, Y. Gao, Y. Sun, B. Zhou, L. Ma, X. Wu, X. Zhang, Synthesis and photoluminescent properties of $CaMoO_4$ nanostructures at room temperature, Mater. Lett. **64**, 602–604 (2010).
[8] X. Li, Z. Yang, L. Guan, J. Guo, Y. Wang, Q. Guo, Synthesis and luminescent properties of $CaMoO_4:Tb^{3+}$, R^+ (Li^+, Na^+, K^+), J. Alloys Compd. **478**, 684–686 (2009).
[9] Z.J. Zhang, H.H. Chen, X.X. Yang, J.T. Zhao, Preparation and luminescent properties of Eu^{3+} and Tb^{3+} ions in the host of $CaMoO_4$, Mater. Sci. Eng. B Solid-State Mater. Adv. Technol. **145**, 34–40 (2007).
[10] F. Lei, B. Yan, Hydrothermal synthesis and luminescence of $CaMO_4:RE^{3+}$ (M=W, Mo; RE=Eu, Tb) submicro-phosphors, J. Solid State Chem. **181**, 855–862 (2008).
[11] M.M. Haque, D.K. Kim, Luminescent properties of Eu^{3+} activated $MLa_2(MoO_4)_4$ based (M = Ba, Sr and Ca) novel red-emitting phosphors, Mater. Lett. **63**, 793–796 (2009).
[12] S.S. Hosseinpour-Mashkani, S.S. Hosseinpour-Mashkani, A. Sobhani-Nasab, Synthesis and characterization of rod-like $CaMoO_4$ nanostructure via free surfactant sonochemical route and its photocatalytic application, J. Mater. Sci. Mater. Electron. **27**, 4351–4355 (2016).

SYNTHESIS OF CATIONIC STARCH USING VARIOUS CATIONIZATION AGENTS

Marius Dragašius, Joana Bendoraitienė

Department of Polymer Chemistry and Technology, Kaunas University of Technology, Lithuania
marius.dragasius@ktu.edu

Biodegradability, low cost and non-toxicity are the main advantages of the biopolymer based flocculants. Cationic starches are effective flocullants and can be used in a wide range of pH. They can be used in wastewater purification processes, in order to get rid of inorganic and organic substances with a negative charge [1]. Also cationic starch derivatives capable of attracting negative charge particles can be very effective sorbents or flocculants in paper and textile industries [2].

Cationic starches (CS) with preserved microgranular structure (see Fig. 1) were obtained by etherification reaction of natural potato starch with 57% glycidyltrimethylammonium chloride (GTAC) or 65,4% 3-chloro-2-hydroxypropyltrimethylammonium chloride (CHPTAC) by using NaOH as a catalyst. The cationization reaction by using CHPTAC was performed without and with an addition of CaO. Molar ratios of the reagents in the reaction mixtures starch (S) : GTAC or CHPTAC : NaOH : CaO : H_2O are shown in Table 1. Reactions were performed at 45 °C for 44-48 h. Obtained CS microgranules were purified by washing with isopropanol and water solvent mixture and when followed by the Soxhlet extraction with methanol.

Table 1. Starch modification reaction conditions and characteristics of obtained CS

Reaction	Cationization agent (CA)	Molar ratio of reaction mixture S : CA : NaOH : CaO : H_2O	Degree of substitution (DS)	Reaction yield, %
1	CHPTAC	1 : 0,10 : 0,11 : 0,04 : 3,0	0,098	98
2	CHPTAC	1 : 0,25 : 0,26 : 0,04 : 3,1	0,236	94
3	CHPTAC	1 : 0,40 : 0,41 : 0,04 : 3,2	0,367	92
4	GTAC	1 : 0,12 : 0,04 : 0 : 3,0	0,115	96
5	GTAC	1 : 0,29 : 0,04 : 0 : 3,0	0,267	92
6	GTAC	1 : 0,46 : 0,04 : 0 : 3,0	0,372	81
7	CHPTAC	1 : 0,10 : 0,11 : 0 : 3,0	0,095	95
8	CHPTAC	1 : 0,25 : 0,26 : 0 : 3,1	0,235	94
9	CHPTAC	1 : 0,40 : 0,41 : 0 : 3,2	0,384	96

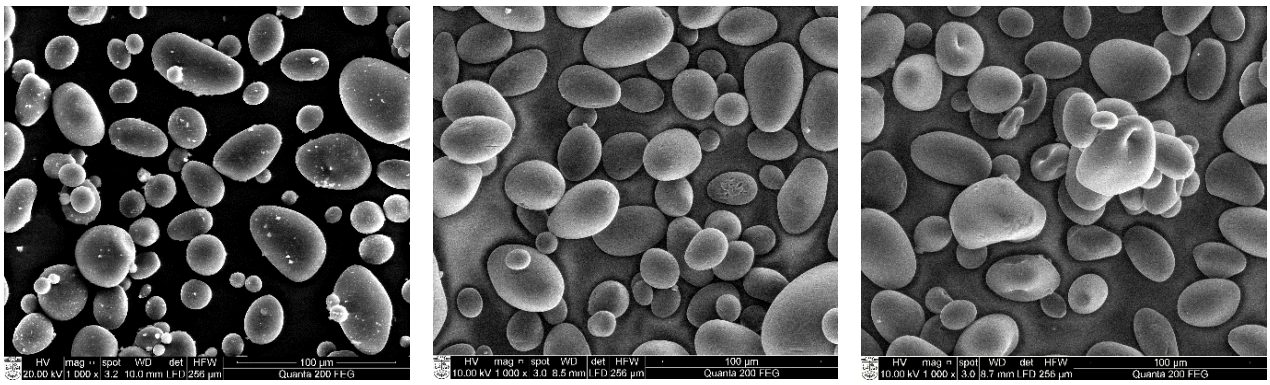

a b c

Fig. 1. Scanning electron microscopy (SEM) images of CS granules obtained in various reactions after purification in methanol: a - reaction 3, b - reaction 6, c- reaction 9.

It was noticed that in the case CaO was used in the modification reaction, even after 48 h of extraction with methanol, the samples were still not fully purified (see Fig. 1, a). However, for other CS derivatives 24 h of purification was sufficient to obtain clean samples. (Fig. 1., b and c).

Acknowledgment. This research was funded by the European Social Fund under the measure No 09.3.3-LMT-K-712 "Development of Competences of Scientists, other Researchers and Students through Practical Research Activities".

[1] S. Pal, D. Mal, and R. P. Singh, "Cationic starch: An effective flocculating agent," Carbohydr. Polym., vol. 59, no. 4, pp. 417–423, 2005.
[2] F. Xie, L. Yu, H. Liu, and L. Chen, "Starch modification using reactive extrusion," Starch/Staerke, vol. 58, no. 3–4, pp. 131–139, 2006.

3D POLYMERIC SCAFFOLD FOR SOFT TISSUE REGENERATION

Lina Ščiupakovaitė, Odeta Baniukaitienė

Department of polymer Chemistry and Technology, Kaunas University of Technology, Lithuania
lina.sciupakovaite@ktu.edu

Nowadays soft tissue regeneration is based on the use of highly porous 3D scaffolds which fully fill the wound, provide space for cell adhesion, proliferation, differentiation. Typically, these scaffolds are made up of natural or synthetic polymers. However, significant attention is focused on natural polymers due to their biocompatibility, non-toxicity, hydrophilicity, and controllable biodegradability [1].

The aim of this work was to prepare 3D scaffolds for soft tissue regeneration. 3D scaffolds were prepared based on natural polymers: sodium alginate, chitosan and hyaluronic acid (Table 1).

Table 1. The composition of the scaffolds

Scaffold number	Polymer			Salt		Purified water
	Sodium alginate	Chitosan	Hyaluronic acid	Glucono delta-lactone	Calcium gluconate	
	Mass portion, %					
1	2	0.1	1	2	1	up to 100
2		0.3				
3		0.6				

The scaffolds were prepared immersing sodium alginate and hyaluronic acid blended frameworks into chitosan solution of glucono delta-lactone. Freeze-drying technique (Freeze dryer, Martin Christ Gefriertrocknungsanlagen GmbH, Germany) was used for the fabrication of highly porous frameworks. The polyelectrolyte networks were formed due to oppositly charged functional groups of the polymers. Additionally, scaffolds were cross-linked with divalent ions.

Fig. 1. Interation between polymers: a) fully miscible system of hyaluronic acid and sodium alginate; b) polyelectrolyte complex formation between chitosan and hyaluronic acid; c) polyelectrolyte complex formation between sodium alginate and chitosan

The optimum scaffold was obtained with the concentration of chitosan 0.3%. This kind of scaffold showed the highest values of liquid uptake and excellent mechanical properties (Fig. 2).

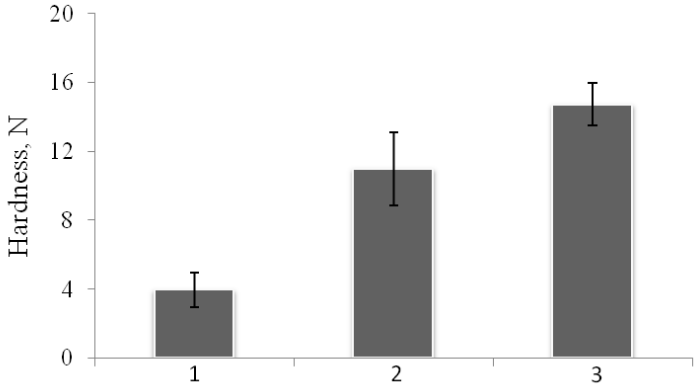

Fig. 2. Mechanical properties of the scaffolds

Water absorption capacity of the composite scaffold reached a value of over 23±2.8 g water /g scaffold.

Acknowledgment: The authors are grateful for Lithuanian Research Council for financial support (project no. 09.3.3-LMT-K-712-03-0102).

[1] W. Paul, C.P. Sharma, Chitosan and alginate wound dressings: a short review, Trends Biomater. Artif. Organs **18**, 18-23 (2004)

STUDY OF PYRROLE ADSORPTION AND ELECTROPOLYMERIZATION ON AU SURFACE FROM PBS SOLUTIONS BY USING ESPR METHOD

Domas Balčiūnas[1], Deivis Plaušinaitis[1]
[1]Vilnius University, Faculty of Chemistry and Geosciences, Institute of Chemistry, Department of Physical Chemistry, 24 Naugarduko, LT-03225 Vilnius, Lithuania
domas.balciunas@chf.stud.vu.lt

Glyphosate-based formulations (the most common being Roundup or *N*-(phosphonomethyl)glycine) are the most widely sold and used herbicide globally. They are used on food crops during cultivation, also used in gardens, along roads and railway tracks. After 40 years of ignorance policy on glyphosate's secondary side effects, many studies in recent years have suggested that glyphosate has worrying health effects at levels regularly detected in food and tap water. In order of such global issue many scientists are trying to discover the best analytical solutions and one of the most popular – research of suitable biosensors.

A biosensor is a device that incorporates a biological recognition (sensing) element in close proximity to, or integrated with the signal transducer, to give a reagentless sensing system specific to a target compound (analyte).

The interest in conducting polymers has proportioned a growing interest on the surface plasmon resonance (SPR) technique due to its high sensitivity, in situ and real time measurements in characterizing films[1]. The combination of SPR with electrochemical measurements (ESPR) has been demonstrated as a powerful technique for the simultaneous characterization and manipulation of electrode/electrolyte interfaces[2].

Main objectives of this study are to reveal biosensor on the basis of polypyrrole (PPy) which would be sensitive to glyphosate (Glyp) by using ESPR method. In order of that we studied pyrrole behavior from phosphate buffer solution such as adsorption and electropolymerization.

The use of SPR, chronoamperometry and electrochemical impedance spectroscopy methods revealed that Py adsorbs from PBS solution on gold surface and after electropolymerization we could see extreme change of SPR angle Θ and reflectivity (Fig. 1). For next step we are going to study Glyp behavior on PPy surface, investigate molecularly imprinted polymer PPy sensitivity on Glyp.

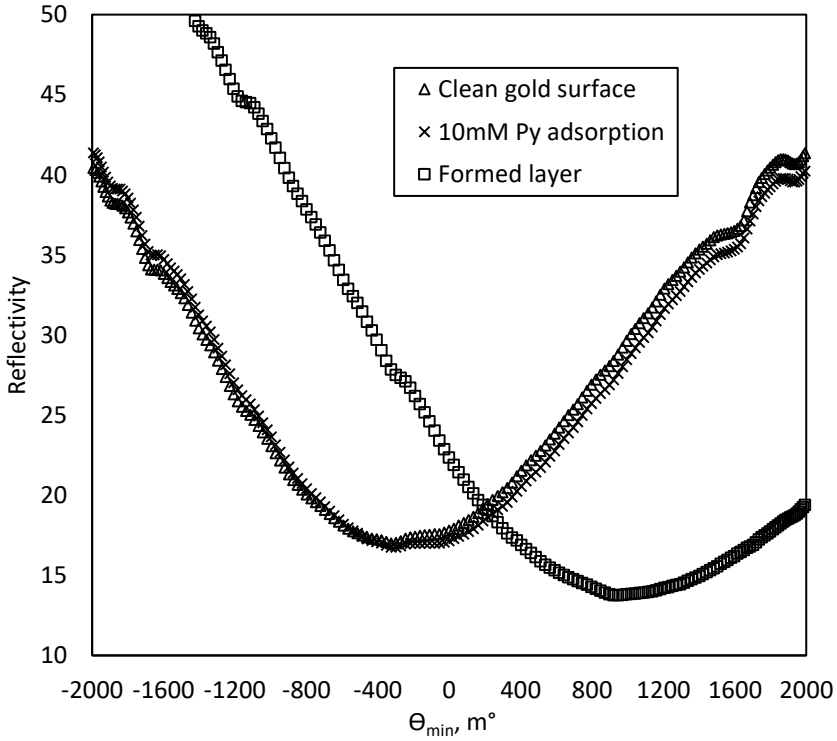

Fig. 1. Reflectivity vs. surface plasmon resonance angle curves recorded on different conditions: a. clean gold surface; b 10mM Py adsorption; c. PPy layer formed from 10mM Py in PBS (pH=7.0).

References
1. Flavio S. Damos, Rita C.S. et al. *Electrochimica Acta 51*, p. 1304 (2006).
2. Akira Baba, Shengjun Tian et al. *Journal of Electroanalytical Chemistry 562*, p. 95 (2004).

MODIFICATION OF TRANSPARENT ITO ELECTRODE WITH ANILINE CO-POLYMERS

Juzef Kucinski[1], Mindaugas Gicevicius[1], Lina Mikoliunaite[1]

[1]Faculty of Chemistry and Geosciences, Vilnius University, Naugarduko 24, LT-03225 Vilnius, Lithuania
juzef.kucinski@gmail.com

Conjugated polymers and their co-polymers possess interesting electrical and optical properties. Due to that they are often used to create sensors, electroactive layers or other polymer coatings [1]. Conjugated polymers are electrically conductive and some of them own interesting electrochromic properties which can be used to improve sensors characteristics, such as selectivity [2]. Using electrochromically active polymer layers two separate response signals: electrical and optical could be measured simultaneously. In this way analytical sensor properties are improved. For this reason the formation of stable and controllable electrochromic layer is of great importance and should be comprehensively investigated. In addition to this, optical properties of the layer could better be evaluated on transparent surfaces, where no additional signal could interfere. Thus, the transparent and conductive indium-tin oxide (ITO) or fluorine doped tin oxide (FTO) glasses are successfully used [3].

The main aim of this research was to electrochemically synthesize co-polymers, consisting of aniline and o,m,p-phenylenediamine or o,m,p-aminophenol on a transparent ITO electrode and characterize their optical, electrical and morphological properties.

The electrochemical deposition of co-polymer layers with varying concentration ratios on a regular ITO electrode was performed by cyclic voltammetry in 0.5M H_2SO_4 aqueous solution using usual three electrode setup. The o-aminophenol synthesis conditions were used according [4] [5] with varying monomer concentrations, scan rate or H_2SO_4 concentration. The obtained spectroscopic properties of the synthesized layer were similar in comparison to polyaniline (Fig. 1), however, the layer was unstable and no further investigation was performed.

M-phenylenediamine (m-PDA) or o-phenylenediamine (o-PDA) and aniline co-polymer was synthesized as recommended in [6], using different concentration ratios and potential intervals. The optimal conditions for both copolymers were determined and the obtained layers were compared with polyaniline layer. Formed polymer coatings were investigated and compared using Raman spectroscopy, Atomic force microscopy and other techniques.

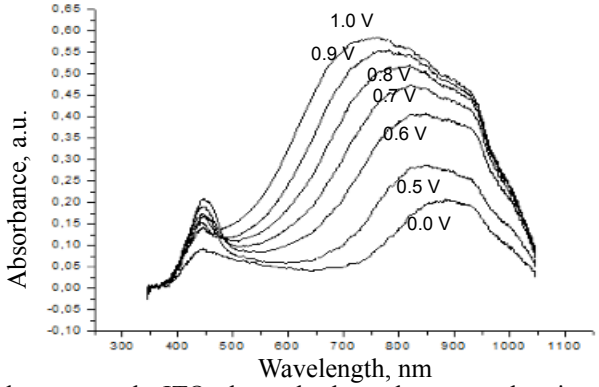

Fig.1. Absorbance of PANI layer coated ITO electrode dependence on electric potential from 0.0 V up to 1.0 V. Synthesis conditions: 0.3 M aniline and 0.5 M H_2SO_4 solution, swept interval -0.25 – -1.2 V.

Acknowledgement:

This research was funded by the European Social Fund under the No. 09.3.3-LMT-K-712 "Development of Competences of Scientists, other Researchers and Students through Practical Research Activities" measure.

[1] N. Nashima, M.Al-Tarawnia, Optimizing low half-wave voltage electro-optic polymer modulator for optical waveguide sensor, Optik - International Journal for Light and Electron Optics Volume 134, April 2017.
[2] M. Ulbricht, Advanced functional polymer membranes, Polymer Volume 47, Issue 7, 22 March 2006.
[3] A.Corradini A.M.Marinangeli et al., Ito as counter-electrode in a polymer based electrochromic device, Electrochimica Acta Volume 35, Issues 11–12, November–December 1990.
[4]J. Zhang, D. Shan et al., Electrochemical copolymerization of aniline with m-aminophenol and novel electrical properties of the copolymer in the wide pH range, Electrochimica Acta 51, 4262–4270, 2006.
[5] A. Shah, R. Holze, Spectroelectrochemistry of aniline-o-aminophenol copolymers Electrochimica Acta 52 1374–1382, 2006
[6]R. Mazeikiene, A. Malinauskas Electrochemical copolymerization of aniline with m-phenylenediamine Synthetic Metals 92 259-263, 1998

SYNTHESIS OF 2-(3-ARYLPROP-2-YNYLTHIO)-1*H*-BENZIMIDAZOLES AND REASEARCH ON THEIR REACTIONS WITH ELECTROPHILES

Justas Pošiūnas, Ieva Karpavičienė

Department of Chemistry and Geosciences, Vilnius University , Lithuania
justposas@gmail.com

It is well-known that electrophile or metal catalyst promoted cyclization reactions of functionally substituted alkynes is an important process in organic synthesis, which allows constructing various carbo- and heterocycles in an efficient way [1]. To the best of our knowledge there are no information about reactivity and electrophile promoted cyclization reactions of heteroaromatic or nonaromatic analogues of 2-(3-arylprop-2-ynylthio)-1*H*-benzimidazoles in the literature. The most alike cyclizations of 2-(2-alkynylphenyl)benzimidazoles induced by iodine have been published in 2016 report [2]. Keeping in mind, that thiazolo[3,2-a]benzimidazole compounds are interesting due to their biological properties [3], we decided to synthesize various 2-(3-arylprop-2-ynylthio)-1*H*-benzimidazoles (1) and to investigate their intramolecular cyclization reactions induced by various electrophile sources.

The starting materials (**1**) were prepared *via* reaction between 2-bromo-1-arylpropynes and 2-thiobenzimidazole, with sodium hydroxide. Then the cyclization reactions of 2-(3-arylprop-2-ynylthio)-1*H*-benzimidazoles (**1**) induced by electrophiles have been studied. It was found that compounds (**1**) can be cyclized to 2,3-dihydro[1,3]thiazolo[3,2-*a*]benzimidazole (2) or 2*H*-[1,3]thiazino[3,2-*a*]benzimidazole (3) heterocyclic systems (Figure 1). Results of cyclization reaction depended only on starting material structure and variation on electrophiles influenced reaction rates and stability of products. The scope and limitations of this reaction will be enlarged in presentation.

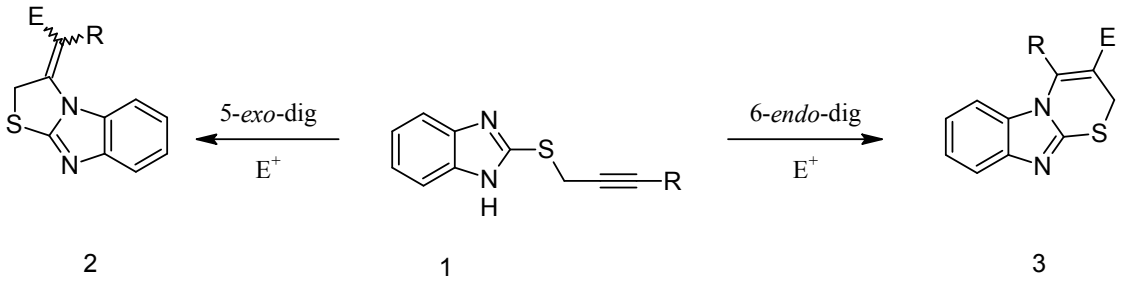

Fig. 1. 2-(3-arylprop-2-ynylthio)-1*H*-benzimidazole cyclization scheme.

[1] (a) A. Palisse and S. F. Kirsch *Org. Biomol. Chem*., **2012**, 10, 8041-8047 (b) R. Bukšnaitienė, I. Čikotienė, *Synlett,* **2015**, 26, 479 – 483 (c) M. Chioua, E. Soriano, L. Infantes, M. L. Jimeno, J. Marco-Contelles, A. Samadi *Eur. J. Org. Chem.* **2013**, 35–39 (d) X. Zhang, T. Yao, M. A. Campo, R. C. Larock *Tetrahedron* **2010**, 66, 1177–1187 (e) K. K. Balasubramanian, R. Nagarajan *Synthesis,* **1976**, 189

[2] S. Matsumoto, S. Kikuchi, N. Norita, H. Masu, M. Akazome *J. Org. Chem.*, **2016**, 81, 5322−5329

[3] Khalid A. Al-Rashood and Hatem A. Abdel-Aziz *Molecules*, **2010**, *15*(6), 3775-3815

CYTOCHROME P450 7B1 F470I MUTATION AFFECTS ON PROTEIN STRUCTURE STABILITY

Yaraslau Dzichenka[1], Evgeniy Gudnyy[2], Sviatlana Smolskaya[1]

[1] Institute of Bioorganic Chemistry, National Academy of Sciences, Belarus
[2] Department of Biology, Belarusian State University, Belarus
dichenko@iboch.by

Human cytochrome P450 7B1 (CYP7B1, EC 1.14.13.100) – microsomal enzyme which takes part in biosynthesis of bile acids precursors, in metabolism of neurosteroids, in regulation of immunoglobulin biosynthesis and in metabolism of estrogen receptor ligands [1]. Dysfunction of CYP7B1 in human body is associated with a neurodegenerative disease – spastic paraplegia type 5 (SPG5) [2, 3]. But molecular reasons of such disorders are still unclear due to lacking of information about chemical and physical properties of mutant form of the enzyme.

In the present study we performed *in silico* and *in vitro* analysis of amino acid substitution F470I influence on CYP7B1 structure.

Analysis of 200 ns accelerated molecular dynamics (aMD) simulation showed that overall fold of mutant protein (CYP7B1_F470I) is conserved and in general this mutation does not lead to the significant changes of the protein structure. Application of principal component analysis showed that there are little changes in CYP7B1 substructures mobility due to F470I substitution. By using of SDM – a server for predicting effects of this mutation on protein stability [4], it was shown that F470I substitution significant increases CYP7B1 stability.

In order to compare thermodynamic properties of CYP7B1_WT and CYP7B1_F470I we overexpressed proteins in *E. coli* cells and obtained highly purified enzymes by using of 2-stage chromatography approach.

Purified enzymes have a typical P450 absorption spectrum with the heme iron in a low-spin state, as evidenced by a Soret region maximum at 419 nm and α, β-bands at 567 and 535 nm, respectively, and a spectrophotometric index $A_{419/280}$=1.4 (for CYP7B1_WT), and $A_{419/280}$=1.2 (for CYP7B1_F470I). The proteins molecular mass corresponds to the expected value of 56 kDa. Upon reduction with sodium dithionite, followed by CO binding, a ferrous-CO complex is formed with a Soret region maximum at 450 nm, indicating that the reduced, substrate-free form is rather stable for both proteins.

Tolerances of the enzymes to chaotropic agent (GuHCl) were compared and thermodynamic stability of the native form was determined. It was demonstrated that the energy barrier for folded-unfolded transition is lower for CYP7B1_WT than for CYP7B1_F470I.This fact is in a good agreement with results of *in silico* analysis.

So, the data obtained indicate that F470I replacement changes CYP7B1 conformational stability in the *in vitro* system and this alteration may be one of the reasons of the SPG5 disorder, when considering *in vivo* system. The influence of F470I substitution on CYP7B1 catalytic properties is under investigation.

[1] S. Steckelbroeck et al, Characterization of the dehydroepiandrosterone (DHEA) metabolism via oxysterol 7alpha-hydroxylase and 17-ketosteroid reductase activity in the human brain, J. Neurochem. **83(3)**, 713-726 (2002).
[2] A.R. Stiles et al, CYP7B1: one cytochrome P450, two human genetic diseases, and multiple physiological functions, J. Biol. Chem. **284(42)**, 28485-28489 (2009).
[3] Y. Akwa et al, Neurosteroid metabolism. 7 alpha-Hydroxylation of dehydroepiandrosterone and pregnenolone by rat brain microsomes, Biochem. J. **288(3)**, 959-964 (1992).
[4] A.P. Pandurangan, SDM: a server for predicting effects of mutations on protein stability, Nucleic Acids Res. **45(1)**, 229-235 (2017).

DAS AND EADS-BASED ANALYSIS OF THE TIME-RESOLVED FLUORESCENCE IN THE AGGREGATES OF PHOTOSYNTHETIC COMPLEXES

Yakov Braver[1], Jevgenij Chmeliov[1,2], Andrius Gelzinis[1,2], Leonas Valkunas[1,2]

[1]Department of Molecular Compound Physics, Centre for Physical Sciences and Technology, Vilnius, Lithuania.
[2]Institute of Chemical Physics, Faculty of Physics, Vilnius University, Vilnius, Lithuania.
jakov.braver@ff.stud.vu.lt

Among the methods of studying characteristics of various molecular systems, time-resolved spectroscopy is known to be particularly insightful. During the experiment, the system under consideration is usually first excited abruptly with a short pulse and then the response of the system (in the form of radiation) is measured. Proper analysis of the resulting time-resolved spectra can contribute remarkably to the understanding of the physical processes governing the behaviour of the system. However, the extraction of the required information is a non-trivial task and due to its significance it is vital to select (or develop) a suitable method of data analysis.

The most-widely used numerical methods to analyse the two-dimensional array of data collected in such a way are based on the calculation of the Decay Associated Spectra (DAS) or the Evolution Associated Difference Spectra (EADS) with the corresponding decay times [1]. The goal is to fit the data with a number of exponentially decaying components (or compartments) by finding their decay times, and then reconstruct the spectra of the components. The DAS describe the system as a set of non-interacting compartments, each decaying with a certain decay time constant after the excitation. Consequently, this model does not take into account any possible energy transfers between the compartments. Such transfers are incorporated into the EADS model, which implies that only one compartment is initially excited. As it decays, it sequentially excites the next compartments causing them to fluoresce. Considering the differences between the models, it may be beneficial to try applying both analysis methods to the measured data.

The first step in applying the models is determining the decay time constants of each compartment. These constants τ_i can be found by solving a minimisation problem: using a computational algorithm one should find such values of parameters τ_i which would make the reconstructed fluorescence intensity function as close to the measured function as possible. If both functions match (with the certain desired tolerance), then we may proceed to examine the spectra and the kinetics of the components to see whether the applied model produced any physically meaningful results.

In this work we studied whether the DAS and EADS models are appropriate for describing the fluorescence decay kinetics in the aggregates of photosynthetic major light-harvesting complexes, that have been measured recently over a wide temperature range [2]. Figure 1a shows the experimental data of fluorescence intensity measurements at 50 K temperature. In order to evaluate the studied analysis methods we used the experimental data and the data given by the models to plot the decay kinetics (Fig. 1b) and the fluorescence spectra (Fig. 1c). Here both DAS and EADS produced similar results, therefore the figures only show the DAS-based results. As we can see, the lines representing the reconstructed kinetics appear to repeat the kinetics of the measured data and the reconstructed spectra are also in agreement with the measurements. At other temperatures the models proved to be able to describe the system accurately as well. At temperatures lower than 130 K the system is described more accurately when a 3-compartmental model is applied which gives an additional component with a decay constant significantly bigger than those of the two other components. A 2-compartmental model is suitable for the systems at temperatures of 130 K and higher.

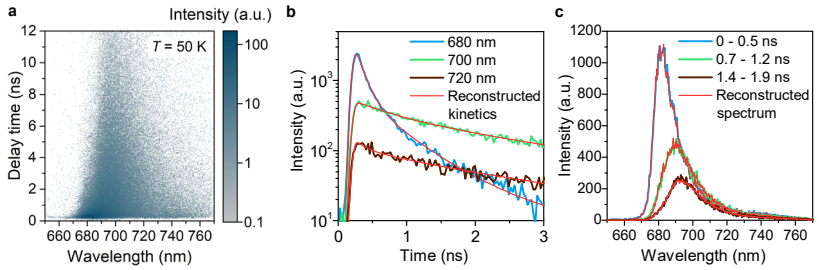

Fig. 1. Fluorescence measurements of LHCII aggregates at 50 K temperature and its analysis. **(a)** Experimental data of the fluorescence intensity measurement. **(b)** Fluorescence decay kinetics integrated over a 6 nm wide region centred at the specified wavelengths as given by the measurements, and the reconstructed kinetics. **(c)** Fluorescence spectra integrated over the specified time period as given by the measurements, and the reconstructed spectra.

The DAS and EADS models are not mathematically complicate, nor do they require special computational power, but nevertheless they are suitable for analysis of time-resolved measurements. Both methods revealed the co-existence of at least two spectrally distinct states of LHCII complexes in the aggregate and allowed us to evaluate the timescale of excitation energy transfer between these states. Therefore, we can conclude that the DAS and EADS models may be used as a reasonable approach to get an initial understanding of the processes in the system in question. However, more detailed structure-based models are required to account for the excitation migration through the aggregate.

[1] I. H. M. van Stokkum et al., Global and target analysis of time-resolved spectra, Biochim. Biophys. Acta **1657**, 82–104 (2004).
[2] J. Chmeliov et al., The nature of self-regulation in photosynthetic light-harvesting antenna, Nat. Plants **2**, (2016).

POLYMERIC FILMS FROM CALCIUM ALGINATE FOR THE PREVENTION OF CATHETER RELATED INFECTIONS

Deimantė Narauskaitė, Odeta Baniukaitienė

Department of polymer Chemistry and Technology, Kaunas University of Technology, Lithuania
deimante.narauskaite@ktu.edu

For the prevention of intravascular catheters and making them with prolonged central venous access polymeric antimicrobial wound-dressings are required. Typically, these wound-dressings contain polymeric films made up of synthetic polymers. Nowadays, significant attention is focused on natural polymers due to their biocompatibility, hydrophilicity, non-toxicity and controllable biodegradability.

The aim of this work was to prepare natural polymer-based flexible films for the prevention of catheter related infections. Polymeric films were prepared by mixing sodium alginate solution with the respective amount of glycerol (**Table 1**). Glycerol was used as a plasticizer in order to improve the flexibility of the films.

Table 1. The composition of the films

Film number	Concentration, %			
	Sodium alginate	Glycerol	Calcium lactate	Purified water
1	1	-	1	up to 100
2	1	1		
3	1	5		
4	2	-		
5	2	1		
6	2	5		
7	3	-		
8	3	1		
9	3	5		

Polymer solution with the respective amount of plasticizer was poured into petri dishes in order to form films. Further, polymer was cross-linked with divalent ions using calcium lactate as a source of calcium ions. The results showed that the mechanical properties of the films depended on the concentration of polymer and plasticizer. The films obtained with 5 % glycerol and with 3 % sodium alginate were the most flexible.

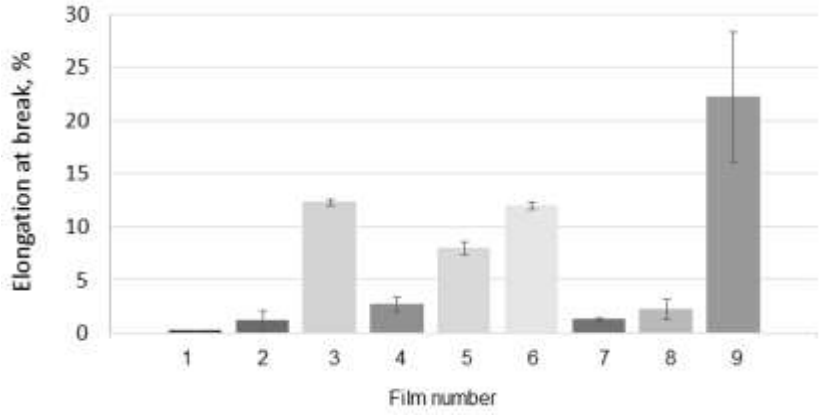

Fig. 2. Mechanical properties of the films

The antibacterial effects of the most suitable films were ensured by spraying polymeric films with a mastic gum solution.

SPLIT-RING RESONATORS FORMATION ON FABRIC USING CONDUCTIVE POLYMER POLYPYRROLE

Monika Kirsnytė[1], Paulius Ragulis[2], Augustas Šukys[3], Rimantas Simniškis[2], Žilvinas Kancleris[2], Arūnas Stirkė[1]

[1] Department of Material Science and Electrical Engineering, Center for Physical Sciences and Technology, Lithuania
[2] Department of Physical Technologies, Center for Physical Sciences and Technology, Lithuania,
[3]*Faculty* of *Chemistry and Geosciences*, Vilnius University, Lithuania
monika.kirsnyte@ftmc.lt

Nowadays a lot of new shielding materials and structures are investigated, developed and commercially available. One promising trend is the application of organic conductors with tunable properties [1]. The structures and composites containing polypyrrole (PPy) are convenient in application as shielding additive material in fabrics making functional textiles for use in electromagnetic radiation shielding [2] or flexible electronics (wearable electronics) e.g. fabricating radio frequency identification (RFID) antennas. The aim of this work was to investigate polymeric split-ring resonators properties on wool fabric in 1-20 GHz frequency range optimizing their transmittance features and observing resonance peaks.

PPy split-ring resonators (SRR) were formed using PPy film formation on wool fabric (electrically conductive composite formation). The coating procedure was performed on fabric sheets of size 35 x 25 cm with polyvinyl alcohol (PVA) and $FeCl_3$ mixture using screen printing with particular split-ring pattern. Adhesive polymeric matrix is used for $FeCl_3$ catalyst over all distribution throughout the textile fabrics to ensure conductive layers strong bond to the fabric. Coated fabrics were dried at condensation temperature 80 °C for 10 min then spray coated with monomer pyrrole and water solution and again dried in laboratory oven. Experimental investigations of transmittance of manufactured samples have been performed in 1-20 GHz frequency range in an anechoic chamber. Experimental results for vertical polarization of electric field together with calculation results are shown in Fig 1. It is seen that dependence of transmittance on

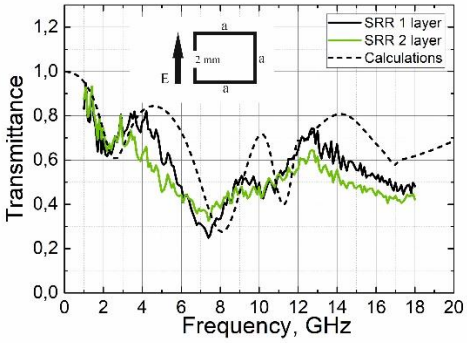

Fig. 1. Dependence of transmittance on frequency, polarization of electric field shown in insert.

frequency demonstrates a few broad minimum peaks on particular frequencies of which theoretical calculations can be determined using the following expression

$$f_r = \frac{nc}{2n_{ef}P}, \text{ where } n = 1, 3, 5; \text{ and } P = 4 \cdot a \quad (1)$$

Results indicate that the measured dependences of transmittance on frequency of polymeric PPy split-ring resonators on wool fabric show two broad resonance peaks at 2 GHz and 7.8 GHz, whereas theoretical calculations demonstrate three resonance peaks. In order to get the sharper peaks corresponding to theoretically calculated and the right number of them, one will need to synthesize a more conductive PPy composites on textile fabrics. Conductive polymer SRR could then be used in developing new functional textiles with lightweight, cost effective and desired design RFID antennas.

[1] Kaynak, A., et al., *A study of microwave transmission, reflection, absorption, and shielding effectiveness of conducting polypyrrole films.* Journal of applied polymer science, 1994. **54**(3): p. 269-278.
[2] Rubežienė, V., et al., *The influence of distribution and deposit of conductive coating on shielding effectiveness of textiles.* The Journal of The Textile Institute, 2018. **109**(3): p. 358-367.

STUDY OF FORMATION OF GALLIUM SELENIDE LAYERS ON POLYCAPROAMIDE

Virginija Ulevičienė, Remigijus Ivanauskas*

Department of Physical and Inorganic Chemistry, Kaunas University of Technology, Lithuania
virginija.balciunaite@ktu.edu

The synthesis and characterization of metal selenides have attracted considerable attention because of their brilliant application prospects. They are widely used as sensor and laser materials, optical recording materials, and thermoelectric cooling materials [1]. Layer-structured group III chalcogenides have highly anisotropic properties and are attractive materials for stable photocathodes and battery electrodes [2]. For the above-mentioned applications, varieties of techniques have been developed to prepare gallium selenides. The polycaproamide belongs to hydrophilic and semi-hydrophilic polymers that are capable of absorbing ions of various electrolytes from aqueous solutions. Therefore, the sorption–diffusion method for the formation of thin layers of metal selenides in the surface of polymer is more convenient [3, 4]. Using this method the thin layers of gallium selenide on polycaproamide substrate in two stages were formed. In the first stage, PA film were treated with the solution of the precursor. As selenium precursor the solution of potassium selenotrithyonate was used. During treatment the anions of lower selenopolythionate – selenotrithionate, $SeS_2O_6^{2-}$, containing chains of divalent selenium atoms of low oxidation state, $-O_3S-Se-SO_3-$ are sorbed by a polymer. In the second stage, polymer were treated with the solution of gallium sulphate. The main task of this work was to prove the suitability of seleniumized polycaproamide films with solution of $K_2SeS_2O_6$ for formation the gallium selenide layers on polymer.

The visual examination of the polymer films colour gave the first indications that the selenotrithionate ions are sorbed–diffused into the tapes: colourless PA tapes depending on the concentration of sorbed–diffused $SeS_2O_6^{2-}$ ions gradually acquires transparent yellow and light red colour. The changing of polymer film colour to darkbrown after its treatment with the gallium sulphate solution indicate the formation of gallium selenide layers on the surface of a polymer by equation:

$$3SeS_2O_6^{2-} + 2Ga^{3+} + 6H_2O \rightarrow Ga_2Se_3\downarrow + 6H_2SO_4$$

The results of X−ray diffraction analysis confirmed the formation of gallium selenide layers in the surface of polyamide. The amount of gallium in the gallium selenide layers increases with the increasing of concentration, of temperature and of pH the solution of thallium salt.

Acknowledgements.
This research is funded by the European Social Fund under the No 09.3.3-LMT-K-712 "Development of Competences of Scientists, other Researchers and Students through Practical Research Activities" measure.

[1] J. Zhu, Y. Koltypin, A. Gadanken, General sonochemical method for the preparation of nanophasic selenides: Synthesis of ZnSe nanoparticles, Chem. Mater. **12**, 1, 73-78 (2000).
[2] N. C Fernelius, Properties of gallium selenide single crystal, Prog. Cryst. Growth Charact. **28**, 4, 275-353 (1994).
[3] R. Ivanauskas, J. Baltrusaitis, Synthesis and surface properties of polyamide–Cu_xSe composite thin films, Appl. Surf. Sci. **283**, 360–366 (2013).
[4] R. Ivanauskas, L. Samardokas, M. Mikolajūnas, D. Viržonis, J. Baltrušaitis, Polyamide–thallium selenide composite materials via temperature and pH controlled adsorption–diffusion method, Appl. Surf. Sci. **317**, 818-827 (2014).

FORMATION AND EVALUATION OF A MOLECULARLY IMPRINTED POLYMER BASED SENSOR FOR URIC ACID

Linas Sinkevičius[1], Deivis Plaušinaitis[1]

[1] Department of Physical Chemistry, Faculty of Chemistry and Geosciences, Vilnius University, Lithuania
linas.sinkevicius@chf.vu.lt

In humans and higher primates, uric acid (UA) is the final oxidation product of purine metabolism and is excreted in urine. However, extreme abnormalities of UA levels are symptoms of several diseases [1]. Thus, the determination of UA concentration in human blood or urine is very important to warn the presence of some diseases, such as gout, Lesch–Nyhan syndrome, immunodeficiency and gouty nephropathy.

Molecularly Imprinted Polymers (MIPs) are synthetic receptors obtained by the molecular imprinting methods [2,3], presenting a number of favorable aspects for sensing in comparison to bioreceptors, for example antibodies [4], including a better stability out of the native environment, reproducibility and low cost. They are porous solids containing specific sites interacting with the molecule of interest according to a "key and lock" model.

Here we present our results in preparation of polypyrrole-based MIPs and evaluation of their properties for sensing. The preparation of MIP sensor was done by electrochemically coating gold electrode surface with polypyrrole matrix containing UA binding sites. The coating was formed by potentiostatic oxidation of pyrrole monomer in the presence of uric acid. Recognition capacity and selectivity of MIP sensors were evaluated using Quartz Crystal Microbalance (QCM) and electrochemical methods.

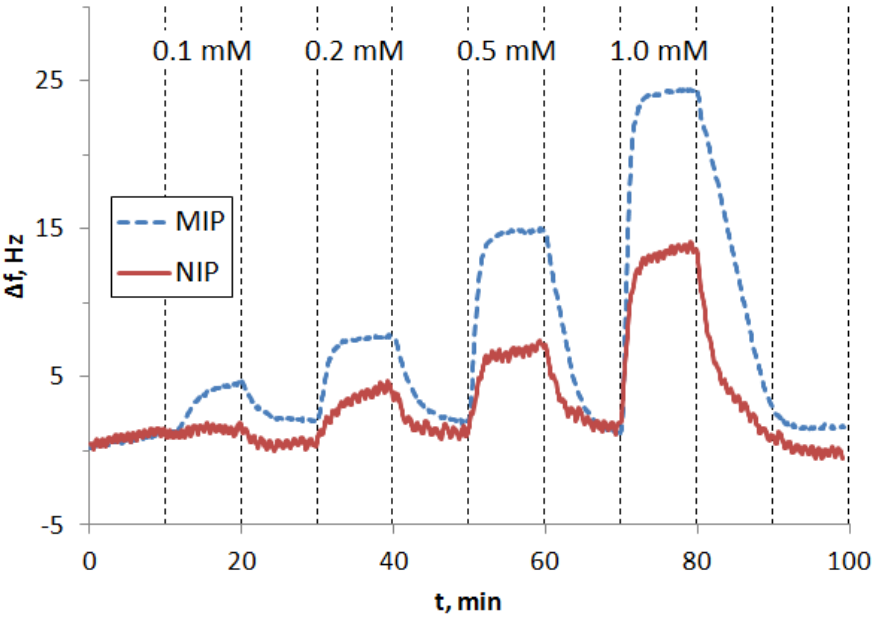

Fig. 1. Change in resonant frequency (Δf, Hz) of the gold coated QCM sensor, modified with uric acid imprinted MIP (dashed line) and non-imprinted NIP (solid line) polypyrrole coating, to the addition of different concentrations of uric acid in phosphate-buffered saline.

[1] V. V. S. Eswara Dutt, H. A. Mottola, Determination of uric acid at the microgram level by a kinetic procedure based on a pseudo-induction period, Analytical Chemistry **46**, 1777-1781 (1974).
[2] B. Sellergren, Noncovalent molecular imprinting: antibody-like molecular recognition in polymeric network materials, Trends in Analytical Chemistry **16**, 310-320 (1997).
[3] A.G. Mayes, K. Mosbach, Molecularly imprinted polymers: useful materials for analytical chemistry, Trends in Analytical Chemistry **16**, 321-332 (1997).
[4] K. Haupt, K. Mosbach., Molecularly Imprinted Polymers and Their Use in Biomimetic Sensors, Chemical Reviews **100**, 2495-2504 (2000).

ELECTRO-REDUCTION OF CO_2 ON GOLD-COPPER ELECTRODE

Andrius Rutkauskas, Aldona Balčiūnaitė, Loreta Tamašauskaitė-Tamašiūnaitė, Eugenijus Norkus

[1] Department of Catalysis, Center for Physical Sciences and Technology, Saulėtekio Ave. 3, LT-10257, Vilnius, Lithuania
[2]Faculty of Chemistry and Geosciences, Vilnius university, Naugarduko 24, LT-03225, Vilnius, Lithuania
andrius.rutkauskas@chf.stud.vu.lt

Fuels that originally originate from fossil resources emit multiple gasses that pose a potential threat to global climate. One of those gasses is carbon dioxide (CO_2). Instead of CO_2 simply being emitted into the atmosphere, it can be used to reproduce multiple different industrial chemicals by electrochemical process that operates at room temperature and atmospheric pressure. The electro-reduction of CO_2 on various catalysts is an intensively studied reaction. Various electrocatalysts, including Au and Cu have been investigated as electrocatalysts for the electro-reduction of CO_2. In the present study, a rapid microwave heating method was used to prepare the graphene or carbon supported Au and Cu electrocatalysts (denoted as AuCu/GR and AuCu/C). The morphology and composition of the catalysts were examined using Field Emission Scanning Electron Microscopy and Inductively Coupled Plasma Optical Emission Spectroscopy. The electrochemical behavior of the fabricated catalysts was examined for the electro-reduction reaction of CO_2 by cyclic voltammetry and linear sweep voltammetry in different phosphate buffers as electrolyte.

In a summary, we developed a facile microwave-assisted chemical reduction method for preparation of the AuCu/GR and AuCu/C electrocatalysts for CO_2 reduction. This work offers a general way to synthesize the graphene or carbon supported Au-Cu materials, which have enhanced electrocatalytic activity for the electro-reduction of CO_2.

FLUORESCENCE PROPERTIES OF PYRANOSE OXIDASE

Augustė Repečkaitė[1], Renata Karpič[2]

[1] Faculty of Fundamental Sciences, Vilnius Gediminas Technical University, Saulėtekio Ave. 11, LT-10223 Vilnius, Lithuania

[2] Institute of Physics, Center for Physical Sciences and Technology, Saulėtekio av. 3, LT-10257 Vilnius, Lithuania.

auguste.repeckaite@stud.vgtu.lt

Enzyme pyranose oxidase (POx) has gained increased attention during the last years because of a number of attractive applications for this enzyme. POx is a unique biocatalyst with high potential for biotransformations of carbohydrates and in synthetic carbohydrate chemistry. Recently, it was shown that POx is useful as bioelement in biofuel cells, replacing glucose oxidase (GOx), which traditionally is used in these applications. POx offers several advantages over GOx for this application, e.g., its much broader substrate specificity. Despite the increasing number of studies on POx, there is little information about the properties of the enzyme at different pH conditions [1].

Spectroscopic properties of pyranose oxidase (POx) and flavin adenine dinucleotide (FAD) were investigated in different acidity environments. The purpose of this research was to evaluate absorption and fluorescence spectra changes and to associate them with changes of POx activity. The study of the absorption and fluorescence spectra and the measurements of relaxation times were carried out using a citric acid sodium phosphate buffer with pH values from 3 to 8.

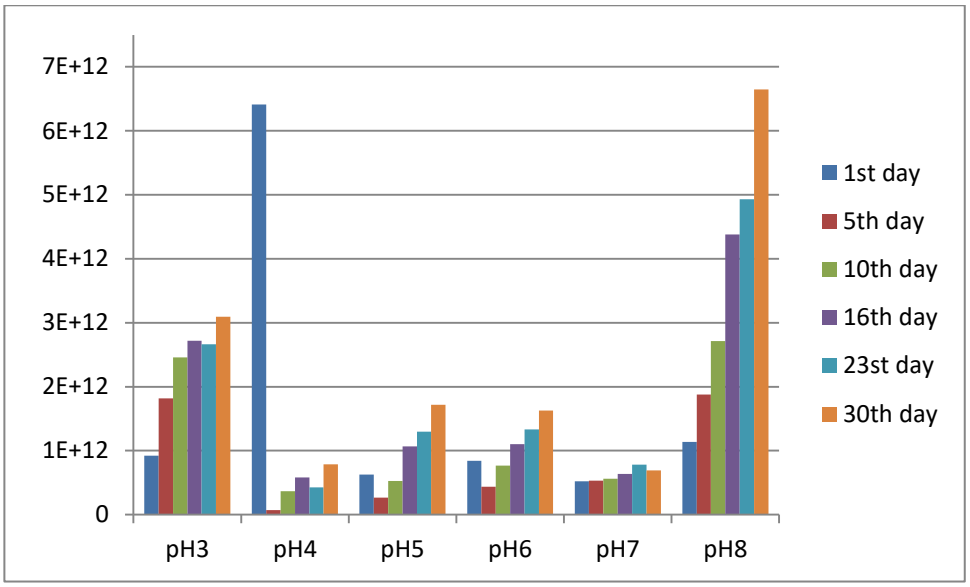

Fig.1. The changes of integrated fluorescence intensity of POx during the 30-day period.

POx is a flavin adenine dinucleotide (FAD) containing glycoprotein. FAD is involved in enzymatic redox reactions and determines the enzyme's activity. POx will lose its activity if FAD dissociates from the enzyme active site.

During this study, POx activity trend was found: over time POx's activity is decreasing. The increased intensity of the fluorescence band of POx at 530 nm is associated with a decreased activity of an enzyme. The changes of fluorescence intensity band are associated with dissociation of FAD from the enzyme. However, the process is not reversible and the decrease of fluorescence intensity is associated with structural changes in the FAD: reduction of FAD, organic molecule aging process.

[1] Salaheddin, Clara et al. Characterisation of Recombinant Pyranose Oxidase from the Cultivated Mycorrhizal Basidiomycete Lyophyllum Shimeji (hon-Shimeji). Microbial Cell Factories 9 (2010): 57.

MOLECULAR DYNAMICS/QUANTUM MECHANICS MODELING OF STRUCTURAL AND NMR PROPERTIES OF ACETIC ACID/CYCLOHEXANE BINARY SOLUTIONS

Dovilė Lengvinaitė[1], Kęstutis Aidas[1]

[1] Institute of Chemical Physics, Vilnius University, Lithuania
dovile.lengvinaite@ff.vu.lt

Acetic acid is considered as a simple organic acid and an important substance in biochemistry. Molecular association in this carboxylic acid has been a subject of extensive investigations. Diffraction techniques as well as spectroscopic measurements and computational methods have also been used to investigate the liquid state of acetic acid (AA). According to the neutron diffraction data, it has been suggested that cyclic dimer clusters yield a good description of the liquid structure [1]. In contrast, molecular dynamics (MD) and Monte Carlo simulations suggest that acetic acid molecules prefer chain structures via hydrogen-bond (HB). The same results have been deduced using large-angle x-ray scattering [2]. Raman spectroscopy and ab-initio calculation lead to the conclusion that acetic acid molecules form a chain structure by inter-molecular HB between the hydroxyl hydrogen atom and the carbonyl oxygen atom. Similar experiments suggested that the equilibrium in AA at 20 ˚C is comprised mainly of cyclic dimers, with some linear dimers, chain polymers, and monomers also present [3].

Measurements of ^{1}H NMR of acetic acid and cyclohexane binary solutions showed a very interesting non-monotonic evolution of the chemical shift of acetic acid protons by changing the concentration of the solution components [4]. This evolution reflects the peculiarities of the association of acetic acid in these systems, which until now have not been thoroughly investigated. The formation of acetic acid dimers or higher order associates and the change in the cis-trans conformational equilibrium are only some of the processes at the molecular level that could be sensitive to the measured NMR spectral parameters. In order to explain the results of NMR parameters of acetic acid and cyclohexane binary solutions, we performed the simulation of the structure, dynamics and NMR spectral parameters of these systems. For this, we used the classical molecular dynamics simulations and combined QM/MM methods for calculating NMR chemical shifts.

In this work, we have performed detailed structural investigations of acetic acid and cyclohexane binary solutions. To describe the intermolecular associations in liquid acetic acid, we have considered three different structures, involving only the trans conformers (Fig. 1). We have performed classical molecular dynamics simulations for these systems, using OPLS-AA and AMBER based force field for acetic acid and cyclohexane molecules. Detailed information concerning local structure was obtained by analyzing relevant radial distribution functions (RDF). A detailed trajectory analysis was performed to estimate the populations of cyclic dimers, cyclic trimers and chain dimers in the pure acetic acid system. Having recorded the trajectories of the systems, we turned to the combined quantum mechanics/molecular mechanics (QM/MM) based calculations of the ^{1}H NMR parameters.

Detailed account of the results will be presented at the conference.

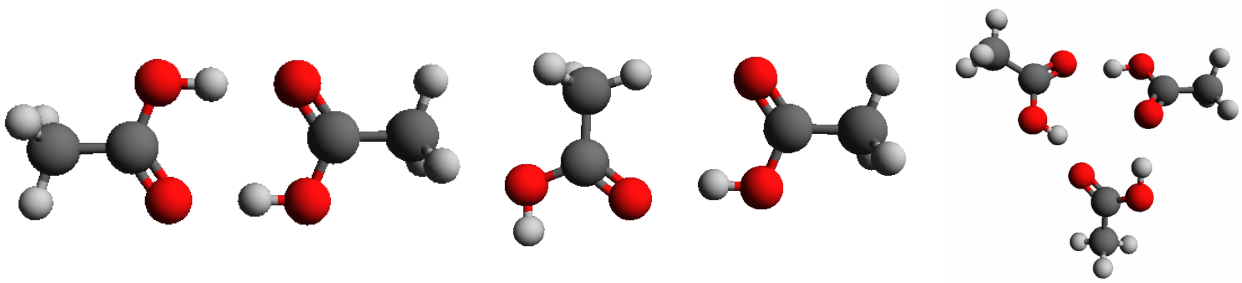

Fig. 1. Structures of the cyclic dimer, chain dimer and cyclic trimer

Computations were performed on resources at the High Performance Computing Center “HPC Sauletekis” in Vilnius University Faculty of Physics.

[1] H. Bertagnolli, H.G. Hertz, Phys.Status Solid A **49**, 463-472 (1978).
[2] T. Takamuku, Y. Kyoshion, H. Noguchi, S.Kusano, T. Yamaguchi, J.Phys.Chem.B **111**, 9270 (2007).
[3] S. Fathi, S. Bouazizi, S. Trabelsi et. al., J. Molec. Liq. **196**, 69-76, (2014).
[4] L.L. Kimtys, V.J. Balevicius, J. Molec. Liq., **15**, 151-161, (1979).

THE ESTABLISHMENT OF METROLOGICAL CHARACTERISTICS OF THREE ANALYTICAL METHODS DURING THE QUANTIFICATION OF VOLATILE COMPOUNDS IN ALCOHOLIC PRODUCTS

Anton Korban[1,2], Siarhei Charapitsa[1], Svetlana Sytova[1]

[1] Institute for Nuclear Problems of Belarusian State University, Belarus
[2] Faculty of Chemistry, Belarusian State University, Belarus
karbonat7@gmail.com

Six standard solutions of volatile compounds in water-ethanol mixture were prepared gravimetrically. These solutions were analysed with three analytical methods: traditional method of internal standard (IS), advanced method of IS and external standard (ES) method. The advanced IS method is called "Ethanol as Internal Standard" and consists in the calculation of relative response factors (RRF) relatively ethanol [1]. The absence of the necessity of IS compound artificial addition and the determination of alcohol by volume content makes the method "Ethanol as Internal Standard" technically better.

The main features of the two most used analytical methods and advanced one were determined by the interlaboratory experiments. Such important analytical characteristics as relative standard deviation (RSD), limit of quantification (LOQ) were obtained for each of the nine most spread volatile impurities. All the experimental data was obtained through the gas chromatography measurements, as it is indicated in the regulatory document [2].

Relative bias, as one of the most demonstrative parameter, which shows the accuracy of a method was calculated for five prepared standard solutions (except one solution used as a calibration point) according to the formula:

$$bias, \% = \frac{\left| C_i(mg/L\ AA) - C_i^{st}(mg/L\ AA) \right|}{C_i^{st}(mg/L\ AA)} \cdot 100\% \qquad (1)$$

Then the demonstrative histograms of relative biases of the three methods were obtained. Each line is relevant to a single analytical method. Lower biases of a method cause smaller area of polygon. Two used IS methods showed high similarity in bias values relatively each other. Oppositely, ES method polygon generally appeared to be quite bigger than the polygons of IS methods. In addition, RSD and LOQ values for ES method had greater values. This can characterize ES method as the worst method among used in the experiment.

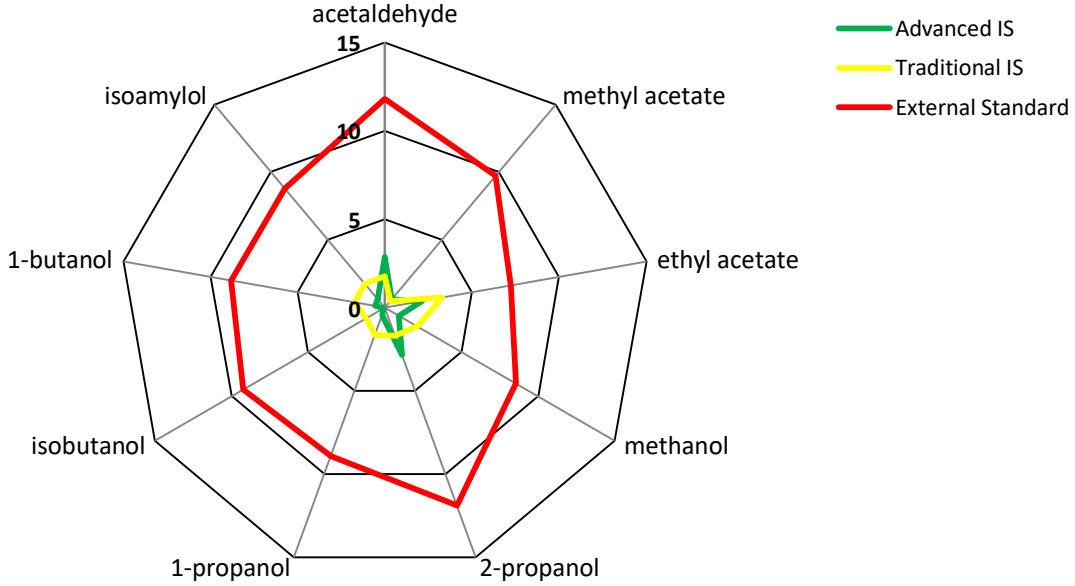

Fig. 1. The example of obtained histogram of biases (%) comparison of three analytical methods.

Analysis of obtained data shows that advanced method of internal standard is comparable with traditional one from analytical point of view. It was showed that this method is robust and can be applied at a great range of volatiles concentrations: from few to more than 5000 mg/L of absolute alcohol. As the result direct quantitative determination of volatile compounds in alcoholic products becomes cheaper faster and easier when the method "Ethanol as Internal Standard" is applied.

[1] S.V. Charapitsa, A.N. Kavalenka, N.V. Kulevich et al., Direct Determination of Volatile Compounds in Spirit Drinks by Gas Chromatography, Journal of Agricultural and Food Chemistry **61**, 2950-2956 (2013).
[2] European Commission EC No. 2870/2000 of 19 December 2000. Off J Eur Communities 333:20–46 (2000).

DEPOSITION OF SELENIUM FILMS ON GLASS USING SELENOPOLYTHIONATES

Viktorija Osipovaite, Algimantas Ivanauskas, Ingrida Ancutiene

Department of Physical and Inorganic Chemistry, Kaunas University of Technology, Lithuania
viktorija.osipovaite@ktu.edu

Selenium is a non-metal with intermediate properties between chalcogen of sulfur and tellurium [1]. In the last two decades, a significant interest in selenium has increased appreciably owing to number of applications such as modern electronics, optoelectronics, new generation sensors and photovoltaic cells [2]. The unique photoelectric and semiconducting properties of selenium find applications in rectifiers, photocells switching electronic devices, memory devices and X-ray photoconductors [1, 2]. Selenium exists in one of four major structures: amorphous, trigonal (hexagonal), and α- or β-monoclinic. The most stable crystal form is the trigonal (hexagonal) Se, consisting of helical Se_n chains. Both monoclinic α and β Se consist of Se_8 rings [3]. Selenium thin films have been prepared by various physical and chemical methods. In present work, selenium films are obtained by chemical bath deposition using a solution of selenpolythionates as selenium precursor.

The glass substrates (20×20×1 mm) with a matte finish on a single side were used. All substrates were washed with liquid soap and distilled water, and dried. Then they were cleaned ultrasonically in an acetone bath for 10 min at 40 °C. For deposition of selenium film, a solution of selenopolythionates was prepared from 0.4 mol/L H_2SeO_3 and 1 mol/L $KHSO_3$ 1:1 mixture. Dark red colored Se film was deposited on glass substrate for 2 or 3 h at 60 °C. Selenium films were characterized by XRD technique using a Bruker AXS D8 Advance diffractometer.

The components of H_2SeO_3 and $KHSO_3$ mixture react with each other and diseleniumtetrathionate acid in solution according to reaction is formed [4]:

$$2H_2SeO_3 + 5KHSO_3 \rightarrow 2H_2Se_2S_2O_6 + 2K_2SO_4 + KHSO_4 + 3H_2O \quad (1)$$

By heating $H_2Se_2S_2O_6$ decomposes and releases elemental selenium, which is deposited on glass substrate:

$$Se_2S_2O_6^{2-} \rightarrow Se + SeS_2O_6^{2-} \quad (2)$$

The amorphoucity or non-crystallinity of the deposited films was confirmed by the absence of crystallization peaks in the XRD pattern as shown in Fig. 1a.

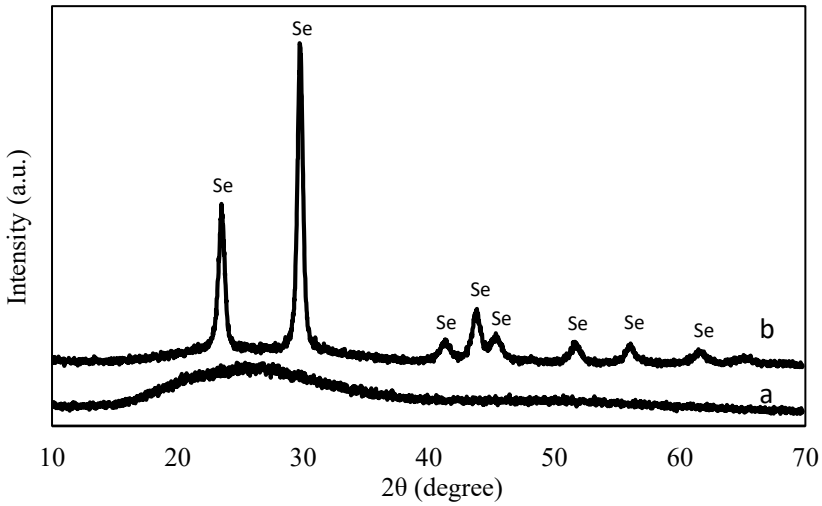

Fig. 1. XRD patterns of selenium films: a – as deposited, b – as annealed.
The peaks were identified as Se – hexagonal selenium (JCPDS: 73-0465).

XRD patterns do not exhibit any difference among all deposited Se films with different deposition time, i.e. all obtained films were amorphous. Lastly, samples were annealed in an inert (nitrogen) atmosphere at 100 °C for 24 h. This process promotes the appearance of hexagonal selenium (JCPDS card No 73-0465) peaks (Fig. 1b). The peaks at 2Θ = 23.5, 29.7, 40.9, 43.8, 45.3, 51.6, 56.3 and 61.3° of selenium phase are found in all samples. This indicates that amorphous elemental selenium has changed to crystal phase.

[1] A.M. Patil, A.C. Lokhande, N.R. Chodankar et al., Electrochemical supercapacitor properties of highly porous sponge-like selenium thin films, International Journal of Hydrogen Energy **41**, 17453-17461 (2016).
[2] A.M. Patil, V.S. Kumbhar, N.R. Chodankar et al., Electrochemical behavior of chemically synthesized selenium thin film, Journal of Colloid and Interface Science **469**, 257-262 (2016).
[3] A.A. Joraid, A.A. Abu-Sehly, S.N. Alamri, Isoconversional kinetic analysis of the crystallization phases of amorphous selenium thin films, Thin Solid Films **517**, 6137-6141 (2009).
[4] J. Sukyte, A. Ivanauskas, I. Ancutiene, Comparative study of selenopolythionic acids H2SenS2O6 as precursors for formation of chalcogenides layers, Chalcogenide Letters **12**, 569-578 (2015).

SYNTHESIS OF 2,3,5-TRISUBSTITUTED-THIOPHENE DERIVATIVES

Mantas Jonušis, Indrė Misiūnaitė, Girius Kisielius, Ieva Karpavičienė, Inga Čikotienė*

Faculty of Chemistry and Geosciences, Vilnius University, Naugarduko 24, Vilnius, LT-03225
mantas.jonusis@chf.vu.lt

Thiophenes are prominent and well-studied π-electron systems in organic chemistry. Our group have synthesized series of substituted thiophenes from 1,3-diarylprop-2-yn-1-ones and corresponding thiols (Fiesselmann thiophene synthesis [1]) or thioureas [2] (Fig. 1).

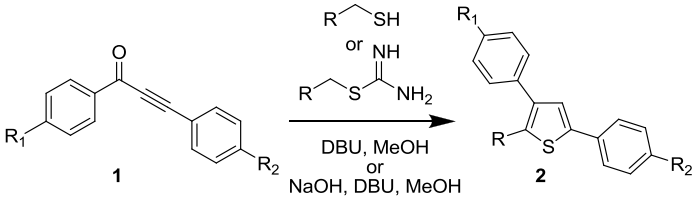

Fig. 1. Synthesis of 3,5-diaryl-2-substituted thiophenes.

Furthermore by establishing known chemical transformations from thiophenes **2** we have derived series of 3,5-diaryl-2-substituted thiophenes containing double C=C bond in 2nd position of thiophene ring (Fig. 2).

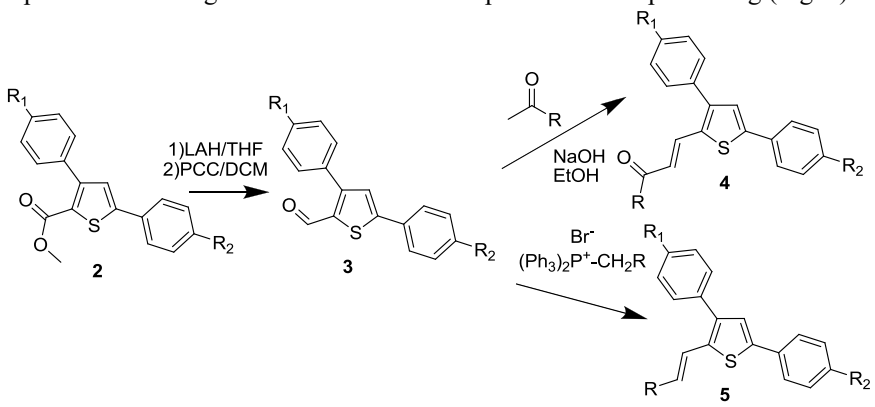

Fig. 1. Modification of thiophenes **2** to **4**; **5**.

All of the synthesized compounds were characterized by spectral analysis. Data table with yields of the reactions is listed below (Table. 1).

Compound	R	R1	R2	Yield (%)
1	n/a	H	H	89
1	n/a	OMe	OMe	75
2	COOMe	OMe	Cl	76
2	COOMe	Cl	OMe	77
2	COOMe	H	H	69/78
2	COOMe	OMe	OMe	71/84
2	2-Benzimidazoyl	OMe	OMe	19/31
2	2-Benzimidazoyl	CF_3	CF_3	26
2	2-Benzimidazoyl	CF_3	OMe	7
2	2-Benzimidazoyl	O*n*Pent	O*n*Pent	72
2	4-Py	OMe	OMe	77
3	n/a	Cl	OMe	60

Compound	R	R1	R2	Yield (%)
3	n/a	OMe	OMe	55
4	4-MeOPh	OMe	Cl	78
4	3-Py	OMe	Cl	54
4	4-*n*BuPh	OMe	Cl	70
4	4-CNPh	OMe	Cl	78
4	4-CNPh	OMe	OMe	86
4	4-CNPh	H	H	87
4	OMe	OMe	OMe	77
4	3-Py	OMe	OMe	90
4	4-BrPh	OMe	OMe	90
4	4-ClPh	OMe	OMe	84
5	Ph	OMe	Cl	42

Table. 1. Yields of the reactions.

This research is funded by the European Social Fund under the No 09.3.3-LMT-K-712 "Development of Competences of Scientists, other Researchers and Students through Practical Research Activities" measure.

2014–2020 metų Europos Sąjungos fondų investicijų veiksmų programa

[1] J. J. Li, Name Reactions: A Collection of Detailed Mechanisms and Synthetic Applications, Springer, Switzerland, 2014, **250**
[2] K. Tamas, J. Jozsef, O. Erzsebet, H. Kalman, Synthetic Communications, 2003, 33(9), **1433-1442**

ECOLOGICAL WATER QUALITY ASSESSMENT OF LITHUANIAN LAKES USING REMOTE SENSING

Dalia Grendaitė[1], Edvinas Stonevičius[1], Jūratė Karosienė[2], Ksenija Savadova[2], Jūratė Kasperovičienė[2]

[1]Hydrology and Climatology Department, Vilnius University, M. K. Čiurlionio str. 21/27, Vilnius, LT-03101, Lithuania
[2]Nature Research Center, Akademijos str. 2, Vilnius, LT-08412, Lithuania
dalia.grendaite@gmail.com

Inland waters are an important habitat for flora and fauna and are also used for aesthetic, recreational, and industrial needs; therefore, it is important to monitor the current state of these waters and apply measures to improve water quality. *In situ* measurements are limited in space and time and cannot ensure water quality monitoring over large areas, thus, to have an efficient monitoring system that could cover large areas, the use of remote sensing data is crucial.

In this study the suitability of the Sentinel 2 Multispectral Imager (MSI) sensor data (satellite measures the reflectance - the relationship between the energy reflected by a surface and the energy incident upon the surface) is being tested for observation of cyanobacteria blooms in lakes and retrieving the chlorophyll-a concentration - an indicator of phytoplankton biomass for estimation of the trophic state of the lake.

The analysis was carried out for four lakes in Lithuania - two eutrophic lakes suffering from recurrent blooms of toxic cyanobacteria and two oligo-mesotrophic non-blooming lakes. The *in situ* chlorophyll-a concentration and six satellite images were used in this study. Seven algorithms for chlorophyll-a concentration retrieval were found in the literature [1, 2, 3].

The lakes appear in different colours in satellite images due to different amounts of phytoplankton and other optically active constituents in the water. Lakes Jieznas and Širvys appear green due to intense chlorophyll-a absorption at the red and blue wavelengths and reflection at the green wavelengths whereas oligo-mesotrophic lakes with low phytoplankton biomass appear almost black as almost all energy is absorbed (Fig. 1). Thus, reflectances are higher in the eutrophic blooming lakes than in non-blooming oligo-mesotrphic lakes due to the presence of chlorophyll-a - a predictor of phytoplankton biomass, that is used as a quick and easy-to-measure surrogate of phytoplankton biomass. The tested algorithms for chlorophyll-a concentration retrieval give errors that are too high (root mean squared error $\geqslant 17\ \mu g\ L^{-1}$) for the methods to be widely used (the chronological graph of chlorophyll-a concentrations is found in Fig. 2). Therefore, a larger *in situ* dataset for algorithm validation is needed.

Fig. 1. Natural Colours Red-Green-Blue (RGB) composite of the lakes studied on the 4th August 2015, from left to right - eutrophic lakes: Jieznas, Širvys, oligo-mesotrophic lakes: Guostus, Šventas

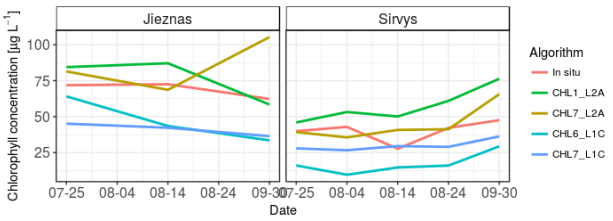

Fig. 2. The *in situ* (red) and four best performing algorithms' chlorophyll-a concentration data (L2A indicates atmospherically corrected data and L1C - the data without atmospheric correction)

The first attempts to map chlorophyll-a concentration in Lithuanian lakes using the data received from the Sentinel 2 MSI sensor show promising results as the changes in reflectance, caused by the changes in chlorophyll-a concentration, can be identified from satellite images. These results suggest that the Sentinel-2 MSI data can be used for monitoring the water quality of the lakes of Lithuania.

[1] W. J. Moses, A. A. Gitelson, S. Berdnikov, V. Povazhnyy. Satellite estimation of chlorophyll-*a* concentration using the red and NIR bands of MERIS—The Azov sea case study. *IEEE Geoscience and Remote Sensing Letters* 6, 845–849 (2009)

[2] M. W. Matthews, S. Bernard, L. Robertson. An algorithm for detecting trophic status (chlorophyll-a), cyanobacterial-dominance, surface scums and floating vegetation in inland and coastal waters. *Remote Sensing of Environment*, 124, 637–652 (2012)

[3] K. Toming, T. Kutser, A. Laas, M. Sepp, B. Paavel, T. Nõges. First experiences in mapping lake water quality parameters with Sentinel-2 MSI imagery. *Remote Sensing*, 8, 640 (2016)